

UNIVERSITÀ
DEGLI STUDI
DI PADOVA

Head Office: Università degli Studi di Padova

Department of Chemical Sciences

Ph.D. COURSE IN: MOLECULAR SCIENCES
CURRICULUM: CHEMICAL SCIENCES
SERIES 37° CYCLE

SYNTHESIS AND PHOTOPHYSICAL CHARACTERIZATION OF NOVEL ELECTROCHEMILUMINESCENT DYES

Thesis written with the financial contribution of European Research Council (ERC) under the European Union's Horizon 2020 research and innovation programme (grant agreement No 949087. ERC Starting Grants 2020", Research Project - BioPoweredCL - "Bright and biologically powered chemiluminescent labels for cell and tissue imaging"

Coordinator: Prof. Stefano Corni
Supervisor: Prof. Alessandro Aliprandi

Ph.D. student : Giulio Pavan

Summary

ABSTRACT OF THE THESIS 1
1. INTRODUCTION 3
1.1 Electrochemiluminescence: energetics and mechanisms 4
1.1.1 ECL mechanisms 4
1.2 ECL emitters 9
1.2.1 Fluorescent emitters 10
1.2.1.1 Polycylic Aromatic Hydrocarbons 10
1.2.1.2 Perylene derivatives 11
1.2.1.3 Fluorene and spirobifluorene derivatives 12
1.2.1.4 BODIPY derivatives 13
1.2.1.5 Coumarin derivatives 16
1.2.2 Phosphorescent emitters 18
1.2.3 Thermally Activated Delayed Fluorescence emitters 21
1.3 Electrochemiluminescence and Electroluminescence emitters: similarities and differences 24
1.4 Scope of the project 27
2. NOVEL IMIDAZOLE-BASED TADF DYES AS ELECTROCHEMILUMINESCENT EMITTERS 29
2.1 Introduction 30
2.2 Results and discussions 31
2.2.1 Synthesis 31
2.2.2 Crystallographic characterization 35
2.2.3 Electrochemical characterization 36
2.2.4 Photophysical characterization 38
2.2.5 Electrochemiluminescence characterization 43
2.2.6 Photophysical and electrochemiluminescence characterization of TADF emitters in aqueous solution 46
2.3 Conclusions 49
2.4 Experimental section 50
2.4.1 Photophysical measurements 50
2.4.2 Electrochemical and electrochemiluminescence measurements 51
2.4.4 XRD analysis – Structural characterization 52
2.4.5 Synthesis route and procedures 53
2.4.5.1 Synthesis of 2,4,6-tris(diphenylamino)-5-fluoroisophthalonitrile (**3DPAFIPN**) 53

2.4.5.2 Synthesis of 2,4,6-tris(diphenylamino)-3,5-difluorobenzonitrile (**3DPA2FBN**)..... 53

2.4.5.3 Synthesis of 2,4,6-tris(diphenylamino)-5-(1H-imidazol-1-yl)isophthalonitrile (**3DPAImIPN**) 53

2.4.5.4 Synthesis of 2,4,6-tris(diphenylamino)-3,5-di(1H-imidazol-1-yl)benzonitrile (**3DPA2ImBN**)..... 54

2.4.5.5 Synthesis of 1-(3,5-dicyano-2,4,6-tris(diphenylamino)phenyl)-3-(2-(2-(2-methoxyethoxy)ethoxy)ethyl)-1H-imidazol-3-ium 4-methylbenzenesulfonate (**[3DPAImIPNTEG]OTs**) 55

2.4.5.6 Synthesis of 1,1'-(5-cyano-2,4,6-tris(diphenylamino)-1,3-phenylene)bis(3-(2-(2-(2-methoxyethoxy)ethoxy)ethyl)-1H-imidazol-3-ium) bis(4-methylbenzenesulfonate) (**[3DPA2ImBN2TEG]2(OTs)**)..... 55

3. NOVEL MONOIMIDAZOLE TADF DYES AS ELECTROCHEMILUMINESCENT EMITTERS 57

3.1 Introduction..... 58

3.2 Results and discussion 59

3.2.1 Synthesis 59

3.2.2 Crystallographic characterization 62

3.2.3 Electrochemical characterization 63

3.2.4 Photophysical characterization 65

3.2.5 Electrochemiluminescence characterization 68

3.3 Conclusions..... 77

3.4 Experimental section..... 78

3.4.1 Photophysical measurements 78

3.4.2 Electrochemical and electrochemiluminescence measurements..... 78

3.4.3 XRD analysis – Structural characterization 80

3.4.4 Synthesis route and procedures..... 81

3.4.4.1 Synthesis of 2,3,5,6-tetrafluoro-4-(1H-imidazol-1-yl)benzonitrile (**4FBNIm**)..... 81

3.4.4.2 Synthesis of 2,3,5,6-tetrasubstituted-4-(1H-imidazol-1-yl)benzonitrile..... 81

3.4.4.3 Synthesis of 2,3,5,6-(tetracarbazol-9-yl)-4-(1H-imidazol-1-yl)benzonitrile (**4CzBNIm**)..... 82

3.4.4.4 Synthesis of 2,3,5,6-tetrakis(3,6-di-tert-butyl-9H-carbazol-9-yl)-4-(1H-imidazol-1-yl)benzonitrile (**4^{tBu}CzBNIm**) 83

3.4.4.5 Synthesis of 2,3,5,6-tetrakis(3,6-dimethoxy -9H-carbazol-9-yl)-4-(1H-imidazol-1-yl)benzonitrile (**4^{OMe}CzBNIm**)..... 83

3.4.4.6 Synthesis of 2,3,5,6-tetrakis(diphenylamino)-4-(1H-imidazol-1-yl)benzonitrile (**4DPABNIm**)..... 84

3.4.4.7 Synthesis of 2,3,5,6-tetrakis(9,9-dimethylacridin-10(9H)-yl)-4-(1H-imidazol-1-yl)benzonitrile (**4DMACBNIm**)....84
3.4.4.8 Synthesis of tert-butyl 14-(tosyloxy)-3,6,9,12-tetraoxatetradecanoate....85
3.4.4.9 Synthesis of 1-(4-cyano-2,3,5,6-tetrakis(diphenylamino)phenyl)-3-(16,16-dimethyl-14-oxo-3,6,9,12,15-pentaoxaheptadecyl)-1H-imidazol-3-ium 4-methylbenzensulfonate (**[4DPABNImTEGCOOtBu]OTs)**....86
4 THE EFFECT OF π-EXTENSION OF THE IMIDAZOLE MOIETY....87
4.1 Introduction....88
4.2 Results and discussion....89
4.2.1 Synthesis....89
4.2.2 Crystallographic characterization....92
4.2.3 Electrochemical characterization....94
4.2.4 Photophysical characterization....95
4.2.5 Electrochemiluminescence characterization....98
4.3 Conclusion....102
4.4 Experimental Section....103
4.4.1 Photophysical measurements....103
4.4.2 Electrochemical and electrochemiluminescence measurements....103
4.4.3 XRD analysis – Structural characterization....103
4.4.4 Synthesis route and procedure....104
4.4.4.1 Synthesis of 2,3,5,6-tetrafluoro-4-(1H-benzo[d]imidazol-1-yl)benzonitrile (**4FBNBenzIm**)....104
4.4.4.2 Synthesis of 2,3,5,6-tetrafluoro-4-(1H-phenanthro[9,10-d]imidazol-1-yl)benzonitrile (**4FBNPhenIm**)....105
4.4.4.3 Synthesis of **4^{tBu}CzBNBenzIm**, **4^{tBu}CzBNPhenIm**, **4DPABNBenzIm** and **4DPABNPhenIm**....105
4.4.4.4 Synthesis of 2,3,5,6-(tetracarbazol-9-yl)-4-(1H-benzo[d]imidazol-1-yl)benzonitrile 106
(**4tBuCzBNBenzIm**)....106
4.4.4.5 Synthesis of 2,3,5,6-(tetracarbazol-9-yl)-4-(1H-phenanthro[9,10-d]imidazol-1-yl)benzonitrile (**4^{tBu}CzBNPhenIm**)....107
4.4.4.6Synthesis of 2,3,5,6-tetrakis(diphenylamino)-4-(1H-benzo[d]imidazol-1-yl)benzonitrile (**4DPABNBenzIm**)....108
4.4.4.7 Synthesis of 2,3,5,6-tetrakis(diphenylamino)-4-(1H-phenanthro[9,10-d]imidazol-1-yl)benzonitrile (**4DPABNPhenIm**)....108
5 TAILORING ACCEPTOR ELECTROCHEMISTRY FOR OXIDATIVE-REDUCTION ECL..109

5.1 Introduction 110
5.2 Result and discussion 111
5.2.1 Synthesis 111
5.2.2 Crystallographic characterization 112
5.2.3 Electrochemical characterization 112
5.2.4 Photophysical characterization 113
5.2.5 Electrochemiluminescence characterization 115
5.2.6 Photophysical and electrochemiluminescence characterization of TADF emitter in water solution 117
5.3 Conclusion 119
5.4 Experimental section 120
5.4.1 Photophysical measurements 120
5.4.2 Electrochemical and electrochemiluminescence measurements 120
5.4.3 XRD analysis – Structural characterization 121
5.4.4 Synthesis route and procedures 122
5.4.4.1 Synthesis of 2,3,5,6-tetrasubstituted-terephthalonitrile derivatives 122
5.4.4.2 Synthesis of 2,3,5,6-diphenyl-amine-terephthalonitrile (**4DPATPN**) 122
5.4.4.3 Synthesis of 2,3,5,6-di-p-tolyl-amine-terephthalonitrile (**4DpTATPN**) 123
5.4.4.4 Synthesis of 2,3,5,6-di-tert-butyl-carbazole-terephthalonitrile (**4^{tBu}CzTPN**) 123
5.4.4.5 Synthesis of 2,3,5,6- diphenilamine-4-sulfonate-terephthalonitrile (**Na_4[4DPASO_3TPN]**) 123
6 NEUTRAL AND CATIONIC TADF DYES IN LIGHT-EMITTING ELECTROCHEMICAL CELLS 125
6.1 Introduction 126
6.2 Synthesis 128
6.3 Electrochemical characterization 129
6.4 Photophysical Characterization in solution state and in powder 130
6.5 Single-Guest LECs 131
6.6 Host-Guest LECs 136
6.7 Conclusion 140
6.8 Experimental Section 141
6.8.1 Electrochemical measurements 141
6.8.2 Photophysical measurements 141
6.8.3 Preparation and characterization of devices 142

6.8.4 Synthesis route and procedures 143
6.8.4.1 Synthesis of 1-(3-(3-(tert-butyl)-9H-carbazol-9-yl)-4-cyano-2,5,6-tris(3,6-di-tert-butyl-9H-carbazol-9-yl)phenyl)-3-dodecyl-1H-imidazol-3-ium iodide (**[4^{tBu}CzBNImC12]I**) 143
6.8.4.2 Synthesis of 1-(4-cyano-2,3,5,6-tetrakis(diphenylamino)phenyl)-3-dodecyl-1H-imidazol-3-ium iodide (**[4DPABNImC12]I**) 144
6.8.4.3 Synthesis of 1-(3-(3-(tert-butyl)-9H-carbazol-9-yl)-4-cyano-2,5,6-tris(3,6-di-tert-butyl-9H-carbazol-9-yl)phenyl)-3-dodecyl-1H-imidazol-3-ium hexafluorophosphate (**[4^{tBu}CzBNImC12]PF$_6$**) 144
6.8.4.4 Synthesis of 1-(4-cyano-3-(cyclohexa-1,4-dien-1-yl(phenyl)amino)-2,5,6-tris(diphenylamino)phenyl)-3-dodecyl-1H-imidazol-3-iumhexafluorophosphate (**[4DPABNImC12]PF$_6$**) 145
7. CONCLUSIONS AND PERSPECTIVES 146
8. BIBLIOGRAPHIC REFERENCES 148
9. APPENDIX 159
Chapter 2 159
2.1 XRD analysis – Structural characterization 159
2.2 ^{1}H NMR Spectra 160
2.3 ^{13}C{^{1}H} NMR Spectra 163
2.4 Absorption-excitation spectra comparisons 165
2.5 Luminescence decay curves 166
2.6 Annihilation ECL-time and current-time profiles 171
Chapter 3 172
3.1 XRD analysis – Structural characterization 172
3.2 ^{1}H NMR and ^{19}F{^{1}H} Spectra 178
3.3 ^{13}C{^{1}H} NMR Spectra 183
3.4 Absorption-excitation spectra comparisons 187
3.5 Luminescence decay curves 189
3.6 Electrochemical characterization 195
3.7 ECL-voltage curves 198
3.8 PL – reductive-oxidation ECL spectra comparisons 200
3.9 PL – oxidative-reduction ECL spectra comparisons 202
3.10 Annihilation ECL-time and current-time profiles 203
3.11 Reductive-oxidation ECL-time and current-time profiles 203
3.12 Oxidative-reduction ECL-time and current-time profiles 205

Chapter 4 206
4.1 XRD analysis – Structural characterization 206
4.2 ^{1}H NMR and ^{19}F{^{1}H} Spectra 208
4.3 ^{13}C{^{1}H} Spectra 212
4.4 Absorption-excitation spectra comparisons 215
4.5 Luminescent decays curves 216
4.6 Electrochemical characterization 220
4.7 ECL-voltage curves 224
4.8 PL – reductive-oxidation ECL spectra comparisons 225
4.9 PL – oxidative-reduction ECL spectra comparisons 227
4.10 Annihilation ECL-time and current-time profiles 228
4.11 Reductive-oxidation ECL-time and current-time profiles 229
4.12 Oxidative-reduction ECL-time and current-time profiles 231
Chapter 5 231
5.1 Single crystal X-ray diffraction analysis 231
5.2 ^{1}H NMR Spectra 233
5.3 ^{13}C{^{1}H} NMR Spectra 235
5.4 Absorption-excitation spectra comparisons 235
5.5 Luminescent decays curves 237
5.6 Electrochemical characterization 239
5.7 PL – oxidative-reduction ECL spectra comparisons 241
5.8 Annihilation ECL-time and current-time profiles 242
5.9 Oxidative-reduction ECL-time and current-time profiles 243
Chapter 6 245
6.1 ^{1}H NMR Spectra 245
6.2 ^{13}C{^{1}H} NMR Spectra 246
6.3 ^{31}P NMR Spectra 247
6.4 ^{19}F NMR Spectra 248
6.5 Absorption-excitation spectra (solution) comparisons 249
6.6 Luminescence decay curves (solution) 249
6.7 Electrochemical and EIS characterization 250
6.8 Emission spectra (Single-Guest thin film) 253
6.9 Excitation spectra (Single-Guest thin film) 254
6.10 Luminescence decay curves (Single-Guest thin film) 256

6.11 Time-dependent Luminance-Intensity-Voltage (Single-Guest thin film).....257
6.12 Time-dependent average voltage and luminance profiles with pulsed current (Single-Guest LECs).....260
6.13 Emission spectra (Host-Guest thin film).....263
6.14 Excitation spectra (Host-Guest thin film).....265
6.15 Luminescence decay curves (Host-Guest thin film).....267
6.16 Time-dependent average voltage and luminance profiles with pulsed current (Host-Guest LECs).....269
Acknowledgments.....271

ABSTRACT OF THE THESIS

Electrogenerated chemiluminescence, or electrochemiluminescence (ECL), represents one of the most powerful analytical techniques available nowadays for biomedical applications. This is due to several factors, including the nearly absent background signal, high sensitivity, large range of linearity and high spatial and temporal control. As ECL is an electron-hole recombination process, only phosphorescent or Thermally Activated Delayed Fluorescence (TADF) emitters can be used efficiently as they harvest triplet excitons.

Purely-organic TADF compounds have been demonstrated to be efficient ECL emitters, offering a cost-effective alternative to expensive phosphorescent heavy metal complexes, which are currently being incorporated into ECL devices and tools.

Nevertheless, TADF compounds exhibit limited water solubility and bioconjugability, thus preventing their practical application in ECL.

However, TADF compounds exhibit limited water solubility and bioconjugability, which hinders their practical deployment in ECL.

This thesis presents the synthesis of novel TADF luminophores and their photophysical and electrochemical characterization, as well as their ECL properties. This is done in order to establish correlations between these properties and to develop a methodology for the design of suitable TADF emitters for ECL applications.

Furthermore, the first instances of water-soluble discrete TADF emitters are presented, along with their photophysical and ECL characterization in aqueous media.

Finally, the compounds with the highest ECL efficiency will be investigated in Light-Emitting Electrochemical Cells, to ascertain whether a relationship exists between ECL and LEC efficiencies.

RIASSUNTO DELLA TESI

La chemiluminescenza elettrogenerata, o elettrochemiluminescenza (ECL), è una delle più potenti tecniche analitiche disponibili al giorno d'oggi nel campo biomedico.

Infatti, questa tecnica possiede svariati vantaggi, tra cui un basso segnale di rumore, un'elevata sensibilità, un ampio intervallo di linearità e un elevato controllo spazio-temporale.

Dal momento che l'ECL è un processo di ricombinazione di tipo elettrone-valenza, possono essere usati efficacemente solo emettitori che permettono di "catturare" gli eccitoni di tripletto, ovvero composti fosforescenti o dotati della cosiddetta "fluorescenza ritardata attivata termicamente" (in inglese TADF, Thermally Activated Delayed Fluorescence).

L'efficacia dei composti aventi proprietà TADF in elettrochemiluminescenza è stata già dimostrata, rendendo questi composti un'alternativa economica rispetto ai costosi complessi metallici fosforescenti attualmente incorporati in tutti i sensori e dispositivi basati sull'ECL.

Tuttavia, i composti TADF possiedono due svantaggi che impediscono la loro applicazione commerciale nei dispositivi ad ECL: infatti, essi non sono idrosolubili ne possiedono porzioni a cui legare gruppi bioconiugabili.

In questa tesi vengono presentati e discussi la sintesi e la caratterizzazione (sia fotofisica che elettrochimica) di differenti composti dotati di proprietà TADF. Inoltre, questi composti vengono studiati come emettitori in elettrochemiluminescenza, con l'intento di stabilire una correlazione tra le proprietà elettrochimiche e fotofisiche e le proprietà elettrochemiluminescenti. Questa indagine viene effettuata per comprendere come sviluppare un emettitore avente proprietà TADF che possa essere efficace in elettrochemiluminescenza.

Infine, vengono mostrati i primi esempi di emettitori idrosolubili e dotati di proprietà TADF e le loro caratterizzazioni in ambiente acquoso.

Infine, i composti con le efficienze ECL più elevate saranno impiegati nelle cosiddette celle elettrochimiche emettitrici di luce.

1. INTRODUCTION

Chiara Alberoni*, Giulio Pavan*, Thomas Scattolin, Alessandro Aliprandi (*these authors contributed equally). *ChemPlusChem*, 2024, **89**(8), e202400142
https://doi.org/10.1002/cplu.202400142

1.1 Electrochemiluminescence: energetics and mechanisms

Electrochemiluminescence, or electrogenerated chemiluminescence (ECL), is a process where reactive radical species formed at an electrode surface undergo electron transfer processes to generate excited species that radiatively relax to the ground state[1,2].

The earliest known reports of electrochemiluminescence can be traced back approximately a century, when the emission of light from metal anodes during the electrolysis of compounds such as aminophthalichydrazide was observed[3,4].

Nevertheless, the theorical framework of electrochemiluminescence was only established four decades later, in the mid-1960s, by Hercules, Bard and Marcus[5–7].

From this point onwards, ECL gained a growing interest since it is one of the most powerful analytical techniques available in fields such as biomarkers, (bio)sensors, environmental analysis, imaging and immunoassays[8–12].

A particular type of ECL-based immunoassays is the one based on the combination of magnetic microbeads and ECL luminophore, which enable the immobilization of the immunoassays on an electrode. This combination represents a milestone in the field of biomedical analysis, and it is now widely used in biomedical and industrial applications.

This is due to its high signal-to-noise ratio, large range of linearity, and low Limit of Detections due to a nearly absent background signal[13,14].

1.1.1 ECL mechanisms

As previously stated, the principal process in electrochemiluminescence is the exergonic electronic transfer between two radical species (namely $A^{\cdot+}$ and $B^{\cdot-}$).

The Gibbs energy of this annihilation reaction can be calculated from the redox potentials of parent compounds A and B using the following equation (**Equation 1.1**)[15]:

$$\Delta G° = F(E^0_{red} - E^0_{ox}) - w_R + w_P \quad \textbf{(1.1)}$$

where F represents the Faraday constant, E^0_{red} and E^0_{ox} are the redox potentials of parent compounds, w_R and w_P are work terms, which are corrective factors.

Substituting the values obtained from the aforementioned equation and the definition of the variation of Gibbs free energy, the enthalpy of the reaction ($\Delta H°$) can be expressed as following (**Equation 1.2**)[1,2]:

$$-\Delta H^0 = -F(E^0_{ox} - E^0_{red} + T\Delta S^0) \quad \textbf{(1.2)}$$

The term $T\Delta S$ at 25 °C can be approximated to 0.1 eV and the preceding equation can be rearranged as following (**Equation 1.3**):

$$-\Delta H^0 = E^0_{ox} - E^0_{red} - 0.1\ eV \quad \textbf{(1.3)}$$

This term is one of the most important parameters during an ECL reaction because the energy levels are quantized, and the electronic transfer must deliver in one step the appropriate amount of energy to generate the excited species.

By comparing the term $-\Delta H^0$ with the energy required to populate the lowest-lying excited singlet state ($E_S = 1239.81/\lambda$, where λ is the emission wavelength in nm), three different "routes" to populate excited species can be found: E-route, S-route or T-route.

In the first case, $A^{\cdot+}$ and $B^{\cdot-}$ generate the activated complex $(A^{\cdot+}\cdots B^{\cdot-})^*$ that is formed in two distinct states, $^1(A^{\cdot+}\cdots B^{\cdot-})^*$ and $^3(A^{\cdot+}\cdots B^{\cdot-})^*$ in a 1:3 statistical ratio.

This ratio is caused by the fact that electrochemiluminescence, as chemiluminescence and electroluminescence, is an electron-hole recombination process[16,17].

If the emission comes only from the transition S_1-S_0, only the exciplex $^1(A^{\cdot+}\cdots B^{\cdot-})^*$ will decay radiatively.

In contrast, the exciplex $^3(A^{\cdot+}\cdots B^{\cdot-})$ cannot decay radiatively as this transition is spin-forbidden, so it can undergo two processes: it can dissociate in the bulk or upconvert to $^1(A^{\cdot+}\cdots B^{\cdot-})$ *via* "triplet-triplet annihilation" (TTA, **Equation 1.4**), with a resulting emission intensity is weaker than the direct emission from singlet state due to higher non-radiative decays.

$$^3(A^{\cdot+}\cdots B^{\cdot-})^* + {}^3(A^{\cdot+}\cdots B^{\cdot-})^* \rightarrow {}^1(A^{\cdot+}\cdots B^{\cdot-})^* + A + B \quad \textbf{(1.4)}$$

$$^1(A^{\cdot+}\cdots B^{\cdot-})^* \rightarrow A + B + h\nu \quad \textbf{(1.5)}$$

The E-route can be found with different fluorescent ECL emitters, and it is concentration-dependent. Moreover, it can be easily identified since the emission is very broad, featureless and typically red-shifted respect to the photoluminescent emission.

In the S-route, the term $-\Delta H^0$ is higher than E_S and the system is called "energy-sufficient" as both singlet and triplet excited states are populated after the electron transfer reaction (**Equations 1.6a-1.6b**):

$$A^{\cdot+} + B^{\cdot-} \rightarrow {}^1A^* + B \quad E_S(A) < E_S(B) \quad \textbf{(1.6a)}$$

$$A^{\cdot+} + B^{\cdot-} \rightarrow {}^1B^* + A \quad E_S(A) > E_S(B) \quad \textbf{(1.6b)}$$

Furthermore, when fluorescent compounds are employed as ECL emitters, emission comes from S_1-S_0 transition, while when phosphorescent emitters are used, emission comes from T_1-S_0 transition (**Equations 1.7a-1.7b**).

$$^1A^* \rightarrow A + h\nu \quad \textbf{(1.7a)}$$

$$^3A^* \rightarrow A + h\nu \quad \textbf{(1.7b)}$$

Conversely, when the term $-\Delta H^0$ is lower than E_s but higher than the energy of the lowest-lying triplet state (E_T) the system is called "energy-deficient" and only triplet states can be directly populated.

These processes follow the so-called T-route (**Equation 1.8a-1.9b**):

$$A^{\cdot+} + B^{\cdot-} \rightarrow {}^3A + B \quad E_T(A) < E_T(B) \qquad \textbf{(1.8a)}$$

$$A^{\cdot+} + B^{\cdot-} \rightarrow {}^3B + A \quad E_T(A) > E_T(B) \qquad \textbf{(1.8b)}$$

$$2\,{}^3A \rightarrow {}^1A^* + A \rightarrow 2A + h\nu_A \qquad \textbf{(1.9a)}$$

$$2\,{}^3B \rightarrow {}^1B^* + B \rightarrow 2B + h\nu_B \qquad \textbf{(1.9b)}$$

T-route ECL is followed by many Polycyclic Aromatic Hydrocarbons, that undergo TTA to generate an excited singlet state.

As just stated, the electron transfer reactions generate excited states rather than ground states and this is because these electronic transfer reactions lie in the inverted Marcus region[7], where the generation of excited states (kinetical products) is faster than the generation of the ground states (thermodynamical products)[18].

The aforementioned E-route, S-route and T-route elucidate the processes through which excited states are populated, while the generation of these excited states can occur in two different ways, named "annihilation ECL" and "co-reactant ECL".

In annihilation ECL the electrode potential is stepped between two voltages to sequentially generate oxidized and reduced forms of a parent molecule that then interact between each other thus generating excited states (**Figure 1.1**) that then decay with the emission of light.

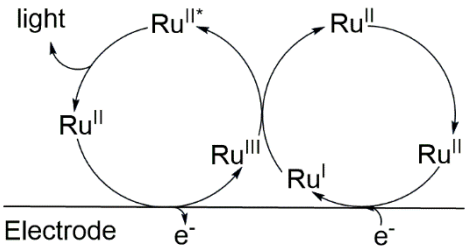


Figure 1.1: Annihilation ECL pathway.

Annihilation ECL was the first method used for investigating electrochemiluminescence[5,19] because of its simplicity (only dye, solvent and supporting electrolyte are required) and nowadays is used very frequently to unravel the stability of both radical cations and anions.

Nevertheless, it comes also with a limitation, as annihilation reactions are very energetic.

Indeed, since the emission is in the visible region (400-700 nm), E_s lies between 2 and 3 eV meaning that the potential window of the solvent must be sufficiently large to allow the generation of the radicals, thereby excluding aqueous solutions as media and preventing analytical application of this technique.

However, by the addition of certain reagents, called co-reactants, to the solution it is possible to generate an ECL signal with the application of a single, fixed potential (both positive or negative).
This is the "co-reactant ECL"[20–23].
A co-reactant is a sacrificial reagent that is present in the solution in heavy excess respect to the luminophore.
This compound generates, upon oxidation or reduction, a reactive intermediate than decomposes into a strong oxidizing or reducing agent which in turn reacts with the reduced or oxidized form of the luminophore yielding its excited state.
This method has two significant advantages over the annihilation method.
Firstly, aqueous solutions can be used as media, as the required potential window is narrower than that required for annihilation ECL[24].
Secondly, it is possible to observe emission from luminophores that undergo only reversible electroreduction or electrooxidation.
It is possible to subdivide co-reactant ECL into two additional mechanisms: "reductive-oxidation ECL" and "oxidative-reduction ECL"[1].
In the reductive-oxidation mechanism co-reactants such as hydrazine, persulfate anion, benzoyl peroxide and hydrogen peroxide are used and this mechanism is very useful for luminophores that possess reversible reduction processes and irreversible oxidation processes
Indeed, a negative potential is applied and radical-anions of both luminophore and co-reactant are formed and, if benzoyl peroxide (BPO) is used as co-reactant, the resulting BPO radical-anion decomposes to generate a benzoyl radical, a highly oxidizing species that extracts an electron from the HOMO of the radical-anion of the luminophore to generate the excited species (**Figure 1.2-left**).
The aforementioned mechanism is the so-called classical reductive-oxidation ECL mechanism.
Along with this mechanism, there is also an "annihilation route" mechanism where the benzoyl radical oxidizes the luminophore, generating a radical-cation that undergo an annihilation reaction with the radical-anion (**Figure 1.2-right**).

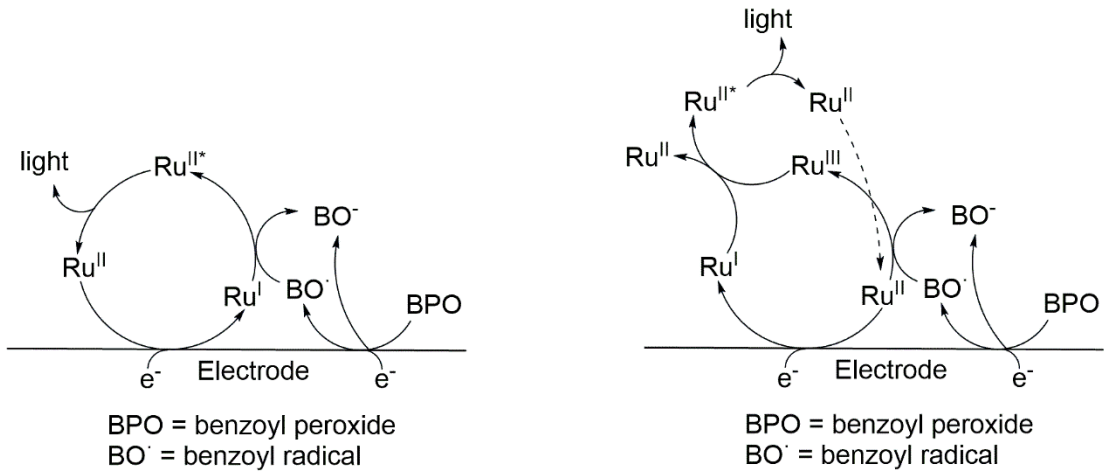


Figure 1.2: Classical "reductive-oxidation" ECL mechanism (left) and "annihilation-route" reductive-oxidation ECL (right).

Conversely to reductive-oxidation mechanism, the oxidative-reduction mechanism is used with luminophores that have stable radical-cations and different co-reactants such as tertiary amines, Ce(III)/pyruvate or oxalate, are used.

In the oxidative-reduction mechanism a positive potential is applied, and radical-cations of luminophore and co-reactant are formed.

If tripropylamine is used as co-reactant, the reactive intermediate is the tripropylamino radical ($TPA^{\cdot}$), a highly reducing species that inject an electron in the LUMO of the luminophore radical-cation to generate the excited species (**Figure 1.3-left**).

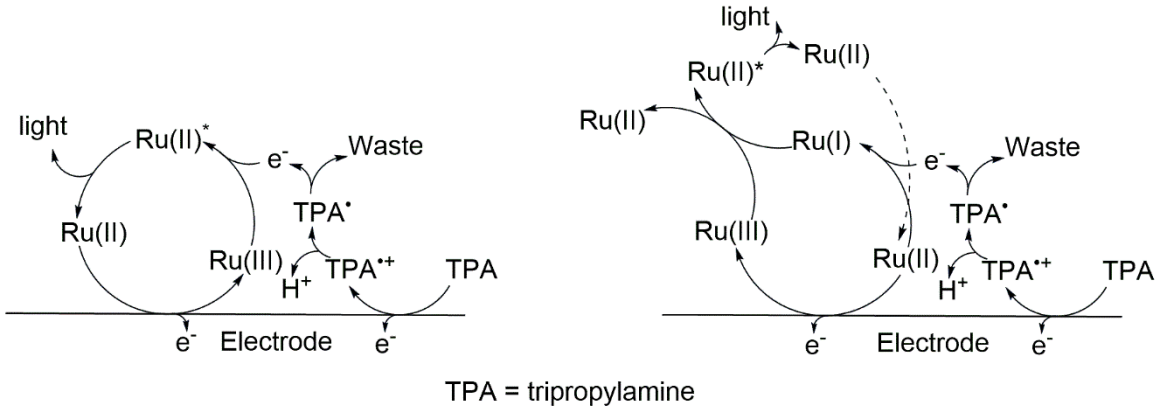


Figure 1.3: Classical "oxidative-reduction" ECL mechanism (left) and "annihilation route" oxidative-reduction ECL (right).

In addition to this "classical" mechanism, there are also the so-called "annihilation route" (**Figure 1.3-right**), the "catalytic route" (**Figure 1.4-left**) and the "remote route" (**Figure 1.4-right**) mechanisms.

Many studies indicate a correlation between these pathways and the applied potential or the concentration ratio between the luminophore and co-reactant[9,25,26].

Indeed, annihilation route can be found along with the classical route when tripropylamine concentration is higher than the luminophore one.

In contrast, the catalytic route is present when the tripropylamine and luminophore concentrations are comparable and the radical-cation of the luminophore promote the oxidation of tripropylamine.
Finally, the remote route can be found at potentials that are insufficient to generate the luminophore radical-cation but enough to generate tripropylamino radical.
The remote route is the typical mechanism of ECL-based sensors, as ECL labels are too much far from electrode surface to be directly oxidized by it.

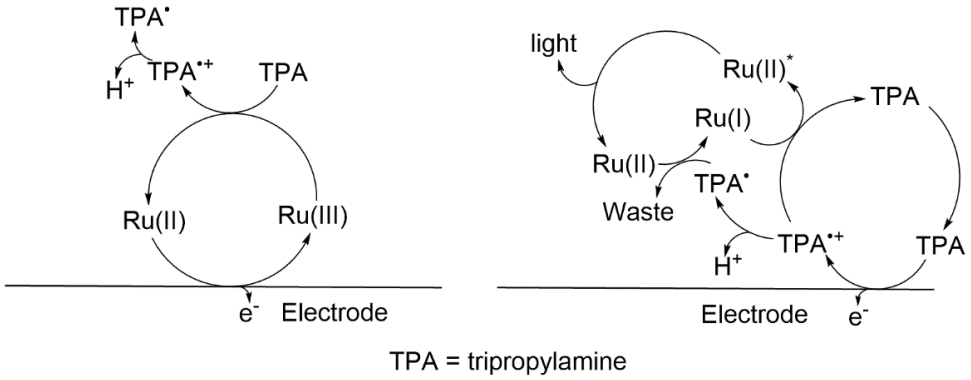


Figure 1.4: "catalytic route" oxidative-reduction ECL (left) and "remote route" oxidative-reduction ECL (right).

To be used as co-reactant, a compound must meet many criteria such as good stability, solubility, suitable electrochemical properties and low quenching towards luminophore emission.
All these criteria can be met in tripropylamine, which is nowadays widely used with $Ru(bpy)_3^{2+}$ in biomedical applications.

1.2 ECL emitters

As previously stated, electrochemiluminescence is an electron-hole recombination process that produces singlet and triplet state in a statistical 1:3 ratio[27], and it is evident that harvesting triplet excitons is of fundamental importance to improve ECL efficiency.
Indeed, many efforts were made during the last 50 years to find highly performing ECL luminophores, also based on the discoveries made in the field of Organic Light Emitting Diodes (OLEDs), that are based on electroluminescence, another electron-hole recombination process.
Based on their composition, ECL luminophore can be divided in discrete luminophores, metallic clusters and nanomaterials-based emitters[8,28–31], with the former class that can be divided into three different classes: fluorescent emitters, phosphorescent emitters and Thermally Activated Delayed Fluorescence (TADF) emitters (**Figure 1.5**).

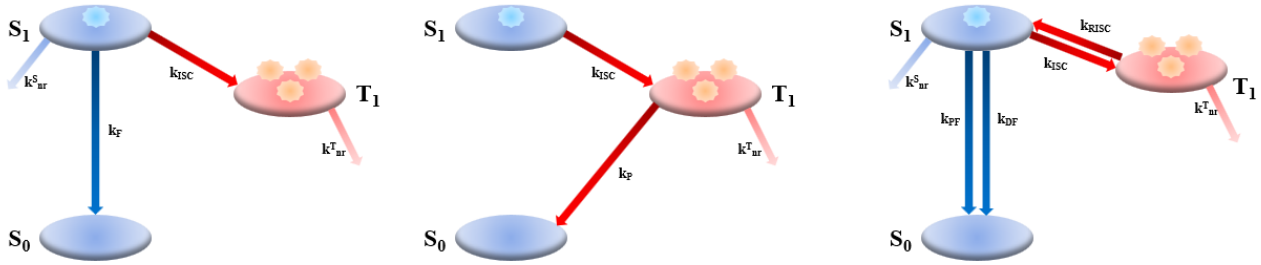


Figure 1.5: Schematic representation of emission mechanism in the fluorescent (left), phosphorescent (center) and TADF (right) emitters. F: fluorescence; P: phosphorescence; PF: prompted fluorescence; DF: delayed fluorescence; ISC: intersystem crossing; nr: non radiative.

1.2.1 Fluorescent emitters

1.2.1.1 Polycylic Aromatic Hydrocarbons

Fluorescent compounds are the first examples of organic dyes applied as electrochemiluminescence emitters owing to their high stability and ease of synthesis.

The first fluorescent dyes studied in ECL were Polycyclic Aromatic Hydrocarbons (PAHs)[5,6] as they form quite stable radicals and possess excited states that can be accessed using the energy released from the annihilation reaction.

Some of these PAHs are reported in **Figure 1.6**.

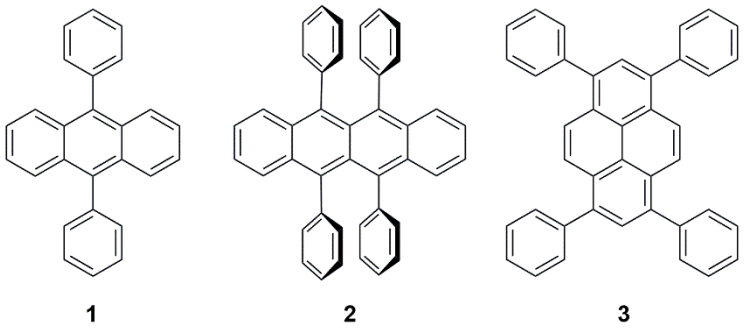


Figure 1.6: From left to right, chemical structures of 9,10-Diphenylanthracene, rubrene and 1,3,6,8-Tetraphenylpyrene.

Among all the PAHs, those that bear substituents (methyl, ethyl or phenyl) on reactive positions exhibit higher ECL efficiencies than their unsubstituted counterparts due to lower collateral reactions. Indeed, the most efficient compound is 9,10-Diphenylanthracene (DPA, **1**) which shows the best absolute ECL efficiency, close to 25%, which is the intrinsic limit for fluorescent systems[32].

This high ECL efficiency is due to the presence of reversible reduction and oxidation processes, a photoluminescent quantum yield (PLQY) approaching unity and because it is an energy-sufficient system.

On contrast, many other PAHs are energy-deficient systems that emits via TTA, which causes low ECL efficiencies.

The outcomes demonstrate that a number of criteria must be met in order to have a good ECL luminophore: high stability of radical-anion and radical-cation (or good electrochemical

reversibility), high PLQYs, an excited singlet state S_1 with a low energy to have an energy-sufficient system, and, for co-reactant ECL, a low quenching from co-reactants[33].

After PAHs, many different PAHs-based fluorescent ECL emitters were investigated, the most important of which are perylene and fluorene/spirobifluorene derivatives.

1.2.1.2 Perylene derivatives

Perylene derivatives are n-type organic semiconductors with high PLQYs and good photostability, absorption and thermal properties[34–36].

They are widely used also in Organic Light-Emitting Diodes (OLEDs), Light-Emitting Electrochemical Cells (LECs), dye lasers and photovoltaic devices[37–40].

While the eponym compound of this class (**4**) exhibits a weak ECL signal with a blue emission, other extended perylenes such as dibenzotetraphenylperflanthene, perylene tetracarboxylic dianhydride or perylene diimides (PDIs, **5**)[41–43] shows higher ECL efficiency, red emission and the possibility to finely tune both electrochemical and photophysical properties by a simple extension or modification in the bay positions of the backbone (**Figure 1.7-right**).

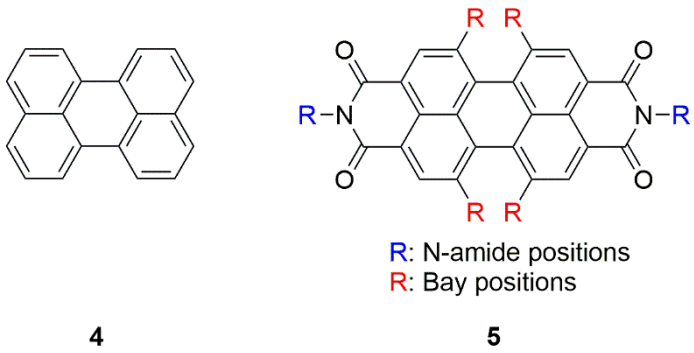


Figure 1.7: Chemical structures of perylene (left) and perylene diimide (PDI, right).

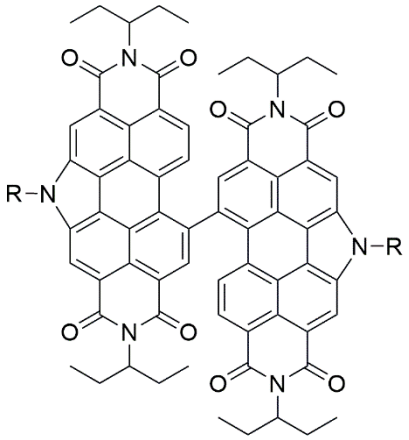
Indeed, Lee *et al.*[42] found that the nature of *N*-substituents has little influence on the electrochemical properties while the extension of the aromatic core between imide groups has a great impact on the oxidation potential and on the emission, with easier oxidation processes and red-shifted emissions.

Moreover, authors found that ECL efficiency tends to decrease with higher conjugation due to lower PLQYs.

Nevertheless, perylene-based derivatives tend to exhibit low solubility in a multitude of organic solvents. Consequently, Williams and Murray[44] synthesized some *N*-polyether PDIs to increase their solubility in organic solvents and water.

They observed that the functionalization with these chains dramatically enhances the solubility in common solvents, enabling a proper investigation of ECL properties of these molecules both in annihilation and co-reactant conditions (with persulfate as co-reactant), as they exhibit reversible reduction processes.

Finally, Ding and coworkers recently reported[45,46] the investigation of two instances of PDI dimers (**Figure 1.8**) as ECL emitters in both annihilation and co-reactant conditions, finding that compound **7** exhibits an ECL efficiency of 1.65 times the standard $Ru(bpy)_3$.



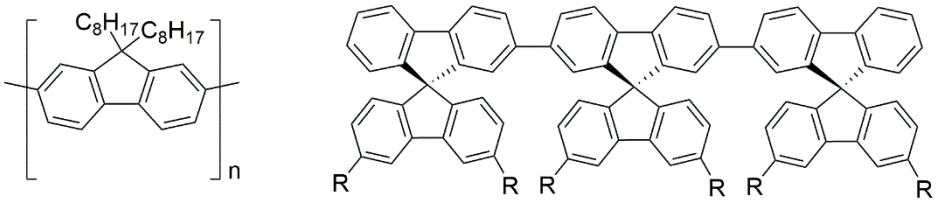
6 R = C_6H_{13}
7 R = trimethylbenzyl

Figure 1.8: Structure of PDI dimers investigated by Ding and coworkers.

1.2.1.3 Fluorene and spirobifluorene derivatives

As for perylene-based emitters, fluorene and spirobifluorene derivatives exhibit high PLQYs and excellent thermal and chemical stabilities, making them suitable compounds for fluorescent blue OLEDs[47].

These compounds gained interest as ECL emitters during the last 25 years since they can be synthesized with a good versatility and shows good ECL efficiencies in the green-blue region that, in some cases, outcome the ECL efficiency of 9,10-Diphenylanthracene.



8

9 R = H
10 R= CH_3

Figure 1.9: Chemical structure of some fluorene and spirobifluorene derivatives investigated by Bard's group.

The first reports about ECL from fluorene and spirobifluorene derivatives (**Figure 1.9**) were published by Bard's group[48–50] two decades ago, where they demonstrated that ECL emissions were different if recorded under annihilation conditions or co-reactant conditions.

Indeed, ECL emission from polymer **8** and compounds **9-10** under annihilation conditions arose from excimers while in presence of BPO no excimer emission was recorded.

The same group in the following years synthesized and investigated many other derivatives with different geometries[50–52], finding that the functionalization increases the radical stability.

However, even if spirobifluorene derivatives exhibit excellent electrochemical reversibility, many of them are energy-deficient systems with low ECL efficiencies.

Starting from these results, in 2012 Polo and coworkers reported three donor-acceptor spirobifluorenes[53] (**11**, **15** and **19**, **Figure 1.10**), finding that **11** and **15** have higher ECL efficiencies than the standard DPA while **19** exhibited only a very weak emission.

These results corroborate the importance of a complete electrochemical reversibility as all of them show similar PLQYs but only compounds **11** and **15** show reversible electrochemistry.

Some years later, Rizzo and coworkers[54] investigated the effect of the insertion of electron-donating or electro-withdrawing group in para position of triphenylamine, making possible the tuning of electrochemical and photophysical properties without decreasing ECL efficiencies.

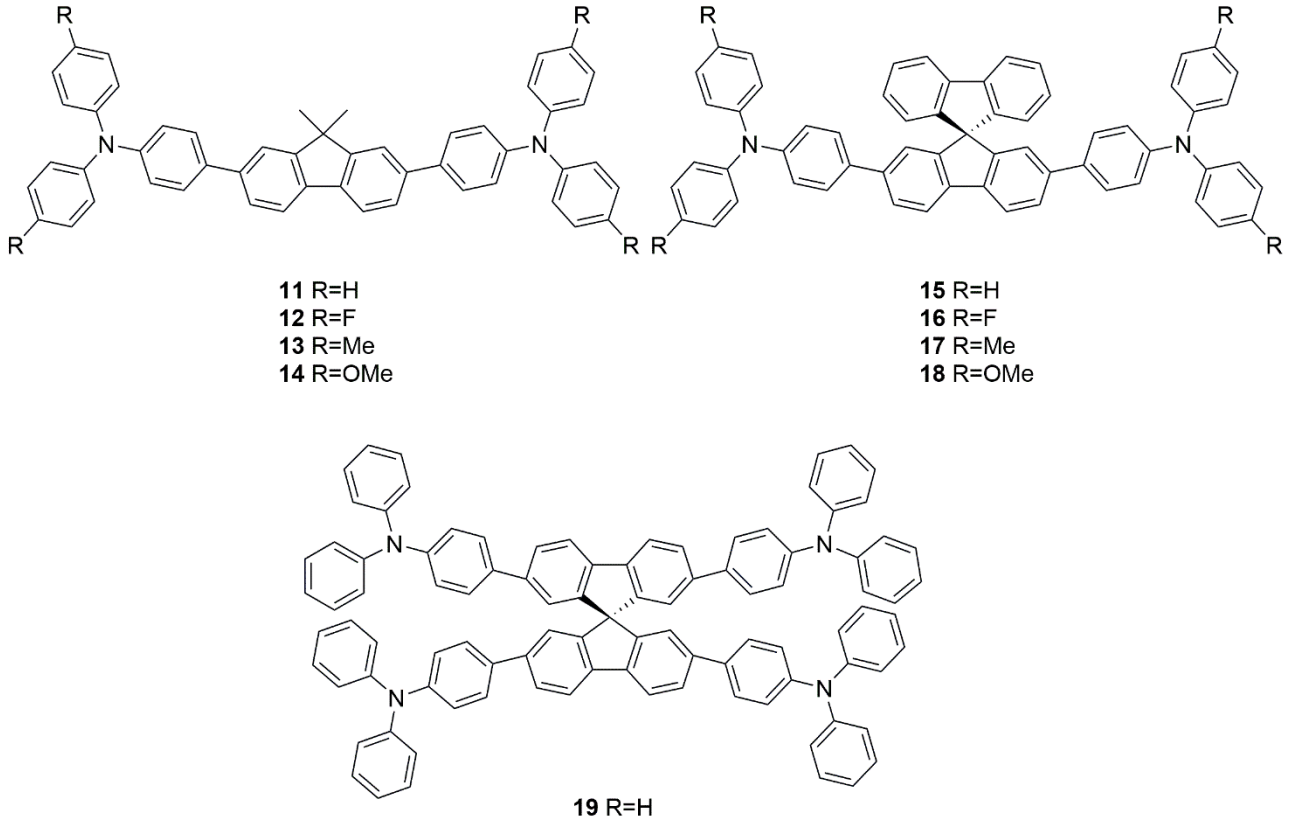


Figure 1.10: Chemical structure of triphenylamine-fluorene and spirobifluorene investigated by Polo and coworkers and Rizzo and coworkers.

1.2.1.4 BODIPY derivatives

BODIPY (4,4-difluoro-4-bora-3a,4a-diaza-s-indacene) derivatives (**Figure 1.11**) are fluorescent dyes widely used as fluorescent labels in biology[55] since they show tunable emissions and a PLQYs close to the unity[56].

They represent a very interesting class of ECL emitters as their photophysical and electrochemical properties strongly depend on the nature of substituents in *meso*, α and β positions.

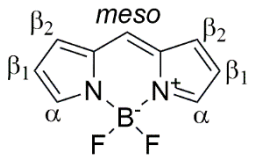


Figure 1.11: Nomenclature of the position in BODIPY structure.

Indeed, the insertion of alkyl groups in β positions causes a redshift of absorption and emission spectra due to an induction effect that is greater for bulkier groups.

The same redshift effect can be obtained by inserting an electron-withdrawing group such as cyanide in *meso* position.

To obtain derivatives with stable radicals all positions must be substituted.

Indeed, the absence of substituents in α and β positions makes the radical-cation instable and the absence of substitution in *meso* position conversely makes the radical-anion instable.

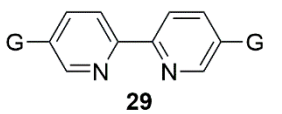
Since the photophysical and electrochemical properties of these properties can be finely tuned, a huge number of these derivatives were synthesized by Bard's and Ding's groups[57–65].

Indeed, Bard and colleagues have systematically investigated the BODIPY compounds reported in **Figure 1.12**, demonstrating that the location and nature of the substituents played a crucial role in predicting the ECL behavior.

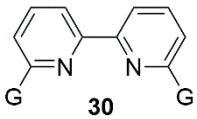


20

21 R_5, R_7 = CH_3
22 R_1, R_3, R_5, R_7 = CH_3
23 R_1, R_3, R_5, R_7, R_8 = CH_3
24 R_1, R_3, R_5, R_7, R_8 = CH_3; R_2, R_4 = CH_2CH_3
25 R_1, R_3, R_5, R_7, R_8 = CH_3; R_2, R_4 = tBu
26 R_1, R_3, R_5, R_7 = CH_3; R_2, R_4 = CH_2CH_3, R_8 = C_5H_{11}
27 R_1, R_3, R_5, R_7 = CH_3; R_2, R_4 = CH_2CH_3; R_8 = C_9H_{19}
28 R_1, R_3, R_5, R_7 = CH_3; R_2, R_4 = CH_2CH_3; R_8 = CN



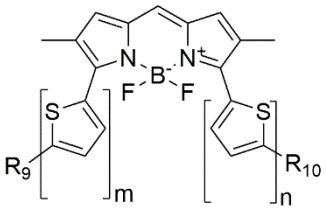
29



30

G:





31 m, n = 1; R_9, R_{10} = H
32 m = 1; n = 2; R_9, R_{10} = H
33 m = 1; n = 2; R_9 = H; R_{10} = C_4H_9
34 m = 3; n= 1; R_9 = C_6H_{13}; R_{10} = H
35 m = 3; n= 1; R_9 = C_6H_{13}; R_{10} = C_4H_9

Figure 1.12: Chemical structure of BODIPY derivatives investigated by Bard's group.

Indeed, the introduction of bulky substituents such as *tert*-butyl groups on the BODIPY backbone blocks dimerization or polymerization processes, leading to higher ECL efficiencies both with annihilation and co-reactant ECL with tripropylamine or benzoyl peroxide as co-reactants.

The same group then varied the conjugation length with a bipyridine spacer (**Figure 1.12**)[58], finding that this spacer does not facilitate efficient electronic communication between the two units, regardless of their position.

Interestingly, for compounds **29** and **30** two emission bands were found under annihilation conditions while only one emission band was found with co-reactant ECL.

This difference was not ascribed to the presence of excimers but to the formation of an unknown byproduct, as the emission was not featureless nor concentration-dependent.

As far as concerned oligothienyl-BODIPY derivatives (**31-35**), they exhibit an irreversible reduction process and oxidation processes that become more reversible with the increase of thiophene rings; however, no one of these compounds exhibited good ECL efficiencies.

More recently "deep red" and Near Infrared (NIR) BODIPY gained a lot of attention since they are of broad interest in biomedical imaging as NIR light can penetrate tissue.

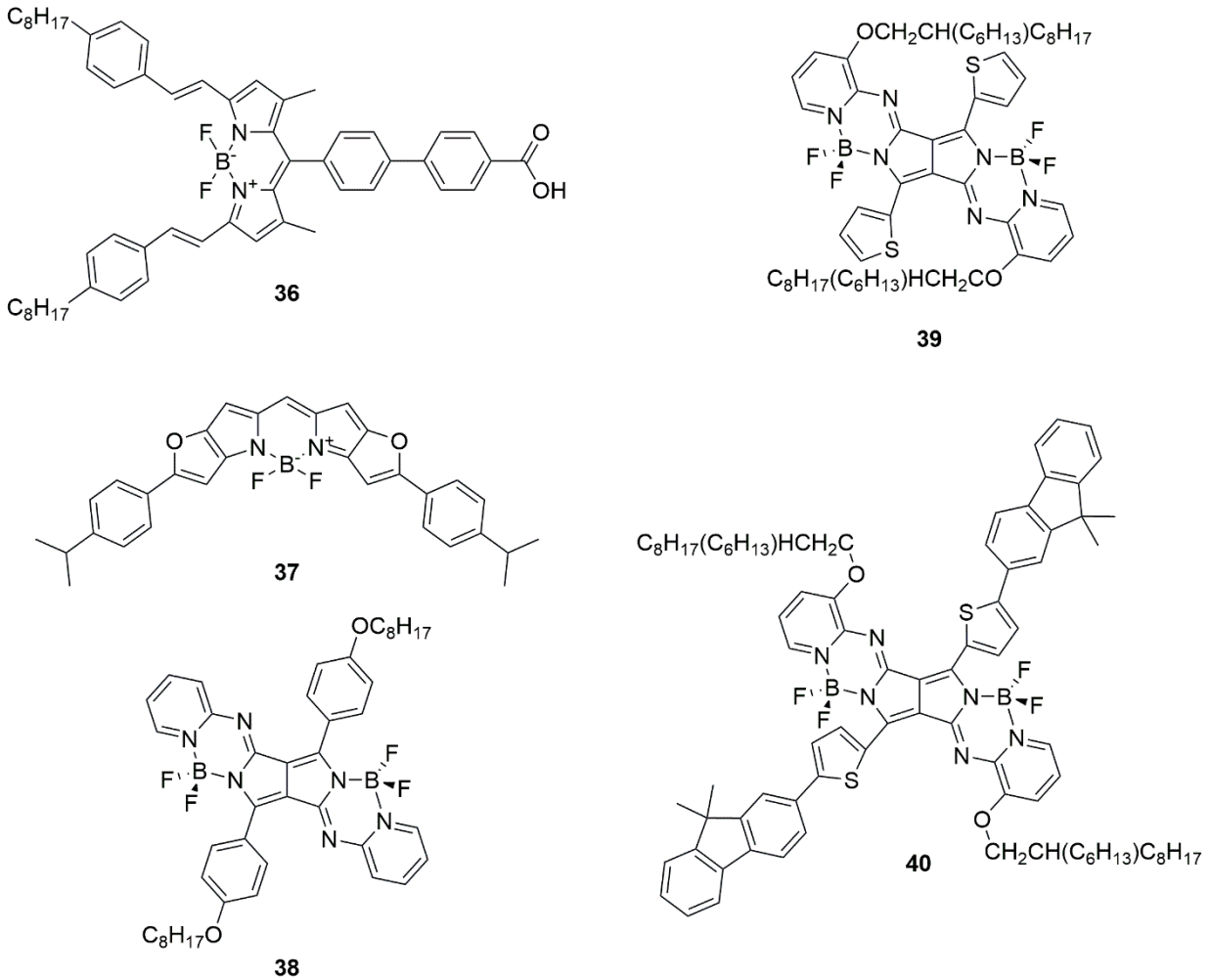


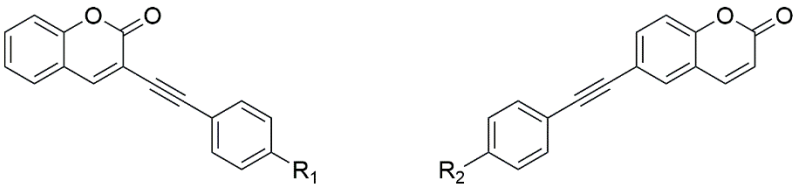
Figure 1.13: Chemical structure of Near InfraRed BODIPY derivatives.

In this context, Ding and colleagues[57] found a deep-red to NIR emission from a BODIPY derivative (**36**) with a long chain (C8) or biphenyl linkers in meso or α position (**Figure 1.13**) while Imato and colleagues[66] investigated electrochemical and ECL properties of compound **37** as it exhibits an outstanding PLQY of 0.97. Nevertheless, this compound is an energy-deficient system and exhibits a weak ECL signal under both annihilation and oxidative-reduction conditions.

In another study, the same group[67] reported that NIR ECL emission can come also from pyrrolopyrrole Aza-BODIPY derivatives (**38-40**), which exhibit an ECL signal that is enhanced by the cooperation of the second lowest-lying excited singlet state (S_2).

1.2.1.5 Coumarin derivatives

Coumarin derivatives represent another class of donor-acceptor fluorescent ECL luminophores[68,69]. The first report of these dyes as ECL luminophores was published by Ho's group[68] in 2004, when they studied the electrochemiluminescence of a series of phenylethynylcoumarins (**Figure 1.14**) with different substituents in position 3 and 6, finding that the substitution position and the nature of the substituents dramatically change photophysical and ECL properties without affecting electrochemical properties.



41 R_1 = H
42 R_1 = CH_3
43 R_1 = OCH_3
44 R_1 = OiPr
45 R_1 = NMe_2

46 R_1 = H
47 R_1 = CH_3
48 R_1 = OCH_3
49 R_1 = OiPr
50 R_1 = NMe_2

Figure 1.14: Coumarin derivatives reported by Ho's group.

Indeed, PLQYs of 6-substituted derivatives is very low (<3%) due to an inefficient communication between moieties following that low ECL efficiencies were achieved for these derivatives.

In contrast 3-substituted derivatives shows higher PLQYs and ECL efficiencies with the formation of excimers.

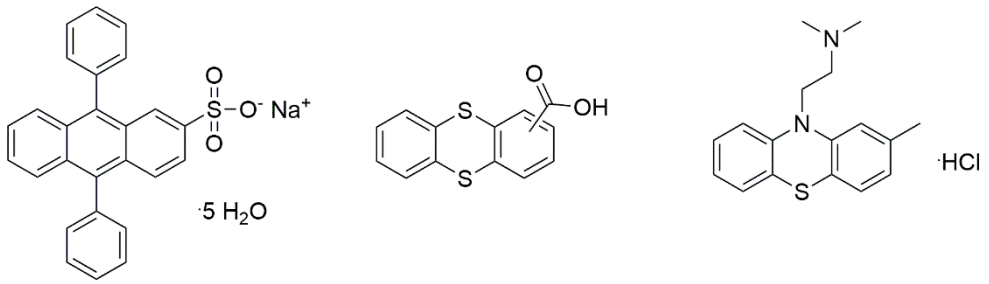
Upon analysis of the ECL efficiencies of the aforementioned luminophores, it becomes apparent that they exhibit superior performances in comparison with the standard 9,10-diphenylanthracene $[Ru(bpy)_3]^{2+}$.

However, it is important to note that these efficiencies have been recorded in organic solvents and often under annihilation conditions.

Conversely, all ECL-based tools operate with aqueous solutions in presence of co-reactant.

The first report about electrochemiluminescence from water-soluble organic fluorescent molecules was published by Richards and Bard[70].

In this paper the authors observed an ECL emission from sodium 9,10-diphenylanthracene-2-sulfonate (DPAS, **51**)), 1- and 2-thiantiirene-carboxylic acid (1-THCOOH and 2-THCOOH, **52-53**) and chlorpromazine (CPZ, **54**) in sodium phosphate buffer with TPA or persulfate as co-reactants.

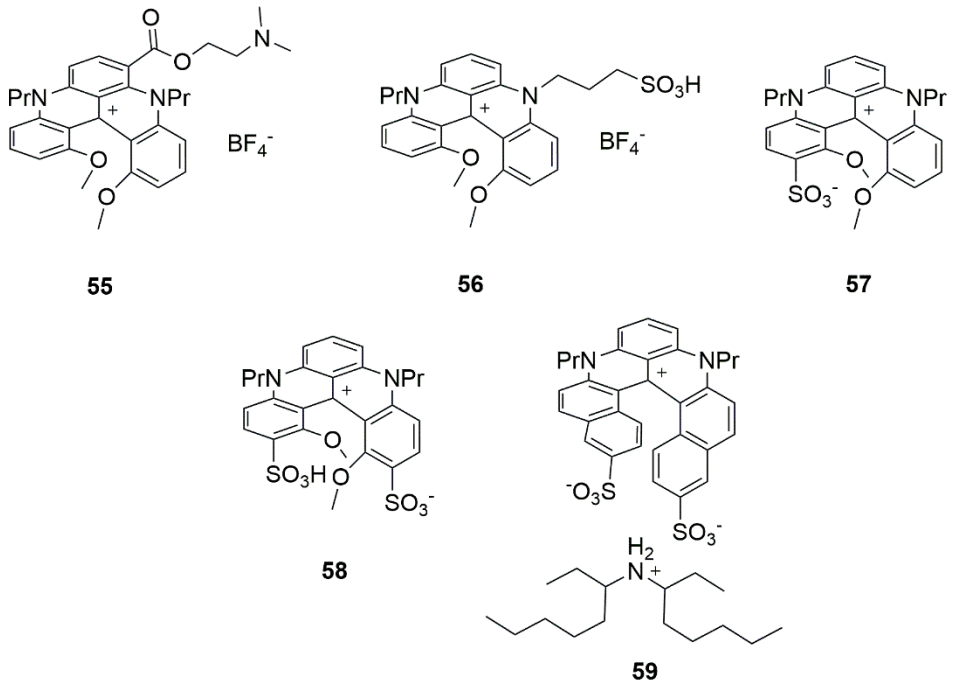


51 **52 (1-THCOOH)** **53 (2-THCOOH)** **54**

Figure 1.15: Structures of water-soluble dyes investigated by Richards and Bard.

Except for chlorpromazine **54**, which showed very low ECL emission, compounds **51-53** show intense ECL emission, that is different from fluorescence for 1THCOOH and 2THCOOH, probably due to the generation of excimers.

An interesting aspect of that work is the behavior of chlorpromazine, which exhibited a kind of "self-annihilation" ECL process, where the dimethylamino group, upon oxidation, generates a reducing group that transferred electrons to the dye core. This phenomenon was also observed by Sojic and colleagues 15 years later[71], when they reported oxidative-reduction ECL in the red region from a cationic helicene with a dimethylamino group (**55**) in absence of co-reactant (**Figure 1.16**).



55 **56** **57** **58** **59**

Figure 1.16: Structures of the water-soluble [4] and [6] helicenes investigated by Sojic and colleagues.

These results are very interesting and can open new research lines as the presence of a dye incorporating the co-reactant can simplify and decrease cost of sensors.

The same group reported near-infrared ECL from water soluble compounds **56–59** by inserting sulfonate groups. All these compounds emit at ca. 700 nm, and they do not exhibit high PLQYs due to energy-gap law and, notably, PLQYs trend is not consistent with ECL efficiency.

1.2.2 Phosphorescent emitters

As previously stated, the main disadvantage of fluorescent emitters in charge-recombination processes is the fact that they have a maximum of Internal Quantum Efficiency (IQE) of 25% since they cannot harvest triplet excitons.

This limit can be overcome with phosphorescent emitters, as they can harvest triplet excitons and reach an IQE of 100%.

Moreover, the parallel growth of the OLED technology (based on electroluminescence), had boosted the investigation of phosphorescent emitters in ECL, since these emitters outperformed fluorescent dyes.

As phosphorescence is a spin-forbidden transition, it can be observed at room temperature only from heavy-metal complexes that show strong spin-orbit coupling, and among all of them[1], Ru(II)- and Ir(III)-based complexes were extensively studied during the last 50 years as ECL emitters.

The first report of electrochemiluminescence from a phosphorescent emitter was published in 1972, when Tokel and Bard[19] reported annihilation ECL from complex $[Ru(bpy)_3]Cl_2$ (**61**, **Figure 1.17**), while some years later co-reactant ECL with this complex was reported[23,24,72], opening a new era in this field that lasts to this day.

In fact, $[Ru(bpy)_3]^{2+}$ is nowadays the benchmark ECL luminophore, since it incorporates nearly all the criteria of the perfect ECL luminophore: good solubility in organic solvents and water, fully electrochemical reversibility, low quenching from the co-reactant, ease of functionalization with bioconjugable groups and high Internal Quantum Efficiency.

However, these properties are counterbalanced by a low PLQY (around 0.06) and low ECL efficiency (0.05)[73] in organic and aqueous solutions.

After 2,2'-bipyridine, many different nitrogen-based chelating ligands (bipyridine, phenanthroline, terpyridine, *N*-heterocyclic carbenes) were used to synthesize novel homoleptic and heteroleptic ruthenium complexes to understand how photophysical and electrochemiluminescent properties are affected by ligands.

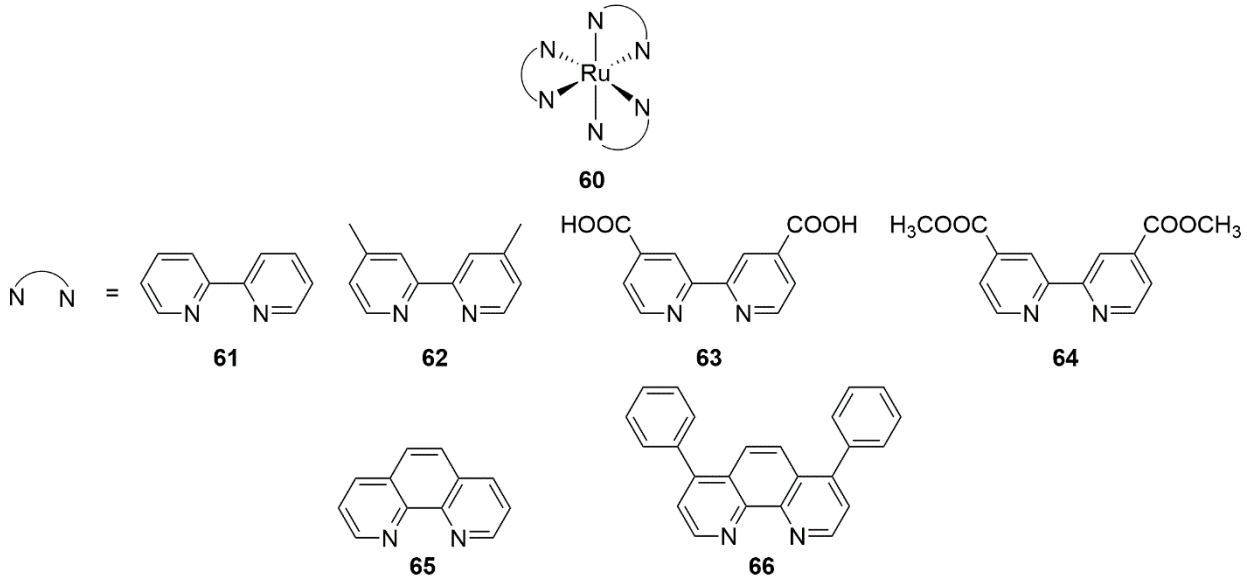


Figure 1.17: Examples of nitrogen-based chelating ligands for Ru(II) complexes investigated in electrochemiluminescence.

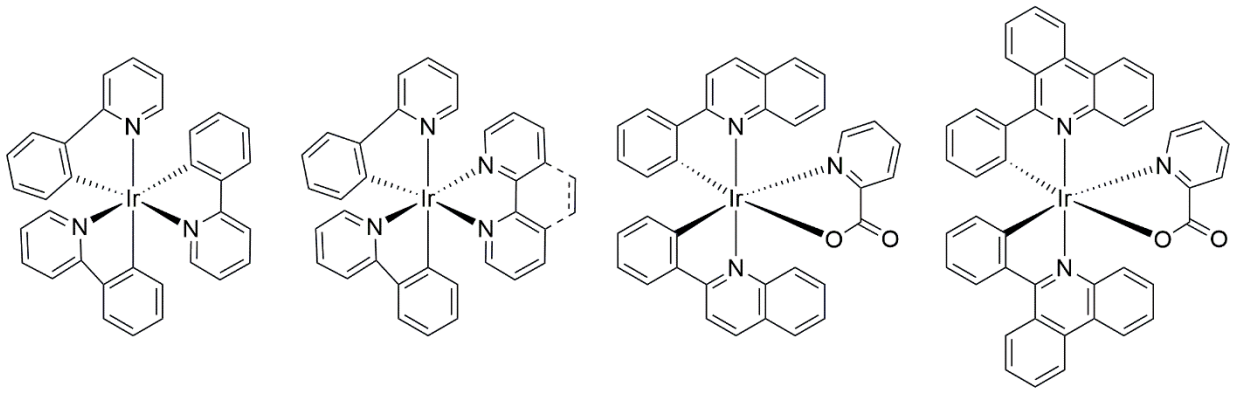
It was found that the different substitution on these ligands affect HOMO and LUMO energies in different modes without affecting the electrochemistry, which generally remains fully reversible.

Furthermore, bipyridine-based complexes exhibit higher annihilation ECL efficiencies than phenanthroline-based complexes except for complex **66** that shows an annihilation ECL efficiency that is half of the $[Ru(bpy)_3]^{2+}$ one and a co-reactant ECL efficiency that is 26-fold the $[Ru(bpy)_3]^{2+}$.

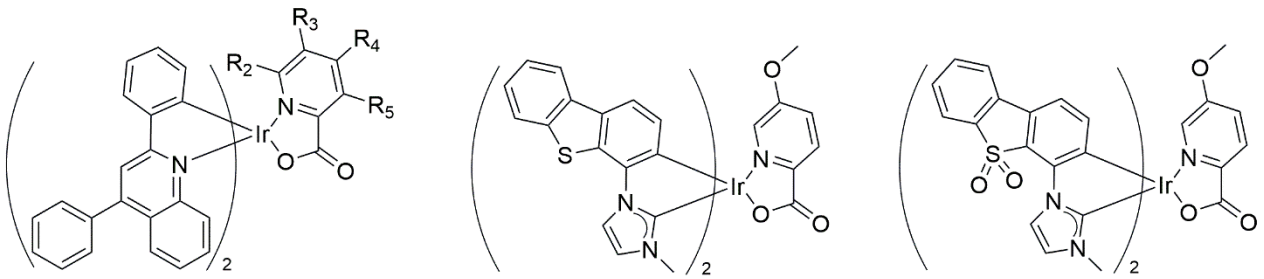
Even if $[Ru(bpy)_3]^{2+}$ is the benchmark ECL luminophore, in the last 20 years, Ir(III) complexes came out as contenders since they show higher PLQYs and easier tunability of emission over the visible spectrum than Ru(II) complexes.

Indeed, emission wavelength in Ir(III) complexes is more tunable because both HOMO and LUMO are delocalized over the ligand framework.

The first investigation of ECL from cyclometalated Ir(III) complexes were reported in 2002 by Gross *et al.* [74] and Bruce *et al.* [75], where they found that complex $Ir(ppy)_3$ (**67**, **Figure 1.18**) shows intense annihilation ECL but low co-reactant ECL.



67 **68/69** **70** **71**



72/73 R_3, R_4, R_5 = H, R_2 = F/OCH_3
74/75 R_2, R_4, R_5 = H, R_3 = F/OCH_3
76/77 R_2, R_3, R_4: H; R_5: F/OCH_3
78/79 R_2, R_4: H; R_3, R_5: F/OCH_3
80 R_2, R_3, R_4, R_5: H

81 **82**

Figure 1.18: Examples of Ir(III) complexes: $Ir(ppy)_3$ (**67**), Ir(III) complexes investigated by Lee and coworkers (**68**, **69**); Ir(III) complexes investigated by De Cola and coworkers (**70**, **71**) and Ir(III) with NHC ligands.

Based on these results, many groups synthesized cyclometalated Ir(III) complexes in order to increase the ECL efficiency and overcome the benchmark $[Ru(bpy)_3]^{2+}$ in organic and aqueous solutions.

During the following years many interesting results were obtained with cyclometalated complexes: in 2005 Lee and coworkers[76] reported some extremely efficient Ir(III) complexes that outperform $[Ru(bpy)_3]^{2+}$ (**68-69**, **Figure 1.18**) while De Cola and coworkers[77] ten years later investigated compound **71**, finding that its ECL efficiency is higher than $[Ru(bpy)_3]^{2+}$ using commercial immunoassays conditions.

In order to make the emission tuning easier, many heteroleptic Ir(III) complexes bearing NHC ligands were investigated[78–82].

Despite many abovementioned compounds are excellent candidates for electrochemiluminescence applications, with the $[Ru(bpy)_3]^{2+}$ as the benchmark to calculate ECL efficiencies of other compounds, they exhibit drawbacks such as economical costs of heavy atoms and geopolitical implications.

1.2.3 Thermally Activated Delayed Fluorescence emitters

Even if some phosphorescent emitters exhibit better electrochemical, electrochemiluminescence and water-solubility properties than fluorescent emitters, they suffer from the aforementioned drawbacks. For these reasons the OLED industry, to which ECL research is linked, began to search for other alternatives to harvest the 75% of excitons[17], and the most promising solution was "Thermally Activated Delayed Fluorescence" (TADF) emitters.

The TADF phenomenon was observed for the first time during the 1960's in eosine[83], an organic compound that showed in the delayed emission spectrum two emission bands, caused by a triplet emission and a singlet emission, the latter of which with a dependence from the temperature.

This singlet emission suggested the existence of a radiative decay from the excited singlet state with a longer decay time than fluorescence one, which was referred to as "Delayed Fluorescence" (DF) while the process was initially referred as "E-type fluorescence".

The TADF phenomenon is composed by the Prompt Fluorescence ("PF") and the Delayed Fluorescence ("DF"), the latter made possible by the so-called "Reverse InterSystem Crossing" (RISC) process, which allows triplet excitons to up-convert into the excited singlet state.

Since this up-conversion is endothermic, the RISC process is temperature-dependent (thermally activated) and this dependence can be expressed in a Boltzmann distribution relation[17] (**Equation 1.10**)

$$k_{RISC} = e^{\frac{\Delta E_{ST}}{k_B T}} \quad \textbf{(1.10)}$$

From **Equation 1.10** follows that a small ΔE_{ST} (≤100 meV) is fundamental to achieve a fast RISC process and an efficient TADF emission.

The energies of the lowest-lying singlet and triplet states (E_S and E_T respectively) are related to many factors, in particular from the orbital energy (E), electron repulsion energy (K) and exchange energy (J) of two unpaired electrons at the excited states (**Equations 1.11a-b**):

$$E_S = E + K + J \quad \textbf{(1.11a)}$$

$$E_T = E + K - J \quad \textbf{(1.11b)}$$

Since the electron arrangements of singlet and triplet states in one molecule are the same, E, K and J are the same so the term ΔE_{ST} is equal to 2J, which can be expressed as follows[17] (**Equation 1.12**):

$$J = \iint \Phi_L(1)\Phi_H(2)\left(\frac{e^2}{r_1 - r_2}\right)\Phi_L(2)\Phi_H(1)dr_1 dr_2 \quad \textbf{(1.12)}$$

where Φ_H and Φ_L represent the HOMO and LUMO wave functions, respectively and e represents the electron charge.

From **Equation 1.12** follows that a small ΔE_{ST} is present with a small overlap integral of $\langle\Phi_H|\Phi_L\rangle$, i.e., via spatial wave function separation of HOMO and LUMO.

This spatial separation between HOMO and LUMO can be obtained from molecules made of electron-rich (donor) and electro-poor (acceptor) moieties that can be directly linked (D-A) or separated by a π-linker (D-π-A).

Moreover, these moieties must be tilted between each other or present spiro connection[17,84–86].

In addition, the spatial separation of HOMO and LUMO makes the tuning of electrochemical and photophysical properties easier.

During the years, TADF was observed in metallic complexes and fullerenes, while the first attempt to introduce TADF compounds in OLED was done in 2009, followed in 2012 by the first highly efficient purely-organic TADF-based OLED, reported by Adachi and coworkers[85].

After this milestone, a huge number of TADF compounds with different acceptors and donors were synthesized and investigated in photocatalysis[87–90], OLEDs[86,91–95], LECs[96–98] and imaging[99,100], while there are only few reports about electrochemiluminescence from TADF molecules.

The first of these reports was published by Imato and colleagues in 2014[101] where they investigated carbazoyldicyanobenzene derivatives under annihilation conditions (**Figure 1.19**).

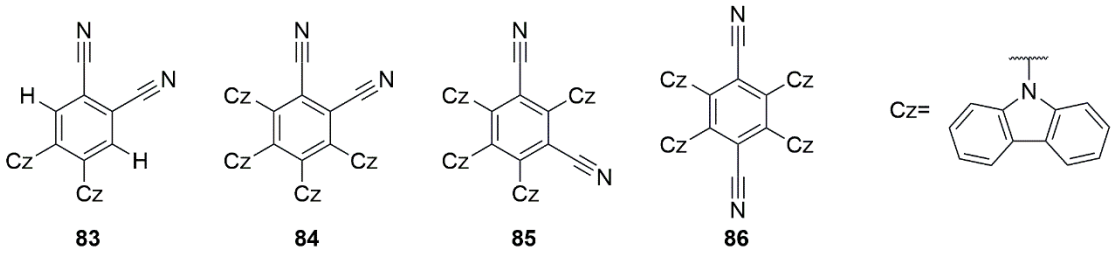


Figure 1.19: Carbazoyl dicyanobenzene derivatives investigated by Imato and colleagues in 2014.

In this paper, the authors found that in some cases the reported compounds showed ECL efficiencies higher than the standard $[Ru(bpy)_3]^{2+}$ and, for compound **85**, ECL efficiency exceeded the limitation of spin statistics, thus making this compound the state of art and demonstrating that spin-up conversion would be very useful for ECL.

Photoluminescent and ECL emissions were superimposable, thus confirming that the S-route was followed, except for compounds **83**-**84**, as they exhibited marked redshifts between PL and ECL emission that were motivated with the formation of oligomers during the oxidation step.

However, the presence of carbazole as donors gave irreversible oxidation processes due to the electropolymerization of this moiety[102] so the same authors two years later chose the best-performing compound (**85**) and tried to figure out how to improve the stability of radicals[103].

This feature, oddly enough, had not been extensively studied in the past for TADF molecules even if it is of critical importance in understanding which TADF compounds can be good candidates for OLEDs.

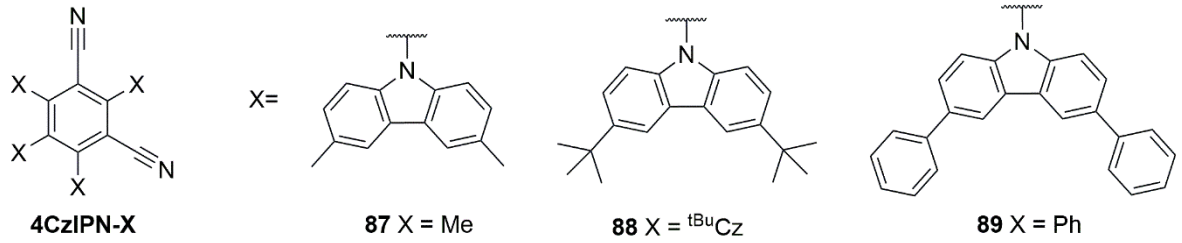


Figure 1.20: Isophthaloderivatives investigated by Imato and colleagues in 2016.

From this examination, they found a direct correlation between radical stability and ECL efficiency: in fact, when *tert*-butyl groups were used as substituents the oxidized form was more stable, leading to higher ECL efficiencies (**Figure 1.20**).

After these two seminal works, the attention was turned to TADF-based polymers, polymer dots or nanoparticles[104–107], until in 2022 Niu and coworkers gave new significant information about ECL of compound **85** under annihilation and co-reactant conditions.

In this article the authors observed that under annihilation conditions the ECL intensity when stepping from negative to positive potentials is greater than ECL intensity generated by a positive-negative step, a behavior that is related to the higher stability of the radical-anion than the radical-cation.

This observation was supported also by the ECL efficiencies in presence of TPA and BPO as co-reactant: in the first case the ECL efficiency is a tenth of the standard ($[Ru(bpy)_3]^{2+}$/TPA) while in the second case it is two times than the same standard.

In the same year, Zysman-Colman and coworkers reported the investigation of ECL from blue-emitting phthalonitrile derivatives containing chalcogenide-substituted carbazole donors[108] (**Figure 1.21**) under annihilation and co-reactant conditions.

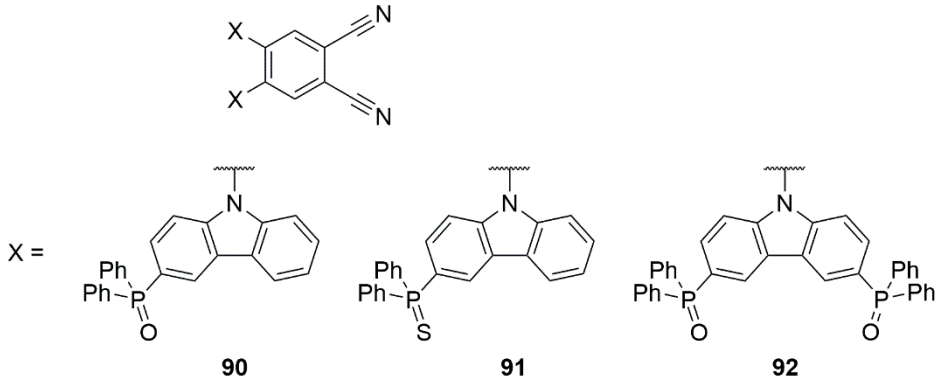


Figure 1.21: Phthalonitrile derivatives investigated by Zysman-Colman and colleagues.

As for the parent compound **83**, these compounds do not show high ECL efficiencies under both conditions because of the instability of their radicals.

Then, the same group reported electrochemiluminescence from compounds **101-105** (**Figure 1.22**) [109,110], the former of which is a MultiResonance TADF (MR-TADF, a TADF molecule where HOMO and LUMO are alternated in the molecule) while the others are through-space charge transfer TADF compound.

Interestingly, these molecules exhibit delays in the onset of ECL signal and a buildup profile which had been already observed by other authors[111].

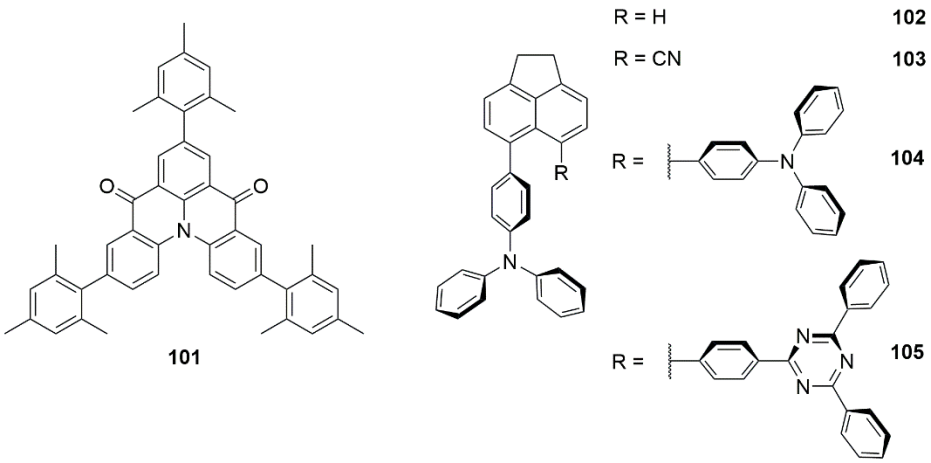


Figure 1.22: Structure of MR -TADF dye (left) and through-space charge transfer TADF dyes (right) investigated by Zysman-Colman and colleagues.

These delays were not reconducted to diffusion issues or to lower electron-transfer constants, but they were attributed to the so-called "Organic Long ElectroChemiLuminescence" (OLECL), a phenomenon similar to the so-called "Organic Long PhotoLuminescence" (OLPL)[112].

Moreover, the authors attributed these delays to either large ΔE_{ST} for compounds **91-92** or aggregate/excimers formation for compounds **102** and **103**, as large redshifts were observed in ECL emission.

Looking at the results to date, it can be argued that TADF compounds represent an attracting alternative to phosphorescent complexes as ECL emitters, as they do not contain scarce and high-costing heavy metals while their photophysical and electrochemical properties can be finely tuned.

Nevertheless, TADF emitters exhibit three main disadvantages that prevent their practical applications: the absence of bioconjugable groups, the lack of water solubility and the PLQYs quenching from oxygen.

While the first, at the best of our knowledge, has never been investigated, some strategies to investigate TADF emitters in aqueous ECL have been successfully employed, such as nanoencapsulation or aggregation induced ECL[107,113], which can in turn inhibit the PLQYs quenching by oxygen.

1.3 Electrochemiluminescence and Electroluminescence emitters: similarities and differences

Light-Emitting Electrochemical Cells (LECs) are a subclass of organic optoelectronic solid-state devices that generate light via electroluminescence[114] that were discovered by Pei and coworkers approximately three decades ago[115].

Indeed, they discovered that by mixing a solid electrolyte and a luminescent semiconducting material the properties of the resulting solid-state device are entirely distinct from those of an OLEDs (**Figure 1.23**).

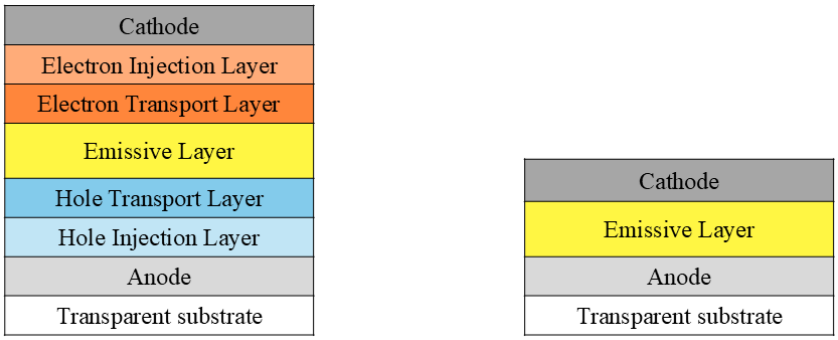


Figure 1.23: Schematic representation of the architectures of a typical OLED (left) and a LEC with a sandwich structure (right).

Indeed, LECs did not behave as a diode as they did not block current in reverse bias. Furthermore, forward- and reverse-bias current-voltage and light-voltage profiles are symmetrical about zero bias, a property not observable in LEDs[115,116].

In addition, the operational mode of a LEC is completely different from that of an OLED.

Following the application of an electric bias, electrons (*p*-type carriers) and holes (*n*-type carriers) are generated at the cathode and the anode, respectively, for both LECs and OLEDs.

In OLEDs, the two carriers are subsequently injected into the Electron Injection Layer (EIL) and Hole Injection Layer (HIL), respectively, and then migrate through the Electron Transport Layer (ETL) and the Hole Transport Layer (HTL) into the emissive layer, where recombination occurs and light is emitted[117].

The multi-stack architecture of these devices dictates that symmetry in carrier injection is of critical importance to avoid a decrease in device efficiency.

Furthermore, the selection of ETL an HTL materials plays a pivotal role in facilitating the carrier transport process[118,119].

In contrast, in LECs after the application of an electric bias, Electric Double Layers (EDLs) are formed in the active layer (LEC architecture will be discussed subsequently) and *p*-type and *n*-type carriers then move towards each other, forming a *p*-*n* junction where they recombine to form excited states[115].

Over the past 30 years of study, both experimental and theoretical evidences has supported two different models: the ElectroDynamic (ED) and the ElectroChemical Doping (ECD) models, which may coexist in devices (**Figure 1.24**).

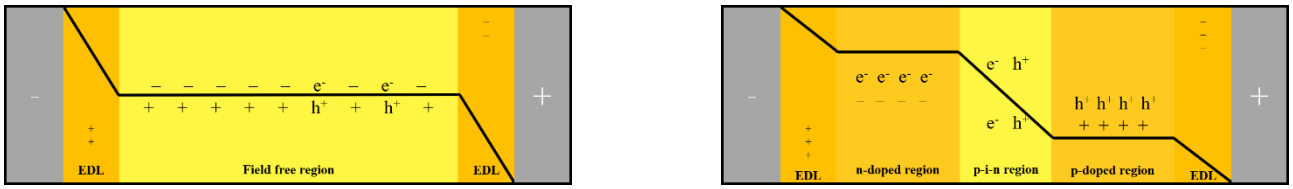


Figure 1.24: Schematic representations of the ElectroDynamic (ED) model (left) and ElectroChemical Doping (ECD) Model (right).

For the ED model, nearly all applied potential drops at the EDLs, which screen the bulk of the active layer from the electric field, resulting in a diffusion-dominated current in the bulk.

In contrast, the ECD model posits the formation of EDLs, accompanied by the presence of *n*-doped and *p*-doped regions within the bulk. These two regions generate a *p*-*n* junction from which light is emitted.

In addition, LECs show some advantages over OLEDs.

The first advantage is the simplicity of their architecture, as previously anticipated.

Indeed, LECs possess a very simple architecture comprising a transparent support (which can be either rigid or flexible[120]); a transparent anode (usually Indium Tin Oxide, ITO) covered with a hole-transport material (PEDOT-PSS); an active layer made of a semiconducting and luminescent material blended with a solid electrolyte and an air-stable metal cathode (e.g. Al).

The presence of an air-stable electrode is made possible by the distinctive mechanism of LECs. The EDL generates robust electric fields, and the potential drop compensates for the initial mismatch in energy between Fermi levels of cathode/anode and the LUMO/HOMO level of the luminophore.

Another advantage is the straightforward manufacturing process of LECs.

Indeed, the PEDOT-PSS and the active layer can be deposited by a multitude of different solution-processable methods including spin-coating, slot-dye coating, gravure printing, blade coating or inkjet printing[120,121].

In contrast, OLED layers are deposited by sequential evaporation processes under high-vacuum conditions, necessitating the encapsulation of all components due to the air-sensitivity of many of the components[122].

Another important advantage is the reduced operational voltage, which is approximately equivalent to the optical energy gap of the luminophore.

Other advantages comprehend higher fault tolerance, higher tolerance to thickness and extended shelf-life.

Despite the numerous advantages of LECs over OLEDs, they present some significant disadvantages that impede commercial viability, such as lower efficacies (which represents the conversion efficiency of electronic carriers in photons) than OLEDs and long turn-on times.

Over the past three decades, many small molecules, phosphorescent metal complexes and fluorescent conjugated polymers have been employed as emitters in LECs[97,120,123–127], with many of them that were also investigated as ECL emitters.

Indeed, Pei and coworkers descripted in their paper[115] the properties of a suitable emitter for LECs: good photoluminescent properties in their undoped state, readily electrochemical oxidation and reduction, electronic conductivity after the redox processes.

The first two requirements are identical to those that a suitable ECL luminophore should possess, thereby reinforcing the idea of using ECL, especially under annihilation conditions, as a testing table for LECs, as it had already done for OLEDs[103,108].

Furthermore, during the first years after the discovery of LECs, some authors[128,129] considered them as an ECL-based devices, as some parallelism with the annihilation ECL were found, such as the generation of radical-anions and radical-cations and the diffusion of these ions in a condensed phase.

Nevertheless, this definition is somehow misleading. Indeed, in LECs the electrons and holes move *via* conductive processes rather than convective processes in the condensed phase. In contrast, in solution-state ECL and in the so-called Electrochemiluminescence devices (ECLDs) electron and holes are delivered via convective processes[130].

Moreover, LECs and ECLDs exhibit a different composition, as in the former the major component is the luminophore while in the latter the luminophore is dispersed in a liquid bulk of electrolyte.

1.4 Scope of the project

As mentioned in **Chapter 1.2.3**, Thermally Activated Delayed Fluorescence (TADF) emitters represent a very valuable alternative to phosphorescent emitters as ECL emitters.

Indeed, they do not contain expensive heavy metals and their electrochemical and photophysical properties can be finely tuned by careful selection of the acceptor and donor moieties, as has been widely reported in the literature.[16,85,86,103]

While, nowadays, TADF emitters are now being extensively studied in optoelectronic devices and incorporated into OLED displays with excellent application prospects, their application in electrochemiluminescence remains rather underestimated, despite notable examples. This is due to the difficulty in designing water-soluble TADF emitters with suitable electrochemical properties and high Photoluminescence Quantum Yields (PLQYs) in aqueous solution, as mentioned above.

The aim of this project is to design novel TADF compounds and investigate them in ECL to understand how to design an efficient ECL emitter.

Furthermore, with the objective of investigating these ECL emitters in aqueous media, water-soluble groups, such as neutral hydrophilic poly(ethylene glycol) chain or anionic groups (e.g. sulfonate group), will be incorporated into them to increase their water solubility.

In order to achieve this goal, different synthetic strategies are followed to understand which one is the best.

Additionally, with the perspective of utilizing these emitters in ECL sensors, the insertion of bioconjugable groups will be explored.

Finally, the emitters with the best ECL properties will be investigated as emitters in Light-Emitting Electrochemical Cells to understand if a relationship exists between these two fields.

2. NOVEL IMIDAZOLE-BASED TADF DYES AS ELECTROCHEMILUMINESCENT EMITTERS

Alessandro Fracassa, Francesco Calogero, Giulio Pavan, Pavlos Nikolaou, Andrea Fermi, Paola Ceroni, Francesco Paolucci, Pier Giorgio Cozzi, Thomas Scattolin, Nicola Demitri, Fabrizia Negri, Andrea Gualandi, Alessandro Aliprandi, Giovanni Valenti.
Chem. Sci., 2024, *accepted article*

2.1 Introduction

As mentioned in **Chapter 1.2.3**, Thermally Activated Delayed Fluorescence compounds have proven to be effective electrochemiluminescence emitters under both annihilation and co-reactant conditions with tunable photophysical and electrochemical properties[86].

Among them, cyanoarene-based compounds represent a very interesting class of TADF compounds, as they can be easily synthesized without the use of palladium catalysts by nucleophilic aromatic substitution from inexpensive reactants and with mild conditions[85,90,103].

Furthermore, by a simple tuning of the donor and acceptor moieties different electrochemical properties can be achieved and high PhotoLuminescence Quantum Yields (PLQYs) can be obtained[90]. Additionally, in the case of isophthalonitrile-based derivatives, noteworthy ECL efficiencies under annihilation conditions were observed.

However, it should be noted that the totality of cyanoarene derivatives investigated in electrochemiluminescence are neither water-soluble nor incorporate moieties that can be functionalized with bioconjugable groups. This presents a significant challenge for practical applications in aqueous media, unless nanoencapsulation is employed.

Among the known isophthalonitrile-based derivatives, compounds 2,4,6-tris(diphenylamino)-5-fluoroisophthalonitrile (**3DPAFIPN**) and 2,4,6-tris(diphenylamino)-3,5-difluorobenzonitrile (**3DPA2FBN**) (**Scheme 2.1**) represent highly promising candidates for ECL applications. Indeed, they exhibit intense PLQYs and unsubstituted fluorine atoms that can be substituted with other moieties that can be themselves functionalized with water-soluble groups (e.g. polyethylene glycol chains) to increase solubility in water. The imidazole group represents an example of these moieties. Indeed, it can be functionalized with hydrophilic chains, thereby allowing the resulting water-soluble imidazolium TADF derivative to be studied as ECL emitters in aqueous media, circumventing the necessity for encapsulation in a water-soluble matrix such as nanoparticles or polymers.

In the present **Chapter**, the synthesis and characterization (both photophysical and electrochemical) in organic solvents of novel imidazole-based TADF derivatives are presented. In addition, the investigation of these compounds as electrochemiluminescent emitters in organic solvent under annihilation conditions is presented.

Finally, ECL in aqueous solution from water-soluble imidazolium-based TADF emitters in presence of tripropylamine as co-reactant is presented and discussed.

2.2 Results and discussions

2.2.1 Synthesis

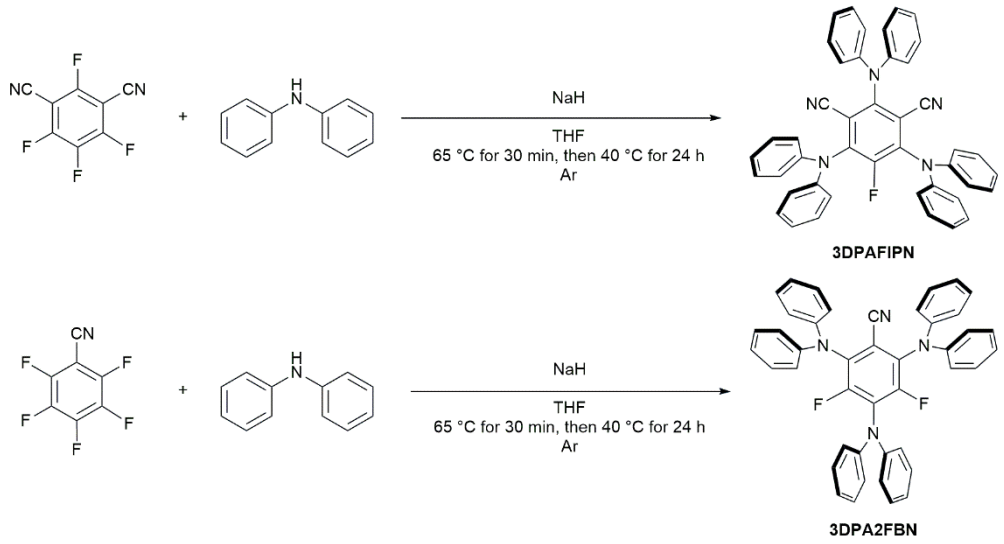
Compounds under analysis show a twisted donor-acceptor structure based on benzonitrile and isophthalonitrile acceptor and diphenylamine as donor.

The syntheses of compounds **3DPAFIPN** and **3DPA2FBN** are carried out according to a literature procedure[90] starting from 2,4,5,6-tetrafluoroisophthalonitrile or 2,3,4,5,6-pentafluorobenzonitrile and diphenylamine in THF in presence of sodium hydride as strong base (**Scheme 2.1**).

Given the high pK_a of diphenylamine (25 in DMSO[131]) the deprotonation step with sodium hydride must be performed at high temperatures (65 °C) for 30 minutes. Then, the temperature is decreased to 40 °C and maintained for 24 h.

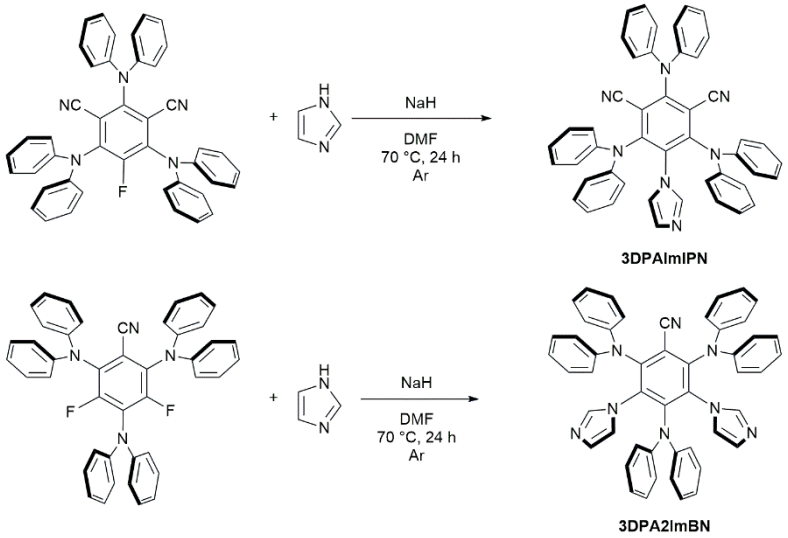
It has been reported, however, that this reaction can be carried out also at room temperature[132], but more than two days are required to achieve complete conversion.

Considering the long reaction time required by this preparative, the original procedure is preferred.



Scheme 2.1: Synthesis of **3DPAFIPN** and **3DPA2FBN**.

The products are isolated with good yields and their ^{1}H NMR spectra are comparable to the one reported in literature[90]. From the ^{19}F NMR spectra can be noticed the presence of one (**3DPAFIPN**) and two (**3DPA2FBN**) unsubstituted fluorine atoms. The next synthetic step consists in the substitution of the remaining fluorine atom/s with imidazole in DMF in presence of sodium hydride as strong base (**Scheme 2.2**).



Scheme 2.2: Synthesis of **3DPAImIPN** and **3DPA2ImBN**.

Although the pK_a of imidazole is considerably lower than the one of diphenylamine (18.6 in DMSO[133]), the reaction of insertion of the imidazolyl moiety is conducted at 70 °C to defy the steric hindrance caused by the other substituent on the central aromatic ring.

The products **3DPAImIPN** and **3DPA2ImBN** are obtained with excellent isolated yields. The successful substitution of the fluorine atoms is verified by the disappearance of the relative signals at -122 ppm in the ^{19}F NMR spectra.

In **Figure 2.1** a comparison of aromatic regions of **3DPAImIPN** and **3DPAFIPN** is depicted.

In the ^{1}H NMR spectrum of **3DPAImIPN** (**Figure 2.1** and **Figure A2.4**) three signals of imidazole protons can be observed between 6.1 and 6.5 ppm, while in the aromatic region many multiplets from phenyl protons split into a complicated system can be observed.

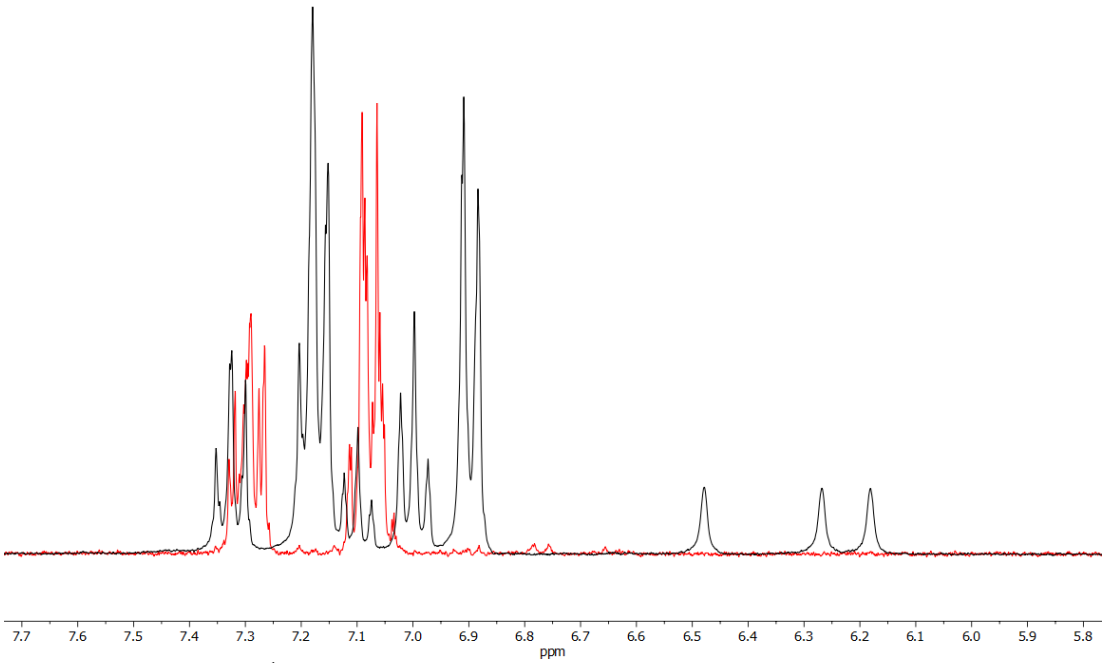


Figure 2.1: Comparison of ^{1}H NMR spectra of **3DPAFIPN** (red) and **3DPAImIPN** (black) in the aromatic region.

Similarly, the ^{1}H NMR spectrum of **3DPA2ImBN** (**Figure 2.2** and **Figure A2.5**) exhibits split signals in the aromatic regions, whereas the signals situated between 6.1 and 6.4 ppm can be attributed to imidazole protons. Furthermore, the molecule exhibits a lower degree of symmetry, as evidenced by the more ambiguous aromatic signals in comparison to those observed in compound **3DPAIPNIm**.

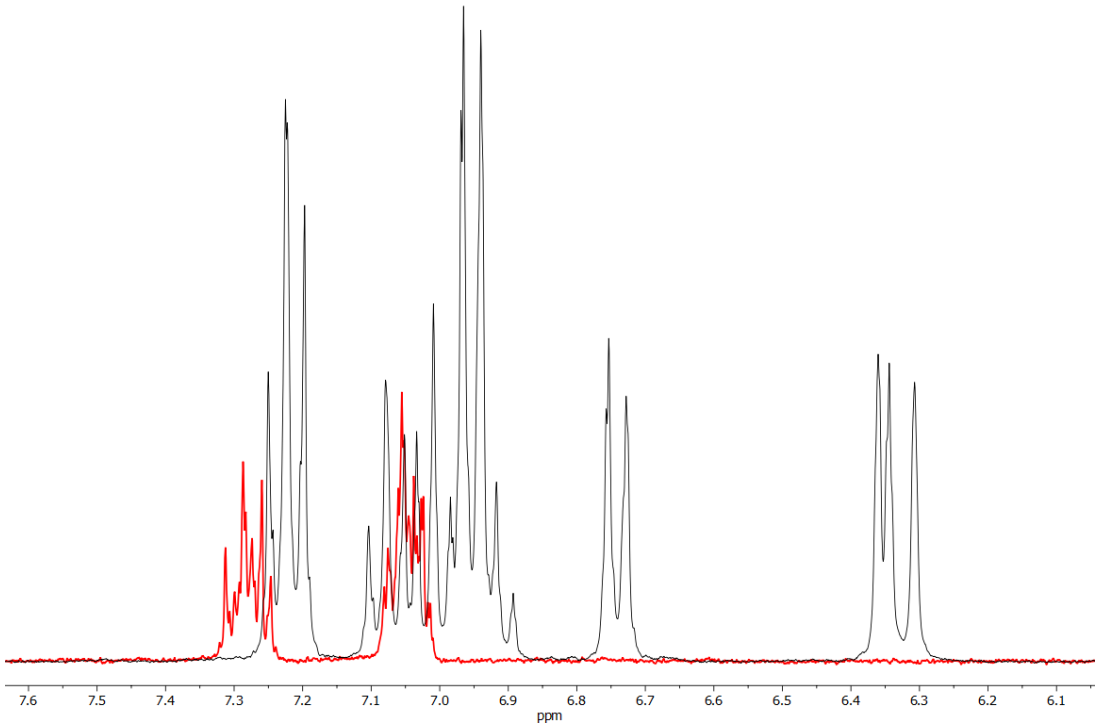
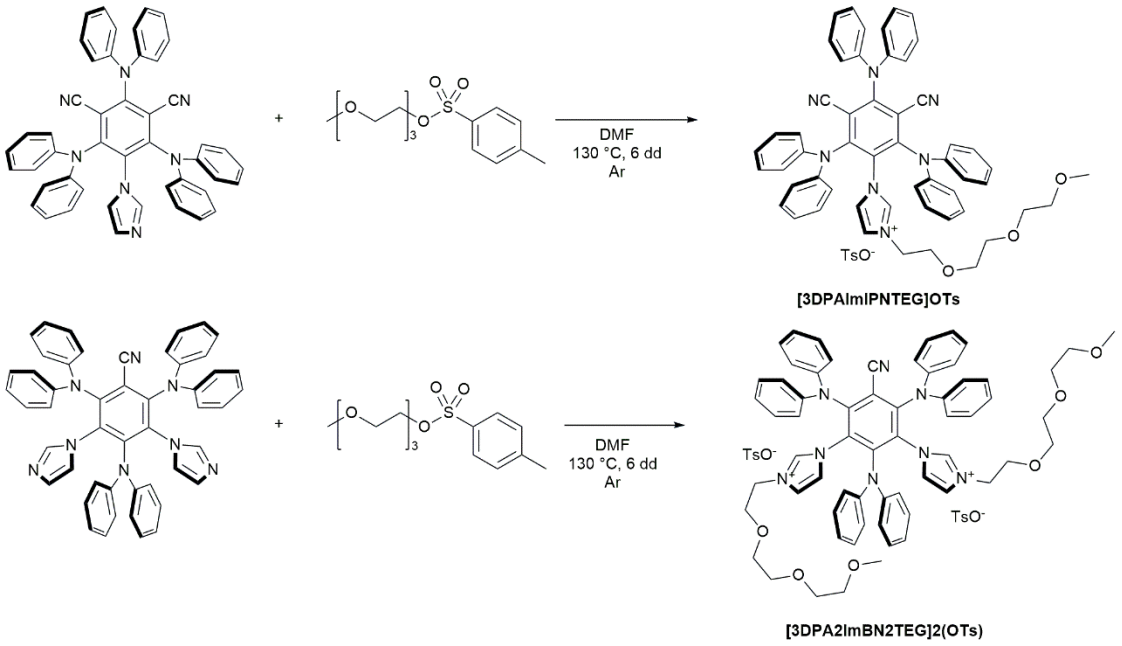


Figure 2.2: Comparison of ^{1}H NMR spectra of **3DPA2FBN** (red) and **3DPA2ImBN** (black) in the aromatic region.

The $^{13}C\{^{1}H\}$ spectra of **3DPAImIPN** and **3DPA2ImBN** are reported in **Figure A2.8-A2.9**.

Finally, the imidazole moieties are functionalized with 2-(2-(2-methoxyethoxy)ethoxy)ethyl 4-methylbenzenesulfonate at high temperature with DMF as solvent to obtain compounds **[3DPAImIPNTEG]OTs** and **[3DPA2ImBNTEG]2(OTs)** with low isolated yields (**Scheme 2.3)**.

Compound 2-(2-(2-methoxyethoxy)ethoxy)ethyl 4-methylbenzenesulfonate is chosen as alkylating agent for the high hydrophilicity of the chain, which enable the investigation of these compounds in aqueous solution, and for its easy synthesis, which require only one step in mild conditions.



Scheme 2.3: Synthesis of **[3DPAImIPNTEG]OTs** and **[3DPA2ImBNTEG]2(OTs)**.

The ^{1}H and $^{13}C\{^{1}H\}$ NMR spectra of **[3DPAImIPNTEG]OTs** is reported in **Figure A2.6-A2.10** while in **Figure 2.3** a comparison between ^{1}H NMR spectra of **3DPAImIPN** and **[3DPAImIPNTEG]OTs** is shown.

This comparison reveals that the aromatic signals maintain the spin system while imidazolium protons are shifted towards lower fields due to the quaternarization of the nitrogen atom.

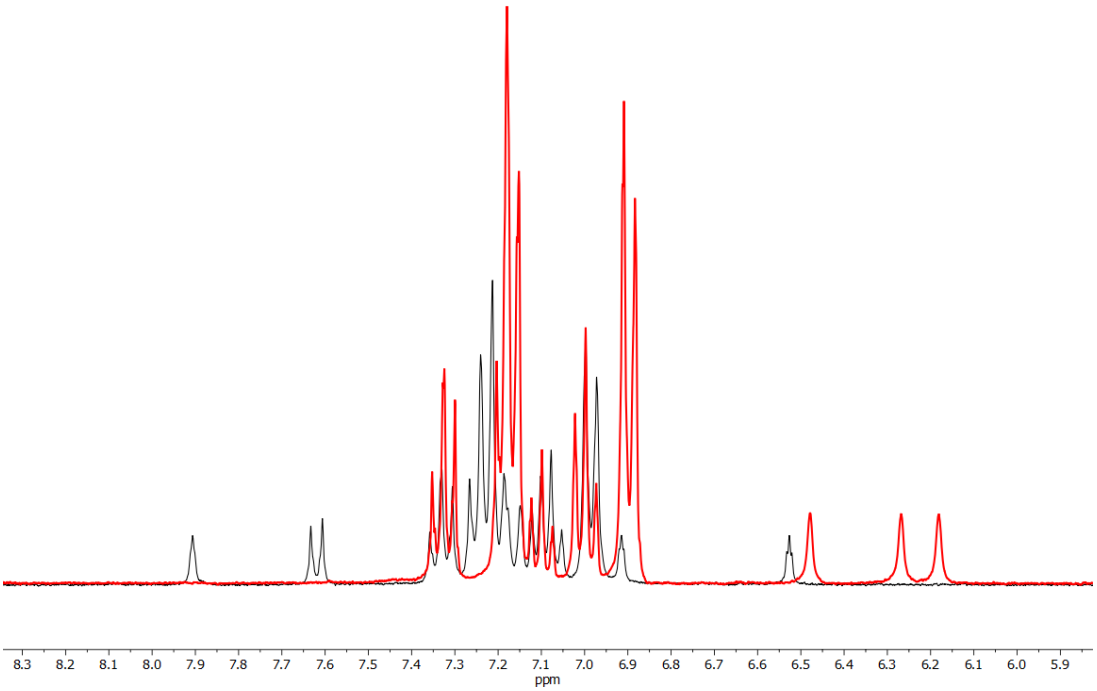


Figure 2.3: Comparison of ^{1}H NMR spectra of **3DPAImIPN** (red) and **[3DPAImIPNTEG]OTs** (black) in the aromatic region.

The ^{1}H and $^{13}C\{^{1}H\}$ NMR spectra of **[3DPA2Im2BNTEG]2(OTs)** are reported in **Figure A2.7-A2.11** and as for the monoimidazolium derivative the alkylation of imidazole shifts imidazolium protons towards lower fields.

2.2.2 Crystallographic characterization

Single crystals of compound **3DPA2ImBN**, suitable for X-ray diffractometric analysis, are grown by slow diffusion of diethylether vapors into chloroform and the XRD structure of the compound is shown in **Figure 2.4**.

This structure confirms the complete absence of fluorine atoms, corroborating the $^{19}F\{^{1}H\}$ NMR, the presence of the imidazole moieties in meta position and the presence of C-N bonds between imidazole moieties and phenyl ring.

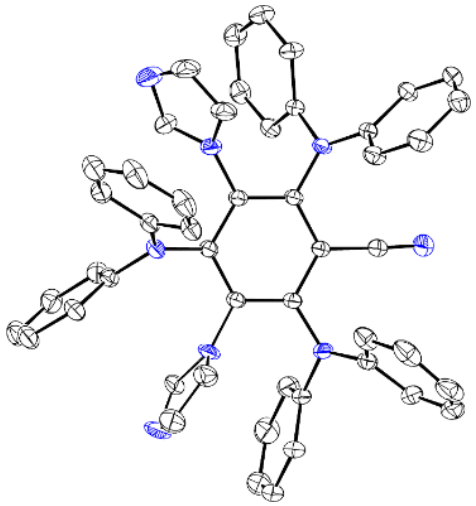


Figure 2.4: Ellipsoid representation of **3DPA2ImBN** asymmetric unit (A.S.U. – 50% probability). Hydrogens are omitted for clarity.

Furthermore, **3DPA2ImBN** crystallizes in a monoclinic centrosymmetric space group with one full molecule in the asymmetric unit. Intramolecular π•••π make the two imidazole rings not equivalent (i.e. only one is locked in a specific orientation) and force them to stack with adjacent phenyl rings (shortest $d_{\pi\cdots\pi} = 3.633(2)$ Å).

Crystal packing show layers of molecules parallel to ab cell face where nitrile group of one molecule stays almost perpendicular to core phenyl ring of a neighbor molecule ($d_{CN\cdots\pi} = 4.663(1)$ Å and $\Lambda_{CN\cdots\pi} = 82.4(1)°$).

Layers are linked by intermolecular CH•••π contacts (shortest one shows $d_{CH\cdots\pi} = 3.584(1)$ Å and $\Lambda_{CH\cdots\pi} = 66.0(1)°$).

2.2.3 Electrochemical characterization

The electrochemical properties of compounds **3DPAFIPN**, **3DPA2FBN**, **3DPAImIPN** and **3DPA2ImBN** are investigated in anhydrous acetonitrile by means of cyclic voltammetry and the voltammograms are depicted in **Figure 2.5**, while all the data are summarized in **Table 2.1**.

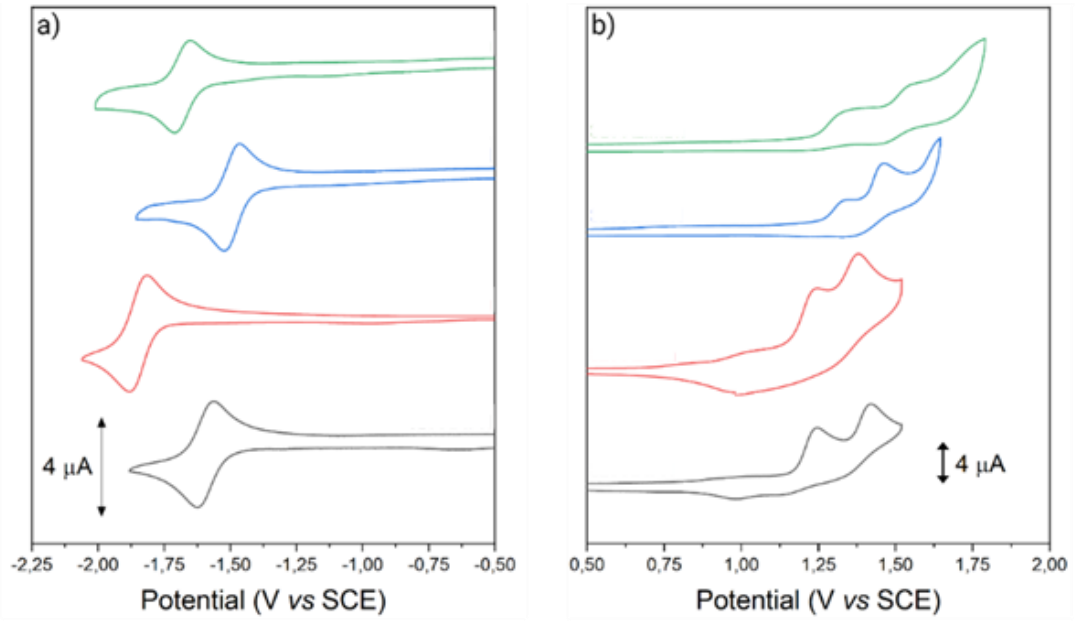


Figure 2.5: Cyclic voltammograms of **3DPAFIPN** (grey line), **3DPA2FBN** (red line), **3DPAImIPN** (blue line), and **3DPA2ImBN** (green line), highlighting the (a) cathodic and the (b) anodic regions.

Table 2.1: Electrochemical properties in acetonitrile solution of investigated compounds.

	3DPAFIPN	**3DPA2FBN**	**3DPAImIPN**	**3DPA2ImBN**
$E_{red}^{1/2}$ **(V)**	-1.59	-1.85	-1.49	-1.68
E_{ox}^{peak} **(V)**[a]	1.24	1.25	1.35	1.35

Measurements are performed in degassed acetonitrile solutions containing 1 mM luminophore and 0.1 M $TBAPF_6$ as the supporting electrolyte. The $Me_{10}Fc^{+}/Me_{10}Fc$ redox couple is used as internal standard. Working Electrode: Glassy Carbon Electrode (1 mm); Reference Electrode: quasi-reference Ag wire electrode; Counter Electrode: Pt wire. Scan rate: 100 mVs^{-1}. [a] Irreversible process, peak potentials are reported.

As these compounds exhibit twisted D-A structure, their HOMO and LUMO are spatially separated, so reduction and oxidation processes involve different moieties: donors for oxidation processes and acceptors for reduction processes.

In the cathodic region, according to the literature data[103], a single, reversible reduction process can be observed, which can be attributed to the formation of a radical-anion delocalized all over the cyanoarene accepting core. Furthermore, no electrochemical process ascribable to the imidazole moiety can be observed with this electrochemical window[134,135].

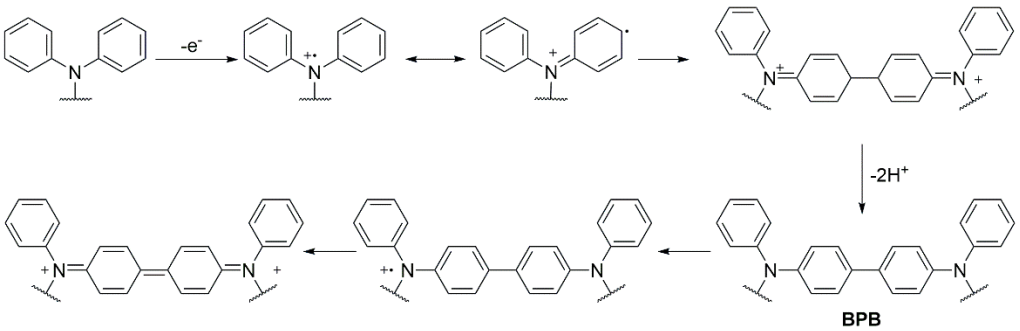
Looking at the half-wave potentials of reduction process, it can be noted that the compounds **3DPAFIPN** and **3DPAImIPN** are less reducing than their benzonitrile-based counterparts, a result in line with the literature data[90] and related to the acceptor strength of these core. Indeed, it is known that the cyano group is more electron-withdrawing than fluorine (σ_m are +0.678 and +0.337 respectively[136]) or imidazole.

Furthermore, by comparing fluorine and imidazole it can be observed that imidazole derivatives exhibit more anodic reduction processes than their fluorinated precursor, a shift that can be reconducted to a stronger σ-acceptor effect (or electron-withdrawing character) of imidazole, which

also possess a weaker π-donor effect, probably due to the fact that the lone pair of the imidazole nitrogen is not in conjugation with the benzene ring.

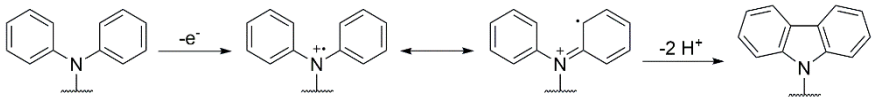
Conversely to the cathodic region, multiple irreversible oxidation processes of diphenylamine moieties can be observed in the anodic region.

These oxidation processes generate *N*-centered radical cations that are destabilized by the high spin density in *para* position which cause a chemical dimerization with the generation of a *N*,*N*'-biphenylbenzidine (BPB) derivatives (**Scheme 2.4**)[137–139].



Scheme 2.4: Mechanism of electrochemical oxidation of diphenylamine moieties.

Moreover, since the BPB product exhibits easier oxidation than diphenylamine, it cannot be excluded that other products, such as dimers or carbazoyl derivatives, are generated (**Scheme 2.5**), a hypothesis that might be corroborated by the presence of small peaks around +1 V vs SCE during the reverse scan, which are typical of these systems.



Scheme 2.5: Possible mechanism of diphenylamine electrooxidation to carbazole.

2.2.4 Photophysical characterization

As it is already known that the compounds **3DPAFIPN** and **3DPA2FBN** are TADF compounds and their photophysical investigation is not the scope of this **Chapter**, the only recorded data are their absorption and emission spectra (to investigate how the imidazole change their optical properties) and their PQLYs in acetonitrile solution.

For all the other compounds, UV-vis absorption spectra, PLQYs, emission and excitation spectra and PhotoLuminescence decay curves were recorded in acetonitrile and dichloromethane solution.

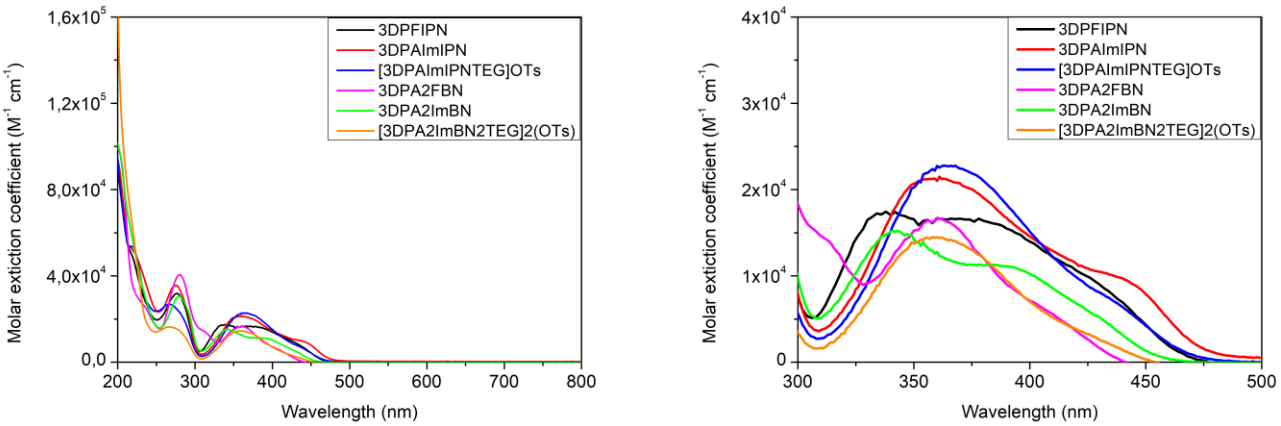


Figure 2.6: Absorption spectra in acetonitrile (left) and zoom of the region 300-500 nm (right).

In **Figure 2.6** UV-vis absorption spectra in acetonitrile are reported, while in **Table 2.2** absorption maxima of ICT region are reported.

In absorption spectra π*←π and σ*←n transitions cause the energy bands very high molar extinction coefficient values (from $5 \cdot 10^5$ to $2 \cdot 10^6$ M^{-1} cm^{-1}) in the region between 200 and 300 nm, while the Internal Charge Transfer (ICT) transitions between donor and acceptor cause the bands with broad profiles and lower molar extinction coefficients (around $2 \cdot 10^4$ M^{-1} cm^{-1}) in the region between 300 and 500 nm.

By comparing absorption spectra of **3DPAFIPN** and **3DPAImIPN** in acetonitrile, it can be observed that in the region between 200 and 300 nm there is a slightly different profile due to the presence of the imidazole. Furthermore, bigger changes are present in the ICT region, as the acceptor structure has changed. Indeed, the insertion of imidazole redshifts the maximum of about 30 nm and generate a shoulder near 440 nm, which can be due to a different conjugation on the acceptor, as donors are the same.

Conversely, the insertion of imidazole in the benzonitrile scaffold leads to bigger changes in the absorption spectra.

Indeed, by passing from **3DPA2FBN** to **3DPA2ImBN** to **[3DPA2ImBN2TEG]2(OTs)** a decrease in the band near 280 nm can be noted while in the ICT region the two-band profile is present for **3DPA2ImBN** but not for the alkylated one, which resembles the spectrum of the fluorinated precursor.

Regarding absorption spectra in dichloromethane (**Figure 2.7**), as expected they exhibit only slight blue-shifts in the ICT region, which are caused by the lower solvent polarity.

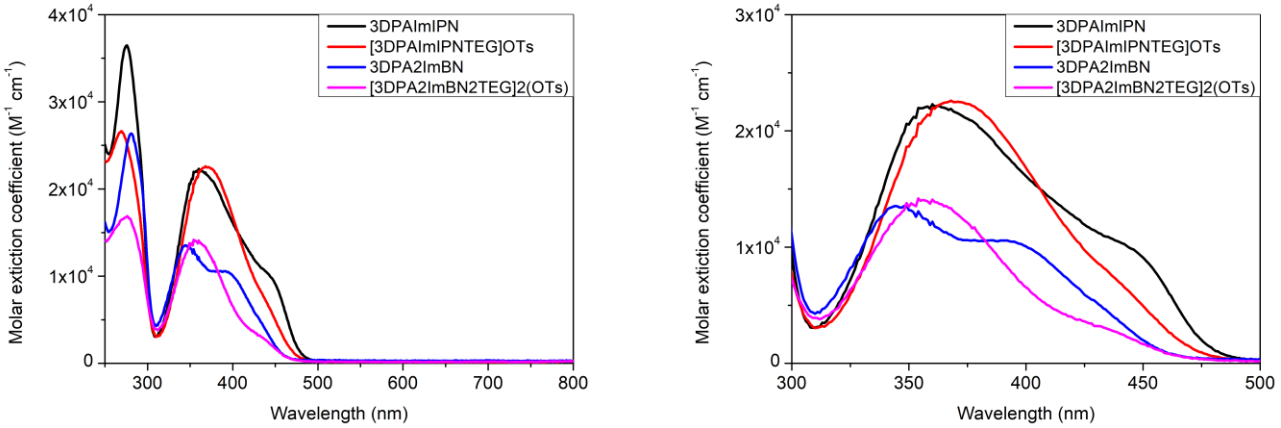


Figure 2.7: Absorption spectra in dichloromethane (left) and zoom of the region 300-500 nm (right).

Table 2.2: Photophysical properties of investigated compounds.

Compound	Solvent	λ_{abs} (nm)	λ_{em} (nm)[a]	Φ_{PL} (%)[b]	Φ_{PL} (%)[c]
3DPAFIPN	**ACN**	334	540	9±1	22±4
3DPAImIPN	**ACN**	361	544	11.3±0.3	32.5±0.8
	DCM	360, 440[sh]	520	10.2±0.5	30±2
[3DPAImIPNTEG]OTs	**ACN**	364	552	4.0±0.4	8.0±0.1
	DCM	369	550	5.7±0.8	17.4±0.8
3DPA2FBN	**ACN**	360	492	10±1	14±1
3DPA2ImBN	**ACN**	340	550	6.6±0.4	35.7±0.5
	DCM	346, 395[sh]	496	10.0±0.4	33.4±0.6
[3DPA2ImBN2TEG]2(OTs)	**ACN**	360	542	7.8±1.1	11.7±1.7
	DCM	356	462	9.7±0.8	14.6±0.9

Measurements are performed with 5 μM solution. [a] λ_{exc} = 340 - 364 nm. [b] Aerated solution, average scan, λ_{exc} = 300 - 410 nm. [c] Ar-purged solution, average scan, λ_{exc} = 300 - 410 nm.

To exclude the formation of excimers, excitation spectra were recorded (**Figure A2.12-2.13**) and for isophthalonitrile derivatives excimers can be ruled out, since absorption and excitation spectra are superimposable as for compound **[3DPA2ImBN2TEG]2(OTs)** in acetonitrile solution.

Conversely, absorption and excitation spectra of compound **3DPA2ImBN** in acetonitrile and dichloromethane are slightly different, since the excitation spectra show only one maximum while in absorption spectra two maxima are present.

This discrepancy, however, cannot be due to the high absorptivity of the sample, as molar extinction coefficients are the same of isophthalonitrile derivatives, nor to the presence of excimers, as excimers emissions are usually featureless and more red-shifted.

For these reasons the hypothesis is that other complicating factors step in for these two compounds.

The emission profiles of compounds are depicted in **Figure 2.8,** and they are characterized by broad emission and large Stokes shifts between absorption and emission maxima which are typical of donor-acceptor molecules[140].

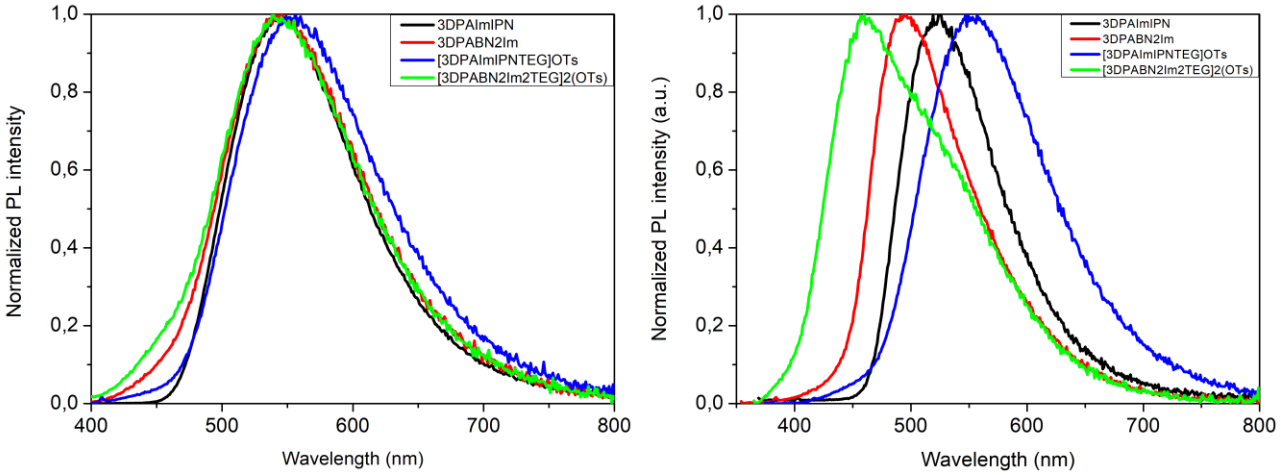


Figure 2.8: Normalized emission spectra in acetonitrile (left) and in dichloromethane (right).

Comparing isophthalonitrile derivatives, a small redshift in emission maxima (ca. 30 nm) can be observed passing from **3DPAFIPN** to **3DPAImIPN**, while the alkylation of the imidazole leads to a very small red-shift, a behavior that reflect a decrease in the HOMO-LUMO gap.

On contrast, in benzonitrile derivatives a big red-shift in emission maxima is present (ca. 60 nm) between **3DPA2FBN** and **3DPA2ImBN**, meaning that the HOMO-LUMO gap in these molecules is lowered in presence of imidazole, reflecting the electrochemical data.

When dichloromethane is used instead of acetonitrile, a solvatochromic effect can be observed, with an evident blue-shift for benzonitrile derivatives, which can be reconducted to the present of high dipole moments of their excited states that are better stabilized by more polar solvents[103,141].

All compounds show low PLQYs in aerated solution that increase upon removal of oxygen, a typical behavior of TADF molecules. The PLQY is also affected by the solvent polarity, that is also a typical feature of TADF, in particular imidazolium derivatives display an increase of the PLQY when solvent polarity is decreased.

By comparing **3DPAFIPN** and **3DPA2FBN**, a higher PLQY of the former can be found, in line with the fact that dicyanobenzene derivatives are acknowledged for enhancing the emission of TADF compounds by mitigating both non-radiative decay and geometric alterations between the ground and the excited state molecule[17,142]. The small fluorine atoms can reduce steric hindrance, thereby increasing the degrees of freedom of the diphenylamine, which favors non-radiative deactivation pathways of the excited state. Notably, an increase in photoluminescence quantum yields (PLQY) is observed going from fluorinated precursors to their imidazole derivatives. This is caused by the imidazole groups, which restrict phenyl rotations, thereby limiting non-radiative decays. Nevertheless, the introduction of flexible TEG chains onto the imidazole moiety reintroduces rotational and vibrational modes, which results in an increase in non-radiative decays and, consequently, a reduction in PLQYs.

The final confirmation of TADF properties however comes from time-resolved fluorescence spectroscopy (**Table 2.3** and **Figures A2.15-2.22**).

Indeed, in these curves bi-exponential profiles can be observed, which confirms that the spin upconversion from T_1 to S_1 states can occur at room temperature.

Table 2.3: Lifetimes of prompted and delayed fluorescence of investigated compounds.

Compound	Solvent	τ_P (ns)[a]	τ_D (µs)[a]	τ_P (ns)[b]	τ_D (µs)[b]
3DPAImIPN	**ACN**	5.18±0.01	0.83±0.03	5.65±0.01	49.6±0.3
	DCM	2.1±0.1 (B_1 5) 4.8±0.3 (B_2 2)	3.05±0.07	3.45±0.02	94.7±0.6
[3DPAImIPNTEG]OTs	**ACN**	2.73±0.02	0.25±0.02 (B_1 179) 2.21±0.02 (B_2 118)	2.91±0.02	15.4±0.1
	DCM	2.44±0.02 (B_1 52) 7.2±0.2 (B_2 4)	2.90±0.05	2.49±0.02 (B_1 0.051) 7.9±0.2 (B_2 0.004)	12.76±0.09
3DPA2ImBN	**ACN**	7.01±0.02	0.247±0.007 (B_1 247) 2.56±0.06 (B_2 46)	8.25±0.02	26.4±0.3
	DCM	2.49±0.02 (B_1 6) 9.21±0.06 (B_2 4)	4.7±0.2	2.73±0.02	82.8±0.7
[3DPA2ImBN2TEG]2(OTs)	**ACN**	6.22±0.06 (B_1 0.013) 16.5±0.2 (B_2 0.03)	10.5±0.2	5.8±0.1 (B_1 0.13) 11.0±0.3 (B_2 0.04)	19.6±0.4
	DCM	9.54±0.01	0.273±0.003	10.39±0.02	0.281±0.004

Measurements are performed with 5 µM solution. λ_{exc} = 402.3 nm, Nanosecond lifetimes are evaluated with TCSPC electronic, while microsecond lifetimes are evaluated with MCS electronic. [a] Aerated solution. [b] Ar-purged solution.

As expected, the presence of oxygen reduces the lifetimes of the delayed fluorescence contribution, as it interacts with the triplet states of compounds increasing non-radiative decays.

Furthermore, with the exception of **[3DPA2ImBN2TEG]2(OTs)** in dichloromethane, very long lifetimes can be found in deoxygenated solutions, in line with literature data.

These long lifetimes may be reconducted to a "large" ΔE_{ST} that decrease the rate constant of the RISC process[103,108].

In contrast, lifetimes of imidazolium derivatives are shorter than their imidazole precursors and decrease going from acetonitrile to dichloromethane. By combining their PLQYs values and lifetimes, the presence of narrower ΔE_{ST} that decrease delayed fluorescence lifetimes can be hypothesized.

Even prompted fluorescence lifetimes are shortened by the presence of oxygen due to interactions between triplet states of a dye and oxygen generate traces of singlet oxygen[143]. Nevertheless, the lifetimes are similar to that of deoxygenated solutions, corroborating the hypothesis that the enhancement of PLQYs is caused by a spin upconversion.

2.2.5 Electrochemiluminescence characterization

As already mentioned in **Chapter 1**, electrochemiluminescence can be generated from two different mechanisms, namely annihilation ECL and co-reactant ECL [2].

The electrochemiluminescence characterization of these molecules has been made by Prof. Giovanni Valenti's group at the University of Bologna.

ECL efficiencies are obtained under annihilation conditions and ECL spectroscopy has been investigated with the presence of benzoyl peroxide as co-reactant by the virtue of the high stability of radical-anions in these compounds[2,144].

Taking advantage of the high stability of radical-anions, a negative potential is initially applied, followed by an anodic one.

Although the scientific community is transitioning its effort from determining a relative ECL quantum yield to an absolute one, the goal of this Chapter is limited to investigate how variations in the D-A architecture impact the ECL emission of TADF emitters [25].

Annihilation-ECL efficiencies (**Equations 2.1-2.4**) and ECL emissions are evaluated only in degassed acetonitrile solutions, and they are reported in **Table 2.4**.

ECL-time and current-time curves are reported in **Figures A2.24-A2.27**.

$$TADF + e^- \rightarrow TADF^{\bullet -} \quad \textbf{(2.1)}$$

$$TADF - e^- \rightarrow TADF^{\bullet +} \quad \textbf{(2.2)}$$

$$TADF^{\bullet +} + TADF^{\bullet -} \rightarrow TADF^* + TADF \quad \textbf{(2.3)}$$

$$TADF^* \rightarrow h\nu + TADF \quad \textbf{(2.4)}$$

Table 2.4: Annihilation ECL efficiencies and ECL emission of compounds.

Compound	Applied potentials (V)	Φ_{ECL} [a]	λ_{ECL} (nm) [b]
3DPAFIPN	-1.7 to +1.35	0.0043	526
3DPAImIPN	-1.6 to +1.45	0.0082	534
3DPA2FBN	-1.9 to +1.35	0.0016	482
3DPA2ImBN	-1.7 to +1.45	0.01	514

Measurements are performed in degassed acetonitrile solutions containing 0.5 mM luminophore and 0.1 M $TBAPF_6$ as supporting electrolyte. WE: Glassy Carbon Electrode (1 mm); RE: quasi-reference Ag wire electrode; CE: Pt wire. [a] Φ_{ECL} determined under annihilation conditions according to **Equation 19**, $[Ru(bpy)_3](PF_6)_2$ as standard (Φ_{ECL} = 0.05). The ECL signal is normalized over the quantum efficiency of spectral response of the PMT at the wavelength of maximum ECL emission. [b] 0.5 mM solution in degassed ACN/$TBAPF_6$ 0.1 M/BPO 10 mM.

A primary consideration for achieving high ECL efficiencies is the energetic demand to populate the excited state, specifically the S-route and T-route.

As previously stated in **Chapter 1**, the S-route is followed when the energy of the annihilation energy is greater than the energy of the singlet state (**Equation 2.5**), which is the case for all derivatives under investigation.

$$E_{p(D/D^+)} - E_{p(A/A^-)} - 0.16 > \frac{1239}{\lambda_{em}(nm)} \quad \textbf{(2.5)}$$

Fluorine-substituted emitters display a notably low Φ_{ECL}, with a decrease from **3DPAFIPN** to **3DPA2FBN**, a behavior that is in line with Φ_{PL} of degassed solutions (22% and 14% respectively).
On the other hand, imidazole-substituted counterparts exhibit a generally higher Φ_{ECL} with **3DPA2ImBN** that surpasses **3DPAImIPN**, defying the previously observed trend with fluorine-substituted emitters.
The reversal of the trend suggests that the imidazole ring is an ancillary substituent not involved in the LUMO, which in turns enhances the charge transfer character of the excited state and leads to a progressively smaller ΔE_{ST} from **3DPAImIPN** to **3DPA2ImBN**.
This outcome is consistent with absorption spectra, lifetimes and cyclic voltammetries.
Indeed, in the absorption spectra only minimal shifts can be noted between imidazole precursors and their pegylated derivatives while Delayed Fluorescence lifetimes decrease from **3DPAImIPN** to **3DPA2ImBN**.
Furthermore, the reduction of the imidazole moiety cannot be observed in the investigated potential window.
Furthermore, by looking at the ECL profiles decreasing trends in ECL intensities during time can be observed for all compounds, which might be caused by the presence of degradation products.
Additionally, a robust ECL signal appears after the oxidation of the radical-anion species while a weaker ECL signal is present after the reduction of the radical-cation species.
These outcomes confirm the higher stability of radical-anions over radical-cations[145].
Interestingly, compound **3DPA2FBN** exhibits the opposite behavior, with a weak signal after the oxidation of the radical-anion species and robust signal after the reduction of the radical-cation species.
This observation is in conflict with the reversible reduction process of this compound and may be due to collateral reactions of the radical-anion.
ECL-voltage experiments are performed under reductive-oxidation conditions in presence of benzoyl peroxide (BPO) as co-reactant to provide insights into ECL behavior under steady radical generation.
Consistently with many other co-reactant ECL systems, the onset of light emission is situated in close proximity to the reduction potential of the luminophore.
Conversely, the reduction of BPO occurs at less cathodic potentials as evidenced by the voltammograms (**Figure 2.9**).

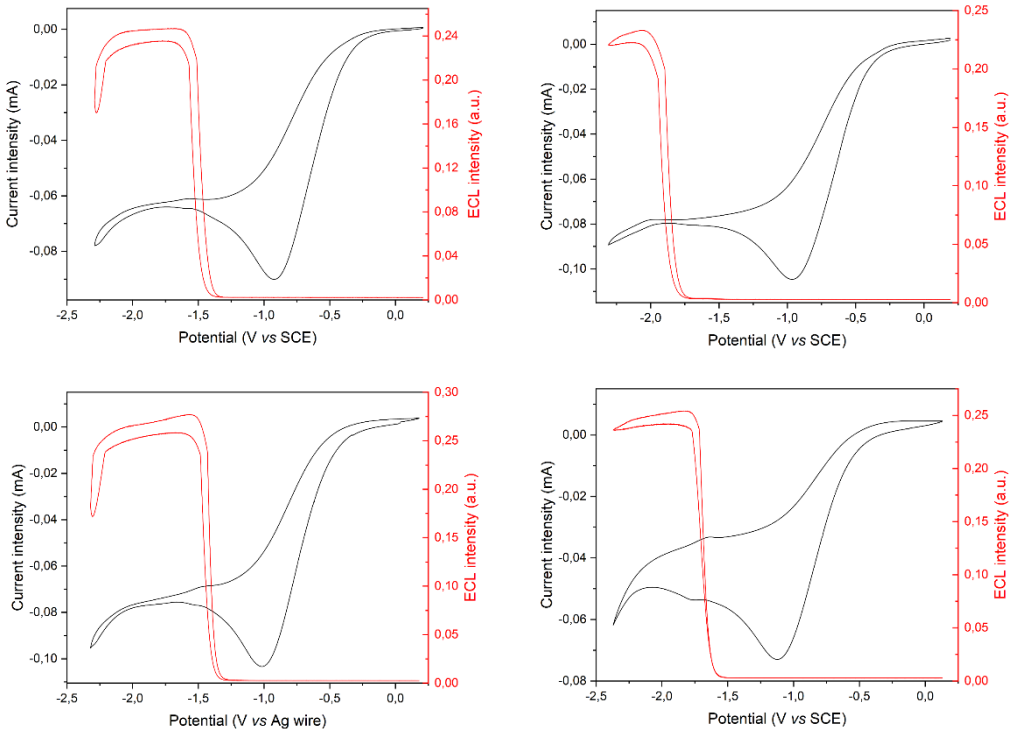


Figure 2.9: ECL-voltage curves of **3DPAFIPN** (upper left), **3DPA2FBN** (upper right), **3DPAImIPN** (lower left) and **3DPA2ImBN** (lower right) in acetonitrile with BPO as co-reactant.

As displayed in **Equations 2.6-2.9**, upon applying a suitable cathodic potential, the radical anions of both species are simultaneously generated. The reduced co-reactant rapidly decomposes into a benzoate anion ($PhCO_2^-$) and the strongly oxidizing benzoate radical ($PhCO_2^{\bullet}$, $E^o_{PhCO2\bullet/PhCO2-} > +1.5$ V *vs* SCE)[146]. This radical subsequently oxidizes the reduced luminophore, yielding its emitting excited state.

$$TADF + e^- \rightarrow TADF^{\bullet -} \quad \textbf{(2.6)}$$

$$BPO + e^- \rightarrow PhCO_2^{\bullet} + PhCO_2^- \quad \textbf{(2.7)}$$

$$TADF^{\bullet -} + PhCO_2^{\bullet} \rightarrow TADF^* + PhCO_2^- \quad \textbf{(2.8)}$$

$$TADF^* \rightarrow h\nu + TADF \quad \textbf{(2.9)}$$

ECL emissions (**Figure 2.10**) are comparable to PL emissions except for a little blue shift[69,111,147], which can be attributed to experimental factors, such as variations in slit width, different instrumentation and sample concentration between PL and ECL measurements.

The alignment between the ECL and PL emission maxima confirm that the implicated transitions are identical across both processes, thus precluding the formation of excimers.

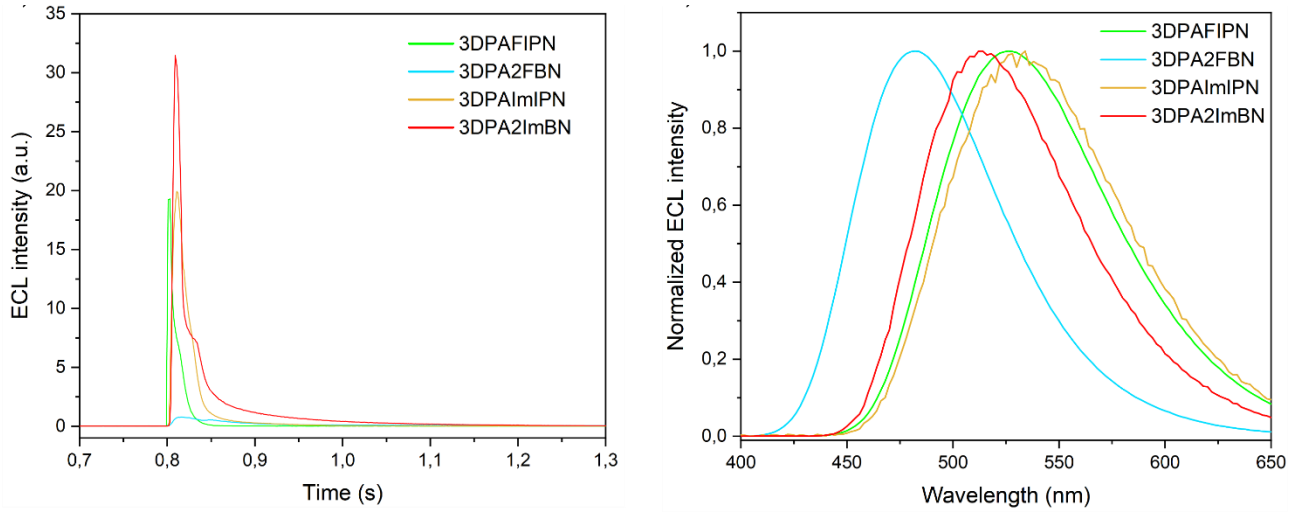


Figure 2.10: First peak of ECL-time intensity of annihilation experiments (left), ECL spectra (right).

2.2.6 Photophysical and electrochemiluminescence characterization of TADF emitters in aqueous solution

As previously stated in **Chapter 1**, all ECL-based sensors in bioanalytical chemistry employ aqueous environments to mimic physiological conditions and to preserve bioanalyte stability. The necessity to work in aqueous conditions is the rationale behind the incorporation of TEG chains into these compounds, thereby yielding the inaugural examples of water-soluble TADF molecules.

To confirm the TADF properties in water, lifetimes of compound **[3DPA2ImBN2TEG]2(OTs)** were evaluated by means of time-resolved fluorescence spectroscopy, which confirmed the presence of a delayed fluorescence contribution (**Table 2.5**).

Table 2.5: Photophysical properties of water-soluble TADF compound in water.

Compound	λ_{abs}	λ_{em} [a]	Φ_{PL} [b]	τ_P (ns)[c]	τ_D (µs)[c]
[3DPA2ImBN2TEG]2(OTs)	355	567	1.7±0.1	1.295±0.004	0.262±0.007

Measurements are performed with 5 µM solution. [a] λ_{exc} = 340 - 364 nm. [b] Aerated solution, average scan, λ_{exc} = 300 - 410 nm. [c] λ_{exc} = 402.3 nm. Lifetimes are evaluated in aerated solution. Nanosecond lifetimes are evaluated with TCSPC electronic, while microsecond lifetimes are evaluated with MCS electronic.

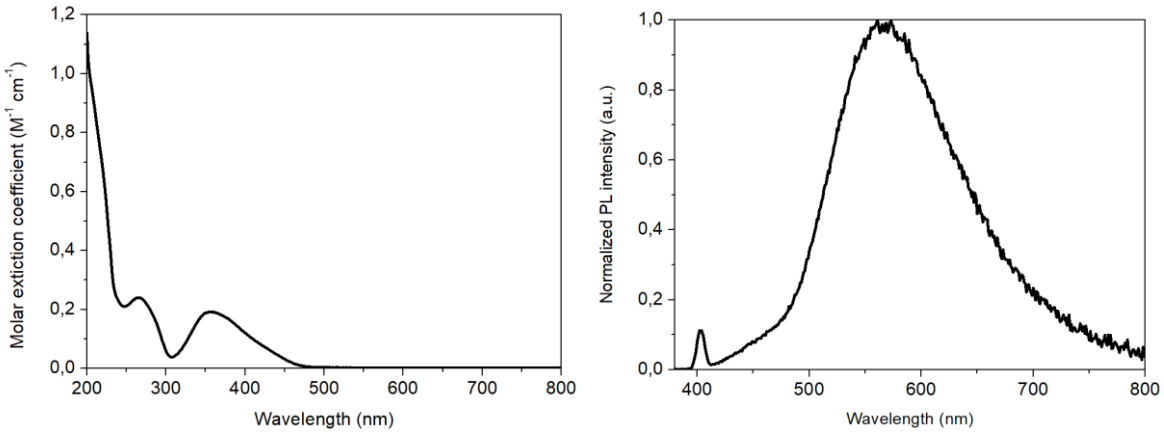


Figure 2.11: Absorption and emission spectra of **[3DPA2ImBN2TEG]2(OTs)** in water.

As expected, a redshift of the emission maximum is observed, along with a quenching of PLQY due to the high polarity of water.

Furthermore, a comparison between absorption and excitation spectra ruled out the presence of excimers.

As this compound exhibits a low PLQY in water, a similar value can be predicted for the compound **[3DPAImIPNTEG]OTs** and very low ECL yields can be predicted for both compounds.

The effectiveness of **[3DPAImIPNTEG]OTs** and **[3DPA2ImBN2TEG]2(OTs)** as ECL emitters is assessed with the aid of ECL-voltage measurements, that were performed using TPA as co-reactant in phosphate buffered solution (PBS) (**Figure 2.12**).

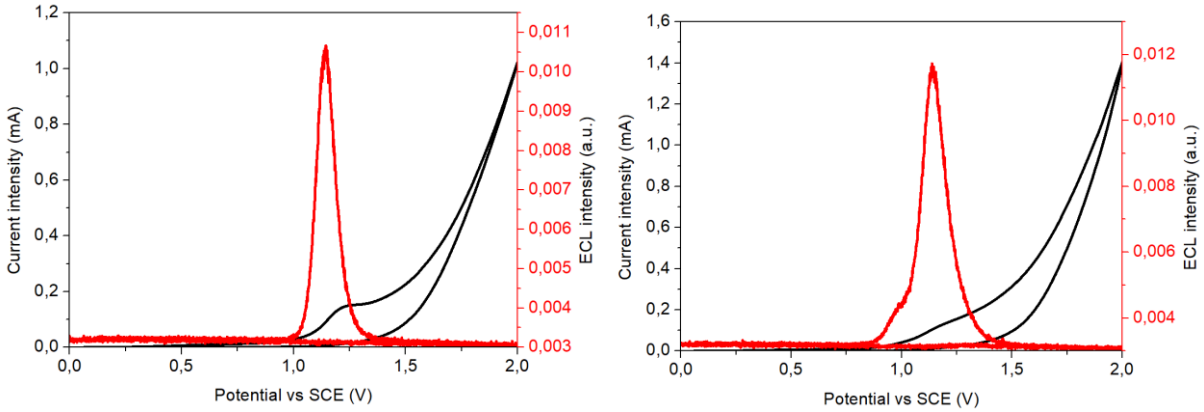


Figure 2.12: ECL-voltage profiles of compounds **[3DPAImIPNTEG]OTs** (left) and **[3DPA2ImBN2TEG]2(OTs)** (right) in Phosphate Buffered aqueous solution with TPA.

Both **[3DPA2ImBN2TEG]2(OTs)** and **[3DPAImIPNTEG]OTs** exhibit an ECL signal, with the former generating a more robust ECL signal than compound **[3DPAImIPNTEG]OTs**.

This outcome is in accordance with the previously observed trend in ECL efficiency for their non-water-soluble counterparts.

Unfortunately, the limited electrochemical window of water prevents the precise determination of the oxidation potentials of imidazolium derivatives. Nevertheless, if a minor effect of PEGylation on both molecules is assumed, their oxidation potentials likely remain comparable to their precursors.

Both compounds exhibit an intense ECL peak close to 1.2 V *vs* SCE, confirming that ECL signal is achieved upon annihilation reaction between the oxidized luminophore and the strongly reducing radical $TPA^{\bullet}$ (homogeneous ECL, **Equations 2.10-2.14**).

$$TPrA - e^- \rightarrow TPrA^{\bullet+} \quad \textbf{(2.10)}$$

$$TPrA^{\bullet+} - H^+ \rightarrow TPrA^{\bullet} \quad \textbf{(2.11)}$$

$$TADF - e^- \rightarrow TADF^{\bullet+} \quad \textbf{(2.12)}$$

$$TADF^{\bullet+} + TPrA^{\bullet} \rightarrow TADF^* + "waste" \quad \textbf{(2.13)}$$

$$TADF^* \rightarrow h\nu + TADF \quad \textbf{(2.14)}$$

While both samples display the homogeneous ECL peak, only the ECL curve of **[3DPA2ImBN2TEG]2(OTs)** exhibits a shoulder at less anodic potentials (ca. 0.9 V vs Ag/AgCl, the

potential at which TPA is oxidized) suggesting the presence of the "remote ECL" pathway (**Equations 2.15-2.17**)

$$TADF + TPrA^{\bullet} \rightarrow TADF^{\bullet -} + "waste" \quad \textbf{(2.15)}$$

$$TADF^{\bullet -} + TPrA^{\bullet +} \rightarrow TADF^{*} + TPrA \quad \textbf{(2.16)}$$

$$TADF^{*} \rightarrow h\nu + TADF \quad \textbf{(2.17)}$$

However, it is well-known in literature that the feasibility of the latter mechanism is limited to few cases, thus it seems reasonable to assume that the remote pathway is active for **[3DPA2ImBN2TEG]2(OTs)** but somehow forbidden for **[3DPAImIPNTEG]OTs**.

To elucidate the factors governing this behavior, a deeper understanding of the thermodynamics of the luminophore/TPA tandem system is crucial.

The first key requirement is that the luminophore reduction potential must be less cathodic than -1.7 V for homogeneous reduction to occur. In addition, the excess energy released by the annihilation reaction in **Equation 2.16** must be sufficient to overcome the HOMO-LUMO energy gap to achieve excitation This condition is described by **Equation 2.18**, which assumes to deal with reducible luminophores by $TPA^{\bullet}$, and the resulting change in free energy governs the feasibility of the remote mechanism.

$$\Delta G = E^{\circ}_{red} - E^{\circ}(TPrA^{\bullet +}) + E_{ES} \quad \textbf{(2.18)}$$

To evaluate the energy sufficiency of the remote ECL pathway for **[3DPA2ImBN2TEG]2(OTs)** and **[3DPAImIPNTEG]OTs**, E^{o}_{red} is considered as the half-wave reduction potential in acetonitrile of the parent molecules **3DPA2ImBN** and **3DPAImIPN**, assuming a minor influence from the PEGylation. $E^{o}_{(TPA^{\bullet +})}$ is set at 0.78 V *vs* SCE and the spectroscopic energy of the excited state [148,149] for **[3DPA2ImBN2TEG]2(OTs)** and **[3DPAImIPNTEG]OTs** is estimated with the ratio $1239/\lambda_{em}$ (nm). ΔG values for the bis- and monoimidazolium derivatives are positive, meaning that these processes should be thermodynamically unfavorable.

Nevertheless, remote ECL is observed for **[3DPA2ImBN2TEG]2(OTs)**, a discrepancy that likely arises from the approximation associated with using the reduction potentials of the parent molecules and from the difference in polarity between the environment used for E_{ES} estimation and for the actual ECL measurement.

2.3 Conclusions

In conclusion, in this **Chapter** novel imidazole and water-soluble imidazolium TADF derivatives synthesized starting from known TADF emitters with metal-free conditions have been reported.

Their photophysical and electrochemical properties has been investigated, finding that the insertion of imidazole increase PLQYs and decrease the reducing behavior of the acceptor core.

Conversely, the insertion of hydrophilic chains decreases PLQYs thus maintaining the TADF properties of these compounds.

ECL yields have been assessed under annihilation conditions, finding an increasing trend moving from fluorinated compounds to imidazole derivatives and going from benzonitrile and isophthalonitrile derivatives. Nevertheless, their ECL yields are lower than the standard $[Ru(bpy)_3]^{2+}$ due to the low stability of radical-cations.

It is of greater significance to note that the inaugural instances of oxidative-reduction ECL from water-soluble TADF emitters in water were reported by means of ECL-voltage experiments, and a remote ECL signal was evident for the compound **[3DPA2ImBN2TEG]2(OTs)**.

These finding marks a significant advancement in the study of ECL emitters as they demonstrate that water-soluble TADF emitters can be effectively synthesized and exhibit ECL emission in aqueous solutions. This suggests promising potential for these molecules as cost-effective alternatives to the established $[Ru(bpy)_3]^{2+}$, which is currently regarded as the gold standard for ECL emitters.

While the results were intriguing, certain factors may restrict the applicability of these scaffolds. For example, the imidazole moiety can be inserted efficiently only if diphenylamine is used as donor and after their insertion into the cyanoarene core.

In addition, from an electrochemical perspective, the primary challenge is the instability of radical-cations, which is known to be detrimental for achieving high ECL efficiencies.

2.4 Experimental section

All reagents, except 2-(2-(2-methoxyethoxy)ethoxy)ethyl 4-methylbenzenesulfonate (synthesized according to literature)[150] were used as received without further purification and they were obtained from Sigma-Aldrich.

All solvents, except those for photophysical measurements, were dried according to literature procedure[151] using 3Å molecular sieves purchased from Thermoscientific.

^{1}H and $^{13}C\{^{1}H\}$ NMR spectra were recorded on a Bruker AVANCE III spectrometer equipped with a BBO probe while ^{19}F NMR were recorded with a Bruker 200 MHz equipped with a QNP probe; ^{1}H and $^{13}C\{^{1}H\}$ NMR chemical shifts were referenced relative to residual solvents peaks while ^{19}F chemical shifts were referenced using indirect referencing[152].

NMR solvents were purchased from Sigma-Aldrich or EurisoTOP and dried with 3Å molecular sieves purchased from Merck.

Multiplicities of signals are reported as s (singlet), d (doublet), t (triplet), q (quartet), quint (quintet), m (multiplet) and combinations of these multiplicities, coupling constants J are reported in Hz, and if not stated otherwise refer to J_{HH} couplings.

HR-MS spectra were recorded on an Agilent Q-TOF equipped with an ESI source. Mass spectra were recorded in positive mode.

All reactions were monitored by thin-layer chromatography using Merck silica gel plates 60 F_{254} (plastic sheets) and spots were visualized with UV light or with iodine/silica staining.

Flash chromatography purifications were performed on a Combiflash Nextgen 300+ using Redisep Bronze column (4, 12, 24, 40 grams) filled with NP silica gel and using Redisep Rf cartridge (4 and 24 grams).

All samples were prepared in spectroscopic-grade Uvasol® acetonitrile and dichloromethane, that were used as received, with a $5 \cdot 10^{-6}$ M concentration.

2.4.1 Photophysical measurements

Absorption spectra were recorded with a Varian Cary 100bio UV-VIS spectrophotometer in 10 mm quartz cuvettes filled with non-degassed solution of investigated compounds.

Emission and excitation spectra were recorded with a Photoluminescence Spectrometer (Edinburgh Instruments, FLS1000) equipped with a 450 W Xe lamp and an air-cooled single-photon counting photomultiplier (Hamamatsu R13456). The solutions of investigated compounds, contained in a10 mm quartz cuvette, were bubbled with argon for 15 minutes prior measurements.

Absolute PhotoLuminescence Quantum Yields of solution were obtained with a Hamamatsu Absolute PL quantum yield spectrometer C11347 Quantaurus QY using a quartz tube filled with non-degassed or Ar-purged solutions of investigated compounds.

Lifetimes were obtained on a FLS1000 in Ar-purged or non-degassed solutions.

Time-resolved lifetime measurements were acquired on the FLS1000 spectrometer equipped with a picosecond laser diode at 402.3 nm. Luminescence decays were recorded using the Time correlated single photon counting (TCSPC) for lifetime in the nanosecond range, or the Multi-channel scaling (MCS) technique for lifetime in the microsecond range. The frequency of the laser was changed according to the lifetime of each sample.

Decay curves were analyzed with the Fluoracle Software using the IRF convolution fitting (for lifetime in ns range) or the tail-fitting for longer lifetimes.

2.4.2 Electrochemical and electrochemiluminescence measurements

The electrochemical characterization was performed using a SP-300 potentiostat (BioLogic Science Instrument, France) equipped with a conventional three-electrode system housed in a glass cell. The three-electrode system contained a glassy carbon working electrode (1 mm diameter), platinum wire counter electrode, and a silver wire quasi-reference electrode. Cyclic voltammograms were performed at a scan rate of 100 mVs^{-1} in anhydrous acetonitrile solutions containing 1 mM luminophore and 0.1 M $TBAPF_6$ as the supporting electrolyte. Before use, the glassy carbon electrode was polished using 0.3 and 0.05 mm alumina powder, sonicated in water, then rinsed with acetone, and eventually dried under Argon flux before use. Prior to analysis, solutions were deoxygenated by purging Argon until the current attributed to the oxygen reduction was negligible. The potentials are referenced to the SCE reference electrode by applying a -0.096 V correction factor to the potentials referenced to the $Me_{10}Fc^{+}/Me_{10}Fc$ redox couple[153]. All electrochemical experiments were carried out at room temperature.

The ECL emission is triggered by chronoamperometric pulses/cyclic voltammetry controlled by a SP-300 potentiostat (BioLogic Science Instrument, France). ECL measurements on purely organic molecules were conducted using a three-electrode system in anhydrous acetonitrile solutions containing 0.5 mM luminophore, 0.1 M $TBAPF_6$ as the supporting electrolyte, and 10 mM BPO when needed. On the other hand, ECL measurements on water-soluble emitters were carried out using the same three-electrode system in aqueous solutions containing 0.5 mM luminophore, 0.3 M PB as the supporting electrolyte, and 180 mM TPA. A platinum side-oriented disk (2 mm diameter) sealed in glass was employed as the working electrode. The counter electrode was a platinum spiral, while a quasi-reference silver wire was used as the reference electrode. These three-electrode system was placed in a one-compartment airtight cell, equipped with high-vacuum O-rings and glass stopcocks.

The cell, housed in a dark box, was carefully placed as close as possible the Hamamatsu R928 photomultiplier tube (PMT; Hamamatsu Photonics K.K., Japan), which was positioned in front of the working electrode. The ECL signal was collected by the PMT and amplified with a Keithley Model 6485 Picoammeter (Keithley Instruments Inc., United States).

The ECL quantum efficiency (Φ_{ECL}) was determined in annihilation conditions. This approach involved applying a square-wave voltage (1.25 Hz) in the diffusion-limited region (i.e., 100 mV past peak current) in anhydrous acetonitrile containing 0.1 M $TBAPF_6$. The Φ_{ECL} was then calculated relatively to the $[Ru(bpy)_3](PF_6)_2$ standard exploiting the following equation (**Equation 19**):

$$\Phi_{ECL,x} = \Phi_{ECL,st} \cdot \left(\frac{ECL_x}{ECL_{st}}\right) \cdot \left(\frac{Q_{st}}{Q_x}\right) \quad \textbf{(19)}$$

Where $\Phi_{ECL,st}$ is the ECL efficiency of the standard under the same conditions ($[Ru(bpy)_3](PF_6)_2$, $\Phi_{ECL} = 0.05$)[154], ECL_x and ECL_{st} are the integrated values of the first ECL emission peak of the given compound and the standard dye, respectively. The integrated ECL value is normalized over the quantum efficiency of spectral response of the PMT at the wavelength of maximum ECL emission. Q_x and Q_{st} are the integrated values of the faradaic current involved in the generation of the first ECL peak for the studied molecule and the standard luminophore, respectively.

2.4.4 XRD analysis – Structural characterization

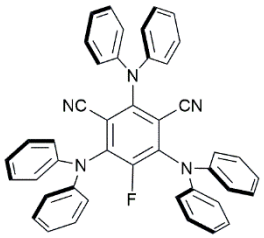
X-Ray diffraction data were collected at the XRD2 beamline of the Elettra Synchrotron, Trieste (Italy) [155]. The crystals were dipped in NHV oil (Jena Bioscience, Jena, Germany) and mounted on the goniometer head with kapton loops (MiTeGen, Ithaca, USA). Complete datasets were collected by the rotation method at 100 K (nitrogen stream supplied through an Oxford Cryostream 700). Data were acquired using monochromatic wavelength of 0.620 Å on a Pilatus 6M hybrid-pixel area detector (DECTRIS Ltd., Baden-Daettwil, Switzerland). Diffraction data were indexed, integrated and scaled using XDS[156]. Structures were solved by the dual space algorithm implemented in the SHELXT program[157]. Fourier analysis and refinement were performed by the full-matrix least-squares methods based on F^2 implemented in SHELXL (Version 2019/3)[158]. The Coot program was used for modeling[159]. Anisotropic thermal motion refinement was used for all atoms. Geometry parameters restrains (SAME and SADI) were applied to disordered fragments. Hydrogen atoms were included at calculated positions with isotropic $U_{factor} = 1.2 \cdot U_{eq}$ (U_{eq} being the equivalent isotropic thermal factor of the bonded non hydrogen atom). Crystals showed solvent molecules trapped into crystal voids. Electron density contribution that couldn't be modeled in **3DPA2ImBN** was removed with Platon SQUEEZE[160] routine. Estimated contributions of these regions (72 electrons in 204 $Å^3$)

are included in the reported crystal properties (**Table A1.1**) and correspond to 2 additional disordered dichloromethane molecules per unit cell. Pictures were prepared using Ortep-3[161] software.

3DPA2ImBN crystallizes in a monoclinic centrosymmetric space group with one full molecule in the asymmetric unit (ASU - **Figure A1.1**). Intramolecular π•••π make the two imidazole rings in **3DPA2ImBN** not equivalent (i.e. only one is locked in a specific orientation) and force them to stack with adjacent phenyl rings (shortest $d_{\pi\cdots\pi}$ = 3.633(2) Å). Crystal packing show layers of molecules parallel to ab cell face where nitrile group of one molecule stays almost perpendicular to core phenyl ring of a neighbor molecule ($d_{CN\cdots\pi}$ = 4.663(1) Å and $\Lambda_{CN\cdots\pi}$ = 82.4(1)°). Layers are linked by intermolecular CH•••π contacts (shortest one shows $d_{CH\cdots\pi}$ = 3.584(1) Å and $\Lambda_{CH\cdots\pi}$ = 66.0(1)°).

2.4.5 Synthesis route and procedures

2.4.5.1 Synthesis of 2,4,6-tris(diphenylamino)-5-fluoroisophthalonitrile (**3DPAFIPN**)

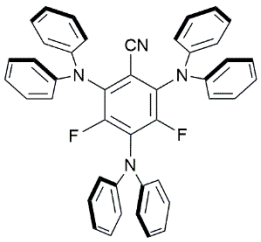


This compound was obtained using a literature method reported elsewhere[90].

^{1}H NMR (300 MHz, CD_3CN) δ 7.36 – 7.25 (m, 12H), 7.17 – 7.00 (m, 18H).

^{19}F NMR (188 MHz, d_6-DMSO) δ -122.15.

2.4.5.2 Synthesis of 2,4,6-tris(diphenylamino)-3,5-difluorobenzonitrile (**3DPA2FBN**)

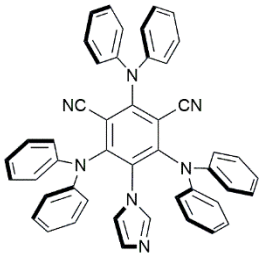


This compound was obtained using a literature method reported elsewhere[90].

^{1}H NMR (300 MHz, CD_3CN) δ 7.34 – 7.22 (m, 13H), 7.11 – 6.98 (m, 16H).

^{19}F NMR (188 MHz, d_6-DMSO) δ -122.15.

2.4.5.3 Synthesis of 2,4,6-tris(diphenylamino)-5-(1H-imidazol-1-yl)isophthalonitrile (**3DPAImIPN**)



To a solution of imidazole (0.5 mmol, 2 equivalents) in dry *N*,*N*-dimethylformamide (5 mL) stirred at room temperature under argon atmosphere, NaH (60% in mineral oil, 0.4 mmol, 1.6 equivalents) was added.

After 25 minutes 2,4,6-tris(diphenylamino)-5-fluoroisophthalonitrile (0.25 mmol, 1 equivalent) is added and the temperature is raised to 70 °C. The solution turned dark green.

After 18 hours, water (1 mL) was added to quench the reaction.

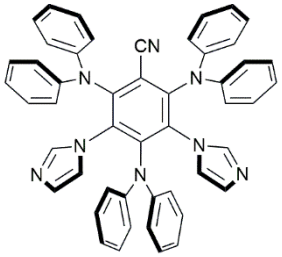
The solvent was then evaporated, the mixture extracted three times with dichloromethane, the organic phase dried with sodium sulphate and the solvent was evaporated to give a dark green crude product. The product was obtained as a yellow solid (0.23 mmol, yield 92%) after flash chromatography (SiO_2, dichloromethane:methanol, from 10:0 to 9:1).

^{1}H NMR (300 MHz, CD_3CN) δ 7.40 – 7.28 (m, 4H), 7.24 – 7.14 (m, 12H), 7.10 (td, *J* = 7.2, 1.2 Hz, 2H), 7.05 – 6.95 (m, 4H), 6.95 – 6.84 (m, 8H), 6.48 (s, 1H), 6.27 (s, 1H), 6.18 (s, 1H).

^{13}C{^{1}H} NMR (75 MHz, CD_3CN) δ 156.41, 154.36, 146.35, 145.79, 137.39, 133.55, 130.42, 130.16, 129.29, 125.35, 124.83, 124.07, 123.05, 113.94, 112.22.

HR-MS (m/z) Calculated: 696.2870 ($[M+H]^+$); Found: 696.2946 ($[M+H]^+$).

2.4.5.4 Synthesis of 2,4,6-tris(diphenylamino)-3,5-di(1H-imidazol-1-yl)benzonitrile (**3DPA2ImBN**)



To a solution of imidazole (1.16 mmol, 2.9 equivalents) in dry *N*,*N*-dimethylformamide (10 mL) stirred at room temperature under argon atmosphere, NaH (60% in mineral oil, 1.3 mmol, 3.3 equivalents) was added.

After 25 minutes 2,4,6-tris(diphenylamino)-3,5-difluorobenzonitrile (0.4 mmol, 1 equivalent) is added and the temperature is raised to 70 °C. The solution turned dark green. After the complete substitution of fluorine atoms (at least 24 h) water (1 mL) was added to quench the reaction. The solvent was then evaporated, the mixture extracted three times with dichloromethane, the organic phase dried with sodium sulphate and the solvent was evaporated to give a dark green solid.

The product was obtained as a yellow solid (0.23 mmol, yield 92%) after flash chromatography (SiO_2, dichloromethane:methanol, from 10:0 to 9:1).

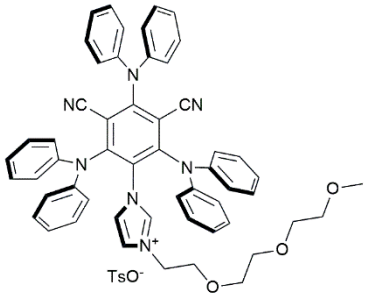
^{1}H NMR (300 MHz, CD_3CN) δ 7.29 – 7.16 (m, 4H), 7.14 – 6.95 (m, 4H), 7.01 – 6.86 (m, 5H), 6.79 – 6.69 (m, 2H), 6.39 – 6.27 (m, 3H).

$^{13}C\{^{1}H\}$ NMR (75 MHz, CD_3CN) δ 151.18, 150.11, 146.22, 146.12, 137.38, 136.32, 130.26, 130.01, 128.92, 124.41, 124.27, 122.58, 122.28, 120.34, 114.59.

HR-MS (m/z) Calculated: 737.3136 ($[M+H]^+$); Found: 737.3199 ($[M+H]^+$).

Suitable crystals for SC-XRD were obtained from slow diffusion of diethylether in chloroform.

2.4.5.5 Synthesis of 1-(3,5-dicyano-2,4,6-tris(diphenylamino)phenyl)-3-(2-(2-(2-methoxyethoxy)ethoxy)ethyl)-1H-imidazol-3-ium 4-methylbenzenesulfonate **([3DPAImIPNTEG]OTs)**



A solution of 2,4,6(diphenylamino)-5-(1*H*-imidazol-1-yl)isophthalonitrile (0.14 mmol, 1 equivalent) and 2-(2-(2-methoxyethoxy)ethoxy)ethyl 4-methylbenzenesulfonate (0.7 mmol, 5 equivalents) in dry *N*,*N*-dimethylformamide (10 mL) was stirred at 130 °C under argon atmosphere.

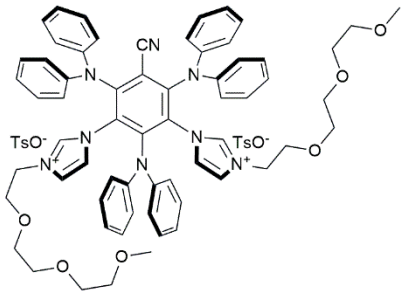
After 6 days the solvent was evaporated and the product was obtained as a yellow solid (0.06 mmol, yield 43%) after flash chromatography (SiO_2, dichloromethane:methanol, from 10:0 to 9:1).

^{1}H NMR (300 MHz, CD_3CN) δ 7.91 (s, 1H), 7.62 (d, J = 8.1 Hz, 2H), 7.39 – 6.88 (m, 32H), 6.53 (s, 1H), 3.81 – 3.72 (m, 2H), 3.59 – 3.37 (m, 8H), 3.42 – 3.25 (m, 2H), 3.23 (s, 3H), 2.34 (s, 2H).

$^{13}C\{^{1}H\}$ NMR (75 MHz, CD_3CN) δ 154.10, 146.35, 145.61, 138.61, 130.70, 130.53, 129.24, 127.02, 126.69, 125.90, 125.85, 125.00, 124.59, 124.23, 124.02, 113.46, 110.07, 72.51, 70.93, 70.89, 70.60, 68.38, 58.86, 50.41, 21.23, 2.09.

HR-MS (m/z) Calculated: 842.3813 ($[M]^+$); Found: 842.3904 ($[M]^+$).

2.4.5.6 Synthesis of 1,1'-(5-cyano-2,4,6-tris(diphenylamino)-1,3-phenylene)bis(3-(2-(2-(2-methoxyethoxy)ethoxy)ethyl)-1H-imidazol-3-ium) bis(4-methylbenzenesulfonate) **([3DPA2ImBN2TEG]2(OTs))**



A solution of 2,4,6(diphenylamino)-3,5-di(1*H*-imidazol-1-yl)benzonitrile (0.14 mmol, 1 equivalent) and 2-(2-(2-methoxyethoxy)ethoxy)ethyl 4-methylbenzenesulfonate (0.7 mmol, 5 equivalents) in dry *N*,*N*-dimethylformamide (10 mL) was stirred at 130 °C under argon atmosphere.

After 6 days the solvent was evaporated and the product was obtained as a yellow solid (0.05 mmol, yield 36%) after flash chromatography (SiO_2, dichloromethane:methanol, from 10:0 to 9:1).

^{1}H NMR (300 MHz, Acetone-d_6) δ 8.88 (s, 1H), 8.37 (s, 1H), 7.89 – 7.80 (m, 5H), 7.37 – 7.09 (m, 38H), 7.00 (td, J = 7.3, 6.6, 5.1 Hz, 9H), 6.63 (s, 1H), 4.07 – 3.99 (m, 5H), 3.66 (s, 6H), 3.52 (dd, J = 5.7, 3.6 Hz, 5H), 3.39 (h, J = 5.2, 4.2 Hz, 20H), 3.22 (s, 8H), 2.37 (s, 8H).

^{13}C{^{1}H} NMR (75 MHz, Acetone-d_6) δ 153.58, 150.13, 147.31, 146.88, 146.47, 146.03, 140.02, 139.70, 139.10, 131.05, 130.75, 130.47, 130.36, 129.98, 129.12, 128.90, 127.13, 125.80, 125.47, 125.31, 125.17, 125.07, 124.33, 124.29, 124.12, 123.68, 123.44, 123.33, 123.09, 122.85, 122.09, 113.49, 112.14, 72.64, 71.07, 70.99, 70.93, 70.89, 68.84, 58.93, 50.50.

HR-MS (m/z) Calculated: 515.25472 ($[M]^+$); Found: 515.2612 ($[M]^+$).

3. NOVEL MONOIMIDAZOLE TADF DYES AS ELECTROCHEMILUMINESCENT EMITTERS

Giulio Pavan, Luca Morgan, Nicola Demitri, Chiara Alberoni, Thomas Scattolin and Alessandro Aliprandi. *Chem. – Eur. J.*, 2023, **29**(55), e202301912
https://doi.org/10.1002/chem.202301912

3.1 Introduction

In **Chapter 2** the characterization of novel TADF dyes as ECL emitters incorporating an imidazole moiety was presented and discussed. Additionally, the first examples of water-soluble TADF dyes were reported along with a preliminary ECL investigation of them in an aqueous media.

As outlined in the **Conclusions** of **Chapter 2**, these molecules exhibit certain limitations, such as the instability of radical-cations and the restriction to diphenylamine as donor. Indeed, the strategy reported in **Chapter 2** is based on the substitution of the fluorine atoms of 2,3,4,5,6-pentafluorobenzonitrile and tetrafluoroisophthalonitrile with diphenylamine and the subsequent incorporation of imidazole groups.

Nevertheless, this strategy cannot be used efficiently for other donors such as the carbazole-based ones since it is known that they will substitute all the fluorine atoms,[85,90,103] thereby preventing the subsequent insertion of imidazole groups.

To circumvent this problem, the insertion of the imidazole group must be performed previous than the donor insertion.

The insertion of a single imidazole group in compound 2,3,4,5,6-pentafluorobenzonitrile has been already reported in literature [162] and the resulting monoimidazole derivative represents an interesting acceptor. Indeed, it can be then kept fixed while systematically varying the donor moieties, thereby yielding a family of novel monoimidazole emitters that exhibit TADF properties.

In the present **Chapter**, the synthesis and characterization of these novel monoimidazole emitters in organic solvents are presented. The aim is to correlate their photophysical and electrochemical properties with their performances in ECL, which are assessed under annihilation, oxidative-reduction and reductive-oxidation conditions.

Furthermore, the presence of a single imidazole moiety is a very valuable feature in an ECL emitters, as it can be functionalized with a single bioconjugable group which can be in turn attached to a specific site of the immunoassay's antibody.

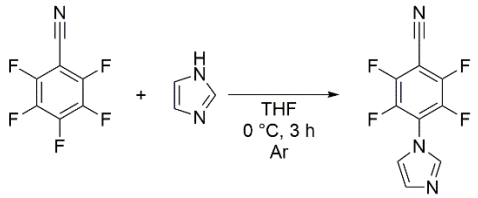
For this reason, the alkylation of the imidazole moiety is conducted with a hydrophilic chain bearing a *tert*-butyl ester group, the protected form of a valuable bioconjugable group.

3.2 Results and discussion

3.2.1 Synthesis

The compounds that will be discussed in this **Chapter** are based on benzonitrile acceptor, which is substituted with imidazole to obtain compound **4FBNIm** following a slightly modified literature procedure[162] (**Scheme 3.1**).

In this reaction the imidazole fulfills two distinct purposes of both reactant and scavenger, thus it is used in excess. In order to increase the stereoselectivity in para position and avoid over functionalization, the temperature is kept around 0 °C.



Scheme 3.1: Synthesis of the compound **4FBNIm**.

The formation of the para-substituted isomer is confirmed by $^{19}F\{^{1}H\}$ NMR (**Figure 3.1**), which reveals the characteristics signals of an AA'BB' spin system of para-disubstituted benzenes, in accordance with the literature data[162].

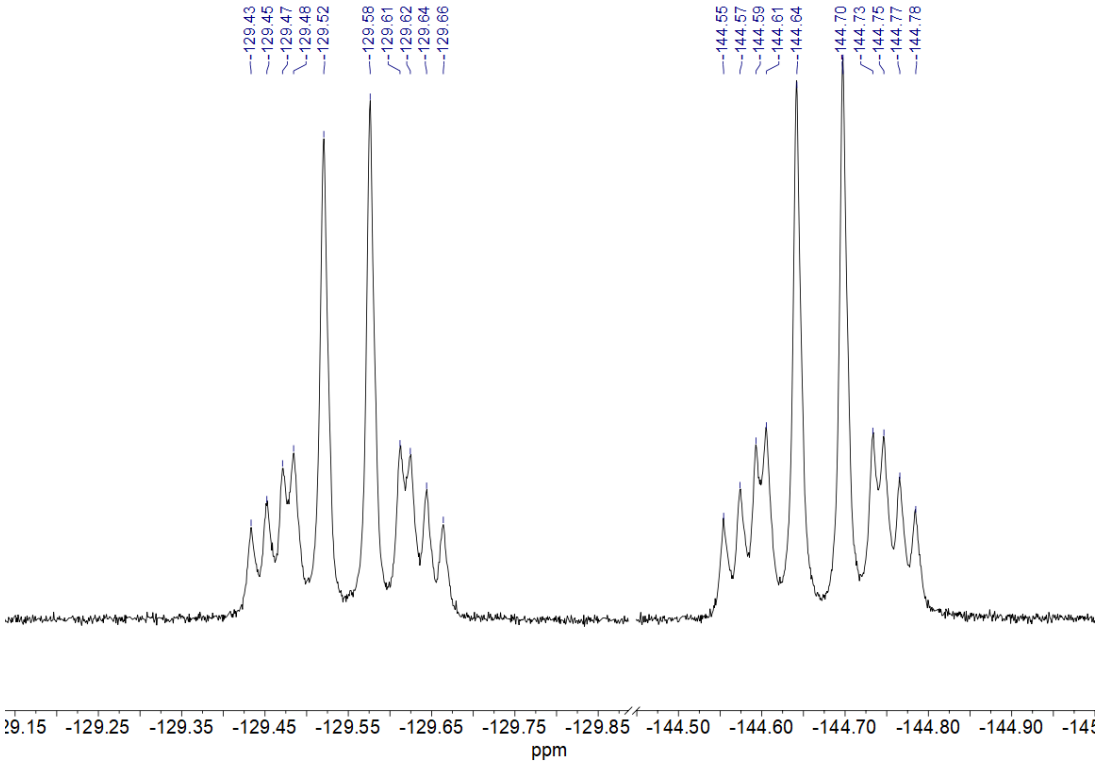


Figure 3.1: $^{19}F\{^{1}H\}$ NMR of the compound **4FBNIm**.

Conversely, the multiplicity of the aromatic proton signals differs slightly from those reported by Fujii *et al.*[162] due to a lower operating frequency of their NMR spectrometer. In addition, imidazole

proton signals exhibit both ^{1}H-^{1}H scalar couplings and ^{1}H-^{19}F scalar couplings/dipolar interactions, which generate a complex system (**Figure 3.2**).

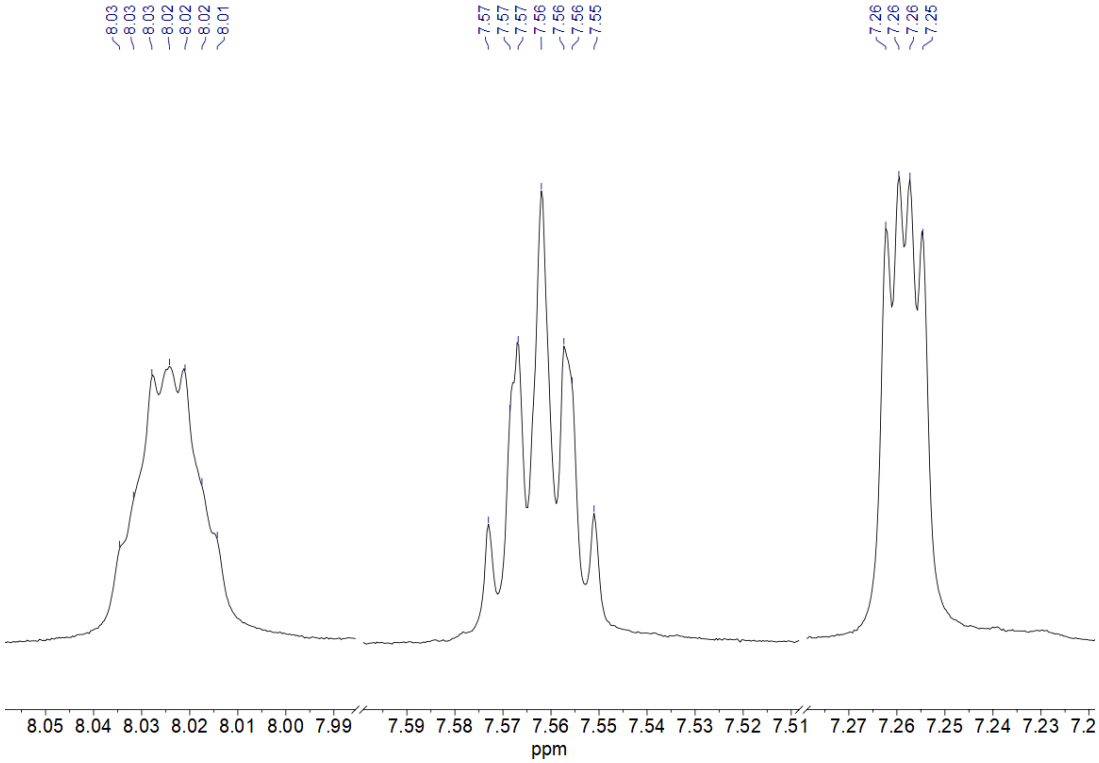
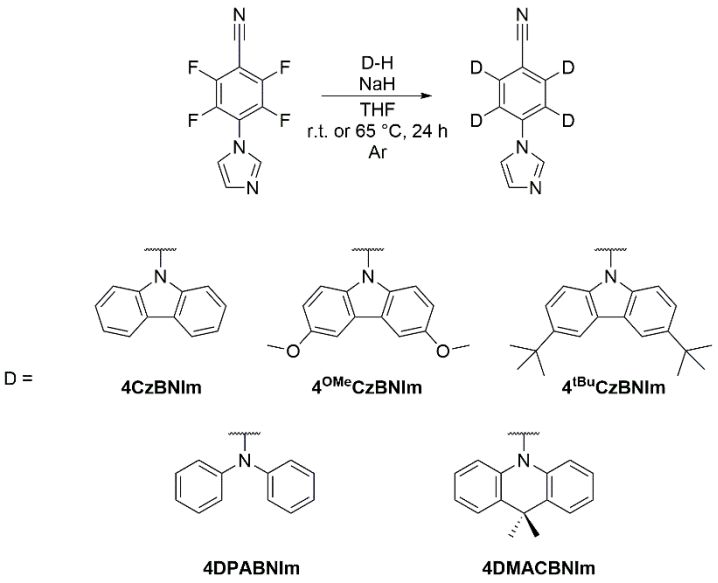


Figure 3.2: Aromatic region of ^{1}H NMR spectrum of the compound **4FBNIm**.

Afterwards, by simple nucleophilic aromatic substitution, all the remaining fluorine atoms are substituted with different donors in presence of sodium hydride as strong base (**Scheme 3.2**) to obtain products in good to quantitative isolated yields.



Scheme 3.2: Syntheses of monoimidazole derivatives.

The insertion of carbazole-based donors occurs at room temperature due to their low steric hindrance and basicity (pK_a = 20 in DMSO[133]). For diphenylamine and 9,9'-dimethyl-9,10-dihydroacridine higher temperatures (65 °C) are required to facilitate the complete substitution of all fluorine atoms.

In all instances, the substitution of all fluorine atoms was confirmed by $^{19}F\{^1H\}$ NMR spectroscopy. ^1H NMR and $^{13}C\{^1H\}$ NMR spectra of compounds are reported in **Figures A3.4-A3.16**.

In the ^1H NMR spectra of compounds **4^{tBu}CzBNIm** and **4^{OMe}CzBNIm** two singlets are observed, which can be attributed to the protons of the *tert*-butyl groups or methoxy groups (**Figure3.3-left and center**).

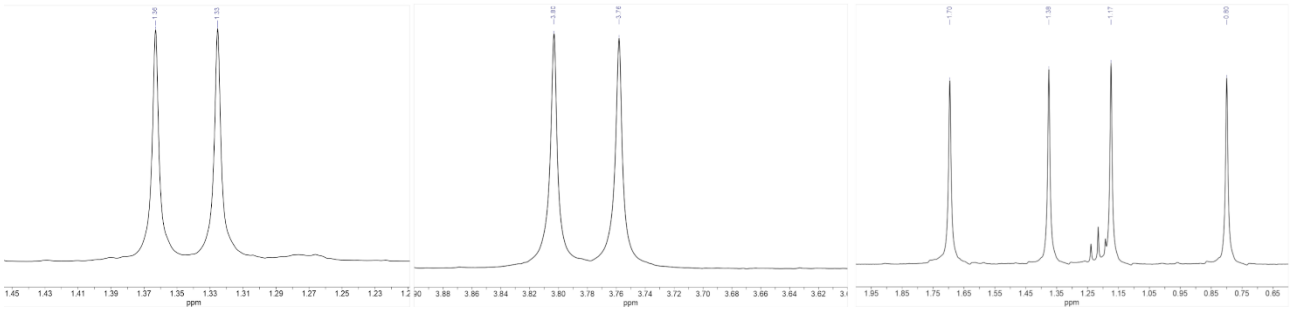
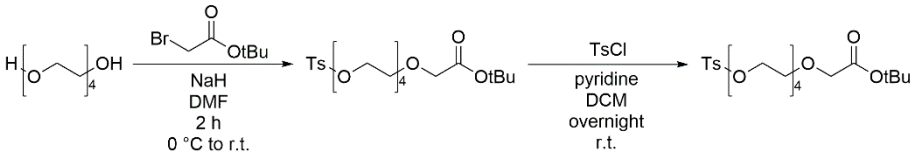


Figure 3.3: Methyl proton signals of the compounds **4^{tBu}CzBNIm** (left), **4^{OMe}CzBNIm** (center) and **4DMACBNIm** (left).

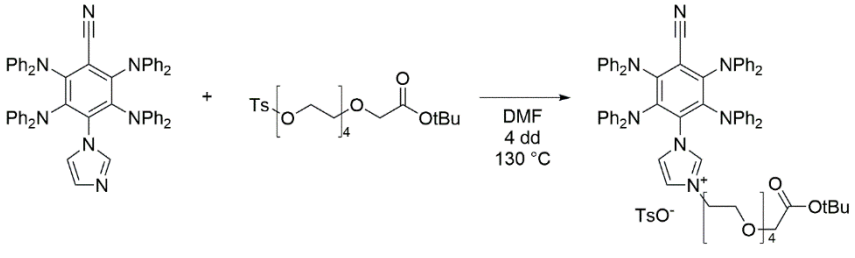
Indeed, these protons resonate at different frequencies due to their proximity to two distinct substituents (cyano and imidazole groups), making them magnetically non-equivalent.

The same behavior is evident in the methyl protons of **4DMACBNIm**, which generate four different singlets (**Figure 3.3-right**).

Finally, with the aim of obtaining a water-soluble TADF emitter with a bioconjugable terminal group, the alkylation of **4DPABNIm** with compound **TsOTEGCOOtBu** (which synthesis is reported in **Scheme 3.3**) is performed at high temperature in *N*,*N*-dimethylformamide to obtain the imidazolium derivative **[4DPABNImTEGCOOtBu]OTs** with good isolated yield.



Scheme 3.3: Synthesis of **TsOTEGCOOtBu**.



[4DPABNImTEGCOOtBu]OTs

Scheme 3.4: Synthesis of **[4DPABNImTEGCOOtBu]OTs**.

^1H NMR and $^{13}C\{^1H\}$ NMR spectra of **[4DPABNImTEGCOOtBu]OTs** are reported in **Figures A3.10-3.17**.

3.2.2 Crystallographic characterization

Single crystals of monoimidazole compounds, suitable for X-ray diffractometric analysis, are grown by slow diffusion of diethyl ether, methanol or n-hexane vapors into chloroform, dichloromethane or *N*,*N*-dimethylformamide (see the **Experimental Section**).

XRD structures of monoimidazole compounds are shown in **Figure 3.4** and confirm the presence of imidazole moiety in the para position and the substitution of all fluorine atoms.

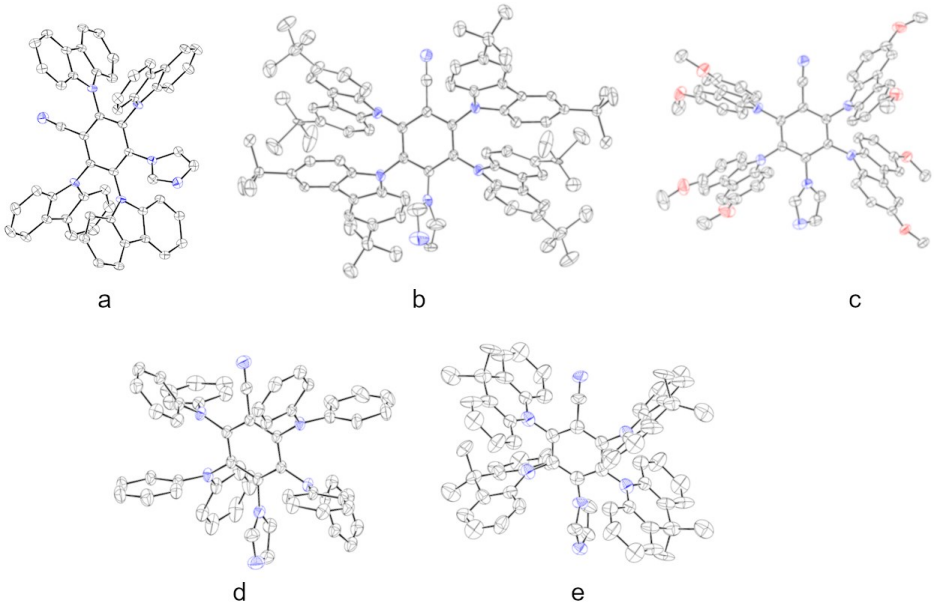


Figure 3.4: Ellipsoid representation of **4CzBNIm** (a), **4^{tBu}CzBNIm** (b), **4^{OMe}CzBNIm** (c), **4DPABNIm** (d) and **4DMACBNIm** (e) asymmetric units (A.S.U. – 50% probability). Hydrogens are omitted for clarity.

Compounds crystallized in centrosymmetric space groups with one full molecule in the asymmetric units (ASU) for **4CzBNIm** (100 K), **4DPABNIm** (100 K), **4DPABNIm** (298 K) and **4^{OMe}CzBNIm** (100 K), adopting a well-defined conformation (**Figure 3.5**). **4^{tBu}CzBNIm** (polymorph a, 100 K), **4^{tBu}CzBNIm** (polymorph a, 298 K), **4^{tBu}CzBNIm** (polymorph b, 298 K), **4DMACBNIm** (100 K) and **4DMACBNIm** (298 K) molecules lies on crystallographic symmetry elements and show static disorder on the polar cyano and imidazolyl heads, suggesting that packed molecules are not forming very strong and specific contacts (i.e. loose and flexible non-covalent interactions, with solvent molecules, are present). Despite the disorder, all the crystal structures are consistent with the expected molecular connectivity; representative models (without disorder) are shown in **Figure A3.1**. Bulky carbazole, diphenylamine and 9,9'-dimethyl-9,10-dihydroacridine sidechains and imidazole ring stay almost perpendicular to the benzonitrile core, despite some degree of freedom is available. Flexibility of sidechains respect to the benzonitrile common scaffold is measured through angles reported in **Table 3.1**, while in **Figure 3.5** an overlap of representative molecules is shown. 9,9'-dimethyl-9,10-dihydroacridine sidechains in the **4DMACBNIm** cubic crystals are adopting multiple conformations with a statistically homogeneous distribution of planar and crooked forms.

Interestingly, in all cases the imidazole ring is almost orthogonal to the benzonitrile ring, thus suggesting a poor orbital overlap.

Table 3.1: Conformations of substituents respect to the central phenyl core: average angles between lateral groups mean planes and central ring are reported for each crystal form analyzed. Representative molecules are overlapped in **Figure 3.5** (light green sticks are used for **4CzBNIm**, dark green sticks for **4^{OMe}CzBNIm**, blue sticks for **4DPABNIm**, pink sticks for **4^{tBu}CzBNIm**, yellow sticks for **4DMACBNIm**).

Compound	PhCore-Imidazole (°)	PhCore-Paddle (°)
4CzBNIm (100 K)	57.53(3)	82.63(1)
4DPABNIm (100 K)	79.96(5)	61.77(3)
4DPABNIm (298 K)	85.28(10)	62.08(5)
4^{tBu}CzBNIm (polymorph a, 100 K)	81.37(22)	63.65(4)
4^{tBu}CzBNIm (polymorph a, 298 K)	86.47(25)	64.48(4)
4^{tBu}CzBNIm (polymorph b, 298 K)	83.78(36)	65.91(4)
4^{OMe}CzBNIm (100 K)	55.49(9)	71.20(3)
4DMACBNIm (100 K)	89.11(1.13)	90.00(3)
4DMACBNIm (298 K)	79.61(76)	89.94(4)

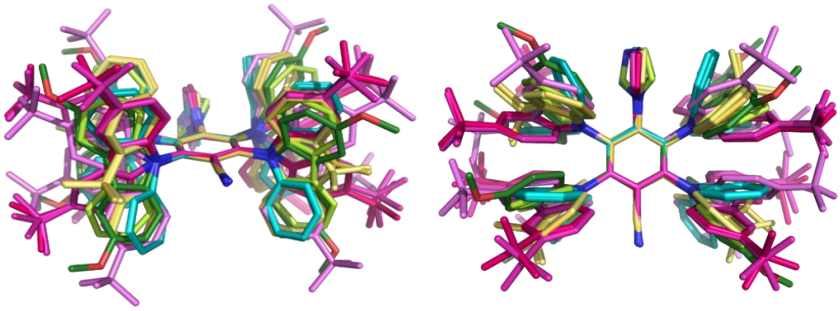


Figure 3.5: Overlap of representative molecules.

Crystal packing contacts essentially involves π•••π stacking and CH•••π contacts through phenyls of sidechains. Small rearrangements of these weak intermolecular interactions are possible and are consistent with the presence of polymorphism in **4^{tBu}CzBNIm** crystal batches.

3.2.3 Electrochemical characterization

Electrochemical properties were studied in anhydrous acetonitrile and dichloromethane solutions by means of cyclic voltammetry. All data are summarized in **Table 3.2**, while cyclic voltammograms are depicted in **Figures A3.36-A3.41**.

Table 3.2: Electrochemical properties of monoimidazole compounds.

Compound	ACN solution		DCM solution	
	$E_{1/2}^{red}$ (V)	$E_{1/2}^{ox}$ (V)	$E_{1/2}^{red}$ (V)	$E_{1/2}^{ox}$ (V)
4CzBNIm	-1.39	1.06[a]	-1.45	1.25
4^{tBu}CzBNIm	-1.45	1.08[a], 1.35[a]	-1.58	1.37
4^{OMe}CzBNIm	-1.46	1.3[a]	-1.50	1.11, 1.4[a]
4DPABNIm	-1.77	1[b], 1.2, 1.4	Not visible	1, 1.2[b]
4DMACBNIm	-1.42	0.95[a], 1.44[a]	-1.48	1.05[a], 1.22[a]
[4DPABNImTEGCOOtBu]OTs	-1.55	0.89[a], 1.15, 1.38	-1.51	0.81[a], 1.09, 1.41

Measurements are performed in degassed solutions containing 1 mM luminophore and 0.1 M $TBAPF_6$. Working Electrode: Glassy Carbon Electrode (3 mm); Reference Electrode: Ag/AgCl(sat.d KCl); Counter Electrode: Pt wire. Scan rate 100 mVs^{-1}. [a] Irreversible process, reported potentials are peak potentials. [b] quasi-reversible process.

As previously stated, these compounds show twisted D-A structure and spatially separated HOMO and LUMO, so reduction and oxidation processes involve, respectively, donor and acceptor.

In the cathodic region, according to the literature data[90,163], a single, reversible reduction process can be observed, attributable to the formation of a radical-anion delocalized all over the benzonitrile accepting core. No electrochemical process ascribable to the imidazole moiety can be observed with this electrochemical window[134,135], even in the case of the imidazolium derivative.

Looking at the half-wave potential of reduction process, it can be noted that the insertion of electro-donating groups (*tert*-butyl and methoxy) at positions 3 and 6 of the carbazole moieties enhances the donating effect, which in turn increase the reducing behavior of the acceptor, as already observed in literature[90,164].

Furthermore, diphenylamine also exhibits a strong donating effect, likely due to the partial conjugation of the nitrogen lone pair with the benzene ring. Nevertheless, this donating effect is diminished upon alkylation of imidazole moiety and the generation of a positive charge on the imidazole ring.

In contrast, in the anodic region different electrochemical behavior can be observed in acetonitrile solutions.

As expected, the oxidation of carbazole moieties in **4CzBNIm** generates *N*-centered radical cations that are destabilized by the high spin density in *para* position, which cause the generation of highly conductive polymers (**Figure 3.6**)[102,165].

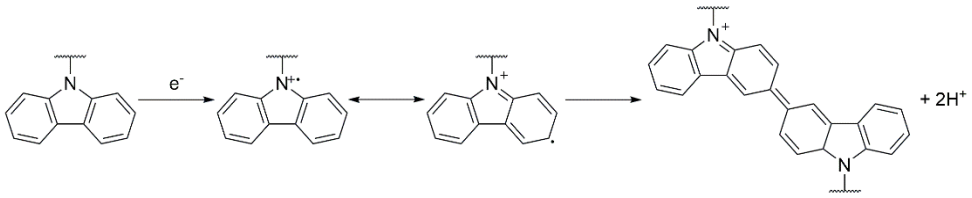


Figure 3.6: Mechanism of electrochemical oxidation of carbazole moieties.

Confirming this, the insertion of *tert*-butyl groups in positions 3 and 6 increases the stability of radical cations[102,103] while for compound **4^{OMe}CzBNIm** irreversible processes can be observed, as in the case of **4DMACBNIm**.

On contrast, compounds **4DPABNIm** and **[4DPABNImTEGCOOtBu]OTs** show more reversible oxidation processes with a ratio i_{pa}/i_{pc} close to 1, an interesting result as usually diphenylamine radical-cations are unstable[139,166].

When dichloromethane is used as solvent instead of acetonitrile, acceptor moieties are reduced at more cathodic potentials, while compound **4DPABNIm** undergo an electrocatalytic process (EC') with dichloromethane that acts as "substrate".

This EC' process is evident from the sigmoid profile, indicating that it falls within the so-called "zone KS"[167,168];

Further confirmation of this EC' process is obtained through cyclic voltammetry at higher scan rates.

Indeed, at higher scan rates the sigmoid profile is no longer observed, and a more common waveform emerged (**Figure 3.7**).

This indicates that the "catalyst" has moved to the so-called "zone KD", a zone that is accessible from zone KS through the use of higher scan rates.

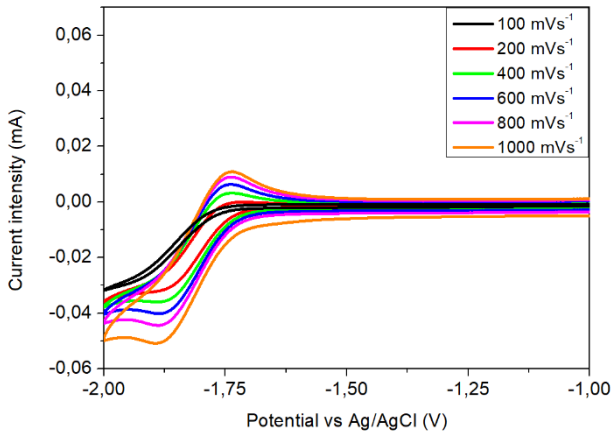


Figure 3.7: CV at different scan rates of **4DPABNIm** in dichloromethane.

In the anodic region, only minor differences can be observed, such as the higher stability of radical-cations of compounds **4^{tBu}CzBNIm** and **4^{OMe}CzBNIm**.

3.2.4 Photophysical characterization

UV-vis absorption spectra, emission and excitation spectra, PLQYs and PhotoLuminescence decay curves of monoimidazole derivatives are recorded both in acetonitrile and dichloromethane solution.

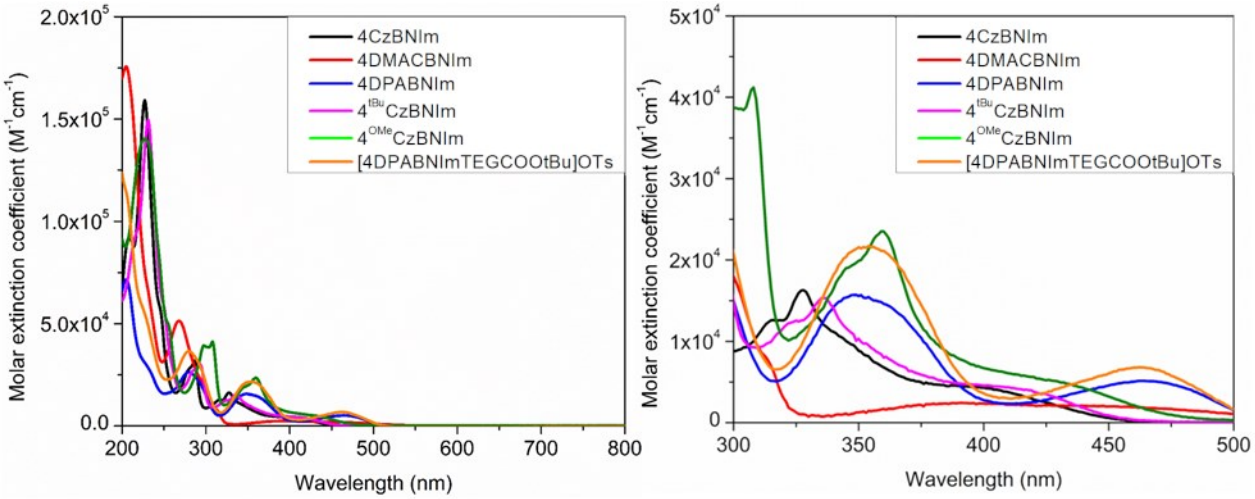


Figure 3.8: Absorption spectra in acetonitrile (left) and zoom of the region 300-500 nm (right).

In **Figure 3.8** UV-vis absorption spectra in acetonitrile are reported, while in **Table 3.3** absorption maxima of ICT region are reported.

In absorption spectra, the π*←π and σ*←n transitions are responsible for the energy bands with very high molar extinction coefficient values observed in the region between 200 and 300 nm. The Internal Charge Transfer (ICT) transitions between donor and acceptor moieties generate the bands with broad

profiles and lower molar extinction coefficients (approximately $2 \cdot 10^4$ M^{-1} cm^{-1}) in the region between 300 and 500 nm.

Compounds **4CzBNIm**, **4^{tBu}CzBNIm** and **4^{OMe}CzBNIm** exhibit similar profiles and, as previously documented in the literature[103,108,169], the presence of electro-donating groups on carbazole moieties results in a redshift of 10-70 nm, consistently with the literature data and attributed to a progressive stabilization of the CT energy[170].

Finally, compounds **4DPABNIm** and **[4DPABNImTEGCOOtBu]OTs** shows two broad peaks with very similar absorption maxima while compound **4DMACBNIm** exhibits a very broad profile with a low molar extinction coefficient as previously reported for DMAC-containing compounds[171,172].

As expected, the absorption spectra in dichloromethane (**Figure 3.9** and **Table 3.3**) demonstrate minimal blueshifts in the ICT region, which can be attributed to the reduced solvent polarity.

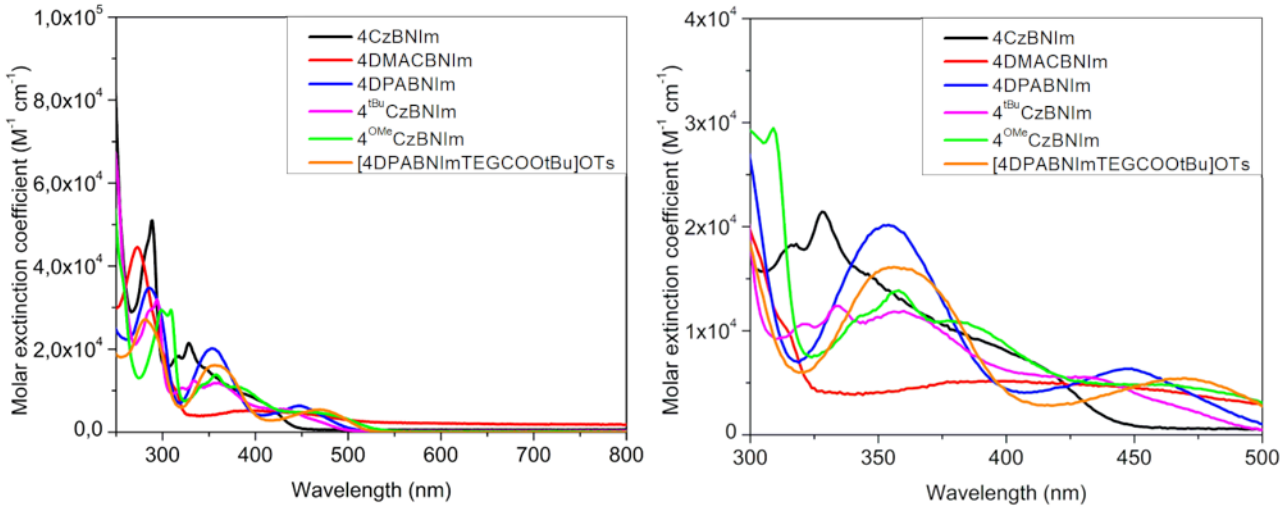


Figure 3.9: Absorption spectra in dichloromethane (left) and zoom of the region 300-500 nm (right).

Table 3.3: Photophysical properties of investigated compounds.

Compound	Solvent	λ_{abs}	λ_{em}[a]	Φ_{PL}[b]	Φ_{PL}[c]
4CzBNIm	**ACN**	316, 329	513	16.4±0.8	40±2
	DCM	315, 328	500	27±1	69±3
4^{tBu}CzBNIm	**ACN**	321, 334, 357	540	13.9±0.8	22±2
	DCM	324^{sh}, 336	525	28±1	58±2
4^{OMe}CzBNIm	**ACN**	342^{sh}, 358	607	<1	<1
	DCM	345^{sh}, 359	576	<1	<1
4DPABNIm	**ACN**	354, 447	536	5.9±0.2	9.8±0.3
	DCM	349, 464	532	7.7±0.2	65±2
4DMACBNIm	**ACN**	407	600	<1	<1
	DCM	423	545	4±2	4±2
[4DPABNImTEGCOOtBu]OTs	**ACN**	357, 471	561	7.0±0.1	46±1
	DCM	354, 464	570	7.7±0.1	37.4±0.7

Measurements are performed with 5 µM solution. [a] λ_{exc}=340 nm. [b] Aerated solution, average scan, λ_{exc} = 300 - 410 nm. [c] Ar-purged solution, average scan, λ_{exc} = 300 - 410 nm.

Excitation spectra are recorded (**Figure A3.18-A3.23**) and they are superimposable on the respective absorption spectra, thus confirming the absence of excimers.

The emission profiles of compounds are reported in **Figure 3.10** and as expected for donor-acceptor molecules they are characterized by broad emission and large Stokes shifts between absorption and emission maxima.

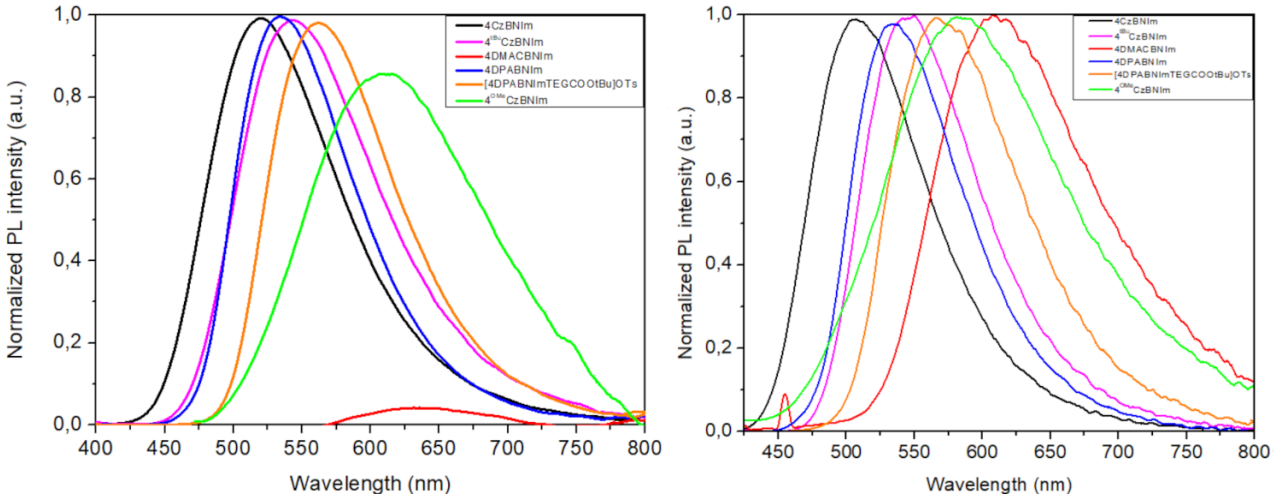


Figure 3.10: Emission spectra in acetonitrile (left) and in dichloromethane (right).

Comparing absorption spectra of the carbazole-containing derivatives, a strong redshift can be observed from **4CzBNIm** to **4^{tBu}CzBNIm** and **4^{OMe}CzBNIm**, with the latter showing near 100 nm of redshift compared to the former, in line with the literature[90,170,173–175].

In addition, compound **4^{OMe}CzBNIm** exhibits a broader profile, in line with the literature data[174,175].

Interestingly, the emission of **[4DPABNImTEGCOOtBu]OTs** is more redshifted than its precursor, meaning that the alkylation of imidazole decrease the HOMO-LUMO gap, reflecting the electrochemical data.

When dichloromethane is used instead of acetonitrile, a solvatochromic effect is present with evident blueshifts for all compounds.

All compounds exhibit low PLQYs in aerated solution that increase upon removal of oxygen, a typical behavior of TADF molecules, or going from acetonitrile to dichloromethane. An exception to this behavior is the imidazolium derivative, that probably suffer from higher non-radiative decays in dichloromethane than in acetonitrile.

Furthermore, the compounds **4DMACBNIm** and **4^{OMe}CzBNIm** do not show an increase of PLQYs upon deoxygenation, meaning that they are not TADF molecules.

In addition, a decrease can be observed when passing from **4CzBNIm** to **4^{tBu}CzBNIm** to **4^{OMe}CzBNIm** and it is due to greater non-radiative decays of the latter two compounds[103].

Very interestingly, compound **[4DPABNImTEGCOOtBu]OTs** shows the highest PLQY in acetonitrile in absence of oxygen, while its precursor shows the second highest PLQY in deoxygenated dichloromethane.

The final confirmation of TADF properties comes from time-resolved fluorescence spectroscopy (**Table 3.4** and **Figures A3.24-A3.35**), where bi-exponential profiles can be observed in deoxygenated solutions.

The only exceptions are the compounds **4DMACBNIm** and **4^{OMe}CzBNIm**, which do not show a delayed fluorescence contribution.

Table 3.4: Lifetimes of prompted and delayed fluorescence of compounds.

Compound	Solvent	τ_P (ns)[a]	τ_D (µs)[a]	τ_P (ns)[b]	τ_D (µs)[b]
4CzBNIm	**ACN**	7.79±0.01	0.319±0.002	28.61±0.05	2.02±0.01
	DCM	15.41±0.02	N.P.[c]	18.20±0.04	2.687±0.004
4^{tBu}CzBNIm	**ACN**	15.75±0.02	0.259±0.002	20.01±0.02	1.407±0.009
	DCM	13.16±0.04	N.P.[c]	15.45±0.03	1.444±0.005
4^{OMe}CzBNIm	**ACN**	0.885±0.005	N.P.[c]	6.92±0.08	N.F.[d]
	DCM	2.435±0.004	N.P.[c]	2.497±0.004	N.F.[d]
4DPABNIm	**ACN**	2.236±0.003	0.407±0.027	2.324±0.004	8.12±0.05
	DCM	2.260±0.003	N.P.[c]	2.329±0.004	10.41±0.06
4DMACBNIm	**ACN**	1.90±0.01	N.P.[c]	2.00±0.02	N.F.[d]
	DCM	20.13±0.03	N.P.[c]	24.55±0.03	N.F.[d]
[4DPABNImTEGCOOtBu]OTs	**ACN**	N.P.[c]	1.13±0.03	3.38±0.01	38.2±0.1
	DCM	N.P.[c]	N.P.[c]	2.52±0.02	16.61±0.06

Measurements are performed with 5 µM solution. λ_{exc} = 402.3 nm, Nanosecond lifetimes were evaluated with TCSPC electronic, while microsecond lifetimes were evaluated with MCS electronic. [a] Aerated solution. [b] Ar-purged solution. [c] Not Performed. [d] Not Found.

As expected, the presence of oxygen reduces delayed fluorescence lifetimes, since it interacts with the triplet states of compounds increasing non-radiative decays.

While carbazole-containing compounds show delayed fluorescence lifetimes around 2 µs, in line with lifetimes of similar carbazole-containing TADF molecules[103,141], **4DPABNIm** and **[4DPABNImTEGCOOtBu]OTs** show longer delayed fluorescence lifetimes that can be ascribed to "large" ΔE_{ST}, in line with the compounds investigated in **Chapter 2**.

Nevertheless, despite a delayed fluorescence lifetime of 10 µs, compound **4DPABNIm** exhibits a remarkably high PLQY in deoxygenated DCM. This indicates that **4DPABNIm** is not subjected to significant non-radiative decays. Conversely, compound **[4DPABNImTEGCOOtBu]OTs** exhibits a behavior close to imidazolium derivatives reported in **Chapter 2**, with a decrease of lifetimes going from acetonitrile to dichloromethane.

Finally, also prompted fluorescence lifetimes are affected by the presence of oxygen due to formation of singlet oxygen.

3.2.5 Electrochemiluminescence characterization

Given the presence of a reversible reduction process, the ECL of these compounds is evaluated under reductive-oxidation conditions with BPO as co-reactant.

Additionally, compounds **4^{tBu}CzBNIm** and **4DPABNIm** are investigated under annihilation conditions and, along with **[4DPABNImTEGCOOtBu]OTs**, in presence of TPA as co-reactant.

Furthermore, ECL spectroscopy was examined with BPO or TPA as co-reactants and ECL-voltage experiments were performed to provide insights into the ECL behavior under steady radical generation.

Consistently, with many other co-reactant ECL systems, the light emission typically starts around the reduction potential of the luminophore (**Figure 3.11** and **Figures A3.42-A3.47**) except for compound **4^{tBu}CzBNIm**, which ECL onset is located at -1.62 V, a more cathodic value than the expected one (ca. -1.45 V).

This discrepancy could be caused to a slow kinetics of electron transfer with benzoyl radical.

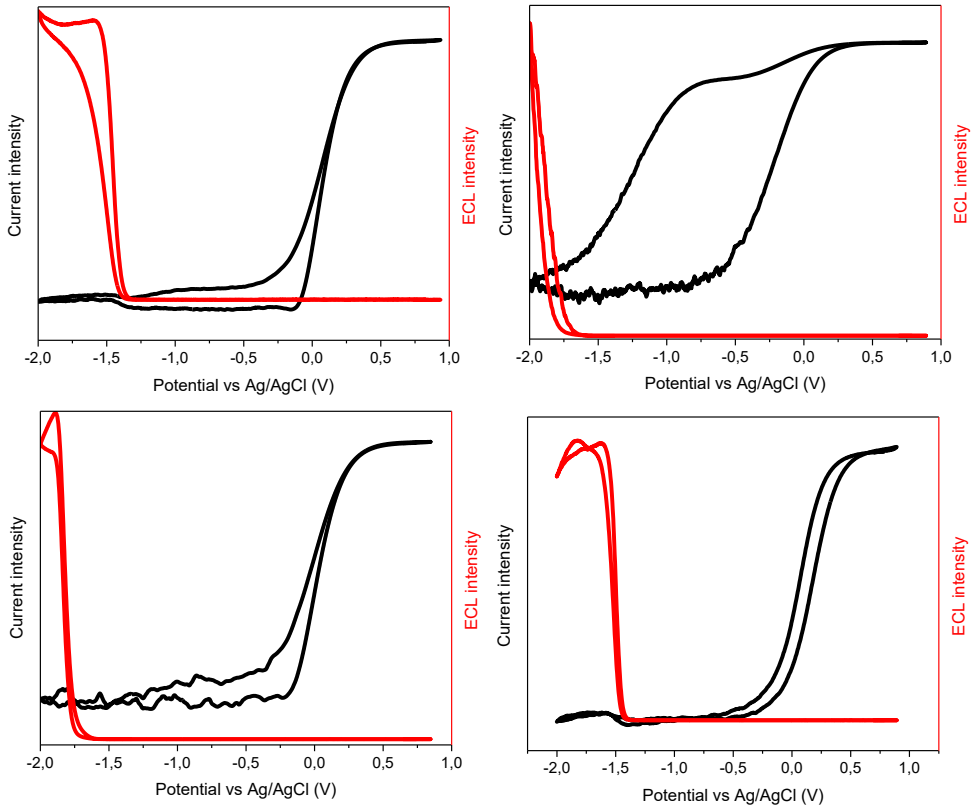


Figure 3.11: ECL-voltage curves of **4CzBNIm** (upper left), **4^{tBu}CzBNIm** (upper right), **4DPABNIm** (lower left) and **[4DPABNImTEGCOOtBu]OTs** (lower right) in acetonitrile with BPO as co-reactant.

As displayed in **Equation 3.1-3.4**, under reductive-oxidation conditions a suitable cathodic potential is applied and the radical-anions of both species are simultaneously generated, with the reduced co-reactant that rapidly decomposes into a benzoyl radical ($PhCO_2^{\bullet}$, $E^{o}_{PhCO2\bullet/PhCO2-}$ > +1.5 V *vs* SCE) that oxidizes the reduced luminophore, yielding its emitting excited state (**Equation 3.4**).

$$TADF + e^- \rightarrow TADF^{\bullet -} \quad \textbf{(3.1)}$$

$$BPO + e^- \rightarrow PhCO_2^{\bullet} + PhCO_2^- \quad \textbf{(3.2)}$$

$$TADF^{\bullet -} + PhCO_2^{\bullet} \rightarrow TADF^* + PhCO_2^- \quad \textbf{(3.3)}$$

$$TADF^* \rightarrow h\nu + TADF \quad \textbf{(3.4)}$$

As the benzoyl radical acts as an oxidizer, emitters must show an oxidation process lower than 0.49 V vs Ag/AgCl, which is the case for all investigated compounds.

In addition, the energy released by the annihilation reaction reported in **Equation 3.3** must be sufficient to overcome the HOMO-LUMO energy gap to achieve excitation, as described by **Equation 3.5** ($E^{o}_{(BO\bullet)}$ is assumed as +1.5 V vs SCE)[149], which is the case of all investigated compounds.

$$\Delta G^{\circ} = E^{\circ}_{red} - E^{\circ}(BO^{\cdot}) + E_{ES} \quad \textbf{(3.5)}$$

Although it is known that such conditions (BPO in organic solvents) are not particularly favorable for the standard ($[Ru(bpy)_3]Cl_2$), the goal of this **Chapter** was limited to investigate how different donors will impact the ECL emission of TADF emitters.

Reductive-oxidation ECL efficiencies are reported in **Table 3.5**, while in **Figures A3.58-A3.63** ECL-time and current-time profiles are reported.

Table 3.5: Reductive-oxidation ECL efficiencies and ECL emissions of monoimidazole derivatives.

Compound	Solvent	Φ_{ECL}	λ_{ECL} (nm)
4CzBNIm	**ACN**	0.38±0.04	522
	DCM	1.3±0.5	514
4^{tBu}CzBNIm	**ACN**	4.7±0.6	545
	DCM	11±3	529
4^{OMe}CzBNIm	**ACN**	0.074±0.005	617
	DCM	0.6±0.2	603
4DPABNIm	**ACN**	12±2	528
	DCM	28±4	533
4DMACBNIm	**ACN**	0.18±0.02	618
	DCM	0.6±0.2	617
[4DPABNImTEGCOOtBu]OTs	**ACN**	3±0.5	550
	DCM	5±2	557

Measurements are performed in degassed solutions containing 50 μM luminophore, 1 mM BPO and 0.1 M $TBAPF_6$. WE: Glassy Carbon Electrode (1 mm); RE: Ag/AgCl (sat.d KCl); CE: Pt wire. Potential sequence (repeated three times): 0 V for 3 s, -2 V for 3 s, 0 V for 3 s. All experiments were performed three times each. [a] Φ_{ECL} determined according to **Equation 3.14**, $[Ru(bpy)_3](Cl)_2$ as standard (ECL efficiency assumes as unitary).

Excluding **4^{OMe}CzBNIm** and **4DMACBNIm**, which are the compounds with the lowest PLQYs and ECL yields, all compounds exhibit an increase of ECL efficiencies moving from acetonitrile to dichloromethane.

More interestingly, the ECL trend does not strictly follow the PLQY trend.

Indeed, ECL trend is in accordance with the trend of energies released from the annihilation reactions reported in **Equation 3.3** (**4DPABNIm** > **[4DPABNImTEGCOOtBu]OTs** > **4^{tBu}CzBNIm** > **4CzBNIm**).

Indeed, compound **4CzBNIm** perform less or slightly more than the standard $[Ru(bpy)_3]Cl_2$, while compounds **4^{tBu}CzBNIm** and **4DPABNIm** outperform the standard by 4.7x and 12x in acetonitrile and 11x and 28x in dichloromethane. These astonishing results might be correlated also to the electrochemical behavior of these molecules: in fact, compounds **4DPABNIm** and **4^{tBu}CzBNIm** possess the most stable radical-cations.

Therefore, apart from the released free energies, two more hypotheses can be drawn out to explain the high efficiencies of compounds bearing diphenylamine and *tert*-butyl carbazole as donors. The first hypothesis is that other mechanisms such as the "annihilation-route" reductive-oxidation ECL (see **Chapter 1.1.1**) are involved in the formation of excited states. The second hypothesis is that an incomplete consumption of radical-anions of the dye is present, causing and accumulation of radical-anions that undergo annihilation reaction with benzoyl radical.

Even if these two hypotheses are partly opposed to each other, they can explain either the higher efficiency of molecules with more stable radical-cations and the increase of ECL emission among pulses.

Conversely, the theory made by Sojic and colleagues[149] that relates ECL efficiencies and cathodic reduction potentials does not seem to be applicable to this class of compounds. Indeed, compound **4^{tBu}CzBNIm** has a higher ECL efficiency than **[4DPABNImTEGCOOtBu]OTs** even if the reduction potential of the former is more anodic than the latter.

Looking at current-time profiles, a Cotrellian behavior of current intensity can be noted after the initial fast double-layer charging (**Figure 3.12**), meaning that the process is under diffusion control and no adsorption phenomena occurs at the electrode.

In contrast ECL-time profiles, especially in dichloromethane, exhibit delays between the application of electrical pulse and the ECL maximum intensity (**Figure 3.13-right**) and build-up profiles, which is particularly clear for compound **4DPABNIm** (**Figure 3.13-left**).

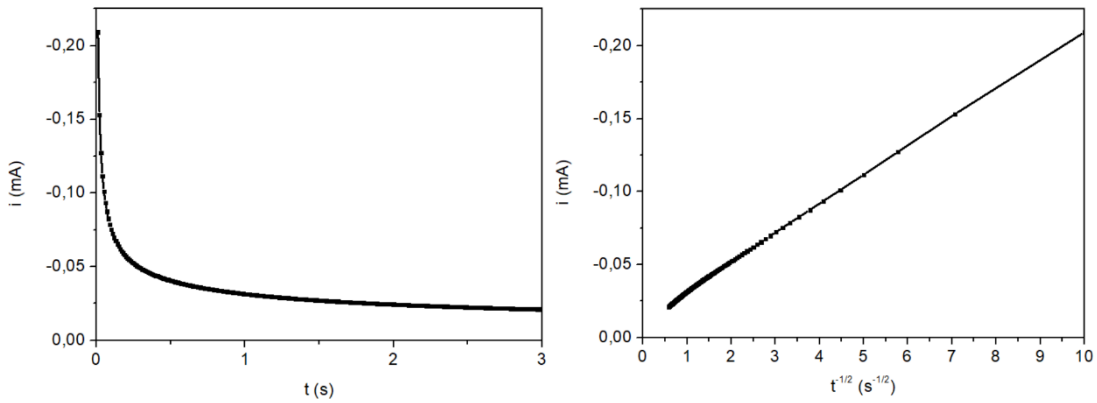


Figure 3.12: Current-time profile of the first pulse of an ECL experiment with **4^{tBu}CzBNIm** as dye and BPO as co-reactant (left). Current-(time)$^{1/2}$ profile of the same pulse (right).

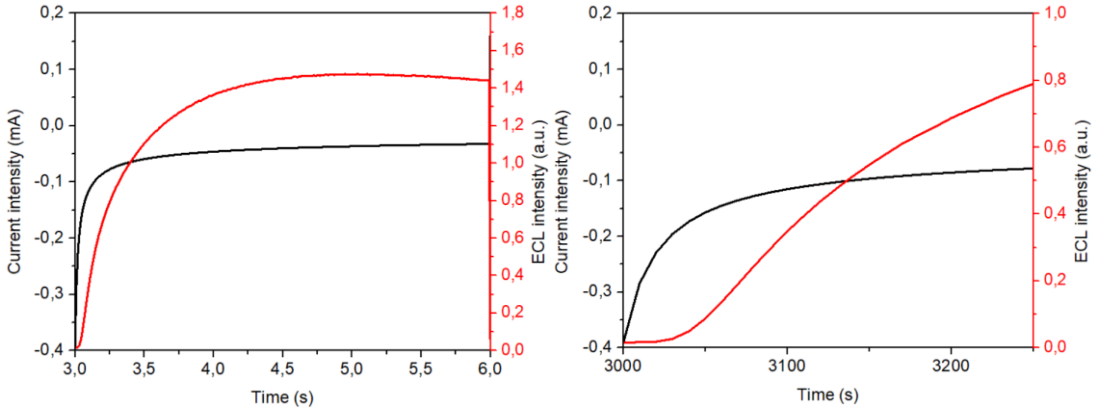


Figure 3.13: Zoom of reductive-oxidation ECL-time (red) and current-time (black) profiles of **4DPABNIm** during the first pulse (left) and during the first 300 ms of the first pulse (right) in dichloromethane.

Such behaviors were already observed in literature and were attributed to the formation of excimers or exciplexes even leading to organic long-persisting ECL (OLECL)[108–110,112], uncompensated solution resistance[176], triplet-triplet annihilation[109], slow diffusions of radicals[111] and slow kinetics of electron-transfer reactions[177].

Among these phenomena, excimers can be ruled out as PL and ECL spectra are comparable (**Figures A3.48-A3.53**). Also, uncompensated solution resistance and TTA can be ruled out since their temporal windows are much shorter than observed delays.

On contrast, diffusion rates and electron-transfer reaction rates can cause these delays, as observed in sulfurated pyrene-cored dendrimers by Valenti and colleagues[111].

By combining all the elements, it seems that the overall ECL emission of these compounds is a complex result of many different mechanisms and energetic requirements.

Nevertheless, the formation of byproduct traces that increase the ECL signal cannot be excluded at all.

Finally, even the imidazolium derivative shows a higher efficiency than the standard, although its efficiencies are lower than its neutral precursor **4DPABNIm**.

ECL emissions are reported in **Figure 3.14** and as already told they are comparable to PL emissions excluding a redshift that can be attributed to experimental factors, such as variations in slit width and different instrumentation.

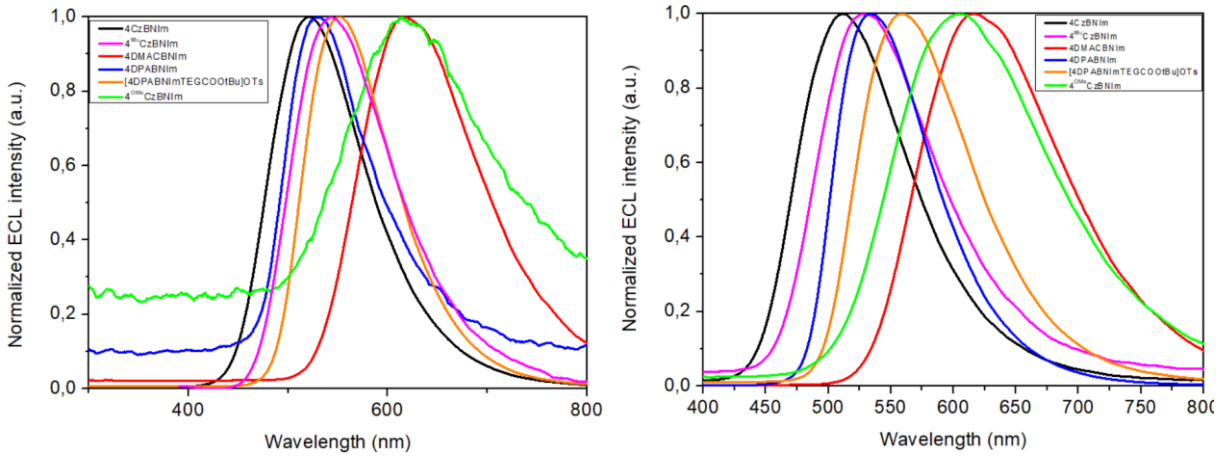


Figure 3.14: ECL spectra in acetonitrile (left) and dichloromethane (right) in presence of BPO as co-reactant.

To unravel the observed behavior, annihilation ECL experiments are performed on **4^{tBu}CzBNIm** and **4DPABNIm**, and their annihilation ECL efficiencies are reported in **Table 3.6**.

Table 3.6: Annihilation ECL efficiencies of monoimidazole derivatives.

Compound	Applied potentials	Φ_{ECL}[a]
4^{tBu}CzBNIm	-1.7 V to +1.3 V	1.4±0.9
4DPABNIm	-2 V to +1.3 V	38±6
	+1.3 V to -2 V	12±4
	-2 V to +1.6 V	9±2
	+1.6 V to -2 V	4±1

Measurements are performed in degassed acetonitrile solutions containing 20 µM luminophore and 0.1 M $TBAPF_6$ as supporting electrolyte. WE: Glassy Carbon Electrode (1 mm); RE: Ag/AgCl (sat.d KCl) electrode; CE: Pt wire. Potentials were stepped with a frequency of 10 Hz. [a] Φ_{ECL} determined under annihilation conditions according to **Equation 3.14**, $[Ru(bpy)_3](Cl)_2$ as standard (ECL efficiency was assumed as unitary).

These two compounds follow the S-route, since the released free energies are greater than the energy of the lowest-lying excited singlet state, and annihilation ECL trend is in accordance with that of reductive-oxidation ECL.

These outcomes confirm the fundamental importance of the radical stability to achieve high ECL efficiencies.

More interestingly, ECL efficiencies of **4DPABNIm** strongly depends on the order of the applied potentials (**Figure 3.15**).

Indeed, when the radical anion is generated first, a strong ECL signal is observed when the potential is stepped to +1.3 V and a weak signal is observed after the subsequent potential step. This behavior can also be observed when the radical-cation is generated first.

In fact, when the potential is stepped between +1.3 V and -2 V, a weak signal appears during the reduction of the radical-cation, and during the subsequent step at +1.3 V a strong ECL signal appears, meaning that the radical-anion is more stable than the radical-cation (**Figure 3.15 upper left and right**).

Furthermore, when potential is increased up to +1.6 V, a higher ECL signal can be observed after every pulse, with the highest intensity that can be observed after the oxidation of radical-anion.

Finally, a decreasing trend of ECL intensity over time can be observed (**Figure 3.15 lower left** and **right**).

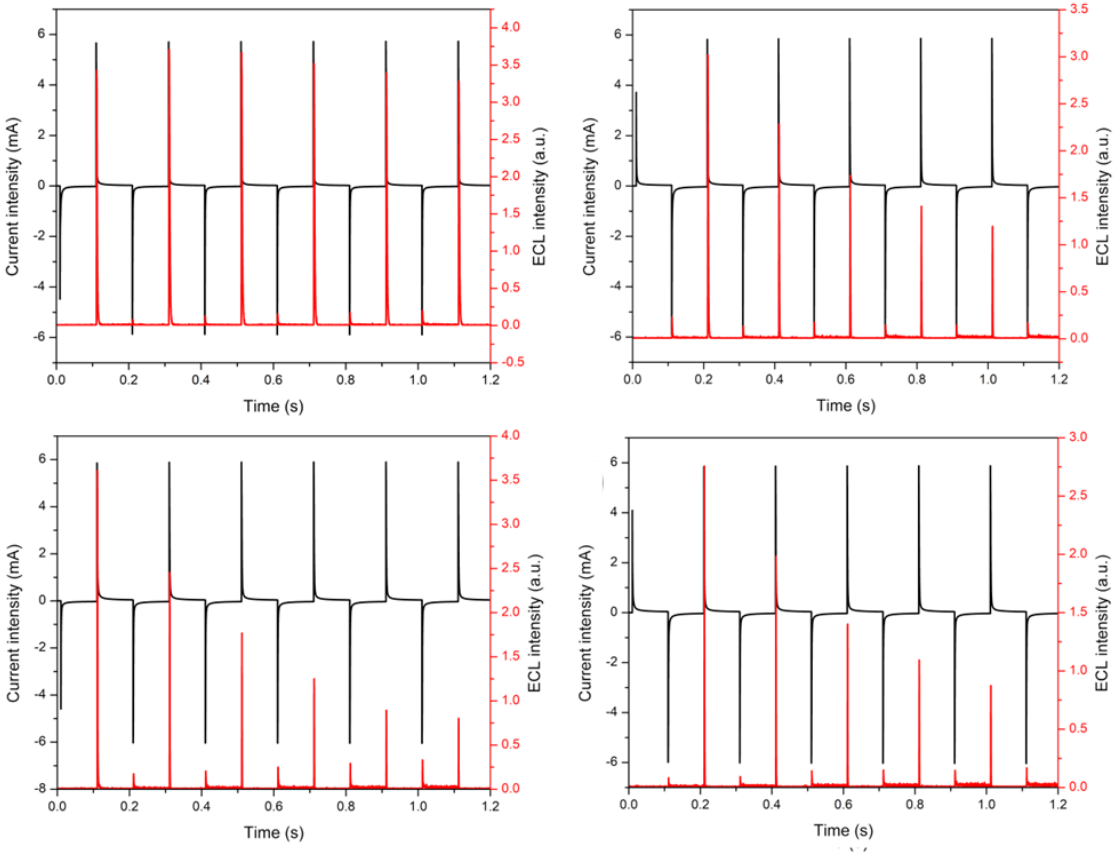


Figure 3.15: ECL-time (red) and chronoamperometric (black) profiles of **4DPABNIm** in ACN during potential stepping experiments at a pulsing frequency of 10 Hz. Potential stepped between -2 and +1.3 V (upper left), +1.3 and -2 V (upper right), -2 and +1.6 V (lower left), and +1.6 and -2 V (lower right).

Furthermore, even in annihilation ECL experiments delays and build-up profile are present (**Figure 3.16**), corroborating the hypothesis that annihilation pathway can collaborate to the generation of ECL signal in co-reactant ECL.

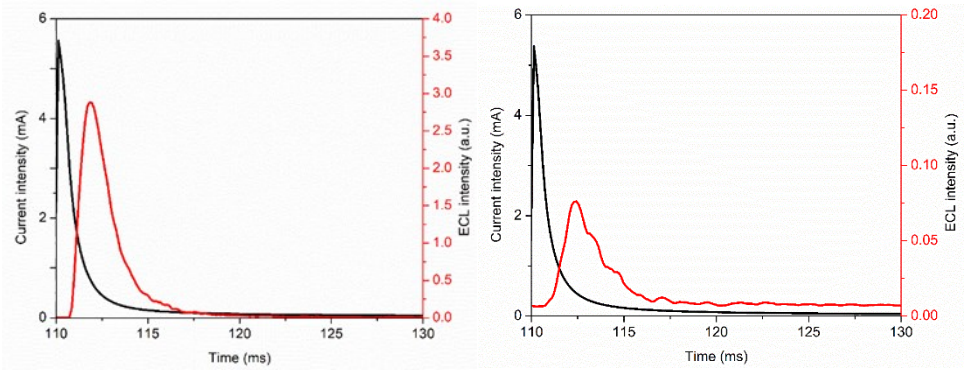


Figure 3.16: Zoom of ECL-time (red) and current-time (black) profiles of **4DPABNIm** in ACN after the potential is stepped from -2V and +1.3V (left). Zoom of ECL-time (red) and chronoamperometric (black) profiles of **4^{tBu}CzBNIm** in acetonitrile after the potential is stepped from -1.7V and +1.3V (right).

Finally, compounds **4^{tBu}CzBNIm**, **4DPABNIm** and **[4DPABNImTEGCOOtBu]OTs** are investigated under oxidative-reduction conditions using TPA as co-reactant in acetonitrile solution.

Consistently with reductive-oxidation ECL-voltage experiments, these compounds display a homogeneous ECL peak after the oxidation of the luminophore (**Equations 3.6-3.10**) while a remote-route mechanism (**Equations 3.11-3.13**) could be present for compound **4DPABNIm**.

Indeed, the onset of the first ECL peak is located around 0.8 V, close to the oxidation of tripropylamine and slightly more cathodic than the first oxidation process.

In contrast, remote ECL pathway can be excluded for compounds **4^{tBu}CzBNIm** and **[4DPABNImTEGCOOtBu]OTs**.

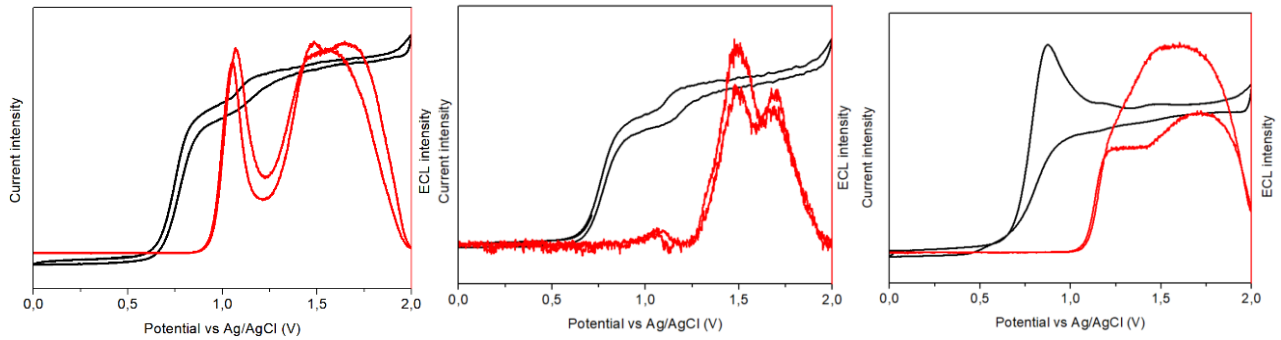


Figure 3.17: ECL-voltage curves of **4DPABNIm** (left), **4^{tBu}CzBNIm** (center) and **[4DPABNImTEGCOOtBu]OTs** (right) in acetonitrile with TPA as co-reactant.

$$TPrA - e^- \rightarrow TPrA^{\bullet+} \quad \textbf{(3.6)}$$

$$TPrA^{\bullet+} - H^+ \rightarrow TPrA^{\bullet} \quad \textbf{(3.7)}$$

$$TADF - e^- \rightarrow TADF^{\bullet+} \quad \textbf{(3.8)}$$

$$TADF^{\bullet+} + TPrA^{\bullet} \rightarrow TADF^* + "waste" \quad \textbf{(3.9)}$$

$$TADF^* \rightarrow h\nu + TADF \quad \textbf{(3.10)}$$

$$TADF + TPrA^{\bullet} \rightarrow TADF^{\bullet-} + "waste" \quad \textbf{(3.11)}$$

$$TADF^{\bullet-} + TPrA^{\bullet+} \rightarrow TADF^* + TPrA \quad \textbf{(3.12)}$$

$$TADF^* \rightarrow h\nu + TADF \quad \textbf{(3.13)}$$

ECL yields are reported in **Table 3.7** and ECL-time and current-time profiles are reported in **Figures A3.64-A3.66**. Finally, ECL emission are depicted in **Figure 3.18**.

Table 3.7: Reductive-oxidation ECL efficiencies and ECL emissions of monoimidazole compounds.

Compound	Φ_{ECL}	λ_{ECL} (nm)
4^{tBu}CzBNIm	0.39	529
4DPABNIm	1.4	533
[4DPABNImTEGCOOtBu]OTs	0.95	562

Measurements are performed in degassed acetonitrile solutions containing 50 µM luminophore, 1 mM TPA and 0.1 M $TBAPF_6$. WE: Glassy Carbon Electrode (1 mm); RE: Ag/AgCl (sat.d KCl); CE: Pt wire. Potential sequence (repeated three times): 0 V for 3 s, +1.5 V for 3 s, 0 V for 3 s. [a] Φ_{ECL} determined according to **Equation 3.14**, $[Ru(bpy)_3](Cl)_2$ as standard (ECL efficiency assumes a unitary).

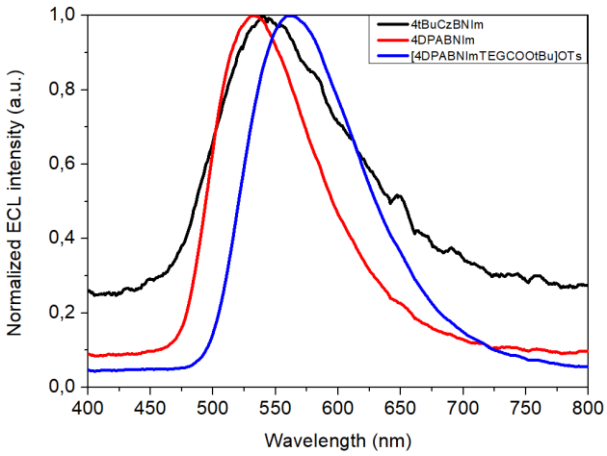


Figure 3.18: ECL spectra in acetonitrile solution in presence of TPA as co-reactant.

The presence of an ECL signal from **4DPABNIm** under these conditions is very surprising and, even better, its ECL yields is higher than the standard $[Ru(bpy)_3]Cl_2$, while the imidazolium derivative performs close to the standard.

Anodic-ECL from **4DPABNIm** appears to be counterintuitive, given that its reduction potential is more cathodic than that of the tripropylamino radical, which, in turn, should not be capable of reducing the radical-cation of the luminophore.

To elucidate this behavior, it is crucial to gain a deeper understanding of the thermodynamics of the **4DPABNIm**/TPA system.

The first requirement is that the reduction potential of the luminophore must be less cathodic than -1.7 V vs Ag/AgCl, which is not the case for compound **4DPABNIm**.

In addition, the energy released from the annihilation reaction (**Equation 3.9**), must be sufficient to overcome the HOMO-LUMO energy gap to achieve excitation[78,148].

$$\Delta G = E^{\circ}_{red} - E^{\circ}(TPrA^{\bullet+}) + E_{ES}$$

The ΔG value is negative for the compounds **4DPABNIm** and **[4DPABNImTEGCOOtBu]OTs**, which means that the reactions that involve these two compounds are thermodynamically favored.

Conversely, the released energy for compound 4^{tBu}CzBNIm is slightly positive, which is reflected in its lower ECL efficiency.

Nevertheless, the most important result remain the ECL signal from compound **[4DPABNImTECOOtBu]OTs** in presence of TPA, which is, at the best of our knowledge, the first example of anodic-ECL with a TADF molecule bearing a hydrophilic chain and the protected form of a bioconjugable group.

3.3 Conclusions

In conclusion, in this **Chapter** novel monoimidazole-based TADF derivatives synthesized starting from a perfluorinated benzonitrile with a metal-free synthesis were reported.

These compounds were structurally characterized, and their photophysical and electrochemical properties were investigated in organic solvents to evaluate how different donors would change their properties.

ECL yields were assessed under reductive-oxidation conditions and, for compounds with the higher electrochemical reversibility in the anodic region, also under annihilation conditions and oxidative-reduction conditions.

By looking at the results, a correlation between ECL performances and the energy released in the annihilation reaction and electrochemical reversibility of redox processes is suggested.

In contrast, the outcomes suggest that photoluminescence properties play a minor role in ECL performances.

A very interesting result is the high ECL efficiencies of compound **4DPABNIm**, surpassing the $[Ru(bpy)_3]Cl_2$ standard under all ECL conditions. Furthermore, the most intriguing result is the high ECL efficiencies of its alkylated derivative **[4DPABNImTEGCOOtBu]OTs**, representing the first example of discrete TADF molecule bearing a hydrophilic chain with a protected bioconjugable group showing good ECL efficiencies in organic solvents.

A critical point of the alkylation of these derivatives is the significant decrease in ECL efficiencies, since it increases non-radiative decays, which can be avoided by strengthening the rigidity of the molecular structure, i.e. with an extended π-system.

3.4 Experimental section

All reagents, except 3,6-di-*tert*-butyl-carbazole (synthesized according to literature[178]) and *tert*-butyl 14-hydroxy-3,6,9,12-tetraoxatetradecanoate (synthesized according to literature[179]) were used as received without further purification and they were obtained from Sigma-Aldrich and Alfa-Aesar (dibenzoyl peroxide, wet with 25% water).

All solvents, except those for photophysical measurements, were dried according to literature procedure[151] using 3Å molecular sieves purchased from Thermoscientific.

^{1}H and $^{13}C\{^{1}H\}$ NMR spectra were recorded on a Bruker AVANCE III spectrometer equipped with a BBO probe while ^{19}F NMR and $^{19}F\{^{1}H\}$ NMR were recorded with a Bruker 200 MHz equipped with a QNP probe; ^{1}H and $^{13}C\{^{1}H\}$ NMR chemical shifts were referenced relative to residual solvents peaks while $^{19}F\{^{1}H\}$ chemical shifts were referenced using indirect referencing[152].

NMR solvents were purchased from Sigma-Aldrich or EurisoTOP and dried with 3Å molecular sieves purchased from Merck.

Multiplicities of signals are reported as s (singlet), d (doublet), t (triplet), q (quartet), quint (quintet), m (multiplet) and combinations of these multiplicities, coupling constants J are reported in Hz, and if not stated otherwise refer to J_{HH} couplings.

HR-MS spectra were recorded on a Thermo Q-Exactive™ equipped with an ESI source. Mass spectra were recorded in positive mode.

All reactions were monitored by thin-layer chromatography using Merck silica gel plates 60 F_{254} (plastic sheets) and spots were visualized with UV light or with iodine/silica staining.

Flash chromatography purifications were performed on a Combiflash Nextgen 300+ using Redisep Bronze column (4, 12, 24, 40 grams) filled with NP silica gel and using Redisep Rf cartridge (4 and 24 grams).

3.4.1 Photophysical measurements

See **Experimental Section** of **Chapter 2**

3.4.2 Electrochemical and electrochemiluminescence measurements

Electrochemical measurements were performed with a Autolab PGstat302N as potentiostat using NOVA 2.1.5 as interface software.

The configuration of electrochemical cell was the three-electrode configuration, which consists in a glassy carbon electrode (diameter 3mm) as working electrode (WE), a silver/silver chloride reference electrode (RE) built according to a literature procedure[180] and a platinum wire as counter electrode (CE).

The glassy electrochemical cell was specially made with a Teflon cap at the head and a flat glass window at the bottom for the detection of the generated ECL signal.

Before every experiment the solution was Ar-bubbled for 5 minutes to remove oxygen and every experiment was performed under a protective atmosphere of argon; finally, after every measurement the working electrode was polished with alumina slurry (0,05 mm).

Cyclic voltammetry measurements were performed with dried HPLC-grade acetonitrile or dichloromethane solution containing 1 mM of investigated compounds and 0.1 M tetrabutylammonium hexafluorophosphate as supporting electrolyte with a scan rate equal to 100 mV/s.

ECL-voltage curve measurements were performed with dried HPLC-grade acetonitrile or dichloromethane solution containing 0.05 mM of investigated compounds, 1 mM of co-reactant (BPO or TPA) and 0.1 M tetrabutylammonium hexafluorophosphate as supporting electrolyte. The scan rate was 20 mV/s and to detect ECL signals the electrochemical cell was put over an Ocean Insight 1 mm optical fiber linked to a Thorlabs 1001/M photomultiplier tube.

PMT 2100 control was used as software interface for photomultiplier tube (PMT gain: 10, Bandwidth 80 MHz).

ECL spectra were performed with dried HPLC-grade acetonitrile or dichloromethane solution containing 0.05 mM of investigated compounds, 1 mM of co-reactant (BPO or TPA) and 0.1 M tetrabutylammonium hexafluorophosphate as supporting electrolyte. The ECL signal was obtained by applying a potential of -2 V to the solution and to detect ECL signals (integration time: 3s) the electrochemical cell was put over a 1 mm optical fiber linked to a CCD QEPro camera.

Co-reactant-ECL measurements were performed with dried HPLC-grade acetonitrile or dichloromethane solution containing 0.05 mM of investigated compounds, 1 mM of co-reactant (BPO or TPA) and 0.1 M tetrabutylammonium hexafluorophosphate as supporting electrolyte; the following scheme was repeated three times: 0 V for 3 seconds, -2 V (if BPO is used as co-reactant) or +1.5 V (if TPA is used as co-reactant) for 3 seconds and 0 V for 3 seconds.

Annihilation-ECL measurements were performed in dried HPLC-grade acetonitrile solution containing 0.02 mM of investigated compounds and 0.1 M tetrabutylammonium hexafluorophosphate as supporting electrolyte; potentials were stepped with a frequency of 10 Hz and their value are reported near every compound.

Every ECL experiment was repeated three times for every compound to calculate average values, and relative efficiencies were determined by comparison with standard $Ru(bpy)Cl_2$ by taking its efficiency as 1.

ECL efficiencies are calculated using **Equation 3.14**[1].

$$\Phi_{x,ECL} = \frac{\left(\frac{\int_a^b ECL\,dt}{\int_a^b i\,dt}\right)_x}{\left(\frac{\int_a^b ECL\,dt}{\int_a^b i\,dt}\right)_{St}} \quad \textbf{(3.14)}$$

where *x* represents the investigated compound and *St* represents the standard $[Ru(bpy)_3]Cl_2$.

3.4.3 XRD analysis – Structural characterization

Suitable single crystals for X-Rays Diffractometry were obtained by slow diffusion or by slow evaporation of solvents.

Solvent mixtures that were employed are reported in **Synthesis route and procedures** part.

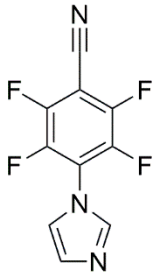
Crystallographic data have been deposited at the Cambridge Crystallographic Data Centre and allocated the deposition numbers CCDC 2242629-2242637 for **4CzBNIm** at 100 K, **4DPABNIm** at 100 K, **4DPABNIm** at 298 K, **4^{tBu}CzBNIm** polymorph *a* at 100 K, **4^{tBu}CzBNIm** polymorph *a* at 298 K, **4^{tBu}CzBNIm** polymorph *b* at 298 K, **4^{OMe}CzBNIm** at 100 K, **4DMACBNIm** at 100 K and **4DMACBNIm** at 298 K. These data can be obtained free of charge via https://www.ccdc.cam.ac.uk/structures.

Data collections were performed at the XRD2 beamline of the Elettra Synchrotron, Trieste (Italy)[155]. The crystals were dipped in NHV oil (Jena Bioscience, Jena, Germany) and mounted on the goniometer head with kapton loops (MiTeGen, Ithaca, USA). Complete datasets were collected at 298K or 100 K (nitrogen stream supplied through an Oxford Cryostream 700) through the rotating crystal method. Data were acquired using monochromatic wavelength of 0.620 Å on a Pilatus hybrid-pixel area detector (DECTRIS Ltd., Baden-Daettwil, Switzerland). Diffraction data were indexed, integrated and scaled using XDS[156]. Complete dataset were obtained merging two independent dataset using CCP4-Aimless code[181,182], for triclinic crystal forms. Structures were solved by the dual space algorithm implemented in the SHELXT code[157]. Fourier analysis and refinement were performed by the full-matrix least-squares methods based on F^2 implemented in SHELXL (Version 2018/3)[158]. The Coot program was used for modeling[159]. Anisotropic thermal motion refinement was used for all atoms with occupancies higher than 40%. Geometry and thermal motion parameters restrains (SIMU, DELU, FLAT, DFIX and DANG) were used on disordered fragments. Hydrogen atoms were included at calculated positions with isotropic $U_{factors} = 1.2 \cdot U_{eq}$ or $U_{factors} = 1.5 \cdot U_{eq}$ for methyl and hydroxyl groups (U_{eq} being the equivalent isotropic thermal factor of the bonded non hydrogen atom). **4^{tBu}CzBNIm** (polymorph a, 100 K), **4^{tBu}CzBNIm** (polymorph a, 298 K), **4DMACBNIm** (100 K) and **4DMACBNIm** (298 K) models were refined as 2-component twins. Twin laws were identified using Platon TWINROTMAT[183] routine and they lead to significant improvements of refinement statistics. Triclinic crystal of **4^{tBu}CzBNIm** (polymorph a) showed two domains related by a 180° rotation around *a** reciprocal lattice direction, while **4DMACBNIm**

twinning was interpreted as a 180° rotation around (1-1-0) reciprocal lattice direction. All the crystal forms showed solvent molecules trapped into crystal voids. Electron density contributions that couldn't be modelled were removed with Platon SQUEEZE[160] routine. Estimated contributions of these regions are included in the reported crystal properties (**Table A3.1**). Pictures were prepared using Ortep-3[161] and Pymol software.

3.4.4 Synthesis route and procedures

3.4.4.1 Synthesis of 2,3,5,6-tetrafluoro-4-(1H-imidazol-1-yl)benzonitrile (**4FBNIm**)



This compound was obtained using a slightly modified literature method[162].

To a solution of imidazole (14.76 mmol, 1.9 equivalents) in dry THF (15 mL) stirred at 0 °C, 2,3,4,5,6-pentafluorobenzonitrile was added (7.77 mmol, 1 equivalent) and the solution was stirred for 3 h under argon atmosphere, during which time it becomes cloudy.

After three hours the reaction mixture was poured into water and extracted three times with ethyl acetate, which was washed with brine. The organic phase was dried over sodium sulphate and the solvent was removed under reduce pressure. The brownish oily crude product was purified by flash chromatography (SiO_2, dichloromethane:methanol from 10:0 to 9:1) to give final product (6.3 mmol, yield 81%) as a brown waxy solid.

^{1}H NMR (300 MHz, Acetone-d_6) δ 8.02 (tt, J = 2.0, 0.9 Hz, 1H), 7.56 (ddd, J = 3.3, 1.9, 1.4 Hz, 1H), 7.26 (dd, J = 1.5, 0.8 Hz, 1H).

^{19}F{^{1}H} NMR (188 MHz, $CDCl_3$) δ -129.38 – -129.76 (m), -144.51 – -144.82 (m).

Chemical shifts are in line with literature data[162].

3.4.4.2 Synthesis of 2,3,5,6-tetrasubstituted-4-(1H-imidazol-1-yl)benzonitrile

Procedure A.

In a flame dried and argon-purged round-bottomed flask equipped with a magnetic stir bar 6 equivalents of sodium hydride (60% in mineral oil) were put in dry THF. Then 5 equivalents of donor were added, and the suspension was stirred for 30 minutes at room temperature. Finally, 1 equivalent of **4FBNIm** was added and the resulting mixture was stirred at room temperature for 24 h.

The reaction was quenched by addition of water and tetrahydrofuran was removed by rotary evaporator. After removal of THF the residue was dissolved in DCM and washed with water.

Then the aqueous phase was extracted three times with DCM and the organic phase was dried over sodium sulphate and the solvent was removed by rotary evaporator. Finally, the crude product was purified by flash chromatography or by precipitation.

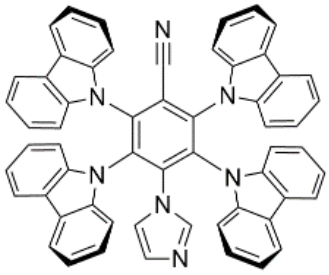
Procedure B.

In a flame dried and argon-purged round-bottomed flask equipped with a magnetic stir bar 6 equivalents of sodium hydride (60% in mineral oil) were put in dry THF. Then 5 equivalents of donor were added, and the suspension was stirred for 30 minutes at 65 °C. Finally, 1 equivalent of **4FBNIm** was added and the resulting mixture was stirred at 65 °C for 24 h.

The reaction was quenched by addition of water and tetrahydrofuran was removed by rotary evaporator. After removal of THF the residue was dissolved in DCM and washed with water.

Then the aqueous phase was extracted thrice with DCM and the organic phase was dried over sodium sulphate and the solvent was removed by rotary evaporator. Finally, the crude product was purified by flash chromatography or by precipitation.

3.4.4.3 Synthesis of 2,3,5,6-(tetracarbazol-9-yl)-4-(1H-imidazol-1-yl)benzonitrile (**4CzBNIm**)



According to procedure A, **4FBNIm** (1.82 mmol, 1 equivalent) and carbazole (9.12 mmol, 4.88 equivalents) as donor were used and a bright yellow precipitate appears during the reaction.

The product was obtained with quantitative yield (1.77 mmol, yield 97%) by precipitation with diethyl ether and it appears as a bright yellow powder.

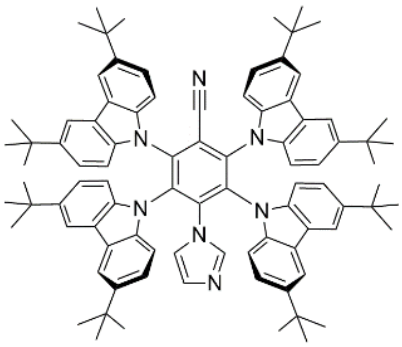
^{1}H NMR (300 MHz, DMF-d_7) δ 7.98 – 7.79 (m, 16H), 7.26 (ddd, J = 8.3, 7.3, 1.3 Hz, 4H), 7.20 – 7.09 (m, 9H), 7.04 (td, J = 7.5, 1.0 Hz, 4H), 6.75 (t, J = 1.1 Hz, 1H), 6.20 (t, J = 1.4 Hz, 1H), 5.96 (t, J = 1.2 Hz, 1H).

^{13}C{^{1}H} NMR (75 MHz, DMF-d_7) δ 163.38, 163.00, 162.61, 144.91, 143.83, 141.00, 140.71, 137.03, 129.43, 126.62, 126.45, 124.54, 124.28, 121.89, 121.66, 121.10, 120.85, 119.20, 112.13, 111.77, 36.33, 36.05, 35.78, 35.50, 35.22, 34.94, 34.67, 31.23, 30.95, 30.68, 30.40, 30.12, 29.84, 29.56.

HR-MS (m/z) Calculated: 830.3020 ([M+H]$^+$); Found: 830.3027 ([M+H]$^+$), 1698.5583 ([2M+K]$^+$).

Suitable crystals for SC-XRD were obtained by slow diffusion of diethyl ether vapors into *N*,*N*-dimethylformamide.

3.4.4.4 Synthesis of 2,3,5,6-tetrakis(3,6-di-tert-butyl-9H-carbazol-9-yl)-4-(1H-imidazol-1-yl)benzonitrile (**4^{tBu}CzBNIm**)



According to procedure A, **4FBNIm** (0.36 mmol, 1 equivalent) and 3,6-di-*tert*-butyl-carbazole (1.95 mmol, 5.4 equivalents) as donor were used and during the reaction a red-brown color appears.

The product was obtained with quantitative yield (0.34 mmol, yield 90%) by purification with flash chromatography (SiO_2, hexane:dichloromethane from 7:3 to 5:5) as a green powder.

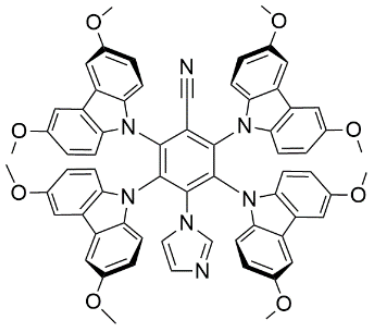
^{1}H NMR (300 MHz, $CDCl_3$) δ 7.64 – 7.40 (m, 8H), 7.06 (t, *J* = 1.1 Hz, 1H), 6.96 (dd, *J* = 8.6, 1.9 Hz, 4H), 6.93 – 6.81 (m, 8H), 6.58 (d, *J* = 8.6 Hz, 4H), 6.40 (t, *J* = 1.4 Hz, 1H), 6.25 (dd, *J* = 1.6, 0.8 Hz, 1H), 1.34 (d, *J* = 11.3 Hz, 82H).

^{13}C{^{1}H} NMR (75 MHz, $CDCl_3$) δ 144.13, 143.84, 141.56, 141.38, 137.65, 136.75, 136.30, 132.15, 129.81, 124.70, 124.22, 123.04, 123.01, 118.37, 117.45, 115.95, 115.88, 113.09, 109.83, 108.26, 77.58, 77.16, 76.74, 34.68, 34.63, 32.02, 31.99, 31.74, 22.80, 14.27.

HR-MS (m/z) Calculated: 1278.8029 ([M+H]$^+$); Found: 1317.7614 ([M+K]$^+$), 1698.5583 ([2M+K]$^+$).

Suitable crystals for SC-XRD were obtained by slow diffusion of methanol into chloroform.

3.4.4.5 Synthesis of 2,3,5,6-tetrakis(3,6-dimethoxy -9H-carbazol-9-yl)-4-(1H-imidazol-1-yl)benzonitrile (**4^{OMe}CzBNIm**)



According to procedure A, **4FBNIm** (0.13 mmol, 1 equivalent) and 3,6-di-methoxy-carbazole (0.63 mmol) as donor were used.

The product was obtained with good yield (0.08 mmol, yield 61%) by purification with flash chromatography (SiO_2, hexane:dichloromethane from 10:0 to 0:10) as a red powder.

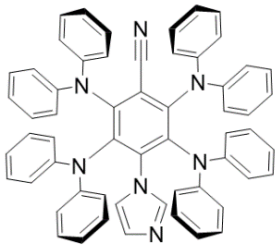
^{1}H NMR (300 MHz, DMF-d_7) δ 7.69 (dd, J = 12.0, 8.9 Hz, 8H), 7.60 (d, J = 2.5 Hz, 4H), 7.48 (d, J = 2.5 Hz, 4H), 6.86 (dd, J = 8.9, 2.6 Hz, 4H), 6.80 – 6.64 (m, 5H), 6.13 (t, J = 1.4 Hz, 1H), 5.99 (dd, J = 1.5, 0.8 Hz, 1H), 3.78 (d, J = 13.6 Hz, 26H).

^{13}C{^{1}H} NMR (75 MHz, DMF-d_7) δ 163.58, 163.19, 162.80, 155.75, 155.50, 144.78, 144.02, 137.08, 136.64, 136.47, 136.26, 129.37, 125.48, 125.20, 119.36, 119.28, 115.76, 115.62, 113.69, 113.01, 112.65, 104.05, 103.74, 56.34, 56.23, 36.51, 36.24, 35.96, 35.68, 35.40, 35.13, 34.85, 31.40, 31.13, 30.85, 30.57, 30.29, 30.01, 29.74.

HR-MS (m/z) Calculated: 1070.3867 ([M+H]$^{+}$); Found: 544.4854 ([M+H_2O+2H]$^{2+}$), 1108.3423 ([M+K]$^{+}$).

Suitable single crystals were obtained by slow diffusion of hexane vapors into chloroform.

3.4.4.6 Synthesis of 2,3,5,6-tetrakis(diphenylamino)-4-(1H-imidazol-1-yl)benzonitrile (**4DPABNIm**)



According to procedure B, **4FBNIm** (1.25 mmol, 1 equivalent) and diphenylamine (5.65 mmol) as donor were used.

The product was obtained with good yield (0.08 mmol, yield 61%) by purification with flash chromatography (SiO_2, hexane:dichloromethane from 10:0 to 0:10) as a yellow powder.

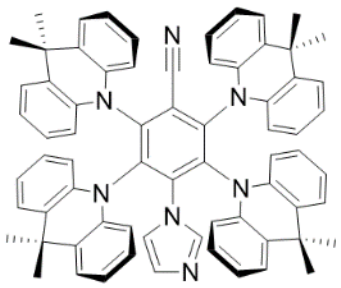
^{1}H NMR (300 MHz, $CDCl_3$) δ 7.14 (s, 2H), 6.96 (dt, J = 17.9, 7.4 Hz, 13H), 6.87 – 6.71 (m, 13H), 6.56 (d, J = 7.8 Hz, 10H), 6.34 (t, J = 1.1 Hz, 1H), 6.25 (t, J = 1.2 Hz, 1H), 5.96 (t, J = 1.4 Hz, 1H).

^{13}C{^{1}H} NMR (75 MHz, $CDCl_3$) δ 148.03, 145.31, 145.13, 144.32, 142.27, 136.07, 129.03, 128.65, 128.00, 123.73, 122.54, 120.97, 119.33, 118.96, 113.57, 77.58, 77.16, 76.74.

HR-MS (m/z) Calculated: 838.3647 ([M+H]$^{+}$); Found: 838.3642 ([M+H]$^{+}$).

Suitable single crystals were obtained by slow diffusion of hexane vapors into chloroform.

3.4.4.7 Synthesis of 2,3,5,6-tetrakis(9,9-dimethylacridin-10(9H)-yl)-4-(1H-imidazol-1-yl)benzonitrile (**4DMACBNIm**)



According to procedure B, **4FBNIm** (0.17 mmol, 1 equivalent) and 9,9-dimethyl-9,10-dihydroacridine (5.65 mmol) as donor were used.

The product was obtained (0.83 mmol, yield 61%) by purification with flash chromatography (SiO_2, hexane:dichloromethane from 10:0 to 5:5) followed by precipitation by diethyl ether as an orange product.

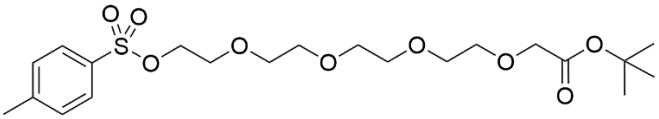
^{1}H NMR (300 MHz, $CDCl_3$) δ 7.30 (dd, *J* = 7.8, 1.5 Hz, 4H), 7.20 – 7.01 (m, 9H), 6.93 (td, *J* = 7.5, 1.2 Hz, 4H), 6.84 – 6.65 (m, 12H), 6.56 – 6.19 (m, 6H), 1.70 (s, 6H), 1.38 (s, 6H), 1.17 (s, 6H), 0.80 (s, 6H).

^{13}C{^{1}H} NMR (75 MHz, $CDCl_3$) δ 150.61, 147.07, 141.06, 137.85, 136.61, 136.20, 131.62, 129.84, 129.59, 128.72, 127.53, 126.15, 122.36, 121.88, 119.42, 114.02, 113.71, 112.73, 77.58, 77.16, 76.74, 35.88, 35.17, 34.70, 34.51, 33.46, 28.06.

HR-MS (m/z) Calculated: 998.4899 ($[M+H]^+$); Found: 998.4887 ($[M+H]^+$), 1996.9770 ($[2M+H]^+$).

Suitable single crystals were obtained by slow diffusion of hexane vapors into chloroform.

3.4.4.8 Synthesis of tert-butyl 14-(tosyloxy)-3,6,9,12-tetraoxatetradecanoate

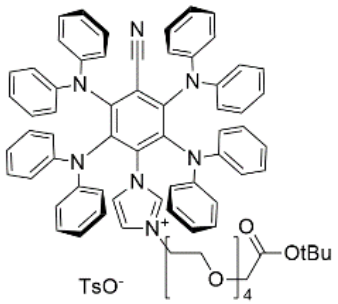


To a solution of *tert*-butyl 14-hydroxy-3,6,9,12-tetraoxatetradecanoate (1.94 mmol) in dichloromethane (5 mL) 4-methylbenzensulfonyl chloride (2.91 mmol, 1.5 equivalents) and pyridine (3.90 mmol, 2 equivalents) were added, and the solution was stirred overnight at room temperature. The reaction was washed with water and aqueous phase was washed thrice with DCM and the organic phase was dried over sodium sulphate and the solvent was removed by rotary evaporator. The product was obtained (1.77 mmol, yield 91%) by purification with flash chromatography (SiO_2, hexane:ethylacetate from 10:0 to 0:10) as a colorless oil.

^{1}H NMR (300 MHz, $CDCl_3$) δ 7.96 – 7.29 (m, 3H), 4.15 (dd, *J* = 5.7, 4.0 Hz, 2H), 4.01 (d, *J* = 2.6 Hz, 2H), 3.77 – 3.62 (m, 12H), 2.44 (s, 3H), 1.47 (s, 11H).

^{13}C{^{1}H} NMR (75 MHz, $CDCl_3$) δ 169.80, 144.93, 133.07, 129.96, 128.13, 81.69, 77.58, 77.37, 77.16, 76.74, 70.87, 70.83, 70.71, 70.65, 69.39, 69.13, 68.80, 28.24, 27.63, 21.80.

3.4.4.9 Synthesis of 1-(4-cyano-2,3,5,6-tetrakis(diphenylamino)phenyl)-3-(16,16-dimethyl-14-oxo-3,6,9,12,15-pentaoxaheptadecyl)-1H-imidazol-3-ium 4-methylbenzensulfonate **([4DPABNImTEGCOOtBu]OTs)**



To a solution of **4DPABNIm** (0.08 mmol) in DMF (10 mL) *tert*-butyl 14-(tosyloxy)-3,6,9,12-tetraoxatetradecanoate (0.8 mmol eq, 10 equivalents) was added and the solution was stirred at 130 °C for 4 days.

Then DMF was removed by rotary evaporator and the crude mixture was purified by column chromatography (SiO_2, dichloromethane:methanol 9:1) to give final product as an orange waxy solid (0.05 mmol, 61%).

^{1}H NMR (300 MHz, CD_2Cl_2) δ 8.44 (s, 1H), 7.87 (d, J = 8.1 Hz, 1H), 7.38 – 6.65 (m, 51H), 6.18 (s, 1H), 4.38 – 3.73 (m, 6H), 3.75 – 3.40 (m, 14H), 3.41 – 3.23 (m, 5H), 3.13 – 2.70 (m, 3H), 2.42 (s, 1H), 1.46 (d, J = 1.7 Hz, 13H).

^{13}C{^{1}H} NMR (75 MHz, CD_2Cl_2) δ 170.03, 147.90, 145.59, 145.22, 145.08, 142.09, 139.61, 137.78, 129.85, 129.69, 129.47, 129.13, 126.54, 124.16, 123.11, 122.85, 122.53, 122.18, 122.06, 113.67, 81.90, 73.00, 71.07, 70.95, 70.86, 70.82, 70.75, 70.66, 70.48, 69.37, 68.91, 62.03, 54.72, 54.36, 54.00, 53.64, 53.28, 50.42, 30.23, 28.38, 28.35.

HR-MS (m/z) Calculated: 1128.5382 ([M]$^+$); Found: 1128.5138 ([M]$^+$).

4 THE EFFECT OF π-EXTENSION OF THE IMIDAZOLE MOIETY

Elisa Pelorosso, Giulio Pavan, Thomas Scattolin, Laura Orian, Sabrina Antonello, Nicola Demitri, Alessandro Aliprandi. *Chem. – Asian J.*, 2024, e202400340
https://doi.org/10.1002/asia.202400340

4.1 Introduction

In **Chapter 3** novel monoimidazole TADF dyes were characterized and investigated as ECL emitters, and the first example of anodic-ECL from a water-soluble TADF dye bearing the protected form of a bioconjugable group was reported.

As outlined in **Conclusion** of **Chapter 3**, the alkylation of imidazole does not affect TADF properties but does impact PLQYs and ECL yields.

Furthermore, the most important result is the fact that ECL performances are related more to the electrochemical reversibility of redox processes rather than to photophysical properties, which nevertheless continue to play a role in ECL efficiencies.

It has been reported that densely combining donors and acceptors along with strengthening the rigidity of the molecular structure can enhance radiative decays, thereby increasing PLQYs[184].

Therefore, with the aim of investigating the role of the imidazole moiety in such scaffolds, the π-extension of the imidazole moiety was increased by using benzimidazole and phenantro[9,10-d]imidazole instead of imidazole, while keeping diphenylamine and 3,6-di-*tert*-butyl carbazole as donors.

In the present **Chapter**, the synthesis and characterization of these novel TADF emitters in organic solvents are presented.

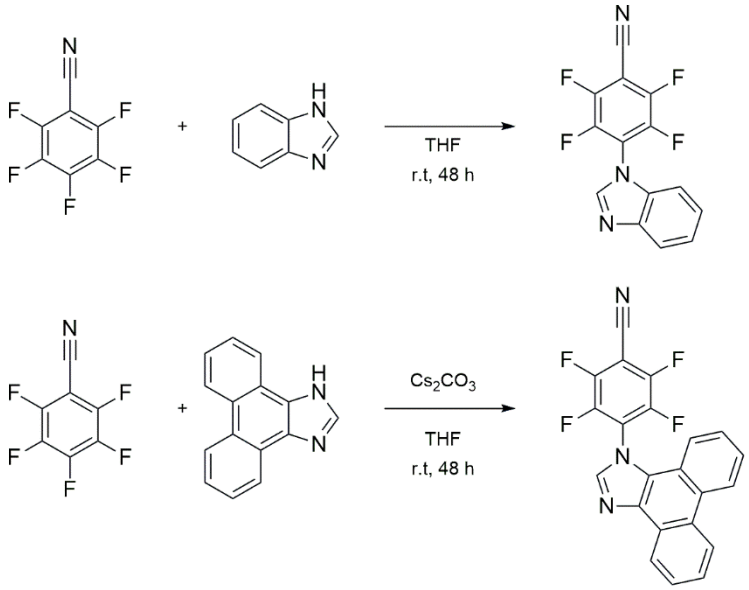
4.2 Results and discussion

4.2.1 Synthesis

As previously indicated, the compound that will be discussed in this Chapter are based on benzonitrile acceptor which was substituted with benzimidazole or phenanthrol[9,10-d]imidazole to obtain compounds **4FBNBenzIm** and **4FBNPhenIm**, respectively (**Scheme 4.1**).

For the synthesis of **4FBNBenzIm** a slightly modified literature procedure was followed[185], and benzimidazole was used in excess since it acts both as reactant and scavenger.

Conversely, for the synthesis of **4FBNPhenIm** a weak base (cesium carbonate) was used in excess to deprotonate phenanthrol[9,10-d]imidazole, since the latter cannot acts as a scavenger.



Scheme 4.1: Syntheses of **4FBNBenzIm** (first row) and synthesis of **4FBNPhenIm** (second row).

The formation of para-substituted isomers was confirmed by $^{19}F\{^{1}H\}$ NMR (**Figure 4.1**), which revealed the characteristics signals of an AA'BB' spin system of p-disubstituted benzene.

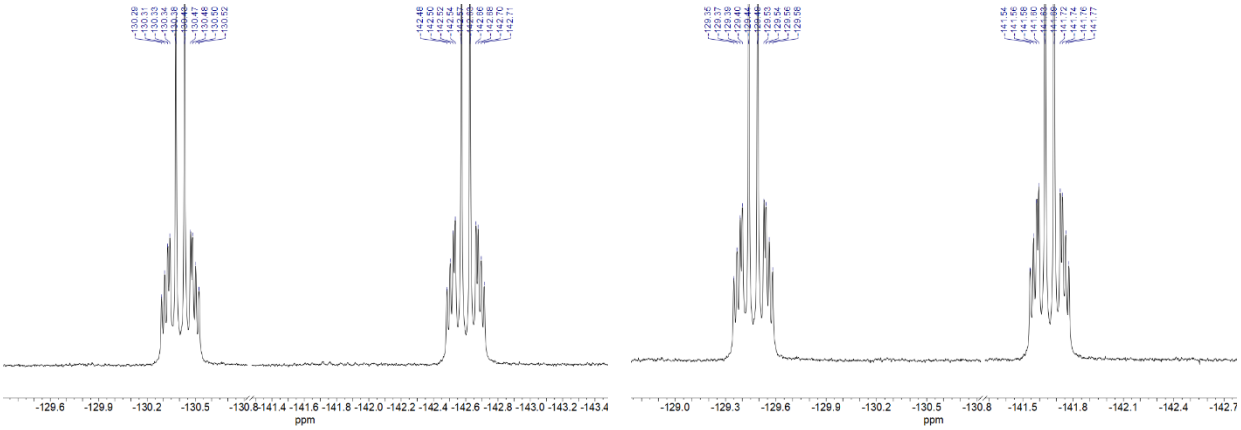


Figure 4.1: $^{19}F\{^{1}H\}$ spectra of **4FBNBenzIm** (left) and **4FBNPhenIm** (right).

In the aromatic region of ^{1}H NMR spectrum of compound **4FBNBenzIm** (**Figure 4.2**) different multiplets caused by aromatic protons are present and they cannot be easily assigned due to the presence of a second-order system and ^{1}H-^{19}F scalar couplings or dipolar interactions

Nevertheless, conversely to literature data, it was found that the proton between the two nitrogen atoms generates a triplet signal instead of a singlet.

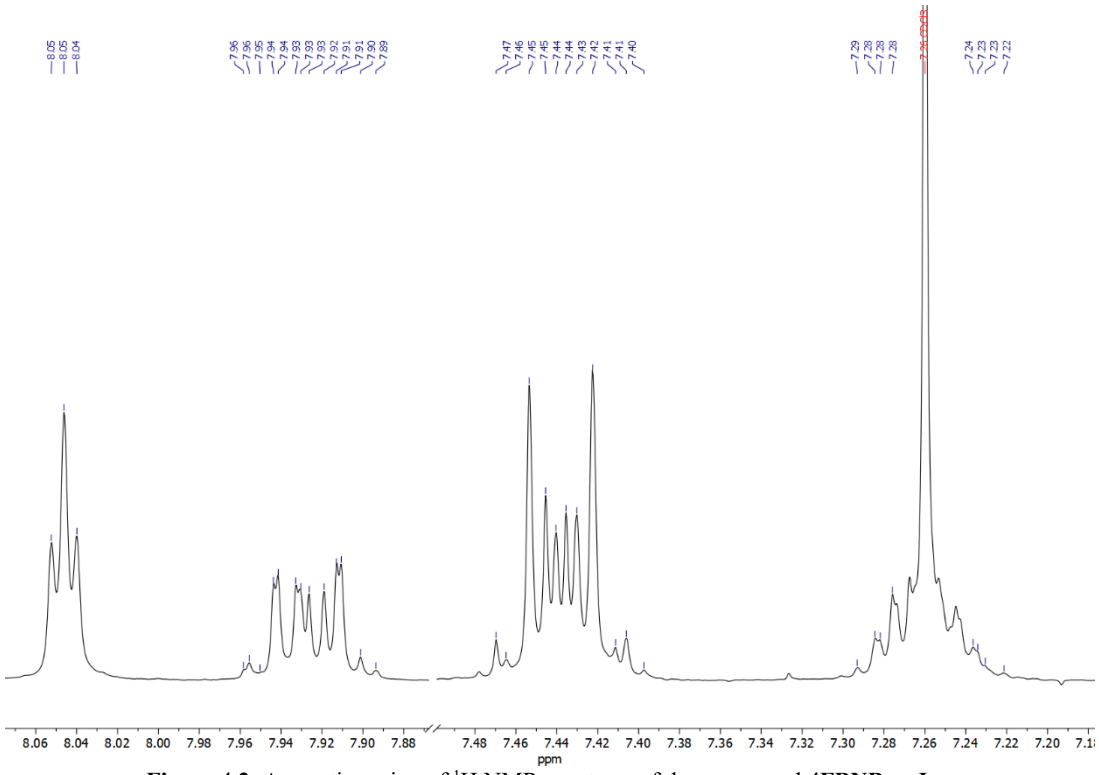


Figure 4.2: Aromatic region of ^{1}H NMR spectrum of the compound **4FBNBenzIm**.

As expected, even in the ^{1}H NMR spectrum of compound **4FPhenBNIm** many complex multiplets showing ^{1}H-^{19}F dipolar interaction are present (**Figure 4.3**).

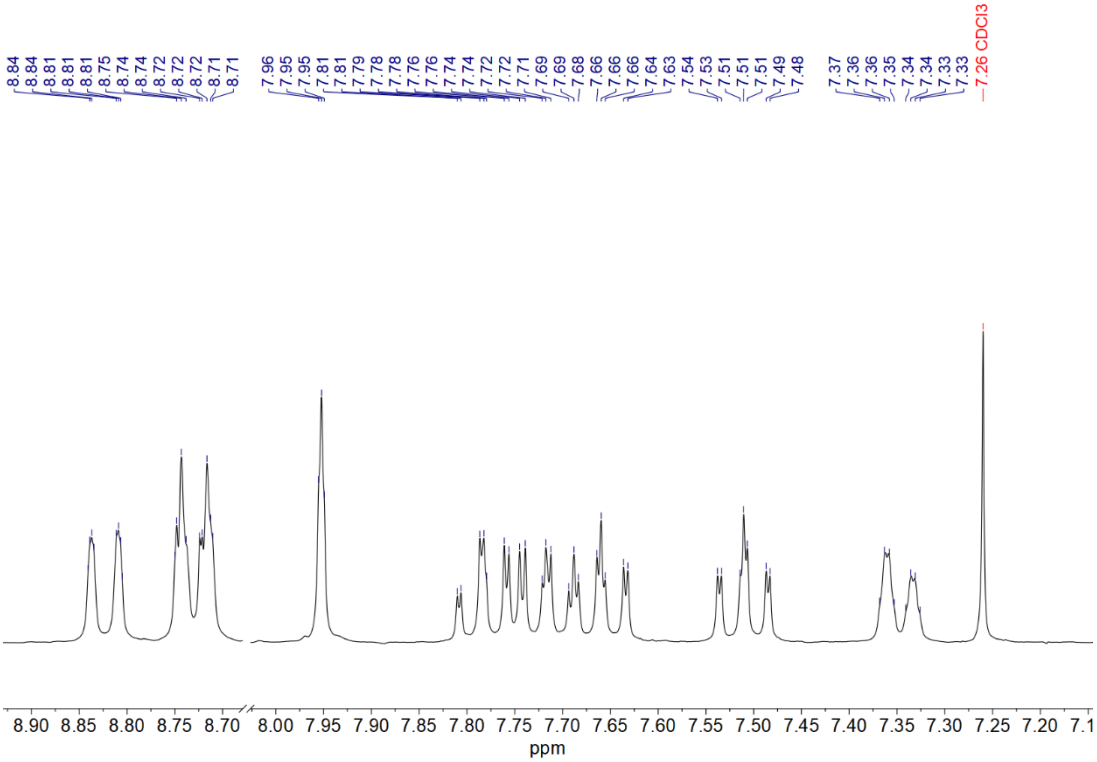
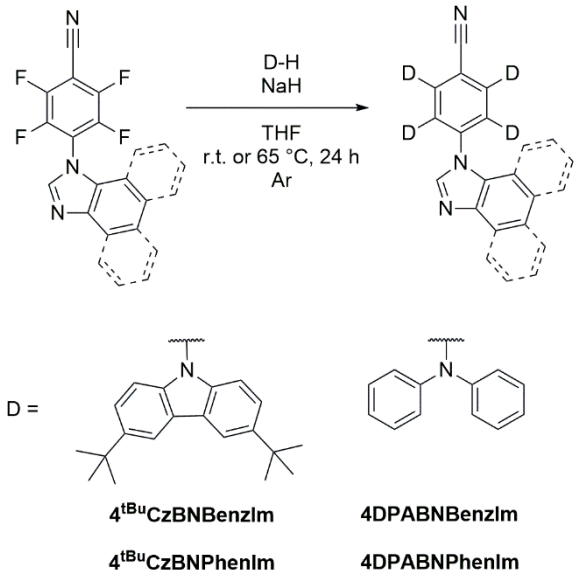


Figure 4.3: Aromatic region of ^{1}H NMR spectrum of the compound **4FBNPhenIm**.

^{13}C{^{1}H} NMR spectrum of compound **4FBNPhenIm** is reported in **Figure A4.10**.

Afterwards, diphenylamine and 3,6-di-*tert*-butyl carbazole were inserted using the same experimental conditions reported in **Chapter 3** (**Scheme 4.2**).



Scheme 4.2: Syntheses of π-extended imidazole derivatives.

^{1}H and ^{13}C{^{1}H} NMR spectra of the products are reported in **Figures A4.6-4.9** and **A4.11-4.14**.

In the ^{1}H NMR spectra of compounds **4^{tBu}CzBNBenzIm** and **4^{tBu}CzBNPhenIm** four singlets attributable to protons of the *tert*-butyl groups can be observed (**Figure 4.4-left**).

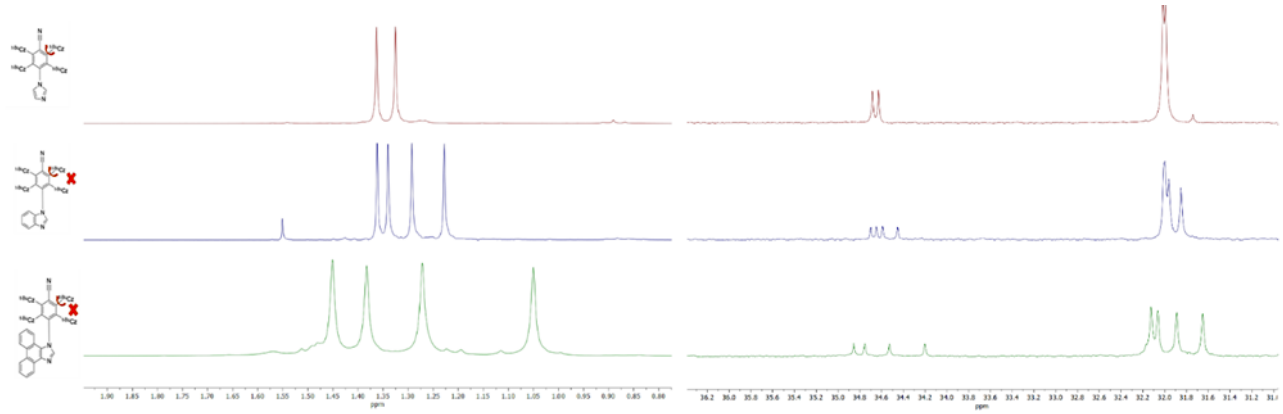


Figure 4.4: Comparison of the aromatic regions of ^{1}H NMR spectra (left) and $^{13}C\{^{1}H\}$ NMR spectra (right) of the compounds **4^{tBu}CzBNIm** (red), **4^{tBu}CzBNBenzIm** (blue) and **4^{tBu}CzBNPhenIm** (green).

Indeed, the intramolecular rotation of carbazole moieties is restricted by the stiffening of the structure going from imidazole to benzimidazole and phenanthro[9,10-d]imidazole, making these protons magnetically non-equivalent, a phenomenon that can be observed also in the $^{13}C\{^{1}H\}$ NMR spectra (**Figure 4.4-right**).

Indeed, in the $^{13}C\{^{1}H\}$ NMR spectrum of **4^{tBu}CzBNBenzIm** four signals can be observed at 35 ppm, which can be attributed to quaternary carbons of *tert*-butyl groups, while at 32 ppm two signals attributable to primary methyl carbon are present.

These signals are caused by different resonance frequencies of carbon nuclei, confirming the presence of a stiffened structure.

A more stiffened structure can be observed in the $^{13}C\{^{1}H\}$ spectrum of compound **4^{tBu}CzBNPhenIm**, since it shows two sets of four singlets at 35 ppm and 32 ppm.

Finally, in order to obtain alkylated derivatives, alkylation of benzimidazole and phenanthro[9,10-d]imidazole moieties with a glycol chain is tried using the compound **TsOTEGCOOtBu** at high temperatures (see **Chapter 3.2.1**). Nevertheless, the charged derivatives are not obtained.

4.2.2 Crystallographic characterization

Single crystals, suitable for X-ray diffractometric analysis, are grown by slow diffusion of methanol or *n*-hexane vapors into chloroform (see the **Experimental section**).

XRD structure of compounds **4^{tBu}CzBNBenzIm**, **4^{tBu}CzBNPhenIm**, **4DPABNPhenIm** are shown in **Figure 4.5** and confirm the presence of benzimidazole and phenanthro[9,10-d]imidazole in the para position and the complete substitution of fluorine atoms.

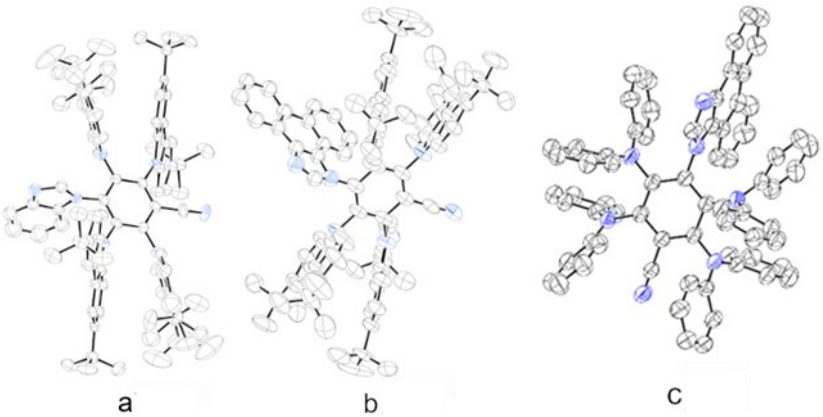


Figure 4.5: Ellipsoid representation of the compounds **4^{tBu}CzBNBenzIm** (a), **4^{tBu}CzBNPhenIm** (b), **4DPABNPhenIm** (c) asymmetric units (A.S.U. – 50% probability). Hydrogens are omitted for clarity.

Compounds crystallize in centrosymmetric space groups with half molecule in the asymmetric units (ASU) for the compounds **4^{tBu}CzBNBenzIm** and **4^{tBu}CzBNPhenIm** while multiple copies have been found for the compound **4DPABNPhenIm** (**Figure A4.1**). Molecules lies on crystallographic inversion centres and show static disorder on the polar cyano and imidazolyl heads, suggesting that packed molecules are not forming very strong and specific contacts (i.e. loose and flexible non-covalent interactions, with solvent molecules, are present). Despite disorder, all the crystal structure are consistent with expected molecular connectivity. Equivalent molecules adopt very similar conformations with minor phenyl rearrangements, as shown in **Figure 4.6** (R.M.S.D. < 1 Å among common atoms). Crystal packing contacts involve multiple CH•••π contacts and poor π•••π stacking of aromatic sidechains. Compound **4DPABNPhenIm** is related to its imidazole congener **4DPABNIm** and show the same orientation of the imidazole substituent (forming an angle of ~81° with the central phenyl core), due to its steric hindrance.

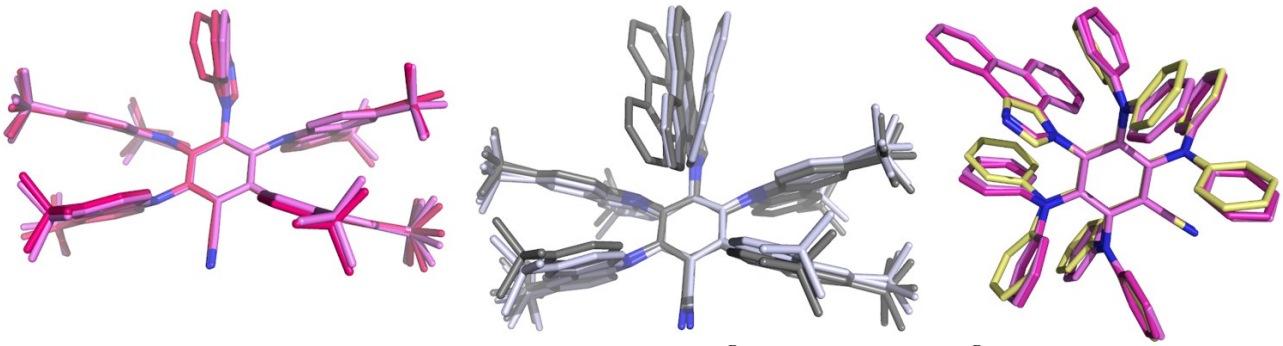


Figure 4.6: Overlap of crystallographically independent molecules of **4^{tBu}CzBNBenzIm** (left), **4^{tBu}CzBNPhenIm** (center) and **4DPABNPhenIm** (purple sticks) with **4DPABNIm** (yellow sticks) as comparison (right) (hydrogens omitted for clarity).

Even in this case, the imidazole derivative moiety is almost orthogonal to the benzonitrile ring, thus suggesting a poor orbital overlap.

4.2.3 Electrochemical characterization

Electrochemical properties of all compounds are studied in anhydrous acetonitrile and dichloromethane by means of cyclic voltammetry, and all the data are summarized in **Table 4.1**, while cyclic voltammograms are depicted in **Figures A4.27-A4.30**.

Table 4.1: Electrochemical properties of π-extended imidazole derivatives.

Compound	ACN solution		DCM solution	
	$E_{1/2}^{red}$ (V)	$E_{1/2}^{ox}$ (V)	$E_{1/2}^{red}$ (V)	$E_{1/2}^{ox}$ (V)
4^{tBu}CzBNBenzIm	-1.46	1.70	-1.54	1.39, 1.66[a]
4^{tBu}CzBNPhenIm	-1.35	1.48[a], 1.66[a]	-1.39	1.39, 1.52[a]
4DPABNBenzIm	-1.76	0.78[a], 1.12, 1.42	-1.8	0.81[a], 1.05, 1.21
4DPABNPhenIm	-1.67	0.79[a], 1.06[a], 1.17[a]	-1.72	1.10, 1.32, 1.62[a]

Measurements are performed in degassed solutions containing 1 mM luminophore and 0.1 M $TBAPF_6$. Working Electrode: Glassy Carbon Electrode (3 mm); Reference Electrode: Ag/AgCl(sat.d KCl); Counter Electrode: Pt wire. Scan rate 100 mVs^{-1}. [a] Irreversible process, reported potentials are peak potentials.

In the cathodic region, a single, reversible reduction process is present and ascribable to the generation of the radical-anion on the benzonitrile core.

Nevertheless, the reducing character of the benzonitrile core decreases by increasing the imidazole π-extension, a peculiar behavior that can be due to a non-innocent character of the π-extended imidazole moiety, in particular for phenanthro[9,10-d]imidazole.

Indeed, a stronger σ-acceptor character of phenanthro[9,10-d]imidazole than benzimidazole and imidazole can be hypothesized, while a partial conjugation of the extended imidazole with the benzene ring cannot be excluded.

As for **4DPABNIm**, **4DPABNBenzIm** shows an EC' process in the cathodic region when dichloromethane is used as solvent (**Figure 4.7**).

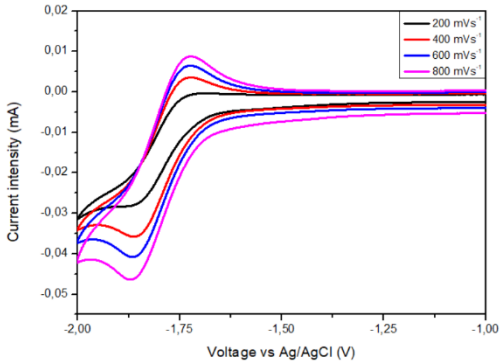


Figure 4.7: CV at different scan rates of **4DPABNBenzIm** in dichloromethane solution.

As expected, in the anodic region multi-electronic oxidation processes are present.

Anodic processes of compounds **4^{tBu}CzBNBenzIm** and **4^{tBu}CzBNPhenIm** are very similar to the one of compound **4^{tBu}CzBNIm**, with a higher electrochemical reversibility in dichloromethane than acetonitrile.

Reversible oxidation processes can be observed also in the anodic regions of compounds **4DPABNBenzIm** and **4DPABNPhenIm** even if the patterns become more complex, meaning that the π-extension of imidazole does not improve stability of radical-cations.

In order to evaluate the difference in diffusive behavior connected to the extension of imidazole, diffusion coefficients are calculated for diphenylamino derivatives at different scan rates through the Randles-Ševčík in acetonitrile and dichloromethane solutions (**Figures A4.31-A4.36**).

As expected, diffusion coefficients smoothly decrease with increasing molecular weight (from $9.1 \cdot 10^{-6}$ cm^2 s^{-1} for **4DPABNIm** to $6.6 \cdot 10^{-6}$ cm^2 s^{-1} for **4DPABNBenzIm** and $2.7 \cdot 10^{-6}$ cm^2 s^{-1} for **4DPABNPhenIm**) and going from acetonitrile to dichloromethane in line with the differences in the solvent viscosity[186].

4.2.4 Photophysical characterization

For all compounds, UV-vis absorption spectra, emission and excitation spectra, PLQYs and PhotoLuminescence decay curves are recorded both in acetonitrile and dichloromethane solution.

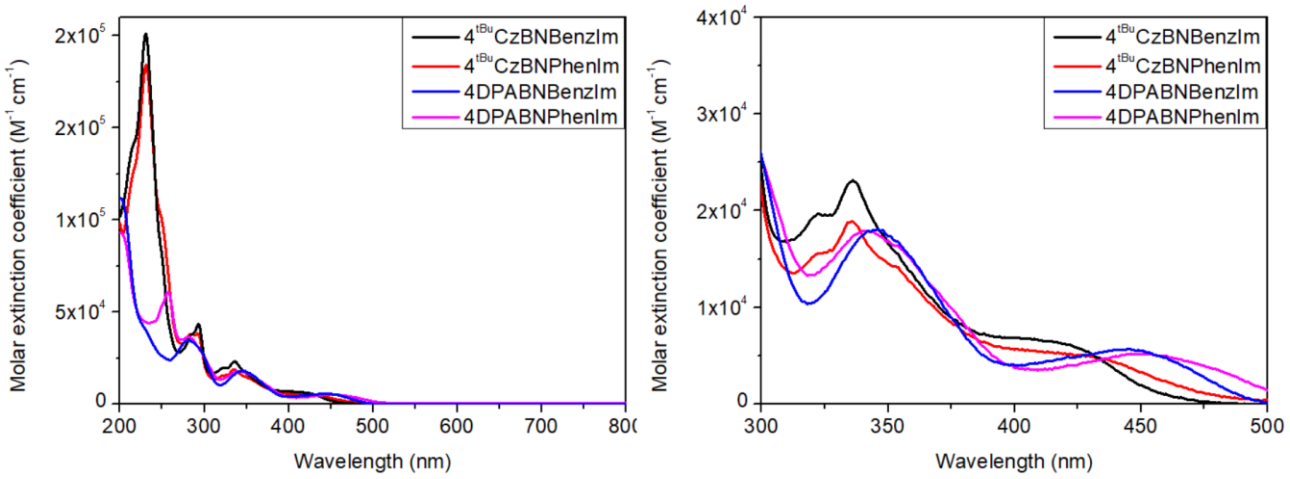


Figure 4.8: Absorption spectra in acetonitrile (left) and zoom of the region 300-500 nm (right).

In **Figure 4.8** UV-vis absorption spectra in acetonitrile are reported, while in **Table 4.2** absorption maxima of ICT region are reported.

In absorption spectra π*←π and σ*←n transitions cause the energy bands with very high molar extinction coefficient values (up to $2 \cdot 10^5$ M^{-1} cm^{-1}) in the region between 200 and 300 nm, while Internal Charge Transfer (ICT) transitions between donor and acceptor moieties generate the bands with broad profiles and lower molar extinction coefficients (around $2 \cdot 10^4$ M^{-1} cm^{-1}) in the region between 300 and 500 nm.

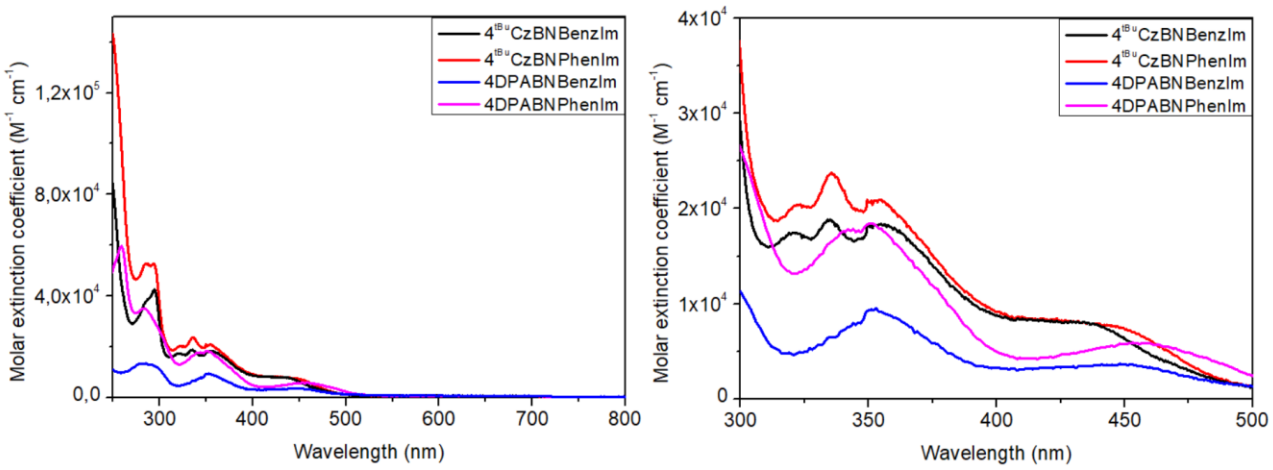


Figure 4.9: Absorption spectra in dichloromethane (left) and zoom of the region 300-500 nm (right).

Table 4.2: Photophysical properties of π-extended imidazole derivatives.

Compound	Solvent	λ_{abs}	λ_{em}[a]	Φ_{PL}[b]	Φ_{PL}[c]
4^{tBu}CzBNBenzIm	**ACN**	322^{sh}, 336	546	13.6 ± 0.5	20.5 ± 0.6
	DCM	320, 335, 354	532	25.5 ± 0.7	49 ± 1
4^{tBu}CzBNPhenIm	**ACN**	322^{sh}, 336	564	8.5 ± 0.4	10.6 ± 0.5
	DCM	322, 336, 354	552	24.5 ± 0.5	31.4 ± 0.8
4DPABNBenzIm	**ACN**	346, 444	518	8 ± 2	38 ± 2
	DCM	352, 451	558	12 ± 3	29 ± 2
4DPABNPhenIm	**ACN**	341, 451	534	8.2 ± 0.9	27 ± 2
	DCM	351, 457	573	9 ± 1	16 ± 1

Measurements are performed with 5 μM solution. [a] λ_{exc}=340 nm. [b] Aerated solution, average scan, λ_{exc} = 300 - 410 nm. [c] Ar-purged solution, average scan, λ_{exc} = 300 - 410 nm.

Moreover, in the ICT region all compounds exhibit profiles that are very similar to the respective monoimidazole derivatives with the absorption maxima located at the same wavelength of the latter, meaning that the extension of imidazole plays a minor role in optical transition.

To exclude the presence of excimers excitation spectra are recorded (**Figures A4.15-A4.18**) and they are superimposable to the respective absorption spectra, thereby excluding the presence of excimers.

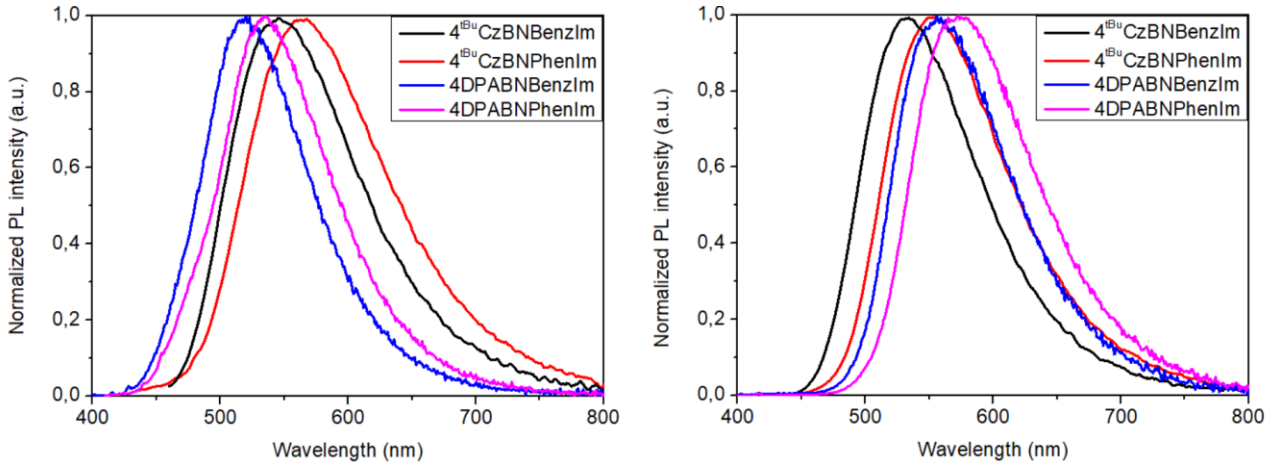


Figure 4.10: Emission spectra in acetonitrile (left) and in dichloromethane (right).

The emission profiles are reported in **Figure 4.10**, and they are characterized by broad emission and large Stokes shift.

Moreover, the extension of the imidazole does impact the HOMO-LUMO gap lowering the LUMO. Indeed, a bathochromic shift can be observed in emission maxima of 3,6-di(*tert*-butyl)carbazoyl derivatives (ca. 6 nm for **4^{tBu}CzBNBenzIm** and ca. 25 nm for **4^{tBu}CzBNPhenIm**) both in acetonitrile and dichloromethane solution, meaning that the HOMO-LUMO gap is decreased, reflecting the electrochemical data.

The PLQYs of 3,6-di(*tert*-butyl)carbazoyl derivatives demonstrate an increase moving from acetonitrile to dichloromethane. However, they remain lower than the imidazole congener, due to the higher non-radiative decays caused by the π-extended imidazole moiety.

In contrast, a less trivial trend can be observed for diphenylamino derivatives, whereby hypsochromic shifts and higher PLQYs can be noted upon increasing solvent polarity.

To the best of our knowledge, this hypsochromic shift with DCM and ACN has never been observed. However, a hypsochromic shift between DCM and ethanol has been reported for a Multi-Resonant TADF compound although no explanation was provided.

Two hypotheses can be proposed to explain this behavior. The first is the formation of aggregates in acetonitrile while the second is an inefficient solvation from acetonitrile molecules[187].

The first hypothesis can be discounted since it would be expected to result in a greater decrease in diffusion coefficients greater than that observed. The second hypothesis is more plausible and may be attributed to the higher rotational degrees of diphenylamine, which may impede efficient solvation.

All these compounds exhibit, as expected, bi-exponential fluorescence decays in deoxygenated solutions, confirming TADF features (**Table 4.3** and **Figures A4.19-A4.26**).

As for TADF compounds reported in the previous chapters, also in this case lifetimes are shortened upon oxygenation.

Table 4.3: Lifetimes of prompted and delayed fluorescence of π-extended imidazole derivatives.

Compound	Solvent	τ_P (ns)[a]	τ_D (μs)[a]	τ_P (ns)[b]	τ_D (μs)[b]
4^{tBu}CzBNBenzIm	**ACN**	13.79 ± 0.02	0.277 ± 0.002	16.15 ± 0.03	1.277 ± 0.007
	DCM	10.92 ± 0.04	0.618 ± 0.002	11.35 ± 0.02	1.7 ± 0.004
4^{tBu}CzBNPhenIm	**ACN**	7.67 ± 0.02	0.322 ± 0.03	7.87 ± 0.05	1.177 ± 0.009
	DCM	9.23 ± 0.02	0.766 ± 0.004	9.58 ± 0.02	1.515 ± 0.007
4DPABNBenzIm	**ACN**	3.02 ± 0.04	N.C.[c]	2.90 ± 0.04	5.93 ± 0.07
	DCM	3.716 ± 0.005	1.59 ± 0.09	3.72 ± 0.01	14.2 ± 0.2
4DPABNPhenIm	**ACN**	3.54 ± 0.02	N.C.[c]	3.71 ± 0.03	28.5 ± 0.7
	DCM	3.946 ± 0.006	1.47 ± 0.04	4.13 ± 0.01	44.2 ± 0.7

Measurements are performed with 5 μM solution. λ_{exc} = 402.3 nm, Nanosecond lifetimes were evaluated with TCSPC electronic, while microsecond lifetimes were evaluated with MCS electronic. [a] Aerated solution. [b] Ar-purged solution. [c] Not Calculated.

As for electrochemical properties, it can be concluded that the π-extension of the imidazole moiety exerts an influence on the photophysical properties, including bathochromic shifts and a declining trend in PLQYs in comparison to their imidazole congeners.

4.2.5 Electrochemiluminescence characterization

Since the scope of this **Chapter** is to evaluate the effect of π-extension of the imidazole moiety in these structures, ECL of these compounds is evaluated under annihilation and co-reactant conditions. Furthermore, ECL spectroscopy and ECL-voltages experiments are examined with the aid of BPO and TPA as co-reactants.

Annihilation ECL efficiencies are reported in **Table 4.2** while ECL-time and current-time profiles are reported in **Figures A4.49-A4.52**.

Table 4.4: Annihilation ECL efficiencies in acetonitrile solution of π-extended imidazole derivatives.

Compound	Applied Potentials (V)	Φ_{ECL}
4^{tBu}CzBNIm	-1.7 to +1.3	1.4±0.9
	+1.3 to -1.7	0.27±0.09
4^{tBu}CzBNBenzIm	-1.6 to +1.5	0.58±0.08
	+1.5 to -1.6	0.56±0.13
4^{tBu}CzBNPhenIm	-1.5 to +1.6	0.12±0.04
	+1.6 to -1.5	0.35±0.14
4DPABNIm	-2 to +1.3	38±6
	+1.3 to -2	12±4
4DPABNBenzIm	-2 to +1.2	0.07±0.02
	+1.2 to -2	0.04±0.02
4DPABNPhenIm	-2 to +1.2	0.14±0.02
	+1.2 to -2	0.16±0.03

Measurements are performed in degassed acetonitrile solutions containing 20 μM luminophore and 0.1 M $TBAPF_6$ as supporting electrolyte. WE: Glassy Carbon Electrode (1 mm); RE: Ag/AgCl (sat.d KCl) electrode; CE: Pt wire. Potentials were stepped with a frequency of 10 Hz. [a] Φ_{ECL} determined under annihilation conditions according to **Equation 3.14**, $[Ru(bpy)_3](Cl)_2$ as standard (ECL efficiency was assumed as unitary).

Independently from the donor, π-extended imidazole derivatives show lower annihilation ECL yields respect to their imidazole congeners, a behavior that can be related to the lower diffusion coefficient of these compounds, which are known to reduce ECL efficiencies[45,111,188], or to a lower stability of their radicals as observed in cyclic voltammetry.

Indeed, for compounds **4DPABNBenzIm** and **4DPABNPhenIm** light appears only after the oxidation of the radical-anion, suggesting a lower lifetime of radical-cations, while for compound **4^{tBu}CzBNBenzIm** and **4^{tBu}CzBNPhenIm** light emission seems to be independent by the pulse sequence.

These results suggest that the π-extension of the imidazole moieties has a detrimental effect on annihilation ECL yields.

Co-reactant ECL experiments are performed in presence of BPO and TPA as co-reactants.

As their imidazole congeners, when BPO is used as co-reactant the light emission arises around the reduction potential of the luminophore (**Figure 4.11** and **Figures A4.37-A4.40**) while when TPA is used as co-reactant light emission arises around the oxidation potential of the luminophore (**Figure 4.12**).

These experiments confirm that the bottleneck is the generation of the radical-anion or radical-cation of the luminophore.

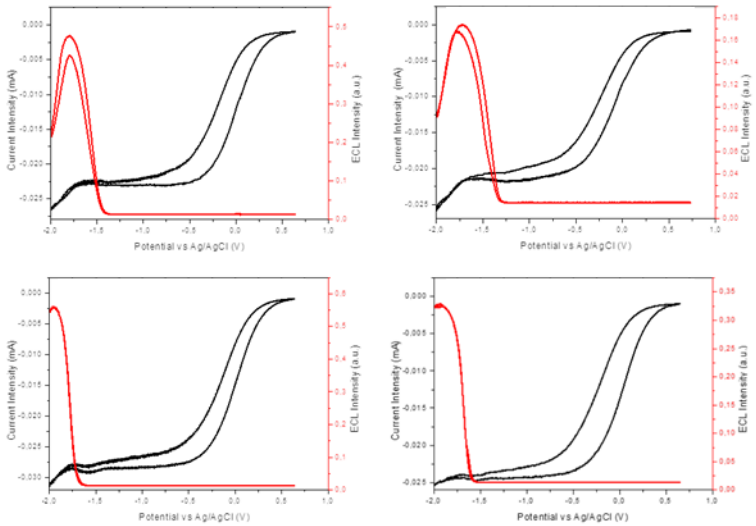


Figure 4.11: ECL-voltage curves of **4^{tBu}CzBNBenzIm** (upper left), **4^{tBu}CzBNPhenIm** (upper right), **4DPABNBenzIm** (lower left), **4DPABNPhenIm** (lower right) in acetonitrile with BPO as co-reactant.

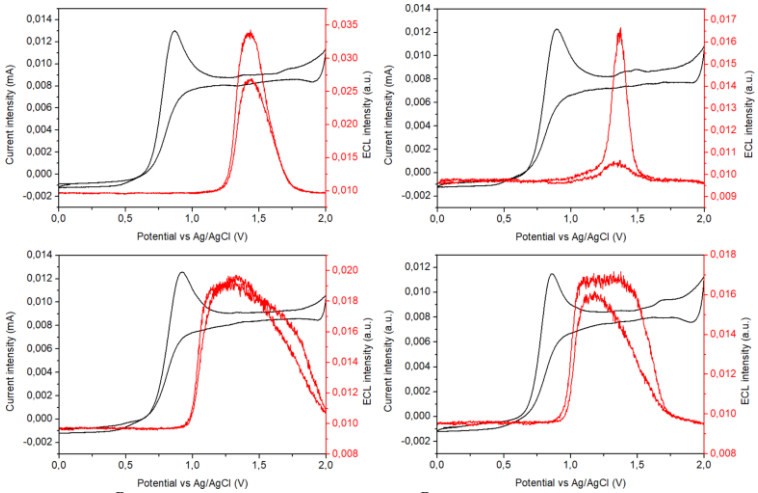


Figure 4.12: ECL-voltage curves of **4^{tBu}CzBNBenzIm** (upper left), **4^{tBu}CzBNPhenIm** (upper right), **4DPABNBenzIm** (lower left), **4DPABNPhenIm** (lower right) in acetonitrile with TPA as co-reactant.

ECL efficiencies and ECL emissions under reductive-oxidation conditions are reported in **Table 4.5** while in **Figures A4.53-A4.56** ECL-time and current-time profiles are reported.

Table 4.5: Reductive-oxidation ECL efficiencies and ECL emissions of π-extended imidazole derivatives.

Compound	Solvent	Φ_{ECL}	λ_{ECL}
4^{tBu}CzBNIm	**ACN**	4.7±0.6	545
	DCM	11±3	529
4^{tBu}CzBNBenzIm	**ACN**	2.3±0.4	545
	DCM	20±3	537
4^{tBu}CzBNPhenIm	**ACN**	1.4±0.5	563
	DCM	3.0±0.4	556
4DPABNIm	**ACN**	12±2	528
	DCM	28±4	533
4DPABNBenzIm	**ACN**	3.2±0.6	529
	DCM	9±2	536
4DPABNPhenIm	**ACN**	0.9±0.2	549

	DCM	5.5±1.4	552

Measurements are performed in degassed solutions containing 50 μM luminophore, 1 mM BPO and 0.1 M $TBAPF_6$. WE: Glassy Carbon Electrode (1 mm); RE: Ag/AgCl (sat.d KCl); CE: Pt wire. Potential sequence (repeated three times): 0 V for 3 s, -2 V for 3 s, 0 V for 3 s. All experiments were performed three times each. [a] Φ_{ECL} determined according to **Equation 3.14**, $[Ru(bpy)_3](Cl)_2$ as standard (ECL efficiency assumes as unitary).

As expected, ECL yields increase passing from acetonitrile to dichloromethane while a general decrease can be observed by extending the imidazole moiety, reflecting PLQYs and a general decrease in ECL yields upon imidazole extension can be noted, in accordance with annihilation experiments.

As for **4DPABNIm**, compounds **4DPABNBenzIm** and **4DPABNPhenIm** exhibit build-up profiles that can be due to the generation of byproducts traces (**Figure 4.13** and **Figures A4.55-A4.56**).

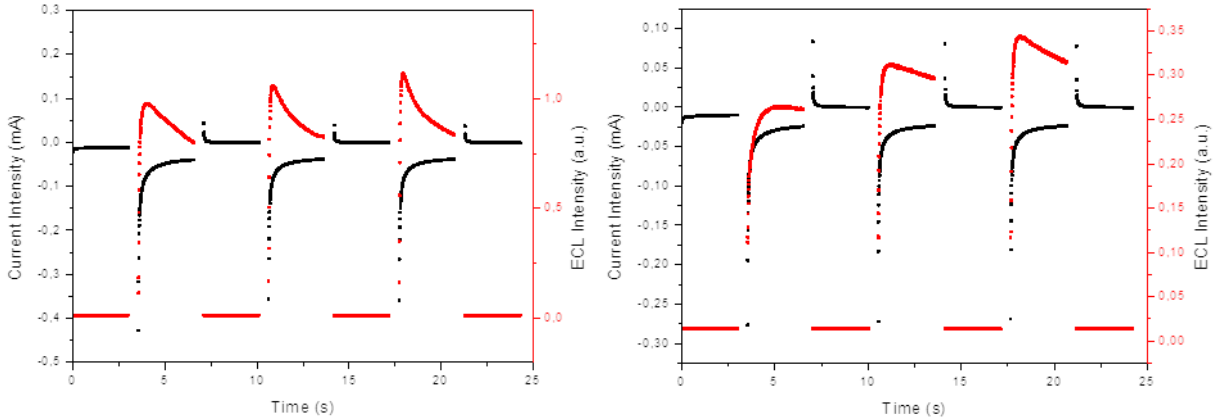


Figure 4.13: Reductive oxidation ECL-time (red) and current-time (black) profiles of **4DPABNBenzIm** (left) and **4DPABNPhenIm** (right) in dichloromethane.

In contrast, no delays between the electrical pulse and light emission can be observed.

Oxidative-reduction ECL efficiencies and emissions are reported in **Table 4.6**, and they follow the same trend of reductive-oxidation ECL efficiencies.

Table 4.6: Oxidative-reduction ECL efficiencies and ECL emissions of π-extended imidazole derivatives.

Compound	Φ_{ECL}	λ_{ECL}
4^{tBu}CzBNIm	0.39	529
4^{tBu}CzBNBenzIm	0.27	548
4^{tBu}CzBNPhenIm	0.03	569
4DPABNIm	1.4	533
4DPABNBenzIm	0.05	537
4DPABNPhenIm	0.06	546

Measurements are performed in degassed acetonitrile solutions containing 50 μM luminophore, 1 mM TPA and 0.1 M $TBAPF_6$. WE: Glassy Carbon Electrode (1 mm); RE: Ag/AgCl (sat.d KCl); CE: Pt wire. Potential sequence (repeated three times): 0 V for 3 s, +1.5 V for 3 s, 0 V for 3 s. [a] Φ_{ECL} determined according to **Equation 3.14**, $[Ru(bpy)_3](Cl)_2$ as standard (ECL efficiency assumes as unitary).

Co-reactant ECL emissions (**Figure 4.13-4.14**) are comparable to PL emission, excluding some little discrepancies caused by different experimental conditions.

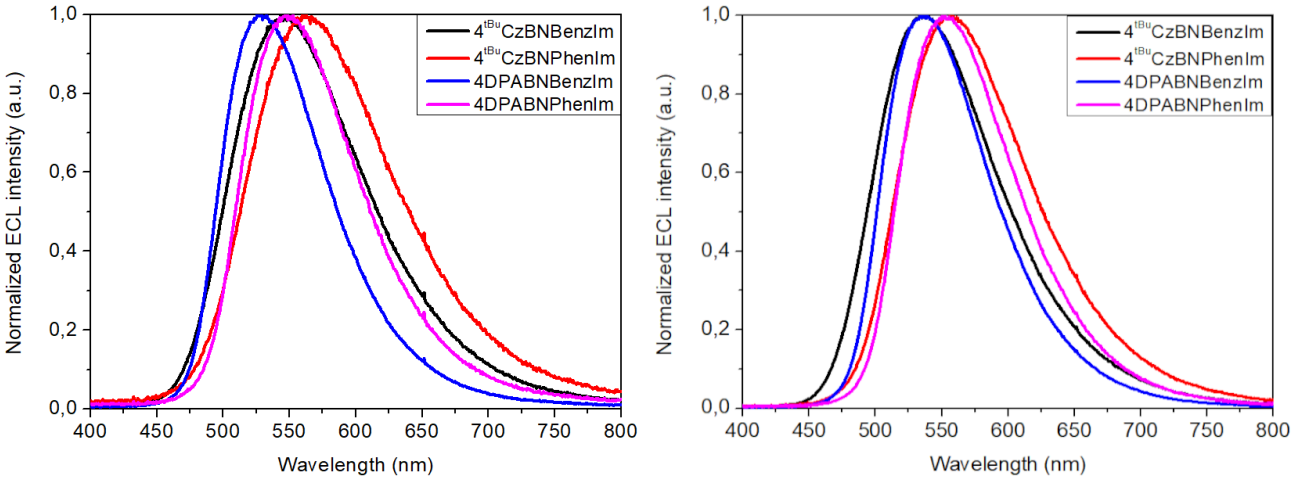


Figure 4.14: ECL spectra in acetonitrile (left) and dichloromethane (right) in presence of BPO as co-reactant.

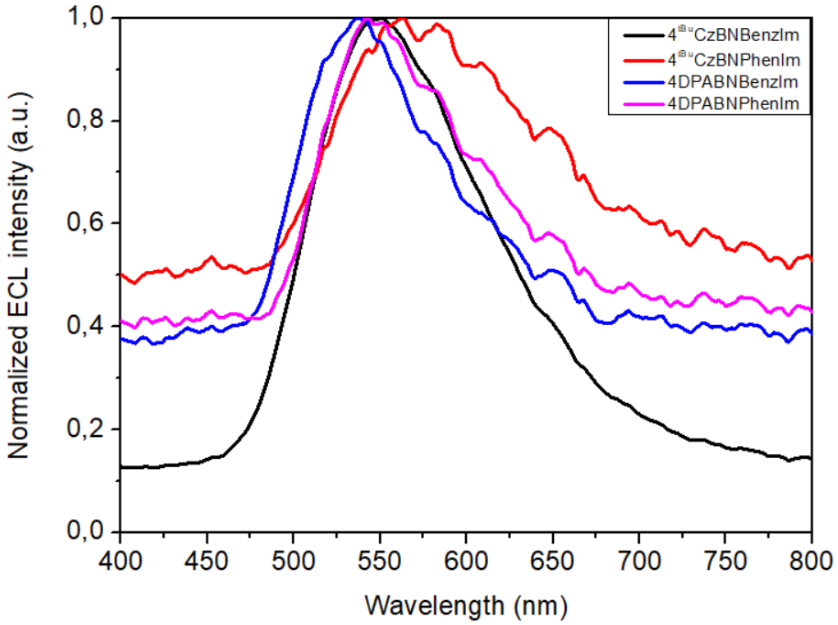


Figure 4.15: ECL spectra in acetonitrile in presence of TPA as co-reactant.

4.3 Conclusion

In conclusion, in this **Chapter** the effect of the π-extension of the imidazole moiety of compounds **4^{tBu}CzBNIm** and **4DPABNIm** on their photophysical, electrochemical and electrochemiluminescence properties was investigated.

Four novel TADF compounds were synthesized and structurally characterized, finding that the extension of the imidazole leads to a restriction of intramolecular rotation (RIR) in solution as observed in ^{1}H NMR experiments.

Their photophysical and electrochemical properties were investigated in organic solvents, finding redshifted emissions, lower PLQYs and a decrease in the reducing character of the acceptor upon extension of the imidazole.

ECL yields were assessed under annihilation and co-reactant conditions, finding lower ECL yields upon extension of the imidazole.

All these results show that the π-extension of the imidazole and the restriction of intramolecular rotation do not improve photophysical and ECL yields.

Nevertheless, these molecules could find a use in other fields such as imaging techniques (two-photon excited fluorescence imaging, fluorescence lifetime imaging…) or as triplet photosensitizers[189–192].

4.4 Experimental Section

All reagents, except 3,6-di-*tert*-butyl-carbazole (synthesized according to literature[178]) were used as received without further purification and they were obtained from Sigma-Aldrich and Alfa-Aesar (dibenzoyl peroxide, wet with 25% water).

All solvents, except those for photophysical measurements, were dried according to literature procedure[151] using 3Å molecular sieves purchased from Thermoscientific.

^{1}H and $^{13}C\{^{1}H\}$ NMR spectra were recorded on a Bruker AVANCE III spectrometer equipped with a BBO probe while $^{19}F\{^{1}H\}$ NMR were recorded with a Bruker 200 MHz equipped with a QNP probe; ^{1}H and $^{13}C\{^{1}H\}$ NMR chemical shifts were referenced relative to residual solvents peaks while $^{19}F\{^{1}H\}$ chemical shifts were referenced using indirect referencing[152].

NMR solvents were purchased from Sigma-Aldrich or EurisoTOP and dried with 3Å molecular sieves purchased from Merck.

Multiplicities of signals are reported as s (singlet), d (doublet), t (triplet), q (quartet), quint (quintet), m (multiplet) and combinations of these multiplicities, coupling constants J are reported in Hz, and if not stated otherwise refer to J_{HH} couplings.

HR-MS spectra were recorded on a Thermo Q-Exactive™ equipped with an ESI source. Mass spectra were recorded in positive mode.

All reactions were monitored by thin-layer chromatography using Merck silica gel plates 60 F_{254} (aluminum sheets) and spots were visualized with UV.

Flash chromatography was performed on a Combiflash Nextgen 300+ using Redisep Bronze column (4, 12, 24, 40 grams) filled with NP silica gel and using Redisep Rf cartridge (4 and 24 grams).

4.4.1 Photophysical measurements

See **Experimental Section** of **Chapter 3**.

4.4.2 Electrochemical and electrochemiluminescence measurements

See **Experimental Section** of **Chapter 3**.

4.4.3 XRD analysis – Structural characterization

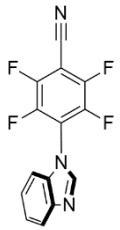
Suitable single crystals for X-Rays Diffractometry were obtained by slow diffusion or by slow evaporation of solvents. Solvent mixtures that were employed are reported in **Synthesis route and procedures** part.

Crystallographic data have been deposited at the Cambridge Crystallographic Data Centre and allocated the deposition numbers CCDC 2322129-2322130 for **4^{tBu}CzBNPhenIm**, **4^{tBu}CzBNBenzIm** and 2284116 for **4DPABNPhenIm**. These data can be obtained free of charge via https://www.ccdc.cam.ac.uk/structures.

Data collections were performed at the XRD2 beamline of the Elettra Synchrotron, Trieste (Italy)[155]. The crystals were dipped in NHV oil (Jena Bioscience, Jena, Germany) and mounted on the goniometer head with kapton loops (MiTeGen, Ithaca, USA). Complete datasets were collected at 100 K (nitrogen stream supplied through an Oxford Cryostream 700) through the rotating crystal method. Data were acquired using monochromatic wavelength of 0.620 Å on a Pilatus hybrid-pixel area detector (DECTRIS Ltd., Baden-Daettwil, Switzerland). Diffraction data were indexed, integrated and scaled using XDS[156]. Complete dataset for **4^{tBu}CzBNPhenIm** and **4DPABNPhenIm** were obtained merging two independent data collections using CCP4-Aimless [182,193] code or SADABS[194] code. Structures were solved by the dual space algorithm implemented in the SHELXT program[157]. Fourier analysis and refinement were performed by the full-matrix least-squares methods based on F2 implemented in SHELXL (Version 2019/3)[158]. The Coot program was used for modeling[159]. Anisotropic thermal motion refinement was used for all atoms with occupancies higher than 50%. Geometry and thermal motion parameters restrains (SIMU, FLAT, DFIX and DANG) were applied to disordered fragments. Hydrogen atoms were included at calculated positions with isotropic $U_{factor} = 1.2 \cdot U_{eq}$ or $U_{factor} = 1.5 \cdot U_{eq}$ for methyl groups (U_{eq} being the equivalent isotropic thermal factor of the bonded non hydrogen atom). All the crystal showed solvent molecules trapped into crystal voids. Electron density contribution that couldn't be modelled in **4^{tBu}CzBNBenzIm** was removed with Platon SQUEEZE routine[160]. Estimated contributions of these regions are included in the reported crystal properties (**Table A4.1** – corresponding to 2 additional disordered methanol molecules per unit cell). Twin laws in **4^{tBu}CzBNBenzIm** have been identified using Platon TWINROTMAT routine[183] (twin fraction refined to 30% and 12% for domains related by 180° rotations around b* and a* reciprocal lattice directions, respectively). Pictures were prepared using Ortep-3[161] and Pymol[195] software.

4.4.4 Synthesis route and procedure

4.4.4.1 Synthesis of 2,3,5,6-tetrafluoro-4-(1H-benzo[d]imidazol-1-yl)benzonitrile (**4FBNBenzIm**)



This compound was obtained using a slightly modified literature method[185].

To a solution of benzimidazole (3.55 mmol, 1.5 equivalents) in THF (50 mL), 2,3,4,5,6-pentafluorobenzonitrile was added (3.0 mmol, 1 equivalent) and the solution was stirred for 48 h at room temperature under argon atmosphere, during which time the solution became cloudy.

After two days the solvent was removed by rotary evaporator, the reaction crude was dissolved in a few milliliters of dichloromethane and filtered by gravity to remove imidazolium salts present as subproducts.

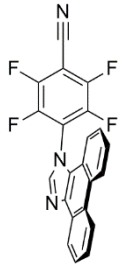
The solvent was removed again by rotary evaporator to obtain the final product (1.95 mmol, yield 65%) as a white solid.

^{1}H NMR (300 MHz, $CDCl_3$) δ 8.05 (t, J = 1.9 Hz, 1H), 7.95 – 7.91 (m, 1H), 7.46 – 7.41 (m, 2H), 7.30 – 7.23 (m, 1H).

^{19}F{^{1}H} NMR (188 MHz, $CDCl_3$) δ -130.27 – -130.50 (m), -142.47 – -142.70 (m).

Chemical shifts are in line with literature data [185].

4.4.4.2 Synthesis of 2,3,5,6-tetrafluoro-4-(1H-phenanthro[9,10-d]imidazol-1-yl)benzonitrile (**4FBNPhenIm**)



To a solution of 1H-phenanthro[9,10-*d*]imidazole (1.77 mmol, 1.5 equivalent) in THF (35 mL), of 2,3,4,5,6-pentafluorobenzonitrile (1.18 mmol, 1 equivalent) and cesium carbonate (3.13 mmol, 3 equivalents) were added and the solution was stirred for 48 h at room temperature under argon atmosphere, during which time the solution became cloudy.

After two days the solvent was removed by rotary evaporator, the reaction crude was dissolved in a few milliliters of dichloromethane and filtered by gravity to remove imidazolium salts present as by-products.

The solvent was removed again by rotary evaporator to obtain the final product (0.85 mmol, yield 72%) as a white solid.

^{1}H NMR (300 MHz, $CDCl_3$) δ 8.86 – 8.78 (m, 1H), 8.77 – 8.67 (m, 2H), 7.95 (d, J = 0.9 Hz, 1H), 7.86 – 7.60 (m, 3H), 7.51 (ddd, J = 8.3, 7.1, 1.2 Hz, 1H), 7.35 (dq, J = 8.1, 1.5 Hz, 1H).

^{13}C{^{1}H} NMR (75 MHz, CDCl3) δ 149.72, 149.58, 146.20, 146.00, 145.37, 145.21, 141.95, 141.87, 141.71, 140.53, 138.79, 129.75, 128.75, 127.99, 127.45, 126.78, 126.72, 126.40, 125.95, 124.78, 123.39, 122.79, 121.90, 119.27, 106.67, 77.58, 77.36, 77.16, 76.74.

^{19}F{^{1}H} NMR (188 MHz, $CDCl_3$) δ -129.35 – -129.55 (m), -141.05 – -141.27 (m).

4.4.4.3 Synthesis of **4^{tBu}CzBNBenzIm**, **4^{tBu}CzBNPhenIm**, **4DPABNBenzIm** and **4DPABNPhenIm** Procedure A.

In a flame dried and argon-purged round-bottomed flask equipped with a magnetic stir bar 6 equivalents of sodium hydride (60% in mineral oil) were put in dry THF. Then 5 equivalents of 3,6-di-*tert*-butyl-carbazole were added, and the suspension was stirred for 30 minutes at room temperature. Finally, 1 equivalent of **4FBNBenzIm** or **4FBNPhenIm** was added and the resulting mixture was stirred at room temperature for 24 h.

The reaction was quenched by addition of water and tetrahydrofuran was removed by rotary evaporator. After removal of THF the residue was dissolved in DCM and washed with water.

Then the aqueous phase was extracted three times with DCM and the organic phase was dried over sodium sulphate and the solvent was removed by rotary evaporator. Finally, the crude product was purified by flash chromatography (hexane:dichloromethane from 10:0 to 5:5).

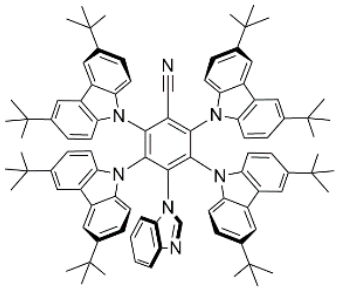
Procedure B.

In a flame dried and argon-purged round-bottomed flask equipped with a magnetic stir bar 6 equivalents of sodium hydride (60% in mineral oil) were put in dry THF. Then 5 equivalents of diphenylamine were added, and the suspension was stirred for 30 minutes at 60 °C. Finally, 1 equivalent of **4FBNBenzIm** or **4FBNPhenIm** was added and the resulting mixture was stirred at 60°C for 24 h.

The reaction was quenched by addition of water and tetrahydrofuran was removed by rotary evaporator. After removal of THF the residue was dissolved in DCM and washed with water.

Then the aqueous phase was extracted thrice with DCM and the organic phase was dried over sodium sulphate and the solvent was removed by rotary evaporator. Finally, the crude product was purified by flash chromatography (hexane:dichloromethane from 10:0 to 5:5).

4.4.4.4 Synthesis of 2,3,5,6-(tetracarbazol-9-yl)-4-(1H-benzo[d]imidazol-1-yl)benzonitrile (**4^{tBu}CzBNBenzIm**)



According to procedure A, **4FBNBenzIm** (0.17 mmol, 1 equivalent) and 3,6-di-*tert*-butyl-carbazole (0.89 mmol, 5.2 equivalents) as donor were used. The product was obtained with quantitative yields (0.125 mmol, yield 97%) by purification with flash chromatography as a bright yellow powder.

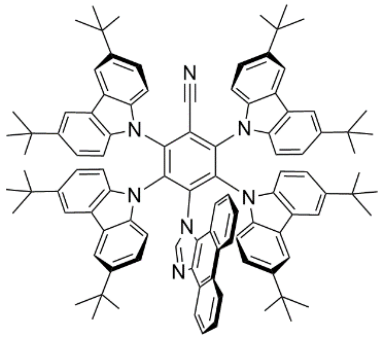
^{1}H NMR (300 MHz, $CDCl_3$) δ 7.65 – 7.47 (m, 4H), 7.47 – 7.29 (m, 5H), 7.11 (dd, J = 22.2, 8.0 Hz, 2H), 7.01 (d, J = 1.2 Hz, 4H), 6.91 – 6.73 (m, 7H), 6.67 (dd, J = 8.2, 4.6 Hz, 3H), 6.51 (d, J = 1.5 Hz, 4H), 1.42 – 1.14 (m, 72H).

{^{1}H}^{13}C NMR (75 MHz, $CDCl_3$) δ 144.09, 144.02, 143.78, 143.47, 142.54, 142.07, 140.88, 140.54, 137.60, 137.55, 136.87, 136.33, 134.08, 132.03, 124.75, 124.57, 124.50, 123.97, 123.45, 123.11, 123.01, 122.64, 122.40, 120.04, 118.10, 116.09, 115.98, 115.85, 115.63, 113.18, 109.97, 109.88, 109.69, 109.06, 108.39, 34.70, 34.65, 34.59, 34.45, 32.01, 31.96, 31.85.

HR-MS (m/z) Calculated: 1329.82 ($[M+H]^+$); Found: 1329.83 ($[M+H]^+$), 1367.78 ($[M+K]^+$).

Suitable crystals for SC-XRD were obtained by slow diffusion of methanol into chloroform.

4.4.4.5 Synthesis of 2,3,5,6-(tetracarbazol-9-yl)-4-(1H-phenanthro[9,10-d]imidazol-1-yl)benzonitrile (**4^{tBu}CzBNPhenIm**)



According to procedure A, **4FBNPhenIm** (0.17 mmol, 1 equivalent) and 3,6-di-*tert*-butyl-carbazole (0.89 mmol, 5.2 equivalents) as donor were used.

The product was obtained by purification with flash cromatography (0.085 mmol, yield 50%) as a yellow powder.

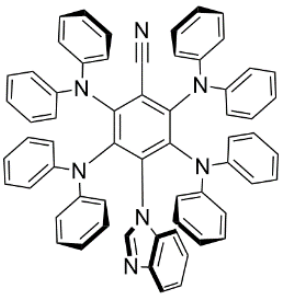
^{1}H NMR (300 MHz, $CDCl_3$) δ 8.34 (dd, J = 41.4, 8.1 Hz, 2H), 8.19 – 7.78 (m, 3H), 7.71 – 7.07 (m, 21H), 6.64 (d, J = 2.1 Hz, 3H), 6.31 – 6.04 (m, 4H), 1.56 – 0.94 (m, 72H).

{^{1}H}^{13}C NMR (75 MHz, $CDCl_3$) δ 144.39, 144.27, 144.19, 143.90, 143.11, 141.45, 141.23, 138.32, 138.07, 137.30, 137.25, 137.01, 136.73, 129.09, 128.01, 126.95, 126.60, 126.01, 125.39, 125.30, 125.21, 125.15, 124.91, 124.41, 124.33, 123.72, 123.49, 123.25, 122.70, 122.50, 122.26, 121.94, 121.27, 119.50, 116.54, 116.30, 115.57, 114.99, 113.15, 109.86, 109.77, 109.31, 108.65, 34.86, 34.75, 34.53, 34.20, 32.17, 32.13, 32.06, 31.89, 31.65.

HR-MS (m/z) Calculated: 1429.85 ($[M+H]^+$); Found: 1429.86 ($[M+H]^+$), 1467.81 ($[M+K]^+$).

Suitable crystals for SC-XRD were obtained by slow diffusion of methanol into chloroform.

4.4.4.6Synthesis of 2,3,5,6-tetrakis(diphenylamino)-4-(1H-benzo[d]imidazol-1-yl)benzonitrile (**4DPABNBenzIm**)



According to procedure B, **4FBNBenzIm** (0.29 mmol, 1 eq) and diphenylamine (1.48 mmol, 5.1 equivalents) as donor were used.

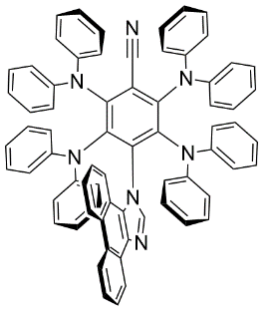
The product was obtained after column chromatography (0.04 mmol, yield 14%) as an olive green solid.

^{1}H NMR (300 MHz, $CDCl_3$) δ 7.79 – 7.51 (m, 1H), 7.41 – 6.48 (m, 42H), 6.30 – 6.14 (m, 2H).

{^{1}H}^{13}C NMR (75 MHz, $CDCl_3$) δ 146.74, 145.42, 144.90, 143.77, 142.14, 141.90, 140.90, 133.09, 129.70, 129.64, 129.03, 128.79, 128.11, 123.60, 122.65, 122.37, 122.28, 121.77, 121.69, 121.14, 119.61, 113.74, 110.46.

HR-MS (m/z) Calculated: 888.37 ([M+H]$^+$); Found: 888.35 ([M+H]$^+$), 926.34 ([M+K]$^+$).

4.4.4.7 Synthesis of 2,3,5,6-tetrakis(diphenylamino)-4-(1H-phenanthro[9,10-d]imidazol-1-yl)benzonitrile (**4DPABNPhenIm**)



According to procedure B, **4FBNPhenIm** (0.29 mmol, 1 equivalent) and diphenylamine (1.48 mmol, 5.1 equivalents) as donor were used.

The product was obtained after column chromatography (0.09 mmol, yield 30%) as an olive green solid.

^{1}H NMR (300 MHz, $CDCl_3$) δ 8.67 – 8.24 (m, 1H), 7.58 (tt, *J* = 12.5, 7.9 Hz, 1H), 7.44 – 7.28 (m, 1H), 7.25 – 7.12 (m, 3H), 6.95 (t, *J* = 7.5 Hz, 4H).

^{13}C NMR (75 MHz, $CDCl_3$) δ 147.43, 145.57, 144.00, 143.29, 138.69, 129.13, 127.86, 126.88, 125.13, 124.97, 124.32, 123.79, 123.45, 123.15, 122.71, 122.25, 122.12, 113.97, 77.58, 77.16, 76.74.

HR-MS (m/z) Calculated: 988.40 ([M+H]$^+$); Found: 988.41 ([M+H]$^+$), 1027.37 ([M+K]$^+$).

Suitable single crystals were obtained by slow diffusion of hexane vapors into chloroform.

5 TAILORING ACCEPTOR ELECTROCHEMISTRY FOR OXIDATIVE-REDUCTION ECL

Luca Morgan, Giulio Pavan, Nicola Demitri, Chiara Alberoni, Thomas Scattolin, Marco Roverso, Sara Bogialli, Alessandro Aliprandi. *RSC Adv.*, 2023, **13**(49), 34520-34523
https://doi.org/10.1039/D3RA06863C

5.1 Introduction

In **Chapter 4** the impact of π-extension of the imidazole moiety on electrochemical and photophysical properties has been examined, and it was found that this π-extension has a detrimental effect on PLQYs and ECL efficiencies, particularly when tripropylamine is used as co-reactant.

Furthermore, it was observed that the π-extension has an impact on the electrochemical properties, as evidenced by a decrease in the reducing character of the acceptor, which consequently results in an anodic shift of the reduction potential.

Nevertheless, further shifting of the acceptor reduction potential towards more anodic values is not feasible with the benzonitrile acceptor. An alternative approach would be to use the terephthalonitrile acceptor in the synthesis of donor-acceptor derivatives that function under oxidative-reduction ECL. Indeed, terephthalonitrile derivatives shows very appealing reduction potential and an orange-red emission that closely resembles that of $[Ru(bpy)_3]^{2+}$.[88,101]

Even if terephthalonitrile derivatives have been the subject of extensive studies in several fields, including Circularly polarized (Electro)Luminescence, Luminescent Solar Concentrator, liquid crystals[196], OLEDs[85,197] and photocatalysis[88,198], there is only one report that investigated the compound **4CzTPN** in electrochemiluminescence[101].

Among all terephthalonitrile derivatives, the compounds **4DPATPN** and **4^{tBu}CzTPN** are particularly promising for oxidative-reduction ECL, as they combine suitable reduction potential of the acceptor and reversible electrochemical processes.

Nevertheless, the low solubility of these compounds prompts the use of di-*para*-tolyl amine as donor to increase the solubility of these derivatives and to assess the impact of diphenylamine substitution on ECL performance.

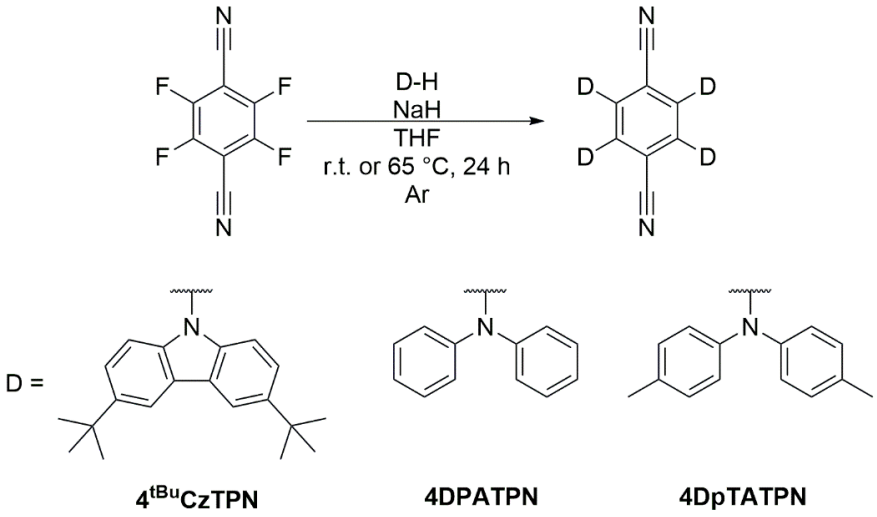
This **Chapter** presents the synthesis and characterization of TADF terephthalonitrile derivatives in organic solvents, with the aim of evaluating the impact of different donors on their photophysical, electrochemical and ECL properties.

In addition, the synthesis and characterization of a novel water-soluble terephthalonitrile derivative is presented.

5.2 Result and discussion

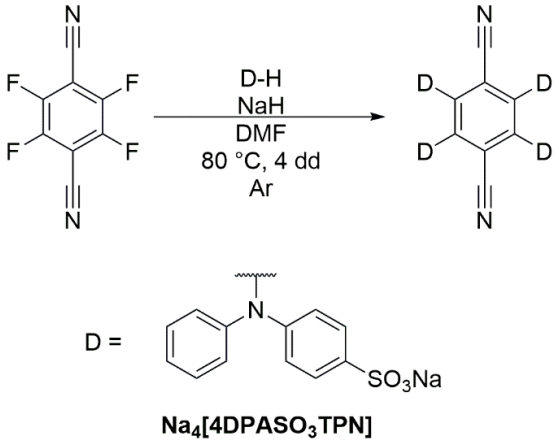
5.2.1 Synthesis

Terephthalonitrile derivatives are synthesized in analogy with the compounds presented in the preceding **Chapters** using a metal-free nucleophilic aromatic substitution reaction (**Scheme 5.1**) in presence of sodium hydride as strong base.



Scheme 5.1: Synthesis of terephthalonitrile derivatives.

With the exception of **Na_4[4DPASO$_3$TPN]**, for which *N,N*-dimethylformamide is employed as solvent to facilitate the solubilization of all reagents (**Scheme 6.2**), tetrahydrofuran is utilized as a solvent in accordance with the synthetic procedure reported by Adachi *et al.*[85].



Scheme 5.2: Synthesis of water-soluble derivative **Na_4[4DPASO$_3$TPN]**.

The substitution of all fluorine atoms is confirmed by means of ^{19}F NMR spectroscopy and all compounds are obtained with good to excellent yields by simple filtration, without requiring any further purification, such as column chromatography.

^{1}H NMR spectra of compounds are reported in **Figures A5.2-A5.5**.

Due to the low solubility of compounds **4^{tBu}CzTPN**, **4DPATPN** and **4DpTATPN**, their $^{13}C\{^{1}H\}$ spectra cannot be recorded, while $^{13}C\{^{1}H\}$ NMR spectra of **Na$_4$[4DPASO$_3$TPN]** is reported in **Figure A5.6**.

5.2.2 Crystallographic characterization

Compounds crystallize in centrosymmetric space groups with half molecule in the asymmetric units (ASU) for compounds **4DPATPN** and **4DpTATPN** (**Figure A5.1**), which molecules lies on crystallographic inversion centres perfectly matching molecular symmetry (**Figure 5.1**). Crystal packing contacts essentially involves π•••π stacking and CH•••π contacts through phenyls of sidechains.

Non-equivalent molecules adopt very similar conformations with minor lateral phenyl rearrangements, as shown in **Figure 5.2** (R.M.S.D. < 0.5 Å among common atoms).

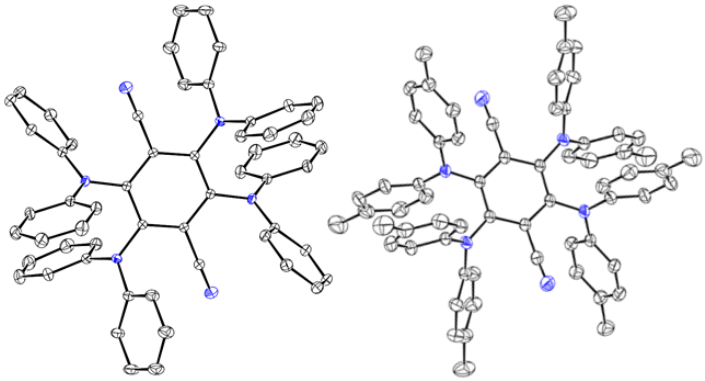


Figure 5.1: Ellipsoid representation of **4DPATPN** (left) and **4DpTATPN** (right) asymmetric units (A.S.U. – 50% probability). Hydrogens are omitted for clarity.

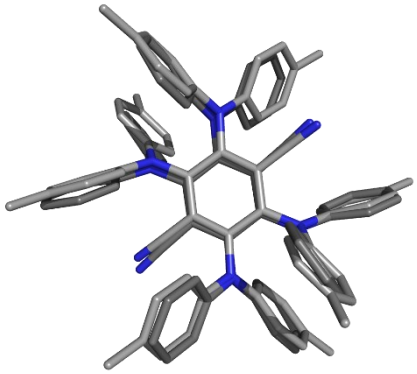


Figure 5.2: Overlap of crystallographically independent molecules of **4DPATPN** and **4DpTATPN**.

5.2.3 Electrochemical characterization

Due to their low solubility, electrochemical properties of terephthalonitrile derivatives are studied only in anhydrous dichloromethane by means of cyclic voltammetry.

All the data are summarized in **Table 5.1**, while cyclic voltammograms are depicted in **Figure A5.15-A5.17**.

Table 5.1: Electrochemical properties in dichoromethane and *N*, *N*-dimethyl formamide solution of terephthalonitrile derivatives.

Compound	4^{tBu}CzTPN	4DPATPN	4DpTATPN	Na_4[4DPASO_3TPN]
$E_{ox}^{1/2}$ (V)	1.44	1.03, 1.26	0.86, 1.04	1.22[a]
$E_{red}^{1/2}$ (V)	-1.09	-1.39	-1.46	-1.32

Measurements are performed in degassed dichloromethane or *N*,*N*-dimethyl formamide (for **Na_4[4DPASO_3TPN]**) solutions containing 1 mM luminophore and 0.1 M $TBAPF_6$ as the supporting electrolyte. Working Electrode: Glassy Carbon Electrode (1 mm); Reference Electrode: Ag/AgCl (sat.d KCl) in agarose; Counter Electrode: Pt wire. Scan rate: 100 mVs^{-1}. [a] Irreversible process, peak potential is reported.

In the cathodic region, a single, reversible reduction process of the dicyanoarene ring can be observed. As expected, the reducing character of the acceptor core is increased upon increasing the donor strength or by inserting electro-donating groups such as in the case of **4DpTATPN** and **4^{tBu}CzTPN**[101].

In contrast, the reducing character of the acceptor is decreased when electro-withdrawing groups (sulfonate groups) are attached to the diphenylamine moiety.

In the anodic region, the compounds **4DPATPN** and **4DpTATPN** exhibit two reversible oxidation processes while compound **4^{tBu}CzTPN** exhibits one quasi-reversible oxidation process.

These oxidation processes generate *N*-centered radical cations that in the case of **4DPATPN** are not destabilized since, as already reported by Hazra and colleagues[199], a low spin density is present in *para* position.

The same effect can be hypothesized for compound **4DpTATPN**, which electrochemical stability is therefore increased by the presence of methyl groups, as already observed by Adams and colleagues[138] in literature.

Conversely, for compound **Na_4[4DPASO_3TPN]** multiple irreversible processes are present, and they might be due to a higher spin density in *para* position which cause chemical dimerization of the donor moieties.

5.2.4 Photophysical characterization

UV-vis absorption spectra, emission and excitation spectra, PLQYs and PhotoLuminescence decay curves of **4^{tBu}CzTPN**, **4DPATPN** and **4DpTATPN** are recorded in dichloromethane solution.

In **Figure 5.3** UV-vis absorption spectra are reported while in **Table 5.2** absorption maxima of ICT region are reported.

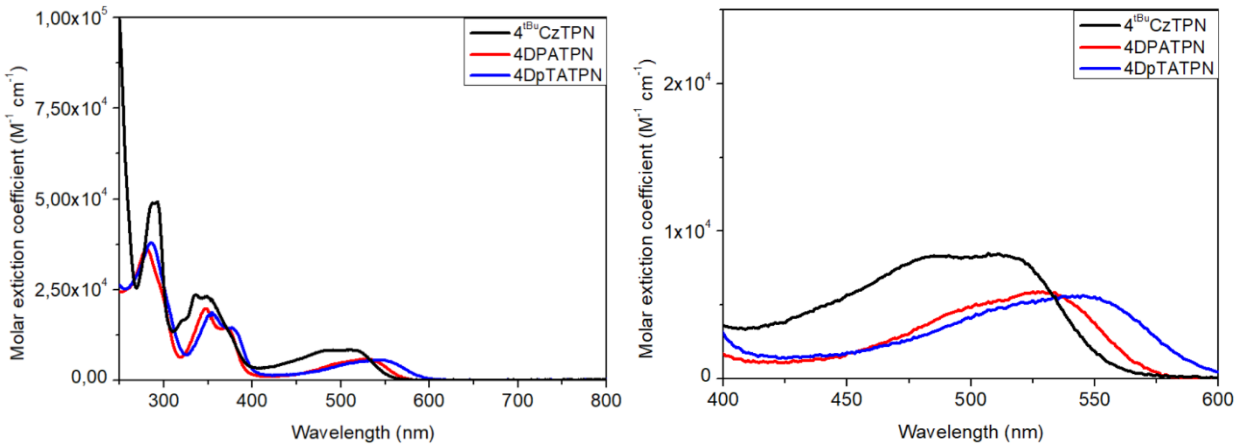


Figure 5.3: Absorption spectra in dichloromethane (left) and zoom of the region 400-600 nm (right).

In absorption spectra, the energy bands related to π*←π transitions are present in the region between 240 and 400 nm while in the region between 400 and 600 nm ICT transition bands with broad profiles are visible. These findings are in accordance with the literature data for compound **4DPATPN**[88,199]. As expected, the insertion of electro-donating group in *para* position to the diphenylamine and carbazole shifts the absorption maxima of ca. 10 nm.

Table 5.2: Photophysical properties of terephthalonitrile derivatives.

Compound	λ_{abs}	λ_{em} [a]	Φ_{PL} [b]	Φ_{PL} [c]
4^{tBu}CzTPN	486, 511	593	6.2±0.2	6.6±0.3
4DPATPN	513	597	8.9±0.3	49.2±1.4
4DpTATPN	543	625	6.8±0.3	15.0±0.6

Measurements are performed with 5 μM dichloromethane solution. [a] λ_{exc} = 460 - 584 nm. [b] Aerated solution, average scan, λ_{exc} = 400-550 nm. [c] Ar-purged solution, average scan, λ_{exc} = 400 - 550 nm.

The formation of excimers can be excluded as the excitation spectra (**Figures A5.7-A5.9**) are superimposable with the respective absorption spectra.

Emission profiles are depicted in **Figure 5.4**, and they are characterized by the typical broad profile of D-A molecules with a redshift passing from **4DPATPN** to **4DpTATPN** due to the presence of methyl groups.

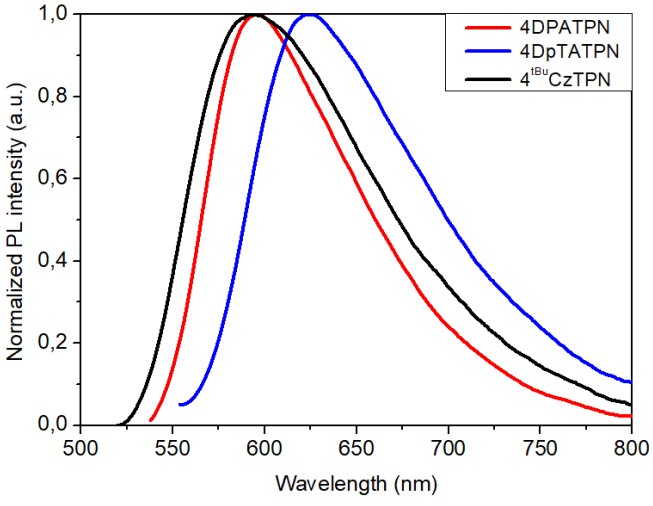


Figure 5.4: Emission spectra in dichloromethane.

All compounds exhibit low PLQYs in aerated solution, which increase upon removal of oxygen, and a bi-exponential fluorescence decay (**Table 5.3** and **Figures A5.11-A5.13**).

Table 5.3: Lifetimes of prompted and delayed fluorescence of terephthalonitrile derivatives.

Compound	τ_P (ns)[a]	τ_D (µs)[a]	τ_P (ns)[b]	τ_D (µs)[b]
4^{tBu}CzTPN	3.587±0.005	0.370±0.008	3.66±0.01	1.91±0.11
4DPATPN	2.06±0.04	2.39±0.07	2.08±0.01	16.53±0.19
4DpTATPN	2.312±0.007	1.28±0.02	2.32±0.02 (B1=0.53) 19.63± 0.09 (B1=0.82)	7.19±0.11

Measurements are performed on 5 µM dichloromethane solution. λ_{exc} = 402.3 nm, Nanosecond lifetimes were evaluated with TCSPC electronic, while microsecond lifetimes were evaluated with MCS electronic. [a] Aerated solution. [b] Ar-purged solution.

5.2.5 Electrochemiluminescence characterization

Given the presence of reversible oxidation processes and a suitable potential of the reduction process, the electrochemiluminescence efficiencies of these compounds are evaluated under annihilation and oxidative-reduction conditions with TPA as co-reactant.

Furthermore, ECL-voltage experiments and ECL spectroscopy are examined with TPA as co-reactant. Annihilation ECL experiments are performed by stepping the potential between the first reduction and the first oxidation processes potentials and annihilation ECL efficiencies are reported in **Table 5.4**.

Table 5.4: Annihilation ECL efficiencies of terephthalonitrile derivatives.

Compound	Applied potentials (V)	Φ_{ECL}[a]
4^{tBu}CzTPN	-1.2 to +1.6	1.3±0.7
	+1.6 to -1.2	1.6±0.7
4DPATPN	-1.6 to +1.1	6±3
	+1.1 to -1.6	6±3
4DpTATPN	-1.6 to +1	5±2
	+1 to -1.6	5±2

Measurements are performed in degassed acetonitrile solutions containing 20 µM luminophore and 0.1 M $TBAPF_6$ as supporting electrolyte. WE: Glassy Carbon Electrode (1 mm); RE: Ag/AgCl (sat.d KCl) electrode; CE: Pt wire. Potentials were stepped with a frequency of 10 Hz. [a] Φ_{ECL} determined under annihilation conditions according to **Equation 3.14**, $[Ru(bpy)_3](PF_6)_2$ as standard (ECL efficiency was assumed as unitary).

All compounds show ECL yields higher than the standard $[Ru(bpy)_3](PF_6)_2$ regardless to the order of applied potentials. Moreover, ECL profiles are stable during time confirming the high stability of both radical-anions and radical-cations (see **Figures A5.22-A5.24**).

ECL-voltage experiments in presence of TPA as co-reactant (**Figure 5.5**) exhibit some interesting results.

As displayed in **Equations 5.1-5.5**, under reductive-oxidation conditions a suitable cathodic potential is applied, and the radical-cations of both species are simultaneously generated. The oxidized co-reactant rapidly releases a proton to form the tripropylamino radical ($TPA^{\bullet}$, $E^{o}_{TPA^{\bullet}/waste}$ = -1.7 V vs Ag/AgCl) that reduces the oxidized luminophore, yielding its emitting excited states (**Equation 5.4**).

$$TPrA - e^- \rightarrow TPrA^{\bullet+} \quad \textbf{(5.1)}$$

$$TPrA^{\bullet+} - H^+ \rightarrow TPrA^{\bullet} \quad \textbf{(5.2)}$$

$$TADF - e^- \rightarrow TADF^{\bullet+} \quad \textbf{(5.3)}$$

$$TADF^{\bullet+} + TPrA^{\bullet} \rightarrow TADF^* + "waste" \quad \textbf{(5.4)}$$

$$TADF^* \rightarrow h\nu + TADF \quad \textbf{(5.5)}$$

Nevertheless, the compounds **4^{tBu}CzTPN** and **4DPATPN** exhibit an ECL signal arising from the remote-route pathway (**Equations 5.6-5.8**).

$$TADF + TPrA^{\bullet} \rightarrow TADF^{\bullet-} + "waste" \quad \textbf{(5.6)}$$

$$TADF^{\bullet-} + TPrA^{\bullet+} \rightarrow TADF^* + TPrA \quad \textbf{(5.7)}$$

$$TADF^* \rightarrow h\nu + TADF \quad \textbf{(5.8)}$$

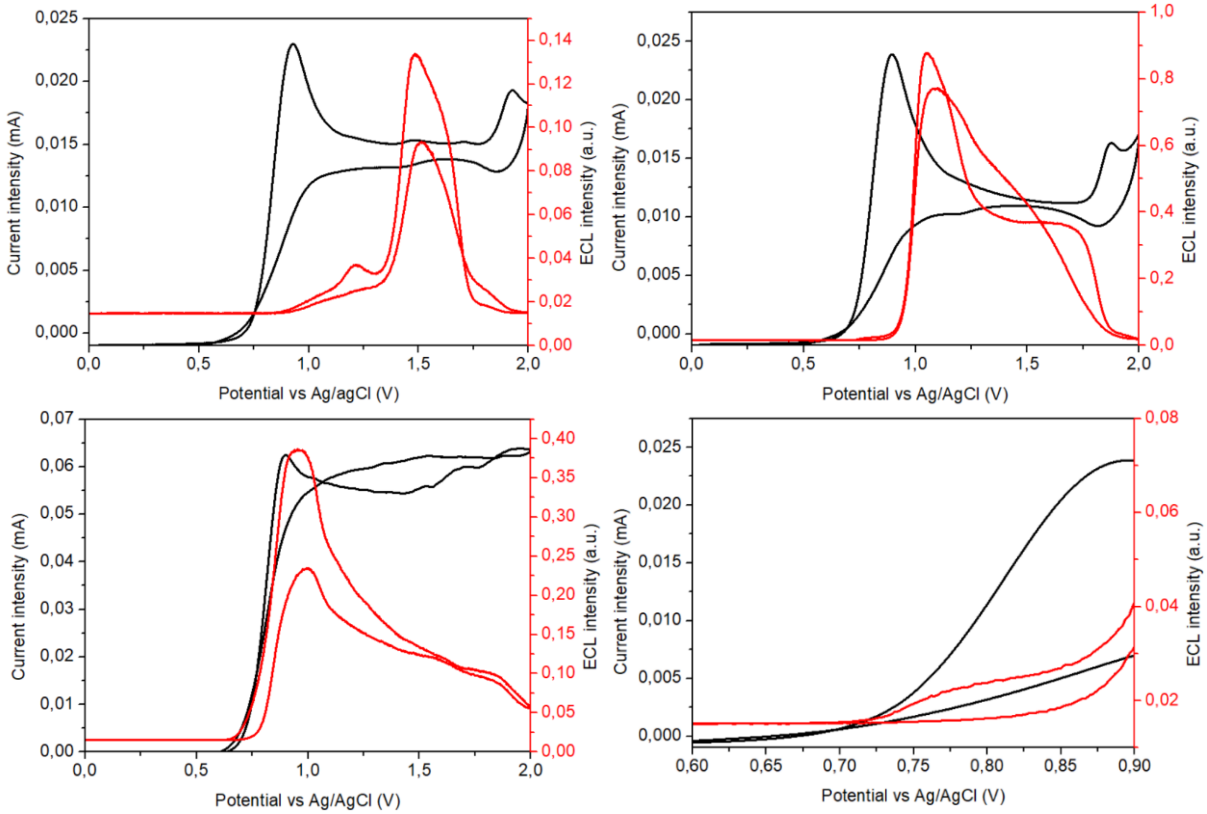


Figure 5.5: ECL-voltage curves of **4^{tBu}CzTPN** (upper left), **4DPATPN** (upper right) and **4DpTATPN** (lower left) in dichloromethane with TPA as co-reactant. Zoom of ECL-voltage curve of compound **4DPATPN** (lower right) in dichloromethane.

Indeed, for compound **4^{tBu}CzTPN** the onset of ECL emission is located close to +0.9 V vs Ag/AgCl while the generation of the radical-cation $4^{tBu}CzTPN^{\cdot+}$ occurs at a more anodic potential.

Furthermore, in the ECL-voltage experiment of compound **4DPATPN** (**Figure 5.5-lower right**) the onset of the ECL signal is located at ca. +0.73 V vs Ag/AgCl.

By considering the energetic requirements, the Gibbs free energy of the annihilation reaction reported in **Equation 5.4** must be negative, which is the case of **4DPATPN** and **4DpTATPN.** Conversely, this term is positive for the compound **4^{tBu}CzTPN**, which is in contrast with the obtained data, divergence probably due to an approximation of the potential of the couple $TPA^{\cdot}$/waste.

Oxidative-reduction ECL efficiencies and emissions are reported in **Table 5.5** while all the ECL-time and current-time profiles are reported in **Figure A5.25-A5.27**.

Table 5.5: Oxidative-reduction ECL efficiencies and ECL emissions of terephthalonitrile derivatives.

Compound	Φ_{ECL}	λ_{ECL}
4^{tBu}CzTPN	0.30±0.08	601
4DPATPN	1.72±0.37	595
4DpTATPN	0.33±0.08	621

Measurements are performed in degassed dichloromethane solutions containing 50 µM luminophore, 1 mM TPA and 0.1 M $TBAPF_6$. WE: Glassy Carbon Electrode (1 mm); RE: Ag/AgCl (sat.d KCl); CE: Pt wire. Potential sequence (repeated three times): 0 V for 3 s, +1.5 V for 3 s, 0 V for 3 s. All experiments were performed three times each [a] Φ_{ECL} determined according to **Equation 3.14**, $[Ru(bpy)_3](PF_6)_2$ as standard (ECL efficiency assumes a unitary).

As expected, the compound **4DPATPN** exhibits the highest ECL efficiency thanks to the high PLQY and highest radical stability. On the other hand, the compounds **4DpTATPN** and **4^{tBu}CzTPN** perform worse due to their lower PLQYs, in line with the annihilation ECL experiments.

As for monoimidazole derivatives investigated in **Chapter 3**, a build-up profile is present for the compound **4^{tBu}CzTPN** at the beginning of every pulse, while no delay can be noted.

ECL emissions are reported in **Figure 5.6**, and they are comparable to PL emission.

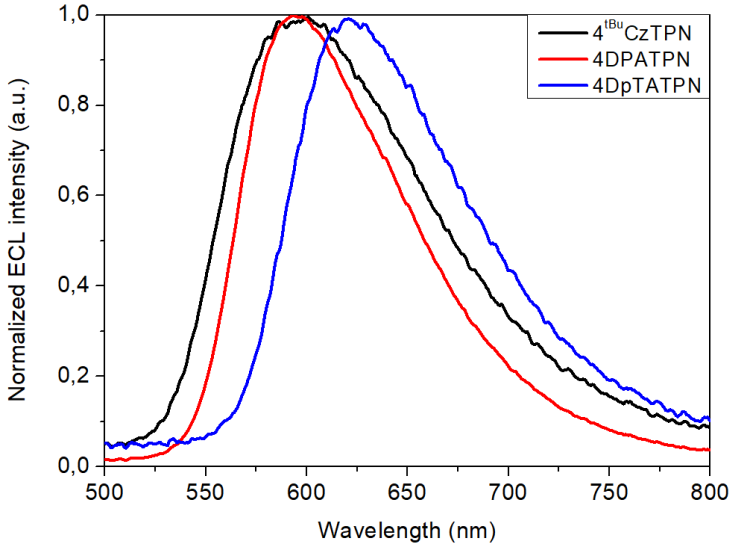


Figure 5.6: ECL spectra in dichloromethane.

5.2.6 Photophysical and electrochemiluminescence characterization of TADF emitter in water solution

As stated in **Introduction**, all ECL-based tools in bioanalytical chemistry work in aqueous media, which is the reason why sodium *p*-(phenylamino)benzenesulfonate is used as donor moiety.

To confirm the TADF properties in water, the lifetimes of compound **Na_4[4DPASO_3TPN]** are evaluated by means of time-resolved fluorescence spectroscopy, which confirmed the presence of a delayed fluorescence contribution (**Table 5.6**).

Table 5.6: Photophysical and ECL properties of water-soluble TADF compound in water.

Compound	λ_{abs}	λ_{em}[a]	Φ_{PL}[b]	τ_P (ns)[c]	τ_D (µs)[c]	Φ_{ECL}	λ_{ECL}
Na_4[4DPASO_3TPN]	534	597	3±1	6.08±0.04	0.31±0.02	0.02±0.01	597

Measurements are performed with 5 µM aqueous solution. [a] λ_{exc} = 400 - 550 nm. [b] Aerated solution, average scan, λ_{exc} = 400 - 550 nm. [c] λ_{exc} = 402.3 nm. Lifetimes were evaluated in aerated solution. Nanosecond lifetimes were evaluated with TCSPC electronic, while microsecond lifetimes were evaluated with MCS electronic.

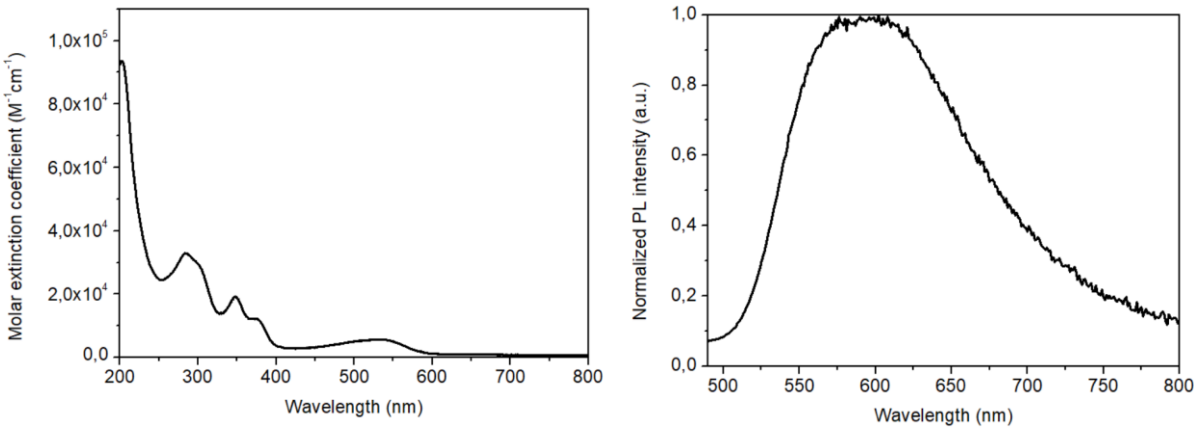


Figure 5.7: Absorption and emission spectra of **Na_4[4DPASO$_3$TPN]** in water.

As expected, a low PLQY is present due to the high solvent polarity, while absorption and excitation spectra are not completely superimposable.

Indeed, similar profiles can be observed in the region 200 – 400 nm while in the ICT region the absorption spectrum show a maximum at 534 nm, while in the excitation spectrum the maximum is shifted to 473 nm. This blueshift can be ascribed to different charge transfer dynamics due to the high solvent polarity or to hydrogen-bonding between sulfonate groups and water molecules.

The effectiveness of compound **Na_4[4DPASO$_3$TPN]** as ECL emitter is assessed in Procell® solution, a buffered aqueous solution (pH 6.8) containing 180 mM tripropylamine and an undisclosed surfactant.

This solution, kindly given by Roche, is the aqueous media used in commercial ECL-based tools.

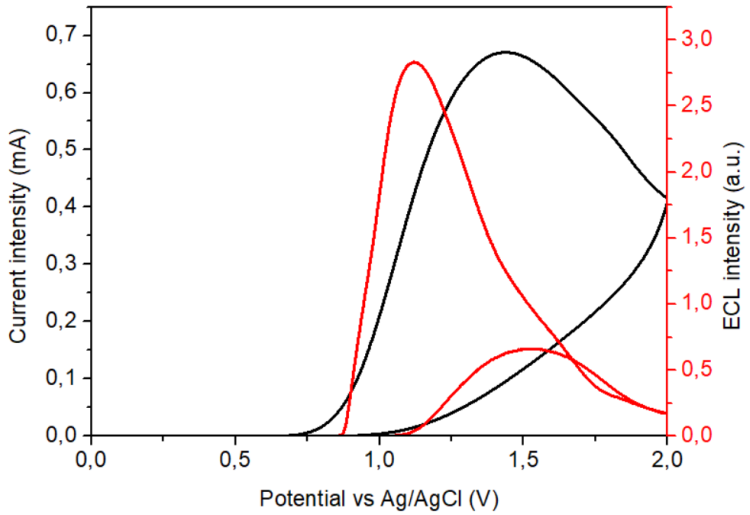


Figure 5.8: ECL-voltage profile of compound **Na_4[4DPASO$_3$TPN]** in Procell® solution.

In the ECL-voltage experiment (**Figure 5.8**), light signal arises when the radical cation is formed, confirming the homogeneous ECL pathway, while, as expected, a low ECL efficiency is obtained due to low PLQYs and irreversible oxidation processes.

5.3 Conclusion

In conclusion, in this **Chapter** terephthalonitrile derivatives exhibiting TADF features are investigated as ECL emitters under annihilation and oxidative-reduction conditions with TPA as co-reactant.

These derivatives exhibit an orange-red emission very similar to the $[Ru(bpy)_3]^{2+}$, only one and highly reversible reduction and oxidation processes, which results in annihilation ECL efficiencies higher than the standard $[Ru(bpy]_3]^{2+}$ in organic solvent.

Furthermore, the compound **4DPATPN** exhibit an ECL efficiency under oxidative-reduction condition which is 1.5 times the standard. In contrast, the compounds **4^{tBu}CzTPN** and **4DpTATPN** exhibit lower ECL efficiencies, that can be reconducted to the lower PLQYs.

Interestingly, a light signal arising from remote-route ECL mechanism can be observed for the compound **4^{tBu}CzTPN**.

In addition, the first example of red-emitting water-soluble TADF emitter is presented, along with its ECL characterization in commercial Procell® solution, which confirms the presence of homogeneous ECL mechanism for this derivative.

Nevertheless, its ECL efficiency in this solution is very low due to irreversible oxidation processes and low PLQYs.

5.4 Experimental section

All reagents, except 3,6-di-*tert*-butyl-carbazole (synthesized according to literature[178]) were used as received without further purification and they are obtained from Sigma-Aldrich and Alfa-Aesar (dibenzoyl peroxide, wet with 25% water).

All solvents, except those for photophysical measurements, were dried according to literature procedure [151] using 3Å molecular sieves purchased from Thermoscientific.

^{1}H and $^{13}C\{^{1}H\}$ NMR spectra were recorded on a Bruker AVANCE III spectrometer equipped with a BBO probe while ^{19}F NMR were recorded with a Bruker 200 MHz equipped with a QNP probe; ^{1}H and $^{13}C\{^{1}H\}$ NMR chemical shifts are referenced relative to residual solvents peaks.[152]

NMR solvents were purchased from Sigma-Aldrich or EurisoTOP and dried with 3Å molecular sieves purchased from Merck.

Multiplicities of signals are reported as s (singlet), d (doublet), t (triplet), q (quartet), quint (quintet), m (multiplet) and combinations of these multiplicities, coupling constants J are reported in Hz, and if not stated otherwise refer to J_{HH} couplings.

HR-MS spectra were recorded on a Thermo Q-Exactive™ equipped with an ESI source. Mass spectra were recorded in positive mode.

All reactions were monitored by thin-layer chromatography using Merck silica gel plates 60 F_{254} (aluminium sheets) and spots were visualized with UV light.

5.4.1 Photophysical measurements

See **Experimental Section** of **Chapter 2**.

5.4.2 Electrochemical and electrochemiluminescence measurements

ECL-voltage curve measurements were performed with dried HPLC-grade dichloromethane solution containing 0.05 mM of investigated compounds, 1 mM of tripropylamine as co-reactant and 0.1 M tetrabutylammonium hexafluorophosphate as supporting electrolyte. The scan rate was 20 mVs^{-1} and to detect ECL signals the electrochemical cell was put over an Ocean Insight 1 mm optical fiber linked to a Thorlabs 1001/M photomultiplier tube.

PMT 2100 control was used as software interface for photomultiplier tube (PMT gain: 40 for **Na_4[4DPASO$_3$TPN]** and 80 for other compounds, Bandwidth 80 MHz).

ECL spectra were performed with dried HPLC-grade dichloromethane solution containing 0.05 mM of investigated compounds, 1 mM of tripropylamine as co-reactant and 0.1 M tetrabutylammonium hexafluorophosphate as supporting electrolyte. The ECL signal was obtained by applying a potential of +1.5 V to the solution and to detect ECL signals (integration time: 3s) the electrochemical cell was put over a 1 mm optical fiber linked to a CCD QEPro camera.

ECL measurements were performed with dried HPLC-grade dichloromethane solution containing 0.05 mM of investigated compounds, 1 mM of tripropylamine as co-reactant and 0.1 M tetrabutylammonium hexafluorophosphate as supporting electrolyte; the following scheme was repeated three times: 0 V for 3 seconds, +1.5 V for 3 seconds and 0 V for 3 seconds.

ECL measurements of **Na_4[4DPASO_3TPN]** were performed with ProCell solution containing 2 μM of investigated compounds and 0.1 M tetrabutylammonium hexafluorophosphate as supporting electrolyte; the following scheme was repeated three times: 0 V for 3 seconds, 1.5 V for 3 seconds and 0 V for 3 seconds.

Every ECL experiment was repeated three times for every compound in order to calculate average values, and relative efficiencies were determined by comparison with standard $[Ru(bpy)_3](PF_6)_2$ by taking its efficiency as 1.

For all the other specifications, see **Experimental Section** of **Chapter 3**.

5.4.3 XRD analysis – Structural characterization

Suitable single crystals for X-Rays diffractometry were obtained by slow diffusion or by slow evaporation of solvents. Solvent mixtures that were employed are reported in **Synthesis route and procedures** part.

Crystallographic data have been deposited at the Cambridge Crystallographic Data Centre and allocated the deposition numbers CCDC 2284117 (for **4DpTATPN**) and 2284118 (for **4DPATPN**). These data can be obtained free of charge via https://www.ccdc.cam.ac.uk/structures.

Data collections were performed at the XRD2 beamline of the Elettra Synchrotron, Trieste (Italy).[155] The crystals were dipped in NHV oil (Jena Bioscience, Jena, Germany) and mounted on the goniometer head with kapton loops (MiTeGen, Ithaca, USA). Complete datasets were collected at 100 K (nitrogen stream supplied through an Oxford Cryostream 700) through the rotating crystal method. Data were acquired using monochromatic wavelength of 0.620 Å on a Pilatus 6M hybrid-pixel area detector (DECTRIS Ltd., Baden-Daettwil, Switzerland). Diffraction data were indexed, integrated and scaled using XDS.[156] Structures were solved by the dual space algorithm implemented in the SHELXT code.[157] Fourier analysis and refinement were performed by the full-matrix least-squares methods based on F2 implemented in SHELXL (Version 2019/3).[158] The Coot program was used for modeling.[159] Anisotropic thermal motion refinement was used for all atoms with occupancies higher than 50%. Geometry and thermal motion parameters restrains (SIMU, DFIX and DANG) were used on disordered solvent molecules. Hydrogen atoms were included at calculated positions with isotropic $U_{factors} = 1.2 \cdot U_{eq}$ or $U_{factors} = 1.5 \cdot U_{eq}$ for methyl groups (U_{eq} being the equivalent isotropic thermal factor of the bonded non hydrogen atom). All the crystals showed solvent molecules trapped into crystal voids. Estimated contributions of these regions were included in the

reported crystal properties (**Table A5.1**). Pictures were prepared using Ortep-3[161] and Pymol[195] software.

5.4.4 Synthesis route and procedures

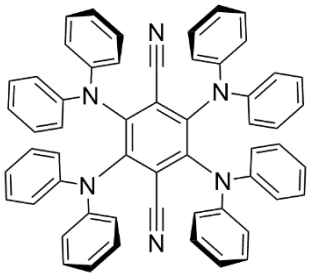
5.4.4.1 Synthesis of 2,3,5,6-tetrasubstituted-terephthalonitrile derivatives

The 2,3,5,6-tetrasubstituted-terephthalonitrile derivatives were synthesized by slight modification of a reported procedure[85] with the aim to uniform the synthetic route for all samples under investigation.

In a flame dried and argon-purged round-bottomed flask equipped with a magnetic stir bar 6 equivalents of donor compound were put in dry THF. Then 10 equivalents of sodium hydride are added (60% in mineral oil), and the suspension was stirred for 1 h at 65 °C. Finally, 1 equivalent of 2,3,5,6-tetrafluorine-terephthalonitrile as acceptor was added and the resulting mixture was stirred at 65 °C for 16 h.

A precipitate was formed, the reaction was quenched by addition of water and the precipitate was filtered on Gooch (porosity 4) and washed with water and diethyl ether. The products are bright red powders, and they were obtained with a good yield.

5.4.4.2 Synthesis of 2,3,5,6-diphenyl-amine-terephthalonitrile (**4DPATPN**)



According to the general procedure, diphenylamine was used as donor and a bright red precipitate appeared during the reaction. The product was obtained with a good yield (86%).

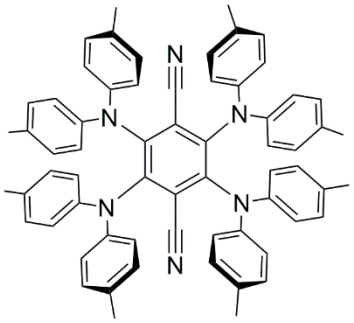
^{1}H NMR (300 MHz, DMF-d_7) δ 7.15 (t, 2H), 7.01 (d, 2H), 6.87 (t, 1H).

^{13}C{^{1}H} NMR could not be obtained due to low solubility of the compound.

HR-MS (*m/z*) Calculated: 819.3207 ([M+Na]$^{+}$); Found: 819.3217 ([M+Na]$^{+}$).

Suitable crystals for SC-XRD were obtained by slow diffusion of acetone vapors into 1,2-dichloroethane.

5.4.4.3 Synthesis of 2,3,5,6-di-p-tolyl-amine-terephthalonitrile (**4DpTATPN**)



According to the general procedure, di-*p*-tolylamine was used as donor and a bright red precipitate appeared during the reaction. The product was obtained with a high yield (86%).

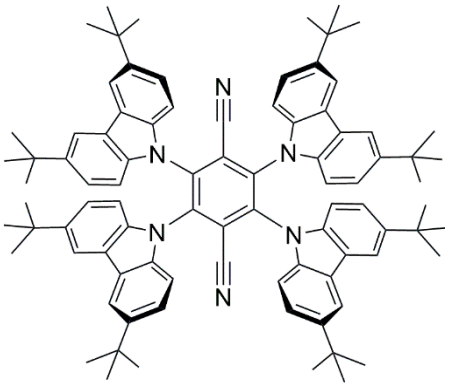
^{1}H NMR (300 MHz, CD_2Cl_2) δ 6.93 (d, 2H), 6.63 (d, 2H), 2.20 (s, 3H).

$^{13}C\{^{1}H\}$ NMR could not be obtained due to low solubility of the compound.

HR-MS (*m/z*) Calculated: 909.4639 ($[M+H]^+$); Found: 909.4636 ($[M+H]^+$).

Suitable crystals for SC-XRD were obtained by slow diffusion of hexane vapors into chloroform.

5.4.4.4 Synthesis of 2,3,5,6-di-tert-butyl-carbazole-terephthalonitrile (**4^{tBu}CzTPN**)



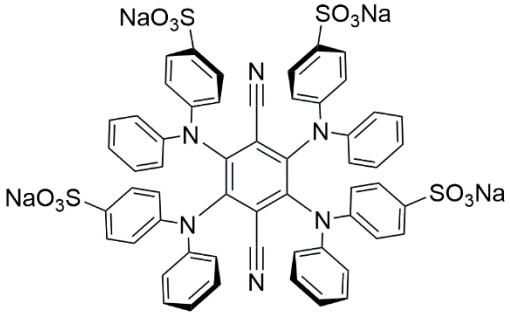
According to the general procedure, di-*tert*-butyl-carbazole was used as donor and a bright red precipitate appeared during the reaction. The product was obtained with a good yield (75%).

^{1}H NMR (300 MHz, CD_2Cl_2) δ 7.66 (d, 1H), 7.11 (dd, 1H), 7.03 (d, 1H), 1.39 (s, 9H).

$^{13}C\{^{1}H\}$ NMR could not be obtained due to low solubility of the compound.

HR-MS (m/z) Calculated: 1237.7769 ($[M+H]^+$); Found: 1237.7802 ($[M+H]^+$) .

5.4.4.5 Synthesis of 2,3,5,6- diphenilamine-4-sulfonate-terephthalonitrile (**Na_4[4DPASO_3TPN]**)



In a flame dried and argon-purged round-bottomed flask equipped with a magnetic stir bar 4.5 equivalents of diphenylamine-4-sulfonate were put in dry DMF. Then 9 equivalents of sodium hydride were added (60% in mineral oil), and the solution was stirred for 1 h at 80 °C. Finally, 1 equivalent of 2,3,5,6-tetrafluorine-terephthalonitrile as acceptor was added and the resulting mixture was stirred at 80 °C for 4 days.

The reaction was quenched by addition of water, the mixture was concentrated at reduced pressure and the precipitation of the product was achieved upon addition of acetonitrile. The precipitate was filtered on Gooch (porosity 4) and washed with acetonitrile. The product was obtained in quantitative yield (92%) as a red powder.

^{1}H NMR (300 MHz, DMSO-d_6) δ 7.35 (d, 2H), 7.15 (t, 1H), 6.90-6.75 (m, 6H).

^{13}C{^{1}H} NMR (75 MHz, D_2O) δ 171.9, 147.2, 145.8, 144.4, 138.1, 130.2, 127.4, 125.5, 123.3, 121.8.

HR-MS (m/z) Calculated: 278.0324 ($[M]^{4-}$); Found: 278.0303 ($[M]^{4-}$).

6 NEUTRAL AND CATIONIC TADF DYES IN LIGHT-EMITTING ELECTROCHEMICAL CELLS

Manuscript in preparation

6.1 Introduction

As previously discussed in **Chapter 1.3**, Light-Emitting Electrochemical Cells (LECs) represent the simplest electroluminescent solid-state devices.

Following their discovery approximately three decades ago, a number of fluorescent, phosphorescent and Thermally Activated Delayed Fluorescence (TADF) luminophores have been incorporated in LECs[125,200].

A distinctive feature of LECs is the incorporation of a solid electrolyte, which enables ionic mobility. Consequently, the synthesis of charged purely-organic emitters for application in LECs has gained significant interest.

Two seminal contributions to the field of charged purely-organic TADF dyes that work as both charge transporters and emitters can be identified: the communication presented by Bolink and colleagues[201] and the article published by Zysman-Colman and colleagues[126].

The second report is of particular significance as it demonstrates the feasibility of utilizing cationic TADF molecules in LECs that incorporate both emitter and charge transporter properties, as lately reported also by He and colleagues[202].

The positive charge of these compound has been generated by alkylating an imidazole group, which can be also found in the TADF derivatives discussed in **Chapter 3**.

Furthermore, in **Chapter 3** the alkylation of the imidazole moiety has been demonstrated, thereby making these molecules interesting candidates for incorporation in LECs.

As asserted by Pei and coworkers[115], a LEC emitter should exhibit good photophysical properties and reversible electrochemical processes.

These properties are analogous to those of a good ECL emitter, and they can be found in the compounds **4^{tBu}CzBNIm** and **4DPABNIm**.

This **Chapter** presents the outcomes obtained under the supervision of Prof. Ruben D. Costa De Riquelme at the Chair of Biogenic Functional Materials in Technical University of Munich – Campus Straubing, Bavaria, Germany.

With the aim of incorporate charged TADF derivatives in LECs, the compounds **4^{tBu}CzBNIm** and **4DPABNIm** are alkylated with a linear alkyl chain, and the electrochemical and photophysical characterization (in both solution and solid state) of the cationic derivatives are presented.

Subsequently, these emitters are incorporated into Single-Guest (or Guest-Only) and Host-Guest Light-Emitting Electrochemical Cells and devices' performances and thin-film photophysical properties are discussed.

The objectives of this **Chapter** are:

- to ascertain whether the ECL trend observed in neutral compounds is upheld;

- to elucidate whether imidazole alkylation could result in an emitter that also facilitates charge transfer;
- to investigate the impact of alkylation on electroluminescent efficacies.

In order to facilitate the comprehension of the present **Chapter**, the following figures of merit are briefly explained:

- Luminance (L): expressed in cd/m^2, describes the amount of luminous power per unit area. It gives a measure of the brightness of the LEC.
- Efficacy (Eff): expressed in cd/A, an expression of electroluminescent efficiency, an important parameter of LEC performance. It relates to the conversion efficiency of electronic carriers in photons. It can be calculated with the following formula $Eff = \frac{L_{max}(cd\ m^{-2})}{i(mA)\cdot 50}$
- Lifetime ($t_{1/2}$): expressed in hours, is the time for the luminance to decay to half-maximum under operation.

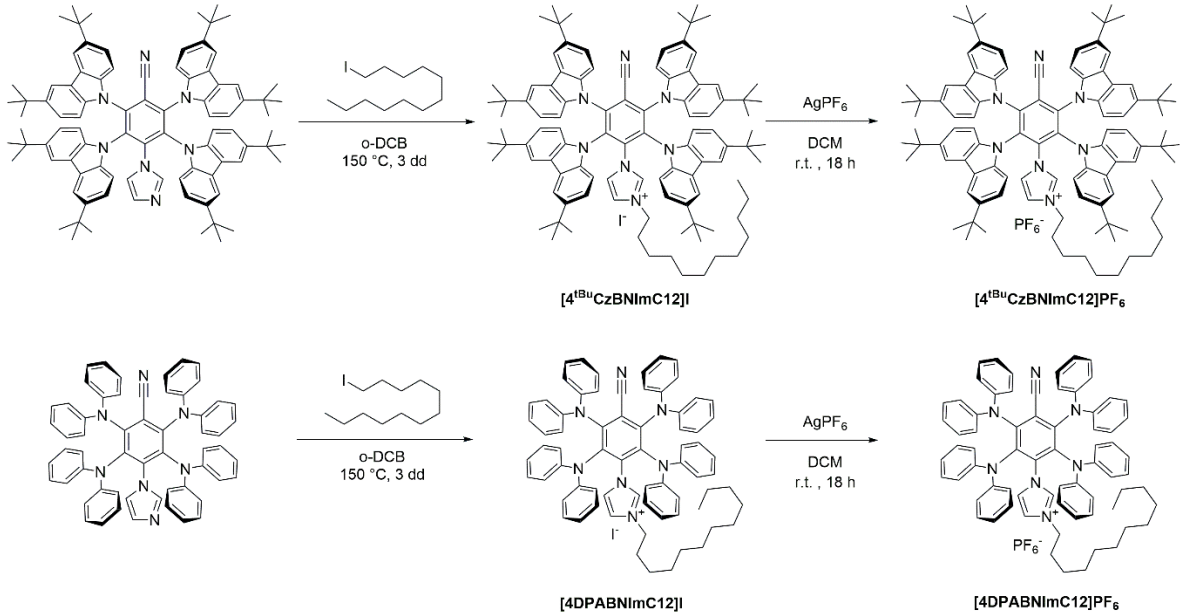
6.2 Synthesis

As previously mentioned, compounds **4^{tBu}CzBNIm** and **4DPABNIm** are alkylated with a linear alkyl chain to yield their charged derivatives.

In order to obtain a good device morphology, the neutral dyes are functionalized with a linear C12 alkyl chain, and iododododecane is chosen as alkylating reagent.

The reactions are performed at high temperatures in *o*-dichlorobenzene in presence of an excess of iododododecane until total conversion is reached (**Scheme 6.1**).

To avoid the formation of iodine-containing subproducts, these reactions are performed in the dark.



Scheme 6.1: Syntheses of the alkylated derivatives **[4^{tBu}CzBNImC12]PF$_6$** (first row) and **[4DPABNImC12]PF$_6$** (second row).

The alkylated derivatives **[4^{tBu}CzBNImC12]I** and **[4DPABNImC12]I** are then purified by column chromatography to remove both the solvent and the unreacted iododododecane. Both products are obtained with good yields

Given the established fact that iodide anion functions as a luminescence quencher[203], the iodide anion is exchanged with hexafluorophosphate anion.

The exchange reaction takes place in dichloromethane with a slight excess of $AgPF_6$ as hexafluorophosphate source and in absence of light.

The reactions yield compounds **[4^{tBu}CzBNImC12]PF$_6$** and **[4DPABNImC12]PF$_6$** in quantitative yields, and their ^{1}H, $^{13}C\{^{1}H\}$, ^{31}P and ^{19}F NMR spectra are reported in **Figures A6.1-A6.8**.

The absence of silver species traces in the final products is confirmed by cyclic voltammetry (see the **Section 6.3**) as no processes around 0 V vs Ag/AgCl can be observed.

6.3 Electrochemical characterization

Electrochemical properties are investigated by cyclic voltammetry (**Table 6.1**) and as expected no great differences can be observed between the anodic region of these compounds and their precursors, as donor moieties are not changed (**FigureA6.13-A6.14**).

In contrast, in the cathodic region some differences can be observed (**Figure 6.1**).

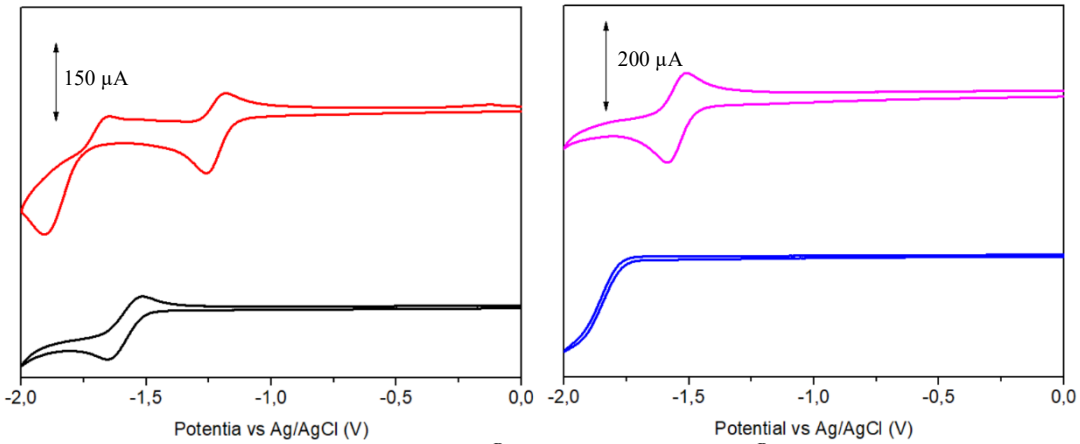


Figure 6.1: Zoom of the cathodic region of the compounds **4^{tBu}CzBNIm** (black line), **[4^{tBu}CzBNImC12]PF$_6$** (red line), **4DPABNIm** (blue line) and **[4DPABNImC12]PF$_6$** (magenta line) in dichloromethane.

Indeed, an examination of the half-wave potential of the reduction process reveals that the positive charge on the imidazolium moiety alters the electronic properties of the molecules, rendering them more electron-deficient and making the cyanoarene ring less reducing.

Table 6.1: Electrochemical properties of neutral and cationic emitters in dichloromethane and HOMO-LUMO energies

Compound	$E^{1/2}_{red}$ (V)	$E^{1/2}_{ox}$ (V)	HOMO^c (eV)	LUMO^c (eV)
4^{tBu}CzBNIm	-1.58	1.37	5.88	3.35
4DPABNIm	Not visible	1, 1.2^a	5.87	3.03
[4^{tBu}CzBNImC12]PF$_6$	-1.22^a, -1.9^b	1.59, 1.77	5.64	3.21
[4DPABNImC12]PF$_6$	-1.54	1.16, 1.41	5.74	2.93

Measurements are performed in degassed dichloromethane solutions containing 1 mM luminophore and 0.1 M $TBAPF_6$. Working Electrode: Glassy Carbon Electrode (3 mm); Reference Electrode: Ag/AgCl(sat.d KCl) in agarose; Counter Electrode: Pt wire. Scan rate 100 mVs^{-1}. ^{a} quasi reversible process. ^{b} Irreversible process. ^{c} Obtained from E_{HOMO}= -($E_{onset,ox}$ vs Fc^+/Fc) + 5.1 eV; E_{LUMO}= -($E_{onset,red}$ vs Fc^+/Fc) + 5.1 eV.

Furthermore, an examination of the i_{pa}/i_{pc} ratios associated with the first reduction process of compounds **4^{tBu}CzBNIm** and its imidazolium derivative reveals a decrease in this ratio (from 0.8 to 0.43).

This phenomenon is likely attributed to a diminished rate of back-electron transfer, which in turn can be attributed to a less favorable conformational state.

Therefore, a second reduction process is observed for compound **[4^{tBu}CzBNImC12]PF$_6$**, with a peak occurring at approximately -1.9 V vs Ag/AgCl.

This second process can be attributed to the reduction of the imidazolium moiety, as previously observed in the literature, which generates a NHC species and hydrogen[134,204].

Nevertheless, for compound **[4^{tBu}CzBNImC12]PF$_6$** a small peak can be observed during the back-scan, indicating that this process does not result in the formation of by-products.

As expected, the alkylation of **4DPABNIm** results in an anodic shift of the reduction process potential. Conversely, no process ascribable to the imidazole can be observed in the electrochemical potential window of dichloromethane.

Furthermore, after scanning multiple times between -2 V and +2 V (vs Ag/AgCl), no changes in voltammograms are observed.

From the onset potentials (vs Fc^+/Fc) HOMO and LUMO energies of emitters are calculated as follows: E_{HOMO}= -($E_{onset,ox}$ vs Fc^+/Fc) + 5.1 eV and E_{LUMO}= -($E_{onset,red}$ vs Fc^+/Fc) + 5.1 eV (**Table 6.1**). The electron-energy diagrams of HOMO and LUMO of the compounds are depicted in **Figure 6.4**.

6.4 Photophysical Characterization in solution state and in powder

Photophysical properties of charged luminophores are evaluated in dichloromethane solution and in powder state.

In **Figure 6.2** UV-vis absorption spectra and emission spectra in dichloromethane solution are depicted, respectively, while in **Table 6.2** maxima of ICT region are reported.

The UV-vis absorption spectra of the compounds exhibit π*←π transition bands that are similar to those of their precursors. However, the ICT transitions are markedly different, particularly in the case of the compound **[4^{tBu}CzBNImC12]PF$_6$**.

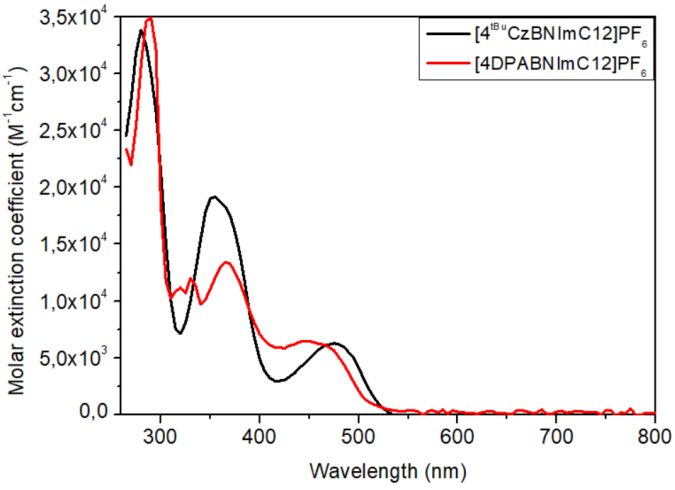


Figure 6.2: UV-vis absorption spectra of imidazolium derivatives in dichloromethane.

Table 6.2: Photophysical properties of neutral and cationic derivatives.

Compound	λ_{abs} (nm)	λ_{em} (nm)[a]	Φ_{PL} (%)[b]	λ_{em} (nm)[c]	Φ_{PL} (%)[d]
4^{tBu}CzBNIm	324^{sh}, 336	525	58±2	510	27.8±1.3
[4^{tBu}CzBNImC12]PF$_6$	354, 474	574	40±4	560	15.6±0.9
4DPABNIm	349, 464	532	65±2	556	10.9±1.1
[4DPABNImC12]PF$_6$	370, 450	597	7.1±0.7	577	17.3±1.1

Measurements are performed with 5 μM dichloromethane solution or in solid state (powder). [a] λ_{exc}=340 nm. [b] Ar-purged solution, average scan, λ_{exc} = 300 - 410 nm. [c] λ_{exc}=340 nm. [d] Aerated solid state (powder), average scan, λ_{exc} = 300 - 410 nm.

Excitation spectra in dichloromethane solution are reported in **Figures A6.9-A6.10** and they are superimposable on the respective absorption spectra, thus confirming the absence of excimers.

The emission spectra of neutral and cationic emitters in dichloromethane and in powder are depicted in **Figure 6.3**.

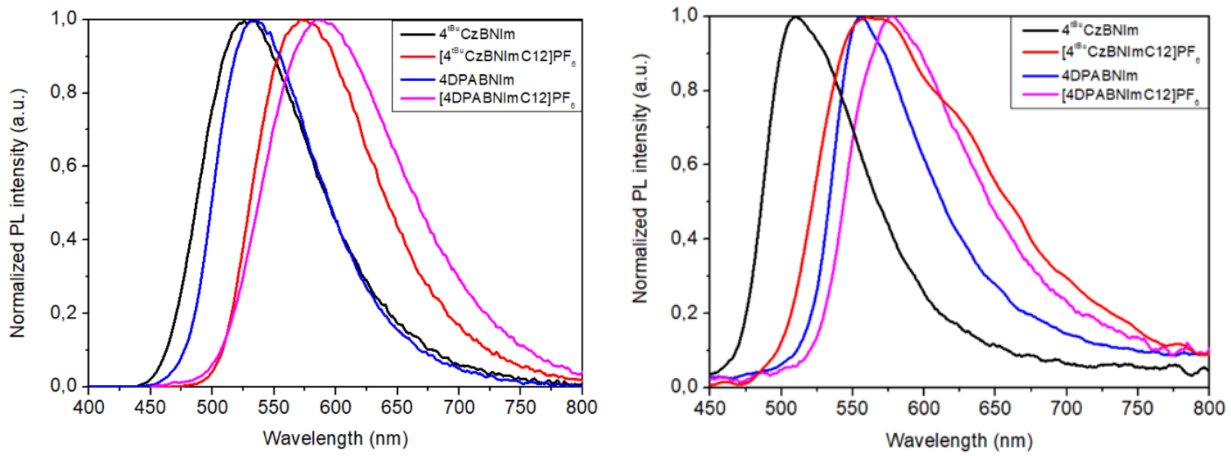


Figure 6.3: Normalized PL emission spectra in dichloromethane (left) and in solid state (powder, right).

In accordance with the electrochemical data, emission wavelengths of cationic emitters are redshifted, and a decrease in PLQYs is present when passing from neutral to cationic derivatives.

Time-resolved fluorescence spectroscopy measurements confirm the retain of TADF properties in the alkylated derivatives (**Table 6.3**).

Table 6.3: Lifetimes of neutral and cationic emitters in Ar-purged dichloromethane solution.

Compound	τ_P (ns)	τ_D (µs)
4^{tBu}CzBNIm	15.45±0.03	1.444±0.005
[4^{tBu}CzBNImC12]PF_6	2.36±0.04	13.76±0.05
4DPABNIm	2.329±0.004	10.41±0.06
[4DPABNImC12]PF_6	5.38±0.04	0.879±0.009

λ_{exc} = 402.3 nm, Nanosecond lifetimes were evaluated with TCSPC electronic, while microsecond lifetimes were evaluated with MCS electronic.

6.5 Single-Guest LECs

As previously outlined in the **Chapter 1.3**, LECs represent the most fundamental concept of an electroluminescent device.

LECs can be classified into two distinct categories, contingent on the composition of their active layer: Single-Guest and Host-Guest LECs.

Single-guest LECs exemplify the LEC concept in its purest form, characterized by an active layer comprising solely the emitter, a solid electrolyte, and a polymeric additive.

In the investigation of the devices, tetrahexylammonium tetrafluoroborate ($THABF_4$) is employed as the electrolyte, while polystyrene (PS) and poly(methyl methacrylate) (PMMA) are utilized as the polymeric additive for neutral and cationic emitters, respectively.

This disparate selection is caused by the disparate solvent employed for spin-coating. Indeed, neutral emitters are solubilized in anisole, whereas cationic emitters are solubilized in acetonitrile.

Furthermore, an optimization of the electrolyte and polymeric additive percentages has been conducted with the objective of achieving higher efficacies.

The following proportions have been identified:

- 100% **4^{tBu}CzBNIm** + 5% PS + 20% $THABF_4$;
- 100% **4DPABNIm** + 5% PS + 20% $THABF_4$;
- 100% **[4^{tBu}CzBNImC12]PF_6**;
- 100% **[4DPABNImC12]PF_6** + 5% PMMA;

Along with thee Single-Guest LECs incorporating these active layers, two more devices incorporating the cationic emitters (100% **[4^{tBu}CzBNImC12]PF_6** + 5% PMMA and 100% **[4DPABNImC12]PF_6**) are investigated.

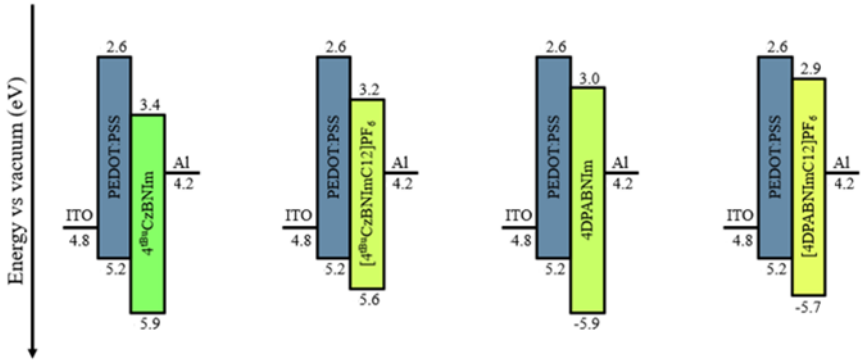


Figure 6.4: Electron-energy diagrams of the single-guest LECs derived from CV data. The electrochemical stability of $THABF_4$ is comprised between -1.5 eV and -6.2 eV[205].

In the initial stage of investigation, the electrochemical properties of Single-Guest LECs with cationic emitters are examined through the use of Electrochemical Impedance Spectroscopy (EIS).

Static EIS measurements are conducted at different applied voltages spanning from 0 V to 5 V, and frequencies ranging from 10 Hz to 1 MHz. EIS analyses of the Nyquist plots are conducted basing on a single resistor/capacitor equivalent circuit model[206] and the EIS raw data and fitted Nyquist plots both exhibit the characteristic semicircular profiles of LECs[207].

From this data, the LEC resistances of the devices can be calculated along with the electrical conductivity, and they are reported in **Table 6.4**.

Table 6.4: Electrochemical Impedance Spectroscopy data of neutral and cationic emitters.

Compound	Additives	DC-Current (V)	C_{eff} (F)	ε_r	σ (Ω^{-1} m^{-1})
[4^{tBu}CzBNImC12]PF_6	No	0.5 V	$4.36 \cdot 10^{-9}$	8.96	$2.68 \cdot 10^{-8}$
	5% PMMA	0 V	$4.24 \cdot 10^{-9}$	8.90	$8.15 \cdot 10^{-9}$
[4DPABNImC12]PF_6	No	0 V	$5.66 \cdot 10^{-9}$	9.59	$1.48 \cdot 10^{-6}$
	5% PMMA	0 V	$4.80 \cdot 10^{-9}$	10	$1.55 \cdot 10^{-7}$

By plotting LEC resistance vs V_{DC} (**Figure A6.15**) a decreasing trend becomes evident for all devices, as its resistance is reduced upon voltage increase.

In addition, devices based on compound **[4^{tBu}CzBNImC12]PF_6** exhibit low electrical conductivities, which may result in shorter device lifetimes and diminished efficacies[206].

In contrast, devices that incorporate the emitter **[4DPABNImC12]PF$_6$** exhibit higher conductivities. Photophysical properties of pristine thin films are evaluated under nitrogen atmosphere (**Table 6.5-6.6**) and emission spectra of pristine thin films are depicted in **Figure 6.5**.

Table 6.5: Photophysical properties of pristine thin film.

Compound	λ_{PL} (nm)	PLQY (%)[a]	τ_p (ns)	τ_d (µs)	ΔE_{ST}[b]
4^{tBu}CzBNIm	510	44	4.7	0.36	0.157
[4^{tBu}CzBNImC12]PF$_6$	555	21	4.2	0.364	0.047
4DPABNIm	550	13	1.6	0.554	0.406
[4DPABNImC12]PF$_6$	566	7	4.8	0.313	0.212

Measurements are obtained from pristine thin films deposited on a quartz slide. λ_{exc} = 402.3 nm. Nanosecond lifetimes are evaluated with TCSPC electronic, while microsecond lifetimes are evaluated with MCS electronic. [a] PLQYs are evaluated under nitrogen atmosphere. [b] ΔE_{ST} are evaluated as reported in literature.[208]

Table 6.6: Kinetics constants values.

Compound	k^S_{rad} (s^{-1})	k^S_{nrad} (s^{-1})	k_{ISC} (s^{-1})	k_{rISC} (s^{-1})
4^{tBu}CzBNIm	$1.52\cdot10^7$	$1.94\cdot10^7$	$1.62\cdot10^8$	$1.66\cdot10^7$
[4^{tBu}CzBNImC12]PF$_6$	$2.74\cdot10^7$	$1.03\cdot10^8$	$5.74\cdot10^7$	$1.08\cdot10^8$
4DPABNIm	$6.09\cdot10^6$	$4.08\cdot10^7$	$1.31\cdot10^7$	$2.32\cdot10^6$
[4DPABNImC12]PF$_6$	$1.21\cdot10^7$	$1.6\cdot10^8$	$3.32\cdot10^7$	$3.81\cdot10^6$

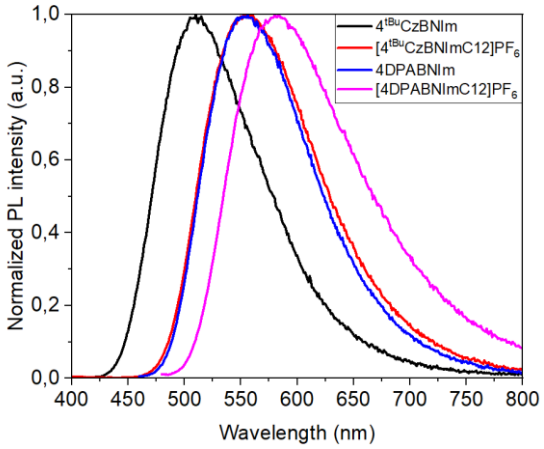


Figure 6.5: Normalized PL emission spectra of pristine thin film.

All samples exhibit TADF properties (**Figure A6.28-A6.31**) and broad emission profiles, which are typical of D-A luminophores. Furthermore, the emission maxima are slightly blue shifted than the powder emission maxima, a discrepancy that arise from the lower guest-guest interactions in pristine thin films.[209]

Thin film PLQYs trend reflect the PLQYs trend in powder, while it is different from the solution one. By observing the kinetics constants (**Table 6.6**), lower nonradiative decays are present for neutral emitters, while **[4^{tBu}CzBNImC12]PF$_6$**-based device exhibits the highest k_{rISC} value among the investigated compounds. Conversely, devices incorporating diphenylamino derivatives display lower k_{rISC} values and higher nonradiative kinetics constants which reflects in lower PLQYs.

In order to gain an insight into LEC behavior at different electrical bias, Time-dependent LIV (Luminance, Intensity and Voltage) experiments are conducted (**Figures A6.32-A6.37**).

Time-dependent LIV experiments of the devices incorporating **4^{tBu}CzBNIm**, **4DPABNIm** and **[4^{tBu}CzBNImC12]PF$_6$** confirm the semiconducting behavior of the devices.

Indeed, current intensity and light signal exhibit an initial flat profile, where no conduction is present, until the injection bandgap is reached, after which current intensity and luminance start to increase.

Furthermore, spikes in current intensity at low voltages are present for the devices with the neutral emitters and they might be caused by the presence of some morphology irregularities.

Time-dependent LIV experiments of the pristine devices incorporating **[4^{tBu}CzBNImC12]PF$_6$** and **[4DPABNImC12]PF$_6$** exhibit a regular profile, thus indicating good morphologies, while the blending with PMMA results in a more irregular morphology.

Furthermore, time-dependent LIV experiment of pristine device incorporating **[4DPABNImC12]PF$_6$** exhibits high driving currents at low voltages, in accordance with EIS data.

Subsequently, devices are tested with pulsed current monitoring the voltage and the luminance over time.

Efficacies and lifetimes of Single-Guest LECs are reported in **Table 6.7** while in **Figure 6.6** the normalized EL emission profiles are depicted.

Table 6.7: Figures of merit of single-guest LEC devices.

Compound	Additives	Current (mA)	Efficacy (cd A^{-1})	Lifetime (h)	λ_{EL} (nm)
4^{tBu}CzBNIm	5% PS, 20%THABF$_4$	3	1	0.42	520
[4^{tBu}CzBNImC12]PF$_6$	No additive	5	0.51	0.005	556
	5% PMMA	5	0.31	0.015	556
4DPABNIm	5% PS, 20%THABF$_4$	3	0.36	11.7	550
[4DPABNImC12]PF$_6$	No additive	40	0.00084	N.R.	566
	5% PMMA	5	0.0024	107	566

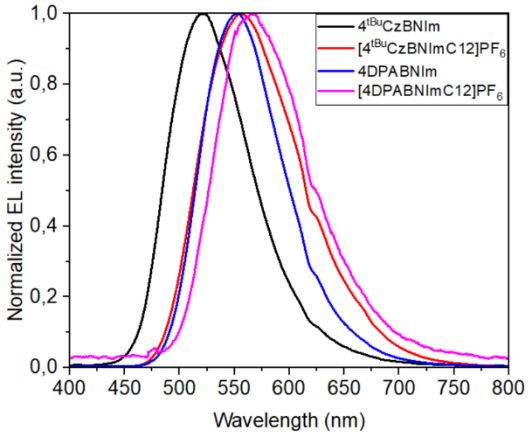


Figure 6.6: Normalized EL emission spectra of single-guest LECs devices, additives are not reported in the caption for simplicity.

A review of the results allows for a number of observations to be made.

In the first instance, the majority of devices exhibit the conventional voltage profile of LECs[126,210] (**Figure A6.38-A6.43**), which is distinguished by an initial decline followed by a steady-state regime.

Indeed, in a LEC, the injection barrier for electron and holes is reduced because of the migration of ions to the electrode interfaces and the formation of doped region. This reduction and the slowly growing of these regions decrease the voltage necessary to sustain the current density. Finally, the steady-state voltage regime is reached as the recombination is self-sustained in the intrinsic zone.
Nevertheless, this steady-state regime is apparent, as the average voltage subsequently begins to increase due to degradation processes.
The sole device that does not exhibit the conventional LEC behavior is the **[4DPABNImC12]PF_6**-based pristine device. Indeed, the average voltage of this device increases during time, exhibiting characteristics more consistent with a capacitor, in line with the EIS data.
The addition of PMMA to the active layer increases the resistivity of the device, thereby approximating its voltage profile to that of a typical LEC profile. However, the diminished thin-film PLQY yields a markedly reduced efficacy (0.0024 cd A^{-1}).
Furthermore, all devices exhibit the typical luminance profile with a buildup profile that originates in a more balanced hole and electron injection when the p-n junctions forms in the active layer.[205]
Another observation regards EL emission wavelengths, which are close to thin-film and powder emission wavelengths, thus confirming the absence of excimers.
Furthermore, LECs incorporating neutral luminophores exhibit good efficacies. Indeed, the **4^{tBu}CzBNIm**-based device exhibit an efficacy higher than that of other TADF-based single-guest LECs (1 cd A^{-1})[126], although it is not yet at the level of the record[202] .
In contrast, the **4DPABNIm**-based device exhibits a lower efficacy (0.36 cd A^{-1}), a result in line with its lower PLQY respect to the **4^{tBu}CzBNIm**-based one (13% vs 44%). Furthermore, these outcomes are not in accordance with ECL performances of these compounds, as the compound **4DPABNIm** exhibits the higher ECL efficiencies.
Furthermore, the efficacies of the LECs incorporating the cationic emitters are inferior to that of devices incorporating their neutral precursors, which can be attributed to the lower PLQYs of the thin films.
These outcomes lend support to the notion that the efficacy of Single-Guest LEC devices can be predicted on the basis of their photophysical properties rather than their electrochemical process. Indeed, while compound **4DPABNIm** exhibits the higher ECL efficiencies under all conditions, when it is incorporated into a Single-Guest LEC the resulting device exhibits a performance that is a third of that of the **4^{tBu}CzBNIm**-based device, which exhibits the higher thin-film PLQY.
Nevertheless, the trend in ECL over time, particularly under annihilation conditions is highly useful for anticipating other device properties, such as device operational lifetimes.

Indeed, LECs incorporating **4DPABNIm** and **[4DPABNImC12]PF_6** as emitters exhibit the longest lifetimes, which can be attributed to their superior electrochemical stability.

Furthermore, the LECs incorporating the cationic emitters do not require the presence of a solid electrolyte, thus confirming their double role of emitters and charge transporters.

6.6 Host-Guest LECs

Although Single-Guest LECs represent the fundamental concept of these devices, they exhibit low luminances due to the presence of exciton-polaron quenching (in organic semiconductors a polaron is an electron or a hole), which is particularly severe in these devices[211].

One potential solution to this issue is the spatial dispersion of the luminophore (guest) into a matrix (host)[201,205,212,213]. The matrix can be composed of one or two small molecules or polymers exhibiting reversible oxidation and reduction processes and it constitutes the principal component of the so-called "Host-Guest LECs". The primary functions of the matrix are to facilitates the physical dispersion of the dye within the active layer, to separate excitons and polarons, to assist in the injection of electron and holes into the active layer and to ensure a balanced charge transport[209,212,214]. It thus follows that matrices must be carefully selected considering their electrochemical and photophysical properties. Ideally, the host emission should be superimposable with the emitter absorption to allow an efficient Förster Resonance Energy transfer (FRET). Additionally, the matrices must be compatible with the guest materials and capable of enhancing charge transport and exciton dynamics.[215]

As these small molecules are the same ones used in OLEDs, numerous combinations are available. Some of them, along with their HOMO-LUMO energies, are presented in **Figure 6.7**.

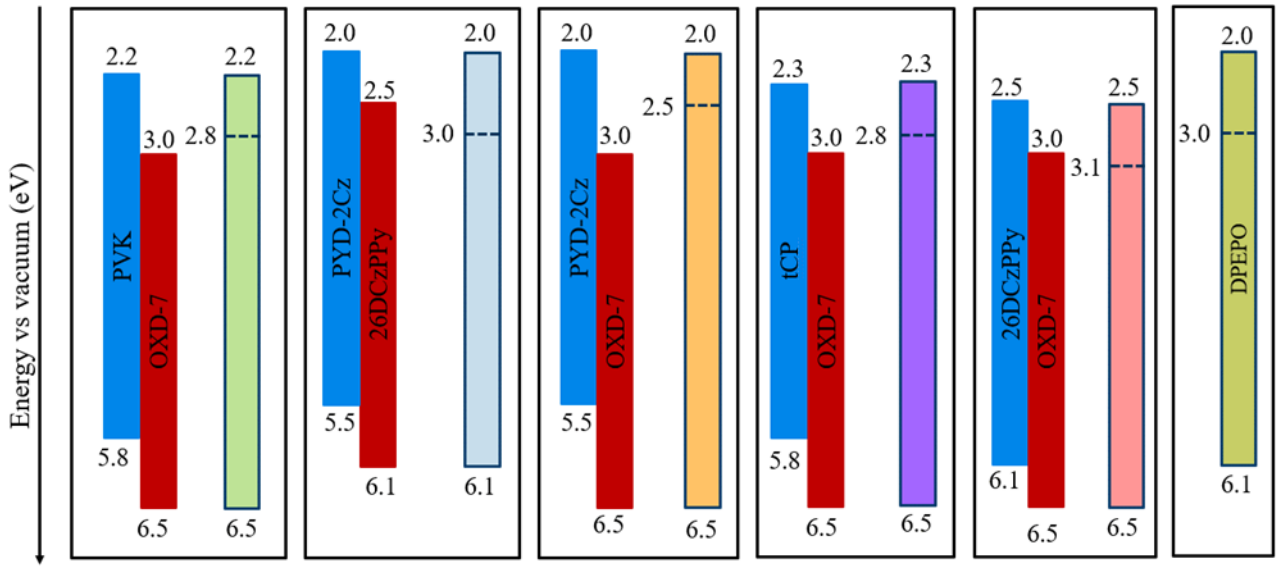


Figure 6.7: Electron-energy diagrams of some matrices with the respective triplet energy. Source: https://www.ossila.com/.

The most suitable matrix has been selected by calculating the electron-trap (E^p_{trap}) and hole-trap depth (E^n_{trap}). The E^p_{trap} is equal to the difference between the highest HOMO of the hosts and the HOMO

of the guest while the E^n_{trap} is the difference between the lowest LUMO of the hosts and the LUMO of the guest[205,212].

The matrix tCP:OXD-7 is selected due to its optimal emission maximum at approximately 400 nm (see below) and its superior trap compromise for all compounds (**Table 6.8**).

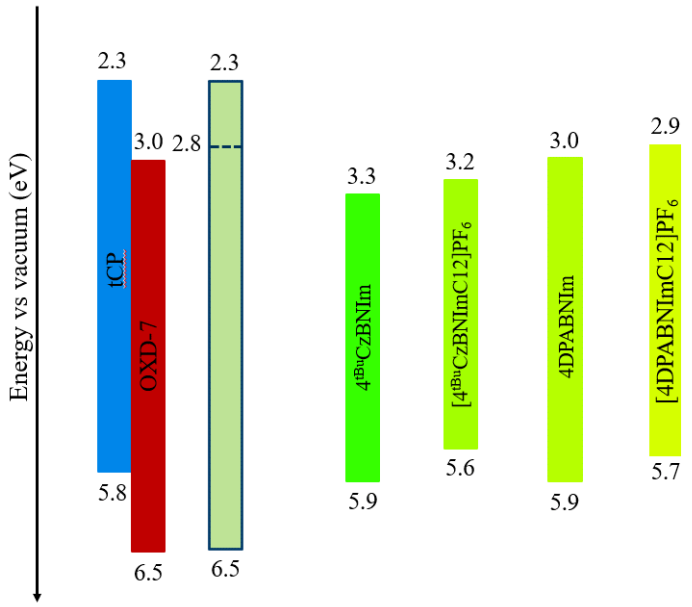


Figure 6.8: Electron-energy diagrams of the matrix and the emitters.

Table 6.8: Electron and hole trap levels for the host-guest systems with the matrix tCP:OXD-7.

Compound	E^p_{trap}	E^n_{trap}
4^{tBu}CzBNIm	0.22	0.35
[4^{tBu}CzBNImC12]PF_6	0.46	0.21
4DPABNIm	0.23	0.03
[4DPABNImC12]PF_6	0.36	-0.07

In order to achieve high efficacies, a DoE (comprising 16 experiments as presented in **Table 6.9**) is conducted with the objective of identifying the optimal concentrations of **[4^{tBu}CzBNImC12]PF_6** and $THABF_4$. The optimized ratio is then utilized for the other three emitters.

Table 6.9: Optimization of **[4^{tBu}CzBNImC12]PF_6** in tCP:OXD-7 matrix.

Exp. No.	$THABF_4$ (%)	[4^{tBu}CzBNImC12]PF_6 (%)	Efficacy (cd A^{-1})	Lifetime (h)
1	0	1	0.129	0.0045
2	11	1	0.1778	0.09667
3	0	10	0.01558	0.033
4	11	10	0.845	0.15
3	0	10	0.01558	0.033
4	11	10	0.845	0.15
5	0	4	0.0765	0.01444
6	11	4	1.164	0.024
7	11	7	1.3	0.039
8	3.66	1	0.46	0.00472
9	7.33	1	0.37	0.0026
10	7.33	10	0.74	0.21
11	5.5	5.5	0.244	0.15
12	5.5	7	0.309	0.28

13	15	15	1.06	0.1
14	15	5.6	1.2	0.04
15	**15**	**6.6**	**1.45**	**0.06**
16	10	15	0.83	0.18

The highest efficacy is obtained with the following tCP:OXD-7:**[4^{tBu}CzBNImC12]PF$_6$**:THABF$_4$ ratio: 100:100:6.6:15.

Photophysical properties of Host-Guest thin films are evaluated under nitrogen atmosphere (**Table 6.10-6.11**) and their normalized emission spectra are depicted in **Figure 6.9**.

Table 6.10: Photophysical properties in thin film.

Compound	λ_{PL} (nm)	PLQY (%)[a]	τ_p (ns)	τ_d (µs)	ΔE_{ST}[b]
4^{tBu}CzBNIm	495	68	6.68	0.767	0.134
[4^{tBu}CzBNImC12]PF$_6$	507	86	6.66	0.829	0.031
4DPABNIm	529	82	2.11	120	0.125
[4DPABNImC12]PF$_6$	539	80	2.03	0.91	0.220

Measurements are obtained from thin films with the following composition: tCP:OXD-7:**[4^{tBu}CzBNImC12]PF$_6$**:THABF$_4$ 100:100:6.6:15. λ_{exc} = 402.3 nm. Nanosecond lifetimes are evaluated with TCSPC electronic, while microsecond lifetimes are evaluated with MCS electronic. [a] PLQYs are evaluated under nitrogen atmosphere. [b] ΔE_{ST} are evaluated as reported in literature.[208]

Table 6.11: Kinetics constants values.

Compound	K^S_{rad} (s^{-1})	K^S_{nrad} (s^{-1})	K_{ISC} (s^{-1})	K_{rISC} (s^{-1})
4^{tBu}CzBNIm	$1.48 \cdot 10^7$	$7 \cdot 10^6$	$1.2 \cdot 10^8$	$8.90 \cdot 10^6$
[4^{tBu}CzBNImC12]PF$_6$	$1.53 \cdot 10^7$	$3.84 \cdot 10^6$	$1.22 \cdot 10^8$	$9.41 \cdot 10^6$
4DPABNIm	$1.85 \cdot 10^5$	$4.09 \cdot 10^4$	$4.56 \cdot 10^8$	$1.72 \cdot 10^7$
[4DPABNImC12]PF$_6$	$1.17 \cdot 10^8$	$2.94 \cdot 10^7$	$3.40 \cdot 10^8$	$3.65 \cdot 10^6$

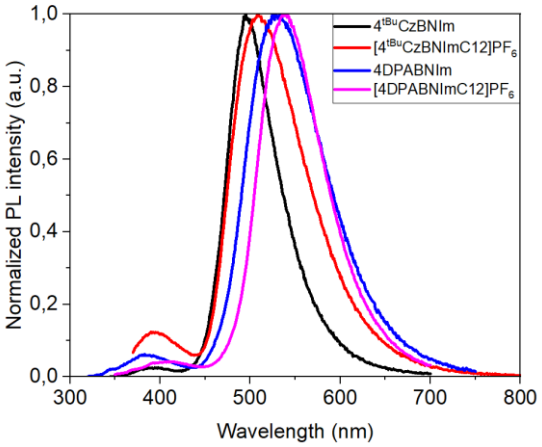


Figure 6.9: Normalized PL emission spectra of Host-Guest thin films.

All samples display TADF properties (**Figure A6.52-6.55**), with the emission maxima exhibiting a blue shift relative to the pristine thin films. This indicates that guest-guest interactions are effectively suppressed.

Furthermore, a second emission at approximately 390 nm is present, which is attributed to a residual emission of the host exciplex[205].

Additionally, the PLQYs of the Host-Guest thin films are higher than those of the pristine thin film, yet the trends do not align. Indeed, the Host-Guest thin film incorporating the emitter

[4^{tBu}CzBNImC12]PF$_6$ exhibits the highest PLQY (86%), whereas the thin film incorporating its neutral precursor displays the lowest PLQY among the investigated emitters (68%).

It its noteworthy that thin films incorporating **4DPABNIm** and **[4DPABNImC12]PF$_6$** exhibit high PLQYs (82% and 80%, respectively), which can be attributed to their lower k_{nr} values in comparison to those of pristine thin films.

Efficacies and lifetimes of Host-Guest LECs are reported in **Table 6.12**.

Table 6.12: Figures of merit of Host-guest LEC devices (tCP:OXD-7:compound:THABF$_4$ ratio: 100:100:6.6:15).

Compound	Current (mA)	Efficacy (cd A^{-1})	Lifetime (h)	λ_{EL} (nm)
4^{tBu}CzBNIm	5	0.03	0.06	510
[4^{tBu}CzBNImC12]PF$_6$	5	1.45	0.05	522
4DPABNIm	2	0.016	2.87	531
[4DPABNImC12]PF$_6$	5	0.12	0.1	550

All devices exhibit the conventional voltage and luminance profiles of LECs[126,205,210] (**Figures A6.56-A6.59**) with the EL emission maxima **(Figure 6.10**) exhibiting a blueshift relative to the Single-Guest EL emissions due to the suppression of the guest-guest interactions.

Except for **4DPABNIm**-based Host-Guest device, that exhibit the longest operational lifetime due to the lower applied current intensity, the other three devices display short lifetimes as the focus of the optimization is the efficacy.

Nevertheless, the devices that incorporate the derivatives **4DPABNIm** and **[4DPABNImC12]PF$_6$** exhibit longer lifetimes, probably due to their superior electrochemical reversibility.

Furthermore, devices incorporating the cationic emitters exhibit higher efficacies when compared to the devices incorporating their neutral precursor. This outcome reflects the PLQYs for di-*tert*butyl carbazole derivatives but does not reflect the PLQYs of diphenylamino derivatives, meaning that other factors might step in.

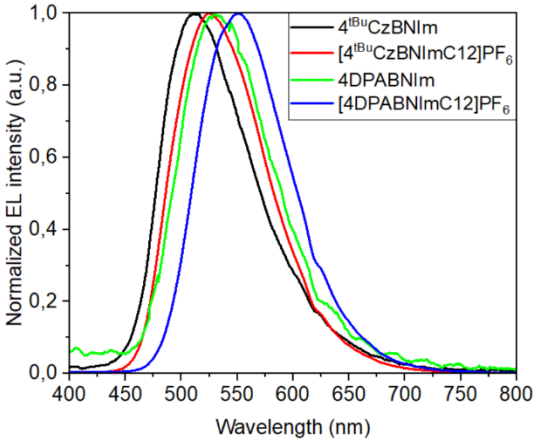


Figure 6.10: Normalized EL emission spectra of Host-Guest LECs.

6.7 Conclusion

In conclusion, this **Chapter** presented the investigation of the highest ECL- yielding, **4^{tBu}CzBNIm** and **4DPABNIm**, along with their alkylated derivatives, **[4^{tBu}CzBNImC12]PF$_6$** and **[4DPABNImC12]PF$_6$**, in Single-Guest and Host-Guest Light-Emitting Electrochemical Cells.

The photophysical properties of the imidazolium derivatives have been evaluated in powder and in dichloromethane solution. It was found that there was a decrease in PLQYs with respect to their neutral precursors upon alkylation. Moreover, the alkylation does not affect TADF properties.

The incorporation of these compounds into Single-Guest Light-Emitting Electrochemical Cells reveals that devices incorporating the neutral emitters display higher efficacies than those incorporating the cationic emitters, approaching the state-of-art performance of TADF-based Single-Guest LECs. Furthermore, the devices incorporating the cationic emitters do not require an ionic source, thereby confirming that these emitters serve also as ionic transporters. Moreover, the devices incorporating the compounds **4DPABNIm** and **[4DPABNImC12]PF$_6$** exhibit enhanced operational lifetimes, attributable to the higher radical stability.

Nevertheless, the trend of Single-Guest LECs efficacies does not align with that of ECL yields, indicating that ECL is an ineffective method for predicting the LEC efficacies while it can be used to predict the operational lifetimes.

Conversely, the thin film PLQYs represent an effective indicator to predict the LEC efficacies.

When incorporated in Host-Guest LECs, an increase of thin film PLQYs has been observed, accompanied by a blueshift due to the reduction in guest-guest interactions.

Furthermore, the optimization of the matrix:electrolyte:dye ratio for the compound **[4^{tBu}CzBNImC12]PF$_6$** resulted in an efficacy of 1.45 cd A^{-1}, which is above of the average and, although lower than the record, still represents a notable result.

Ultimately, the cationic derivatives exhibited higher efficacies than their neutral precursors.

6.8 Experimental Section

All reagents, except 3,6-di-*tert*-butyl-carbazole (synthesized according to literature[178]) were used as received without further purification and they are obtained from Sigma-Aldrich and Alfa-Aesar.

All solvents were dried according to literature procedure[151] using 3Å molecular sieves purchased from Sigma Aldrich.

^{1}H and $^{13}C\{^{1}H\}$ and ^{31}P NMR spectra were recorded on a Bruker AVANCE III spectrometer equipped with a BBO probe and ^{19}F NMR were recorded with a Bruker 200 MHz equipped with a QNP probe; ^{1}H and $^{13}C\{^{1}H\}$ NMR chemical shifts are referenced relative to residual solvents peaks while ^{19}F and ^{31}P chemical shifts are referenced using indirect referencing[4].

NMR solvents were purchased from Sigma-Aldrich or EurisoTOP and dried with 3Å molecular sieves purchased from Merck.

Multiplicities of signals are reported as s (singlet), d (doublet), t (triplet), q (quartet), quint (quintet), m (multiplet) and combinations of these multiplicities, coupling constants J are reported in Hz, and if not stated otherwise refer to J_{HH} couplings.

HR-MS spectra were recorded on an Agilent Q-TOF equipped with an ESI source. Mass spectra were recorded in positive mode.

All reactions were monitored by thin-layer chromatography using Merck silica gel plates 60 F_{254} (plastic sheets) and spots were visualized with UV light.

Flash chromatography was performed on a Combiflash Nextgen 300+ using Redisep Bronze column (4, 12, 24 grams) filled with NP silica gel and using Redisep Rf cartridge (4 and 24 grams).

6.8.1 Electrochemical measurements

See **Experimental Section** of **Chapter 3**.

6.8.2 Photophysical measurements

All samples were prepared with a $5 \cdot 10^{-6}$ M concentration using spectroscopic grade Uvasol dichloromethane, that was used as received.

Absorption spectra were recorded with a Agilent Cary 60 UV-VIS spectrophotometer in 10 mm quartz cuvettes filled with non-degassed solution of investigated compounds.

Emission and excitation spectra were recorded with a Photoluminescence Spectrometer (Edinburgh Instruments, FLS1000) equipped with a 450 W Xe lamp and an air-cooled single-photon counting photomultiplier (Hamamatsu R13456). The solutions of investigated compounds, contained in a10 mm quartz cuvette, were bubbled with argon for 15 minutes prior measurements.

Absolute PhotoLuminescence Quantum Yields in solution, powder and thin film were obtained with a Hamamatsu Absolute PL quantum yield spectrometer C11347 Quantaurus QY using a quartz tube

filled with Ar-purged solutions of investigated compounds; on a Petri dish (for powder) and by spin-coating the emitter on a quartz slide (for thin-film).

Lifetimes, emission spectra and excitation spectra in solution were obtained on a FLS1000 in Ar-purged or aerated solutions and lifetimes, emission spectra and excitation spectra in thin film were obtained on a FLS5 in N_2-purged environment.

Time-resolved lifetime measurements were acquired on the spectrometer equipped with a picosecond laser diode at 402.3 nm. Luminescence decays were recorded using the time correlated single photon counting (TCSPC) for lifetime in the nanosecond range, or the Multi-channel scaling (MCS) technique for lifetime in the microsecond range. The frequency of the laser was changed according to the lifetime of each sample.

Decay curves were analyzed with the Fluoracle Software using the IRF convolution fitting (for lifetime in ns range) or the tail-fitting for longer lifetimes.

For thin film preparation via spin coating, emitters were dissolved in anisole or acetonitrile (for Single-Guest LECs, 15 mg mL^{-1}) or chlorobenzene (for Host-Guest LECs, 5 mg mL^{-1} + the matrix and the solid electrolyte) and then dispersed on a quartz slide via spin-coating.

6.8.3 Preparation and characterization of devices

ITO substrates were purchased from Naranjo Substrates with a sheet resistance <15 Ω.sq. They were extensively cleaned using detergent, water, ethanol and iso-propanol as solvents in an ultrasonic bath (frequency 37-70 Hz) for 30 minutes each.

Afterward, the slides were dried with nitrogen and put in a UV-ozone cleaner for 8 minutes.

The clean plates were then coated with 80-nm PEDOT:PSS layer via spin coating to increase the device reproducibility.

To this end, an aqueous solution of PEDOT:PSS was filtered and mixed with iso-propanol in a ratio of 3:1, and 50 µL of this solution were dropped onto the substrate at a rotation speed of 1000 rpm for 60 seconds and then 2500 rpm for 25 seconds.

The resulting layers were dried on a hotplate at 120 °C for 10 minutes and stored under vacuum.

50 µL of blend solutions containing the emitters were deposited via spin coating at a rotation speed of 800 rpm for 30 seconds, 1200 rpm for 30 seconds and 3000 rpm for 10 seconds.

After the active layer deposition, the devices were transferred to an inert-atmosphere glovebox.

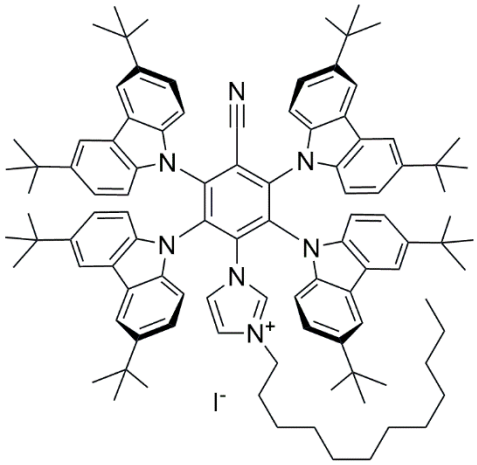
Finally, the aluminum cathode (>100 nm) was thermally evaporated onto the active layer using a shadow mask under high vacuum (<10^{-6} mbar) in an Angstrom Covap evaporator integrated into the inert-atmosphere glovebox.

Time dependence of luminance, voltage, and current intensity were measured by applying constant and/or pulsed voltage and current by monitoring the desired parameters simultaneously using an

Avantes spectrophotometer (Avaspec-ULS2048L-USB2) in conjunction with a calibrated integrated sphere Avasphere 30-Irrad and Botest OLT OLED Lifetime-Test System. EL spectra were recorded using the above-mentioned spectrophotometer. EIS assays were carried out with a potentiostat/galvanostat (Metrohm μAutolabIII) equipped with a frequency response analyzer module (FRA2). Measurements were performed at the applied voltage range from 0 to 5 V and fitted with the Nova 2.1 software using the circuit model reported in literature[206]. R_{LEC} represents the effective resistance of the active layer, including injection resistances, CPE_{LEC} represents the capacitance of the two electrodes contacting the film. The second resistor (R_{series}) represents all external resistances, including those of the ITO and Al electrodes. The AC signal amplitude was set to 10 mV, modulated in a frequency range from 10^1 to 10^6 MHz.

6.8.4 Synthesis route and procedures

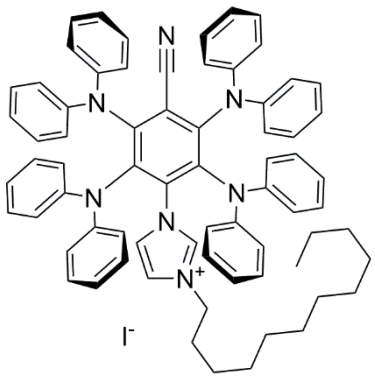
6.8.4.1 Synthesis of 1-(3-(3-(tert-butyl)-9H-carbazol-9-yl)-4-cyano-2,5,6-tris(3,6-di-tert-butyl-9H-carbazol-9-yl)phenyl)-3-dodecyl-1H-imidazol-3-ium iodide (**[4^{tBu}CzBNImC12]I**)



In a flame dried and argon-purged round-bottomed flask equipped with a magnetic stir bar, 2,3,5,6-tetrakis(3,6-di-*tert*-butyl-9H-carbazol-9-yl)-4-(1H-imidazol-1-yl)benzonitrile (**4^{tBu}CzBNIm**) (0.156 mmol, 1 equivalent) and iododododecane (0.936, 6 equivalents) were put in dry o-dichlorobenzene and heated in the dark at 150 °C until total conversion.

The resulting mixture was then purified by flash chromatography (100% DCM to 90%/10% DCM/methanol) to remove o-dichlorobenzene and iododododecane in excess to obtain the final product with good yield (0.117, yield 75%).

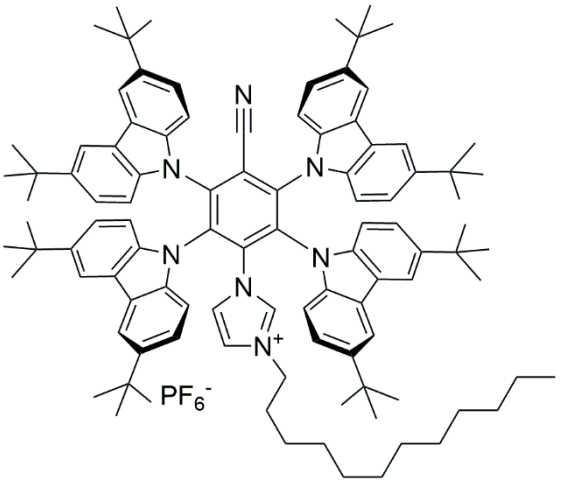
6.8.4.2 Synthesis of 1-(4-cyano-2,3,5,6-tetrakis(diphenylamino)phenyl)-3-dodecyl-1H-imidazol-3-ium iodide (**[4DPABNImC12]I**)



In a flame dried and argon-purged round-bottomed flask equipped with a magnetic stir bar, 2,3,5,6-tetrakis(3,6-di-*tert*-butyl-9H-carbazol-9-yl)-4-(1H-imidazol-1-yl)benzonitrile (**4DPABNIm**) (0.2 mmol, 1 equivalent) and iododododecane (1.2, 6 equivalents) were put in dry o-dichlorobenzene and heated in the dark at 150 °C until total conversion.

The resulting mixture was then purified by flash chromatography (100% DCM to 90%/10% DCM/methanol) to remove o-dichlorobenzene and iododododecane in excess to obtain the final product with good yield (0.134, yield 67%).

6.8.4.3 Synthesis of 1-(3-(3-(tert-butyl)-9H-carbazol-9-yl)-4-cyano-2,5,6-tris(3,6-di-tert-butyl-9H-carbazol-9-yl)phenyl)-3-dodecyl-1H-imidazol-3-ium hexafluorophosphate (**[4^{tBu}CzBNImC12]PF$_6$**)



In a flame dried and argon-purged round-bottomed flask equipped with a magnetic stir bar, 1-(3-(3-(tert-butyl)-9H-carbazol-9-yl)-4-cyano-2,5,6-tris(3,6-di-tert-butyl-9H-carbazol-9-yl)phenyl)-3-dodecyl-1H-imidazol-3-ium iodide (0.117 mmol, 1 equivalent) and silver hexafluorophosphate (0.12 mmol, 1.04 mmol) were put in dry dichloromethane and the mixture is stirred in the dark for 18 h at room temperature.

The mixture was then purified through a silica gel plug (100% DCM to 90%/10% DCM/methanol) to obtain the final product in quantitative yield (0.11 mmol, yield 96%).

^{1}H NMR (400 MHz, CD_3CN) δ 8.10 (d, *J* = 1.7 Hz, 1H), 7.93 (s, 1H), 7.79 (dd, *J* = 42.4, 1.9 Hz, 7H), 7.41 – 6.99 (m, 15H), 6.83 (t, *J* = 1.9 Hz, 1H), 6.62 (t, *J* = 1.9 Hz, 1H), 3.39 (t, *J* = 7.2 Hz, 2H), 1.34 (d, *J* = 16.1 Hz, 84H).

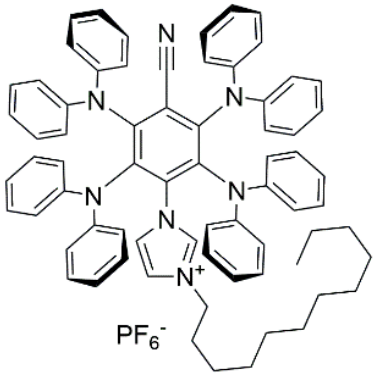
^{13}C{^{1}H} NMR (101 MHz, CD_3CN) δ 145.57, 145.49, 138.60, 137.95, 135.78, 125.18, 125.02, 124.25, 124.11, 118.26, 117.36, 111.29, 110.65, 35.28, 35.24, 32.58, 32.05, 30.29, 30.21, 30.15, 30.01, 29.60, 29.06, 25.55, 23.35, 14.34, 1.89, 1.68, 1.47, 1.41, 1.27, 1.06.

^{31}P NMR (121 MHz, CD_3CN) δ -144.18 (h, *J* = 712 Hz).

^{19}F NMR (188 MHz, CD_3CN) δ -72.59 (d, *J* = 712 Hz).

HR-MS (m/z) Calculated: 1447.99 ($[M]^+$); Found: 1448.01 ($[M]^+$).

6.8.4.4 Synthesis of 1-(4-cyano-3-(cyclohexa-1,4-dien-1-yl(phenyl)amino)-2,5,6-tris(diphenylamino)phenyl)-3-dodecyl-1H-imidazol-3-iumhexafluorophosphate (**[4DPABNImC12]PF_6**)



In a flame dried and argon-purged round-bottomed flask equipped with a magnetic stir bar, 1-(4-cyano-2,3,5,6-tetrakis(diphenylamino)phenyl)-3-dodecyl-1H-imidazol-3-ium iodide (0.134 mmol, 1 equivalent) and silver hexafluorophosphate (0.14 mmol, 1.04 mmol) were put in dry dichloromethane and the mixture is stirred in the dark for 18 h at room temperature.

The mixture was then purified through a silica gel plug (100% DCM to 90%/10% DCM/methanol) to obtain the final product in quantitative yield (0.13 mmol, yield 97%).

^{1}H NMR (300 MHz, Acetone-d_6) δ 7.57 (t, *J* = 1.9 Hz, 1H), 7.47 (t, *J* = 1.8 Hz, 1H), 7.32 – 6.67 (m, 44H), 6.54 (t, *J* = 1.6 Hz, 1H), 3.66 – 3.48 (m, 2H), 1.72 – 1.05 (m, 28H).

^{13}C{^{1}H} NMR (75 MHz, CD_2Cl_2) δ 147.65, 145.45, 144.01, 140.83, 136.10, 129.33, 129.01, 124.18, 123.71, 121.73, 120.91, 120.66, 53.81, 53.77, 53.40, 53.04, 52.68, 31.88, 29.68, 29.54, 29.40, 29.30, 29.18, 28.86, 28.77, 26.01, 22.66, 13.85.

^{31}P NMR (121 MHz, Acetone-d_6) δ -144.18 (h, *J* = 712 Hz).

^{19}F NMR (188 MHz, Acetone-d_6) δ -72.59 (d, *J* = 712 Hz).

HR-MS (m/z) Calculated: 1007.36 ($[M]^+$); Found: 1006.56 ($[M]^+$).

7. CONCLUSIONS AND PERSPECTIVES

In conclusion, in this Thesis different novel TADF emitters have been synthesized and their electrochemical, photophysical and ECL properties were investigated.

In particular, in **Chapter 2** the tuning of the acceptor strength of TADF emitters was investigated and the inaugural instances of oxidative-reduction ECL from water-soluble TADF emitters in an aqueous media were presented, thereby marking a significant advancement in the study of ECL emitters displaying TADF properties.

Furthermore, the first instance of "remote-route" ECL mechanism from a TADF emitters was shown.

Nevertheless, the TADF emitters investigated in this chapter exhibited electrochemical issues, the restriction to diphenylamine as donor and the impossibility to decide *a priori* the position of the imidazole group.

To circumvent these problems, in **Chapter 3** the insertion of a single imidazole moiety in a benzonitrile acceptor, followed by the systematically insertion of different donors, was performed, thereby yielding a class of novel TADF emitters which photophysical, electrochemical and ECL properties were investigated.

Additionally, the alkylation of imidazole was demonstrated using a short glycol chain incorporating the protected form of a bioconjugable group.

Moreover, the emitters that displayed high radical stability displayed higher ECL efficiencies under different conditions, thereby confirming the critical importance of this property to achieve high ECL yields.

These outcomes pushed us to stiffen these structures by increasing the π-extension of the imidazole moiety by keeping fixed the donors that exhibited higher electrochemical stability, thereby increasing PLQYs and, consequently, ECL efficiencies.

The restriction of intramolecular rotation was confirmed by NMR experiments but these compounds, as discussed in **Chapter 4**, exhibited lower ECL yields than their non-extended congeners due to their lower PLQYs, lower radical stability and lower diffusion coefficients.

Moreover, the acceptor reduction potential could not be further shifted towards more anodic values.

For this reason, terephthalonitrile was employed as acceptor core and it was functionalized with the donor exhibiting the better electrochemical properties.

Even if these compounds did not display high ECL efficiencies due to low PLQYs, some of them exhibited a remote-route ECL mechanism.

Moreover, a sulfonated donor was utilized to synthesize the first instance of red-emitting water-soluble TADF emitter, which ECL properties were evaluated in an aqueous solution.

Finally, the emitter with the best ECL properties were evaluated, along with their alkyl imidazolium derivatives, in Single-Guest and Host-Guest Electrochemical Cells (**Chapter 5**) to try to establish a relationship between ECL efficiencies and LECs efficacies. Nevertheless, this relationship was not observed, even if it was observed that the compound with the most stable ECL trend over time under annihilation conditions exhibited the longest operation lifetimes.

A review of the outcomes obtained in the present Thesis permits the identification of the properties that a suitable TADF emitters should have for electrochemiluminescence application:

- High PLQYs with low quenching from oxygen, which can be achieved by a careful molecular design (for example by introducing bulky peripherical groups, by coordinating the imidazolium to heavy metals or shifting to the Hybridized Local and Charge Transfer - HLCT);
- High radical-anion and radical-cation stability (remote ECL mechanism);
- Suitable half-wave potential and emission, in order to have a negative ΔG of the annihilation reaction;
- High diffusion coefficients (not relevant for bead-based immunoassays).

Additionally, it is suspected that, at high concentration, the co-reactant can act as a quencher towards emitters, as already observed for some fluorescent emitters in the past. Thus, it cannot be excluded at all that some emitters reported in this Thesis are quenched by the co-reactant in a greater mode.

Starting from the outcomes of the present Thesis, a number of different perspectives may be drawn out.

Firstly, the study of the quenching of ECL emitters by the co-reactant has the potential to be a valuable tool in predicting the ECL efficiency of the emitters.

Other valuable perspectives include the proper functionalization of the bis imidazolium derivative reported in the **Chapter 2** with a glycol chain incorporating a bioconjugable moiety, which would enhance its investigation in ECL sensors.

Nevertheless, the low stability of the radical-cations of those emitters should be increased by inserting in the reactive positions of diphenylamine alkyl groups (e.g. *tert*-butyl groups).

Furthermore, all the TADF emitters reported in the present work might be investigated as photocatalysts or, after proper functionalization, as imaging probes thanks to their long Delayed Fluorescence lifetimes.

8. BIBLIOGRAPHIC REFERENCES

[1] M. M. Richter, *Chem. Rev.* **2004**, *104*, 3003–3036.

[2] W. Miao, *Chem. Rev.* **2008**, *108*, 2506–2553.

[3] N. Harvey, *J. Phys. Chem* **1929**, *33*, 1456–1459.

[4] H. B. Lemon, *Science (1979)* **1918**, *47*, 170.

[5] K. S. V. Santhanam, A. J. Bard, *J. Am. Chem. Soc.* **1965**, *87*, 139–140.

[6] D. M. Hercules, *Science (1979)* **1964**, *145*, 808–809.

[7] R. A. Marcus, *J. Chem. Phys.* **1965**, *43*, 2654–2657.

[8] K. Wu, Y. Zheng, R. Chen, Z. Zhou, S. Liu, Y. Shen, Y. Zhang, *Biosens. Bioelectron.* **2023**, *223*, 115031.

[9] A. Zanut, A. Fiorani, S. Canola, T. Saito, N. Ziebart, S. Rapino, S. Rebeccani, A. Barbon, T. Irie, H.-P. Josel, F. Negri, M. Marcaccio, M. Windfuhr, K. Imai, G. Valenti, F. Paolucci, *Nat. Commun.* **2020**, *11*, 2668.

[10] L. Chen, D. J. Hayne, E. H. Doeven, J. Agugiaro, D. J. D. Wilson, L. C. Henderson, T. U. Connell, Y. H. Nai, R. Alexander, S. Carrara, C. F. Hogan, P. S. Donnelly, P. S. Francis, *Chem. Sci.* **2019**, *10*, 8654–8667.

[11] J. Dong, Y. Lu, Y. Xu, F. Chen, J. Yang, Y. Chen, J. Feng, *Nature* **2021**, *596*, 244–249.

[12] K. Sakanoue, A. Fiorani, C. I. Santo, Irkham, G. Valenti, F. Paolucci, Y. Einaga, *ACS Sens.* **2022**, *7*, 1145–1155.

[13] S. Senthil Kumar, A. J. Bard, *Anal. Chem.* **2013**, *85*, 292–295.

[14] K. Muzyka, *Biosens. Bioelectron.* **2014**, *54*, 393–407.

[15] A. J. Bard, *Electrogenerated Chemiluminescence*, Marcel Dekker, New York, **2004**.

[16] M. Y. Wong, E. Zysman-Colman, *Adv. Mater.* **2017**, *29*, 1605444.

[17] Y. Tao, K. Yuan, T. Chen, P. Xu, H. Li, R. Chen, C. Zheng, L. Zhang, W. Huang, *Adv. Mater.* **2014**, *26*, 7931–7958.

[18] R. J. Forster, P. Bertoncello, T. E. Keyes, *Annu. Rev. Anal. Chem.* **2009**, *2*, 359–385.

[19] N. E. Tokel, A. J. Bard, *J. Am. Chem. Soc.* **1972**, *94*, 2862–2863.

[20] M.-M. Chang, T. Saji, A. J. Bard, *J. Am. Chem. Soc.* **1977**, *99*, 5399–5403.

[21] H. S. White, A. J. Bard, *J. Am. Chem. Soc.* **1982**, *104*, 6891–6895.

[22] J. B. Noffsinger, N. D. Danielson, *Anal. Chem* **1987**, *59*, 865–868.

[23] J. K. Leland, M. J. Powell, *J. Electrochem. Soc* **1990**, *137*, 3127–3131.

[24] I. Rubinstein, A. J. Bard, *J. Am. Chem. Soc* **1981**, *103*, 512–516.

[25] A. Fracassa, C. Mariani, M. Marcaccio, G. Xu, N. Sojic, G. Valenti, F. Paolucci, *Curr. Opin. Electrochem.* **2023**, *41*, 101375.

[26] W. Miao, J. P. Choi, A. J. Bard, *J. Am. Chem. Soc.* **2002**, *124*, 14478–14485.

[27] F. Fang, L. Zhu, M. Li, Y. Song, M. Sun, D. Zhao, J. Zhang, *Adv. Sci.* **2021**, *8*, 2102970.

[28] Y. Chen, S. Zhou, L. Li, J. Zhu, *Nano Today* **2017**, *12*, 98–115.

[29] A. Abdussalam, G. Xu, *Anal. Bioanal. Chem.* **2017**, *414*, 131.

[30] J. Ge, X. Chen, J. Yang, Y. Wang, *Analyst* **2021**, *146*, 803–815.

[31] Y. Fang, Z. Zhou, Y. Hou, C. Wang, X. Cao, S. Liu, Y. Shen, Y. Zhang, *Anal. Chem.* **2023**, *95*, 6620–6628.

[32] K. M. Maness, R. M. Wightman, *J. Electroanal. Chem.* **1995**, *396*, 85–95.

[33] R. Y. Lai, A. J. Bard, *J. Phys. Chem. A* **2003**, *107*, 3335–3340.

[34] L. Feiler, H. Langhals, K. Polborn, *Liebigs Ann.* **1995**, *1995*, 1229–1244.

[35] H. Quante, Y. Geerts, K. Müllen, *Chem. Mater.* **1997**, *9*, 495–500.

[36] S. Demmig, H. Langhals, *Chem. Ber.* **1988**, *121*, 225–230.

[37] Z. B. Hill, D. B. Rodovsky, J. M. Leger, G. P. Bartholomew, *Chem. Commun.* **2008**, 6594–6596.

[38] D. Schlettwein, D. Woehrle, E. Karmann, U. Melville, *Chem. Mater.* **1994**, *6*, 3–6.

[39] M. Sadrai, L. Hadel, R. R. Sauers, S. Husain, K. Krogh-Jespersen, J. D. Westbrook, G. R. Bird, *J. Phys. Chem.* **1992**, *96*, 7988–7996.

[40] E. Kozma, W. Mróz, F. Villafiorita-Monteleone, F. Galeotti, A. Andicsová-Eckstein, M. Catellani, C. Botta, *RSC Adv.* **2016**, *6*, 61175–61179.

[41] J. D. Debad, J. C. Morris, V. Lynch, P. Magnus, A. J. Bard, *J. Am. Chem. Soc.* **1996**, *118*, 2374–2379.

[42] S. K. Lee, Y. Zu, A. Herrmann, Y. Geerts, K. Müllen, A. J. Bard, *J. Am. Chem. Soc.* **1999**, *121*, 3513–3520.

[43] Y. Wang, Y. Li, W. Zhang, P. Yin, L. Shang, R. Ma, L. Jia, Q. Xue, S. He, H. Wang, *Analyst* **2021**, *146*, 3679–3685.

[44] M. E. Williams, R. W. Murray, *Chem. Mater.* **1998**, *10*, 3603–3610.

[45] X. Qin, L. Yang, Z. Zhan, E. Cieplechowicz, K. Chu, C. Zhang, S. Jahanghiri, G. C. Welch, Z. Ding, *Electrochim. Acta* **2023**, *450*, 142226.

[46] L. Yang, A. D. Hendsbee, Q. Xue, S. He, C. R. De-Jager, G. Xie, G. C. Welch, Z. Ding, *ACS Appl. Mater. Interfaces* **2020**, *12*, 51736–51743.

[47] U. Scherf, E. J. W. List, *Adv. Mater.* **2002**, *14*, 477–487.

[48] I. Prieto, J. Teetsov, M. A. Fox, D. A. Vanden Bout, A. J. Bard, *J. Phys. Chem. A* **2001**, *105*, 520–523.

[49] J. P. Choi, K. T. Wong, Y. M. Chen, J. K. Yu, P. T. Chou, A. J. Bard, *J. Phys. Chem. B* **2003**, *107*, 14407–14413.

[50] F. Fungo, K. T. Wong, S. Y. Ku, Y. Y. Hung, A. J. Bard, *J. Phys. Chem. B* **2005**, *109*, 3984–3989.

[51] K. M. Omer, S. Y. Ku, Y. C. Chen, K. T. Wong, A. J. Bard, *J. Am. Chem. Soc.* **2010**, *132*, 10944–10952.

[52] K. M. Omer, A. L. Kanibolotsky, P. J. Skabara, I. F. Perepichka, A. J. Bard, *J. Phys. Chem. B* **2007**, *111*, 6612–6619.

[53] F. Polo, F. Rizzo, M. Veiga-Gutierrez, L. De Cola, S. Quici, *J. Am. Chem. Soc.* **2012**, *134*, 15402–15409.

[54] F. Rizzo, F. Polo, G. Bottaro, S. Fantacci, S. Antonello, L. Armelao, S. Quici, F. Maran, *J. Am. Chem. Soc.* **2017**, *139*, 2060–2069.

[55] J. Bañuelos, *Chem. Rec.* **2016**, *16*, 335–348.

[56] A. B. Nepomnyashchii, A. J. Bard, *Acc. Chem. Res.* **2012**, *45*, 1844–1853.

[57] M. Hesari, J. Lu, S. Wang, Z. Ding, *Chem. Commun.* **2015**, *51*, 1081–1084.

[58] H. Qi, J. J. Teesdale, R. C. Pupillo, J. Rosenthal, A. J. Bard, *J. Am. Chem. Soc.* **2013**, *135*, 13558–13566.

[59] M. M. Sartin, F. Camerel, R. Ziessel, A. J. Bard, *J. Phys. Chem. C* **2008**, *112*, 10833–10841.

[60] J. Suk, K. M. Omer, T. Bura, R. Ziessel, A. J. Bard, *J. Phys. Chem. C* **2011**, *115*, 15361–15368.

[61] J. E. Dick, A. Poirel, R. Ziessel, A. J. Bard, *Electrochim. Acta* **2015**, *178*, 234–239.

[62] A. B. Nepomnyashchii, M. Bröring, J. Ahrens, A. J. Bard, *J. Am. Chem. Soc.* **2011**, *133*, 19498–19504.

[63] A. B. Nepomnyashchii, M. Bröring, J. Ahrens, A. J. Bard, *J. Am. Chem. Soc.* **2011**, *133*, 8633–8645.

[64] A. B. Nepomnyashchii, M. Bröring, J. Ahrens, R. Krüger, A. J. Bard, *J. Phys. Chem. C* **2010**, *114*, 14453–14460.

[65] A. B. Nepomnyashchii, S. Cho, P. J. Rossky, A. J. Bard, *J. Am. Chem. Soc.* **2010**, *132*, 17550–17559.

[66] R. Ishimatsu, H. Shintaku, C. Adachi, K. Nakano, T. Imato, *ChemistrySelect* **2017**, *2*, 10531–10536.

[67] R. Ishimatsu, H. Shintaku, Y. Kage, M. Kamioka, S. Shimizu, K. Nakano, H. Furuta, T. Imato, *J. Am. Chem. Soc.* **2019**, *141*, 11791–11795.

[68] A. Elangovan, J. H. Lin, S. W. Yang, H. Y. Hsu, T. I. Ho, *J. Org. Chem.* **2004**, *69*, 8086–8092.

[69] T. Mikysek, P. Nikolaou, M. Kafexholli, P. Šimůnek, J. Váňa, A. Marková, M. Vala, G. Valenti, *ChemElectroChem* **2020**, *7*, 1550–1557.

[70] T. C. Richards, A. J. Bard, *Anal. Chem* **1995**, *67*, 3140–3147.

[71] S. Voci, R. Duwald, S. Grass, D. J. Hayne, L. Bouffier, P. S. Francis, J. Lacour, N. Sojic, *Chem. Sci.* **2020**, *11*, 4508–4515.

[72] H. S. White, A. J. Bard, *J. Am. Chem. Soc.* **1982**, *104*, 6891–6895.

[73] G. J. Barbante, C. F. Hogan, D. J. D. Wilson, N. A. Lewcenko, F. M. Pfeffer, N. W. Barnett, P. S. Francis, *Analyst* **2011**, *136*, 1329–1338.

[74] E. M. Gross, N. R. Armstrong, R. M. Wightman, *J. Electrochem. Soc.* **2002**, *149*, E137–E142.

[75] D. Bruce, M. M. Richter, *Anal. Chem* **2002**, *74*, 1340–1342.

[76] J. Il Kim, I.-S. Shin, H. Kim, J.-K. Lee, *J. Am. Chem. Soc.* **2005**, *127*, 1614–1615.

[77] J. M. Fernandez-Hernandez, E. Longhi, R. Cysewski, F. Polo, H. P. Josel, L. De Cola, *Anal. Chem.* **2016**, *88*, 4174–4178.

[78] B. D. Stringer, L. M. Quan, P. J. Barnard, D. J. D. Wilson, C. F. Hogan, *Organometallics* **2014**, *33*, 4860–4872.

[79] L. M. Quan, B. D. Stringer, M. A. Haghighatbin, J. Agugiaro, G. J. Barbante, D. J. D. Wilson, C. F. Hogan, P. J. Barnard, *Dalton Trans.* **2019**, *48*, 653–663.

[80] R. E. Karmis, S. Carrara, A. A. Baxter, C. F. Hogan, M. D. Hulett, P. J. Barnard, *Dalton Trans.* **2019**, *48*, 9998–10010.

[81] Y. Zhou, Y. Ding, J. Dong, Y. Zhao, F. Chen, Y. He, *J. Electrochem. Soc.* **2021**, *895*, 115534.

[82] Y. Zhou, L. Kong, K. Xie, C. Liu, *J. Organomet. Chem.* **2017**, *846*, 335–342.

[83] C. A. Parker, C. G. Hatchard, *Trans. Faraday Soc.* **1961**, *57*, 1894–1904.

[84] L. Bergmann, D. M. Zink, S. Bräse, T. Baumann, D. Volz, *Top. Curr. Chem. (Z)* **2016**, *374*, 22.

[85] H. Uoyama, K. Goushi, K. Shizu, H. Nomura, C. Adachi, *Nature* **2012**, *492*, 234–238.

[86] J. H. Kim, J. H. Yun, J. Y. Lee, *Adv. Opt. Mater.* **2018**, *6*, 1800255.

[87] M. A. Bryden, E. Zysman-Colman, *Chem. Soc. Rev.* **2021**, *50*, 7587–7680.

[88] A. Sahari, J. Puumi, J. K. Mannisto, T. Repo, *J. Org. Chem.* **2023**, *88*, 3822–3829.

[89] H. Huang, X. Li, C. Yu, Y. Zhang, P. S. Mariano, W. Wang, *Angew. Chem. Int. Ed.* **2017**, *56*, 1500–1505.

[90] E. Speckmeier, T. G. Fischer, K. Zeitler, *J. Am. Chem. Soc.* **2018**, *140*, 15353–15365.

[91] G. Hong, C. Si, A. K. Gupta, C. Bizzarri, M. Nieger, I. D. W. Samuel, E. Zysman-Colman, S. Bräse, *J. Mater. Chem. C* **2021**, *10*, 4757–4766.

[92] J.-X. Chen, W.-W. Tao, W.-C. Chen, Y.-F. Xiao, K. Wang, C. Cao, J. Yu, S. Li, F.-X. Geng, C. Adachi, C.-S. Lee, X.-H. Zhang, *Angew. Chem. Int. Ed.* **2019**, *58*, 14660–14665.

[93] X. Li, S. Fu, Y. Xie, Z. Li, *Rep. Prog. Phys* **2023**, *86*, 096501.

[94] Y. Liu, C. Li, Z. Ren, S. Yan, M. R. Bryce, *Nat. Rev. Mater.* **2018**, *3*, 18020.

[95] S. Y. Lee, T. Yasuda, Y. S. Yang, Q. Zhang, C. Adachi, *Angew. Chem. Int. Ed.* **2014**, *53*, 6402–6406.

[96] S. Tang, P. Lundberg, Y. Tsuchiya, J. Ràfols-Ribé, Y. Liu, J. Wang, C. Adachi, L. Edman, *Adv. Funct. Mater.* **2022**, *32*, 2205967.

[97] S. Tang, J. M. dos Santos, J. Ràfols-Ribé, J. Wang, E. Zysman-Colman, L. Edman, *Adv. Funct. Mater.* **2023**, *33*, 2306170.

[98] K. Zhang, X. Pang, Y. Song, Y. Xiu, R. Yu, L. He, *Adv. Opt. Mater* **2024**, *12*, 2400467.

[99] F. Ni, N. Li, L. Zhan, C. Yang, *Adv. Opt. Mater.* **2020**, *8*, 1902187.

[100] W. Ma, Y. Su, Q. Zhang, C. Deng, L. Pasquali, W. Zhu, Y. Tian, P. Ran, Z. Chen, G. Yang, G. Liang, T. Liu, H. Zhu, P. Huang, H. Zhong, K. Wang, S. Peng, J. Xia, H. Liu, X. Liu, Y. (Michael) Yang, *Nat. Mater.* **2022**, *21*, 210–216.

[101] R. Ishimatsu, S. Matsunami, T. Kasahara, J. Mizuno, T. Edura, C. Adachi, K. Nakano, T. Imato, *Angew. Chem. Int. Ed.* **2014**, *53*, 6993–6996.

[102] K. Karon, M. Lapkowski, *J. Solid State Electrochem.* **2015**, *19*, 2601–2610.

[103] R. Ishimatsu, T. Edura, C. Adachi, K. Nakano, T. Imato, *Chem. - Eur. J.* **2016**, *22*, 4889–4898.

[104] Y. Luo, B. Zhao, B. Zhang, Y. Lan, L. Chen, Y. Zhang, Y. Bao, L. Niu, *Analyst* **2022**, *147*, 2442–2451.

[105] X. Zou, Z. Zeng, B. Zhao, Y. Yue, Z. Xu, Y. Zhang, Y. Fu, Z. Xie, L. Niu, B. Zhang, *ACS Appl. Polym. Mater.* **2023**, *5*, 10116–10126.

[106] P. Huang, B. Zhang, Q. Hu, B. Zhao, Y. Zhu, Y. Zhang, Y. Kong, Z. Zeng, Y. Bao, W. Wang, Y. Cheng, L. Niu, *ChemPhysChem* **2021**, *22*, 726–732.

[107] B. Zhang, Y. Kong, H. Liu, B. Chen, B. Zhao, Y. Luo, L. Chen, Y. Zhang, D. Han, Z. Zhao, B. Z. Tang, L. Niu, *Chem. Sci.* **2021**, *12*, 13283–13291.

[108] S. Kumar, P. Tourneur, J. R. Adsetts, M. Y. Wong, P. Rajamalli, D. Chen, R. Lazzaroni, P. Viville, D. B. Cordes, A. M. Z. Slawin, Y. Olivier, J. Rô Me Cornil, Z. Ding, E. Zysman-Colman, *J. Mater. Chem. C* **2022**, *10*, 4646–4667.

[109] L. Yang, L. Dong, D. Hall, M. Hesari, Y. Olivier, E. Zysman-Colman, Z. Ding, *SmartMat* **2023**, *4*, e1149.

[110] K. Chu, J. R. Adsetts, Z. Whitworth, S. Kumar, E. Zysman-Colman, Z. Ding, *Langmuir* **2023**, *39*, 2829–2837.

[111] G. Valenti, A. Fiorani, S. Di Motta, G. Bergamini, M. Gingras, P. Ceroni, F. Negri, F. Paolucci, M. Marcaccio, *Chem. - Eur. J.* **2015**, *21*, 2936–2947.

[112] R. Kabe, C. Adachi, *Nature* **2017**, *550*, 384–387.

[113] X. Wei, M. J. Zhu, H. Yan, C. Lu, J. J. Xu, *Chem. - Eur. J.* **2019**, *25*, 12671–12683.

[114] S. van Reenen, M. Kemerink, in *Light-Emitting Electrochemical Cells: Concepts, Advances and Challenges*, Springer International Publishing, **2017**, pp. 3–45.

[115] Q. Pei, G. Yu, C. Zhang, Y. Yang, A. J. Heeger, *Science (1979)* **1995**, *269*, 1086–1088.

[116] J. H. Burroughes, D. D. C. Bradley, A. R. Brown, R. N. Marks, K. Mackay, R. H. Friend, P. L. Burns, A. B. Holmes, *Nature* **1990**, *347*, 539–541.

[117] G. Hong, X. Gan, C. Leonhardt, Z. Zhang, J. Seibert, J. M. Busch, S. Bräse, *Adv. Mater.* **2021**, *33*, 2005630.

[118] D. Volz, M. Wallesch, C. Fléchon, M. Danz, A. Verma, J. M. Navarro, D. M. Zink, S. Bräse, T. Baumann, *Green Chem.* **2015**, *17*, 1988–2011.

[119] J. Shinar, in *Organic Light-Emitting Devices. A Survey*, Springer-Verlag, New York, **2004**.

[120] K. Schlingman, Y. Chen, R. S. Carmichael, T. B. Carmichael, *Adv. Mater.* **2021**, *33*, 2006863.

[121] E. M. Lindh, A. Sandström, L. Edman, *Small* **2014**, *10*, 4148–4153.

[122] S. B. Meier, D. Tordera, A. Pertegás, C. Roldán-Carmona, E. Ortí, H. J. Bolink, *Mater. Today* **2014**, *17*, 217–223.

[123] S. Hu, J. Gao, in *Handbook of Organic Materials for Electronic and Photonic Devices, Second Edition*, Elsevier, **2018**, pp. 727–757.

[124] Z. B. Hill, D. B. Rodovsky, J. M. Leger, G. P. Bartholomew, *Chem. Commun.* **2008**, 6594–6596.

[125] M. Y. Wong, E. Zysman-Colman, in *Light-Emitting Electrochemical Cells: Concepts, Advances and Challenges*, Springer International Publishing, **2017**, pp. 237–266.

[126] M. Y. Wong, G. J. Hedley, G. Xie, L. S. Kölln, I. D. W. Samuel, A. Pertegás, H. J. Bolink, E. Zysman-Colman, *Chem. Mater.* **2015**, *27*, 6535–6542.

[127] S. Kanagaraj, A. Puthanveedu, Y. Choe, *Adv. Funct. Mater.* **2020**, *30*, 1907126.

[128] D. Dini, *Chem. Mater.* **2005**, *17*, 1933–1945.

[129] T. Nobeshima, M. Nakakomi, K. Nakamura, N. Kobayashi, *Adv. Opt. Mater.* **2013**, *1*, 144–149.

[130] S. H. Kong, J. I. Lee, S. Kim, M. S. Kang, *ACS Photonics* **2018**, *5*, 267–277.

[131] F. G. Bordwell, J. C. Branca, D. L. Hughes, W. N. Olmstead, *J. Org. Chem.* **1980**, *45*, 3305–3313.

[132] E. Pinosa, E. Bassan, S. Cetin, M. Villa, S. Potenti, F. Calogero, A. Gualandi, A. Fermi, P. Ceroni, P. G. Cozzi, *J. Org. Chem.* **2022**, *88*, 6390–6400.

[133] F. G. Bordwell, *Acc. Chem. Res.* **1988**, *21*, 456–463.

[134] C. Rizzo, S. Marullo, M. Feroci, V. Accurso, F. D'Anna, *Dyes Pigm.* **2021**, *186*, 109035.

[135] B. Gorodetsky, T. Ramnial, N. R. Branda, J. A. C. Clyburne, *Chem. Commun.* **2004**, 1972–1973.

[136] L. P. Hammett, *J. Am. Chem. Soc.* **1937**, *59*, 96–103.

[137] O. Yurchenko, D. Freytag, L. Zur Borg, R. Zentel, J. Heinze, S. Ludwigs, *J. Phys. Chem. B* **2012**, *116*, 30–39.

[138] E. T. Seo, R. F. Nelson, J. M. Fritsch, L. S. Marcoux, D. W. Leedy, R. N. Adams, *J. Am. Chem. Soc.* **1966**, *88*, 3498–3503.

[139] R. F. Nelson, R. N. Adams, *J. Am. Chem. Soc.* **1968**, *90*, 3925–3930.

[140] A. Wakamiya, K. Mori, S. Yamaguchi, *Angew. Chem., Int. Ed.* **2007**, *46*, 4273–4276.

[141] R. Ishimatsu, S. Matsunami, K. Shizu, C. Adachi, K. Nakano, T. Imato, *J. Phys. Chem. A* **2013**, *117*, 5607–5612.

[142] N. Akai, S. Kudoh, M. Nakata, *Chem. Phys. Lett.* **2003**, *371*, 655–661.

[143] C. Schweitzer, R. Schmidt, *Chem. Rev.* **2003**, *103*, 1685–1757.

[144] G. Valenti, C. Bruno, S. Rapino, A. Fiorani, E. A. Jackson, L. T. Scott, F. Paolucci, M. Marcaccio, *J. Phys. Chem. C* **2010**, *114*, 19467–19472.

[145] H. Li, S. Voci, A. Wallabregue, C. Adam, G. M. Labrador, R. Duwald, I. Hernández Delgado, S. Pascal, J. Bosson, J. Lacour, L. Bouffier, N. Sojic, *ChemElectroChem* **2017**, *4*, 1750–1756.

[146] E. A. Chandross, F. I. Sonntag, *J Am Chem Soc* **1966**, *88*, 1089–1096.

[147] E. K. Galván-Miranda, H. M. Castro-Cruz, J. Arturo Arias-Orea, M. Iurlo, G. Valenti, M. Marcaccio, N. A. Macías-Ruvalcaba, *Phys. Chem. Chem. Phys.* **2016**, *18*, 15025–15038.

[148] E. Kerr, E. H. Doeven, D. J. D. Wilson, C. F. Hogan, P. S. Francis, *Analyst* **2016**, *141*, 62–69.

[149] C. Adam, A. Wallabregue, H. Li, J. Gouin, R. Vanel, S. Grass, J. Bosson, L. Bouffier, J. Lacour, N. Sojic, *Chem. - Eur. J.* **2015**, *21*, 19243–19249.

[150] M. R. Molla, S. Ghosh, *Chem. - Eur. J.* **2012**, *18*, 9860–9869.

[151] D. B. G. Williams, M. Lawton, *J. Org. Chem.* **2010**, *75*, 8351–8354.

[152] R. K. Harris, E. D. Becker, S. M. Cabral De Menezes, R. Goodfellow, P. Granger, *Pure Appl. Chem.* **2001**, *73*, 1795–1818.

[153] A. Paul, R. Borrelli, H. Bouyanfif, S. Gottis, F. Sauvage, *ACS Omega* **2019**, *4*, 14780–14789.

[154] W. L. Wallace, A. J. Bard, *J. Phys. Chem.* **1979**, *83*, 1350–1357.

[155] A. Lausi, M. Polentarutti, S. Onesti, J. R. Plaisier, E. Busetto, G. Bais, L. Barba, A. Cassetta, G. Campi, D. Lamba, A. Pifferi, S. C. Mande, D. D. Sarma, S. M. Sharma, G. Paolucci, *Eur. Phys. J. Plus* **2015**, *130*, 1–8.

[156] W. Kabsch, *Acta Crystallogr,, Sect. D: Biol. Crystallogr.* **2010**, *66*, 125–132.

[157] G. M. Sheldrick, *Acta Crystallogr., Sect. A: Found. Adv.* **2015**, *71*, 3–8.

[158] G. M. Sheldrick, *Acta Crystallogr., Sect. C: Struct. Chem.* **2015**, *71*, 3–8.

[159] P. Emsley, B. Lohkamp, W. G. Scott, K. Cowtan, *Acta Crystallogr., Sect. D: Biol. Crystallogr.* **2010**, *66*, 486–501.

[160] A. L. Spek, *Acta Crystallogr., Sect. C: Struct. Chem.* **2015**, *71*, 9–18.

[161] L. J. Farrugia, *J. Appl. Crystallogr.* **2012**, *45*, 849–854.

[162] S. Fujii, Y. Maki, H. Kimoto, *J. Fluorine Chem.* **1989**, *43*, 131–144.

[163] A. Maggiore, Y. Qu, R. Guillot, P. Pander, M. Vasylieva, P. Data, F. B. Dias, P. Audebert, G. Clavier, F. Miomandre, *J. Phys. Chem. B* **2022**, *126*, 2740–2753.

[164] J. S. Ward, R. S. Nobuyasu, M. A. Fox, J. A. Aguilar, D. Hall, A. S. Batsanov, Z. Ren, F. B. Dias, M. R. Bryce, *J. Org. Chem.* **2019**, *84*, 3801–3816.

[165] J. F. Ambrose, R. F. Nelson, *J. Electrochem. Soc.* **1968**, *115*, 1159–1164.

[166] P. Blanchard, C. Malacrida, C. Cabanetos, J. Roncali, S. Ludwigs, *Polym Int* **2019**, *68*, 589–606.

[167] E. S. Rountree, B. D. McCarthy, T. T. Eisenhart, J. L. Dempsey, *Inorg. Chem.* **2014**, *53*, 9983–10002.

[168] K. J. Lee, B. D. McCarthy, J. L. Dempsey, *Chem. Soc. Rev.* **2019**, *48*, 2927–2945.

[169] T. D. Bortolato Mateusz; Vega-Peñaloza Alberto; Dell'Amico Luca, *Synthesis (Stuttg)* **2022**, *54*, 3409–3413.

[170] H. Liu, J. Li, G. Li, B. Zhang, Q. Zhan, Z. Liu, C. Zhou, K. Li, Z. Wang, C. Yang, *Dyes Pigm.* **2020**, *180*, 108521.

[171] J. Luo, S. Gong, T. Zhang, C. Zhong, G. Xie, Z. H. Lu, C. Yang, *Dyes Pigm.* **2017**, *147*, 350–356.

[172] Z. He, J. Li, D. Liu, Y. Mei, H. Wan, *Dyes Pigm.* **2023**, *212*, 111104.

[173] Q. A. Wu, F. Chen, C. C. Ren, X. F. Liu, H. Chen, L. X. Xu, X. C. Yu, S. P. Luo, *Org. Biomol. Chem.* **2020**, *18*, 3707–3716.

[174] C.-Y. Chan, L.-S. Cui, J. U. Kim, H. Nakanotani, C. Adachi, *Adv. Funct. Mater.* **2018**, *28*, 1706023.

[175] W. Yuan, D. Hu, M. Zhu, W. Shi, C. Shi, N. Sun, Y. Tao, *Dyes Pigm.* **2021**, *191*, 109395.

[176] J. Rosenmund, K. Doblhofer, *J. Electroanal. Chem.* **1995**, *396*, 77–83.

[177] D. L. Akins, R. L. Birke, *Chem. Phys. Lett.* **1974**, *29*, 428–435.

[178] Y. Liu, M. Nishiura, Y. Wang, Z. Hou, *J. Am. Chem. Soc.* **2006**, *128*, 5592–5593.

[179] A. P. Crew, K. Raina, H. Dong, Y. Qian, J. Wang, D. Vigil, Y. V. Serebrenik, B. D. Hamman, A. Morgan, C. Ferraro, K. Siu, T. K. Neklesa, J. D. Winkler, K. G. Coleman, C. M. Crews, *J. Med. Chem.* **2018**, *61*, 583–598.

[180] J. M. Thomas, *J. Chem. Educ.* **1999**, *76*, 97–98.

[181] M. D. Winn, C. C. Ballard, K. D. Cowtan, E. J. Dodson, P. Emsley, P. R. Evans, R. M. Keegan, E. B. Krissinel, A. G. W. Leslie, A. McCoy, S. J. McNicholas, G. N. Murshudov, N. S. Pannu, E. A. Potterton, H. R. Powell, R. J. Read, A. Vagin, K. S. Wilson, *Acta Crystallogr., Sect. D: Biol. Crystallogr.* **2011**, *67*, 235–242.

[182] P. R. Evans, G. N. Murshudov, *Acta Crystallogr., Sect. D: Biol. Crystallogr.* **2013**, *69*, 1204–1214.

[183] A. L. Spek, *Acta Crystallogr,, Sect. D: Biol. Crystallogr.* **2009**, *65*, 148–155.

[184] Z. Yang, Z. Mao, Z. Xie, Y. Zhang, S. Liu, J. Zhao, J. Xu, Z. Chi, M. P. Aldred, *Chem. Soc. Rev.* **2017**, *46*, 915–1016.

[185] H. I. Althagbi, J. R. Lane, G. C. Saunders, S. J. Webb, *J. Fluorine Chem.* **2014**, *166*, 88–95.

[186] K. Izutsu, *Electrochemistry in Nonaqueous Solutions*, Wiley-VCH, **2009**.

[187] T. Hatakeyama, K. Shiren, K. Nakajima, S. Nomura, S. Nakatsuka, K. Kinoshita, J. Ni, Y. Ono, T. Ikuta, *Adv. Mater.* **2016**, *28*, 2777–2781.

[188] I. Svir, A. Oleinick, O. V Klymenko, C. Amatore, *ChemElectroChem* **2015**, *2*, 811–818.

[189] L. Kacenauskaite, N. Bisballe, R. Mucci, M. Santella, T. Pullerits, J. Chen, T. Vosch, B. W. Laursen, *J. Am. Chem. Soc.* **2021**, *143*, 1377–1385.

[190] M. Zheng, Y. Li, Y. Wei, L. Chen, S. Liu, X. Zhou, *J. Phys. Chem. C* **2023**, *127*, 2846–2854.

[191] K. Y. Zhang, Q. Yu, H. Wei, S. Liu, Q. Zhao, W. Huang, *Chem. Rev.* **2018**, *118*, 1770–1839.

[192] T. He, C. Ren, Z. Li, S. Xiao, J. Li, X. Lin, C. Ye, J. Zhang, L. Guo, W. Hu, R. Chen, *Appl. Phys. Lett.* **2018**, *112*, 211102.

[193] J. Agirre, M. Atanasova, H. Bagdonas, C. B. Ballard, A. Baslé, J. Beilsten-Edmands, R. J. Borges, D. G. Brown, J. J. Burgos-Mármol, J. M. Berrisford, P. S. Bond, I. Caballero, L. Catapano, G. Chojnowski, A. G. Cook, K. D. Cowtan, T. I. Croll, J. É. Debreczeni, N. E. Devenish, E. J. Dodson, T. R. Drevon, P. Emsley, G. Evans, P. R. Evans, M. Fando, J. Foadi, L. Fuentes-Montero, E. F. Garman, M. Gerstel, R. J. Gildea, K. Hatti, M. L. Hekkelman, P. Heuser, S. W. Hoh, M. A. Hough, H. T. Jenkins, E. Jiménez, R. P. Joosten, R. M. Keegan, N. Keep, E. B. Krissinel, P. Kolenko, O. Kovalevskiy, V. S. Lamzin, D. M. Lawson, A. A. Lebedev, A. G. W. Leslie, B. Lohkamp, F. Long, M. Malý, A. J. McCoy, S. J. McNicholas, A. Medina, C. Millán, J. W. Murray, G. N. Murshudov, R. A. Nicholls, M. E. M. Noble, R. Oeffner, N. S. Pannu, J. M. Parkhurst, N. Pearce, J. Pereira, A. Perrakis, H. R. Powell, R. J. Read, D. J. Rigden, W. Rochira, M. Sammito, F. Sánchez Rodr\'\iguez, G. M. Sheldrick, K. L. Shelley, F. Simkovic, A. J. Simpkin, P. Skubak, E. Sobolev, R. A. Steiner, K. Stevenson, I. Tews, J. M. H. Thomas, A. Thorn, J. T. Valls, V. Uski, I. Usón, A. Vagin, S. Velankar, M. Vollmar, H. Walden, D. Waterman, K. S. Wilson, M. D. Winn, G. Winter, M. Wojdyr, K. Yamashita, *Acta Crystallogr., Sect. D: Struct. Biol.* **2023**, *79*, 449–461.

[194] Sheldrick, *SADABS Version 2014/5 University of Göttingen, Germany*, **2014**.

[195] L. Schrodinger, *The PyMOL Molecular Graphics System. Schrodinger, LLC*, **2015**.

[196] A. F. Suleymanova, M. Z. Shafikov, A. C. Whitwood, R. Czerwieniec, D. W. Bruce, *J. Mater. Chem. C* **2021**, *9*, 6528–6535.

[197] S. Wang, L. Peng, F. He, Y. Ming, H. Qi, Y. Liu, D. Ma, S. Ying, S. Yan, *Adv. Opt. Mater.* **2024**, *12*, 2400503.

[198] N. Noto, A. Yada, T. Yanai, S. Saito, *Angew. Chem. Int. Ed.* **2023**, *62*, e202219107.

[199] A. Chatterjee, J. Chatterjee, S. Sappati, R. Tanwar, M. D. Ambhore, H. Arfin, R. M. Umesh, M. Lahiri, P. Mandal, P. Hazra, *Chem. Sci.* **2023**, *14*, 13832–13841.

[200] Y. Choe, C. D. Sunesh, M. S. Subeesh, K. Shanmugasundaram, in *Light-Emitting Electrochemical Cells: Concepts, Advances and Challenges*, Springer International Publishing, **2017**, pp. 329–349.

[201] A. Pertegás, D. Tordera, J. J. Serrano-Pérez, E. Ortí, H. J. Bolink, *J. Am. Chem. Soc.* **2013**, *135*, 18008–18011.

[202] R. Yu, Y. Song, K. Zhang, X. Pang, M. Tian, L. He, *Adv. Funct. Mater.* **2022**, *32*, 2110623.

[203] Joseph R. Lakowicz, *Principles of Fluorescence Spectroscopy*, Springer New York, **2006**.

[204] T. O. Villaseñor-Granados, G. Rodríguez-López, I. Ramos-García, D. Morales-Martínez, F. J. González, A. Flores-Parra, *ChemPhysChem* **2020**, *21*, 1177–1183.

[205] P. Lundberg, Y. Tsuchiya, E. M. Lindh, S. Tang, C. Adachi, L. Edman, *Nat. Commun.* **2019**, *10*, 5307.

[206] E. Fresta, G. U. Mahoro, L. M. Cavinato, J.-F. Lohier, J.-L. Renaud, S. Gaillard, R. D. Costa, *Adv. Opt. Mater.* **2022**, *10*, 2101999.

[207] Y. Li, J. Gao, G. Yu, Y. Cao, A. J. Heeger, *Chem. Phys. Lett.* **1998**, *287*, 83–88.

[208] Q. Zhang, B. Li, S. Huang, H. Nomura, H. Tanaka, C. Adachi, *Nat. Photonics* **2014**, *8*, 326–332.

[209] P. Lundberg, E. M. Lindh, S. Tang, L. Edman, *ACS Appl. Mater. Interfaces* **2017**, *9*, 28810–28816.

[210] E. Fresta, G. Volpi, M. Milanesio, C. Garino, C. Barolo, R. D. Costa, *Inorg. Chem.* **2018**, *57*, 10469–10479.

[211] S. van Reenen, R. A. J. Janssen, M. Kemerink, *Adv. Funct. Mater.* **2015**, *25*, 3066–3073.

[212] S. Tang, A. Sandström, P. Lundberg, T. Lanz, C. Larsen, S. Van Reenen, M. Kemerink, L. Edman, *Nat. Commun.* **2017**, *8*, 1190.

[213] S. Jenatsch, L. Wang, N. Leclaire, E. Hack, R. Steim, S. B. Anantharaman, J. Heier, B. Ruhstaller, L. Penninck, F. Nüesch, R. Hany, *Org. Electron.* **2017**, *48*, 77–84.

[214] C.-T. Liao, H.-F. Chen, H.-C. Su, K.-T. Wong, *Phys. Chem. Chem. Phys.* **2012**, *14*, 1262–1269.

[215] K. S. Yook, J. Y. Lee, *Adv. Mater.* **2014**, *26*, 4218–4233.

9. APPENDIX

Chapter 2

2.1 XRD analysis – Structural characterization

Table A2.1: Crystallographic data and refinement details.

	3DPA2ImBN
CCDC Number	2359842
Chemical Formula	$C_{49}H_{36}N_8 \cdot {}^1/_2CH_2Cl_2$
Formula weight	779.32 g/mol
Temperature	100(2) K
Wavelength	0.620 Å
Crystal system	Monoclinic
Space Group	P $2_1/c$
Unit cell dimensions	a = 13.982(3) Å b = 12.019(2) Å c = 23.870(5) Å α = 90° β = 97.56(3)° γ = 90°
Volume	3976.4(14) $Å^3$
Z	4
Density (calculated)	1.302 $g \cdot cm^{-3}$
Absorption coefficient	0.103 mm^{-1}
F(000)	1628
Theta range for data collection	1.3° to 31.1°
Index ranges	$-23 \leq h \leq 23$, $-19 \leq k \leq 19$, $-37 \leq l \leq 37$
Resolution	0.60 Å
Reflections collected	92549
Independent reflections	17263, 15309 data with I>2σ(I)
Data multiplicity (max resltn)	4.75 (2.79)
I/σ(I) (max resltn)	24.67 (11.31)
R_{merge} (max resltn)	0.0336 (0.0790)
Data completeness (max resltn)	89.9% (72.9%)
Refinement method	Full-matrix least-squares on F^2
Data / restraints / parameters	17263 / 21 / 560
Goodness-of-fit on F^2	1.018
Δ/σ_{max}	0.004
Final R indices [I>2σ(I)]	R_1 = 0.0497, wR_2 = 0.1385
R indices (all data)	R_1 = 0.0540, wR_2 = 0.1428
Largest diff. peak and hole	0.538 and -0.583 $eÅ^{-3}$
R.M.S. deviation from mean	0.063 $eÅ^{-3}$

$R_1 = \Sigma \; ||Fo|-|Fc|| \; / \; \Sigma \; |Fo|$, $wR_2 = \{ \Sigma \; [w(Fo^2 - Fc^2)^2] \; / \; \Sigma \; [w(Fo^2)^2] \}^{½}$

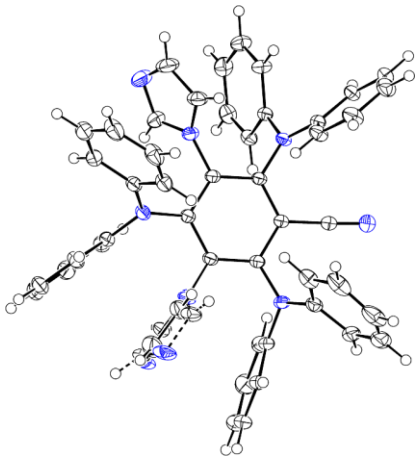


Figure A2.1: Ellipsoids representation of **3DPA2ImBN** asymmetric unit (A.S.U. - 50% probability).

2.2 ^{1}H NMR Spectra

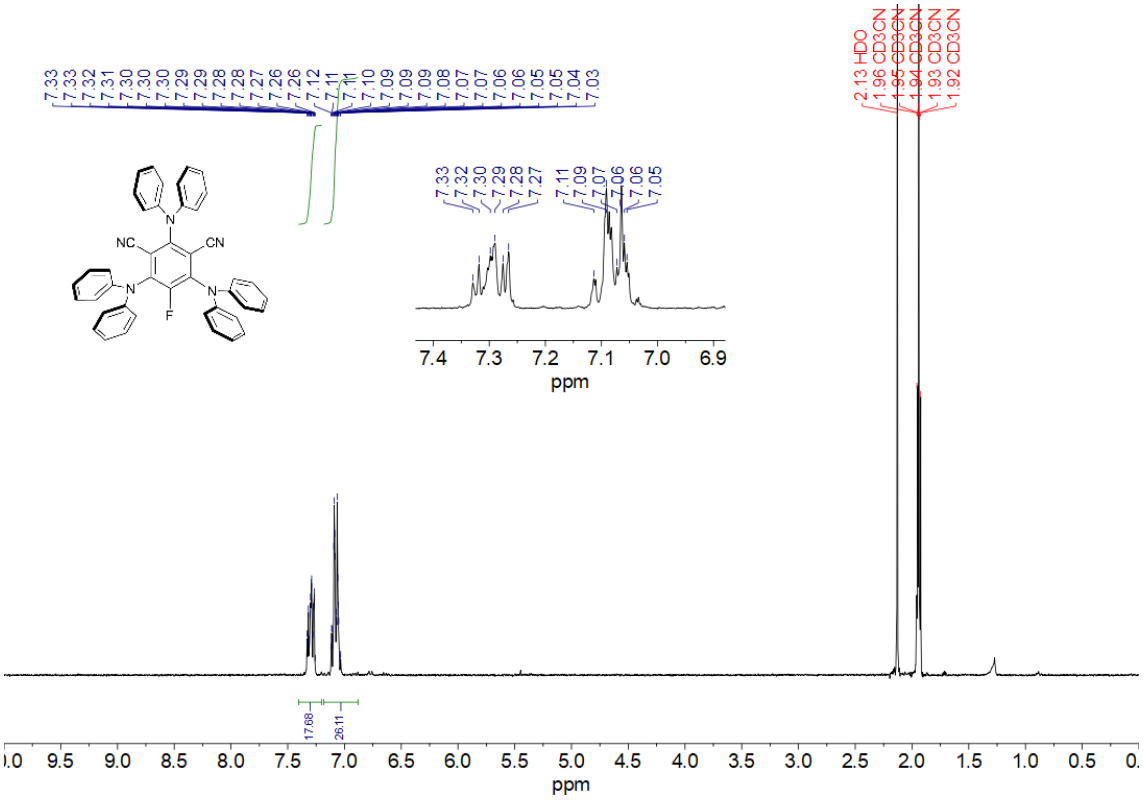


Figure A2.2: ^{1}H NMR spectrum of **3DPAFIPN** (CD_3CN).

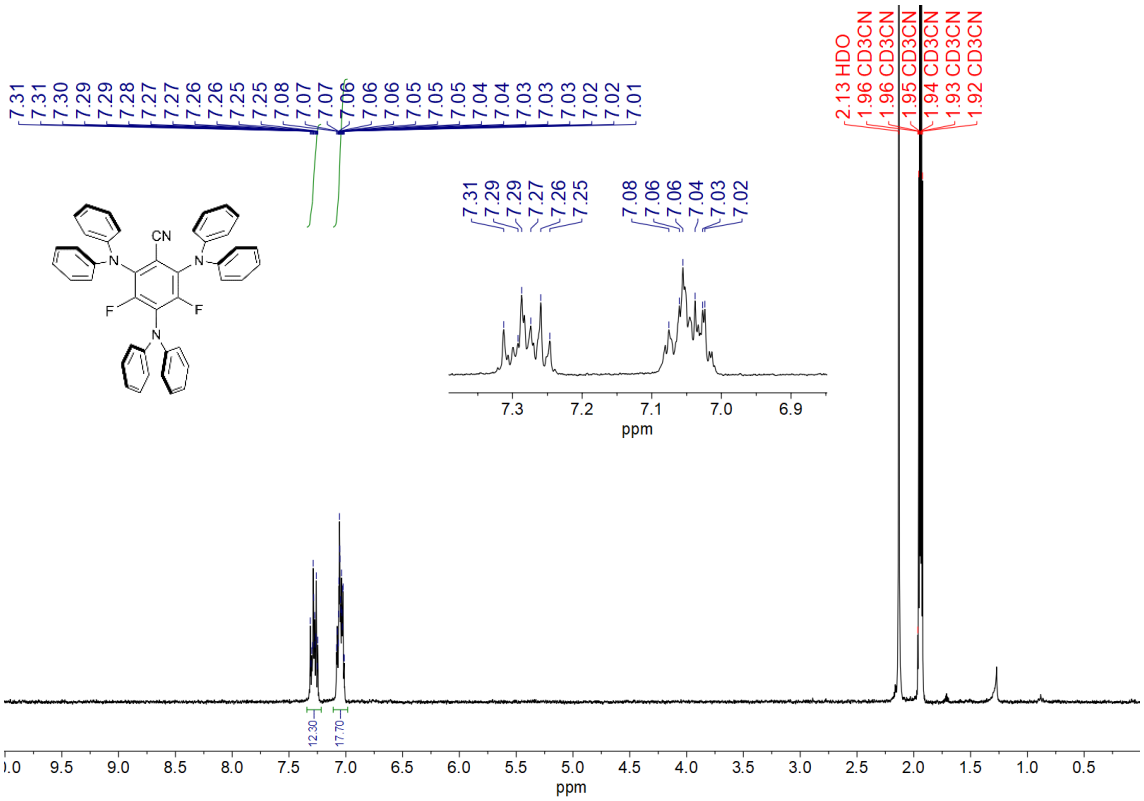


Figure A2.3: ^{1}H NMR spectrum of **3DPA2FBN** (CD_3CN).

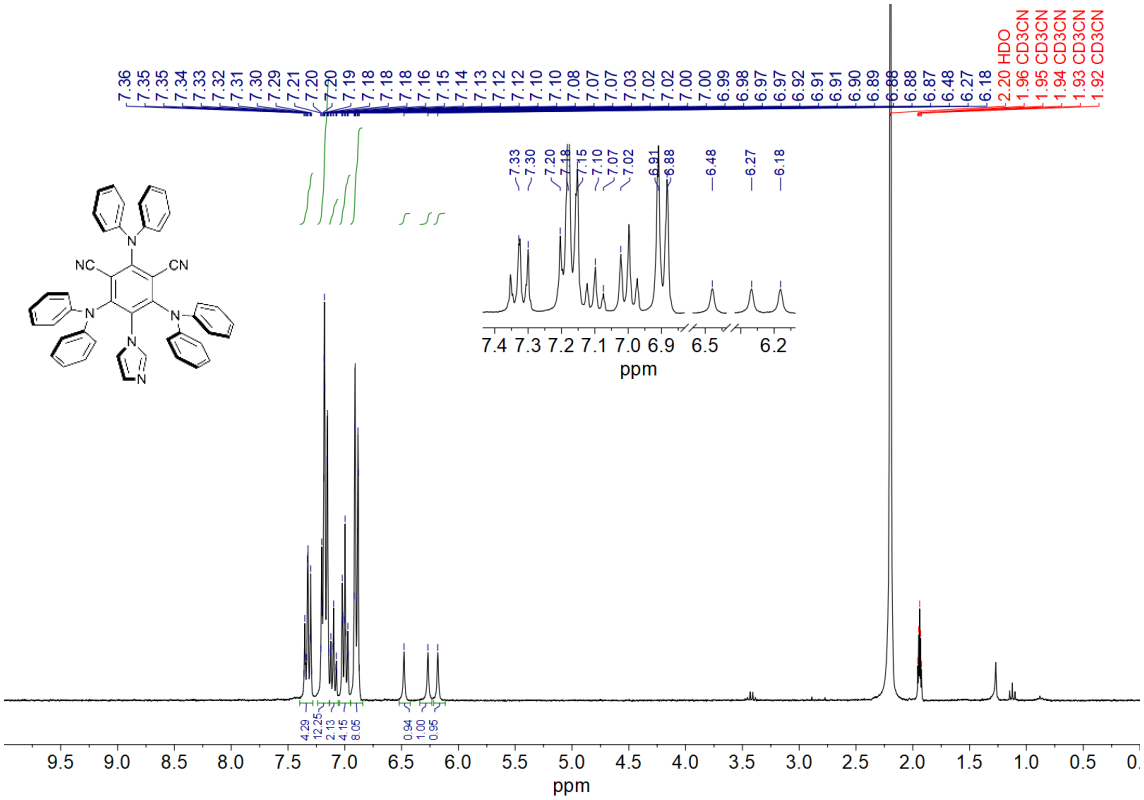


Figure A2.4: ^{1}H NMR spectrum of **3DPAImIPN** (CD_3CN).

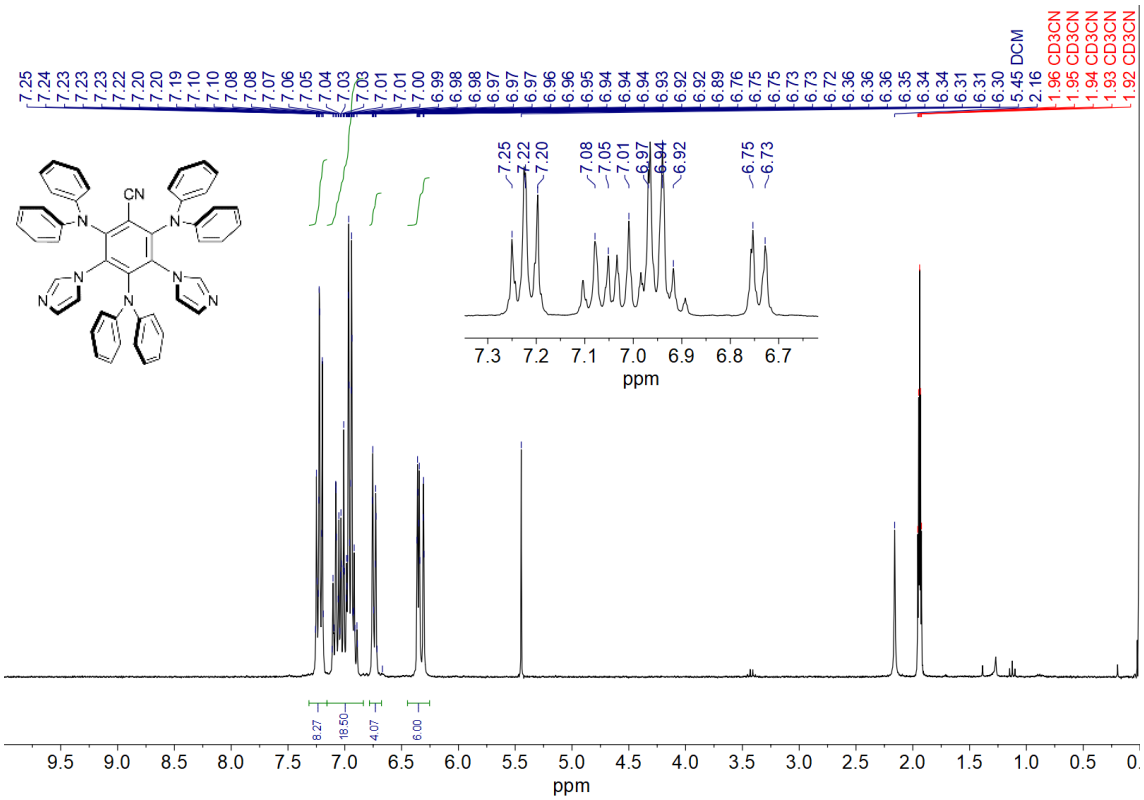


Figure A2.5: ^{1}H NMR spectrum of **3DPA2ImBN** (CD_3CN).

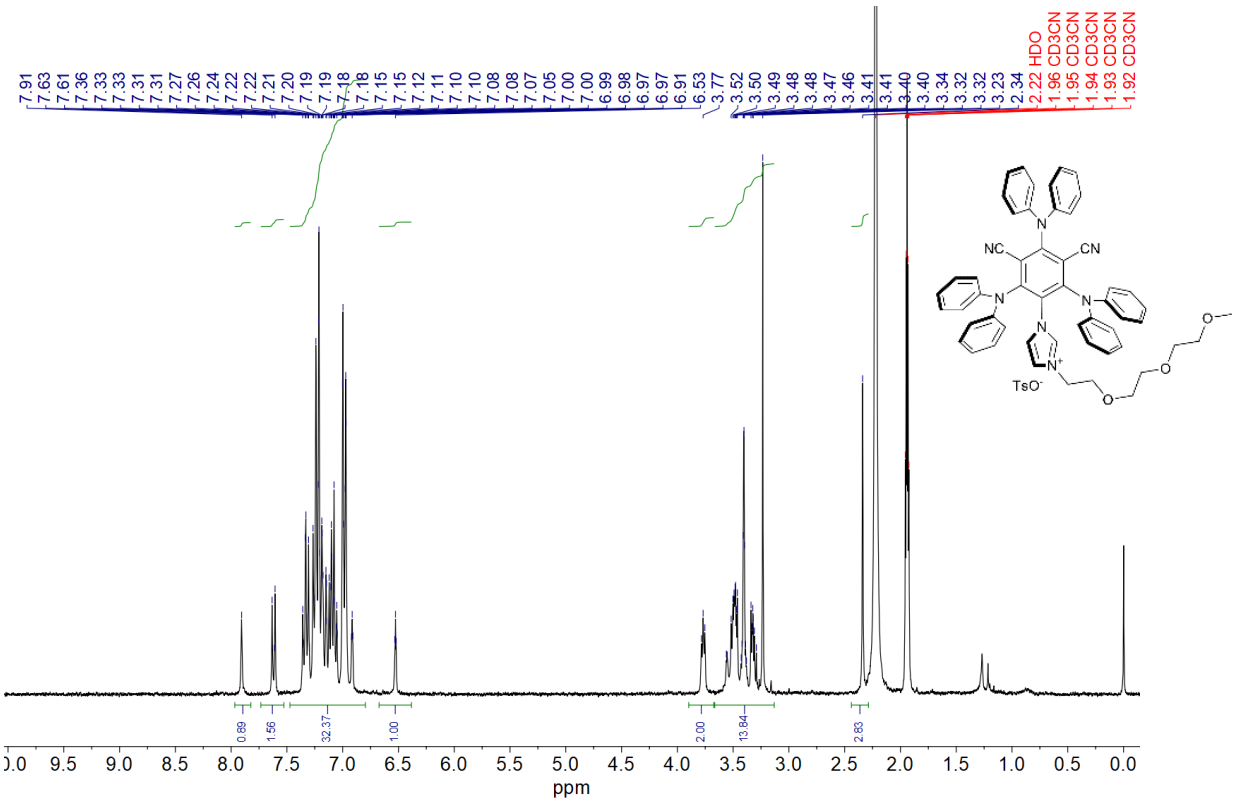


Figure A2.6: ^{1}H NMR spectrum of **[3DPAImIPNTEG]OTs** (CD_3CN).

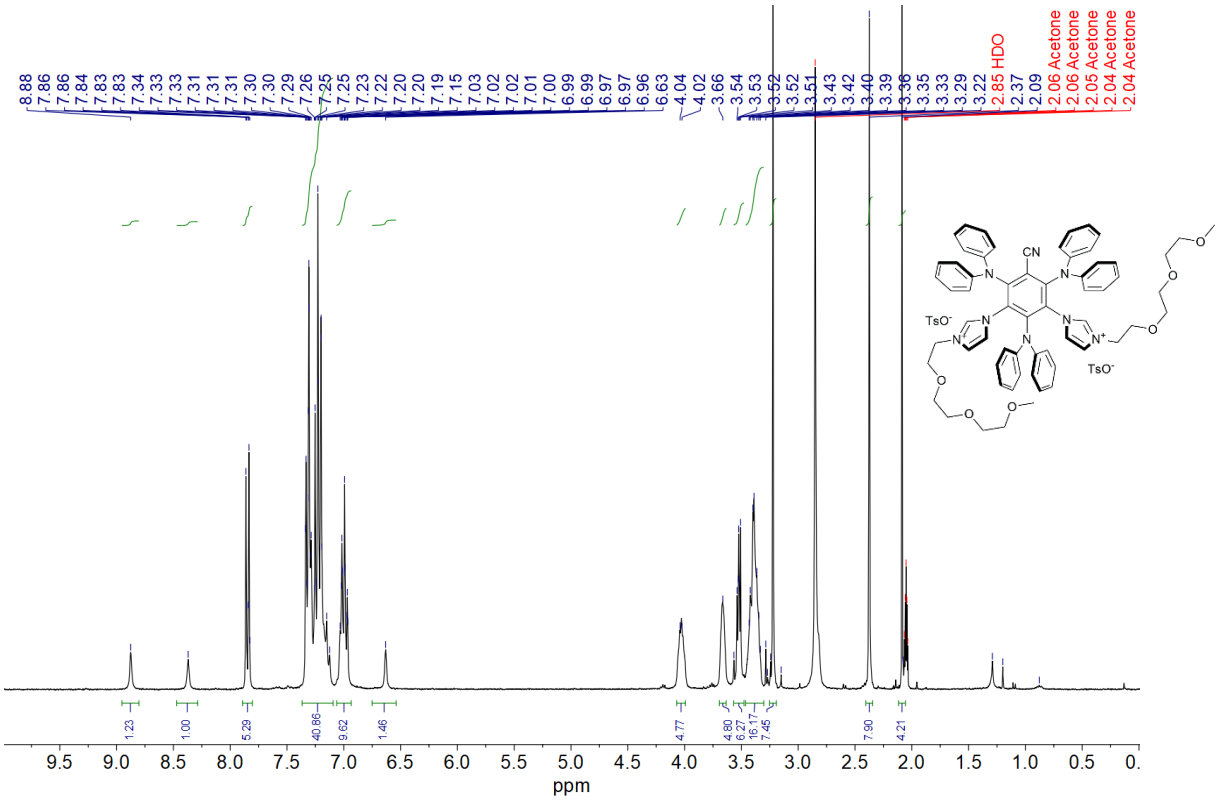


Figure A2.7: ^{1}H NMR spectrum of **[3DPA2ImBN2TEG]2(OTs)** (Acetone-d_6).

2.3 ^{13}C{^{1}H} NMR Spectra

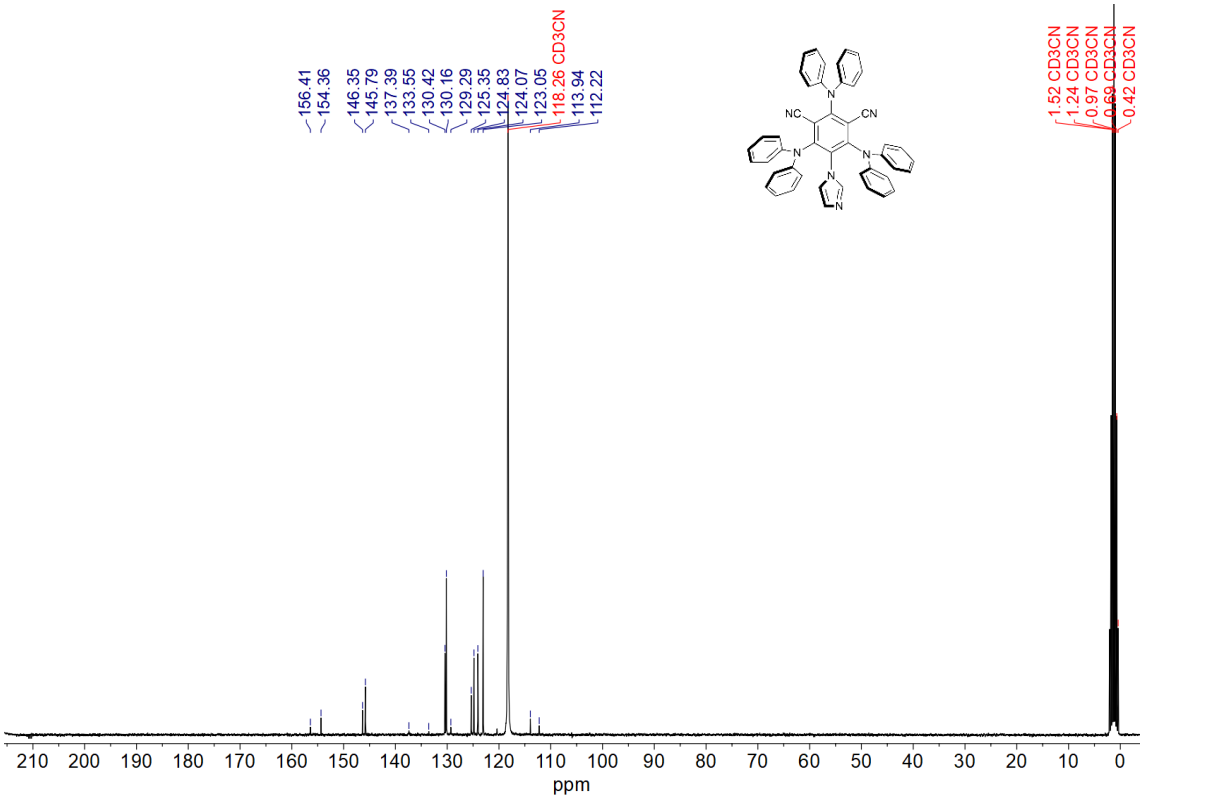


Figure A2.8: ^{13}C{^{1}H} NMR spectrum of **3DPAImIPN** (CD_3CN).

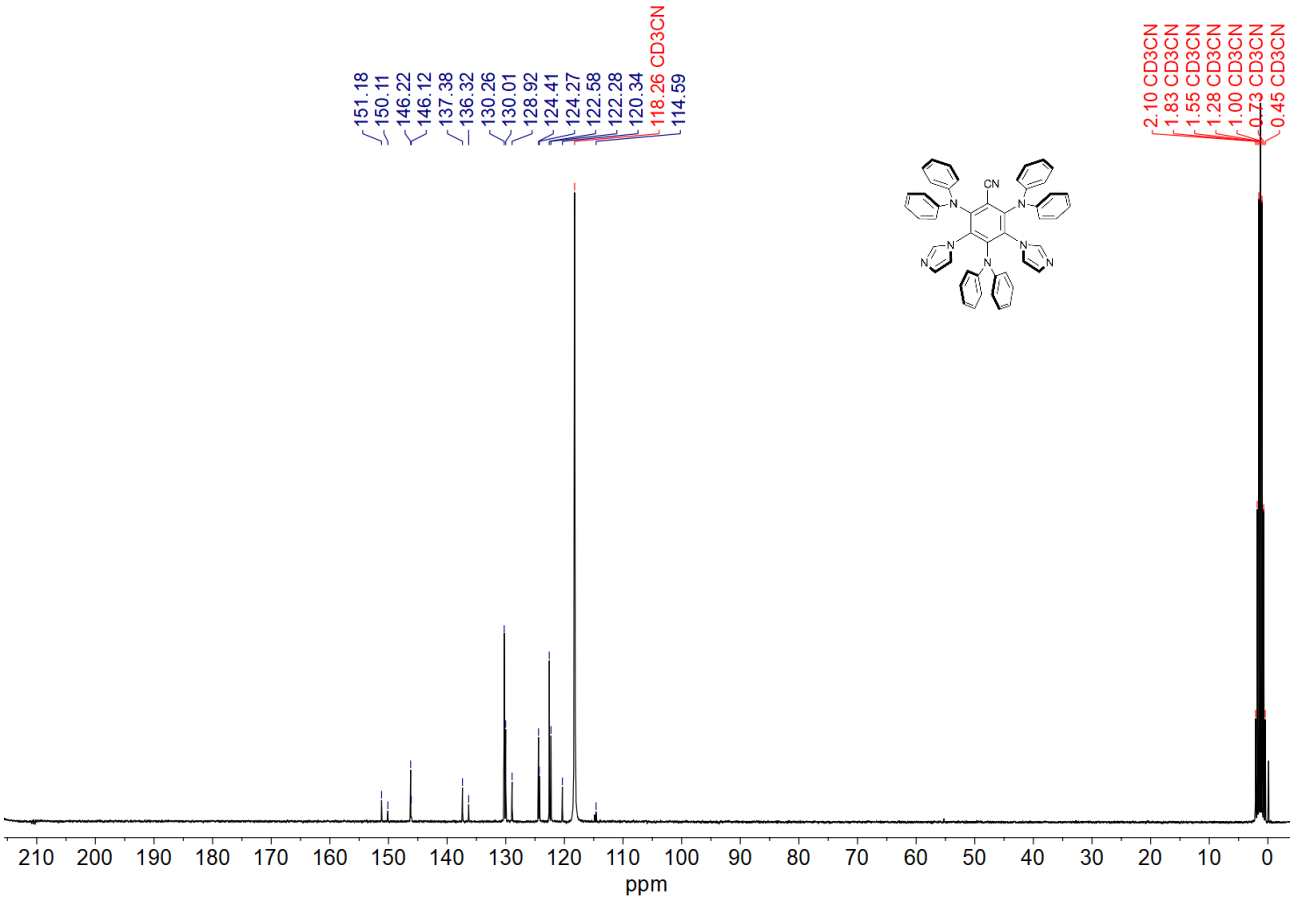


Figure A2.9: $^{13}C\{^{1}H\}$ NMR spectrum of **3DPA2ImBN** (CD_3CN).

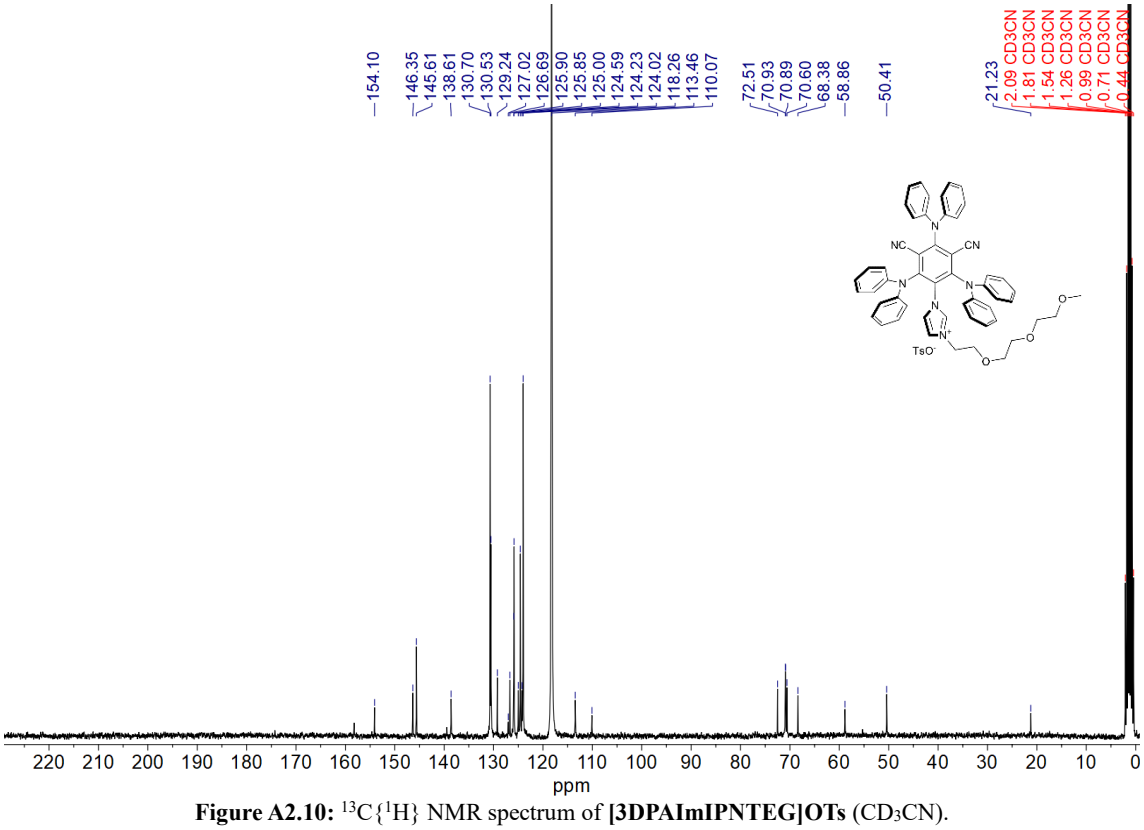


Figure A2.10: $^{13}C\{^{1}H\}$ NMR spectrum of **[3DPAImIPNTEG]OTs** (CD_3CN).

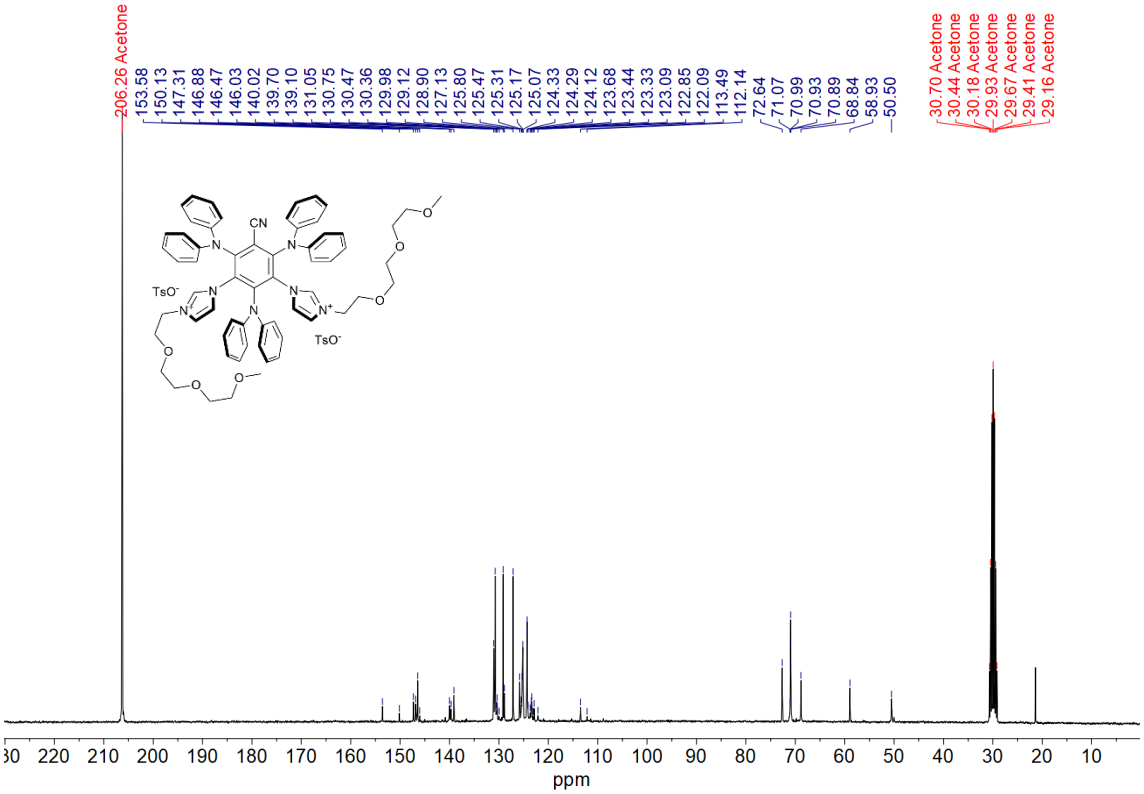


Figure A2.11: $^{13}C\{^{1}H\}$ NMR spectrum of **[3DPA2ImBN2TEG]2(OTs)** (Acetone-d_6).

2.4 Absorption-excitation spectra comparisons

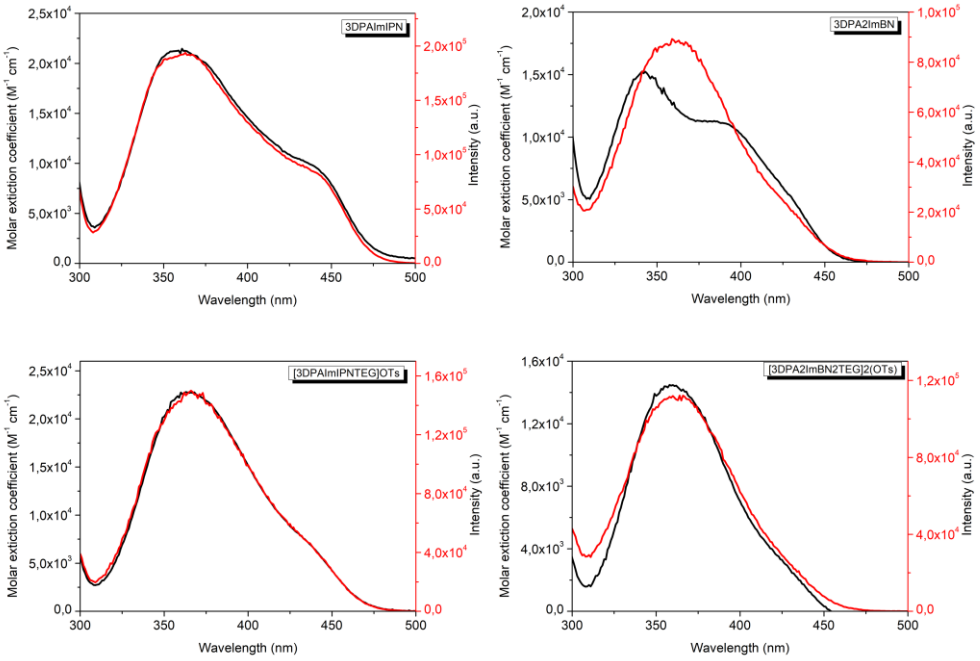


Figure A2.12: Comparison of absorption (black line) and excitation (red line) spectra of compounds in acetonitrile solution. The names of compounds are reported in the inset.

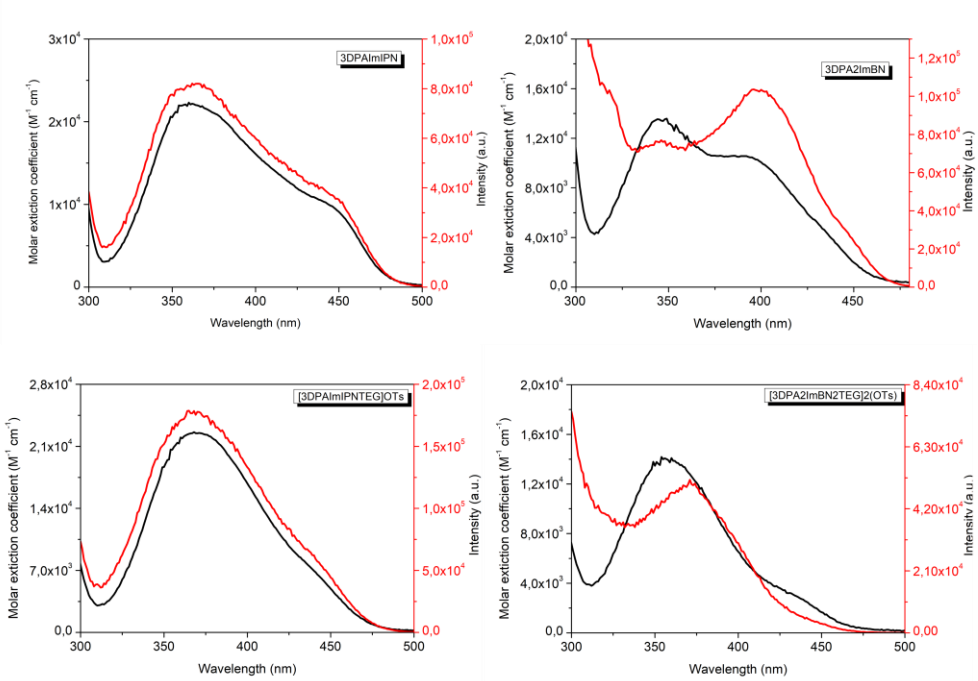


Figure A2.13: Comparison of absorption (black line) and excitation (red line) spectra in dichloromethane solution. The names of compounds are reported in the inset.

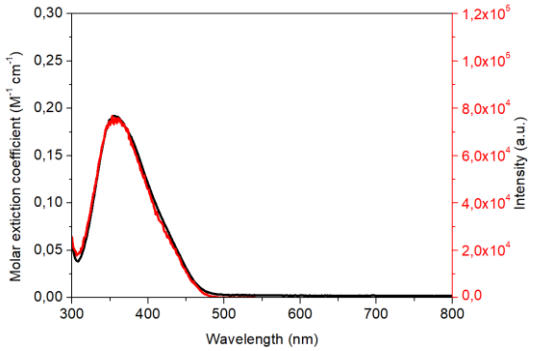
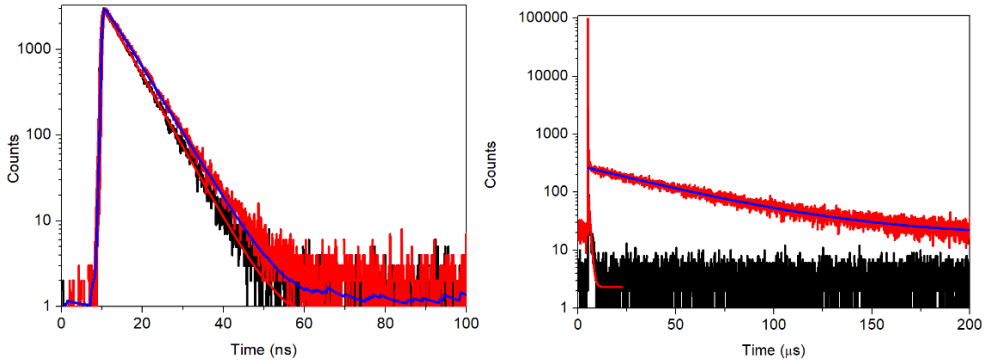


Figure A2.14: Comparison of absorption (black line) and excitation (red line) of **[3DPA2ImBN2TEG]2(OTs)** in water.

2.5 Luminescence decay curves



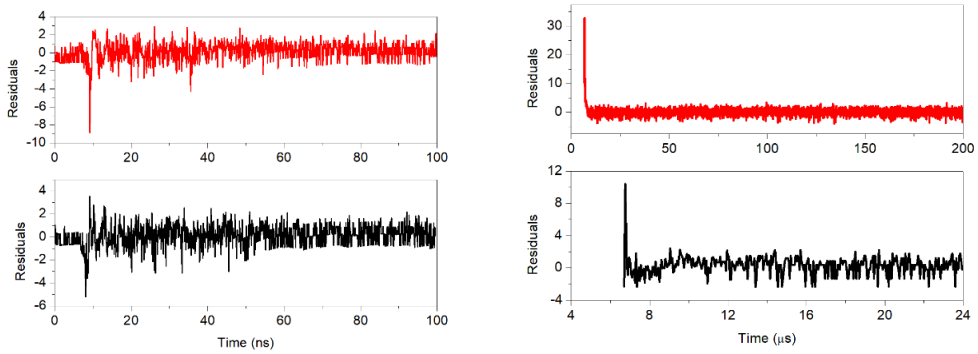


Figure A2.15: Luminescence decay curves of **3DPAImIPN** in aerated acetonitrile (black curves) and in Ar-purged acetonitrile solutions (red curves) with their fittings and residuals. Left: decays in the nanosecond scale; Right: decays in the microsecond scale.

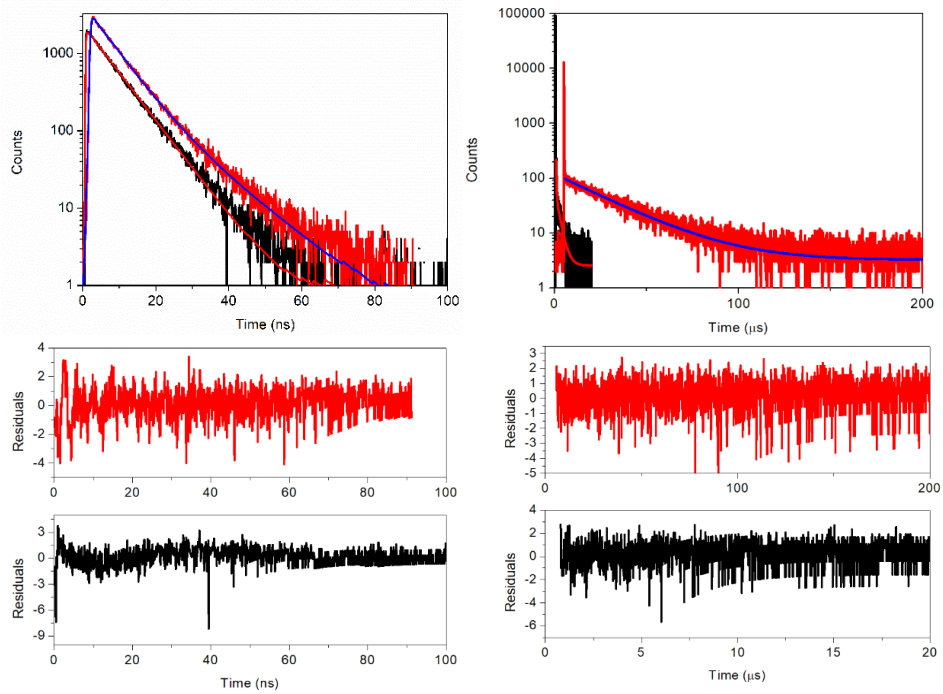
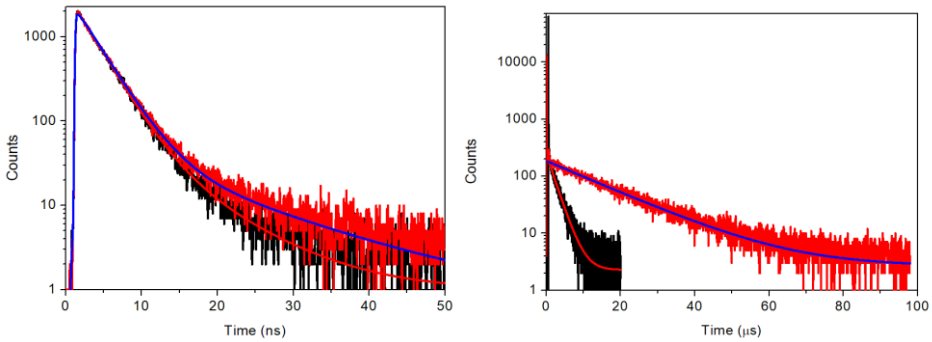


Figure A2.16: Luminescence decay curves of **3DPA2ImBN** in aerated acetonitrile (black curves) and in Ar-purged acetonitrile solutions (red curves) with their fittings and residuals. Left: decays in the nanosecond scale; Right: decays in the microsecond scale.



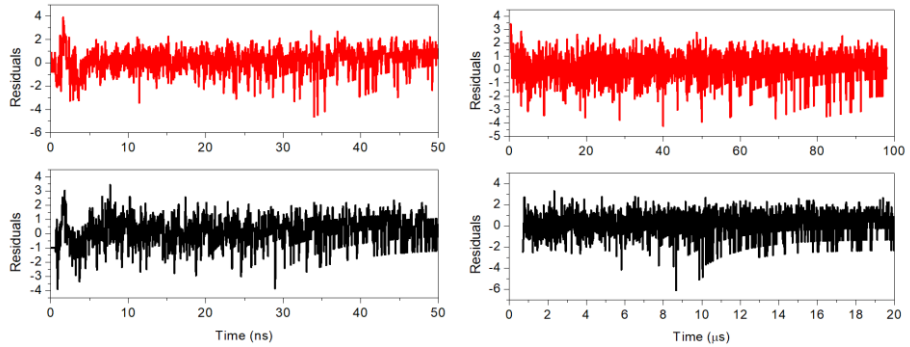


Figure A2.17: Luminescence decay curves of **[3DPAImIPNTEG]OTs** in aerated acetonitrile (black curves) and in Ar-purged acetonitrile solutions (red curves) with their fittings and residuals. Left: decays in the nanosecond scale; Right: decays in the microsecond scale.

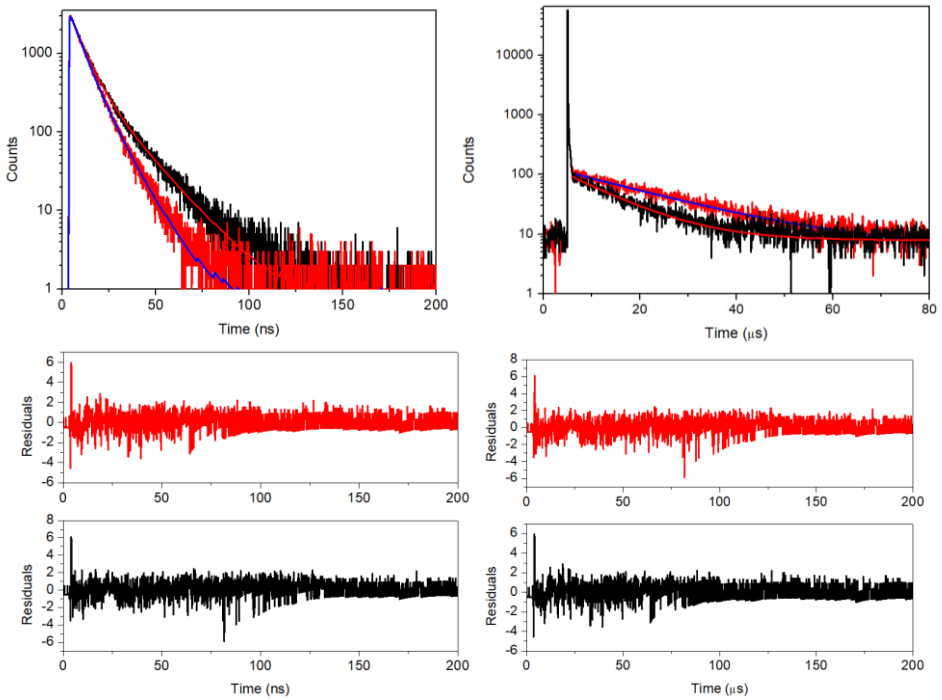
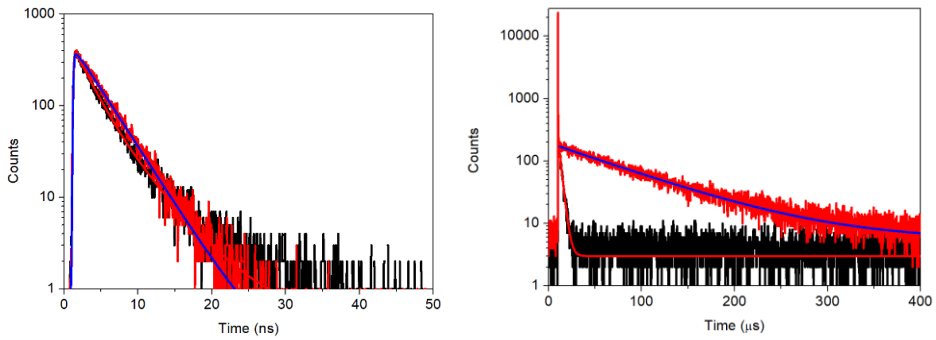


Figure A2.18: Luminescence decay curves of **[3DPA2ImBN2TEG]2(OTs)** in aerated acetonitrile (black curves) and in Ar-purged acetonitrile solutions (red curves) with their fittings and residuals. Left: decays in the nanosecond scale; Right: decays in the microsecond scale.



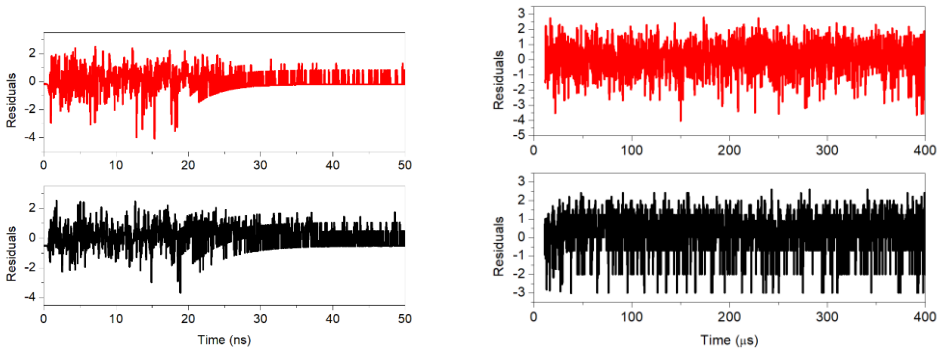


Figure A2.19: Luminescence decay curves of **3DPAImIPN** in aerated dichloromethane (black curves) and in Ar-purged dichloromethane solutions (red curves) with their fittings and residuals. Left: decays in the nanosecond scale; Right: decays in the microsecond scale.

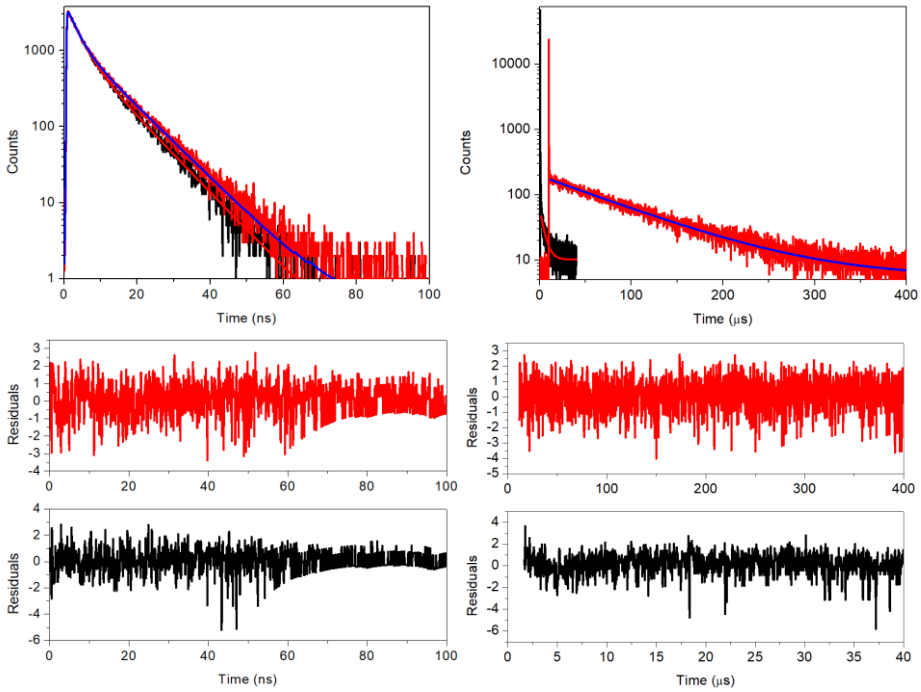
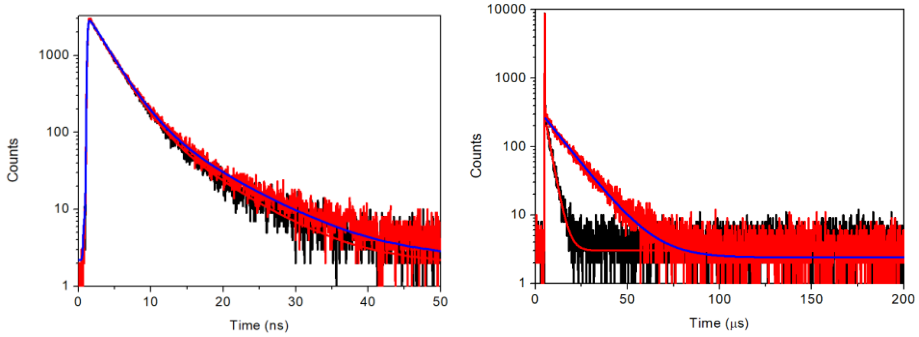


Figure A2.20: Luminescence decay curves of **3DPA2ImBN** in aerated dichloromethane (black curves) and in Ar-purged dichloromethane solutions (red curves) with their fittings and residuals. Left: decays in the nanosecond scale; Right: decays in the microsecond scale.



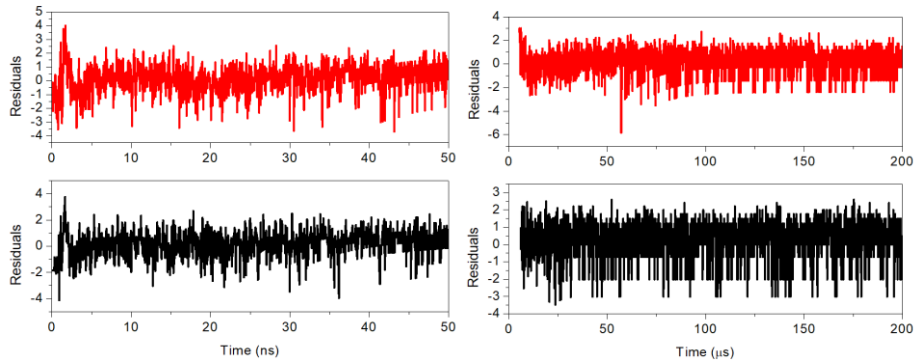


Figure A2.21: Luminescence decay curves of **[3DPAImIPNTEG]OTs** in aerated dichloromethane (black curves) and in Ar-purged dichloromethane solutions (red curves) with their fittings and residuals. Left: decays in the nanosecond scale; Right: decays in the microsecond scale.

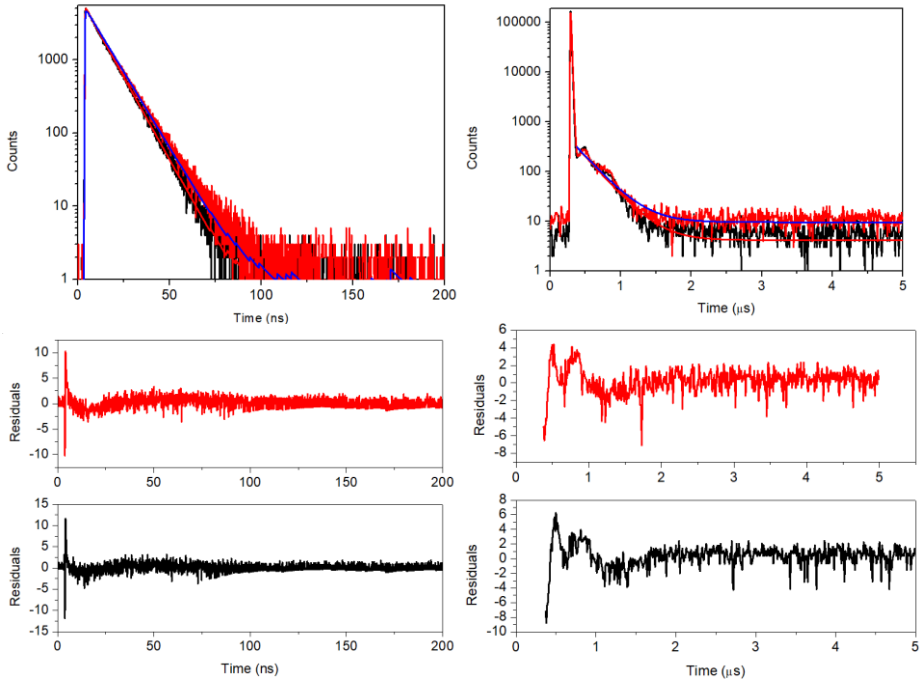
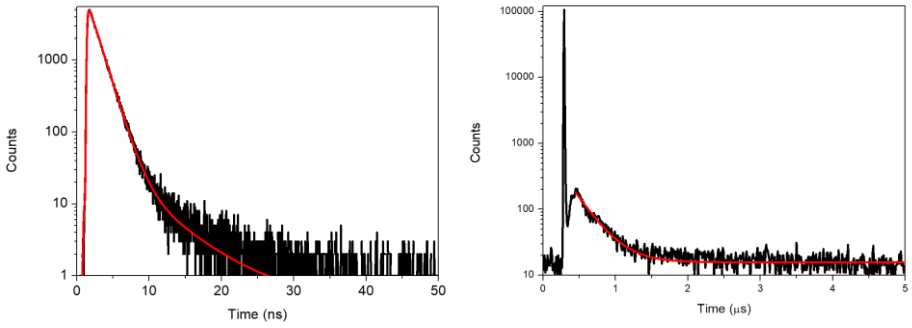


Figure A2.22: Luminescence decay curves of **[3DPA2ImBN2TEG]2(OTs)** in aerated dichloromethane (black curves) and in Ar-purged dichloromethane solutions (red curves) with their fittings and residuals. Left: decays in the nanosecond scale; Right: decays in the microsecond scale.



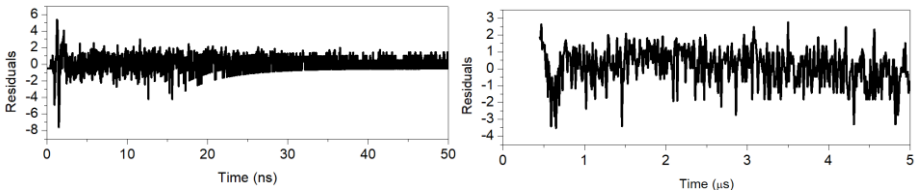


Figure A2.23: Luminescence decay curve of **[3DPA2ImBN2TEG]2(OTs)** in aerated water with fittings and residuals. Left: decays in the nanosecond scale; Right: decays in the microsecond scale.

2.6 Annihilation ECL-time and current-time profiles

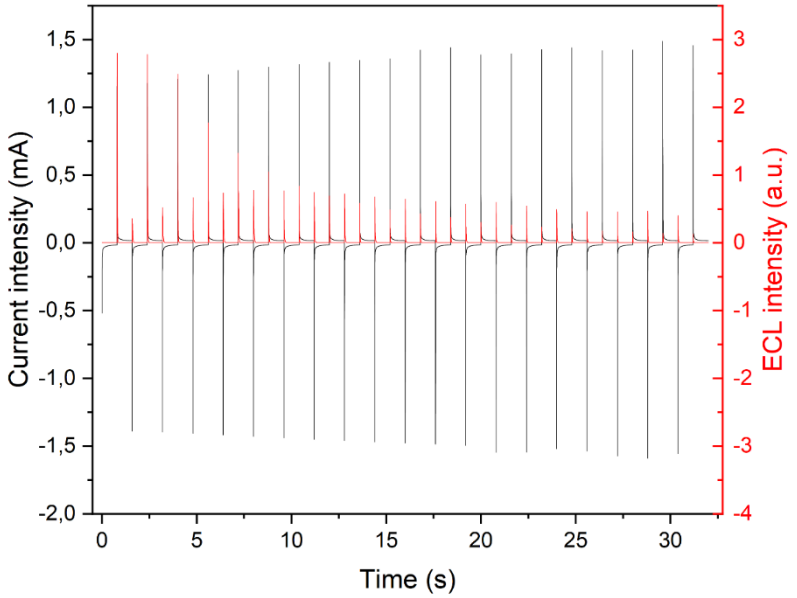


Figure A2.24: Annihilation ECL-time (red curve) and current-time (black curve) of **3DPAFIPN** in acetonitrile.

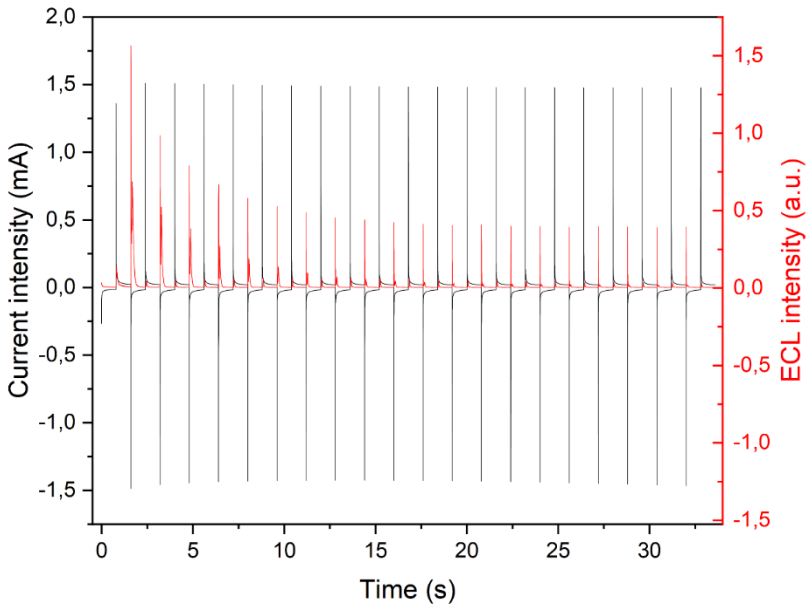


Figure A2.25: Annihilation ECL-time (red curve) and current-time (black curve) of **3DPA2FBN** in acetonitrile.

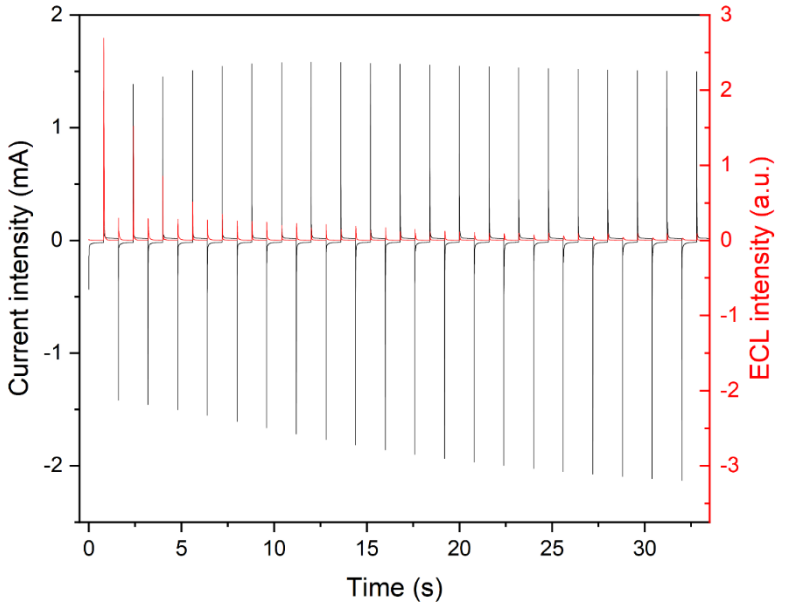


Figure A2.26: Annihilation ECL-time (red curve) and current-time (black curve) of **3DPAImIPN** in acetonitrile.

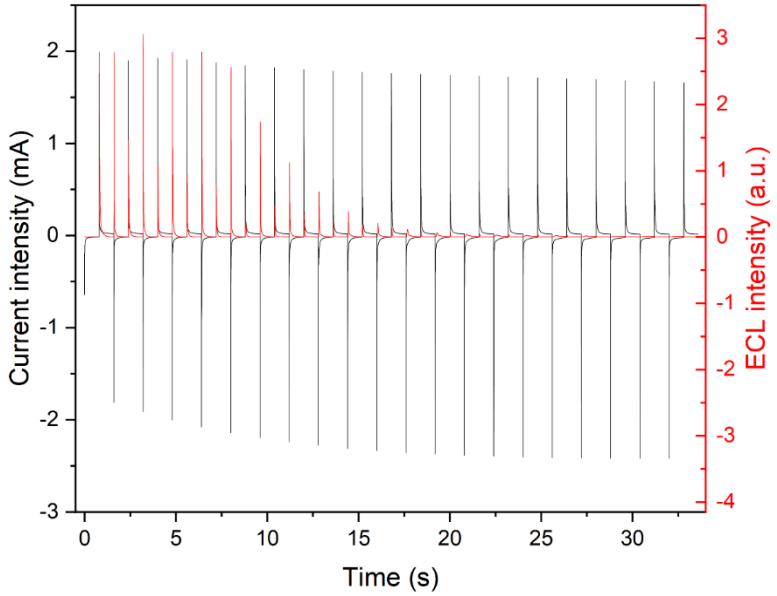


Figure A2.27: Annihilation ECL-time (red curve) and current-time (black curve) of **3DPA2ImBN** in acetonitrile.

Chapter 3

3.1 XRD analysis – Structural characterization

Table A3.1. Crystallographic data and refinement details.

	4CzBNIm	**4DPABNIm**	**4DPABNIm**
CCDC Number	2242629	2242630	2242631
Chemical Formula	$C_{58}H_{35}N_7 \cdot 4C_3H_7NO$	$C_{58}H_{43}N_7 \cdot 2CHCl_3$	$C_{58}H_{43}N_7 \cdot 2CHCl_3$
Formula weight	1122.31 g/mol	1076.73 g/mol	1076.73 g/mol
Temperature	100(2) K	100(2) K	298(2) K
Wavelength	0.620 Å	0.620 Å	0.620 Å
Crystal system	Triclinic	Monoclinic	Monoclinic
Space Group	*P* -1	*P* $2_1/n$	*P* $2_1/n$
Unit cell dimensions	*a* = 11.095(2) Å *b* = 15.143(3) Å *c* = 18.412(4) Å *α* = 98.19(3)° *β* = 92.72(3)° γ = 107.55(3)°	*a* = 12.449(2) Å *b* = 11.579(2) Å *c* = 38.635(8) Å *α* = 90° *β* = 98.61(3)° γ = 90°	*a* = 12.584(3) Å *b* = 11.805(2) Å *c* = 38.951(8) Å *α* = 90° *β* = 98.29(3)° γ = 90°
Volume	2905.8(11) $Å^3$	5506(2) $Å^3$	5726(2) $Å^3$
Z	2	4	4
Density (calculated)	1.283 $g \cdot cm^{-3}$	1.299 $g \cdot cm^{-3}$	1.249 $g \cdot cm^{-3}$
Absorption coefficient	0.062 mm^{-1}	0.244 mm^{-1}	0.234 mm^{-1}
F(000)	1184	2224	2224
Theta range for data collection	1.0° to 31.1°	1.4° to 31.1°	0.9° to 28.0°
Index ranges	$-18 \le h \le 18$, $-25 \le k \le 25$, $-28 \le l \le 28$	$-20 \le h \le 20$, $-19 \le k \le 19$, $-63 \le l \le 63$	$-19 \le h \le 19$, $-17 \le k \le 17$, $-59 \le l \le 59$
Resolution	0.60 Å	0.60 Å	0.66 Å
Reflections collected	129282	126720	120534
Independent reflections	24356, 18925 data with I>2σ(I)	24021, 19264 data with I>2 σ (I)	20741, 12806 data with I>2 σ (I)
Data multiplicity (max resltn)	4.57 (2.73)	4.69 (2.80)	5.69 (4.93)
I/□(I) (max resltn)	234.20 (41.69)	19.08 (6.16)	14.05 (2.17)
R_{merge} (max resltn)	0.1015 (0.3211)	0.0357 (0.1222)	0.0337 (0.3965)
Data completeness (max resltn)	86.2% (67.9%)	90.2% (73.8%)	99.7% (99.7%)
Refinement method	Full-matrix least-squares on F^2	Full-matrix least-squares on F^2	Full-matrix least-squares on F^2
Data / restraints / parameters	24356 / 18 / 797	24021 / 12 / 694	20741 / 45 / 694
Goodness-of-fit on F^2	1.039	1.044	1.043
Δ/σ_{max}	0.001	0.010	0.001
Final R indices [I>2□(I)]	R_1 = 0.0553, wR_2 = 0.1453	R_1 = 0.0728, wR_2 = 0.2272	R_1 = 0.0873, wR_2 = 0.1643
R indices (all data)	R_1 = 0.0747, wR_2 = 0.1574	R_1 = 0.0834, wR_2 = 0.2382	R_1 = 0.1153, wR_2 = 0.1743
Largest diff. peak and hole	0.485 and -0.448 $eÅ^{-3}$	1.470 and -0.907 $eÅ^{-3}$	0.863 and -0.448 $eÅ^{-3}$
R.M.S. deviation from mean	0.066 $eÅ^{-3}$	0.083 $eÅ^{-3}$	0.051 $eÅ^{-3}$

$$R_1 = \Sigma \, ||Fo|-|Fc|| \, / \, \Sigma \, |Fo|, \; wR_2 = \{\Sigma \, [w(Fo^2 - Fc^2)^2] \, / \, \Sigma \, [w(Fo^2)^2]\}^{1/2}$$

Table A3.1 (continued). Crystallographic data and refinement details.

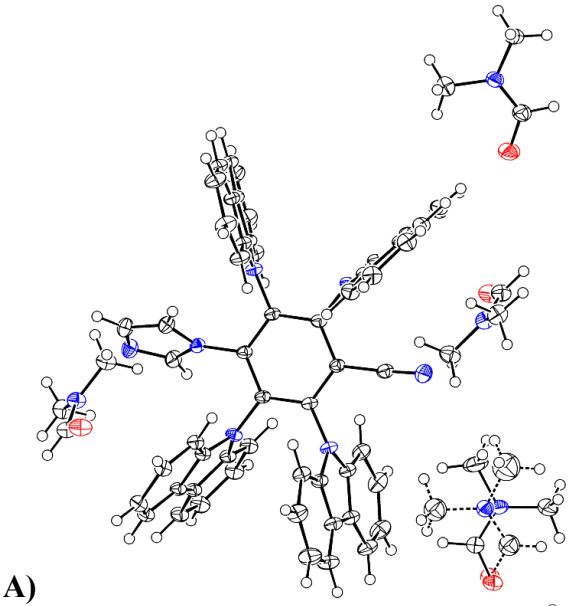
	4^{tBu}CzBNIm	**4^{tBu}CzBNIm**	**4^{tBu}CzBNIm**
CCDC Number	2242632	2242633	2242634
Chemical Formula	$C_{90}H_{99}N_7 \cdot 2CHCl_3$	$C_{90}H_{99}N_7 \cdot {}^3/_2CHCl_3$	$C_{90}H_{99}N_7 \cdot 2CHCl_3$
Formula weight	1517.49g/mol	1457.81 g/mol	1517.49g/mol
Temperature	100(2) K	298(2) K	298(2) K
Wavelength	0.620 Å	0.620 Å	0.620 Å
Crystal system	Triclinic	Triclinic	Triclinic
Space Group	*P* -1	*P* -1	*P* -1
Unit cell dimensions	*a* = 12.304(2) Å *b* = 18.369(4) Å *c* = 20.171(4) Å *α* = 106.24(3)° *β* = 90.17(3)° γ = 96.69(3)°	*a* = 12.487(3) Å *b* = 18.531(4) Å *c* = 20.244(4) Å *α* = 105.78(3)° *β* = 90.14(3)° γ = 97.17(3)°	*a* = 12.439(2) Å *b* = 18.484(4) Å *c* = 28.745(6) Å *α* = 88.79(3)° *β* = 81.24(3)° γ = 81.88(3)°
Volume	4344.6(17) Å^3	4469.3(17) Å^3	6467(2) Å^3
Z	2	2	3
Density (calculated)	1.160 g·cm^{-3}	1.083 g·cm^{-3}	1.169 g·cm^{-3}
Absorption coefficient	0.169 mm^{-1}	0.134 mm^{-1}	0.170 mm^{-1}
F(000)	1608	1550	2412
Theta range for data collection	0.9° to 27.2°	0.9° to 25.6°	1.0° to 24.8°
Index ranges	-18 ≤ h ≤ 18, -27 ≤ k ≤ 27, -29 ≤ l ≤ 29	-17 ≤ h ≤ 17, -25 ≤ k ≤ 25, -28 ≤ l ≤ 28	-16 ≤ h ≤ 16, -24 ≤ k ≤ 24, -38 ≤ l ≤ 38
Resolution	0.68 Å	0.78 Å	0.74 Å
Reflections collected	125012	98355	138277
Independent reflections	28713, 20816 data with I>2 σ (I)	24443, 16297 data with I>2 σ (I)	32712, 21184 data with I>2 σ (I)
Data multiplicity (max resltn)	4.32 (3.83)	3.81 (3.43)	4.14 (4.17)
I/□(I) (max resltn)	10.17 (3.94)	9.60 (2.64)	6.69 (2.12)
R_{merge} (max resltn)	0.0896 (0.2269)	0.1004 (0.3462)	0.0618 (0.3972)
Data completeness (max resltn)	99.4% (98.9%)	96.5% (92.9%)	98.1% (97.4%)
Refinement method	Full-matrix least-squares on F^2	Full-matrix least-squares on F^2	Full-matrix least-squares on F^2
Data / restraints / parameters	28713 / 150 / 1104	24443 / 102 / 1121	32712 / 363 / 1662
Goodness-of-fit on F^2	1.048	1.041	1.092
Δ/σ_{max}	0.002	0.006	0.004
Final R indices [I>2□(I)]	R_1 = 0.1233, wR_2 = 0.2545	R_1 = 0.1150, wR_2 = 0.2329	R_1 = 0.1115, wR_2 = 0.2284
R indices (all data)	R_1 = 0.1466, wR_2 = 0.2661	R_1 = 0.1426, wR_2 = 0.2467	R_1 = 0.1472, wR_2 = 0.2461
Largest diff. peak and hole	1.642 and -0.787 eÅ^{-3}	0.503 and -0.303 eÅ^{-3}	0.861 and -0.800 eÅ^{-3}
R.M.S. deviation from mean	0.097 eÅ^{-3}	0.062 eÅ^{-3}	0.068 eÅ^{-3}

$R_1 = \Sigma \, ||Fo|-|Fc|| \, / \, \Sigma \, |Fo|$, $wR_2 = \{\Sigma \, [w(Fo^2 - Fc^2)^2] \, / \, \Sigma \, [w(Fo^2)^2]\}^{½}$

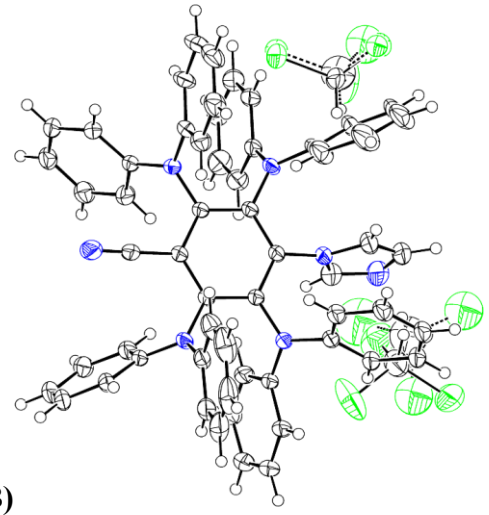
Table A3.1 (continued). Crystallographic data and refinement details.

	4^{OMe}CzBNIm	**4DMACBNIm**	**4DMACBNIm**
CCDC Number	2242635	2242636	2242637
Chemical Formula	$C_{66}H_{51}N_7O_8 \cdot CHCl_3 \cdot 2H_2O$	$C_{70}H_{59}N_7 \cdot {}^5/_{12}CH_2Cl_2$	$C_{70}H_{59}N_7 \cdot {}^5/_{12}CH_2Cl_2$
Formula weight	1225.53 g/mol	1033.62 g/mol	1033.62 g/mol
Temperature	100(2) K	100(2) K	298(2) K
Wavelength	0.620 Å	0.620 Å	0.620 Å
Crystal system	Triclinic	Cubic	Cubic
Space Group	*P* -1	*I m*-3	*I m*-3
Unit cell dimensions	*a* = 11.322(2) Å *b* = 14.907(3) Å *c* = 18.281(4) Å *α* = 94.58(3)° *β* = 91.02(3)° γ = 103.85(3)°	*a* = 20.242(2) Å *b* = 20.242(2) Å *c* = 20.242(2) Å *α* = 90° *β* = 90° γ = 90°	*a* = 20.464(2) Å *b* = 20.464(2) Å *c* = 20.464(2) Å *α* = 90° *β* = 90° γ = 90°
Volume	2984.0(11) Å^3	8294(3) Å^3	8570(3) Å^3
Z	2	6	6
Density (calculated)	1.364 g·cm^{-3}	1.242 g·cm^{-3}	1.202 g·cm^{-3}
Absorption coefficient	0.154 mm^{-1}	0.082 mm^{-1}	0.079 mm^{-1}
F(000)	1276	3273	3273
Theta range for data collection	1.0° to 31.1°	1.2° to 29.0°	1.2° to 27.1°
Index ranges	-18 ≤ h ≤ 18, -24 ≤ k ≤ 24, -30 ≤ l ≤ 30	-22 ≤ h ≤ 21, -21 ≤ k ≤ 22, -31 ≤ l ≤ 31	-19 ≤ h ≤ 19, -19 ≤ k ≤ 19, -27 ≤ l ≤ 27
Resolution	0.60 Å	0.64 Å	0.74 Å
Reflections collected	136553	56886	23500
Independent reflections	24869, 15723 data with I>2 σ (I)	2955, 2404 data with I>2 σ (I)	1978, 1167 data with I>2 σ (I)
Data multiplicity (max resltn)	4.72 (2.79)	18.15 (15.88)	9.18 (8.57)
I/□(I) (max resltn)	4.47 (1.76)	15.63 (3.87)	8.12 (0.50)
R_{merge} (max resltn)	0.0954 (0.5482)	0.0764 (0.3868)	0.0777 (0.9698)
Data completeness (max resltn)	86.0% (67.8%)	100.0% (100.0%)	100.0% (100.0%)
Refinement method	Full-matrix least-squares on F^2	Full-matrix least-squares on F^2	Full-matrix least-squares on F^2
Data / restraints / parameters	24869 / 115 / 822	2955 / 96 / 204	1978 / 186 / 205
Goodness-of-fit on F^2	0.993	1.098	1.009
Δ/σ_{max}	0.013	0.002	0.008
Final R indices [I>2□(I)]	R_1 = 0.0996, wR_2 = 0.2576	R_1 = 0.1325, wR_2 = 0.2185	R_1 = 0.0998, wR_2 = 0.1842
R indices (all data)	R_1 = 0.1425, wR_2 = 0.2927	R_1 = 0.1447, wR_2 = 0.2224	R_1 = 0.1306, wR_2 = 0.1961
Largest diff. peak and hole	0.968 and -1.211 eÅ^{-3}	0.483 and -0.394 eÅ^{-3}	0.289 and -0.199 eÅ^{-3}
R.M.S. deviation from mean	0.088 eÅ^{-3}	0.064 eÅ^{-3}	0.042 eÅ^{-3}

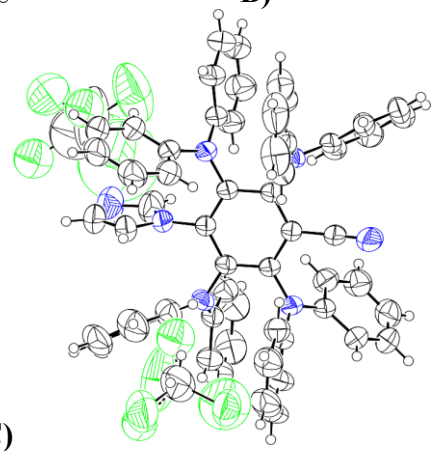
$$R_1 = \Sigma \, ||Fo|-|Fc|| \, / \, \Sigma \, |Fo|, \; wR_2 = \{\Sigma \, [w(Fo^2 - Fc^2)^2] \, / \, \Sigma \, [w(Fo^2)^2]\}^{1/2}$$



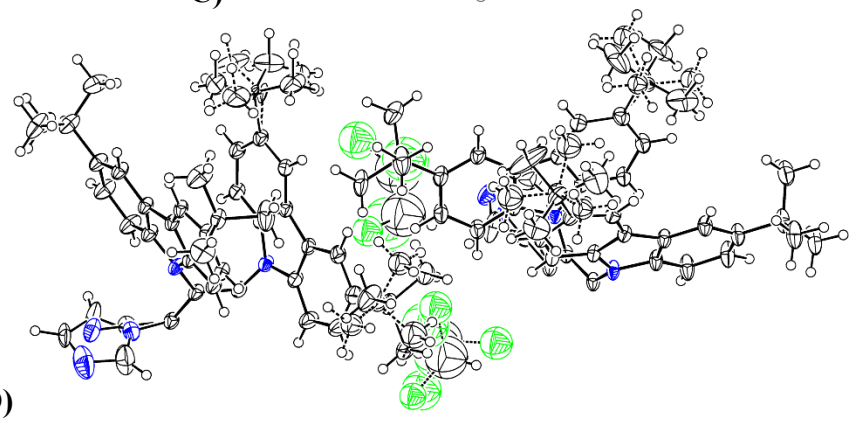
A)



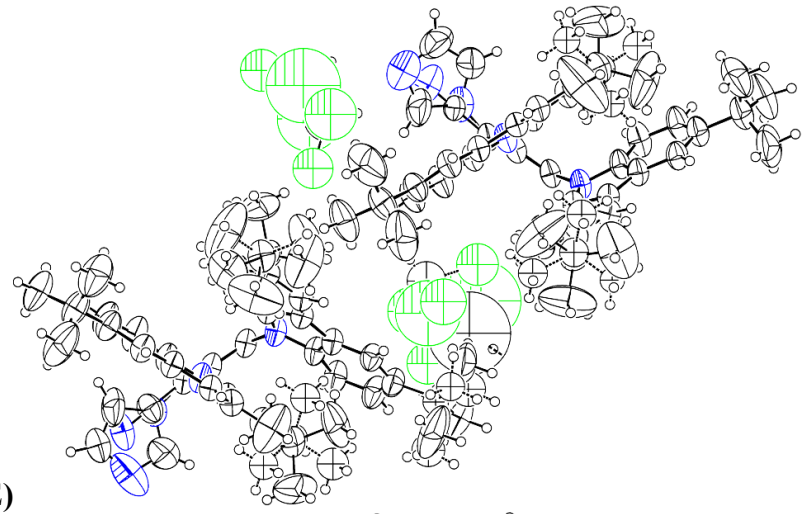
B)



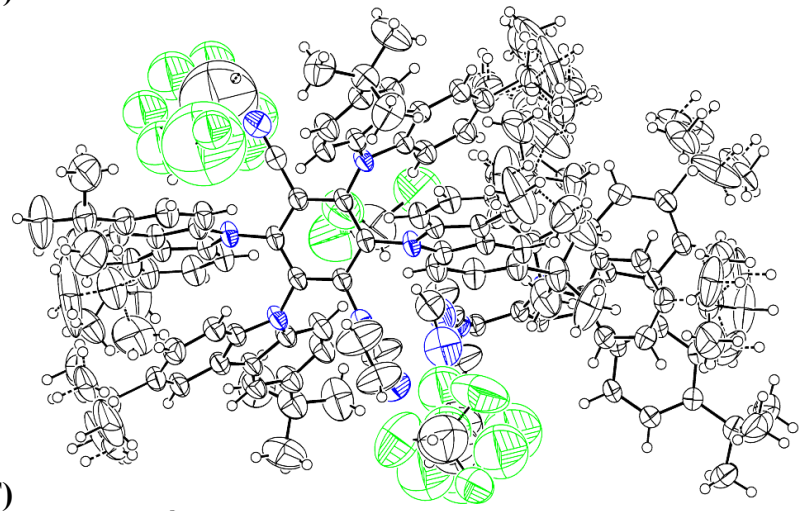
C)



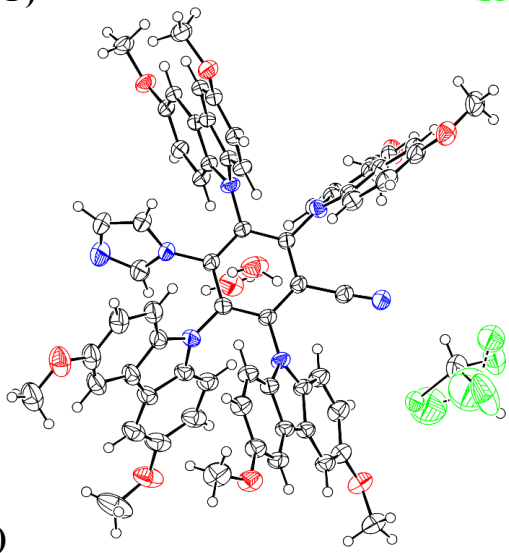
D)



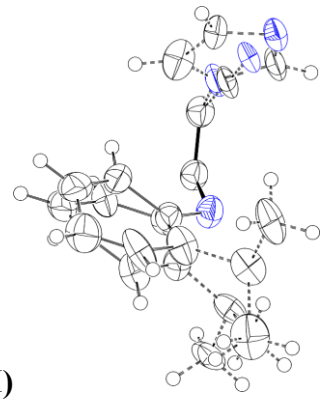
E)



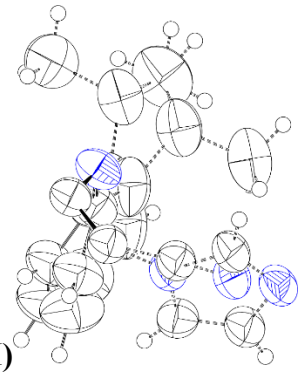
F)



G)



H)



I)

Figure A3.1: Ellipsoids representation of **4CzBNIm** at 100 K (A), **4DPABNIm** at 100 K (B), **4DPABNIm** at 298 K (C), **4^{tBu}CzBNIm** polymorph a at 100 K (D), **4^{tBu}CzBNIm** polymorph a at 298 K (E), **4^{tBu}CzBNIm** polymorph b at 298 K (F), **4^{OMe}CzBNIm** at 100 K (G), **4DMACNBIm** at 100 K (H) and **4DMACNBIm** at 298 K (I) asymmetric unit contents (A.S.U. - 50% probability).

3.2 ^{1}H NMR and ^{19}F{^{1}H} Spectra

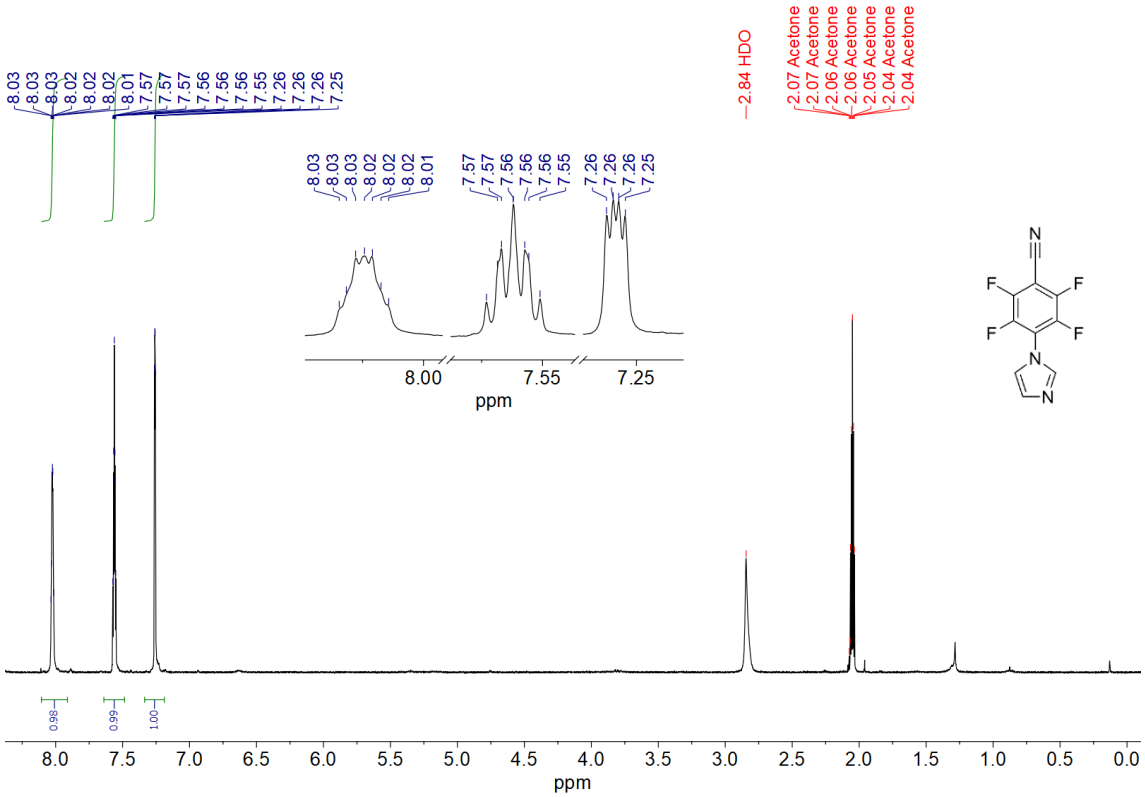


Figure A3.2: ^{1}H NMR spectrum of **4FBNIm** (Acetone-d_6).

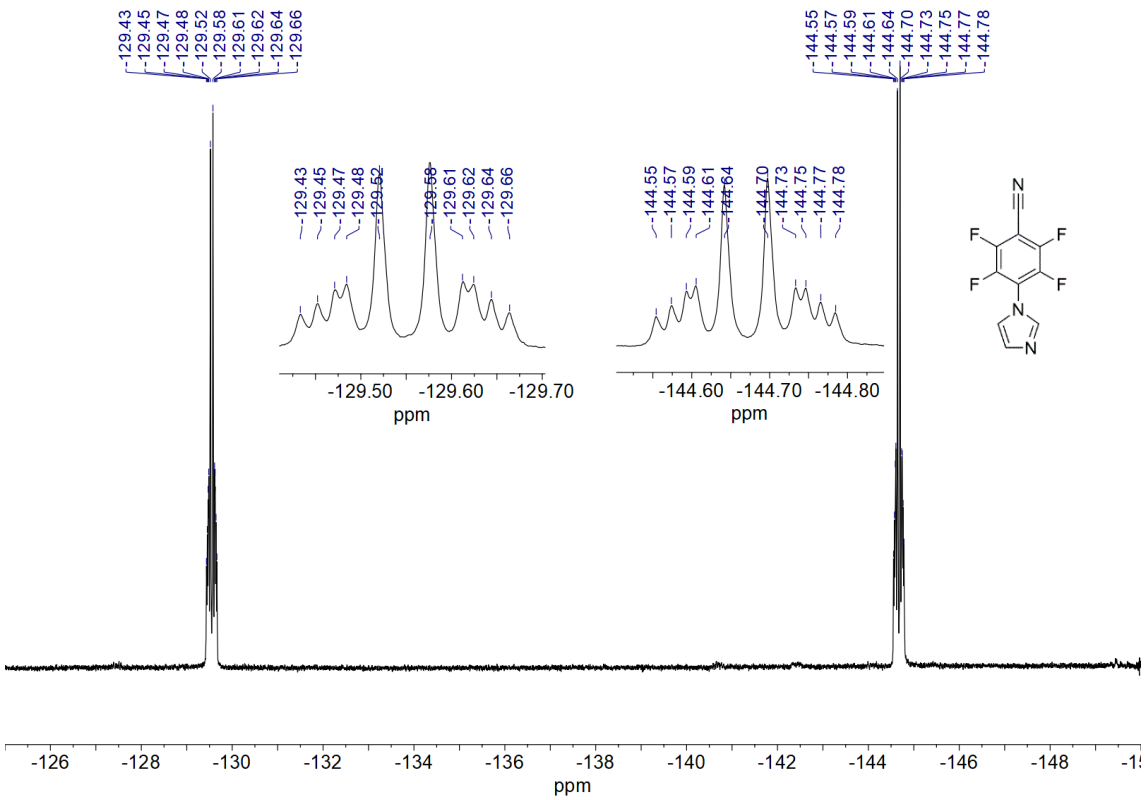


Figure A3.3: $^{19}F\{^{1}H\}$ NMR spectrum of **4FBNIm** ($CDCl_3$).

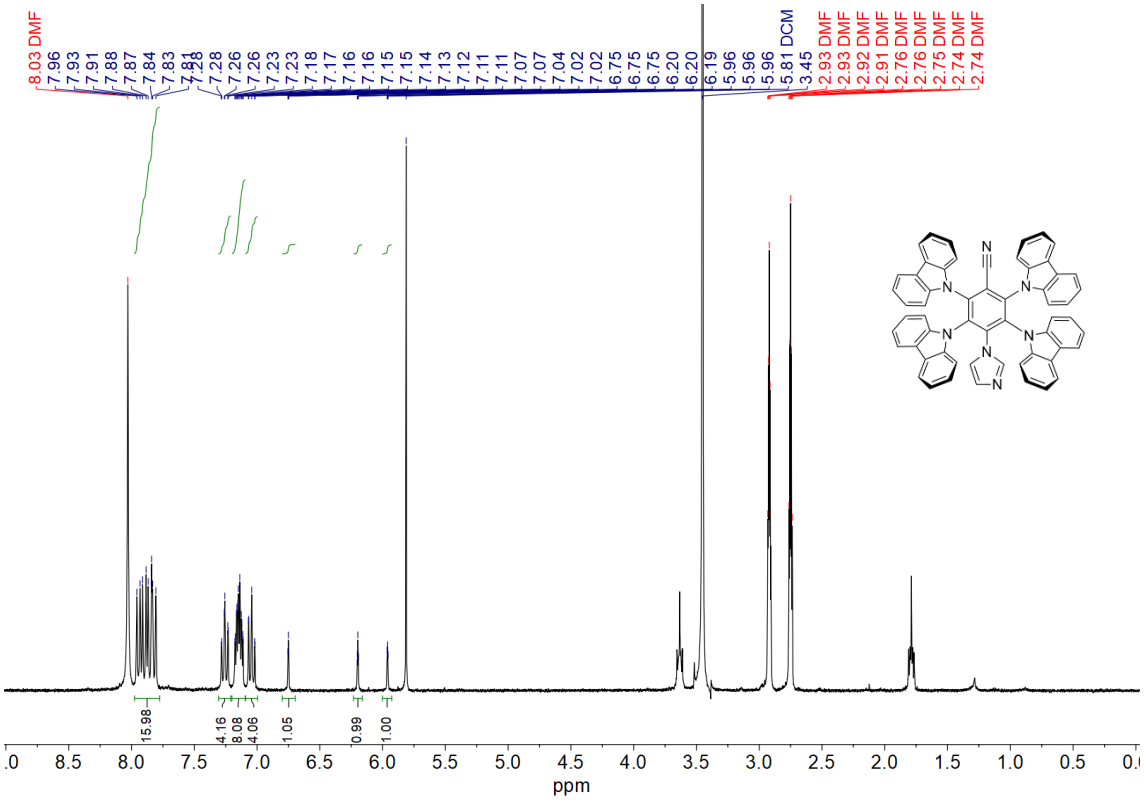


Figure A3.4: ^{1}H NMR spectrum of **4CzBNIm** ($DMF\text{-}d_7$).

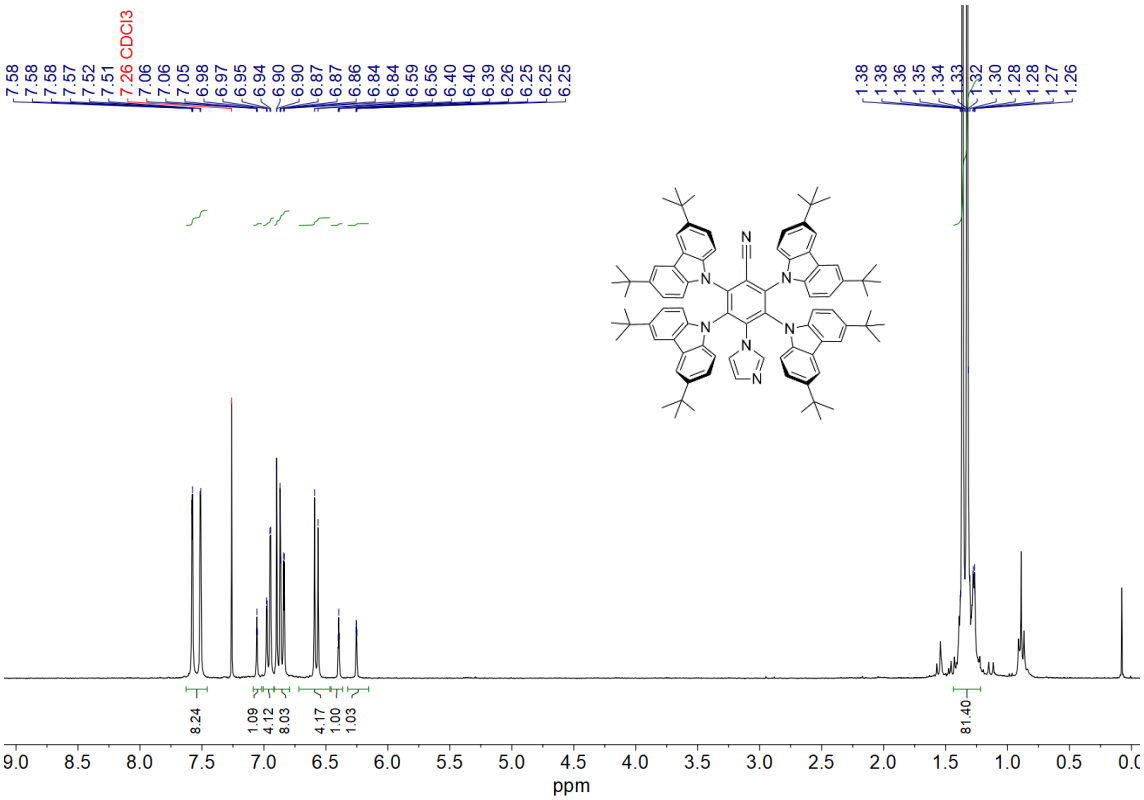


Figure A3.5: ^{1}H NMR spectrum of **4^{tBu}CzBNIm** ($CDCl_3$).

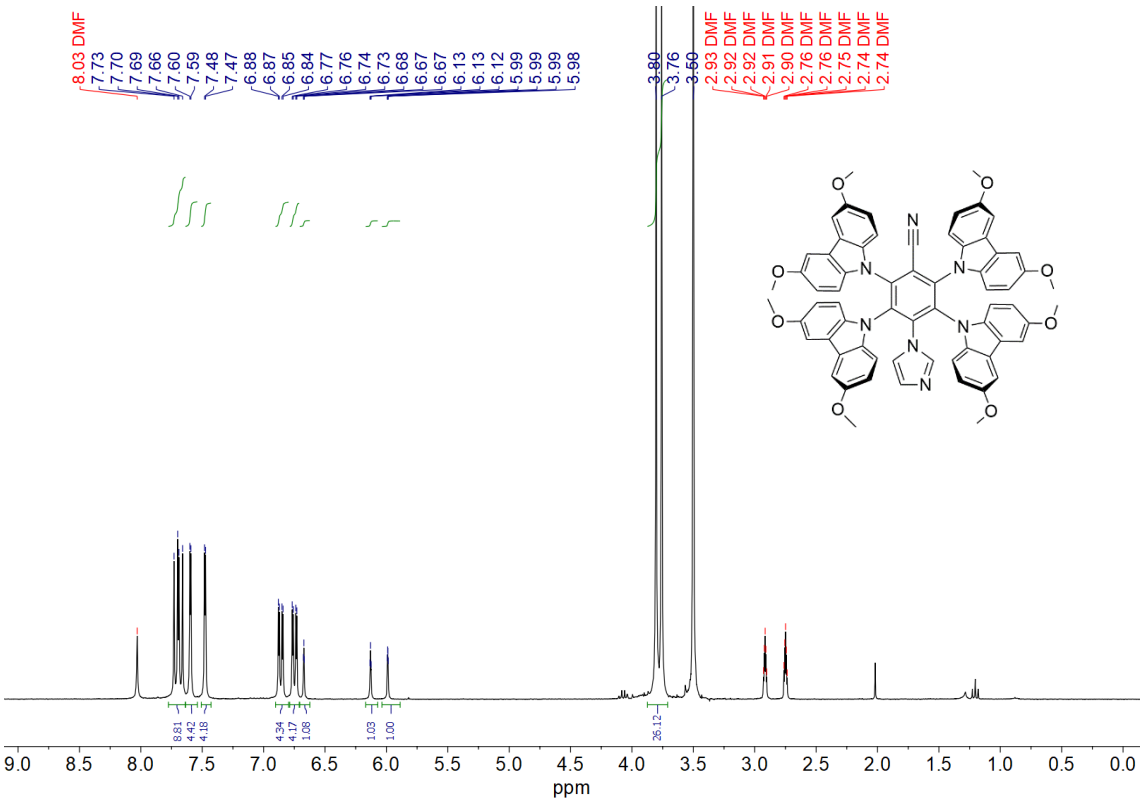


Figure A3.6: ^{1}H NMR spectrum of **4^{OMe}CzBNIm** (DMF-d_7).

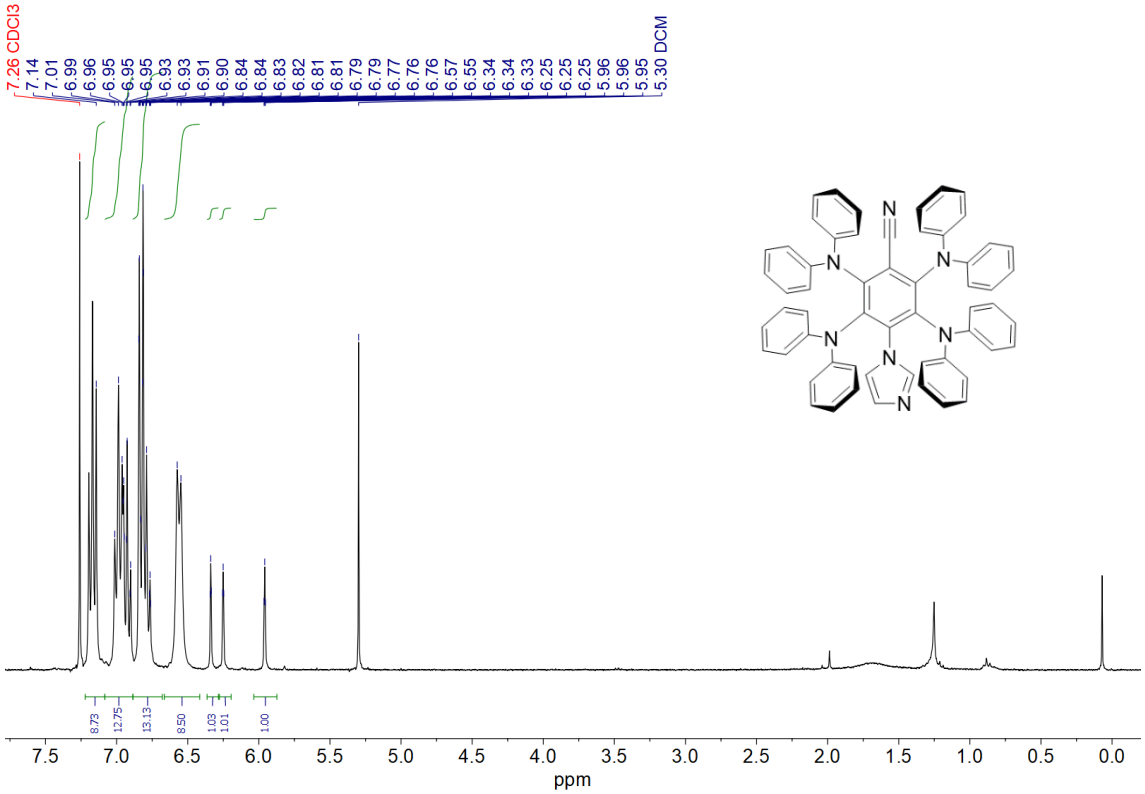


Figure A3.7: ^{1}H NMR spectrum of **4DPABNIm** ($CDCl_3$).

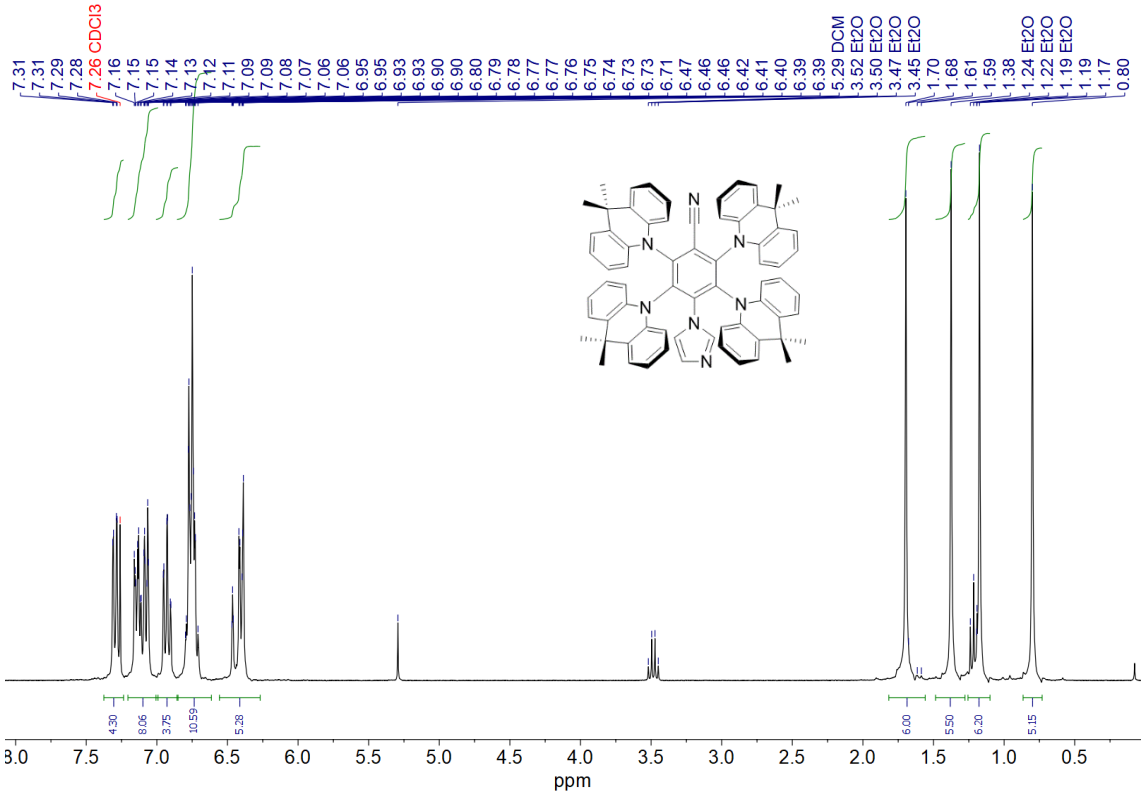


Figure A3.8: ^{1}H NMR spectrum of **4DMACBNIm** ($CDCl_3$).

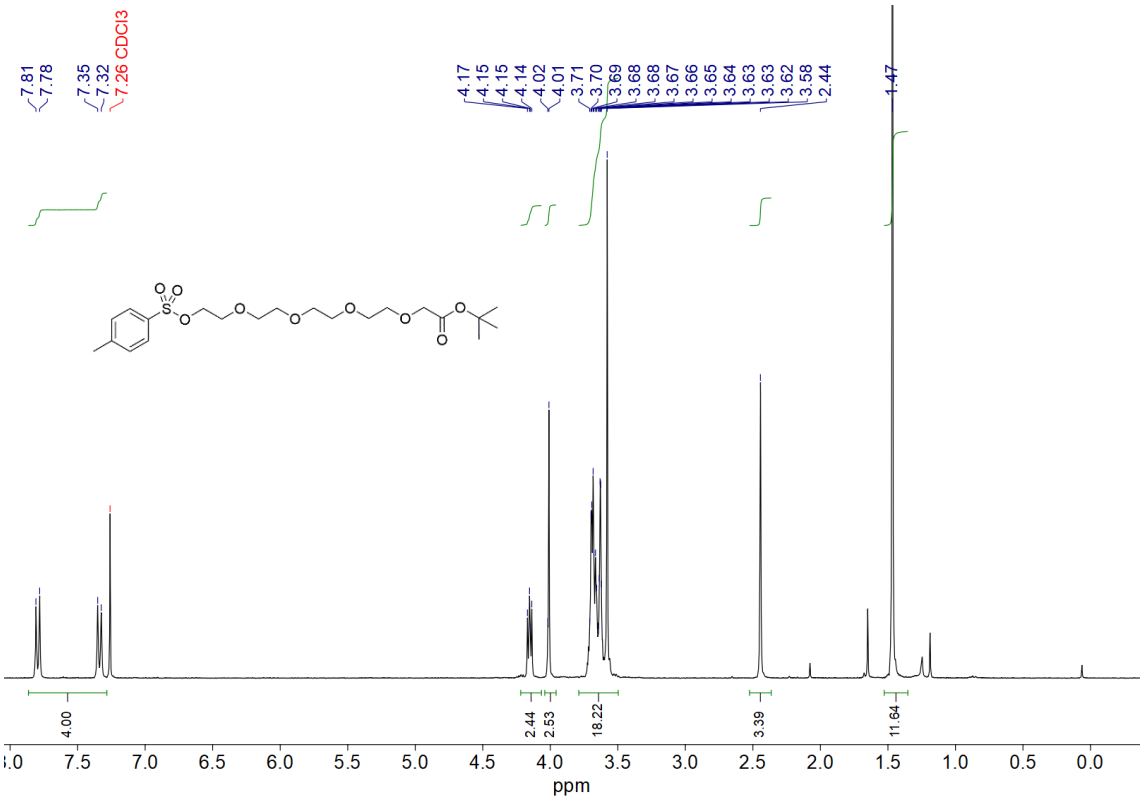


Figure A3.9: ^{1}H NMR spectrum of *tert*-butyl 14-(tosyloxy)-3,6,9,12-tetraoxatetradecanoate ($CDCl_3$).

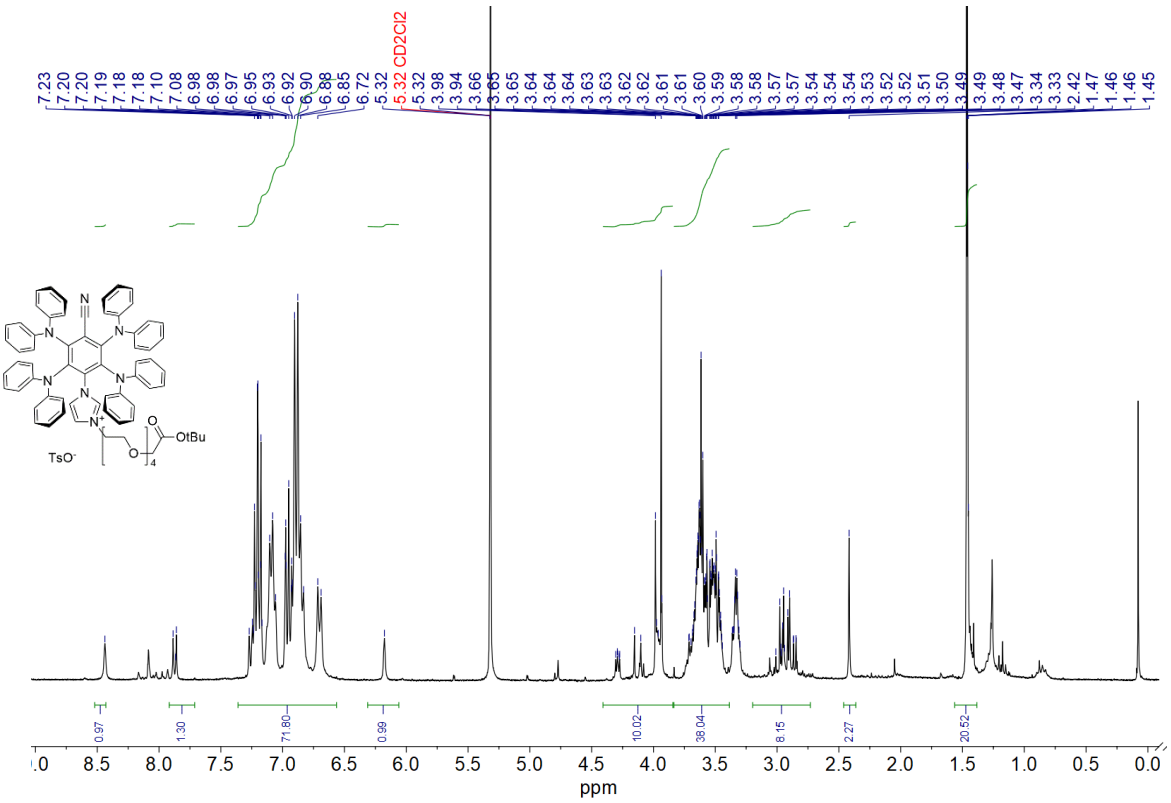


Figure A3.10: ^{1}H NMR spectrum of **[4DPABNImTEGCOOtBu]OTs** (CD_2Cl_2).

3.3 $^{13}C\{^{1}H\}$ NMR Spectra

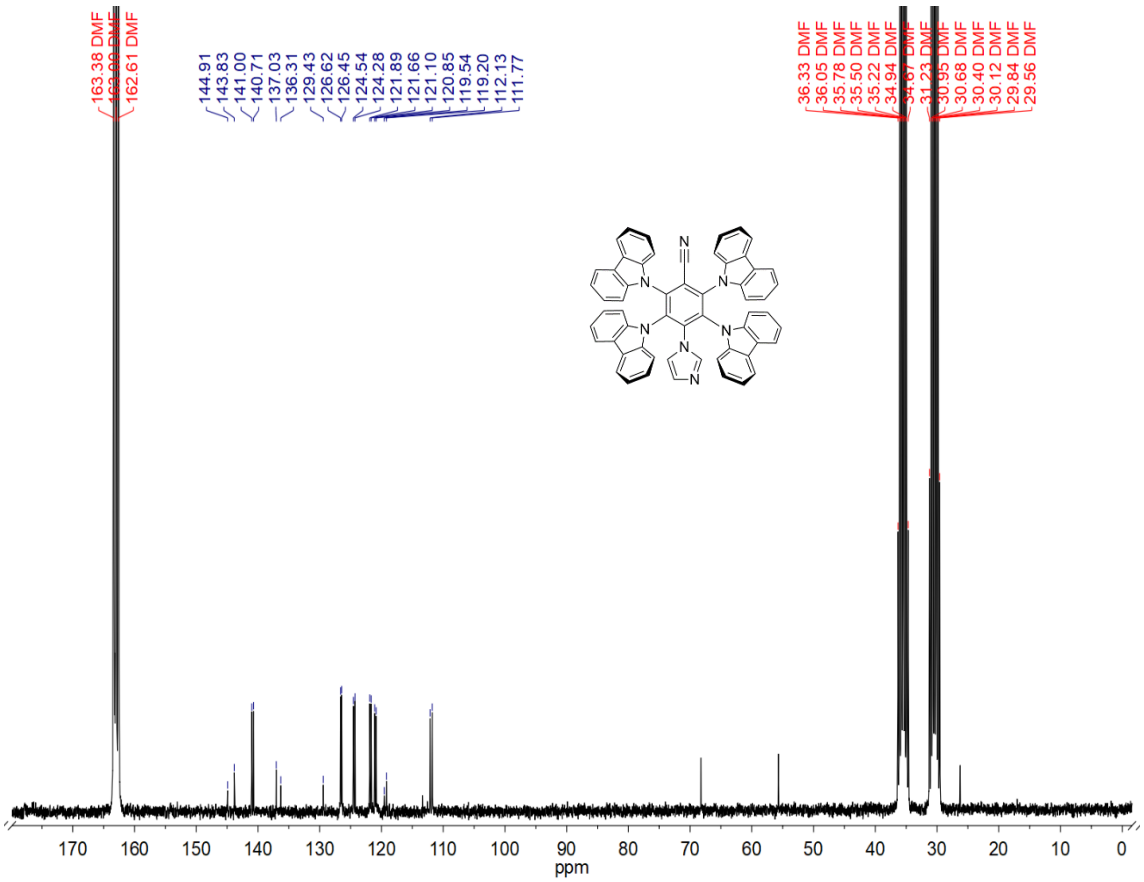


Figure A3.11: $^{13}C\{^{1}H\}$ NMR spectrum of **4CzBNIm** (DMF-d_7).

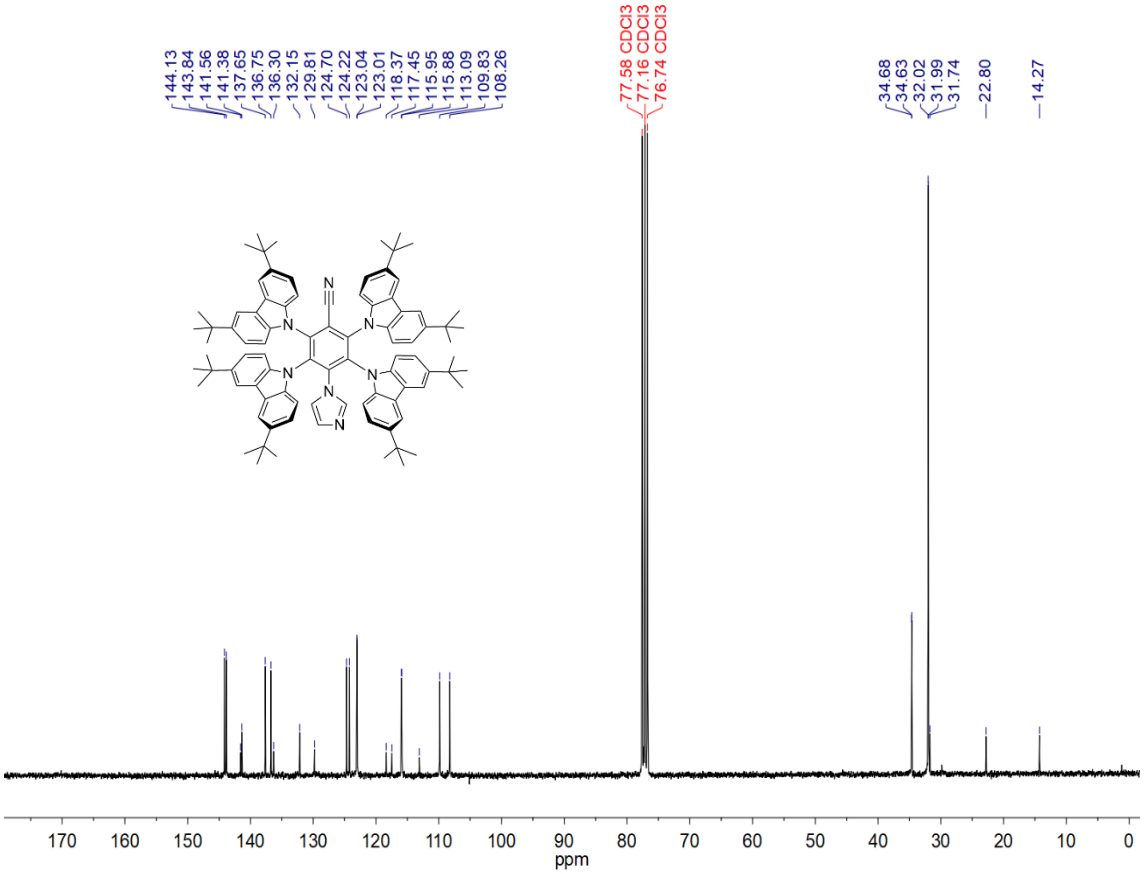


Figure A3.12: $^{13}C\{^{1}H\}$ NMR spectrum of **4^{tBu}CzBNIm** ($CDCl_3$).

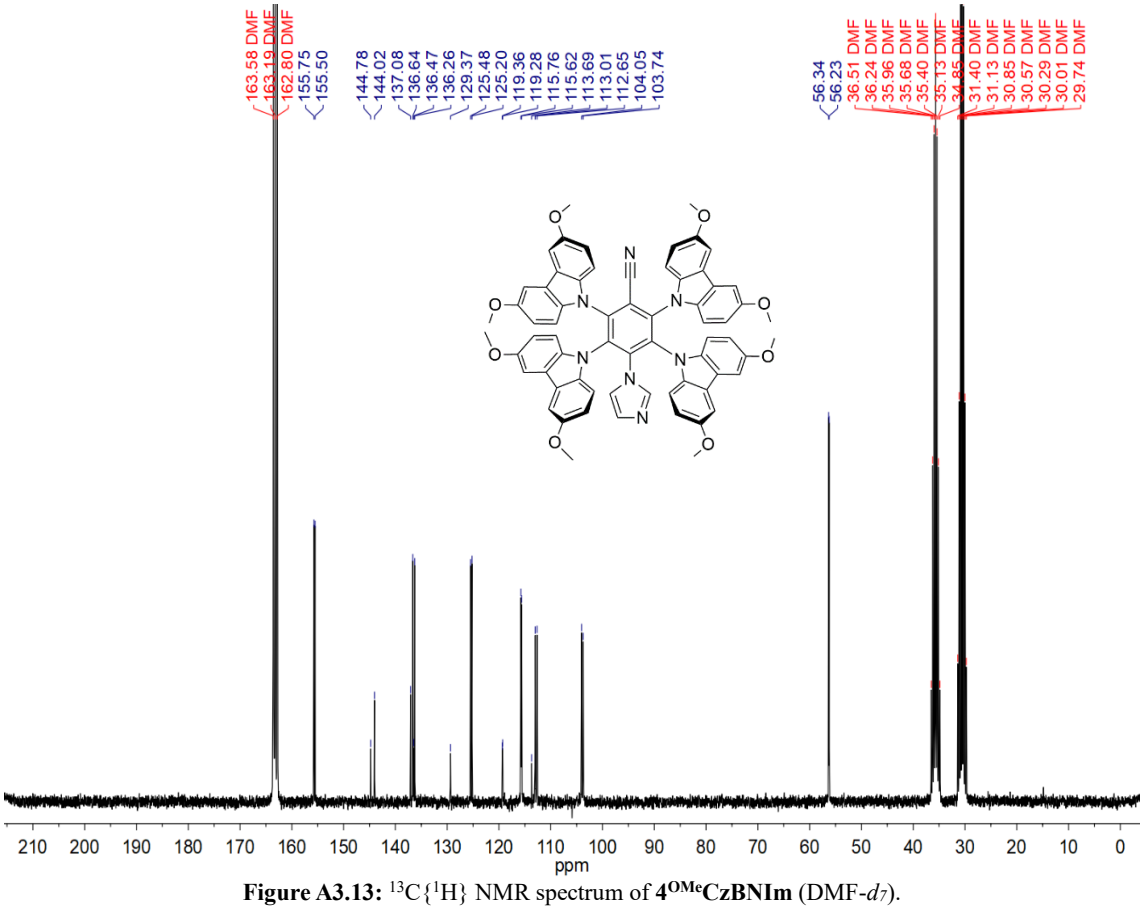


Figure A3.13: $^{13}C\{^{1}H\}$ NMR spectrum of **4^{OMe}CzBNIm** (DMF-d_7).

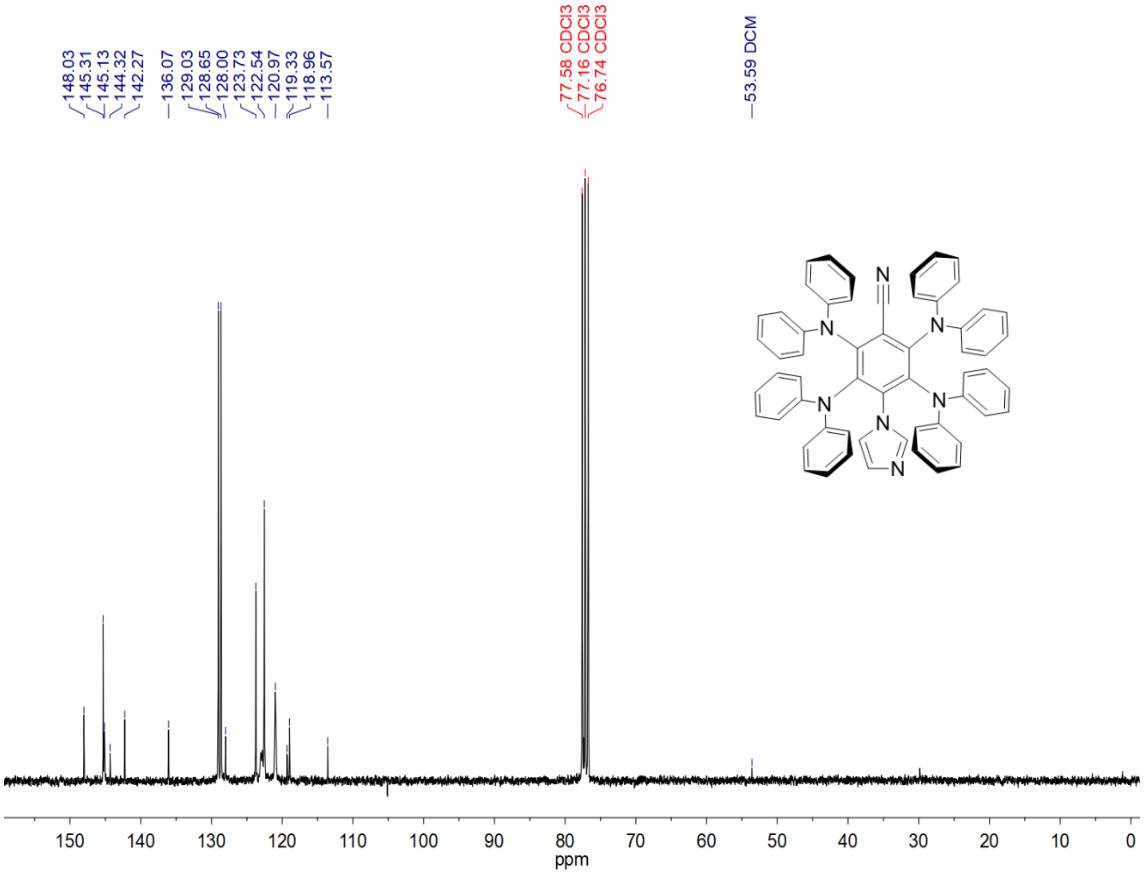


Figure A3.14: $^{13}C\{^{1}H\}$ NMR spectrum of **4DPABNIm** ($CDCl_3$).

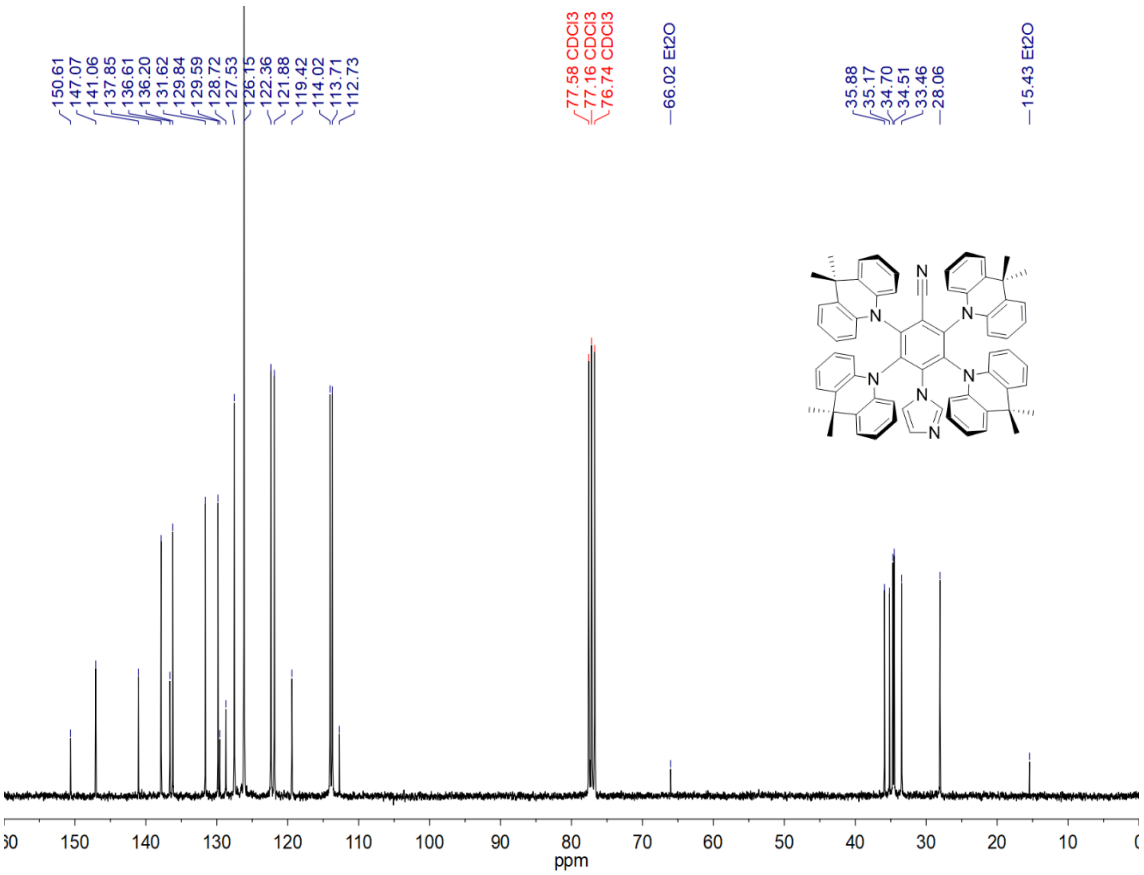


Figure A3.15: $^{13}C\{^{1}H\}$ NMR spectrum of **4DMACBNIm** ($CDCl_3$).

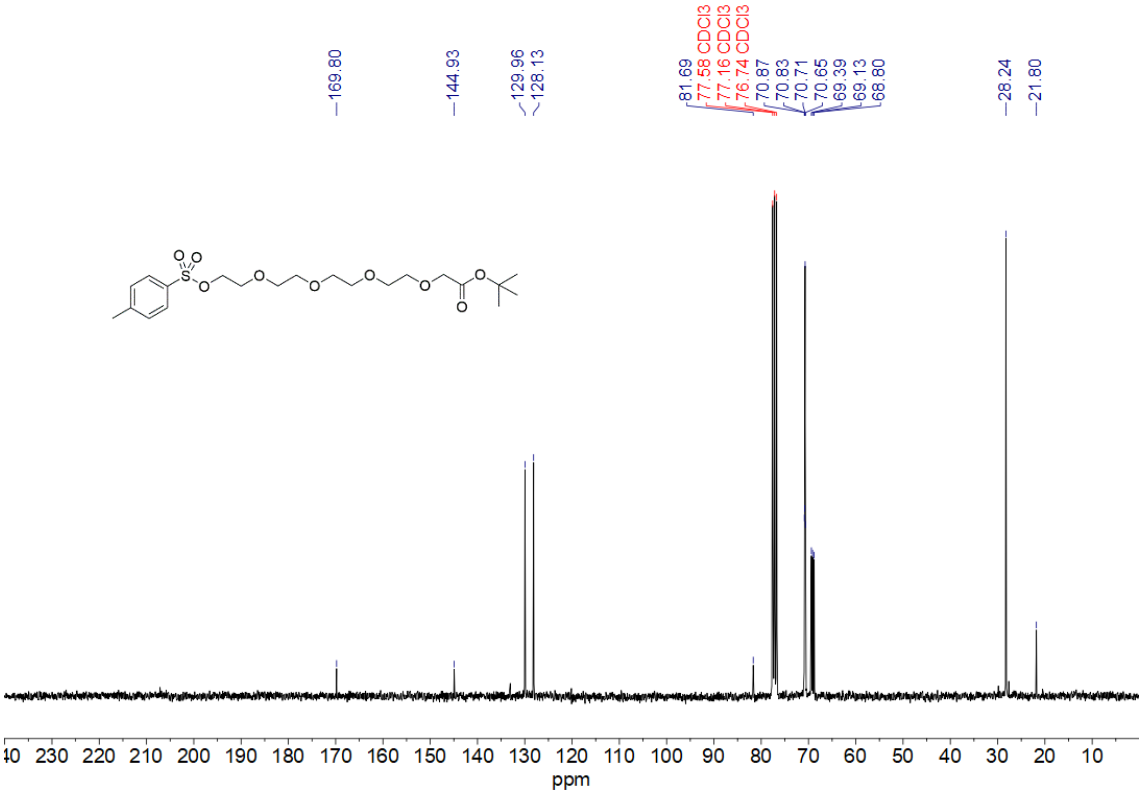


Figure A3.16: $^{13}C\{^{1}H\}$ NMR spectrum of *tert*-butyl 14-(tosyloxy)-3,6,9,12-tetraoxatetradecanoate ($CDCl_3$).

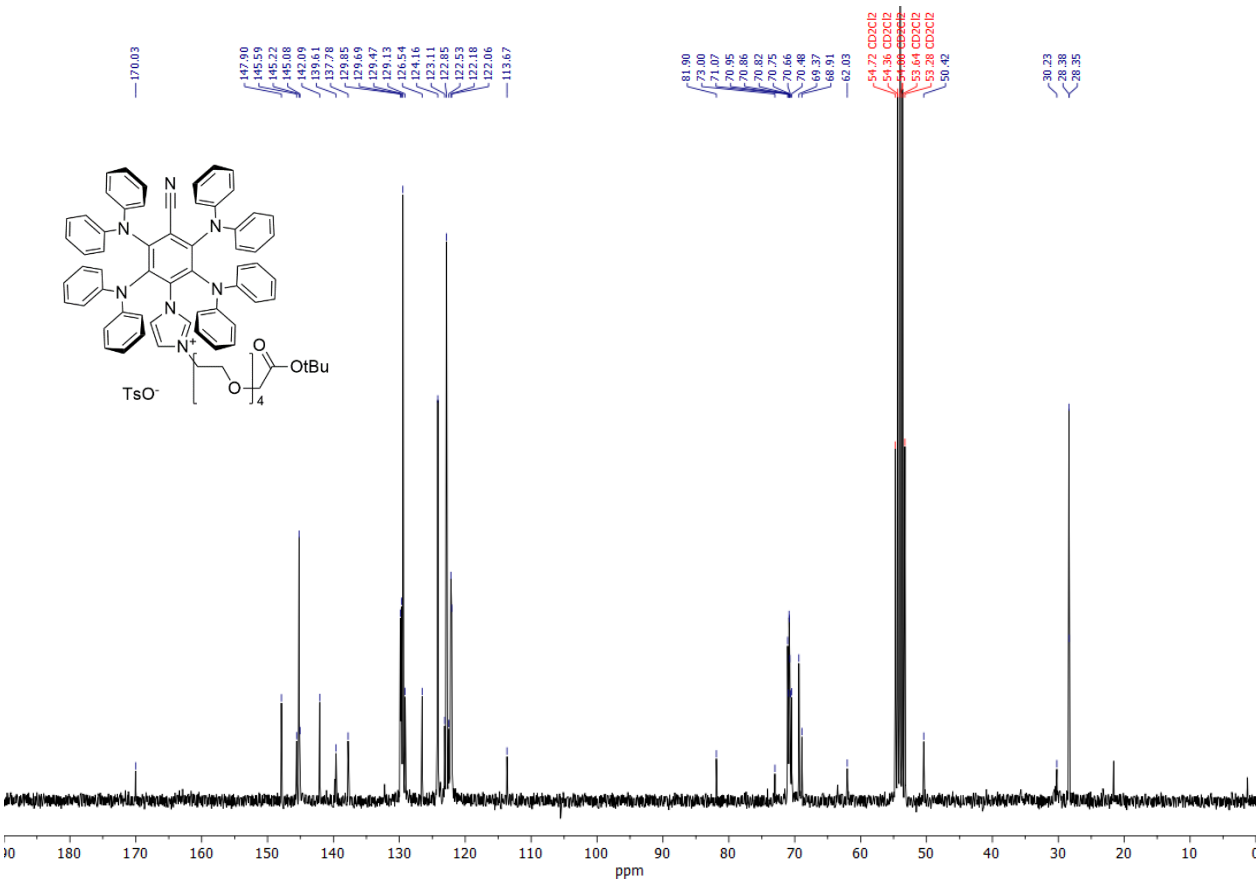


Figure A3.17: $^{13}C\{^{1}H\}$ NMR spectrum of **[4DPABNImTEGCOOtBu]OTs** (CD_2Cl_2).

3.4 Absorption-excitation spectra comparisons

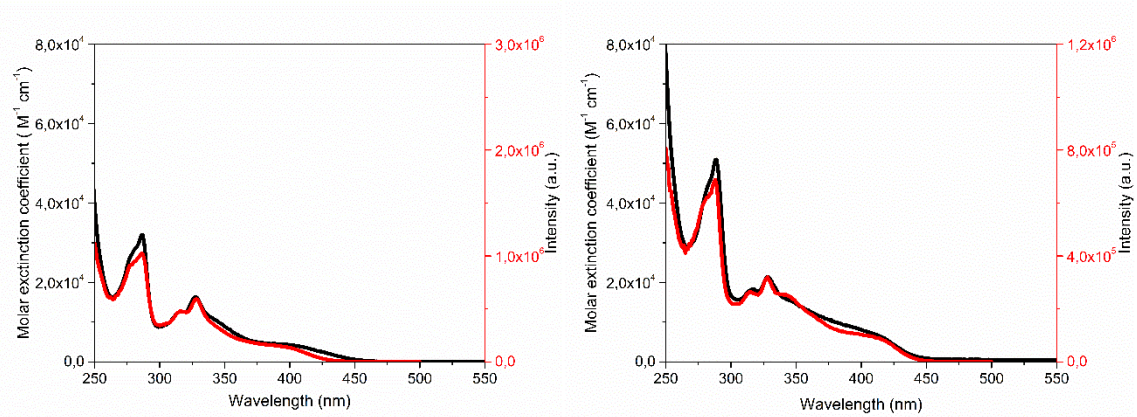


Figure A3.18: Absorption (black line) and excitation (red line) spectra of **4CzBNIm** in acetonitrile (left) and dichloromethane (right).

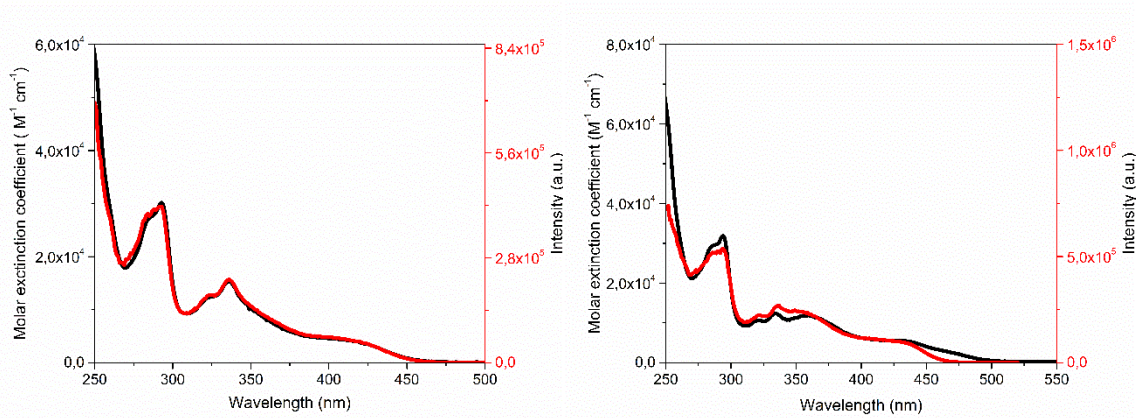


Figure A3.19: Absorption (black line) and excitation (red line) spectra of **4^{tBu}CzBNIm** in acetonitrile (left) and dichloromethane (right).

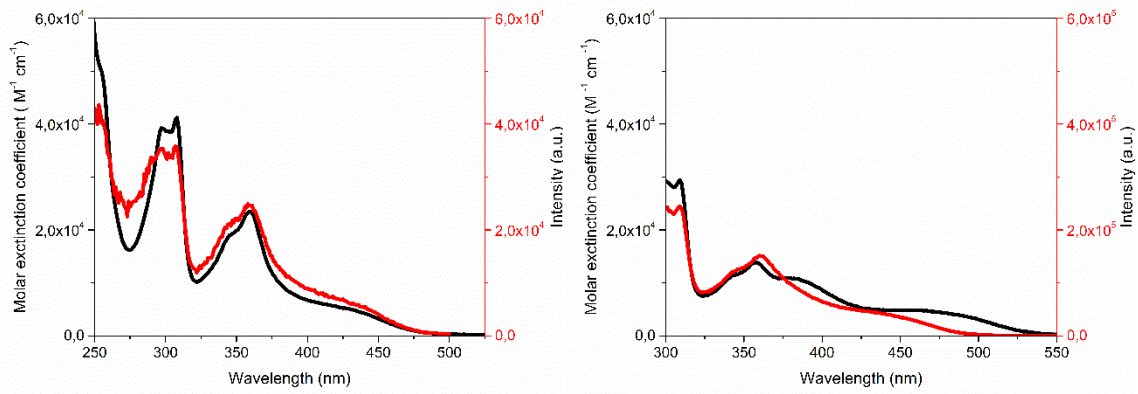


Figure A3.20: Absorption (black line) and excitation (red line) spectra of **4^{OMe}CzBNIm** in acetonitrile (left) and dichloromethane (right).

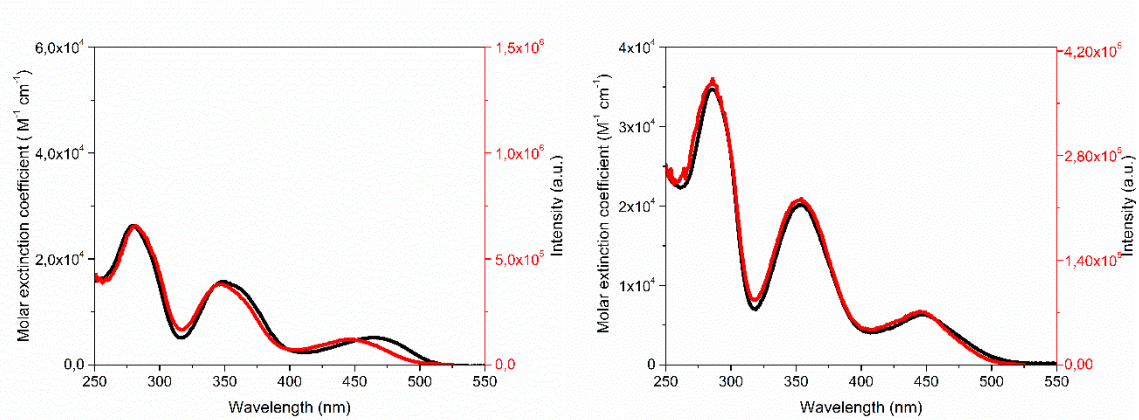


Figure A3.21: Absorption (black line) and excitation (red line) spectra of **4DPABNIm** in acetonitrile (left) and dichloromethane (right).

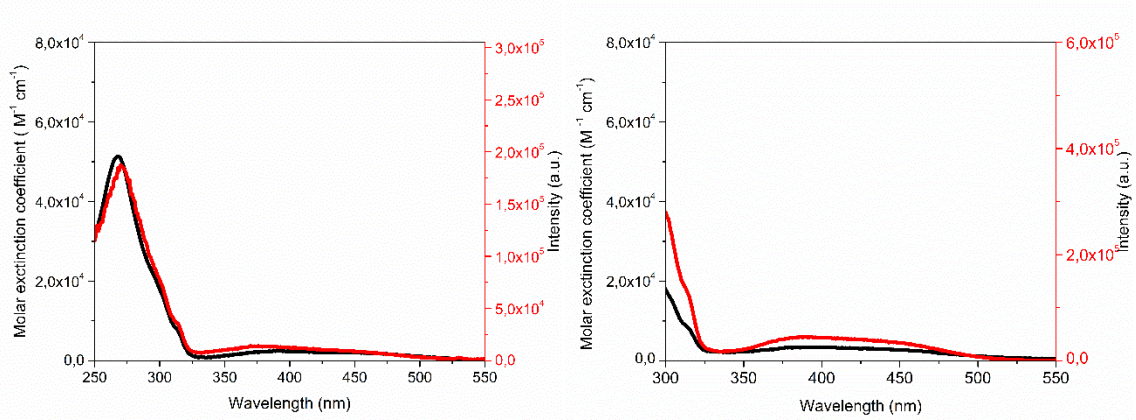


Figure A3.22: Absorption (black line) and excitation (red line) spectra of **4DMACBNIm** in acetonitrile (left) and dichloromethane (right).

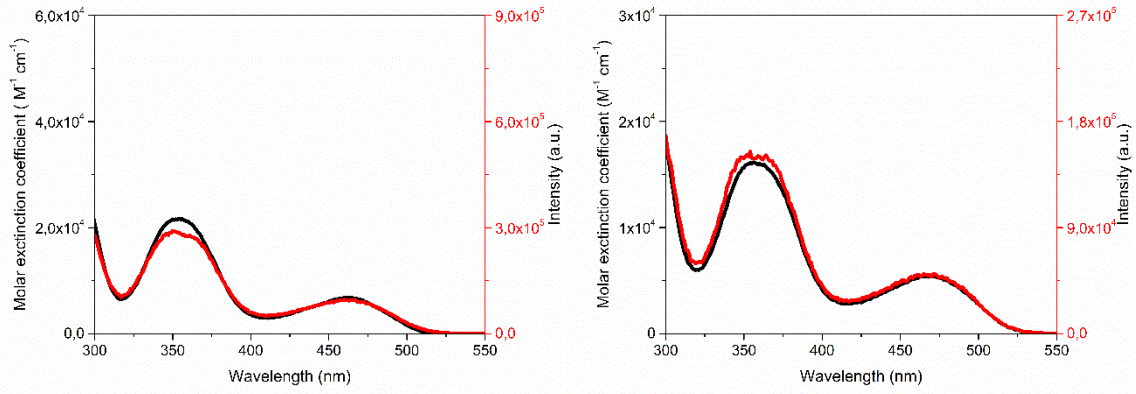


Figure A3.23: Absorption (black line) and excitation (red line) spectra of **[4DPABNImTEGCOOtBu]OTs** in acetonitrile (left) and dichloromethane (right).

3.5 Luminescence decay curves

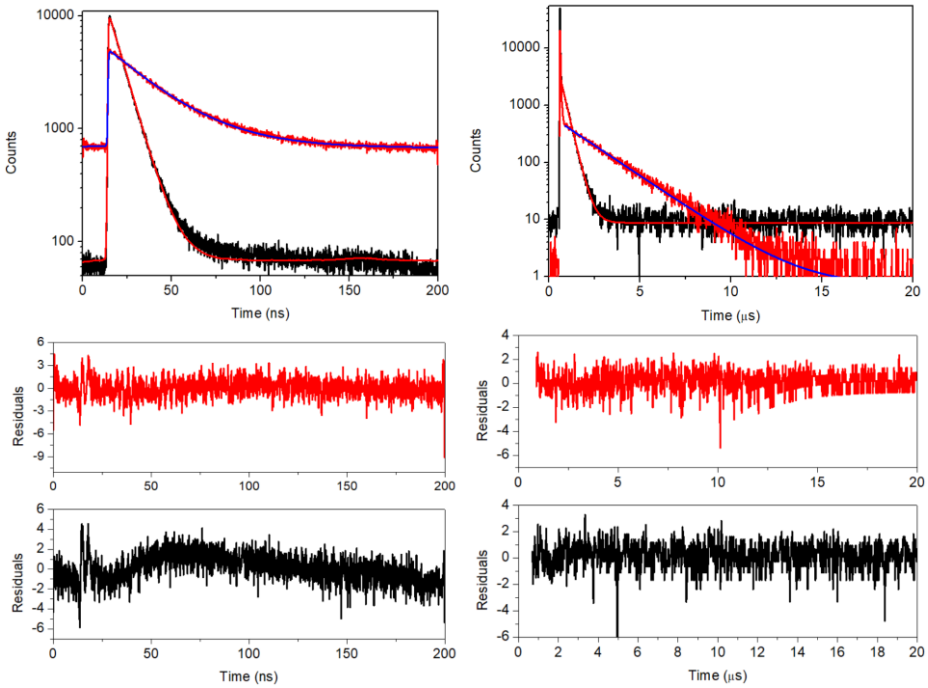


Figure A3.24: Luminescence decay curves of **4CzBNIm** in aerated acetonitrile (black curves) and in Ar-purged acetonitrile solutions (red curves) with their fittings and residuals. Left: decays in the nanosecond scale; Right: decays in the microsecond scale.

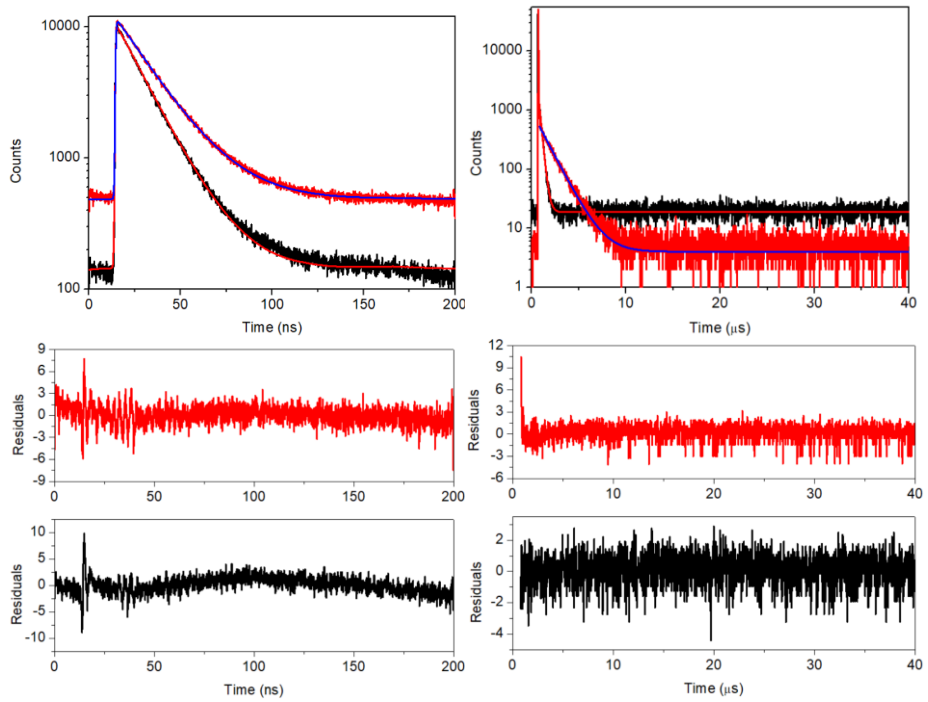


Figure A3.25: Luminescence decay curves of **4^{tBu}CzBNIm** in aerated acetonitrile (black curves) and in Ar-purged acetonitrile solutions (red curves) with their fittings and residuals. Left: decays in the nanosecond scale; Right: decays in the microsecond scale.

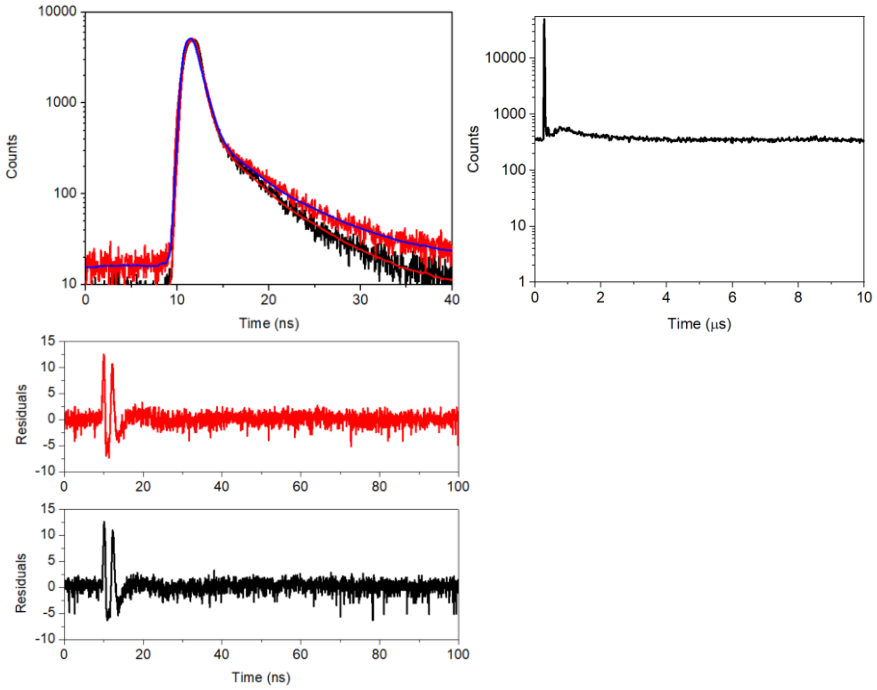


Figure A3.26: Luminescence decay curves of **4^{OMe}CzBNIm** in aerated acetonitrile (black curves) and in Ar-purged acetonitrile solutions (red curves) with their fittings and residuals. Left: decays in the nanosecond scale; Right: decays in the microsecond scale.

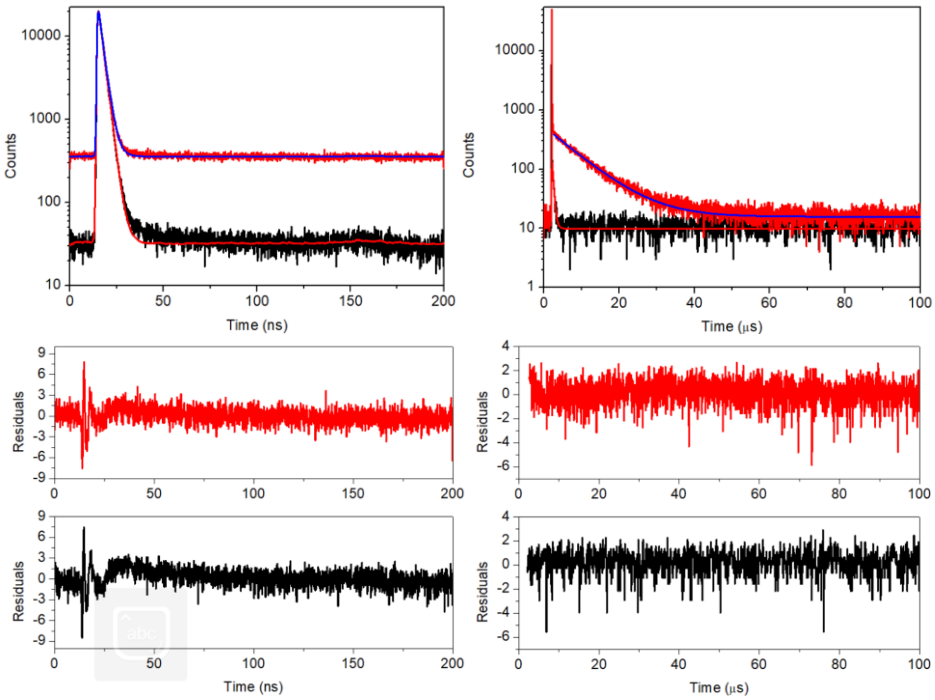


Figure A3.27: Luminescence decay curves of **4DPABNIm** in aerated acetonitrile (black curves) and in Ar-purged acetonitrile solutions (red curves) with their fittings and residuals. Left: decays in the nanosecond scale; Right: decays in the microsecond scale.

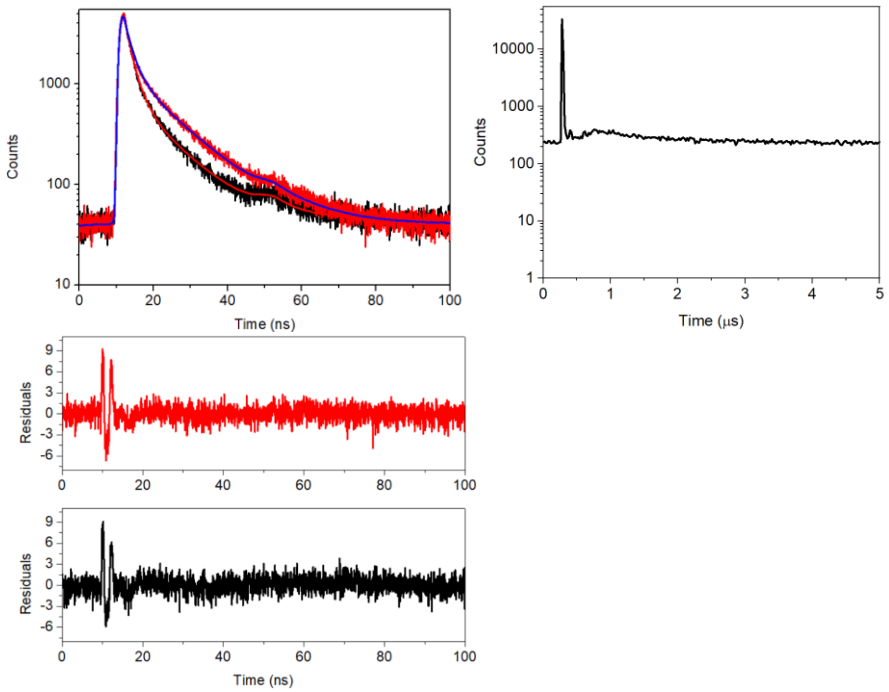


Figure A3.28: Luminescence decay curves of **4DMACBNIm** in aerated acetonitrile (black curves) and in Ar-purged acetonitrile solutions (red curves) with their fittings and residuals. Left: decays in the nanosecond scale; Right: decays in the microsecond scale.

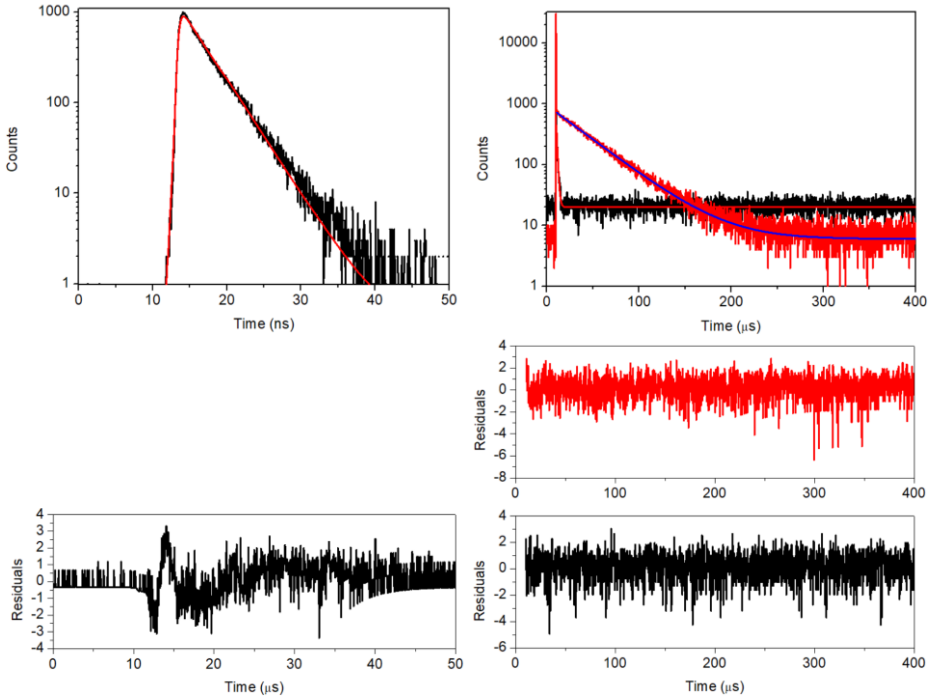


Figure A3.29: Luminescence decay curves of **[4DPABNImTEGCOOtBu]OTs** in aerated acetonitrile (black curves) and in Ar-purged acetonitrile solutions (red curves) with their fittings and residuals. Left: decay in the nanosecond scale; Right: decays in the microsecond scale.

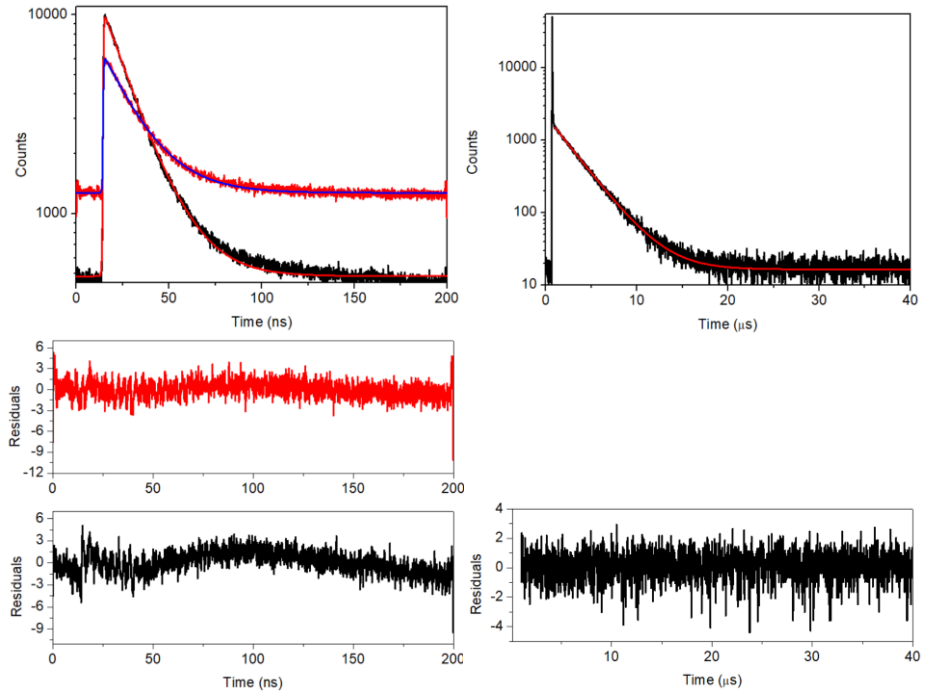


Figure A3.30: Luminescence decay curves of **4CzBNIm** in aerated dichloromethane (black curves) and in Ar-purged dichloromethane solutions (red curves) with their fittings and residuals. Left: decays in the nanosecond scale; Right: decay in the microsecond scale of the Ar-purged dichloromethane solution.

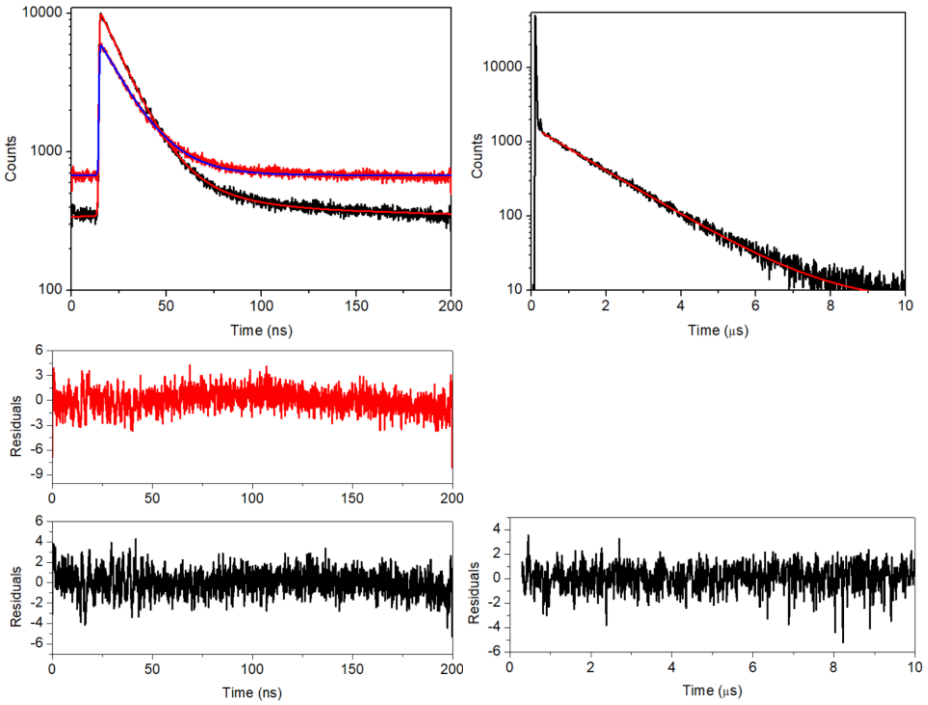


Figure A3.31: Luminescence decay curves of **4^{tBu}CzBNIm** in aerated dichloromethane (black curves) and in Ar-purged dichloromethane solutions (red curves) with their fittings and residuals. Left: decays in the nanosecond scale; Right: decay in the microsecond scale of the Ar-purged dichloromethane solution.

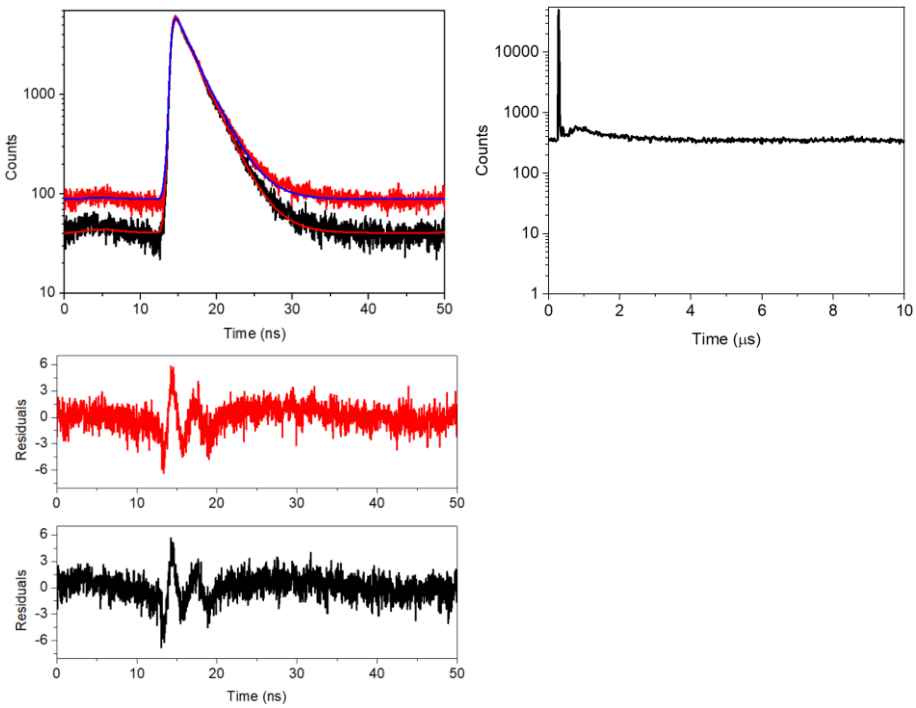


Figure A3.32: Luminescence decay curves of **4^{OMe}CzBNIm** in aerated dichloromethane (black curves) and in Ar-purged dichloromethane solutions (red curves) with their fittings and residuals. Left: decays in the nanosecond scale; Right: decay in the microsecond scale of the Ar-purged dichloromethane solution.

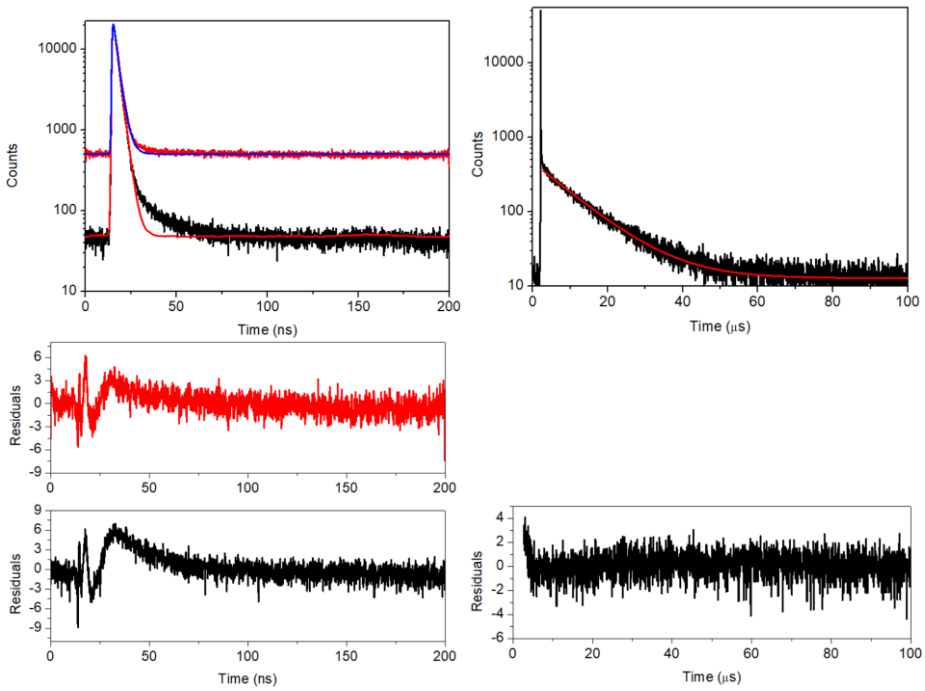


Figure A3.33: Luminescence decay curves of **4DPABNIm** in aerated dichloromethane (black curves) and in Ar-purged dichloromethane solutions (red curves) with their fittings and residuals. Left: decays in the nanosecond scale; Right: decay in the microsecond scale of the Ar-purged dichloromethane solution.

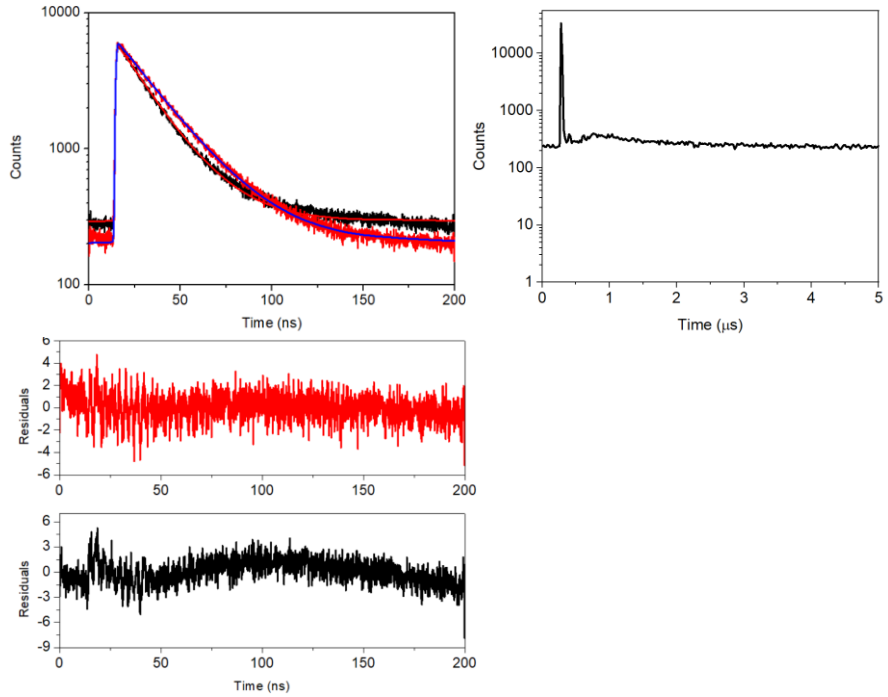


Figure A3.34: Luminescence decay curves of **4DMACBNIm** in aerated dichloromethane (black curves) and in Ar-purged dichloromethane solutions (red curves) with their fittings and residuals. Decays in the nanosecond scale.

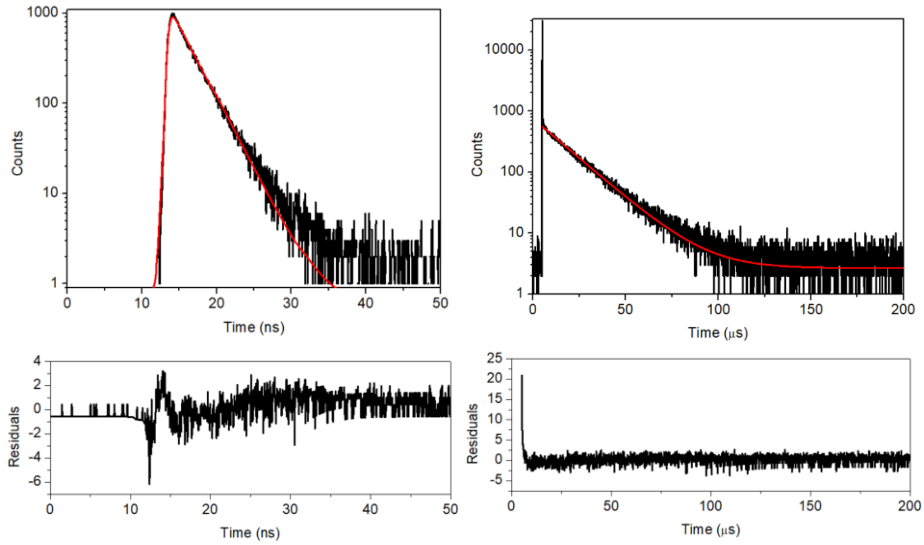


Figure A3.35: Luminescence decay curves of **[4DPABNImTEGCOOtBu]OTs** in Ar-purged dichloromethane solution with their fittings and residuals. Left: decay in the nanosecond scale; Right: decay in the microsecond scale.

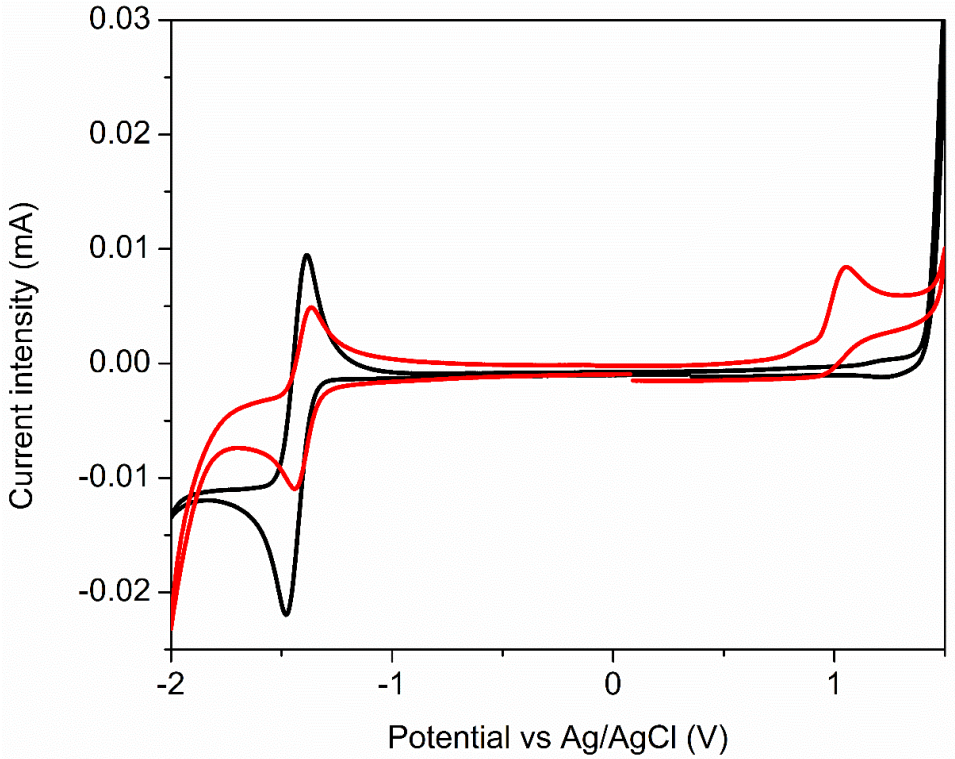


Figure A3.36: CV of **4CzBNIm** in acetonitrile (red curve) and dichloromethane (black curve).

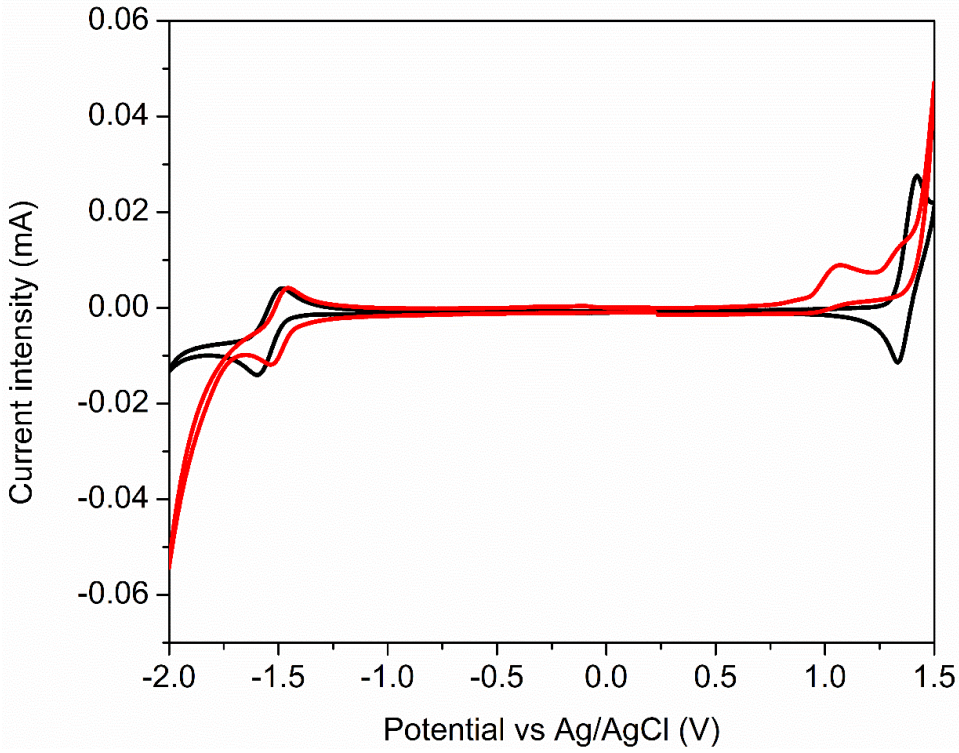


Figure A3.37: CV of **4^{tBu}CzBNIm** in acetonitrile (red curve) and dichloromethane (black curve).

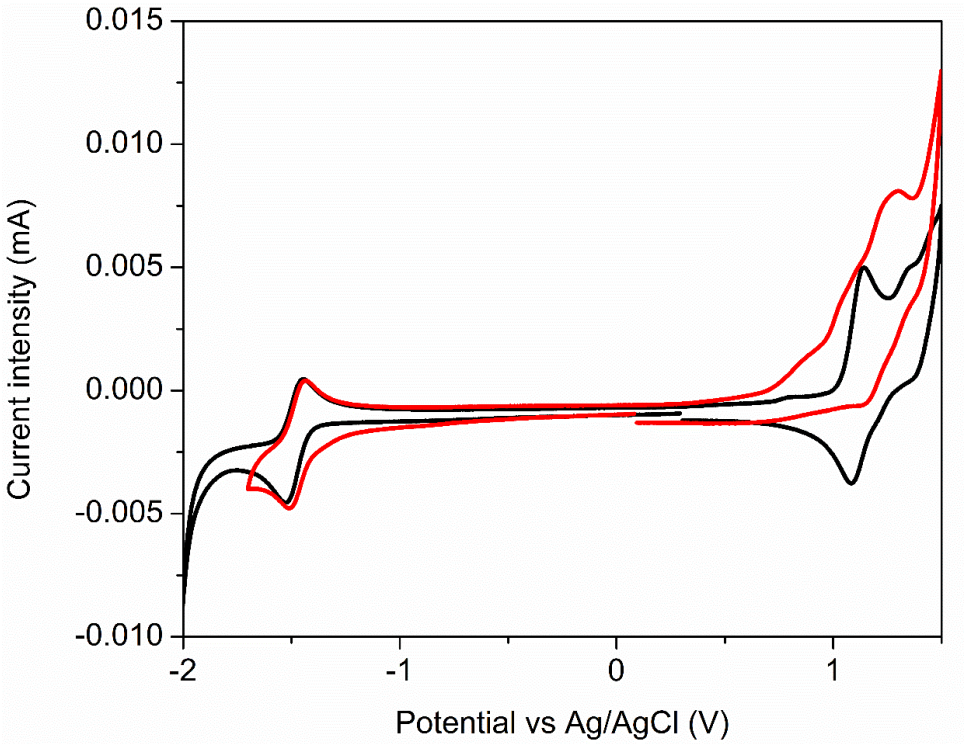


Figure A3.38: CV of **4^{OMe}CzBNIm** in acetonitrile (red curve) and dichloromethane (black curve).

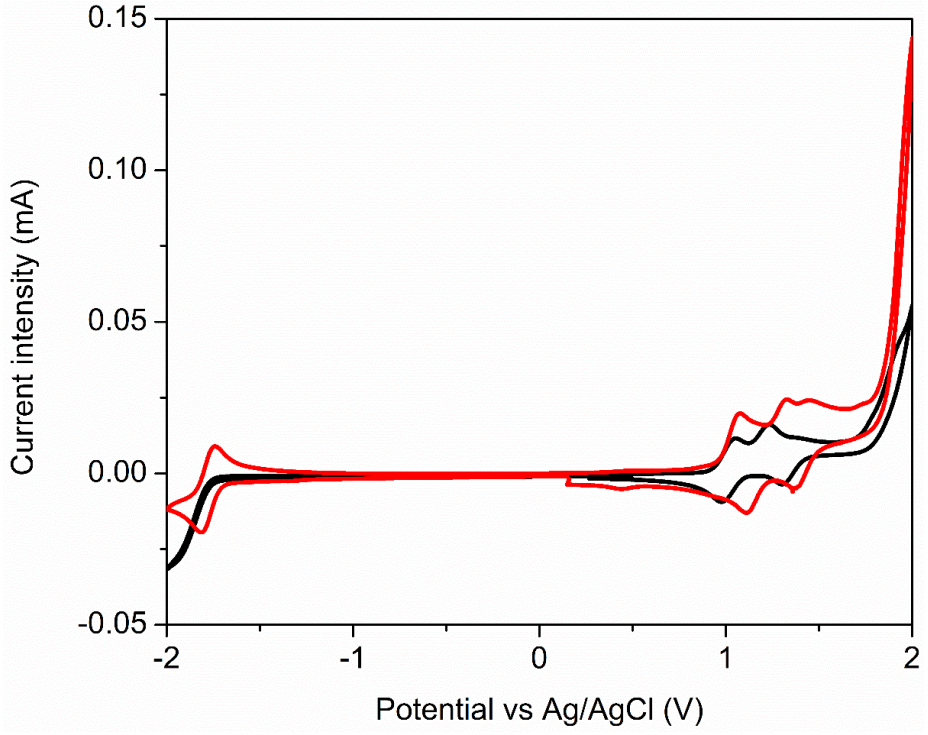


Figure A3.39: CV of **4DPABNIm** in acetonitrile (red curve) and dichloromethane (black curve).

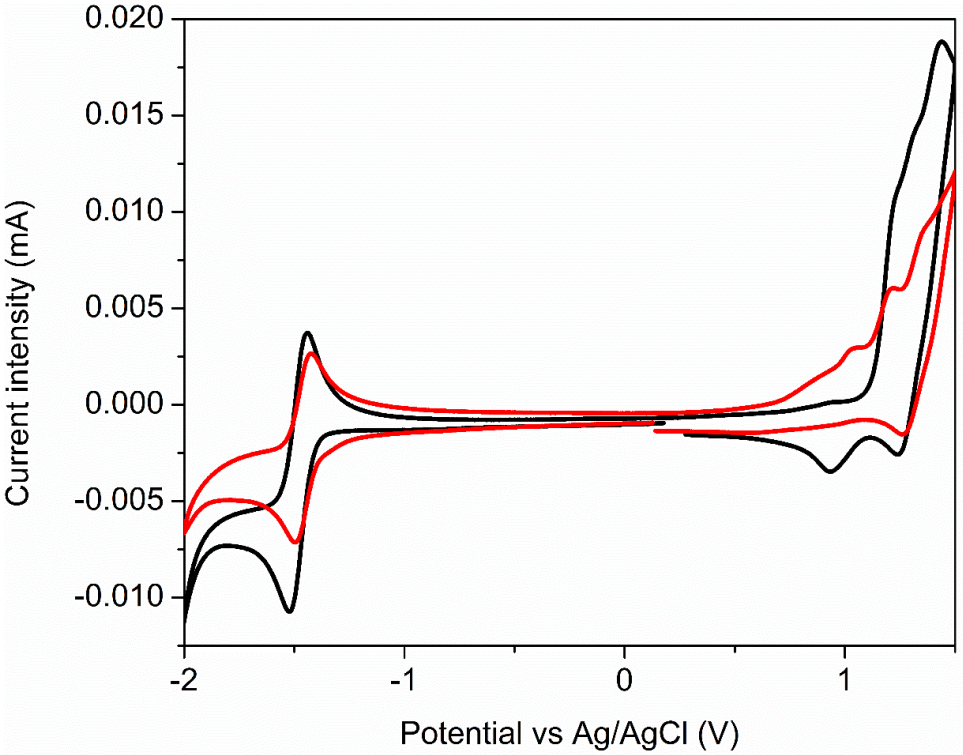


Figure A3.40: CV of **4DMACBNIm** in acetonitrile (red curve) and dichloromethane (black curve).

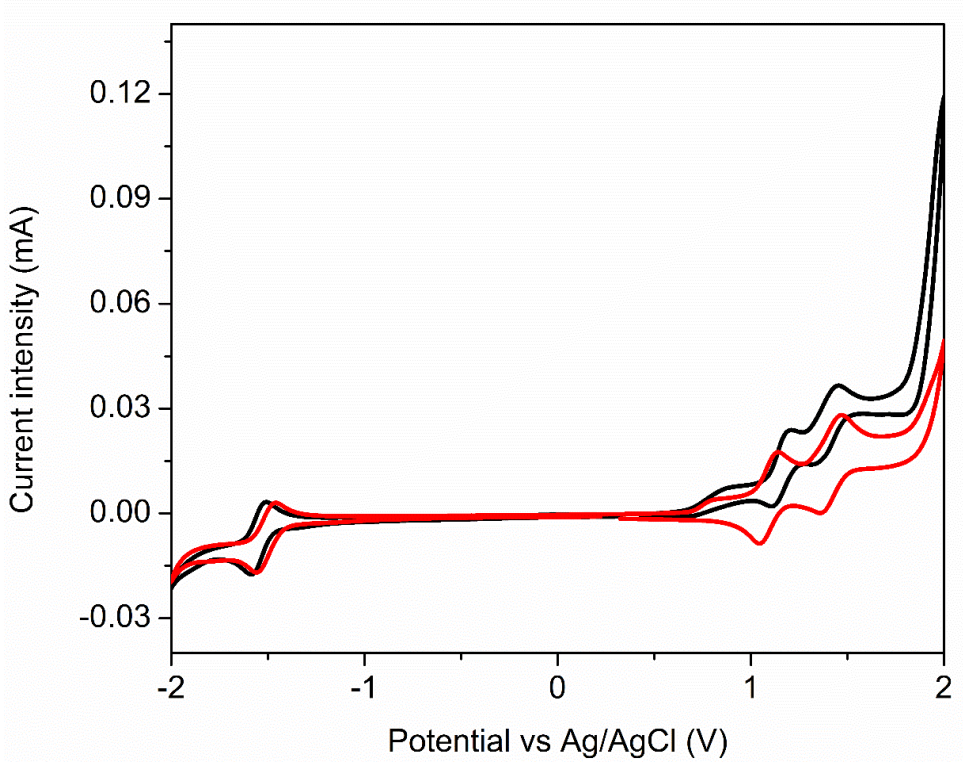


Figure A3.41: CV of **[4DPABNImTEGCOOtBu]OTs** in acetonitrile (red curve) and dichloromethane (black curve).

3.7 ECL-voltage curves

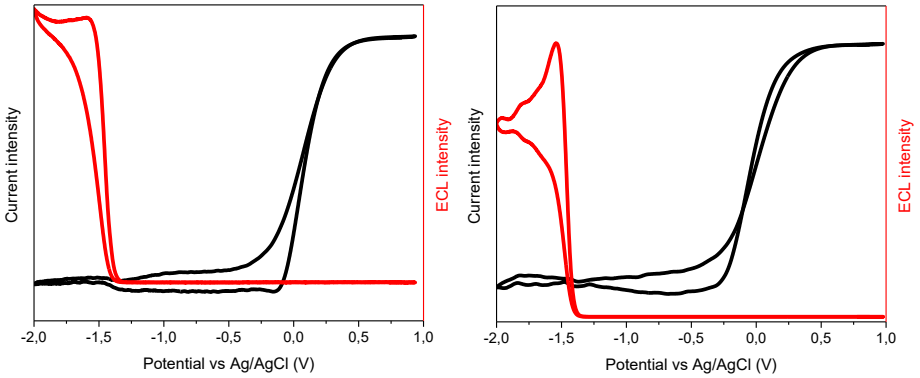


Figure A3.42: ECL-voltage curves of **4CzBNIm** in acetonitrile (left) and dichloromethane (right).

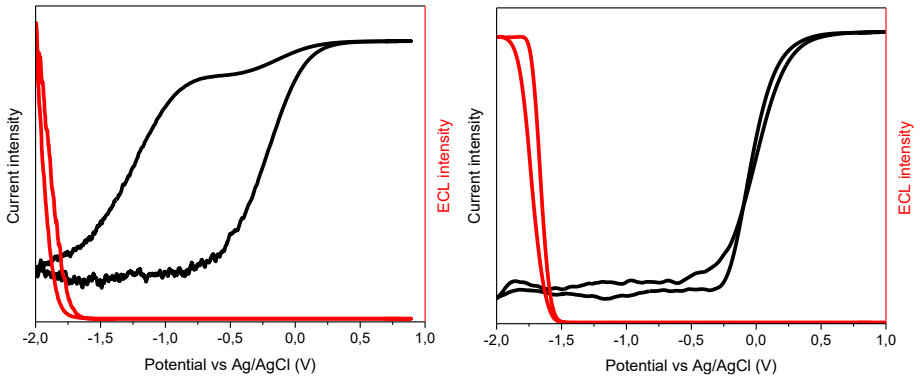


Figure A3.43: ECL-voltage curves of **4^{tBu}CzBNIm** in acetonitrile (left) and dichloromethane (right).

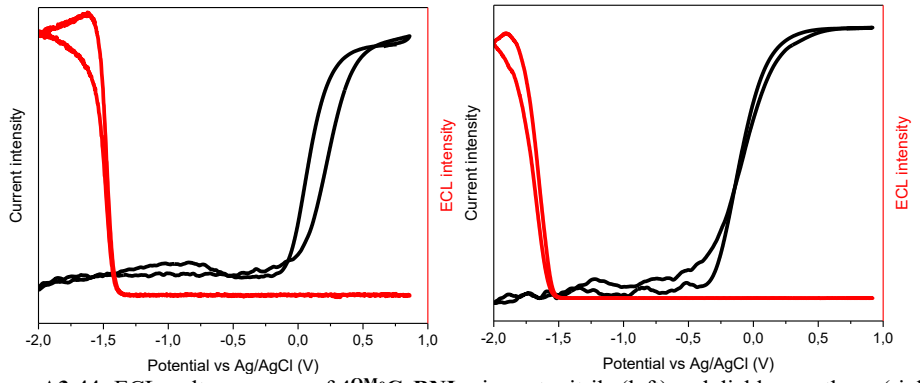


Figure A3.44: ECL-voltage curves of **4^{OMe}CzBNIm** in acetonitrile (left) and dichloromethane (right).

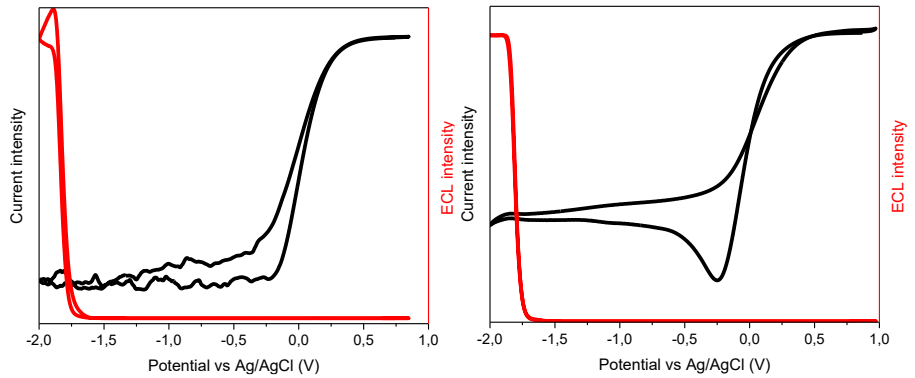


Figure A3.45: ECL-voltage curve of **4DPABNIm** in acetonitrile (left) and dichloromethane (right).

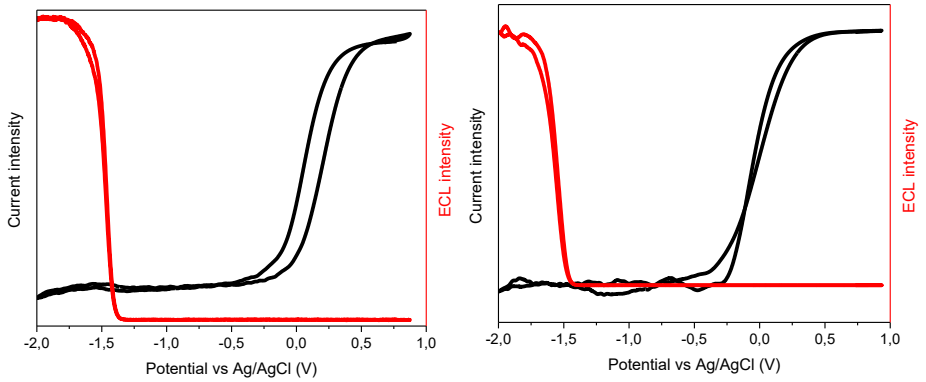


Figure A3.46: ECL-voltage curve of **4DMACBNIm** in acetonitrile (left) and dichloromethane (right).

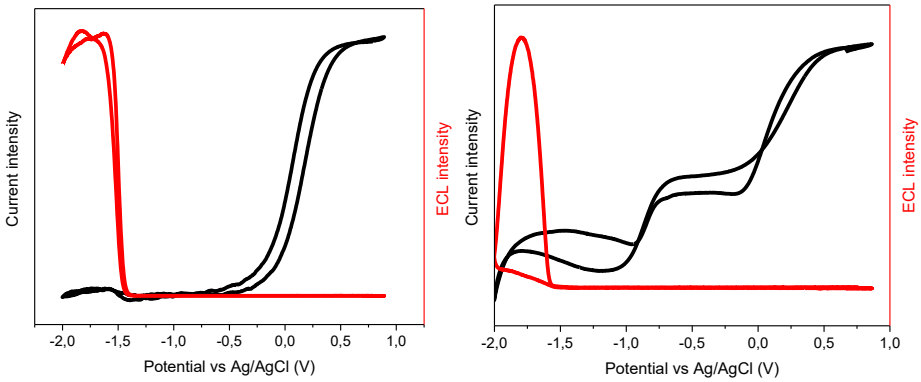


Figure A3.47: ECL-voltage curve of **[4DPABNImTEGCOOtBu]OTs** in acetonitrile (left) and dichloromethane (right)

3.8 PL – reductive-oxidation ECL spectra comparisons

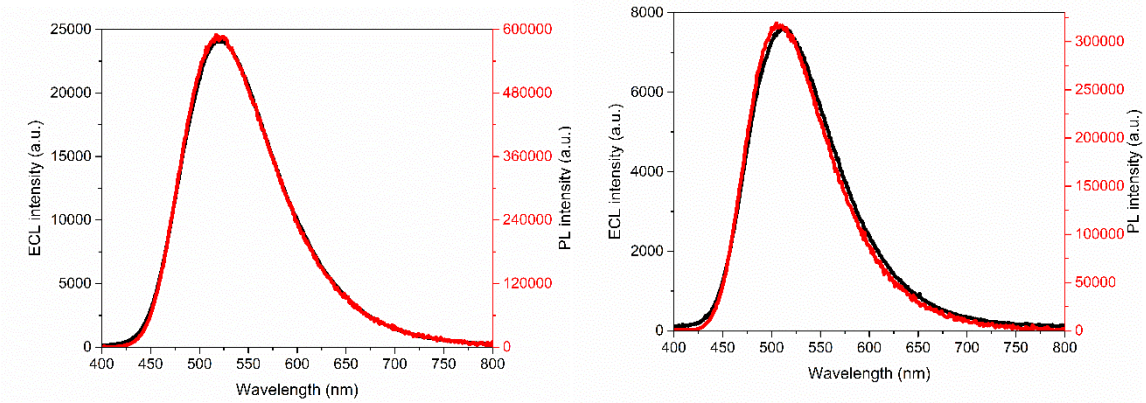


Figure A3.48: ECL (black curve) and PL (red curve) spectra of **4CzBNIm** in acetonitrile (left) and dichloromethane (right).

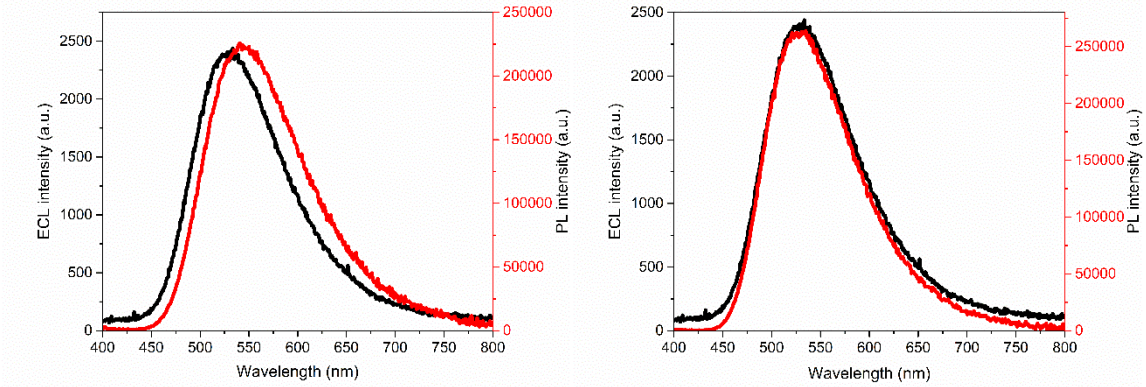


Figure A3.49: ECL (black curve) and PL (red curve) spectra of **4^{tBu}CzBNIm** in acetonitrile (left) and dichloromethane (right).

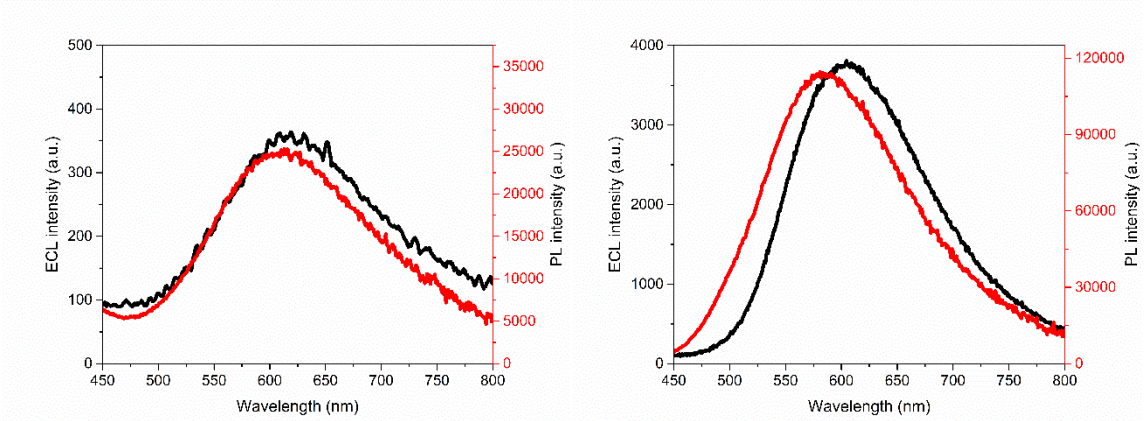


Figure A3.50: ECL (black curve) and PL (red curve) spectra of **4^{OMe}CzBNIm** in acetonitrile (left) and dichloromethane (right).

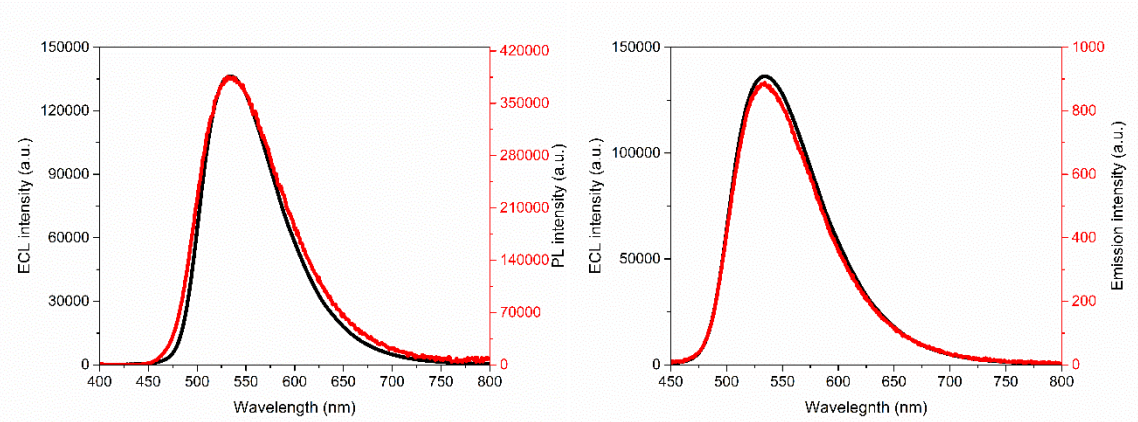


Figure A3.51: ECL (black curve) and PL (red curve) spectra of **4DPABNIm** in acetonitrile (left) and dichloromethane (right).

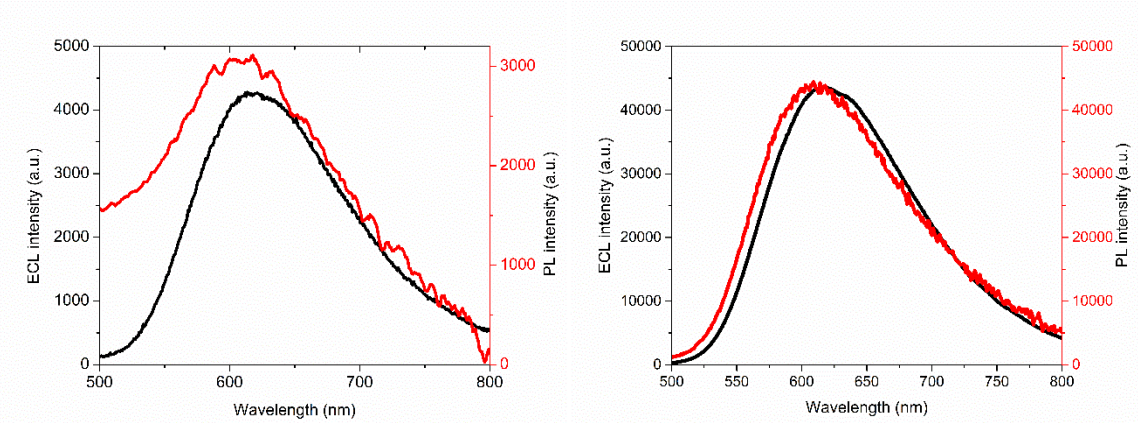


Figure A3.52: ECL (black curve) and PL (red curve) spectra of **4DMACBNIm** in acetonitrile (left) and dichloromethane (right).

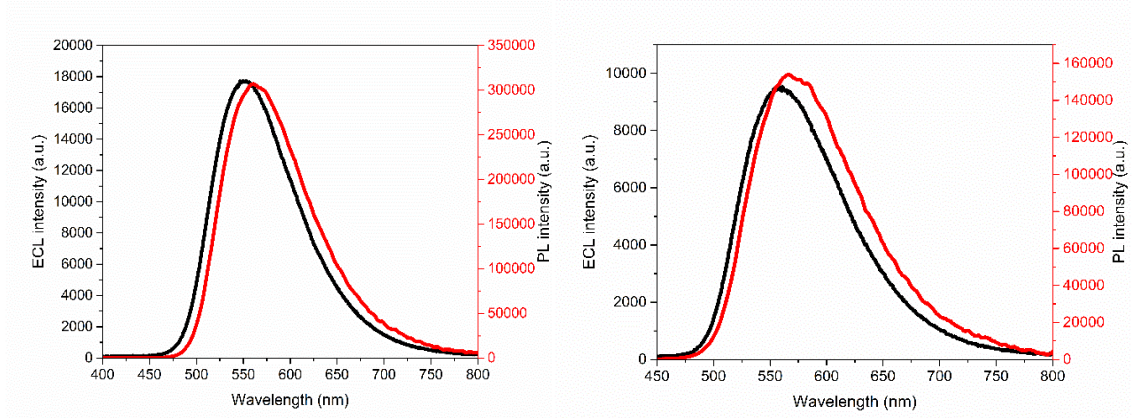


Figure A3.53: ECL (black curve) and PL (red curve) spectra of **[4DPABNImTEGCOOtBu]OTs** in acetonitrile (left) and dichloromethane (right).

3.9 PL – oxidative-reduction ECL spectra comparisons

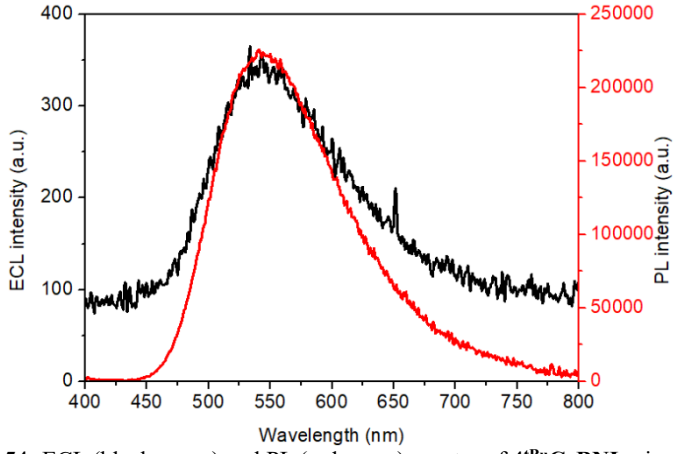


Figure A3.54: ECL (black curve) and PL (red curve) spectra of **4^{tBu}CzBNIm** in acetonitrile.

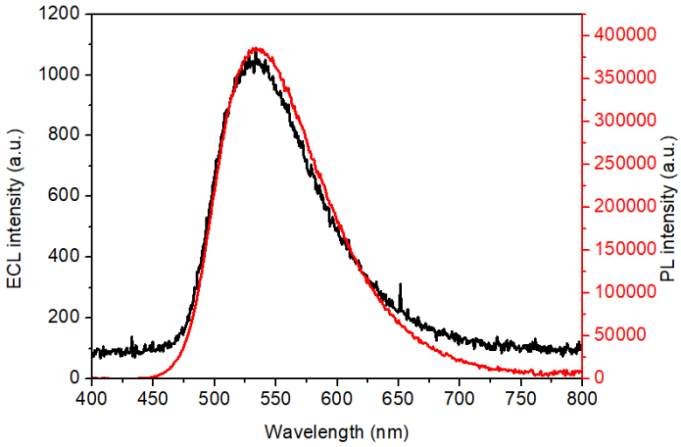


Figure A3.55: ECL (black curve) and PL (red curve) spectra of **4DPABNIm** in acetonitrile.

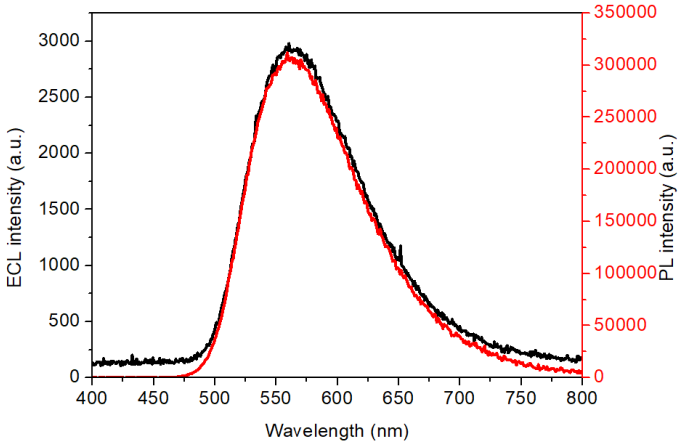


Figure A3.56: ECL (black curve) and PL (red curve) spectra of **[4DPABNImTEGCOOtBu]OTs** in acetonitrile.

3.10 Annihilation ECL-time and current-time profiles

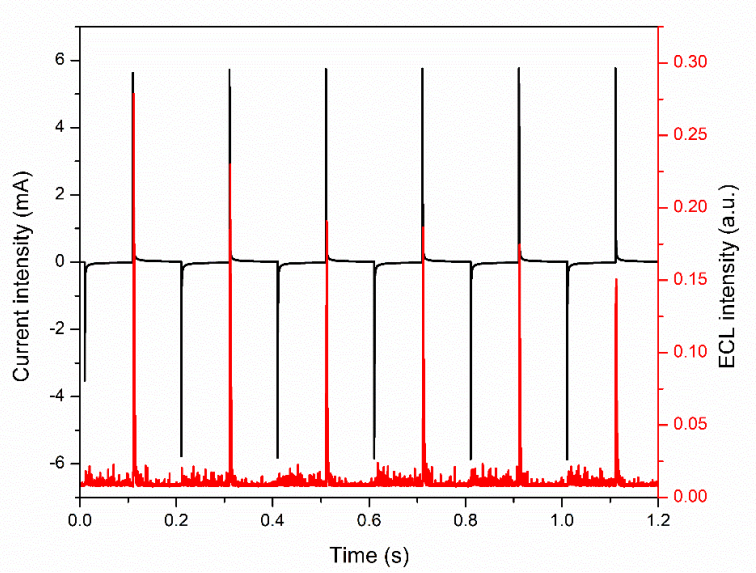


Figure A3.57: ECL-time (red) and chronoamperometric (black) profiles of **4^{tBu}CzBNIm** in acetonitrile. Potential stepped between -1.7 V and +1.3 V.

3.11 Reductive-oxidation ECL-time and current-time profiles

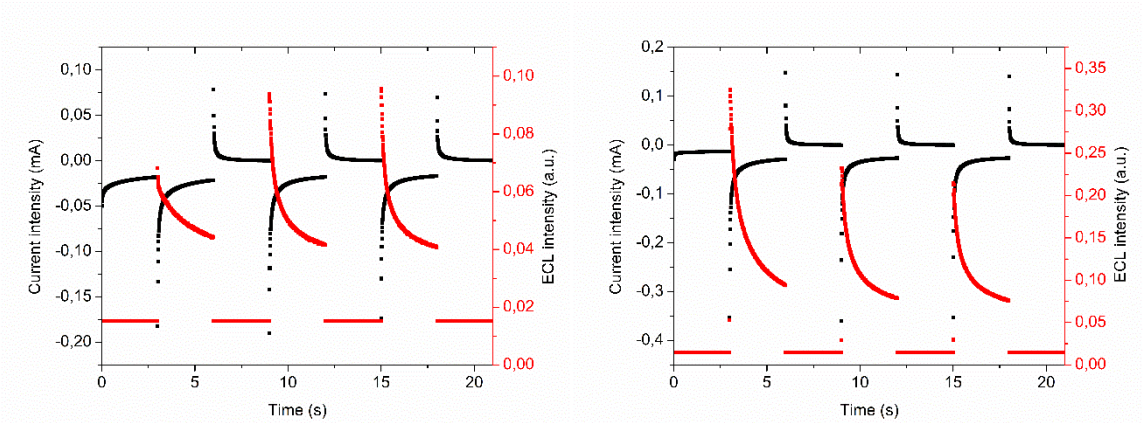


Figure A3.58: Co-reactant ECL-time (red curve) and current-time (black curve) profiles of **4CzBNIm** in acetonitrile (left) and dichloromethane (right).

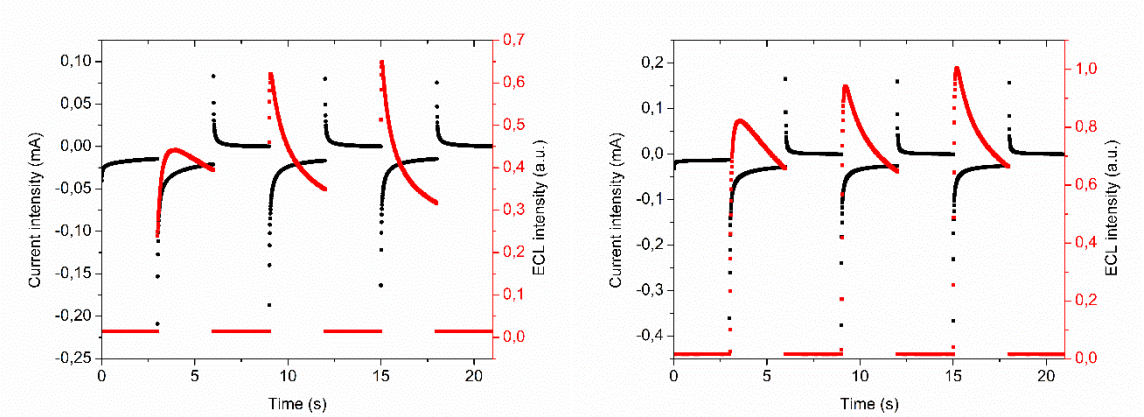


Figure A3.59: Co-reactant ECL-time (red curve) and current-time (black curve) profiles of **4^{tBu}CzBNIm** in acetonitrile (left) and dichloromethane (right).

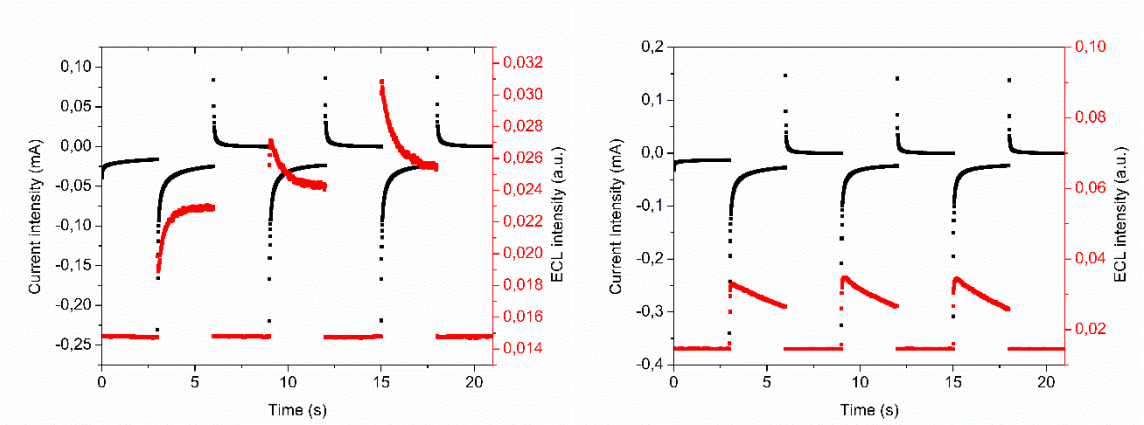


Figure A3.60: Co-reactant ECL-time (red curve) and current-time (black curve) profiles of **4^{OMe}CzBNIm** in acetonitrile (left) and dichloromethane (right).

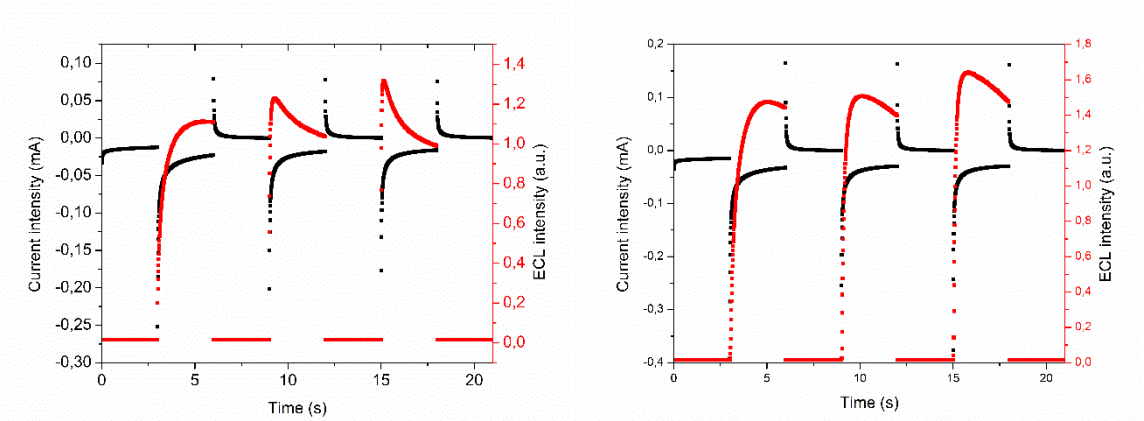


Figure A3.61: Co-reactant ECL-time (red curve) and current-time (black curve) profiles of **4DPABNIm** in acetonitrile (left) and dichloromethane (right).

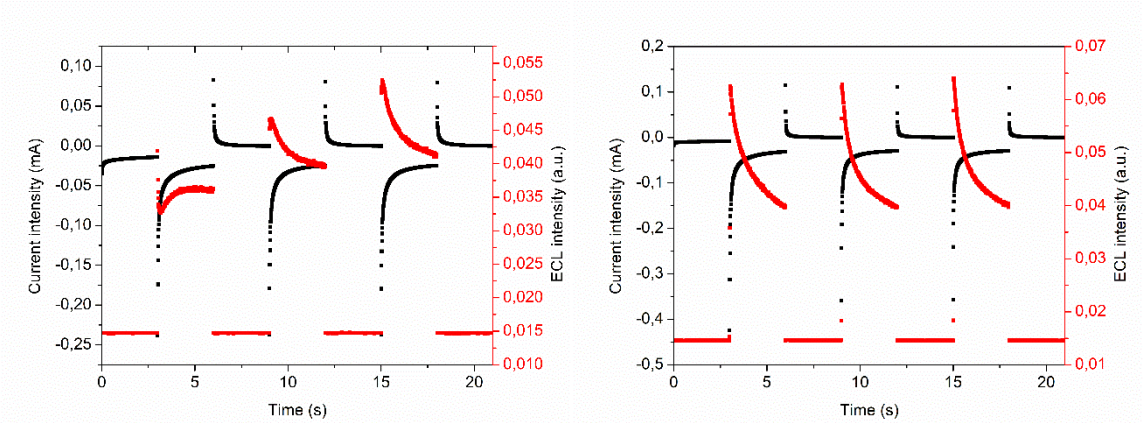


Figure A3.62: Co-reactant ECL-time (red curve) and current-time (black curve) profiles of **4DMACBNIm** in acetonitrile (left) and dichloromethane (right).

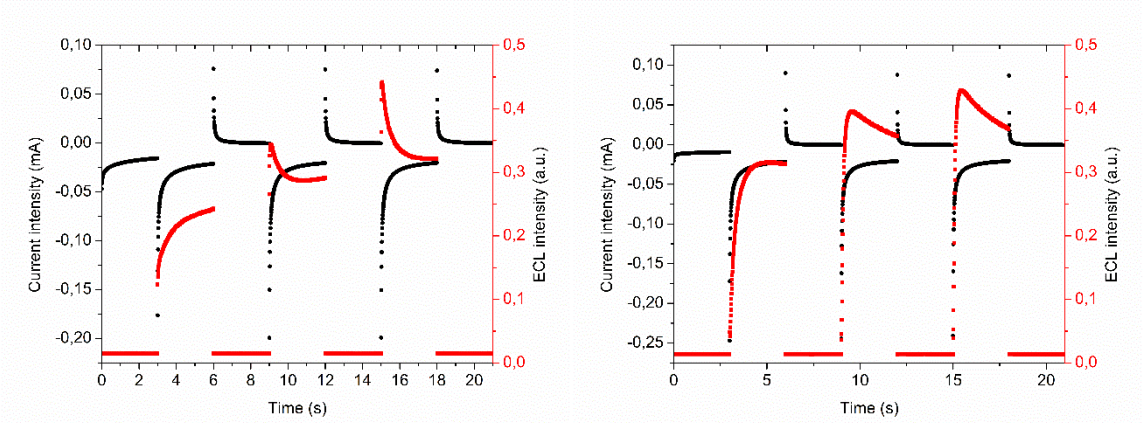


Figure A3.63: Co-reactant ECL-time (red curve) and current-time (black curve) profiles of **[4DPABNImTEGCOOtBu]OTs** in acetonitrile (left) and dichloromethane (right).

3.12 Oxidative-reduction ECL-time and current-time profiles

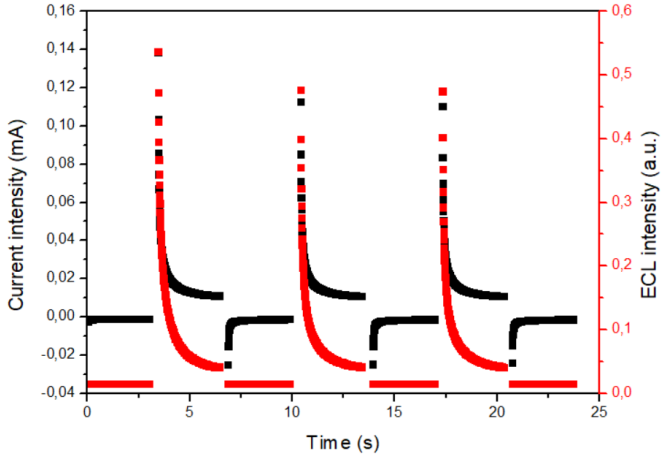


Figure A3.64: Co-reactant ECL-time (red curve) and current-time (black curve) profiles of **4^{tBu}CzBNIm** in acetonitrile.

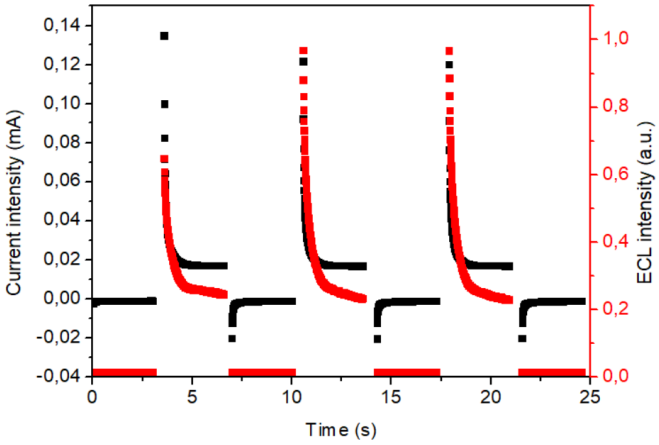


Figure A3.65: Co-reactant ECL-time (red curve) and current-time (black curve) profiles of **4DPABNIm** in acetonitrile.

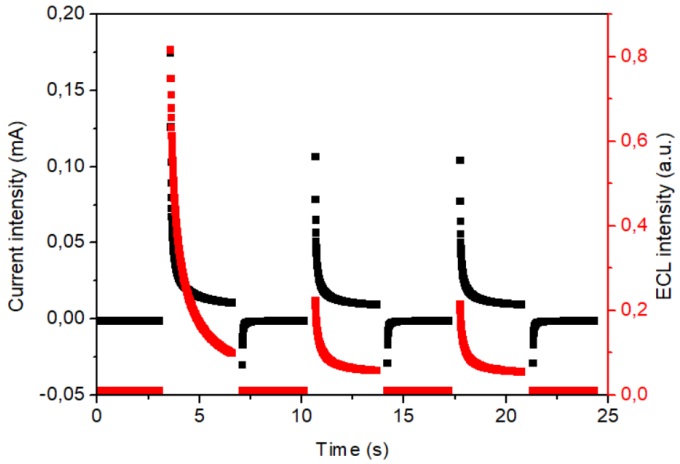


Figure A3.66: Co-reactant ECL-time (red curve) and current-time (black curve) profiles of [**4DPABNImTEGCOOtBu]OTs** in acetonitrile.

Chapter 4

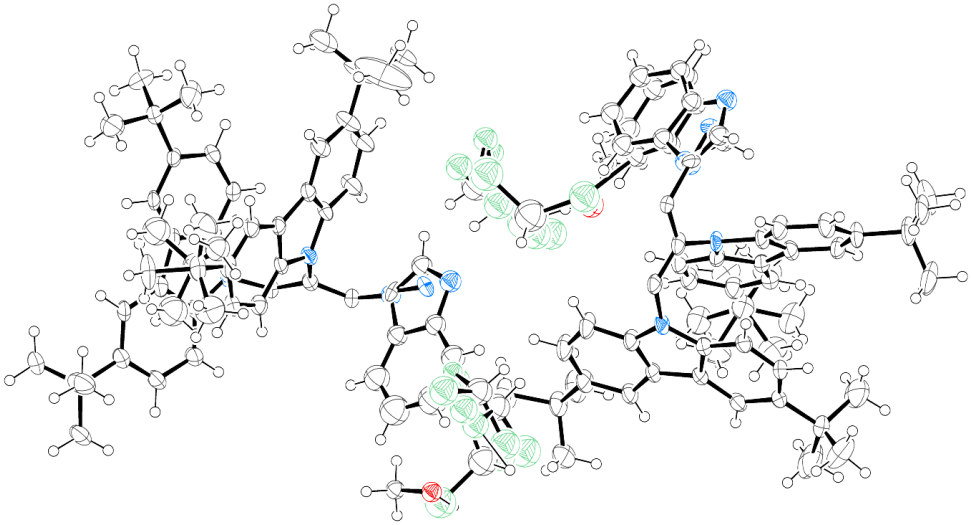
4.1 XRD analysis – Structural characterization

Table A4.1. Crystallographic data and refinement details.

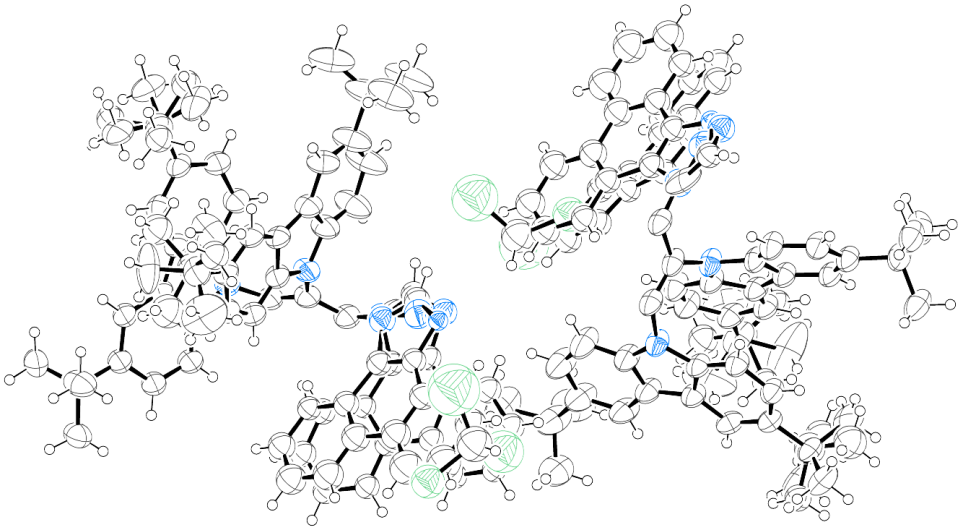
	4^{tBu}CzBNBenzIm	**4^{tBu}CzBNPhenIm**	**4DPABNPhenIm**
CCDC Number	2322130	2322129	2284116
Chemical Formula	$C_{94}H_{101}N_7 \cdot CHCl_3 \cdot 3/2CH4O$	C102H105N7×1/2CHCl3	C70H49N7×1/2C6H14
Formula weight	1496.24 g/mol	1488.61 g/mol	1031.24 g/mol
Temperature	100(2) K	100(2) K	100(2) K
Wavelength	0.620 Å	0.620 Å	0.620 Å
Crystal system	Triclinic	Triclinic	Triclinic
Space Group	*P* -1	*P* -1	*P* -1
Unit cell dimensions	*a* = 12.542(3) Å *b* = 18.330(4) Å *c* = 19.990(4) Å *α* = 106.30(3)° *β* = 90.11(3)° *γ* = 96.82 (3)	*a* = 12.123(2) Å *b* = 18.406(4) Å *c* = 20.343(4) Å *α* = 106.59(3)° *β* = 90.07(3)° *γ* = 97.26(3)	*a* = 12.101(2) Å *b* = 17.185(3)Å *c* = 27.914(6) Å *α* = 103.09(3)° *β* = 95.77(3)° *γ* = 98.85(3)
Volume	4376.7(17) Å3	4312.2(17) Å3	5531(2) Å^3
Z	2	2	4
Density (calculated)	1.135 g·cm^{-3}	1.146 g·cm^{-3}	1.238 g·cm^{-3}
Absorption coefficient	0.110 mm^{-1}	0.081 mm^{-1}	0.056 mm^{-1}
F(000)	1598	1590	2172
Theta range for data collection	0.9° to 22.1°	0.9° to 31.1°	0.7° to 28.1°
Index ranges	-15 ≤ h ≤ 15, -22 ≤ k ≤ 22, -24 ≤ l ≤ 24	-18 ≤ h ≤ 18, -29 ≤ k ≤ 29, -32 ≤ l ≤ 32	-17 ≤ h ≤ 17, -25 ≤ k ≤ 25, -41 ≤ l ≤ 42
Resolution	0.82 Å	0.66 Å	0.66 Å
Reflections collected	80457	189029	172670
Independent reflections	15867, 13514 data with I>2σ(I)	34744, 17763 data with I>2σ(I)	30749, 14991 data with I>2σ(I)
Data multiplicity (max resltn)	2.40 (2.40)	4.53 (1.97)	4.24 (0.97)
I/σ(I) (max resltn)	4.73 (3.41)	6.63 (0.91)	5.88 (0.65)
R_{merge} (max resltn)	0.0785 (0.1431)	0.0780 (0.6619)	0.1026 (0.8119)
Data completeness (max resltn)	97.2% (98.2%)	83.2% (55.2%)	75.6% (31.1%)

Refinement method	Full-matrix least-squares on F^2	Full-matrix least-squares on F^2	Full-matrix least-squares on F^2
Data / restraints / parameters	15867 / 671 / 1121	34744 / 671 / 1165	30749 / 0 / 1441
Goodness-of-fit on F^2	0.915	1.068	1.030
Δ/σ_{max}	0.028	0.001	0.006
Final R indices [I>2σ(I)]	$R_1 = 0.1504$, $wR_2 = 0.3458$	$R_1 = 0.1431$, $wR_2 = 0.2818$	$R_1 = 0.0900$, $wR_2 = 0.2248$
R indices (all data)	$R_1 = 0.1623$, $wR_2 = 0.3549$	$R_1 = 0.20367$, $wR_2 = 0.3083$	$R_1 = 0.1713$, $wR_2 = 0.2770$
Largest diff. peak and hole	1.194 and -0.545 eÅ^{-3}	1.253 and -0.547 eÅ^{-3}	0.464 and -0.360 eÅ^{-3}
R.M.S. deviation from mean	0.111 eÅ^{-3}	0.078 eÅ^{-3}	0.058 eÅ^{-3}

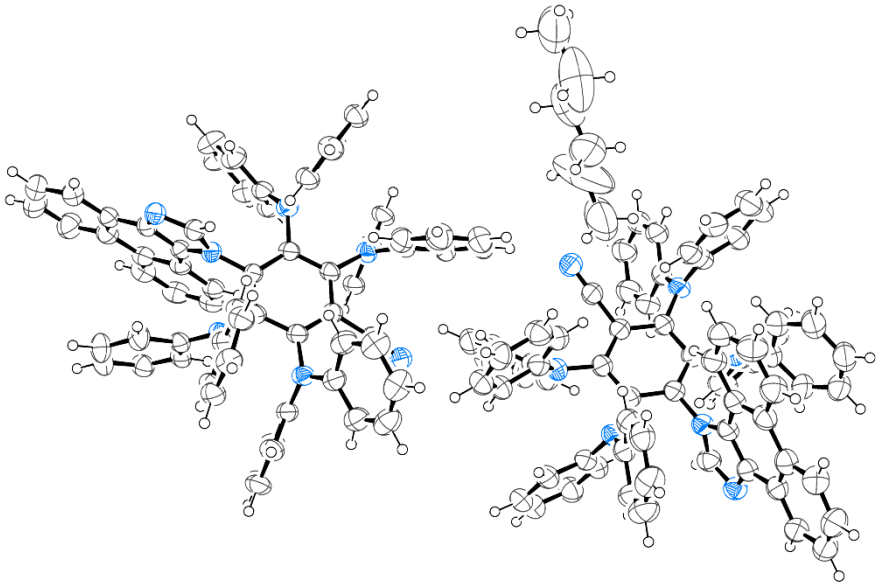
$R_1 = \Sigma \, ||Fo|-|Fc|| \, / \, \Sigma \, |Fo|$, $wR_2 = \{ \Sigma \, [w(Fo^2 - Fc^2)^2] \, / \, \Sigma \, [w(Fo^2)^2] \}^{½}$



(A)



(B)



(C)

Figure A4.1: Ellipsoids representation of **4^{tBu}CzBNBenzIm** (A), **4^{tBu}CzBNPhenIm** (B) and **4DPABNPhenIm** (C) at 100 K (A.S.U. - 50% probability).

4.2 ^{1}H NMR and ^{19}F{^{1}H} Spectra

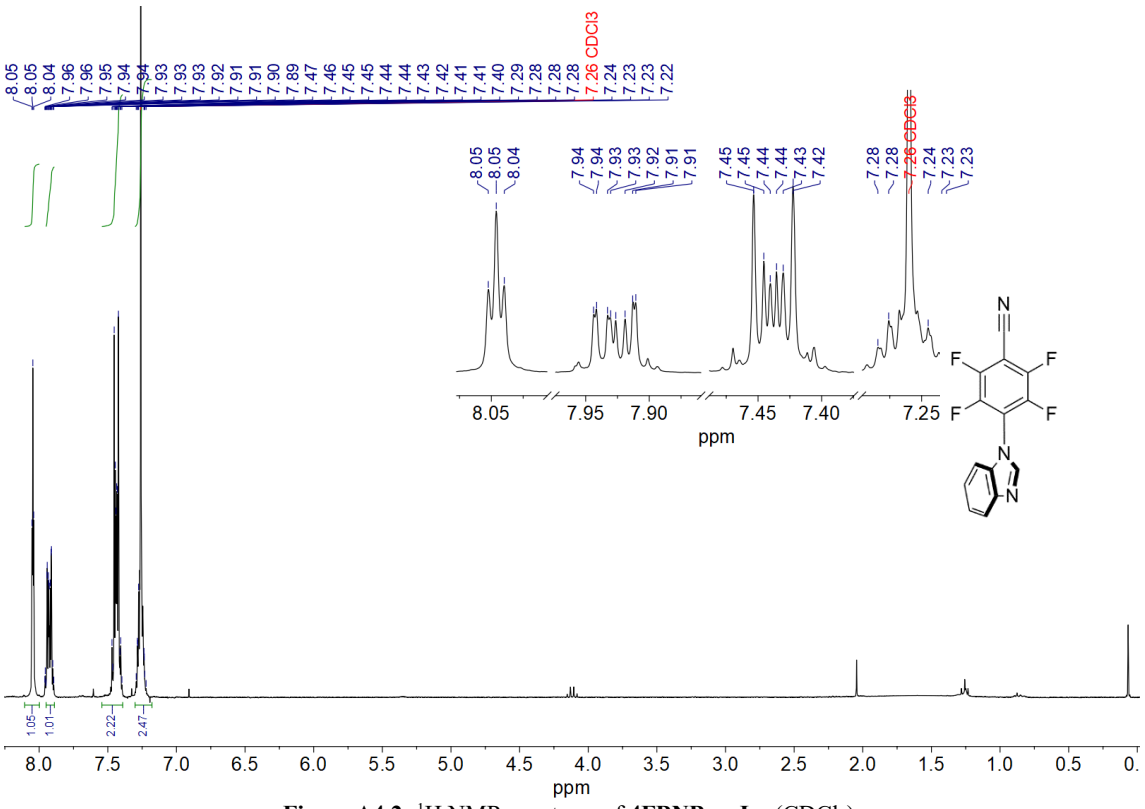


Figure A4.2: ^{1}H NMR spectrum of **4FBNBenzIm** ($CDCl_3$).

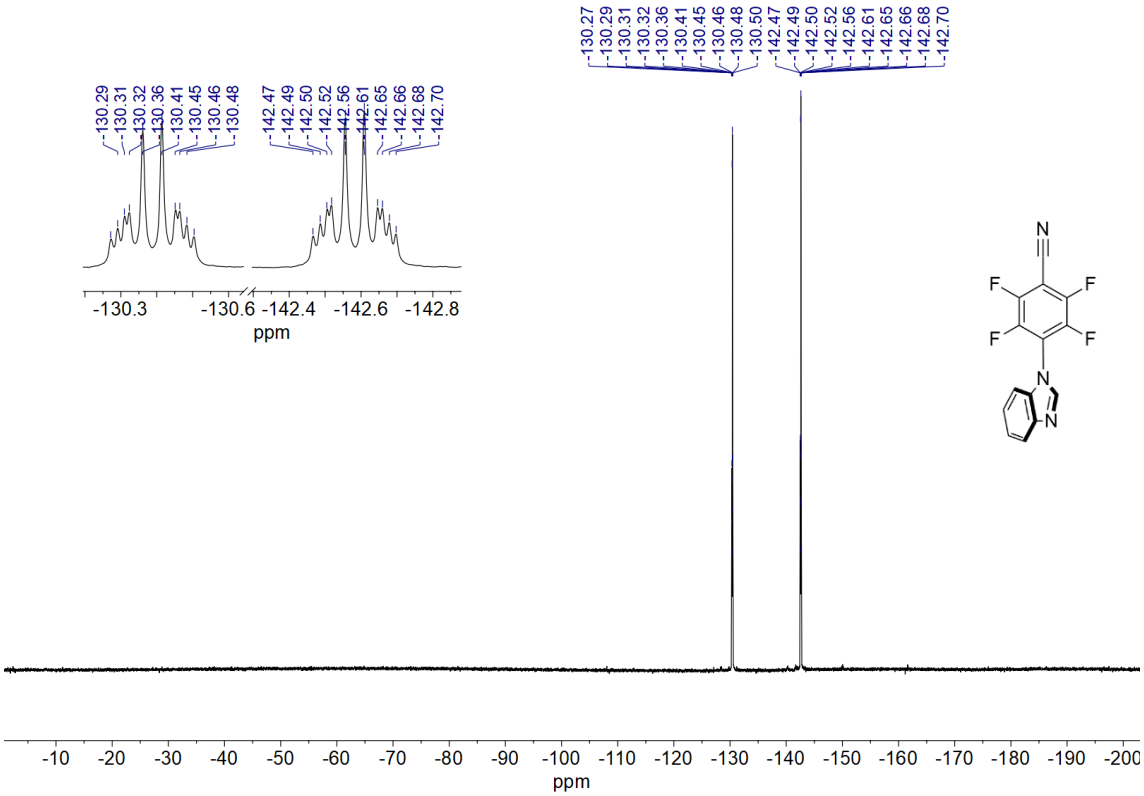


Figure A4.3: $^{19}F\{^{1}H\}$ NMR spectrum of **4FBNBenzIm** ($CDCl_3$).

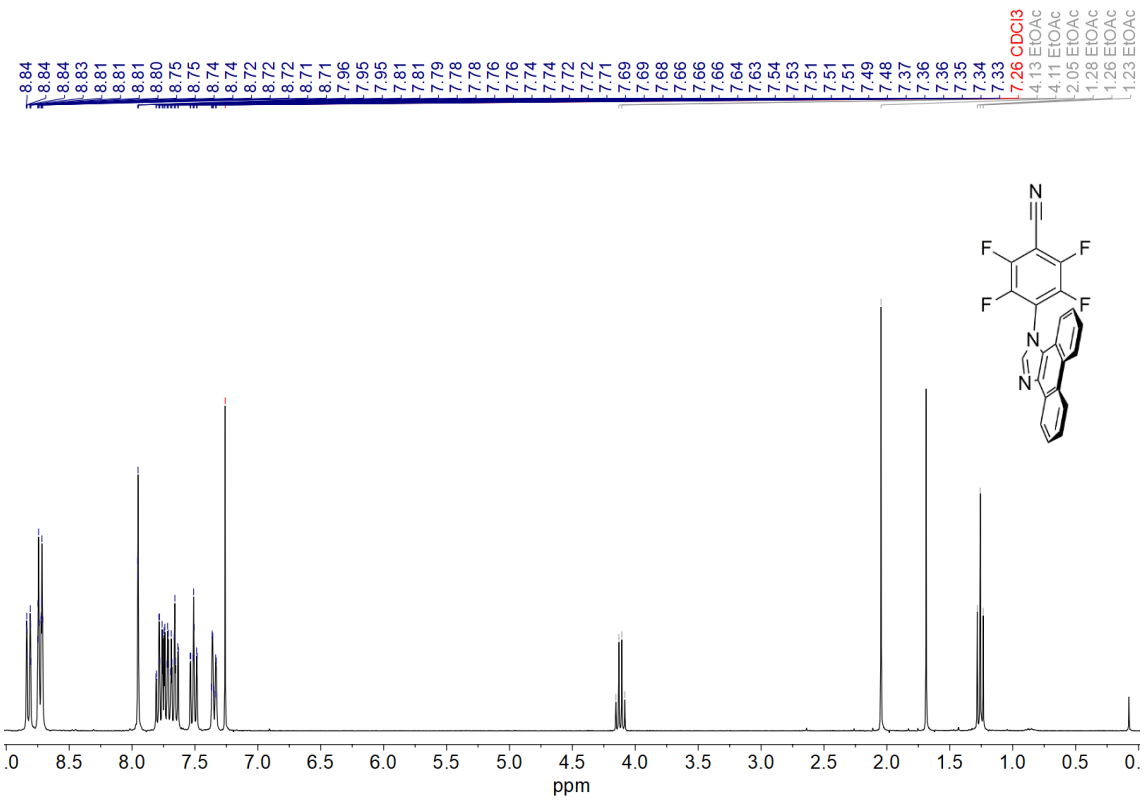


Figure A4.4: ^{1}H NMR spectrum of **4FBNPhenIm** ($CDCl_3$).

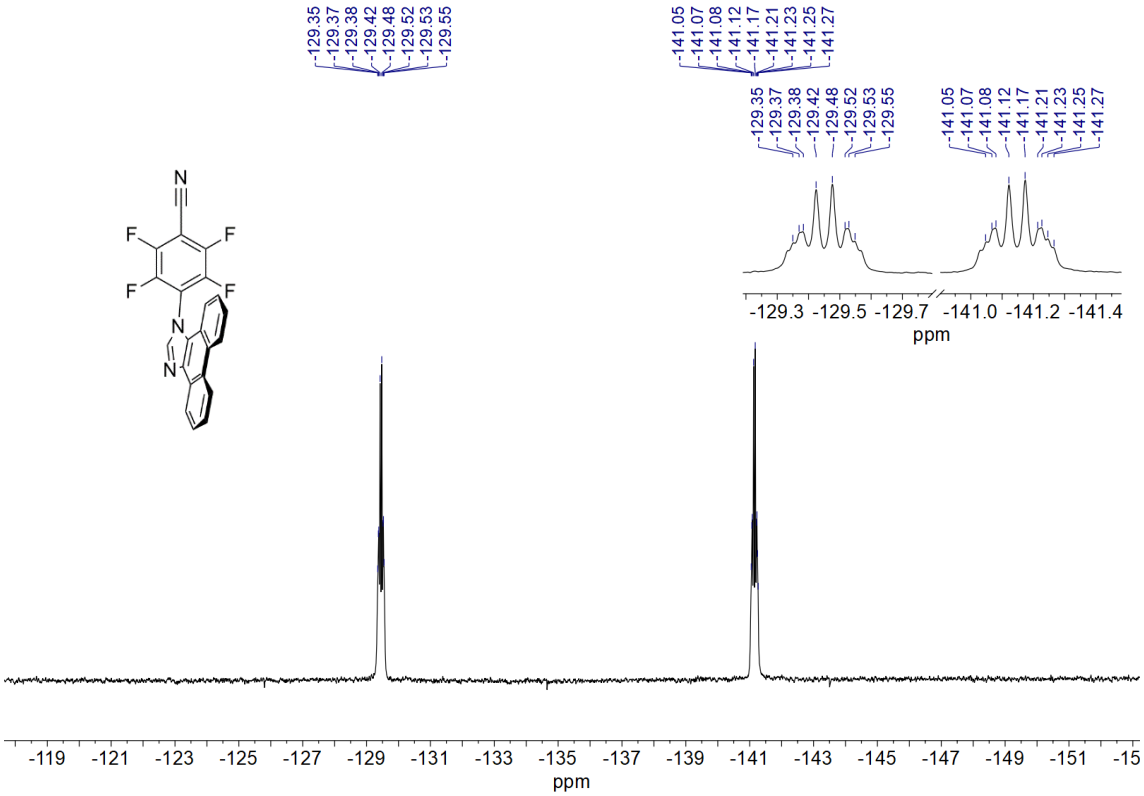


Figure A4.5: $^{19}F\{^{1}H\}$ NMR spectrum of **4FBNPhenIm** ($CDCl_3$).

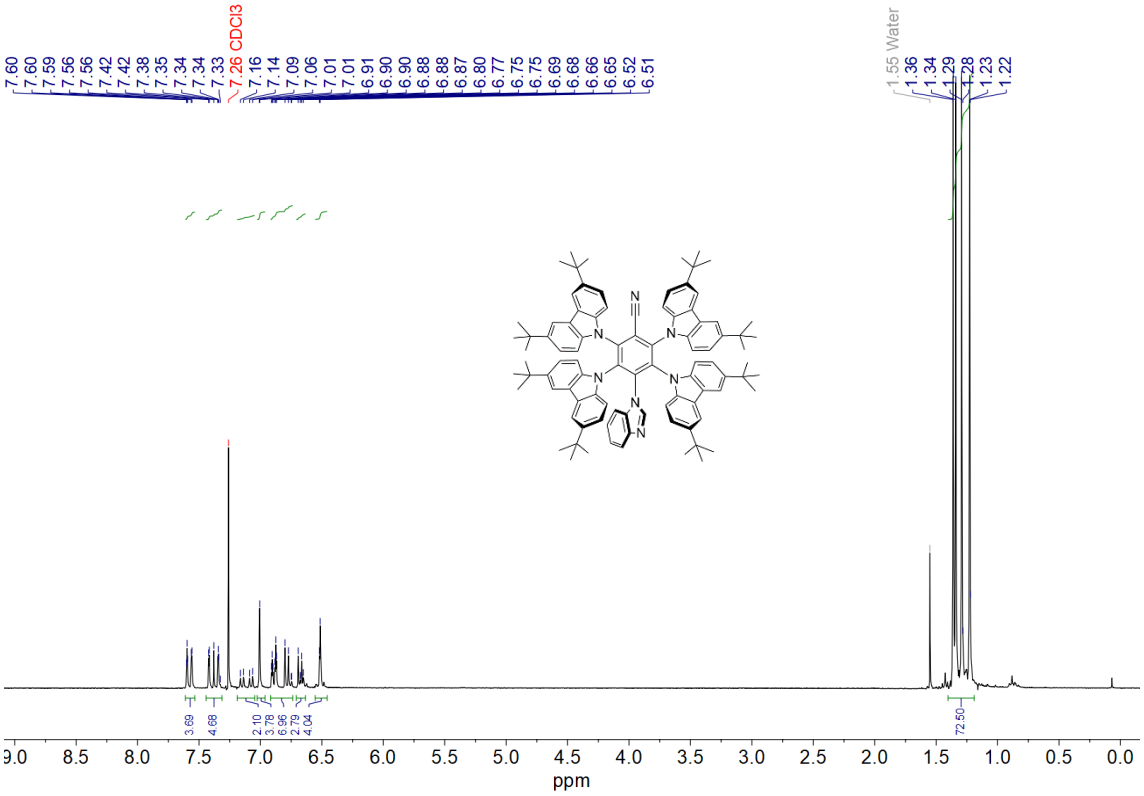


Figure A4.6: ^{1}H NMR spectrum of **4^{tBu}CzBNBenzIm** ($CDCl_3$).

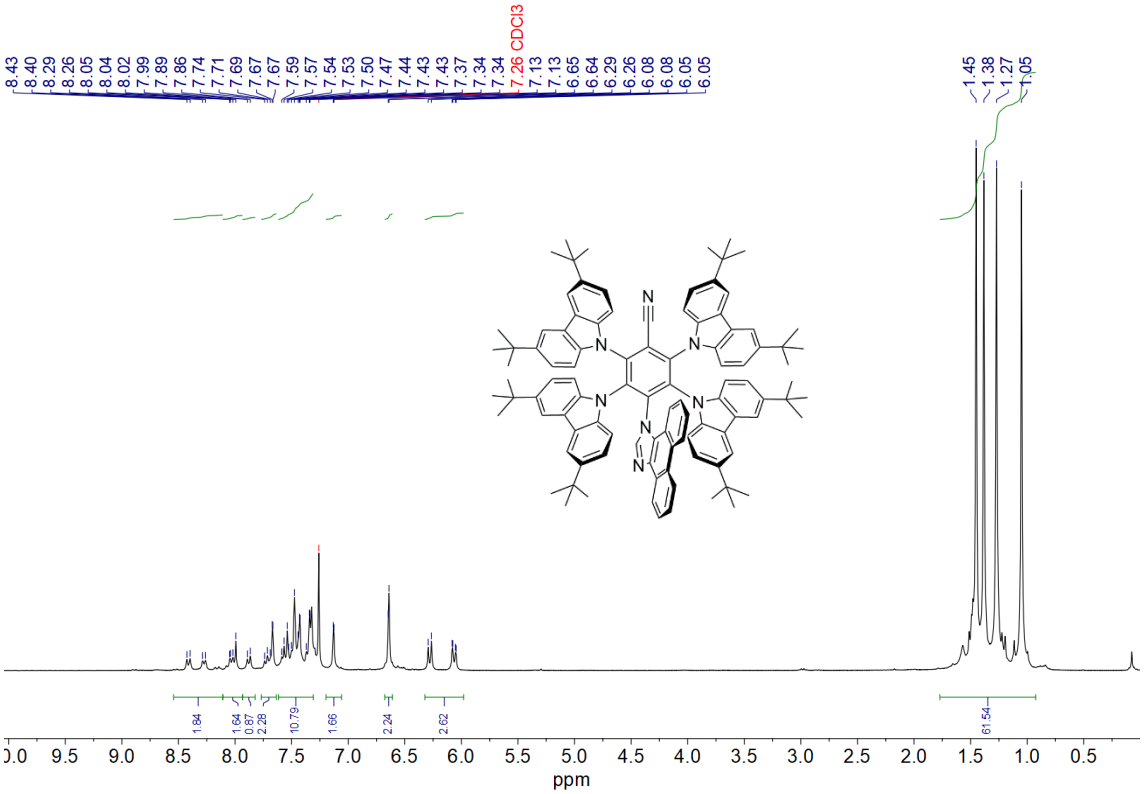


Figure A4.7: ^{1}H NMR spectrum of **4^{tBu}CzBNPhenIm** ($CDCl_3$).

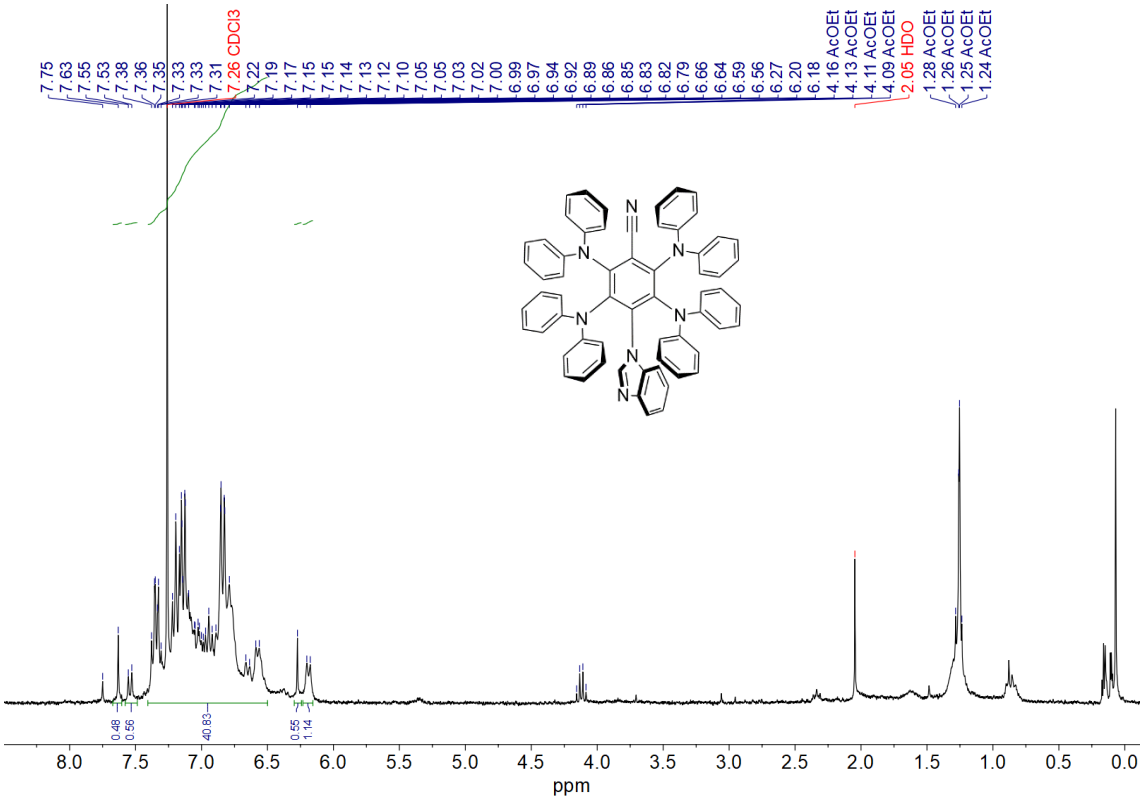


Figure A4.8: ^{1}H NMR spectrum of **4DPABNBenzIm** ($CDCl_3$).

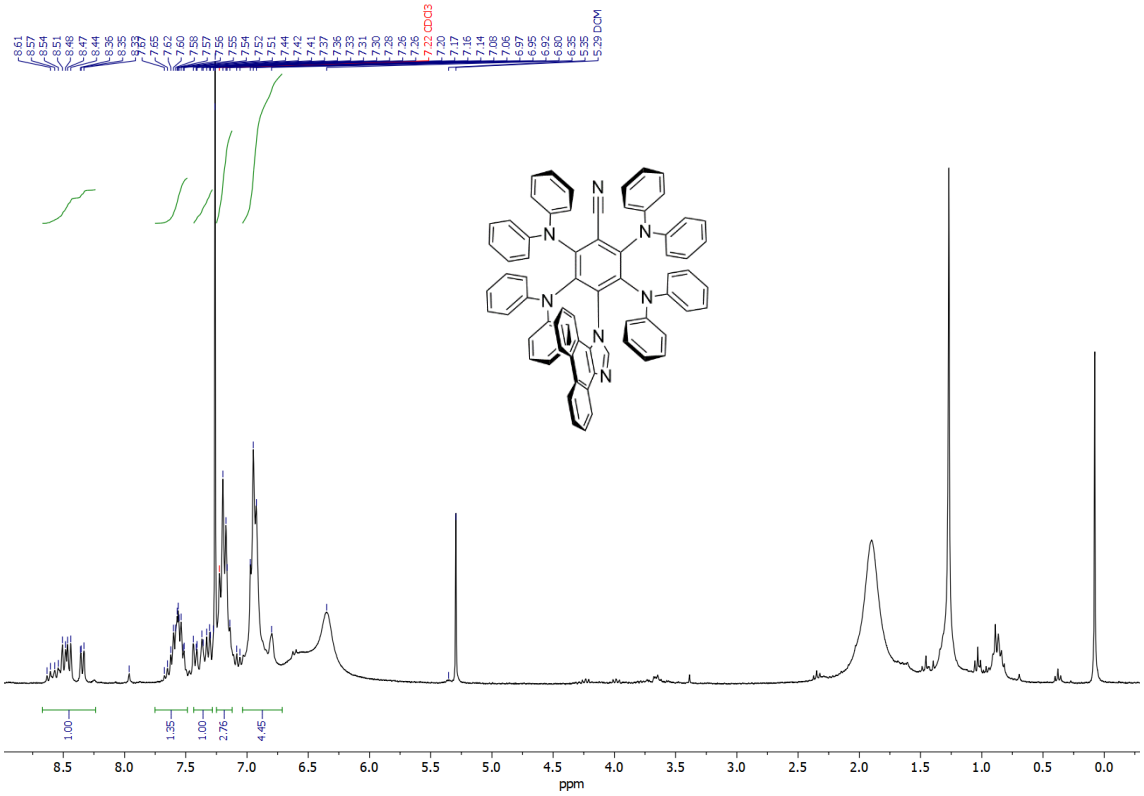


Figure A4.9: ^{1}H NMR spectrum of **4DPABNPhenIm** ($CDCl_3$).

4.3 $^{13}C\{^{1}H\}$ Spectra

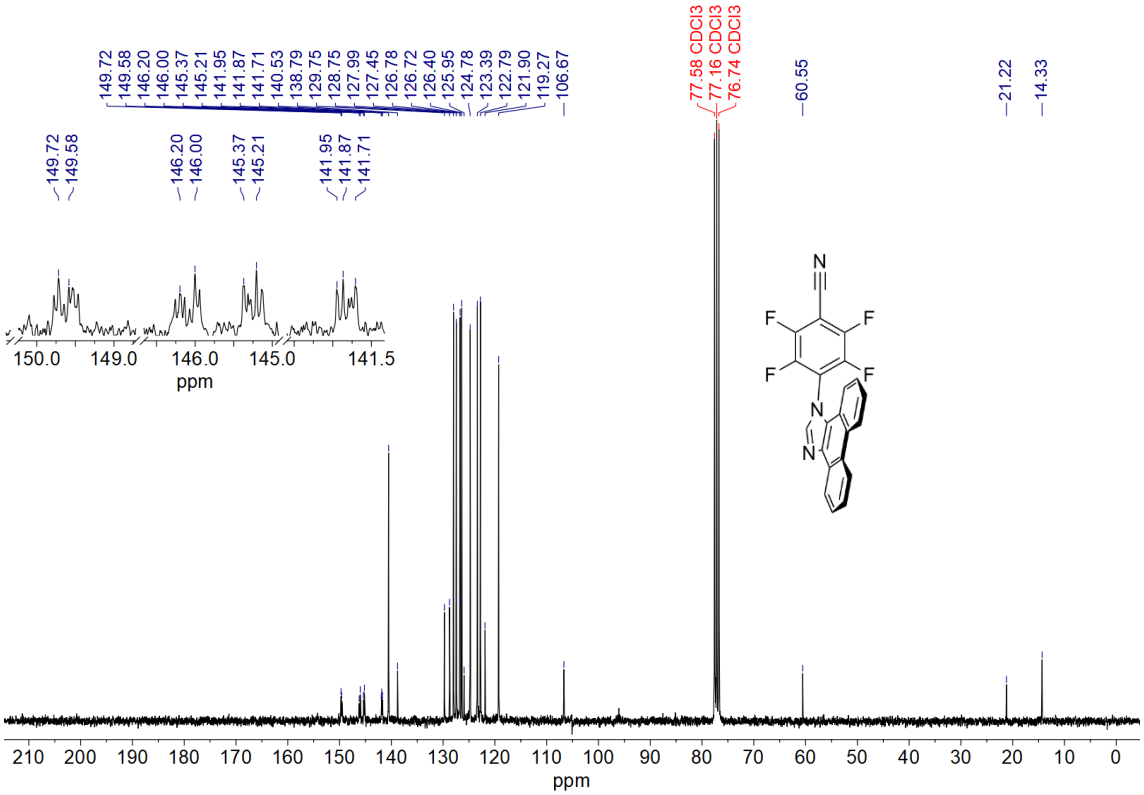


Figure A4.10: $^{13}C\{^{1}H\}$ NMR spectrum of **4FBNPhenIm** ($CDCl_3$).

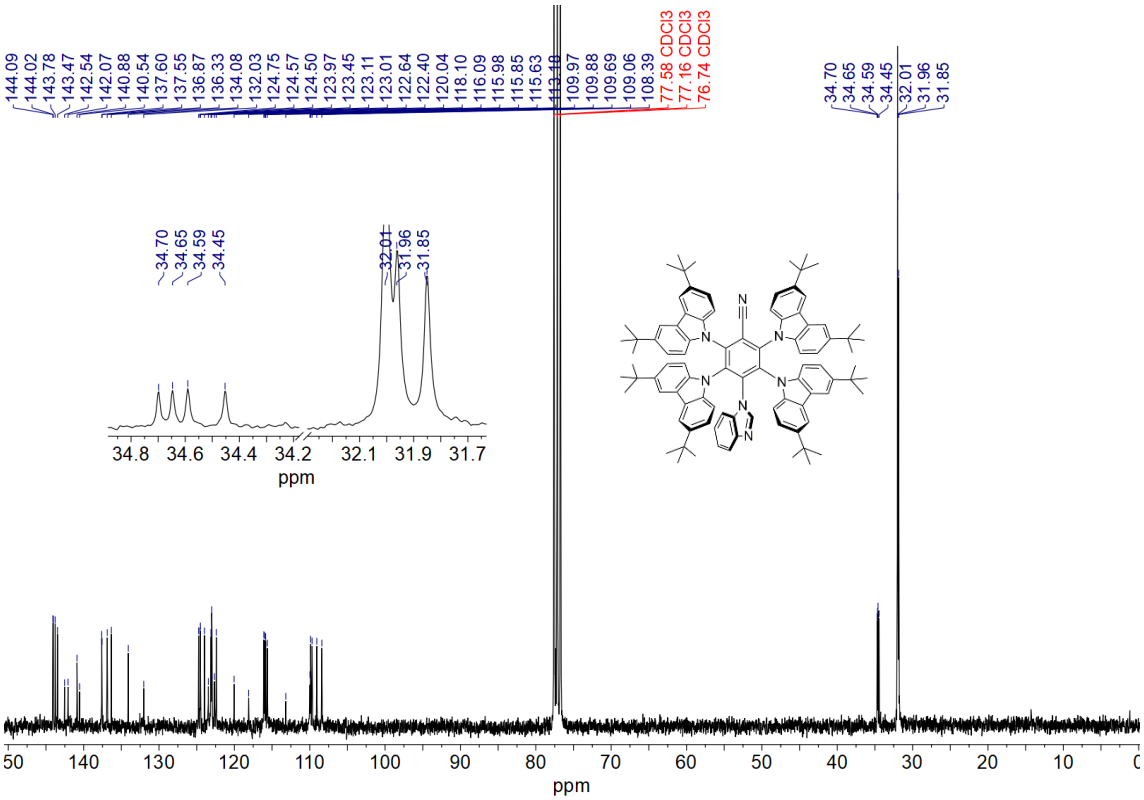


Figure A4.11: $^{13}C\{^{1}H\}$ NMR spectrum of **4^{tBu}CzBNBenzIm** ($CDCl_3$).

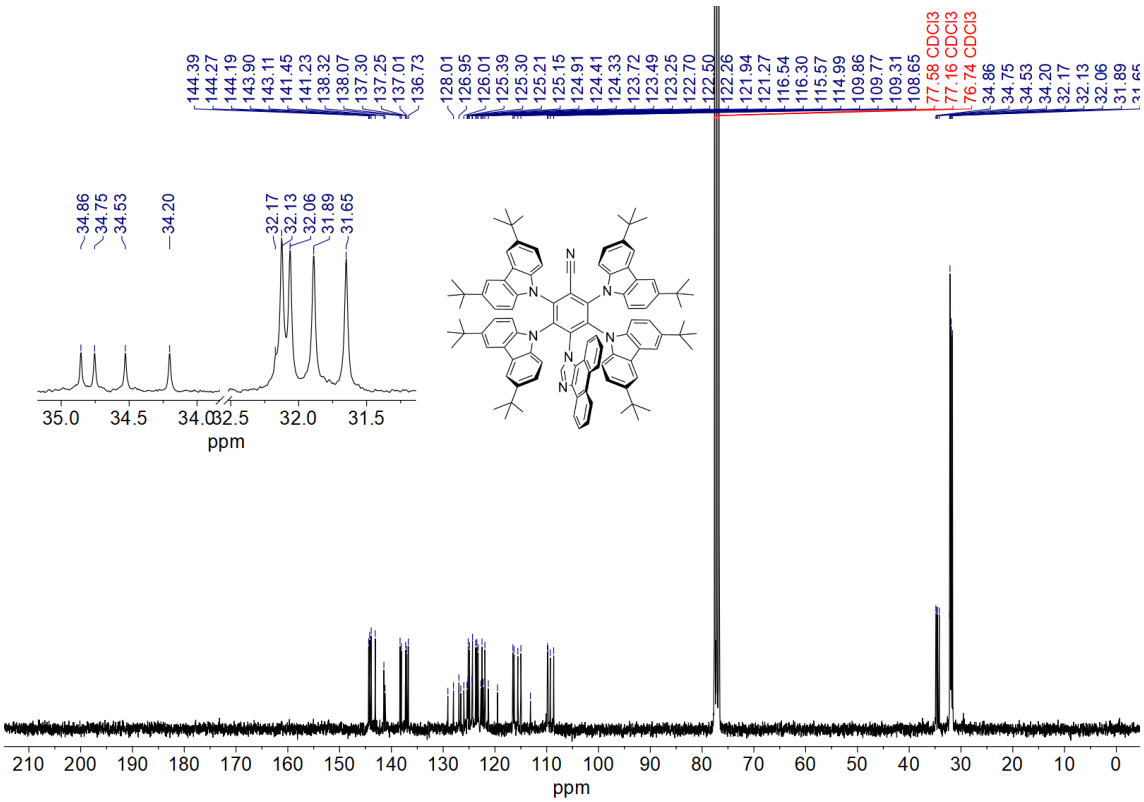


Figure A4.12: $^{13}C\{^{1}H\}$ NMR spectrum of **4^{tBu}CzBNPhenIm** ($CDCl_3$).

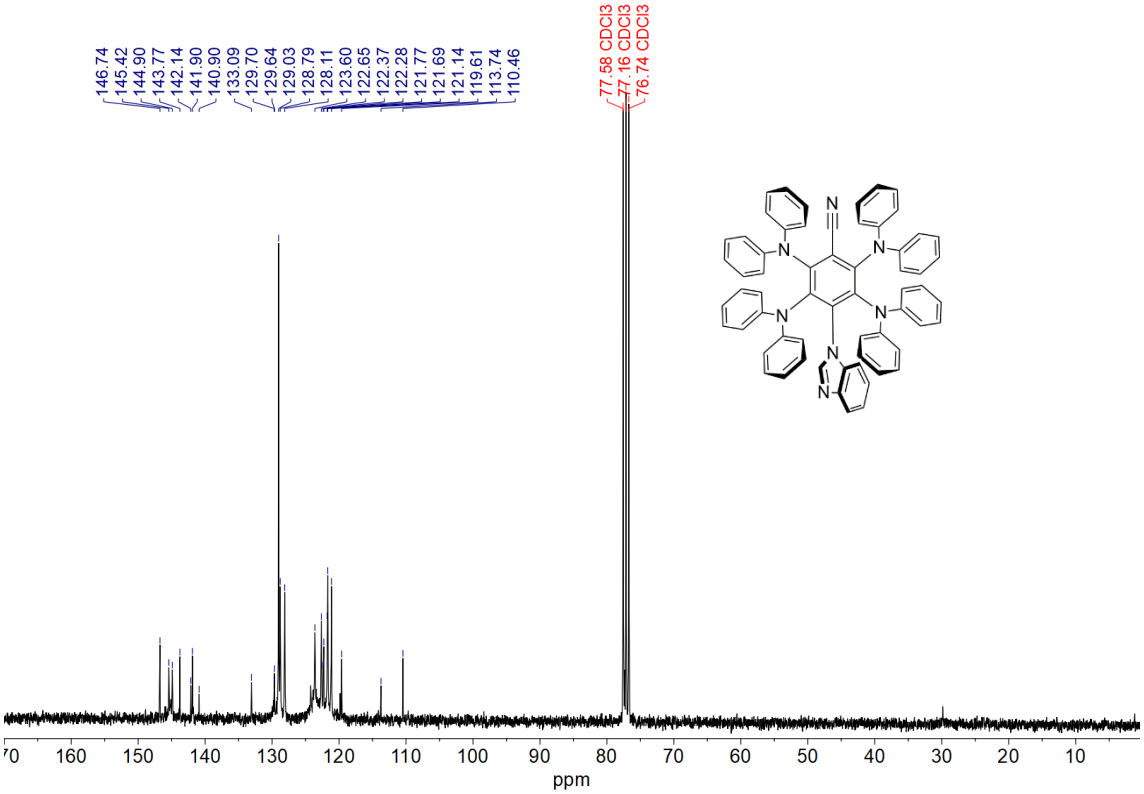


Figure A4.13: $^{13}C\{^{1}H\}$ NMR spectrum of **4DPABNBenzIm** ($CDCl_3$).

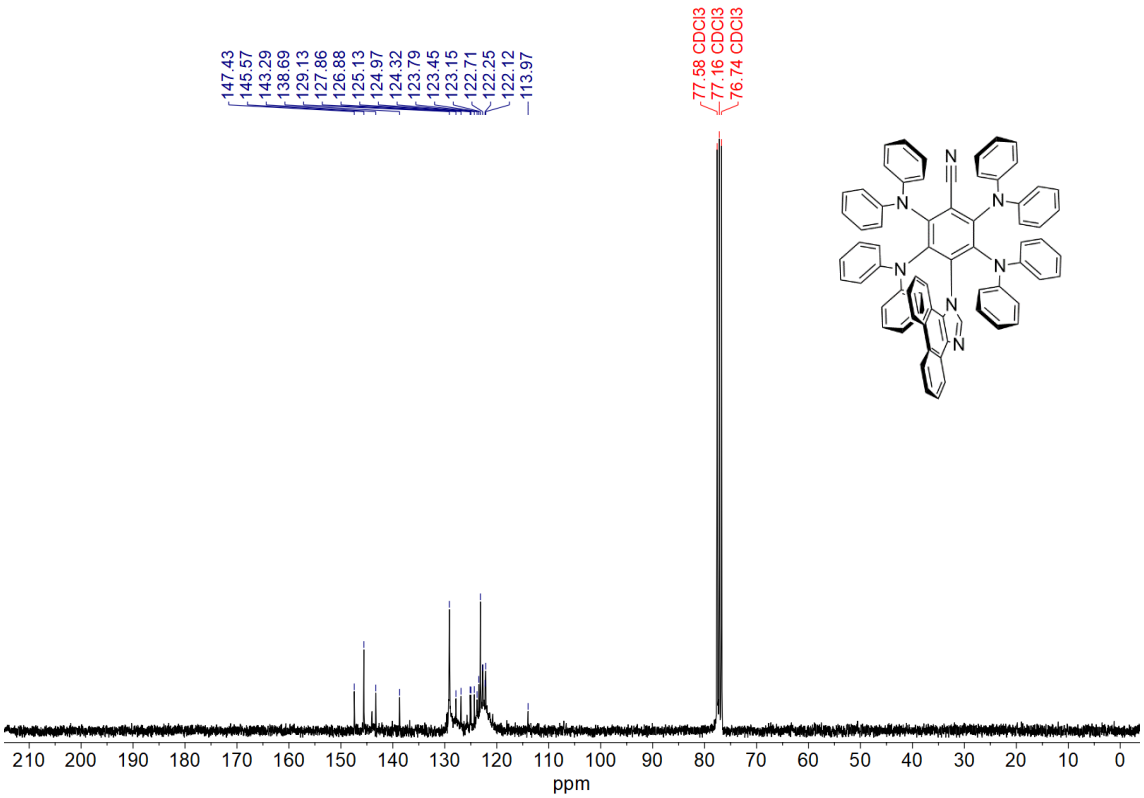


Figure 4.14: $^{13}C\{^{1}H\}$ NMR spectrum of **4DPABNPhenIm** ($CDCl_3$).

4.4 Absorption-excitation spectra comparisons

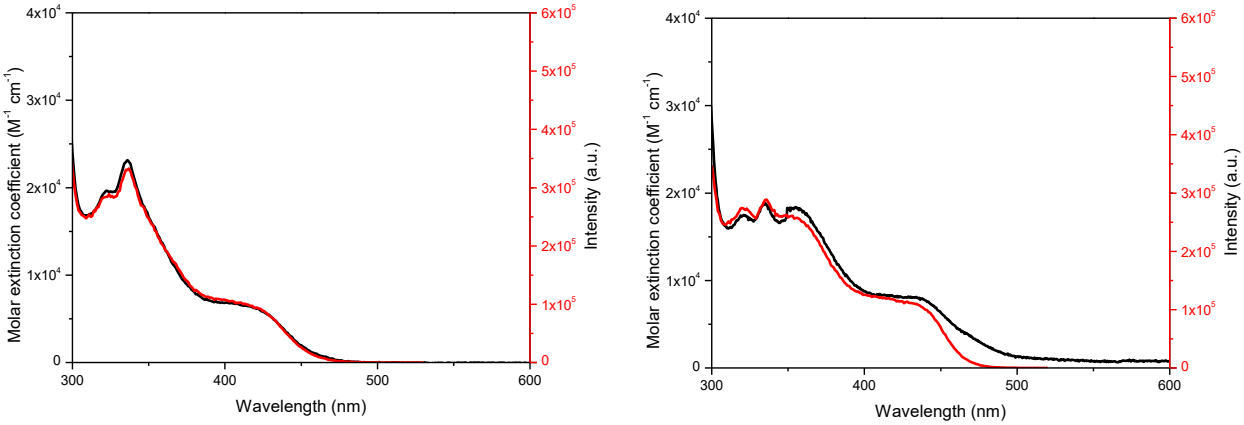


Figure A4.15: Absorption (black curve) and excitation (red curve) spectra of **4^{tBu}CzBNBenzIm** in acetonitrile (left) and dichloromethane (right).

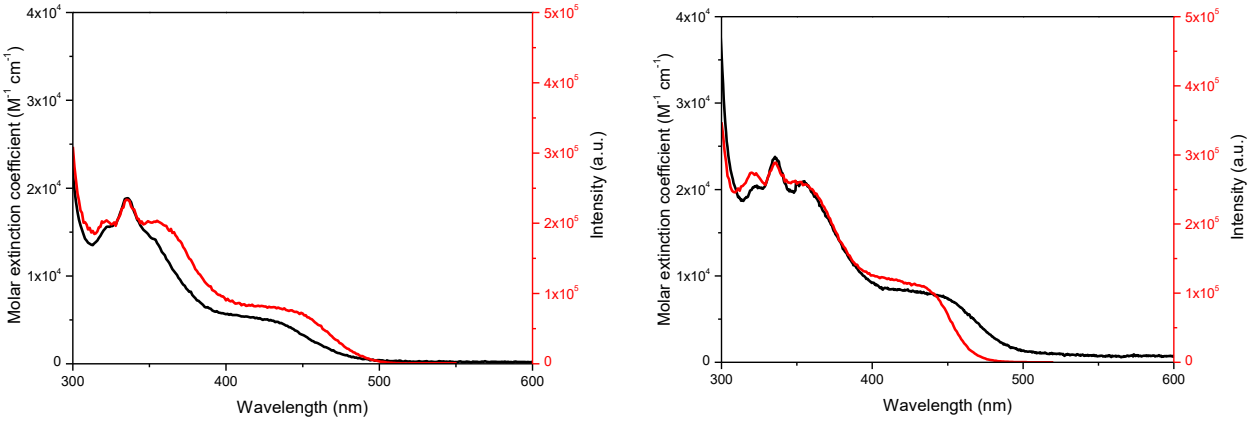


Figure A4.16: Absorption (black curve) and excitation (red curve) spectra of **4^{tBu}CzBNPhenIm** in acetonitrile (left) and dichloromethane (right).

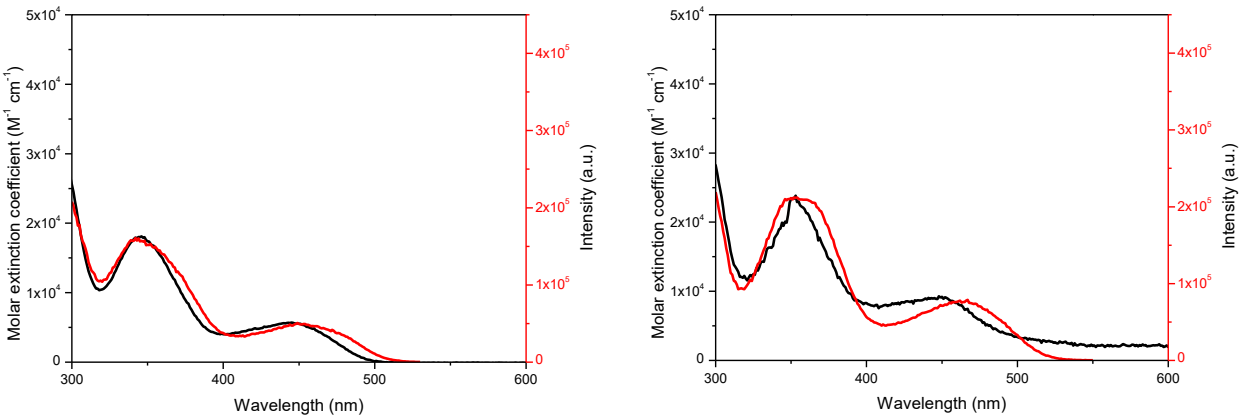


Figure A4.17: Absorption (black curve) and excitation (red curve) spectra of **4DPABNBenzIm** in acetonitrile (left) and dichloromethane (right).

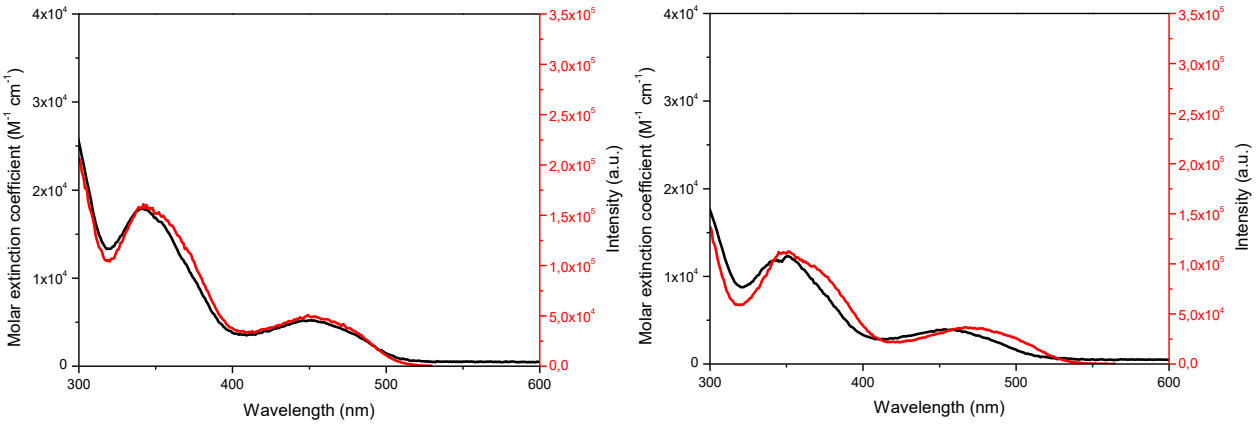


Figure A4.18: Absorption (black curve) and excitation (red curve) spectra of **4DPABNPhenIm** in acetonitrile (left) and dichloromethane (right).

4.5 Luminescent decays curves

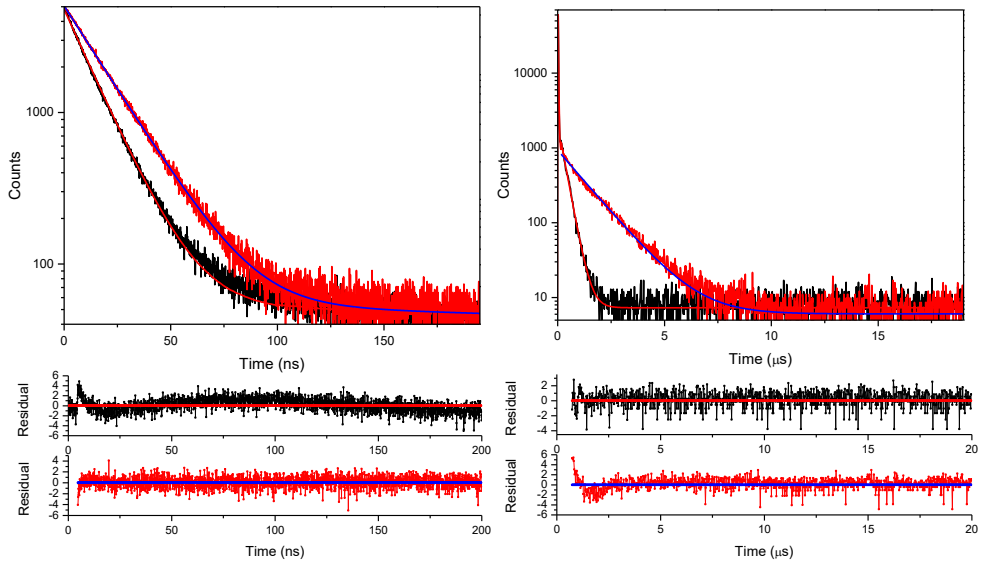


Figure A4.19: Luminescence decay curves of **4^{tBu}CzBNBenzIm** in aerated acetonitrile (black curves) and in Ar-purged acetonitrile solutions (red curves) with their fittings and residuals. Left: decays in the nanosecond scale; Right: decays in the microsecond scale.

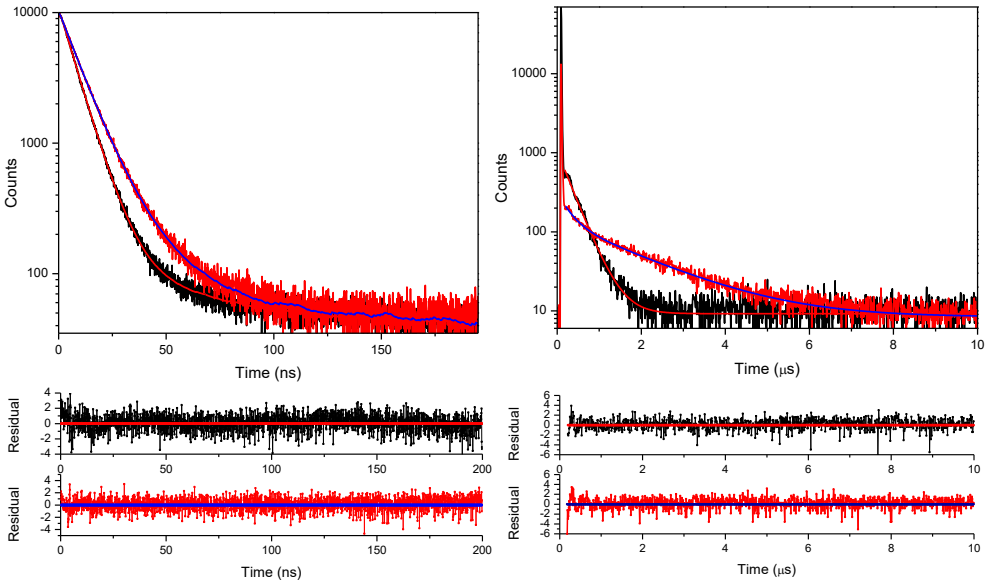


Figure A4.20: Luminescence decay curves of **4^{tBu}CzBNPhenIm** in aerated acetonitrile (black curves) and in Ar-purged acetonitrile solutions (red curves) with their fittings and residuals. Left: decays in the nanosecond scale; Right: decays in the microsecond scale.

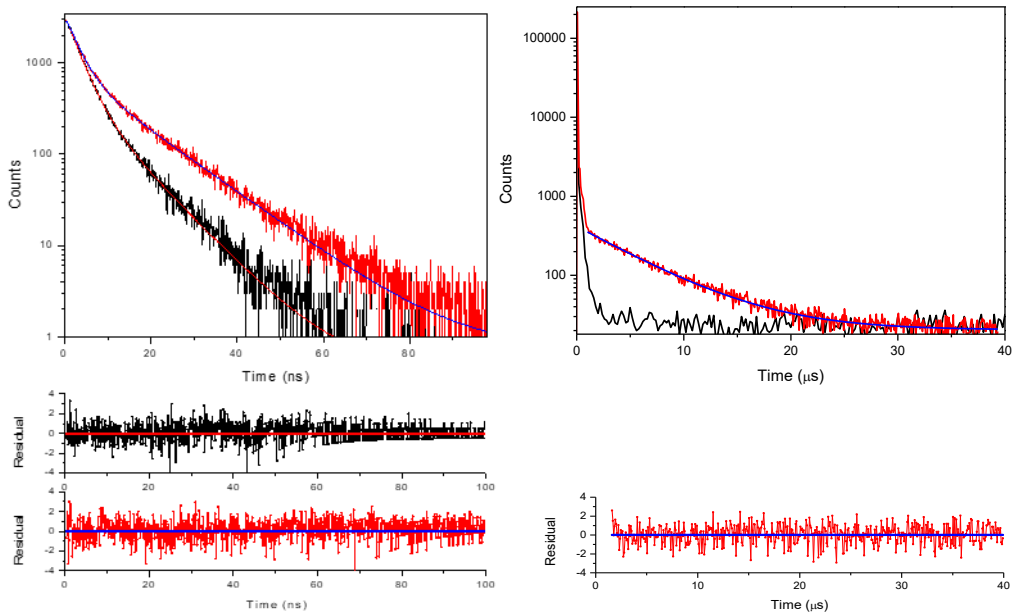


Figure A4.21: Luminescence decay curves of **4DPABNBenzIm** in aerated acetonitrile (black curves) and in Ar-purged acetonitrile solutions (red curves) with their fittings and residuals. Left: decays in the nanosecond scale; Right: decays in the microsecond scale.

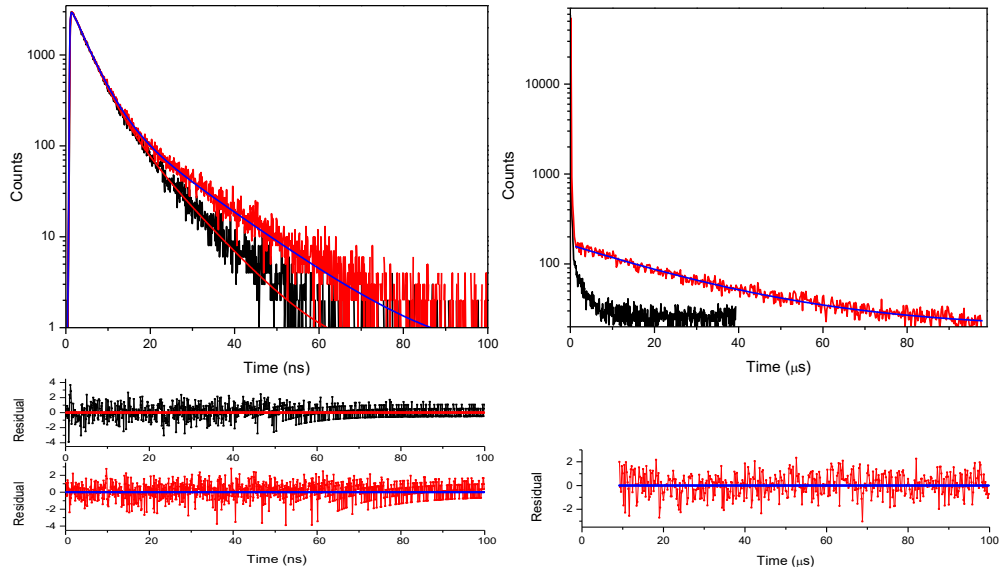


Figure A4.22: Luminescence decay curves of **4DPABNPhenIm** in aerated acetonitrile (black curves) and in Ar-purged acetonitrile solutions (red curves) with their fittings and residuals. Left: decays in the nanosecond scale; Right: decays in the microsecond scale.

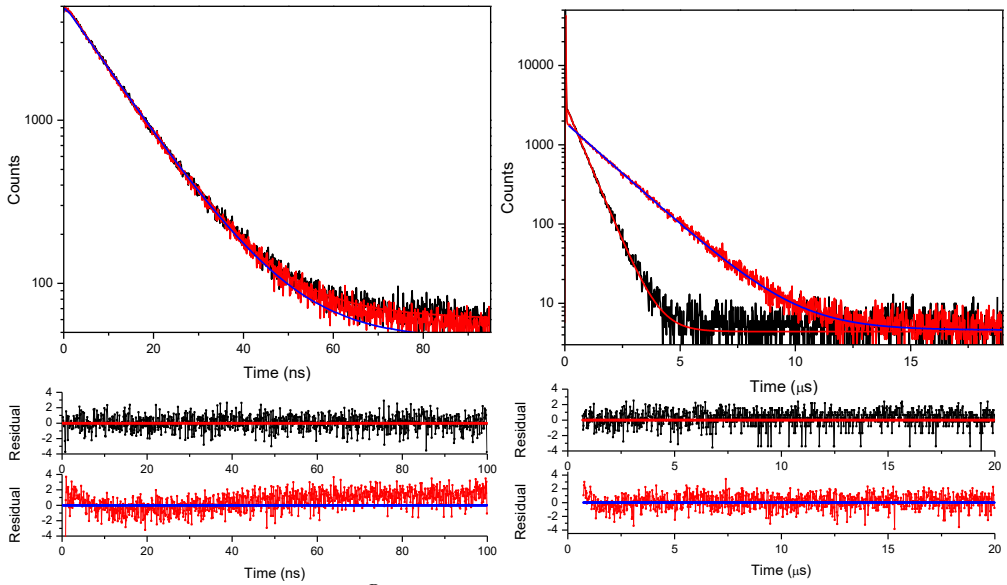


Figure A4.23: Luminescence decay curves of **4^{tBu}CzBNBenzIm** in aerated dichloromethane (black curves) and in Ar-purged dichloromethane solutions (red curves) with their fittings and residuals. Left: decays in the nanosecond scale; Right: decays in the microsecond scale.

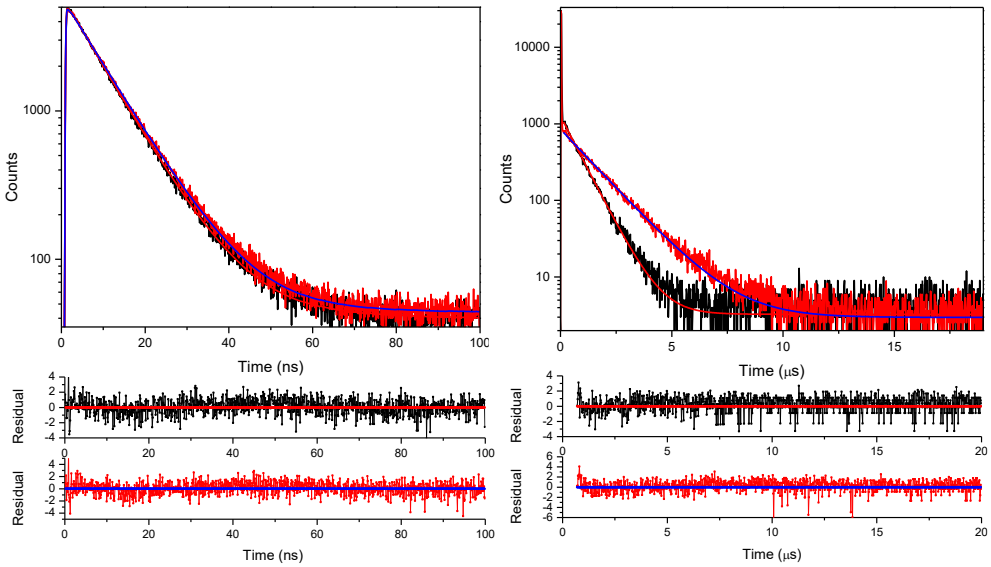


Figure A4.24: Luminescence decay curves of **4^{tBu}CzBNPhenIm** in aerated dichloromethane (black curves) and in Ar-purged dichloromethane solutions (red curves) with their fittings and residuals. Left: decays in the nanosecond scale; Right: decays in the microsecond scale.

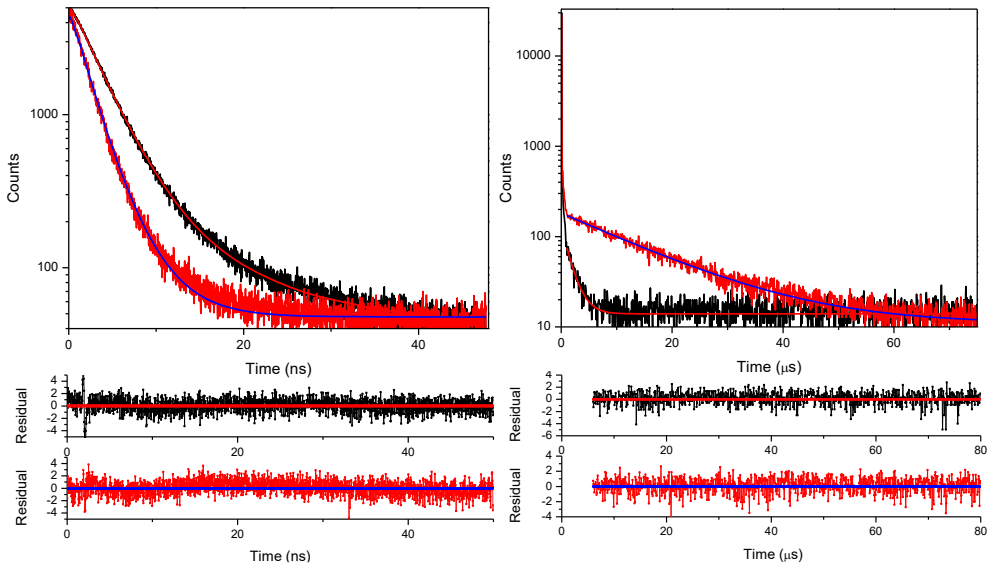


Figure A4.25: Luminescence decay curves of **4DPABNBenzIm** in aerated dichloromethane (black curves) and in Ar-purged dichloromethane solutions (red curves) with their fittings and residuals. Left: decays in the nanosecond scale; Right: decays in the microsecond scale.

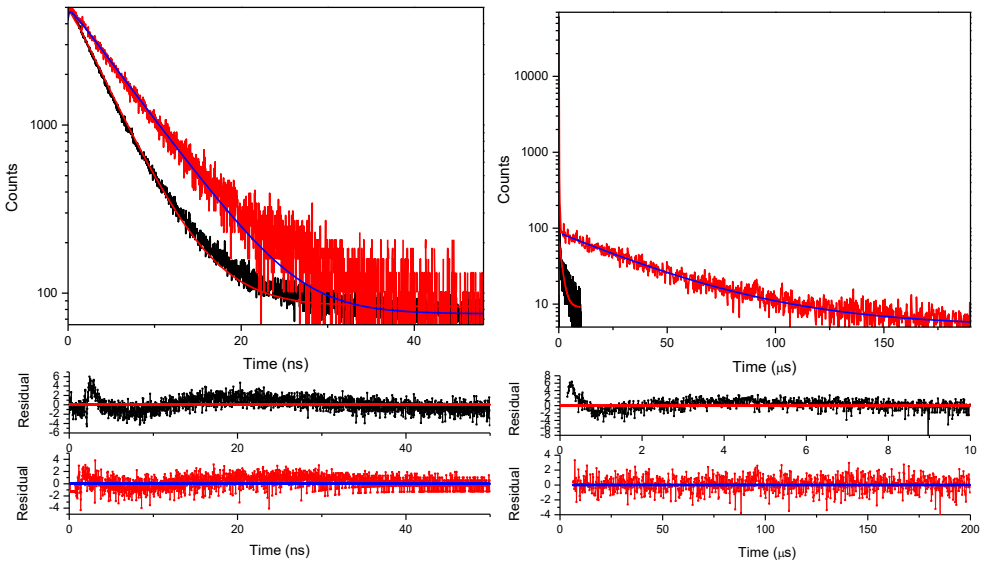


Figure A4.26: Luminescence decay curve of **4DPABNPhenIm** in aerated dichloromethane (black curves) and in Ar-purged dichloromethane (red curves) with their fittings and residuals. Left: decays in the nanosecond scale; Right: decays in the microsecond scale.

4.6 Electrochemical characterization

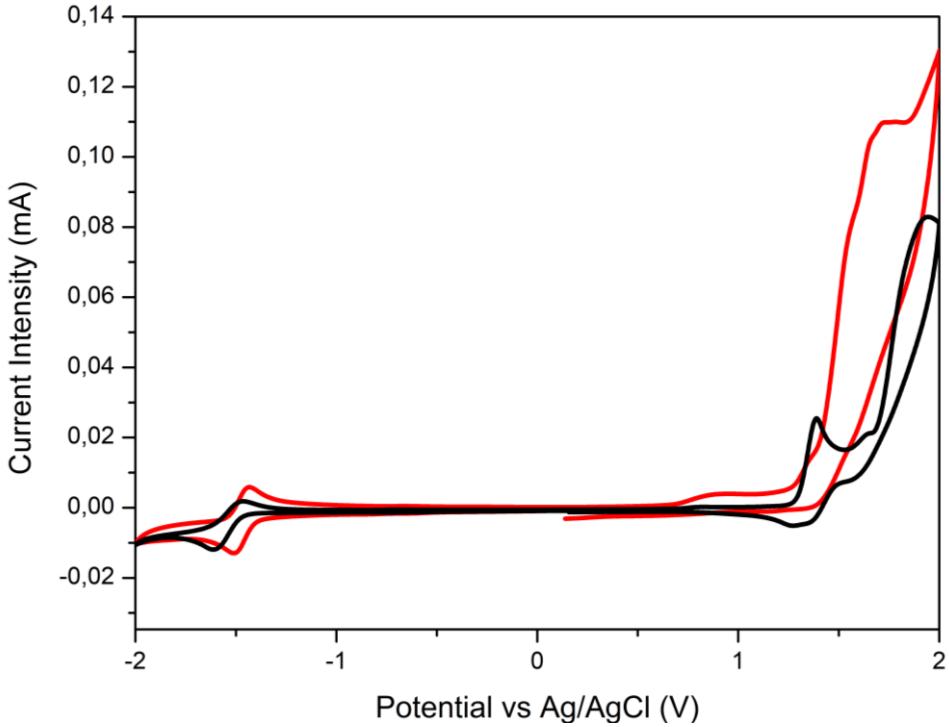


Figure A4.27: CV of **4^{tBu}CzBNBenzIm** in acetonitrile (red curve) and dichloromethane (black curve).

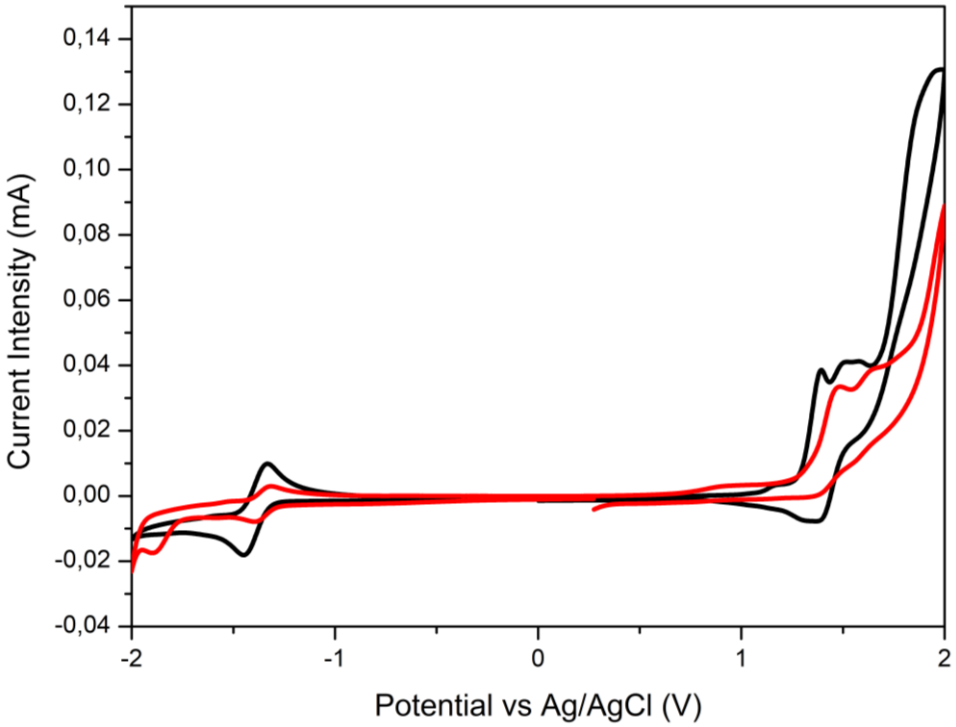


Figure A4.28: CV of **4^{tBu}CzBNPhenIm** in acetonitrile (red curve) and dichloromethane (black curve).

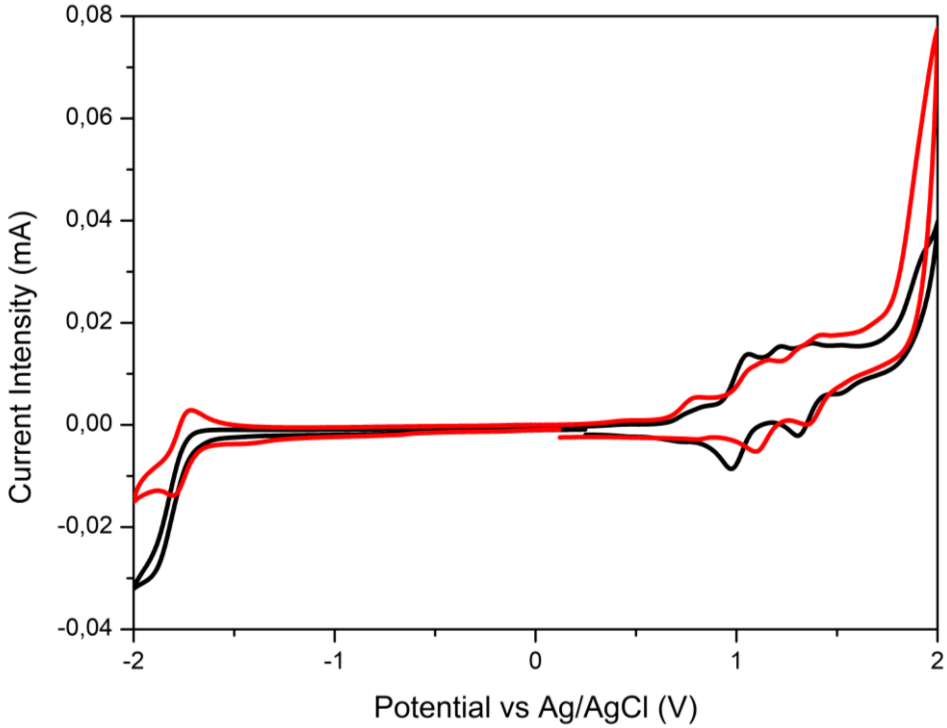


Figure A4.29: CV of **4DPABNBenzIm** in acetonitrile (red curve) and dichloromethane (black curve).

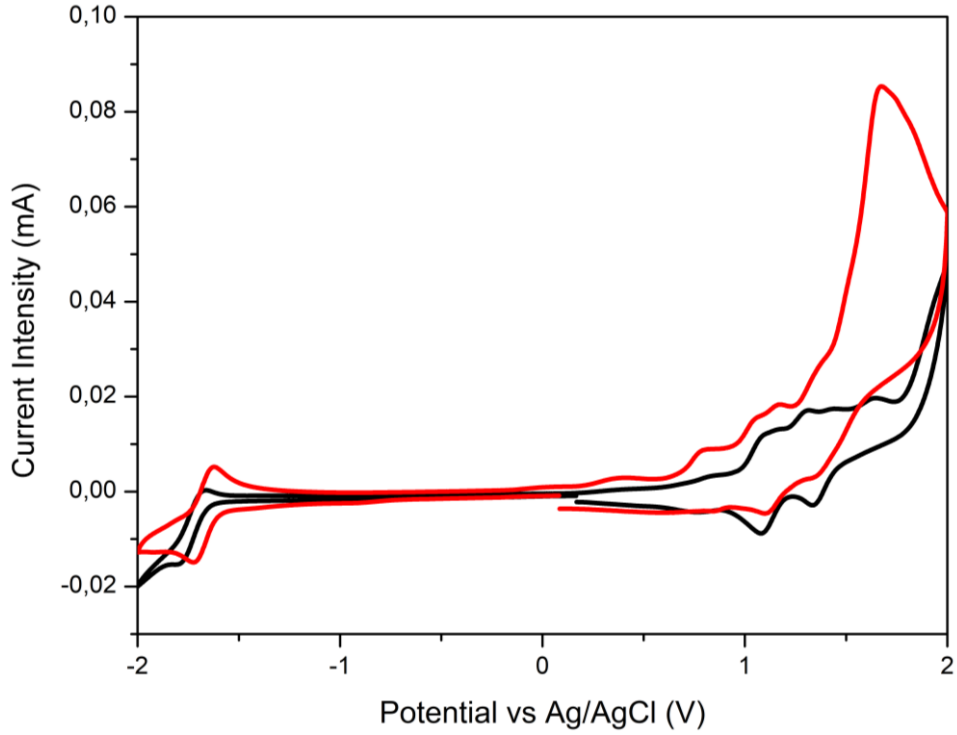


Figure A4.30: CV of **4DPABNPhenIm** in acetonitrile (red curve) and dichloromethane (black curve).

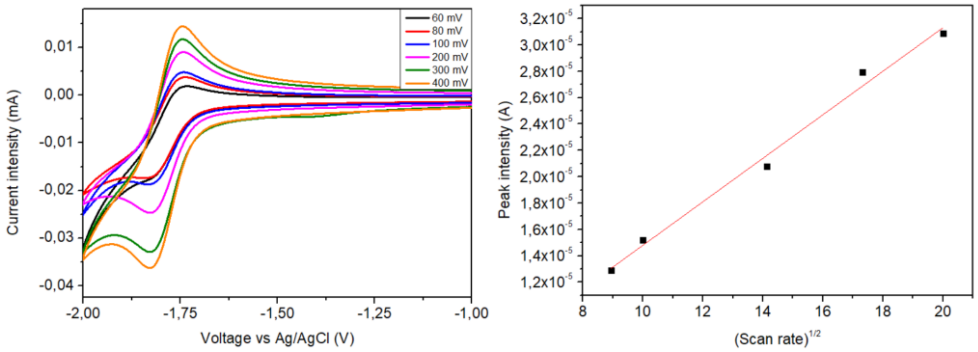


Figure A4.31: Cyclic voltammetries at different scan rates of compound **4DPABNIm** in acetonitrile (left) and plot of i_{pc} over square root of scan rate (right, the equation is $y = 1.65 \cdot 10^{-6}x - 1.72 \cdot 10^{-6}$).

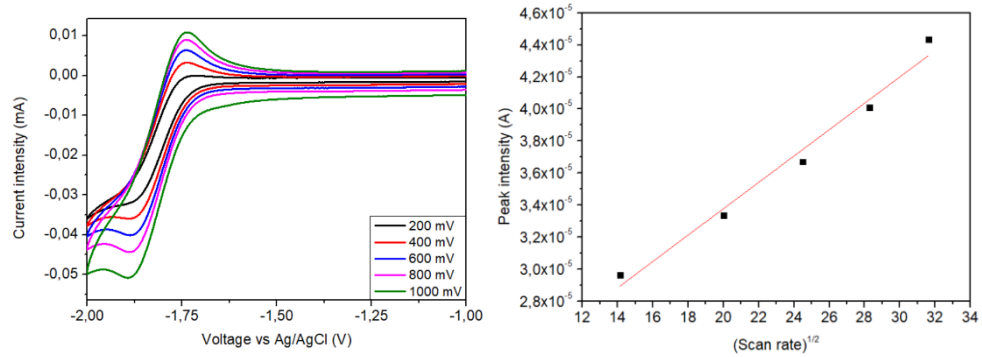


Figure A4.32: Cyclic voltammetries at different scan rates of compound **4DPABNIm** in dichloromethane (left) and plot of i_{pc} over square root of scan rate (right, the equation is $y = 8.23 \cdot 10^{-7}x - 1.73 \cdot 10^{-5}$).

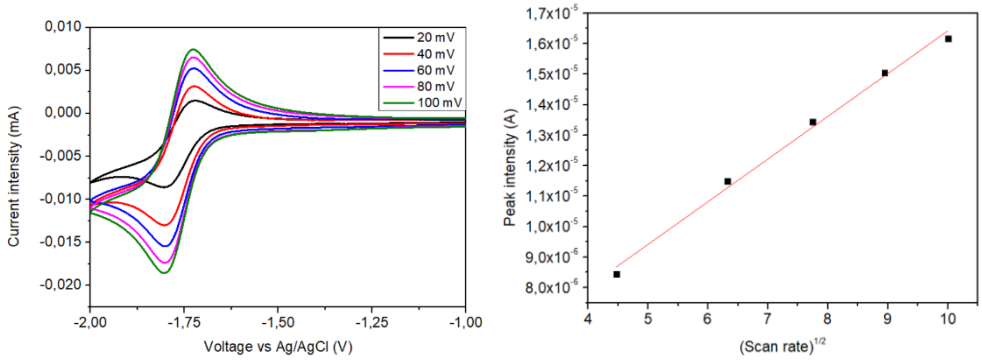


Figure A4.33: Cyclic voltammetries at different scan rates of compound **4DPABNBenzIm** in acetonitrile (left) and plot of i_{pc} over square root of scan rate (right, the equation is $y = 1.4 \cdot 10^{-6}x - 2.42 \cdot 10^{-6}$).

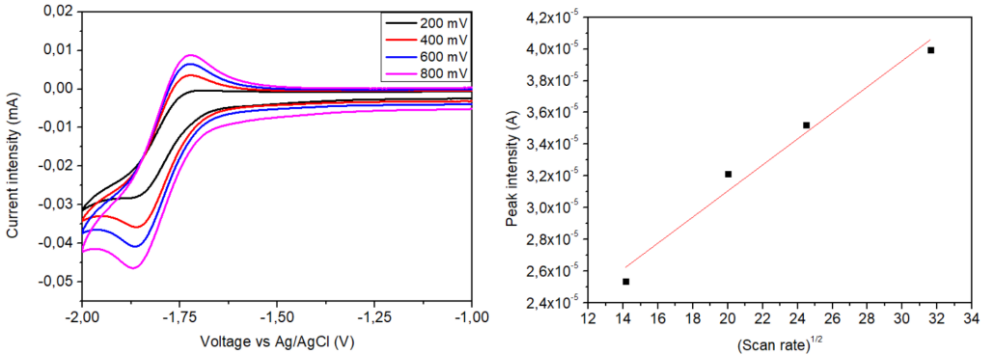


Figure A4.34: Cyclic voltammetries at different scan rates of compound **4DPABNBenzIm** in dichloromethane (left) and plot of i_{pc} over square root of scan rate (right, the equation is $y = 1.4 \cdot 10^{-5}x - 8.21 \cdot 10^{-7}$).

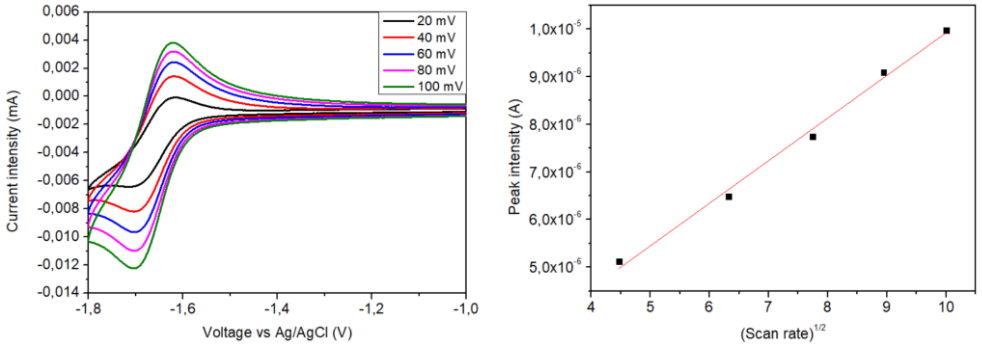


Figure A4.35: Cyclic voltammetries at different scan rates of compound **4DPABNBenzIm** in dichloromethane (left) and plot of i_{pc} over square root of scan rate (right, the equation is $y = 8.94 \cdot 10^{-7}x - 9.78 \cdot 10^{-7}$).

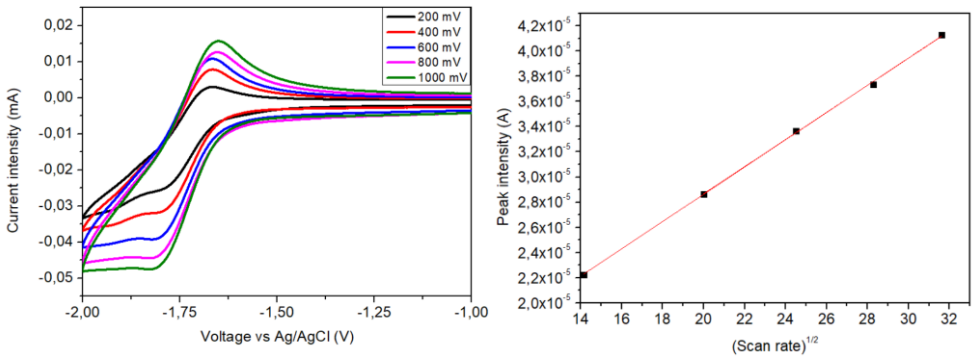


Figure A4.36: Cyclic voltammetries at different scan rates of compound **4DPABNBenzIm** in dichloromethane (left) and plot of i_{pc} over square root of scan rate (right, the equation is $y = 1.08 \cdot 10^{-6}x - 6.99 \cdot 10^{-6}$).

4.7 ECL-voltage curves

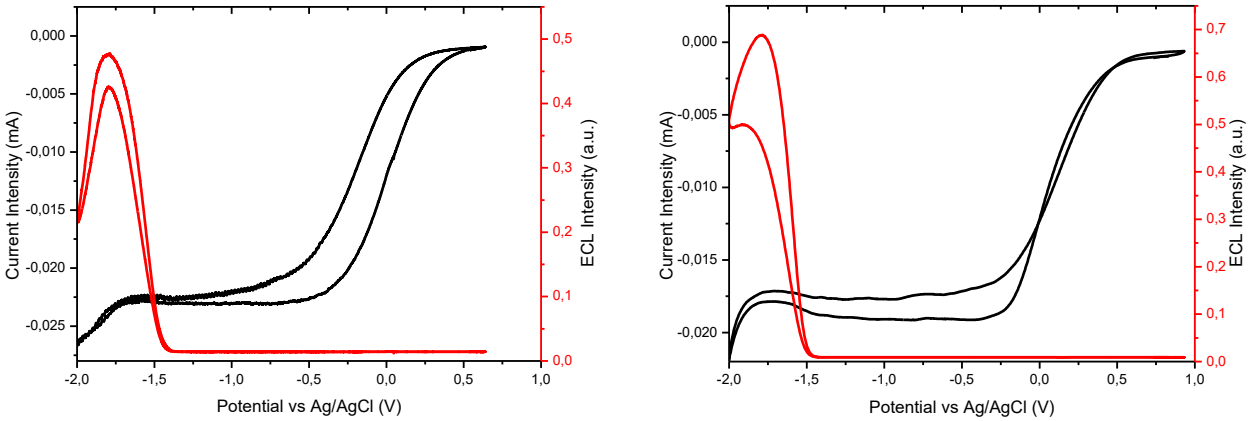


Figure A4.37: ECL-voltage curves of **4^{tBu}CzBNBenzIm** in acetonitrile (left) and dichloromethane (right).

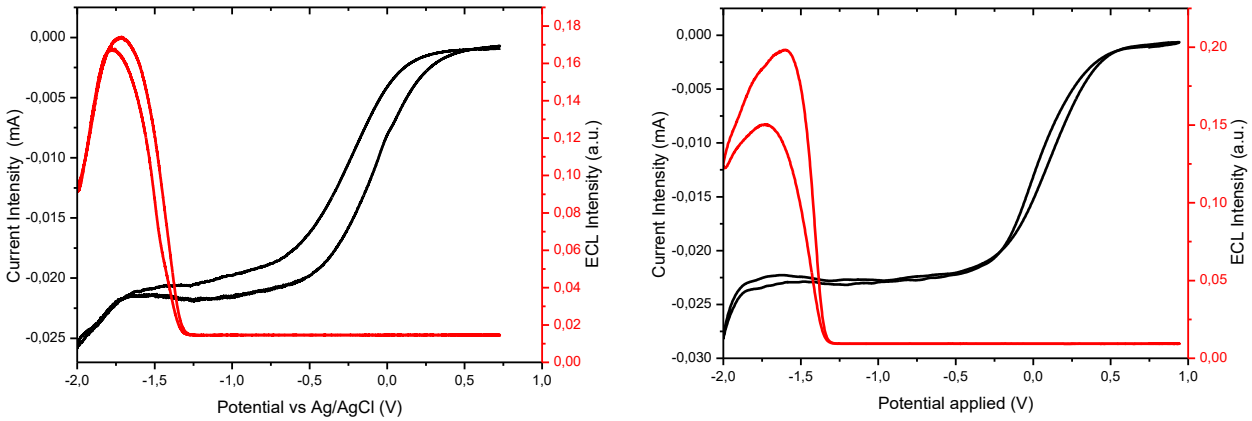


Figure A4.38: ECL-voltage curves of **4^{tBu}CzBNPhenIm** in acetonitrile (left) and dichloromethane (right).

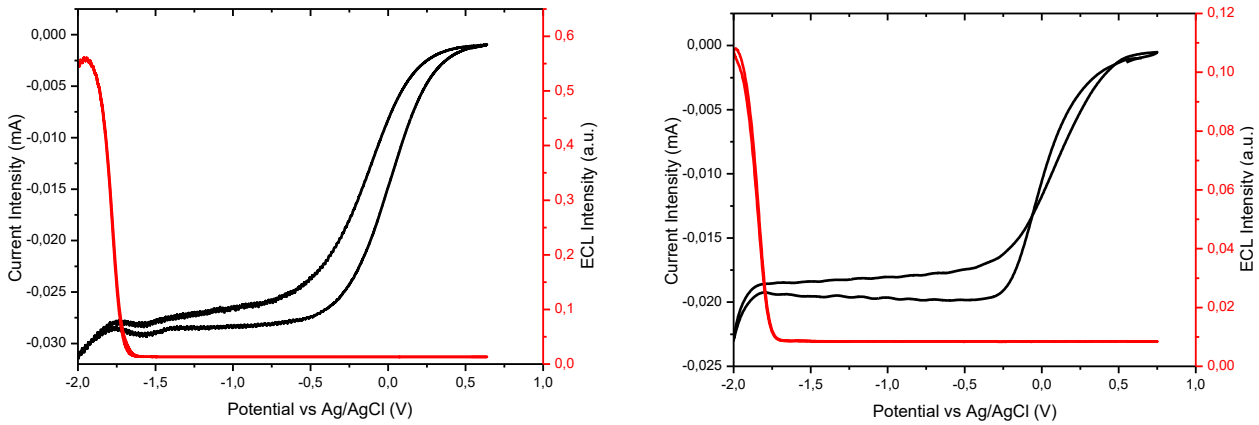


Figure A4.39: ECL-voltage curves of **4DPABNBenzIm** in acetonitrile (left) and dichloromethane (right).

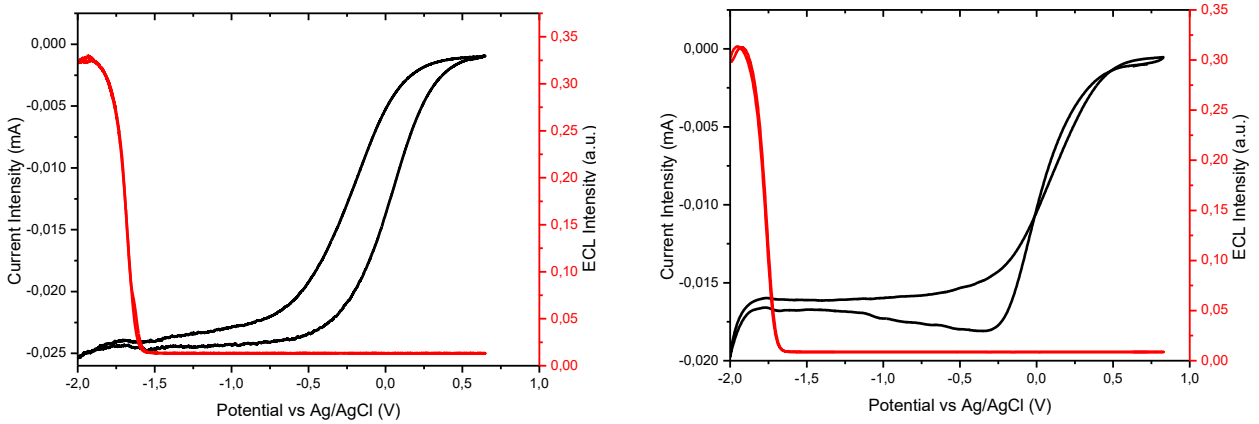


Figure A4.40: ECL-voltage curve of **4DPABNPhenIm** in acetonitrile (left) and dichloromethane (right).

4.8 PL – reductive-oxidation ECL spectra comparisons

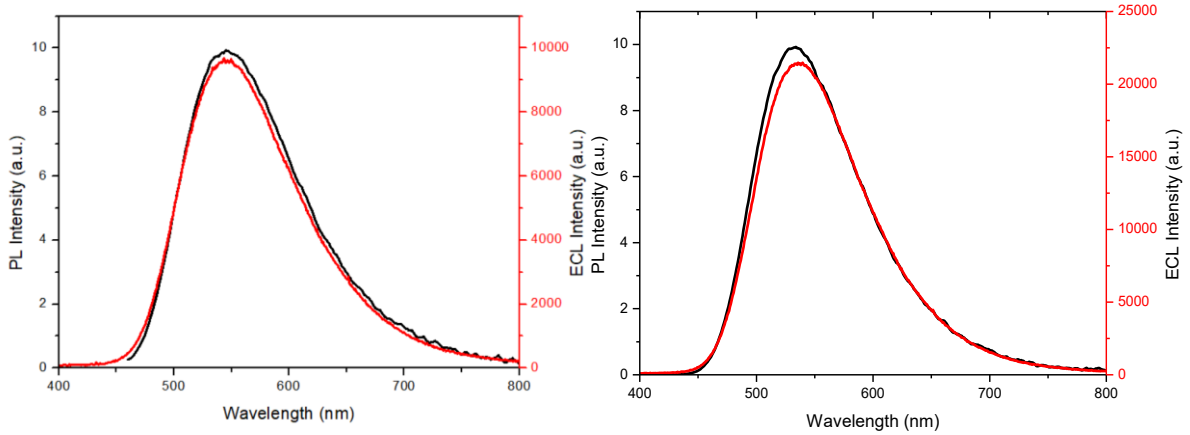


Figure A4.41: PL (black curve) and ECL (red curve) spectra of **4^{tBu}CzBNBenzIm** in acetonitrile (left) and dichloromethane (right).

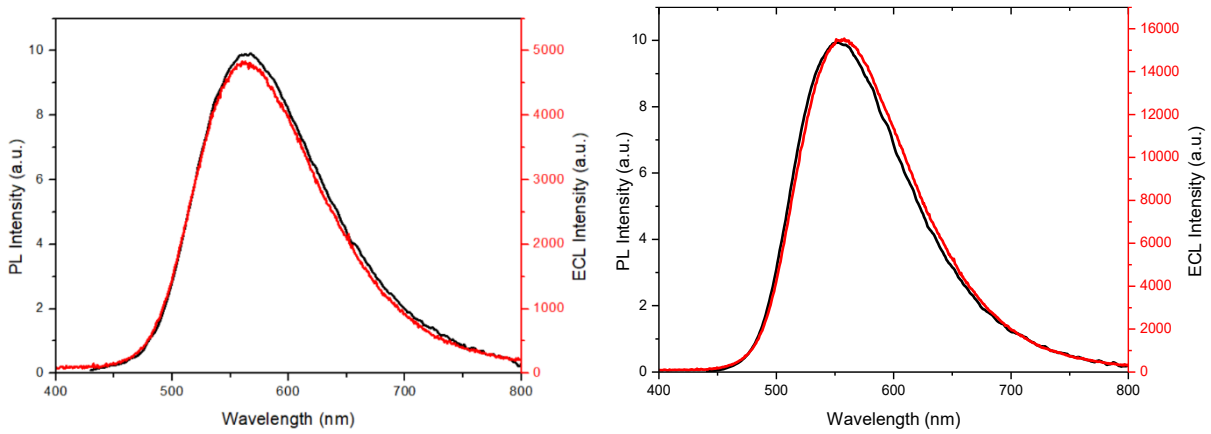


Figure A4.42: PL (black curve) and ECL (red curve) spectra of **4^{tBu}CzBNPhenIm** in acetonitrile (left) and dichloromethane (right).

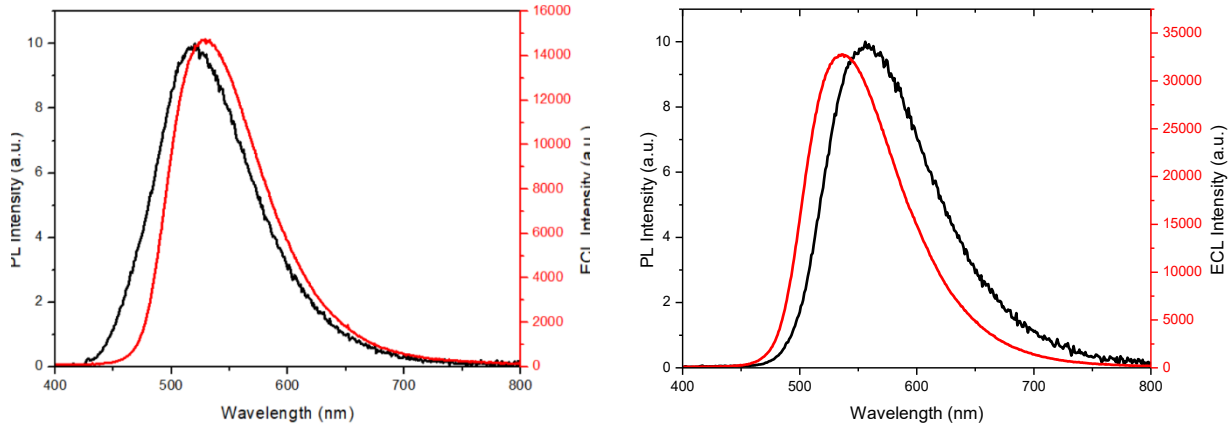


Figure A4.43: PL (black curve) and ECL (red curve) spectra of **4DPABNBenzIm** in acetonitrile (left) and dichloromethane (right).

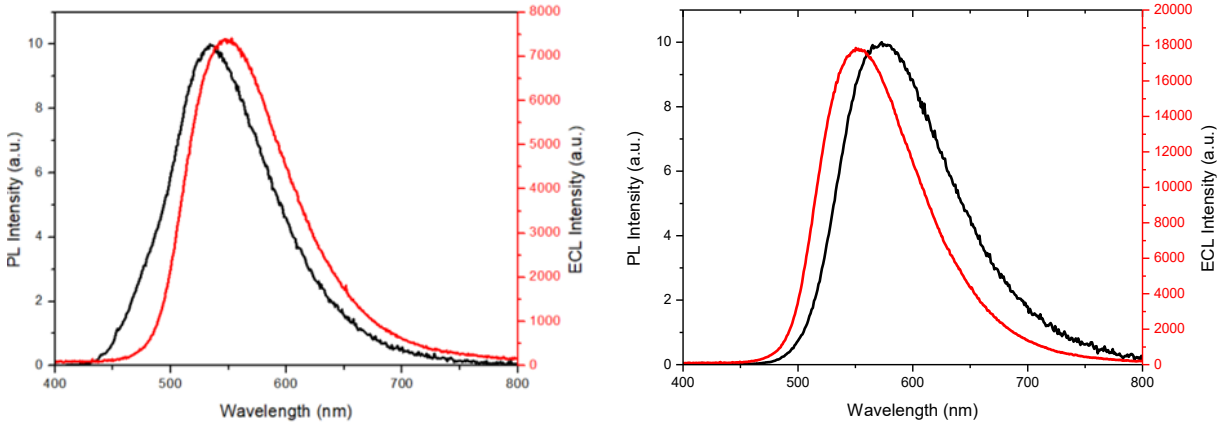


Figure A4.44: PL (black curve) and ECL (red and blue curves) spectra of **4DPABNPhenIm** in acetonitrile (left) and dichloromethane (right).

4.9 PL – oxidative-reduction ECL spectra comparisons

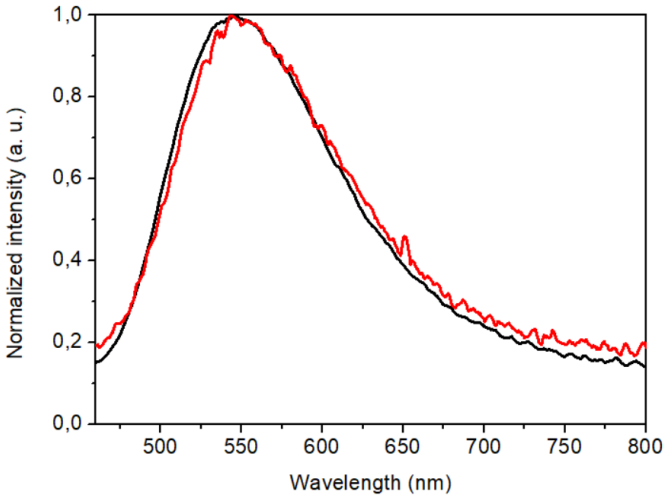


Figure A4.45: PL (black curve) and ECL (red curve) spectra of **4^{tBu}CzBNBenzIm** in acetonitrile.

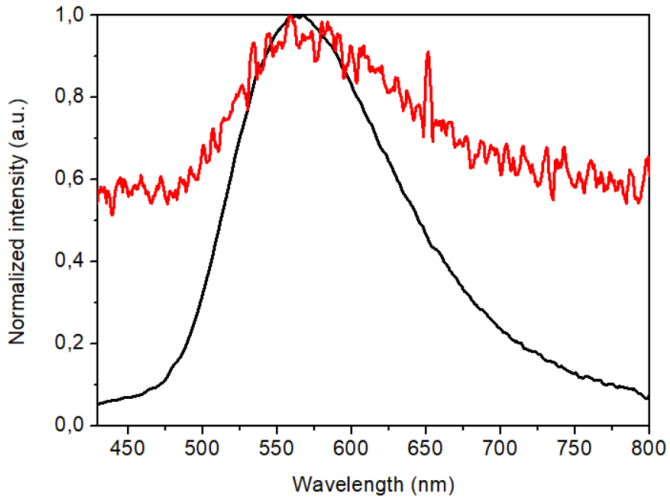


Figure A4.46: PL (black curve) and ECL (red curve) spectra of **4^{tBu}CzBNPhenIm** in acetonitrile.

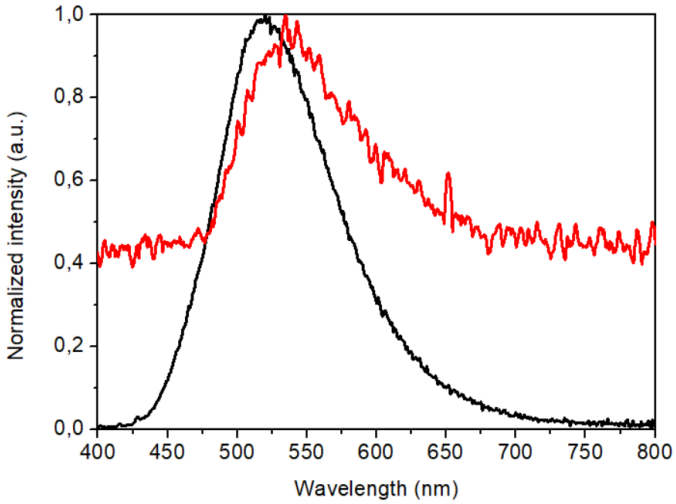


Figure A4.47: PL (black curve) and ECL (red curve) spectra of **4DPABNBenzIm** in acetonitrile.

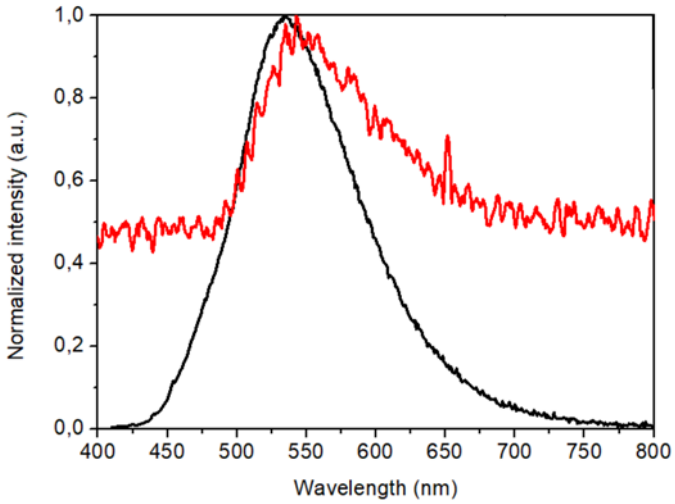


Figure A4.48: PL (black curve) and ECL (red curve) spectra of **4DPABNPhenIm** in acetonitrile.

4.10 Annihilation ECL-time and current-time profiles

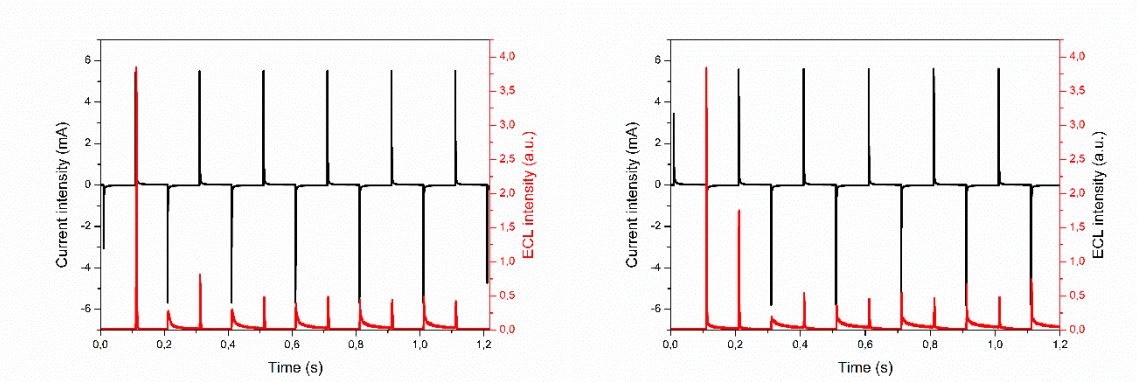


Figure A4.49: ECL-time (red) and chronoamperometric (black) profiles of **4^{tBu}CzBNBenzIm** in acetonitrile. Potential stepped between -1.6 V and +1.5 V (left) and between +1.5 V and -1.6 V (right).

.

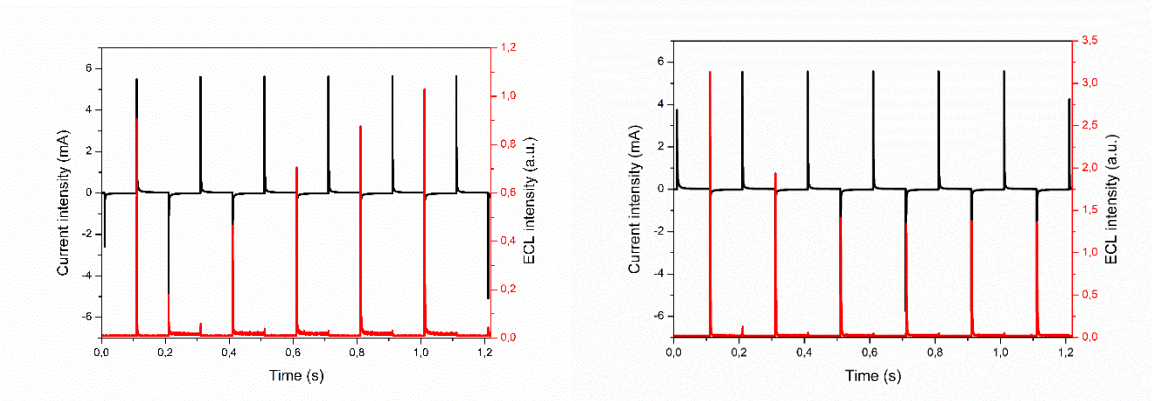


Figure A4.50: ECL-time (red) and chronoamperometric (black) profiles of **4^{tBu}CzBNPhenIm** in acetonitrile. Potential stepped between -1.5 V and +1.6 V (left) and between +1.6 V and -1.5 V (right).

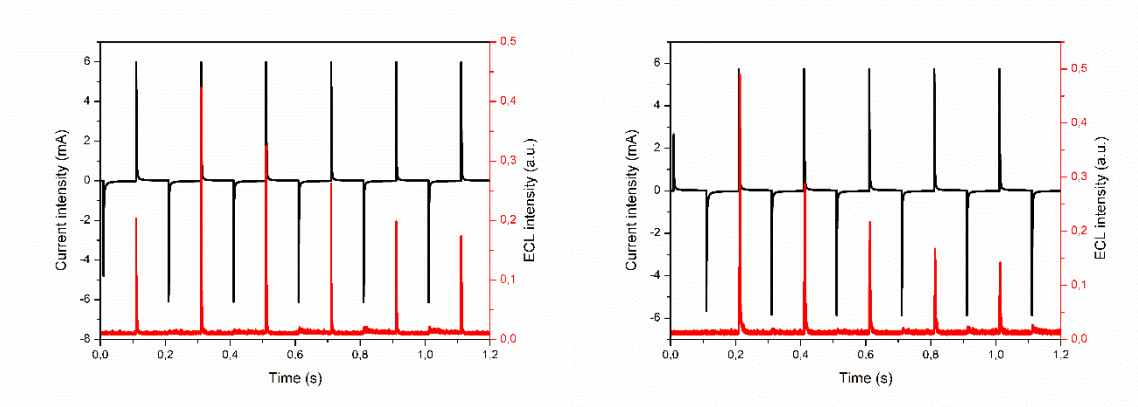


Figure A4.51: ECL-time (red) and chronoamperometric (black) profiles of **4DPABNBenzIm** in acetonitrile. Potential stepped between -2 V and +1.2 V (left) and between +1.2 V and -2 V (right).

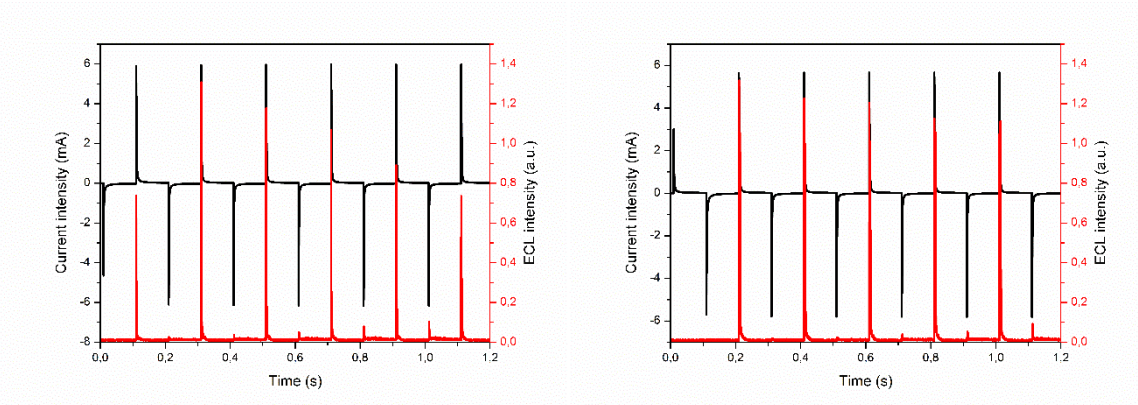


Figure A4.52: ECL-time (red) and chronoamperometric (black) profiles of **4DPABNPhenIm** in acetonitrile. Potential stepped between -2 V and +1.2 V (left) and between +1.2 V and -2 V (right).

4.11 Reductive-oxidation ECL-time and current-time profiles

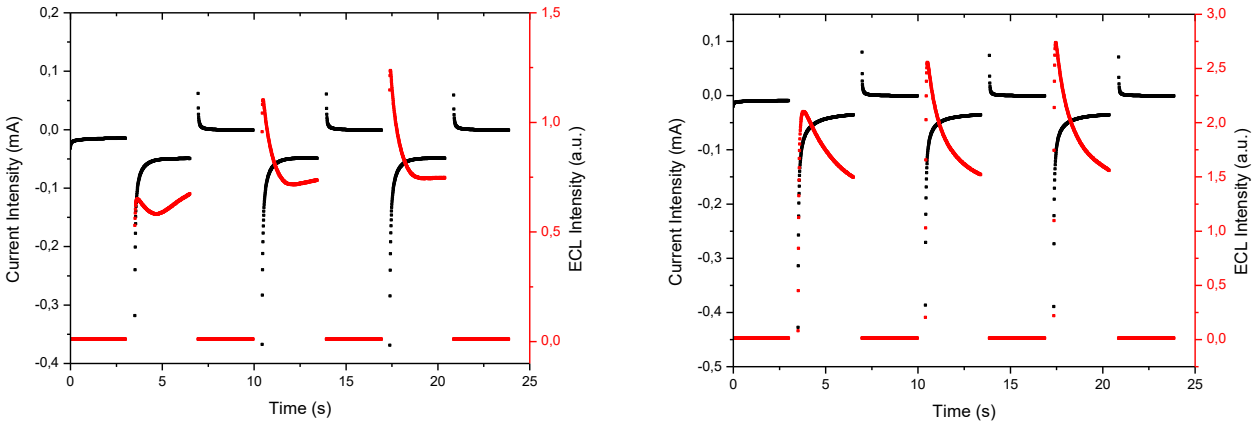


Figure A4.53: Co-reactant ECL-time (red curve) and current-time (black curve) profiles of **4^{tBu}CzBNBenzIm** in acetonitrile (left) and dichloromethane (right).

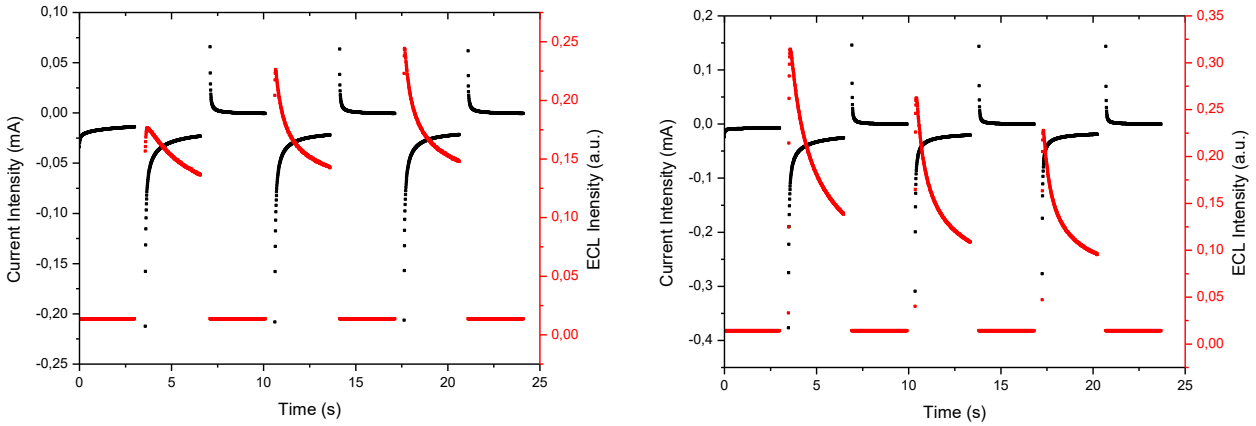


Figure A4.54: Co-reactant ECL-time (red curve) and current-time (black curve) profiles of **4^{tBu}CzBNPhenIm** in acetonitrile (left) and dichloromethane (right).

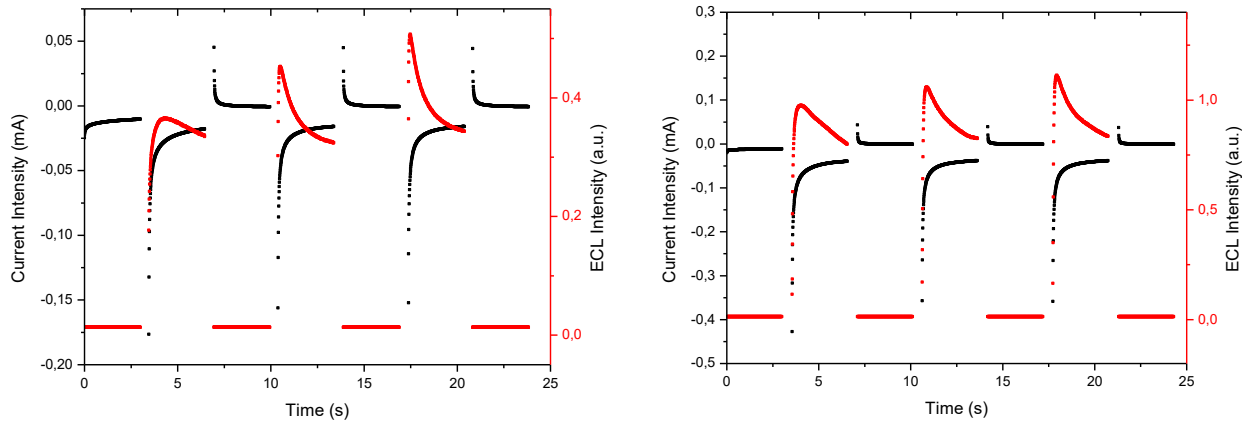


Figure A4.55: Co-reactant ECL-time (red curve) and current-time (black curve) profiles of **4DPABNBenzIm** in acetonitrile (left) and dichloromethane (right).

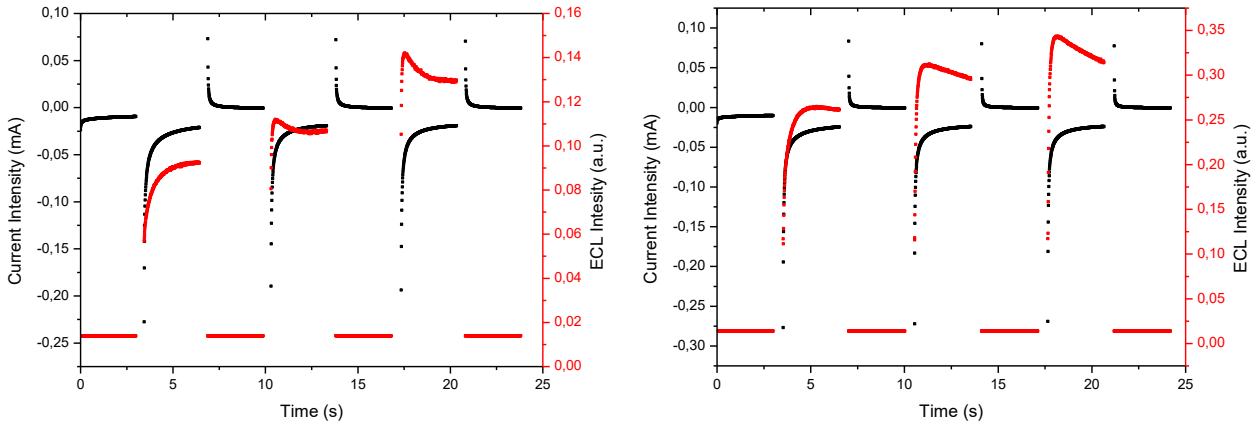


Figure A4.56: Co-reactant ECL-time (red curve) and current-time (black curve) profiles of **4DPABNPhenIm** in acetonitrile (left) and dichloromethane (right).

4.12 Oxidative-reduction ECL-time and current-time profiles

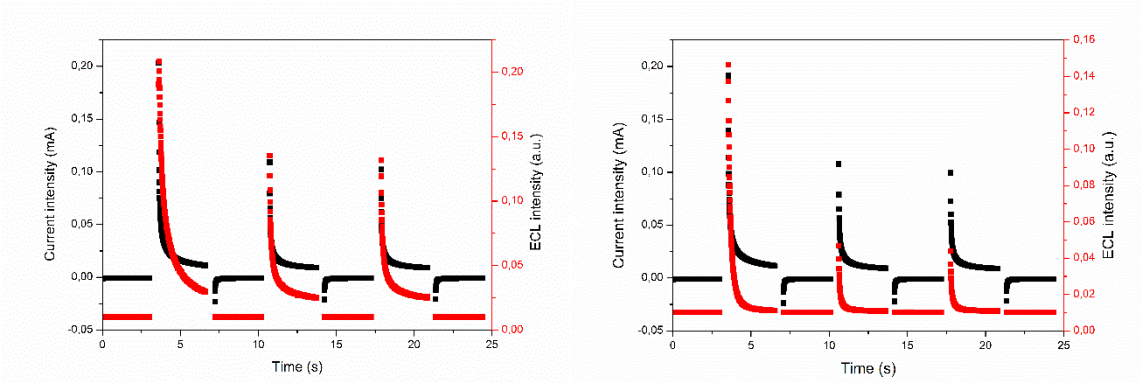


Figure A4.57: Co-reactant ECL-time (red curve) and current-time (black curve) profiles of **4^{tBu}CzBNBenzIm** (left) and **4^{tBu}CzBNPhenIm** (right) in acetonitrile.

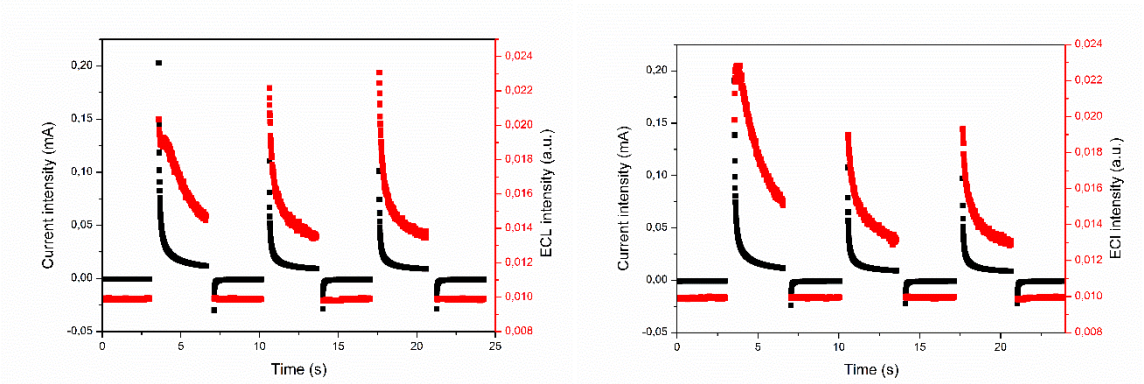


Figure A4.58: Co-reactant ECL-time (red curve) and current-time (black curve) profiles of **4DPABNBenzIm** (left) and **4DPABNPhenIm** (right) in acetonitrile.

Chapter 5

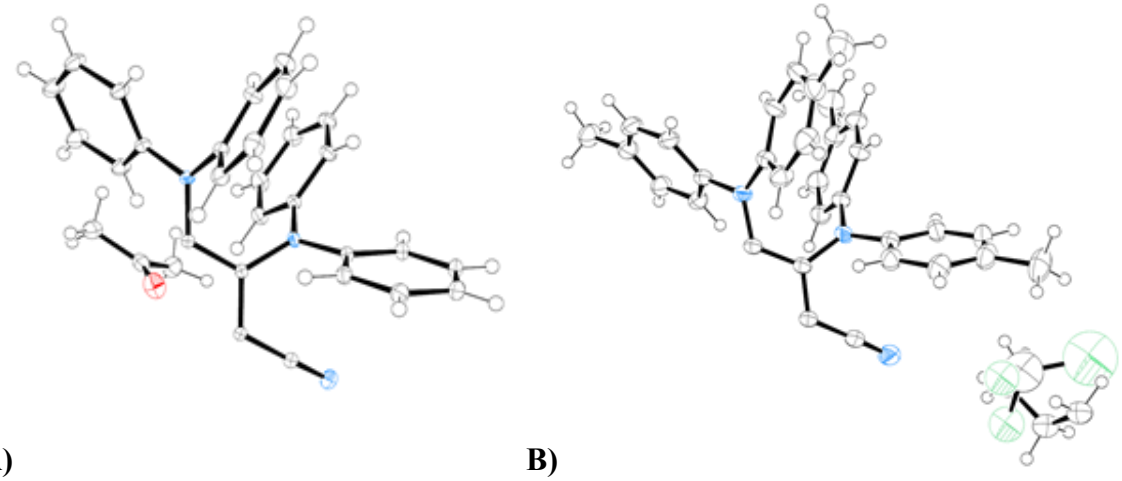
5.1 Single crystal X-ray diffraction analysis

Table A5.1: Crystallographic data and refinement details.

	4DpTATPN	**4DPATPN**
CCDC Number	2284117	2284118
Chemical Formula	$C_{64}H_{56}N_6 \cdot {}^1/_7CHCl_3 \cdot {}^6/_7C_6H_{14}$	$C_{56}H_{40}N_6 \cdot 2C_3H_6O$
Formula weight	1000.30 g/mol	913.09 g/mol
Temperature	100(2) K	100(2) K
Wavelength	0.620 Å	0.620 Å
Crystal system	Monoclinic	Monoclinic
Space Group	*P* $2_1/c$	P 21/n
Unit cell dimensions	*a* = 12.857(3) Å	a = 11.156(2) Å
	b = 12.102(2) Å	b = 12.563(3) Å
	c = 18.856(4) Å	c = 17.063(3) Å
	α = 90°	α = 90°
	β = 104.22(3)°	β = 96.40(3)°
	γ = 90°	γ = 90°
Volume	2844.0(11) Å^3	2376.5(8) Å^3
Z	2	2
Density (calculated)	1.168 g·cm^{-3}	1.276 g·cm^{-3}
Absorption coefficient	0.066 mm^{-1}	0.060 mm^{-1}
F(000)	1066	964

Theta range for data collection	1.4° to 31.1°	1.8° to 31.1°
Index ranges	-20 ≤ h ≤ 20, -20 ≤ k ≤ 20, -30 ≤ l ≤ 29	-20 ≤ h ≤ 20, -20 ≤ k ≤ 20, -30 ≤ l ≤ 29
Resolution	0.60 Å	0.60 Å
Reflections collected	66828	56097
Independent reflections	12438, 9693 data with I>2σ(I)	10394, 9555 data with I>2σ(I)
Data multiplicity (max resltn)	4.79 (2.84)	4.81 (2.77)
I/σ(I) (max resltn)	19.58 (6.35)	25.55 (15.67)
R_{merge} (max resltn)	0.0361 (0.1422)	0.0390 (0.0565)
Data completeness (max resltn)	90.4% (74.0%)	90.4% (74.3%)
Refinement method	Full-matrix least-squares on F^2	Full-matrix least-squares on F^2
Data / restraints / parameters	12438 / 12 / 366	10394 / 0 / 318
Goodness-of-fit on F^2	1.061	1.043
Δ/σ_{max}	0.000	0.001
Final R indices [I>2σ(I)]	R_1 = 0.0749, wR_2 = 0.2106	R_1 = 0.0437, wR_2 = 0.1255
R indices (all data)	R_1 = 0.0902, wR_2 = 0.2234	R_1 = 0.0466, wR_2 = 0.1291
Largest diff. peak and hole	0.633 and -0.394 eÅ^{-3}	0.586 and -0.280 eÅ^{-3}
R.M.S. deviation from mean	0.066 eÅ^{-3}	0.064 eÅ^{-3}

$R_1 = \Sigma \; ||Fo|-|Fc|| \; / \; \Sigma \; |Fo|$, $wR_2 = \{ \Sigma \; [w(Fo^2 - Fc^2)^2] \; / \; \Sigma \; [w(Fo^2)^2] \}^{½}$



A) **B)**

Figure A5.1: Ellipsoids representation of **4DPATPN** (A) and **4DpTATPN** (B) asymmetric unit contents (A.S.U. - 50% probability). Hydrogen atoms were omitted for clarity.

5.2 ^{1}H NMR Spectra

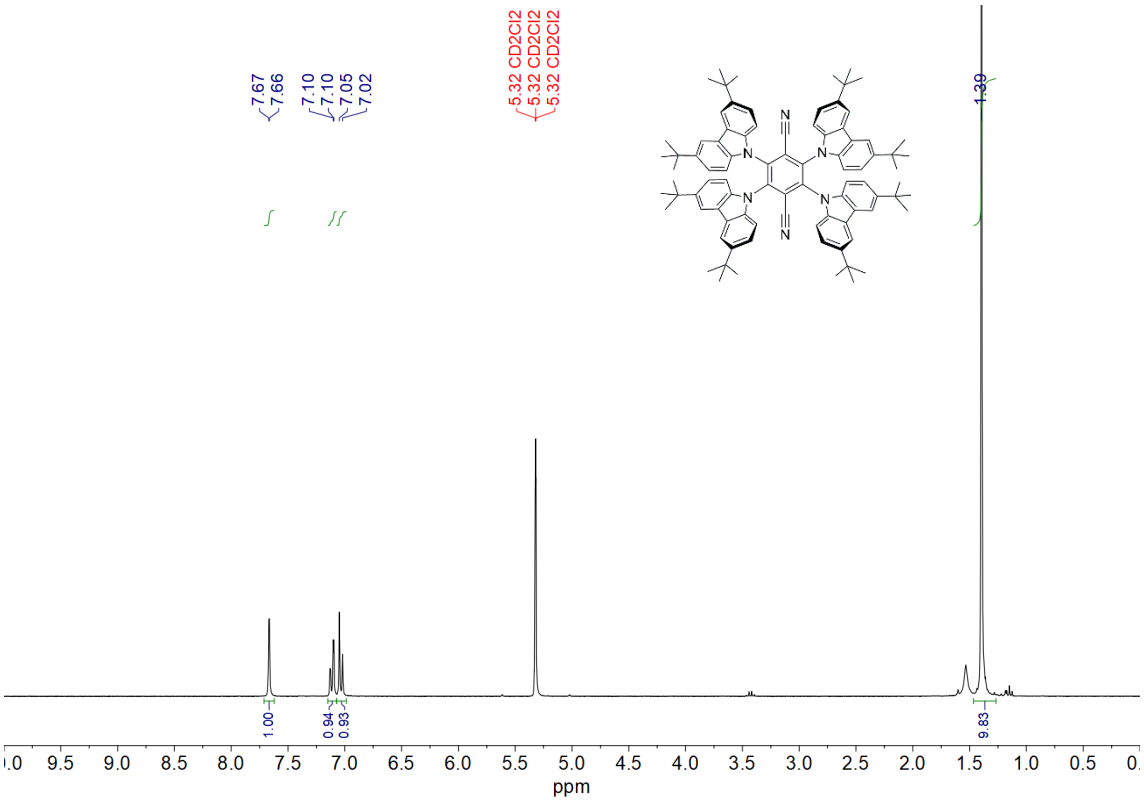


Figure A5.2: ^{1}H NMR of spectrum of **4^{tBu}CzTPN** (CD_2Cl_2).

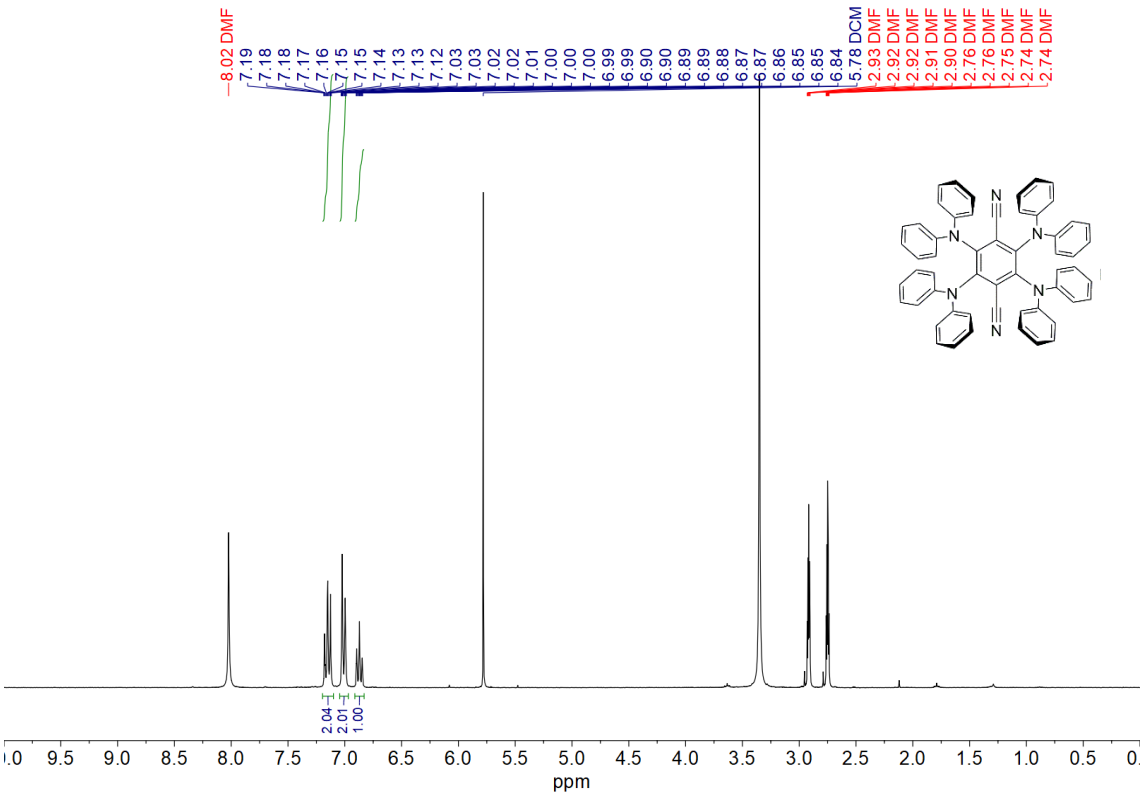


Figure A5.3: ^{1}H NMR of spectrum of **4DPATPN** (DMF-d_7).

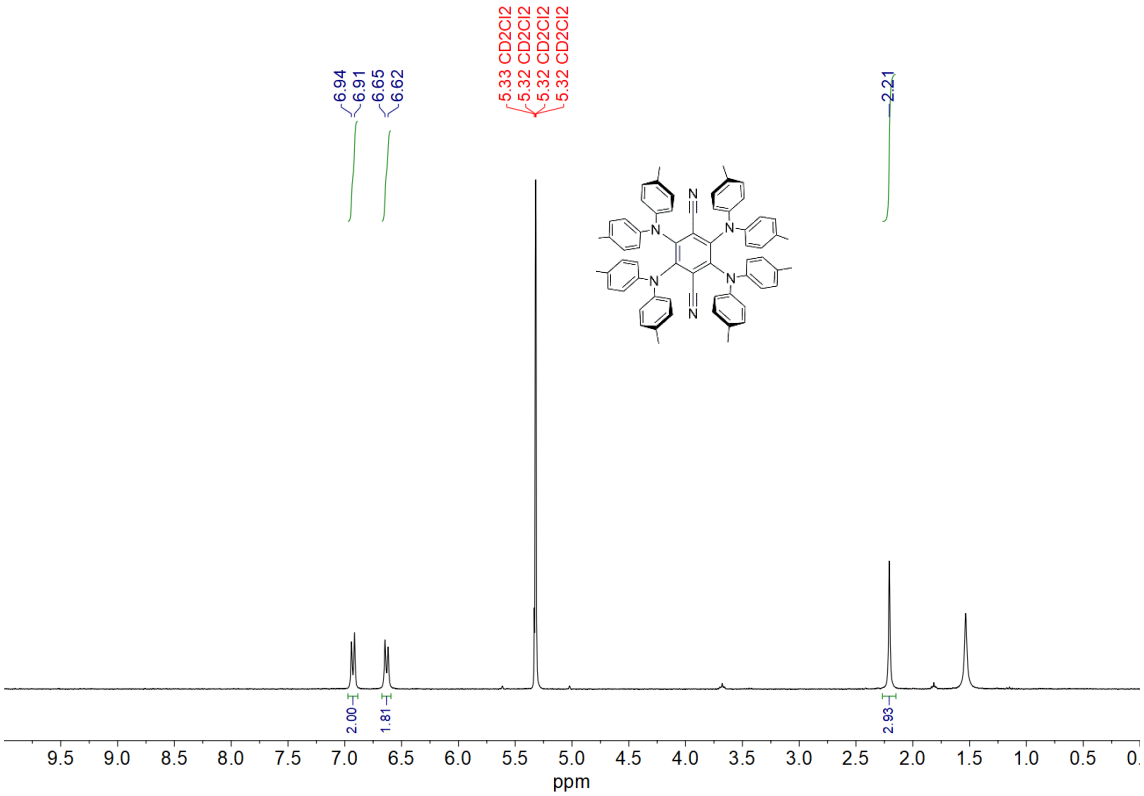


Figure A5.4: ^{1}H NMR of spectrum of **4DpTATPN** (CD_2Cl_2).

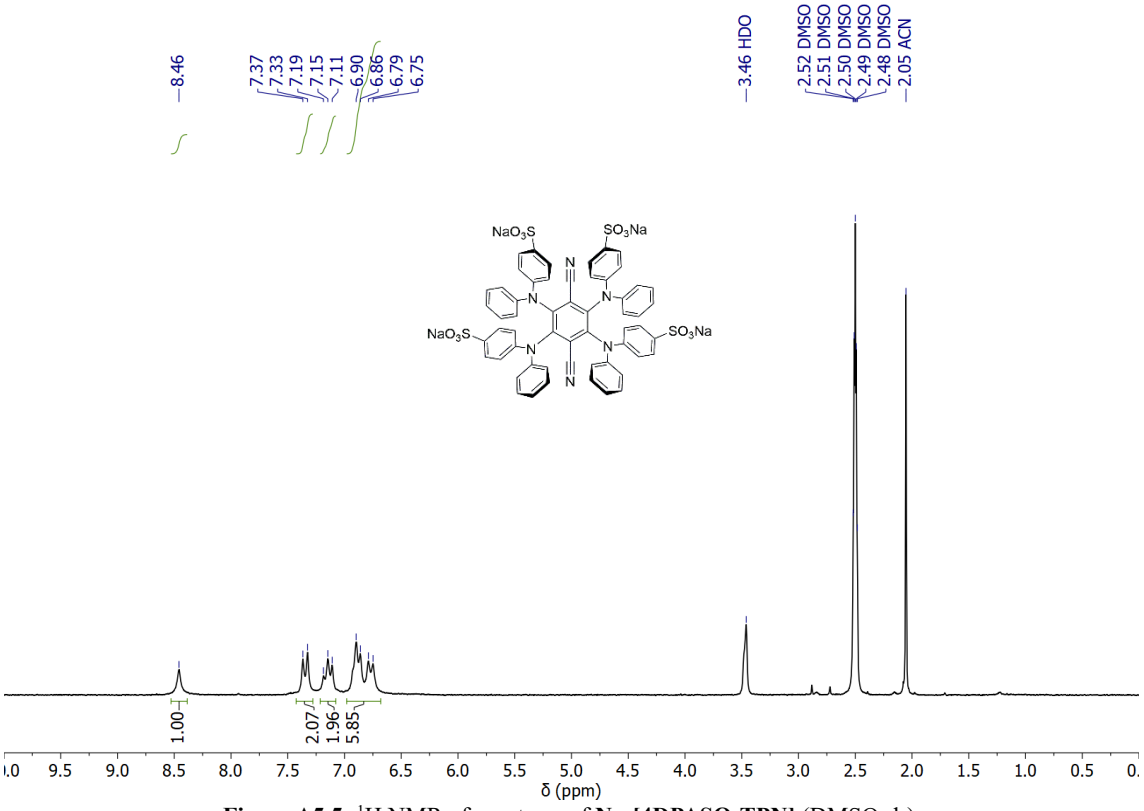


Figure A5.5: ^{1}H NMR of spectrum of **Na_4[4DPASO$_3$TPN]** (DMSO-d_6).

5.3 $^{13}C\{^{1}H\}$ NMR Spectra

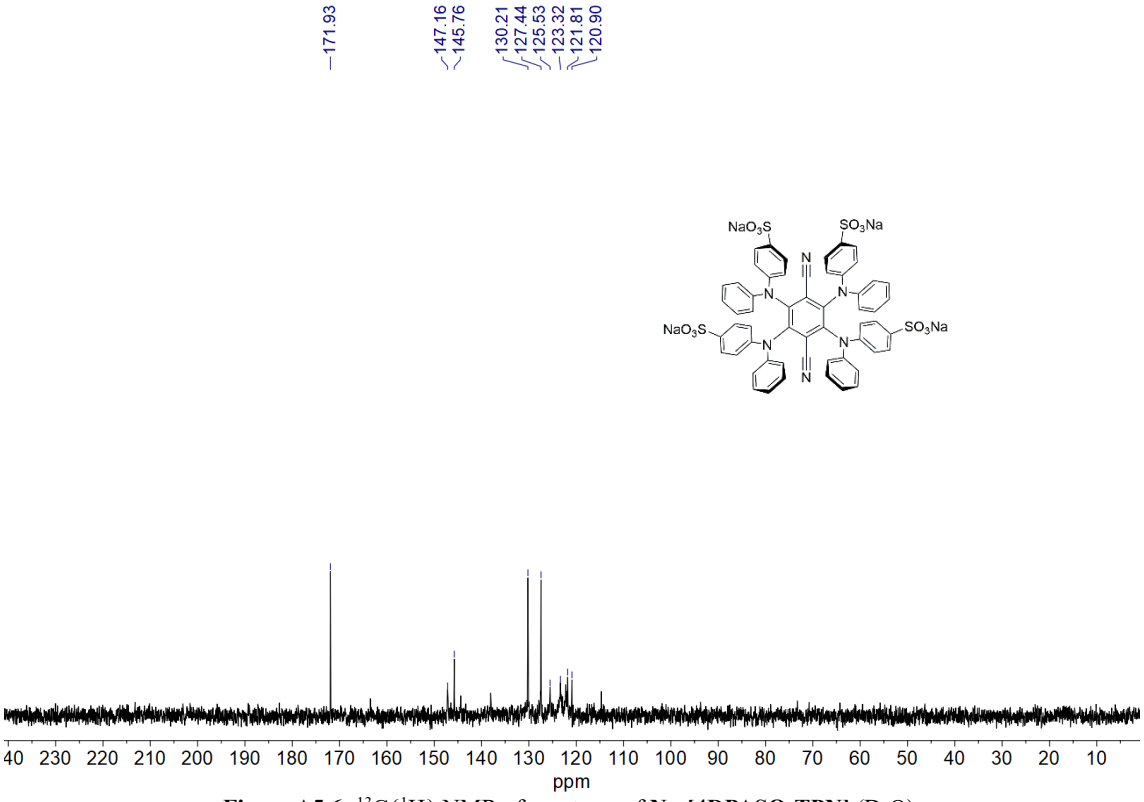


Figure A5.6: $^{13}C\{^{1}H\}$ NMR of spectrum of **Na_4[4DPASO$_3$TPN]** (D_2O).

5.4 Absorption-excitation spectra comparisons

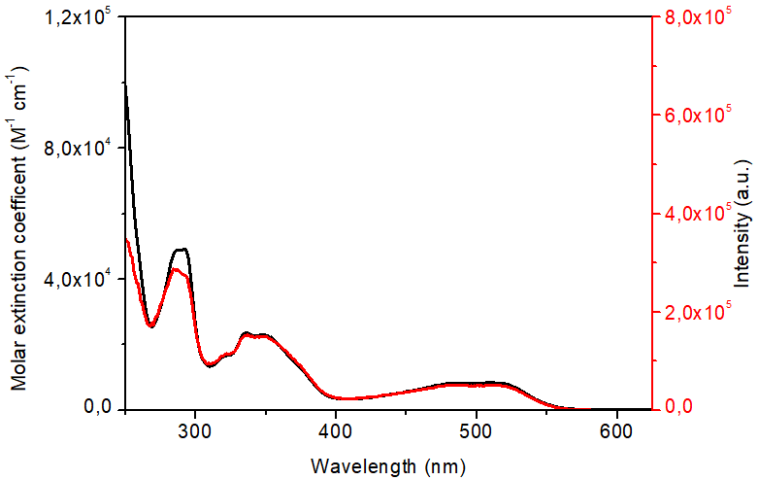


Figure A5.7: Absorption (black curve) and excitation (red curve) spectra of **4^{tBu}CzTPN** in dichloromethane.

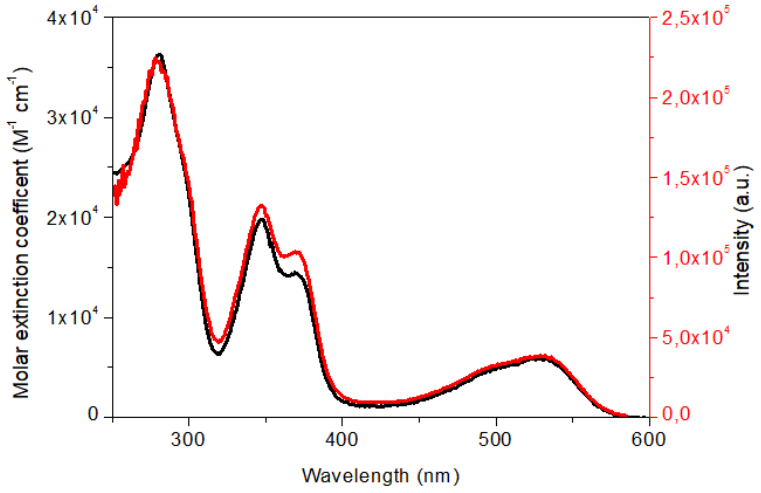


Figure A5.8: Absorption (black curve) and excitation (red curve) spectra of **4DPATPN** in dichloromethane.

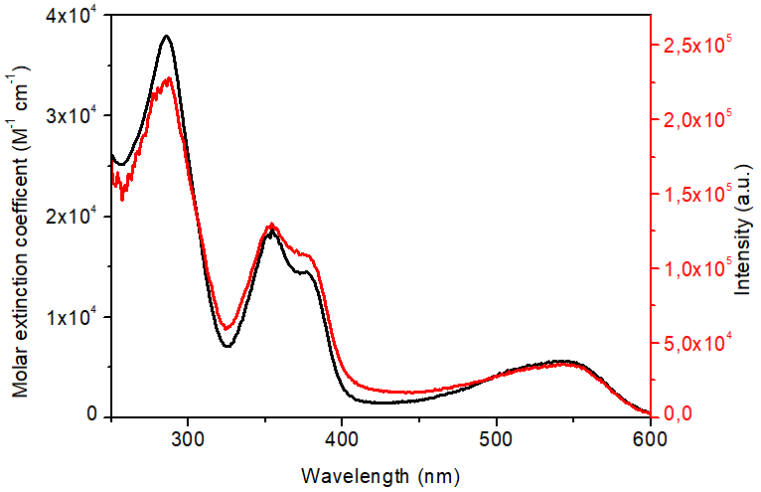


Figure A5.9: Absorption (black curve) and excitation (red curve) spectra of **4DpTATPN** in dichloromethane.

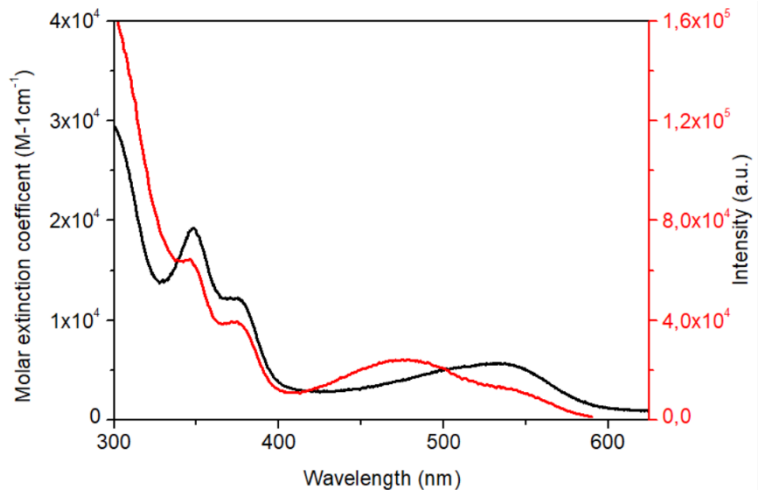


Figure A5.10: Absorption (black curve) and excitation (red curve) spectra of **Na_4[4DPASO_3TPN]** in water.

5.5 Luminescent decays curves

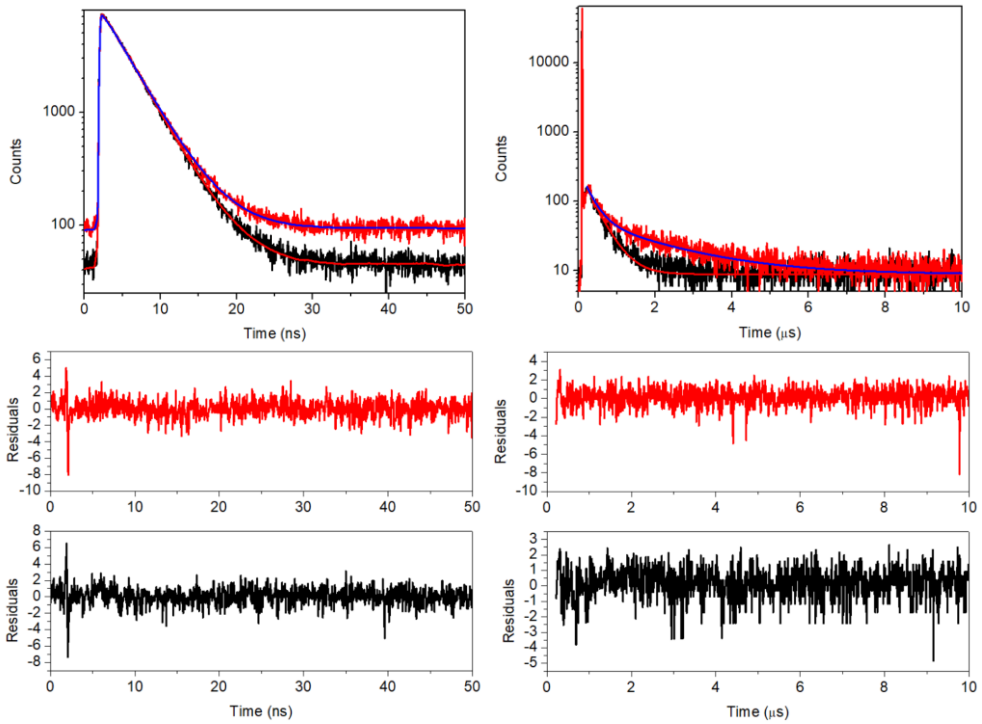


Figure A5.11: Luminescence decay curves of **4^{tBu}CzTPN** in aerated dichloromethane (black curves) and in Ar-purged dichloromethane solutions (red curves) with their fittings and residuals. Left: decays in the nanosecond scale; Right: decays in the microsecond scale.

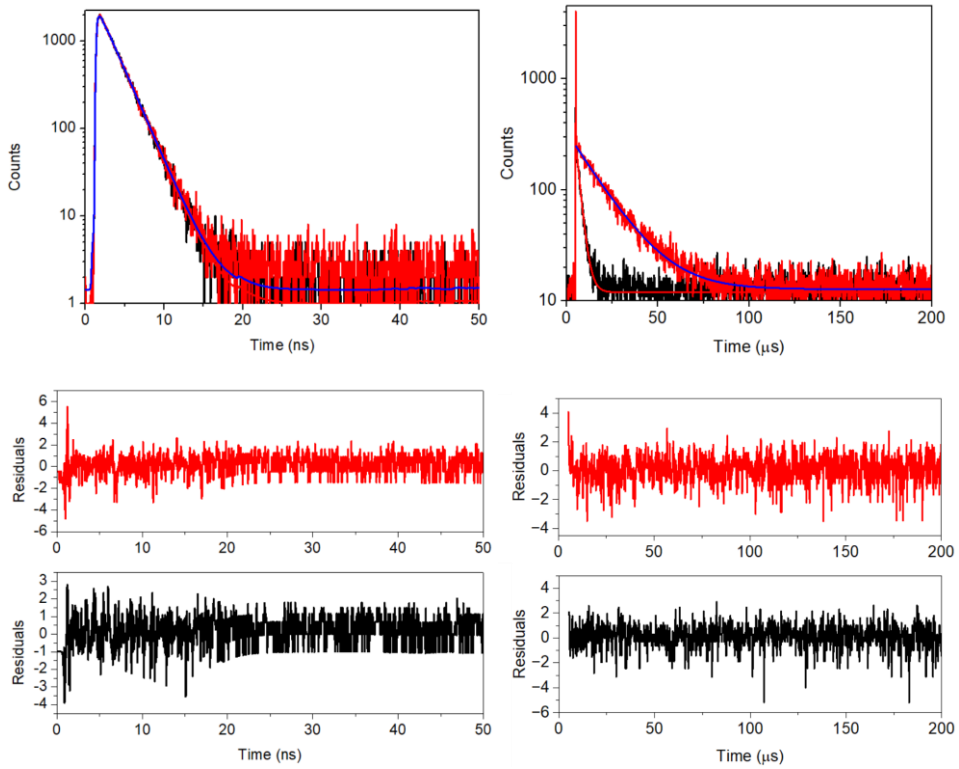


Figure A5.12: Luminescence decay curves of **4DPATPN** in aerated dichloromethane (black curves) and in Ar-purged dichloromethane solutions (red curves) with their fittings and residuals. Left: decays in the nanosecond scale; Right: decays in the microsecond scale.

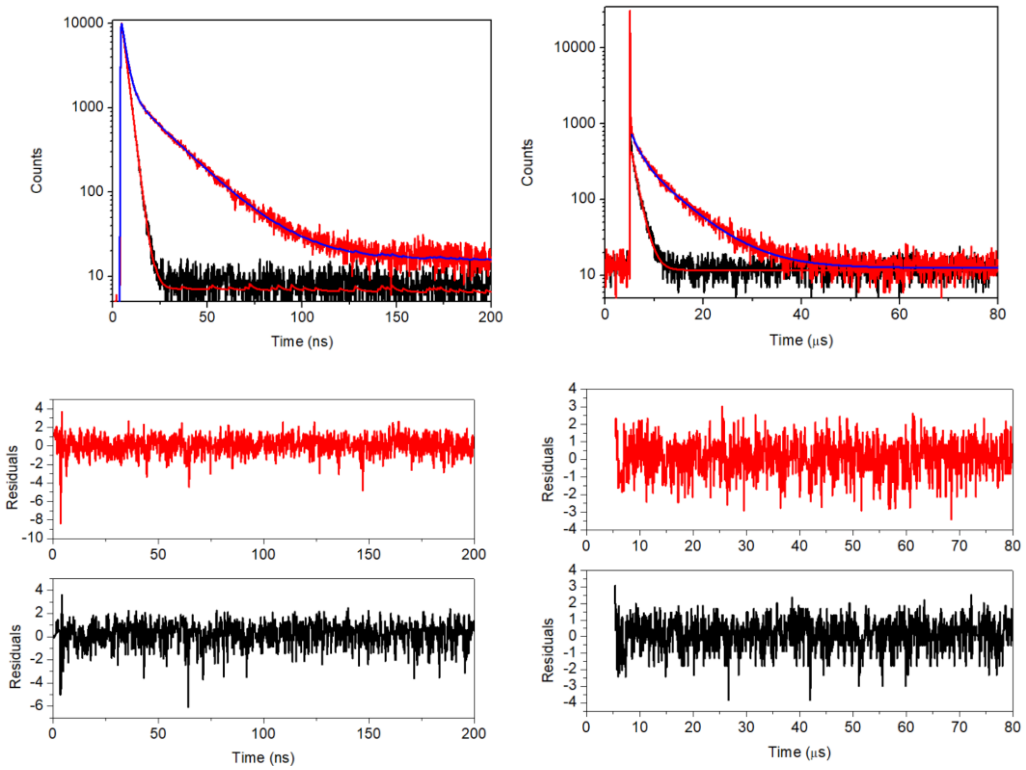


Figure A5.13: Luminescence decay curves of **4DpTATPN** in aerated dichloromethane (black curves) and in Ar-purged dichloromethane solutions (red curves) with their fittings and residuals. Left: decays in the nanosecond scale; Right: decays in the microsecond scale.

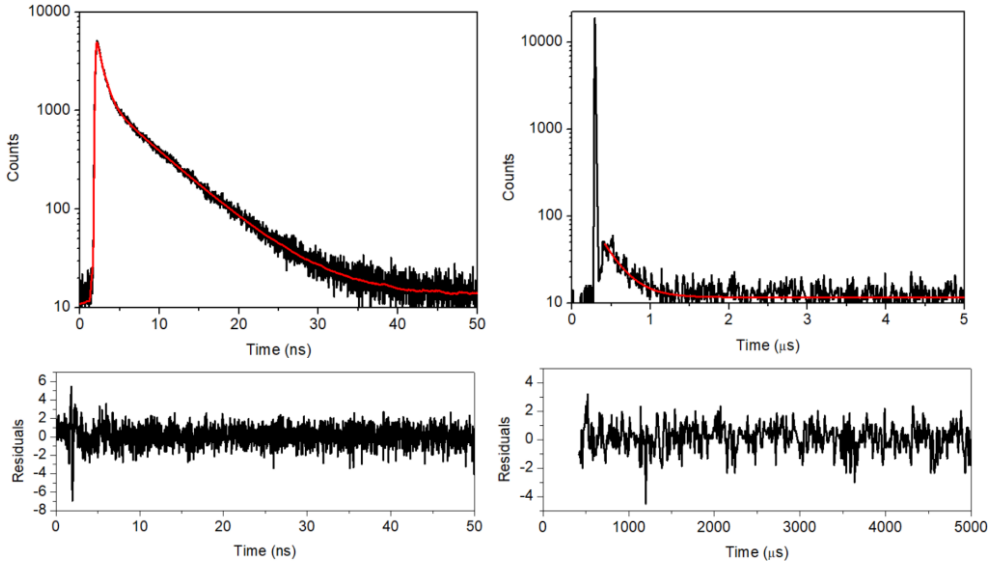


Figure A5.14: Luminescence decay curves of **Na_4[4DPASO_3TPN]** in aerated water with their fittings and residuals. Left: decays in the nanosecond scale; Right: decays in the microsecond scale.

5.6 Electrochemical characterization

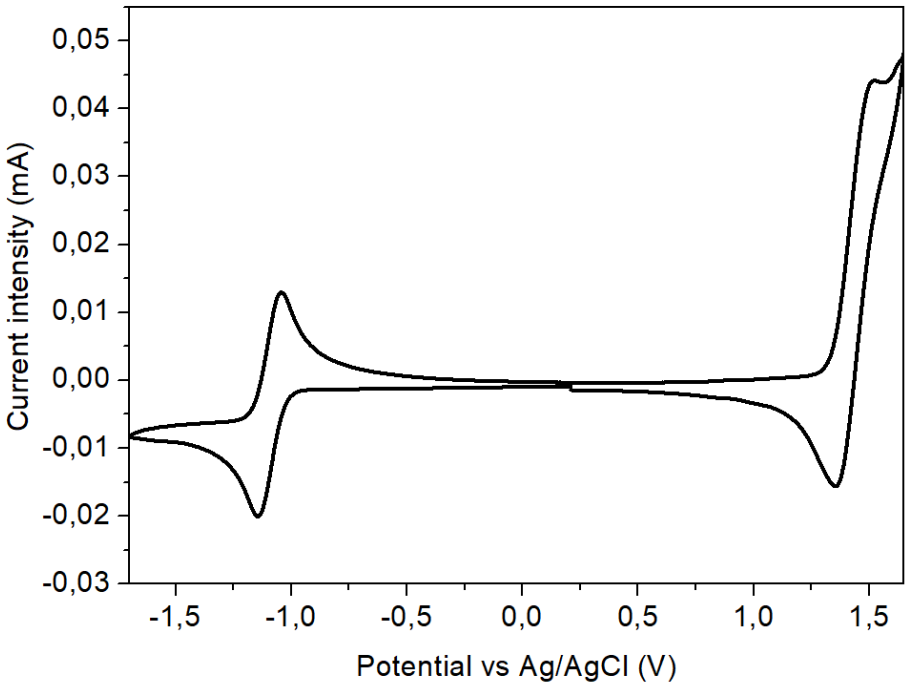


Figure A5.15: CV of **4^{tBu}CzTPN** in dichloromethane.

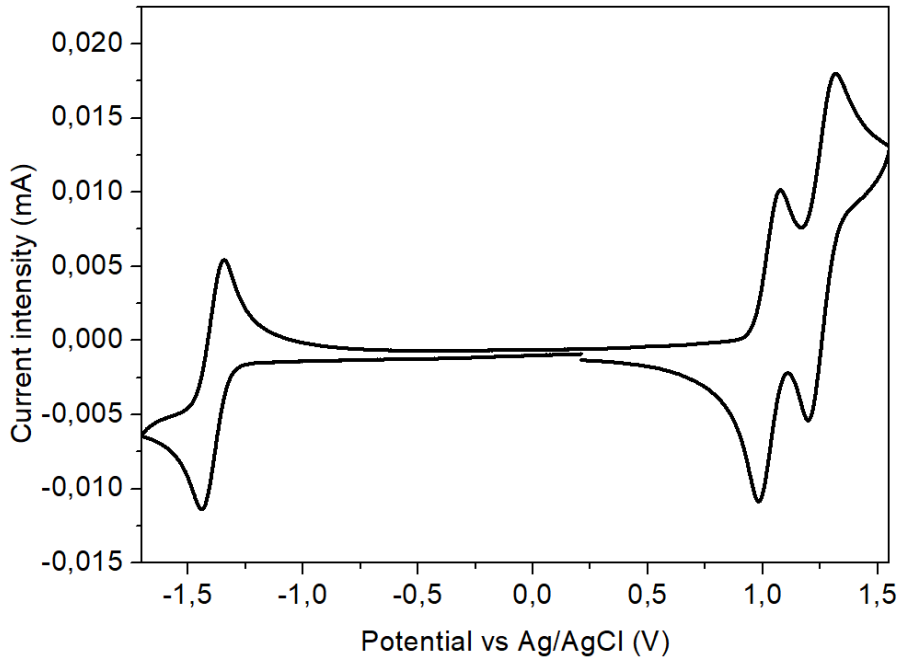


Figure A5.16: CV of **4DPATPN** in dichloromethane.

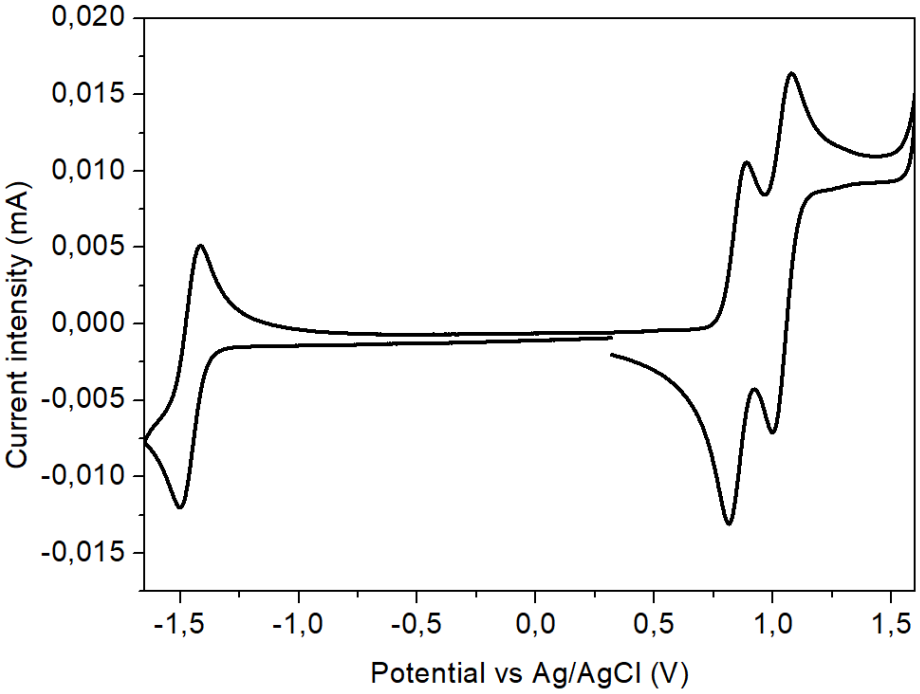


Figure A5.17: CV of **4DpTATPN** in dichloromethane.

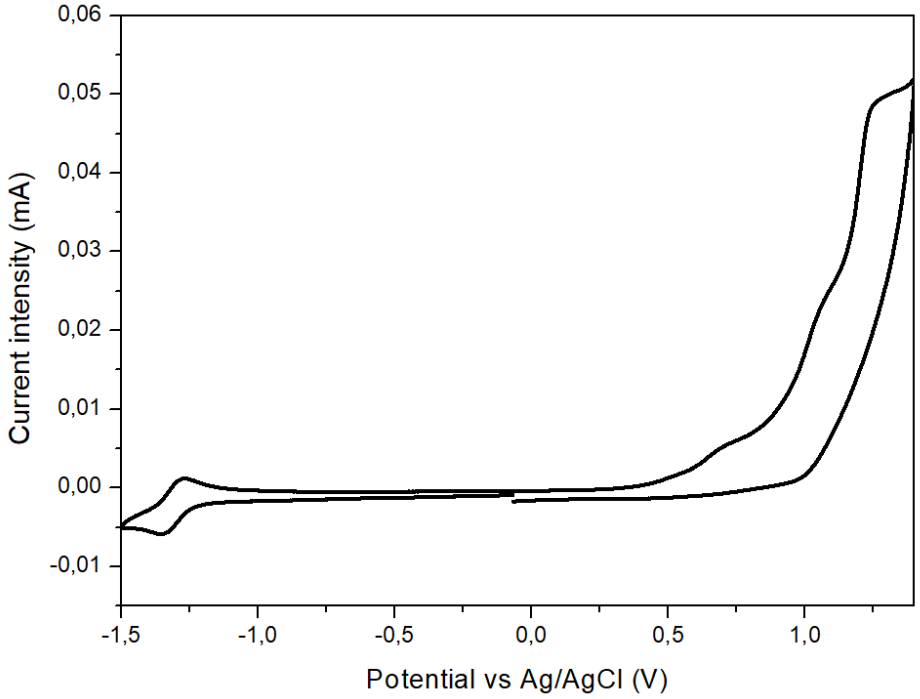


Figure A5.18: CV of **Na_4[4DPASO_3TPN]** in DMF.

5.7 PL – oxidative-reduction ECL spectra comparisons

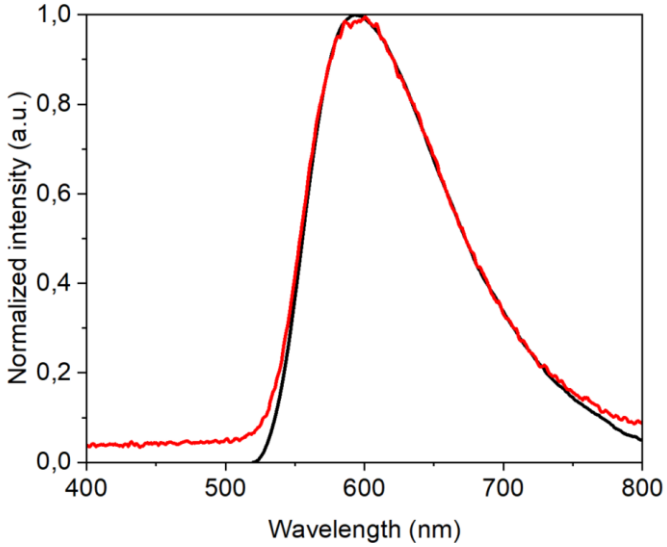


Figure A5.19: PL (black curve) and ECL (red curve) spectra of **4^{tBu}CzTPN** in dichloromethane.

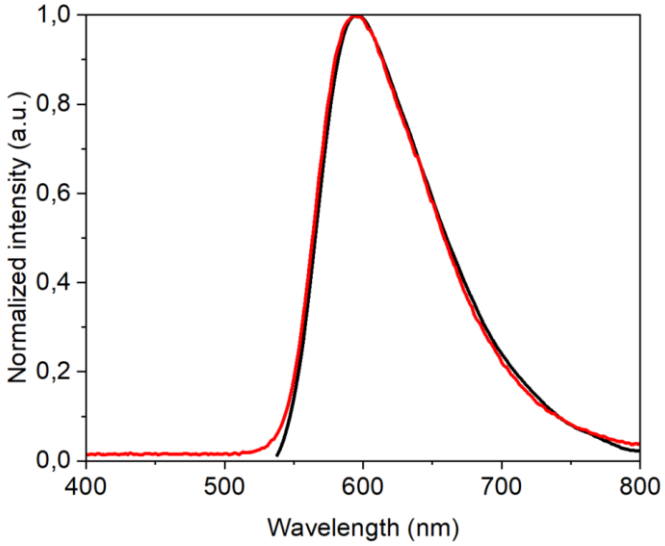


Figure A5.20: PL (black curve) and ECL (red curve) spectra of **4DPATPN** in dichloromethane.

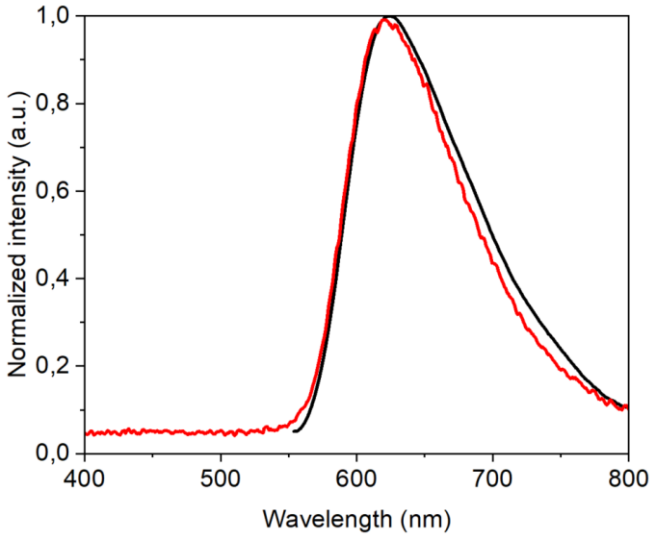


Figure A5.21: PL (black curve) and ECL (red curve) spectra of **4DPATPN** in dichloromethane.

5.8 Annihilation ECL-time and current-time profiles

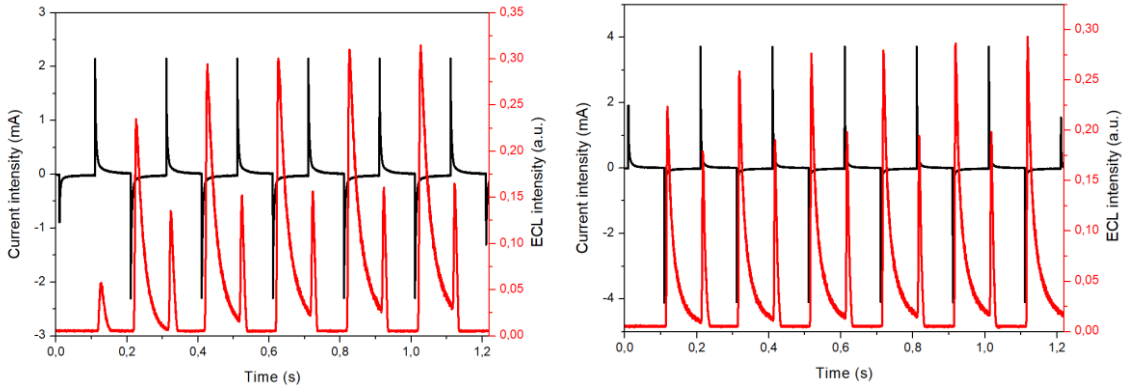


Figure A5.22: ECL-time (red) and chronoamperometric (black) profiles of **4^{tBu}CzTPN** in dichloromethane. Potential stepped between -1.2 V and +1.6 V (left) and between +1.6 V and -1.2 V (right).

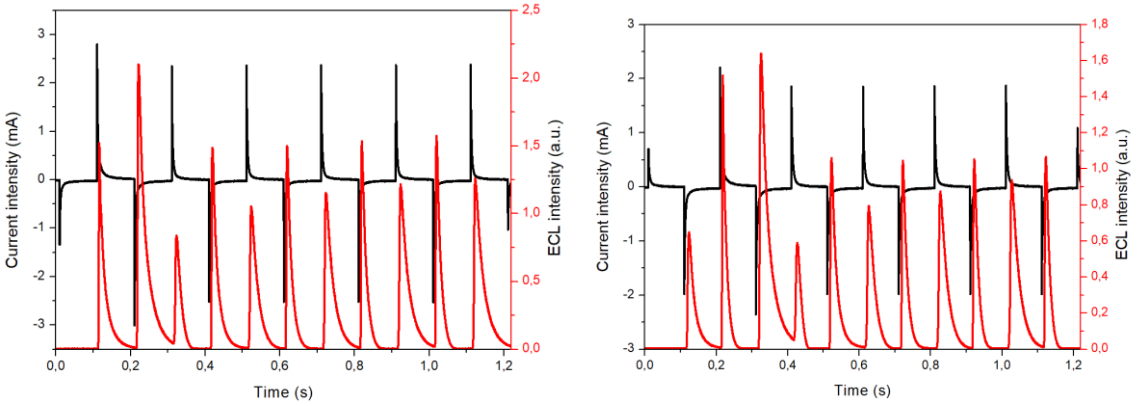


Figure A5.23: ECL-time (red) and chronoamperometric (black) profiles of **4DPATPN** in dichloromethane. Potential stepped between -1.6 V and +1.1 V (left) and between +1.1 V and -1.6 V (right).

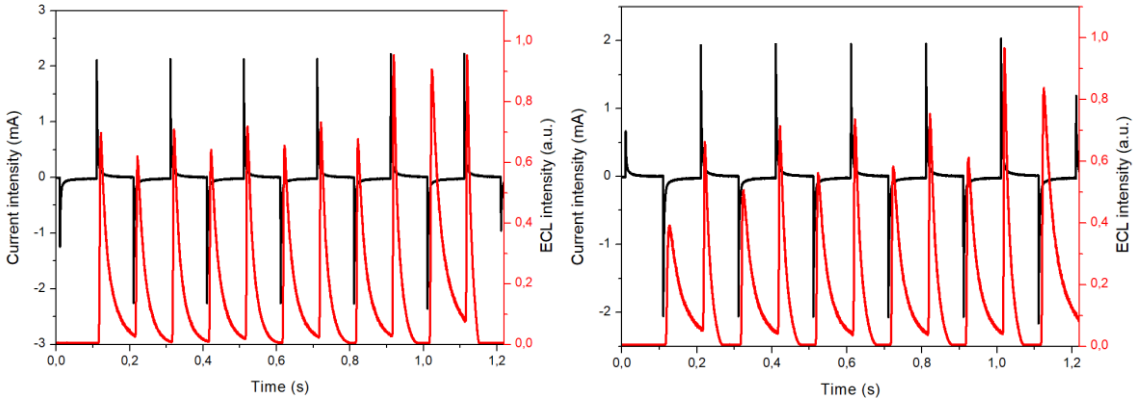


Figure A5.24: ECL-time (red) and chronoamperometric (black) profiles of **4DpTATPN** in dichloromethane. Potential stepped between -1.6 V and +1 V (left) and between +1 V and -1.6 V (right).

5.9 Oxidative-reduction ECL-time and current-time profiles

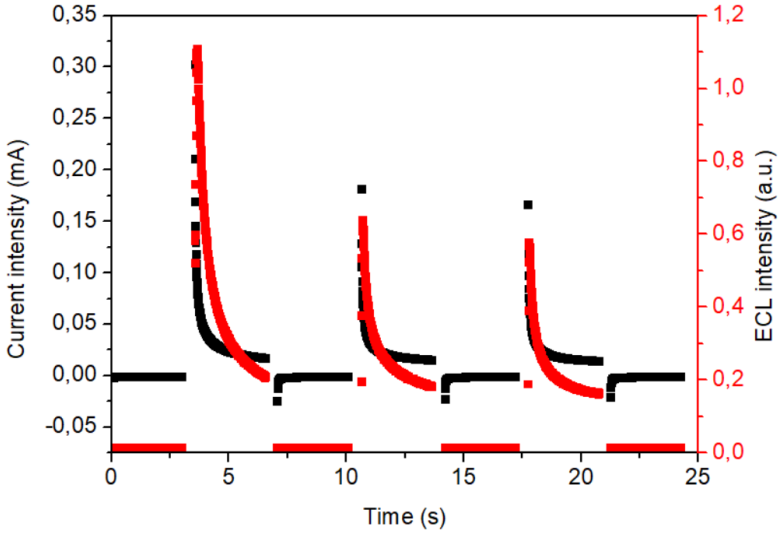


Figure A5.25: Co-reactant ECL-time (red curve) and current-time (black curve) profiles of **4^{tBu}CzTPN** in dichloromethane.

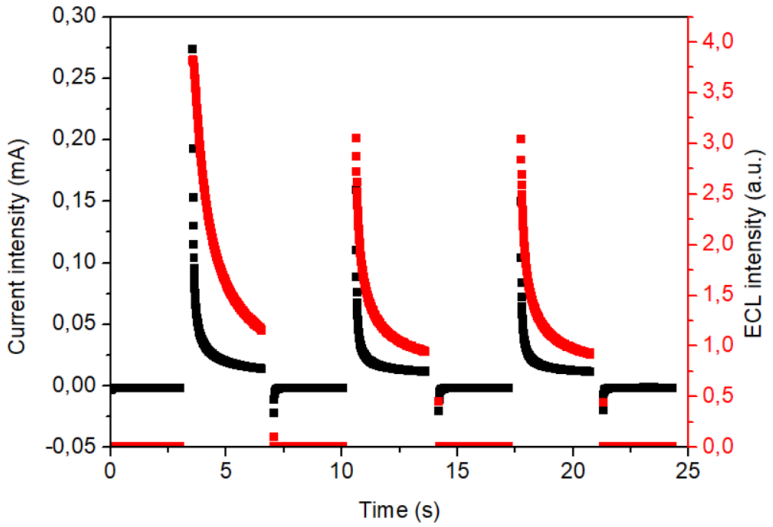


Figure A5.26: Co-reactant ECL-time (red curve) and current-time (black curve) profiles of **4DPATPN** in dichloromethane.

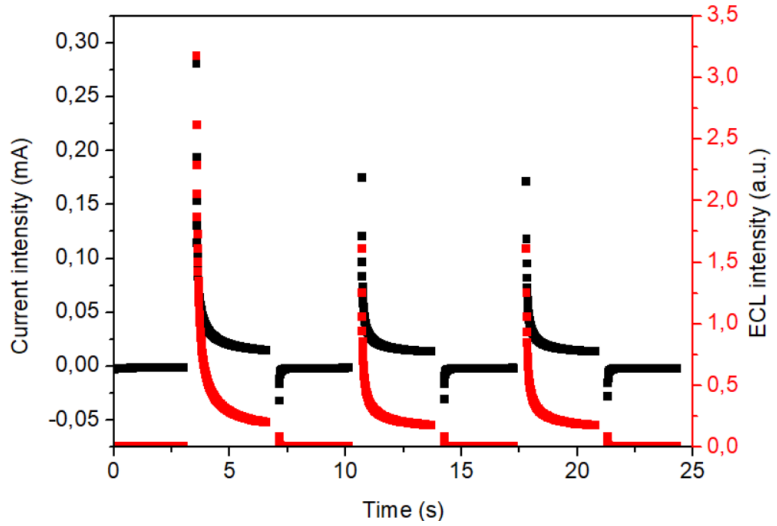


Figure A5.27: Co-reactant ECL-time (red curve) and current-time (black curve) profiles of **4DpTATPN** in dichloromethane.

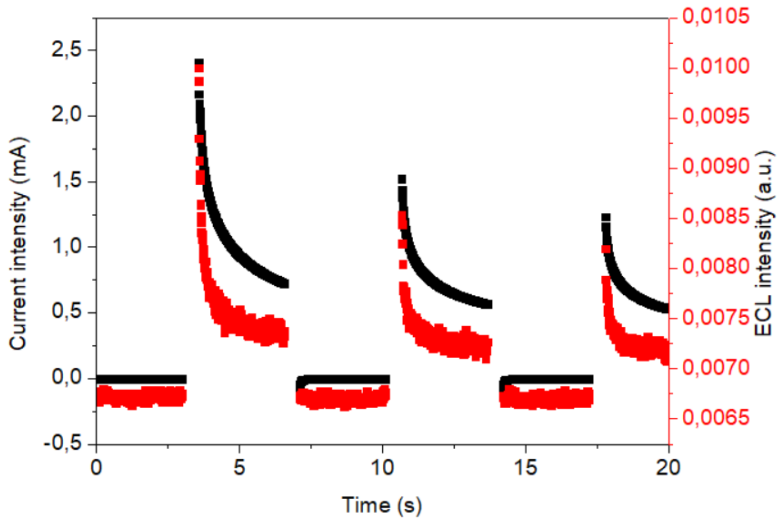


Figure A5.28: Co-reactant ECL-time (red curve) and current-time (black curve) profiles of **Na_4[4DPASO$_3$TPN]** in Procell® solution.

Chapter 6

6.1 ^{1}H NMR Spectra

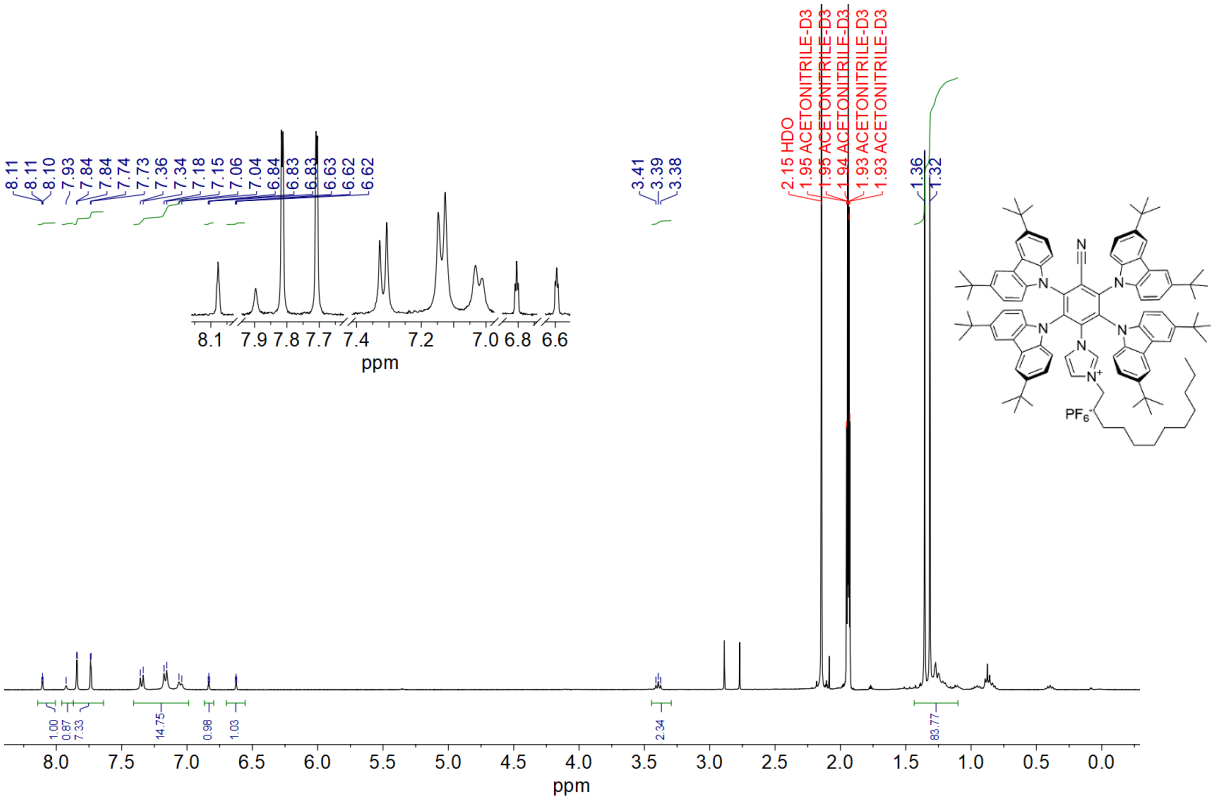


Figure A6.1: ^{1}H NMR spectrum of **[4^{tBu}CzBNImC12]PF$_6$** (CD_3CN).

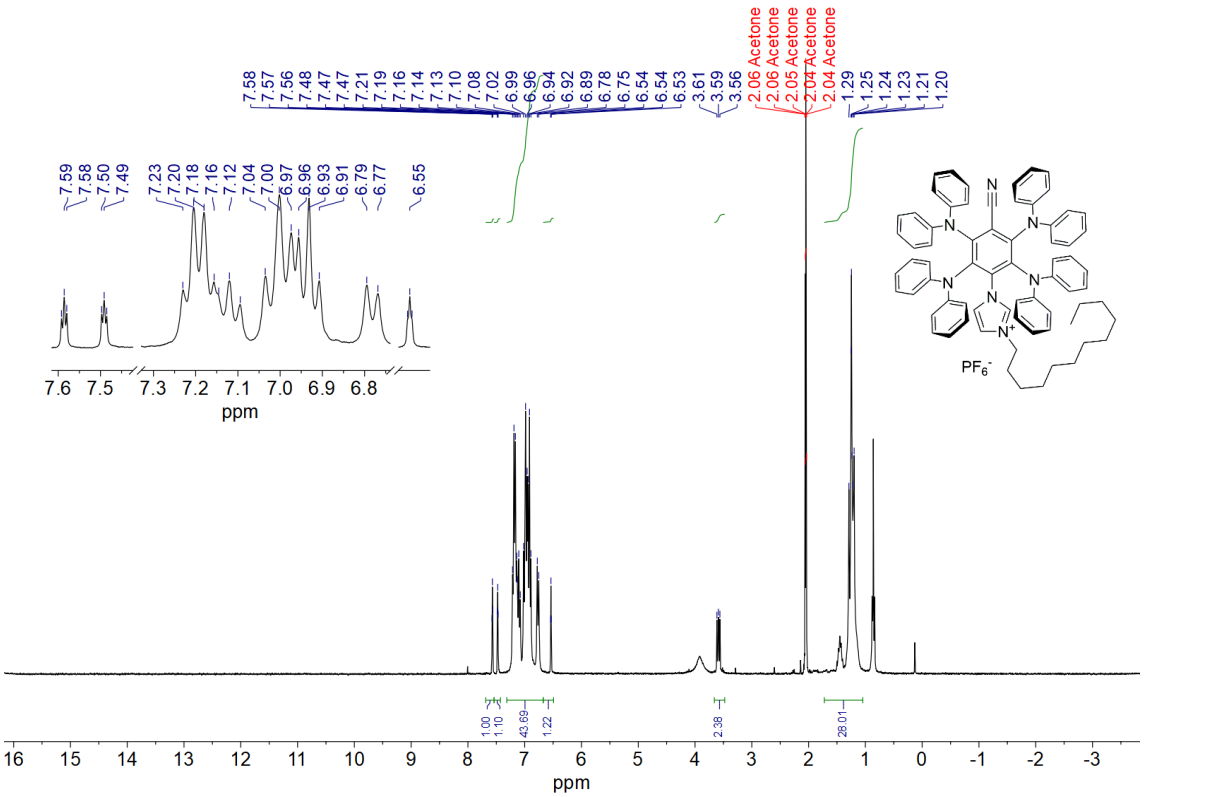


Figure A6.2: ^{1}H NMR spectrum of **[4DPABNImC12]PF$_6$** (Acetone-d_6).

6.2 $^{13}C\{^{1}H\}$ NMR Spectra

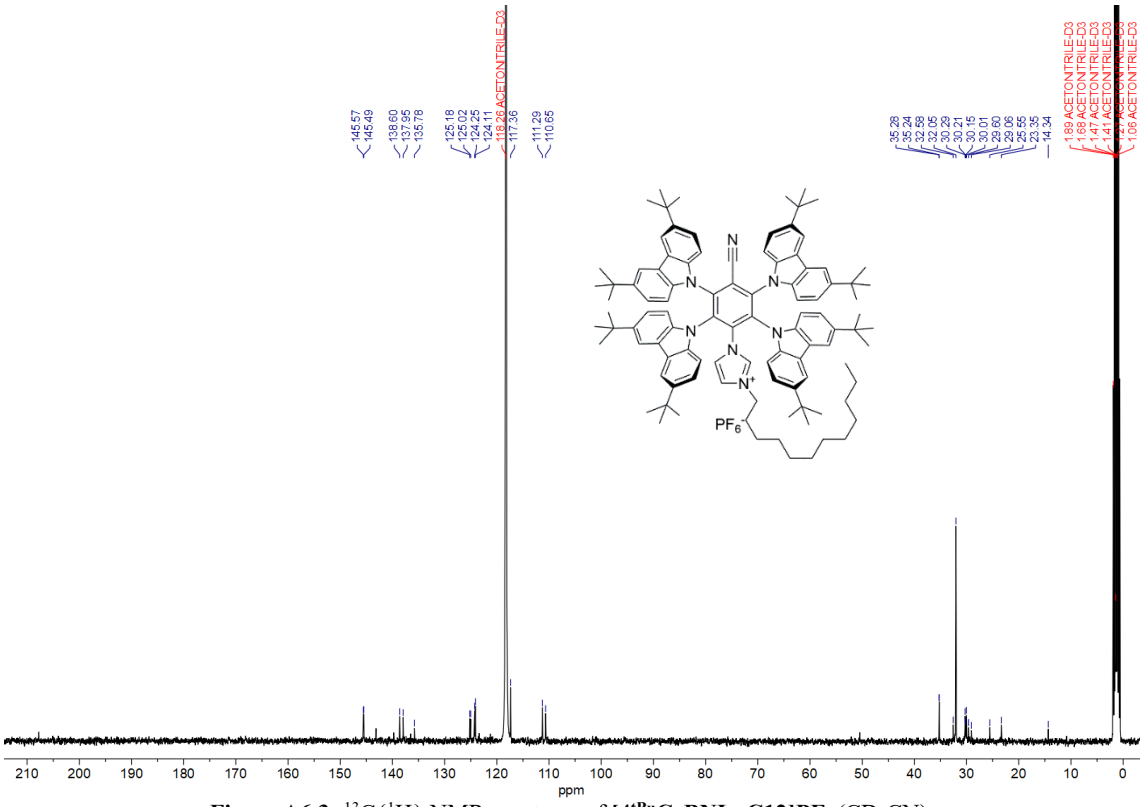


Figure A6.3: $^{13}C\{^{1}H\}$ NMR spectrum of **[4^{tBu}CzBNImC12]PF$_6$** (CD_3CN).

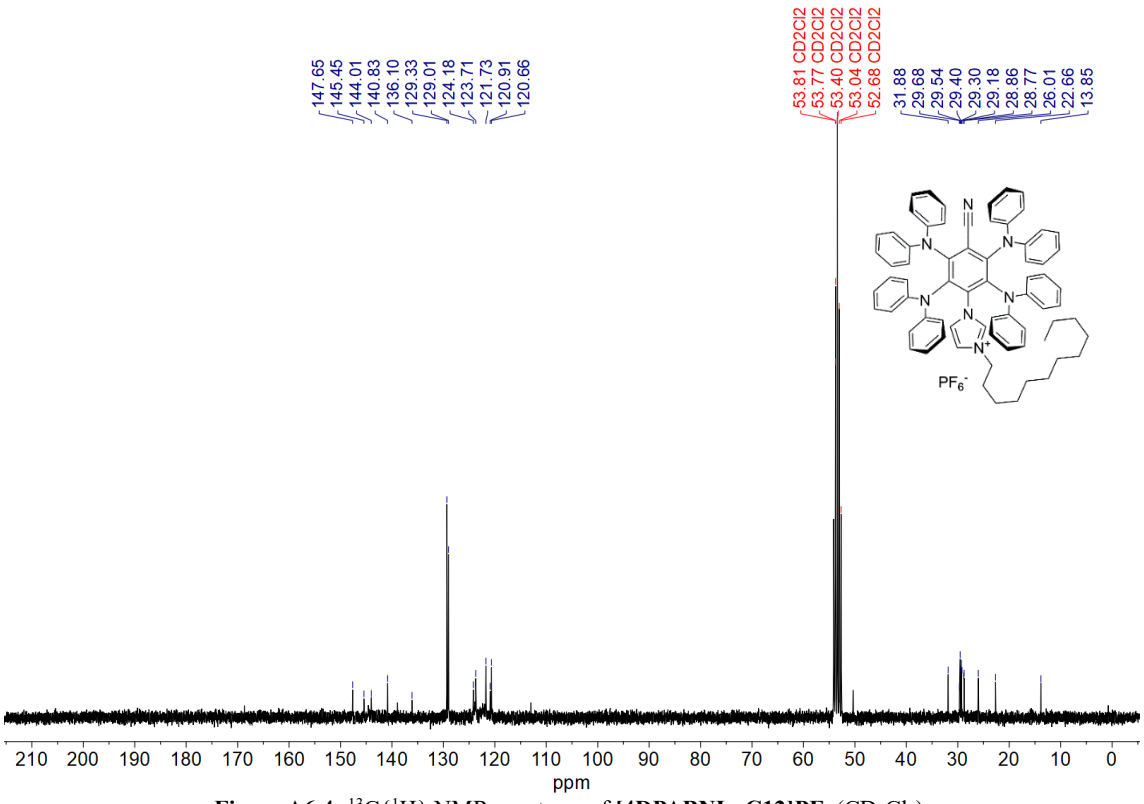


Figure A6.4: $^{13}C\{^{1}H\}$ NMR spectrum of **[4DPABNImC12]PF$_6$** (CD_2Cl_2).

6.3 ^{31}P NMR Spectra

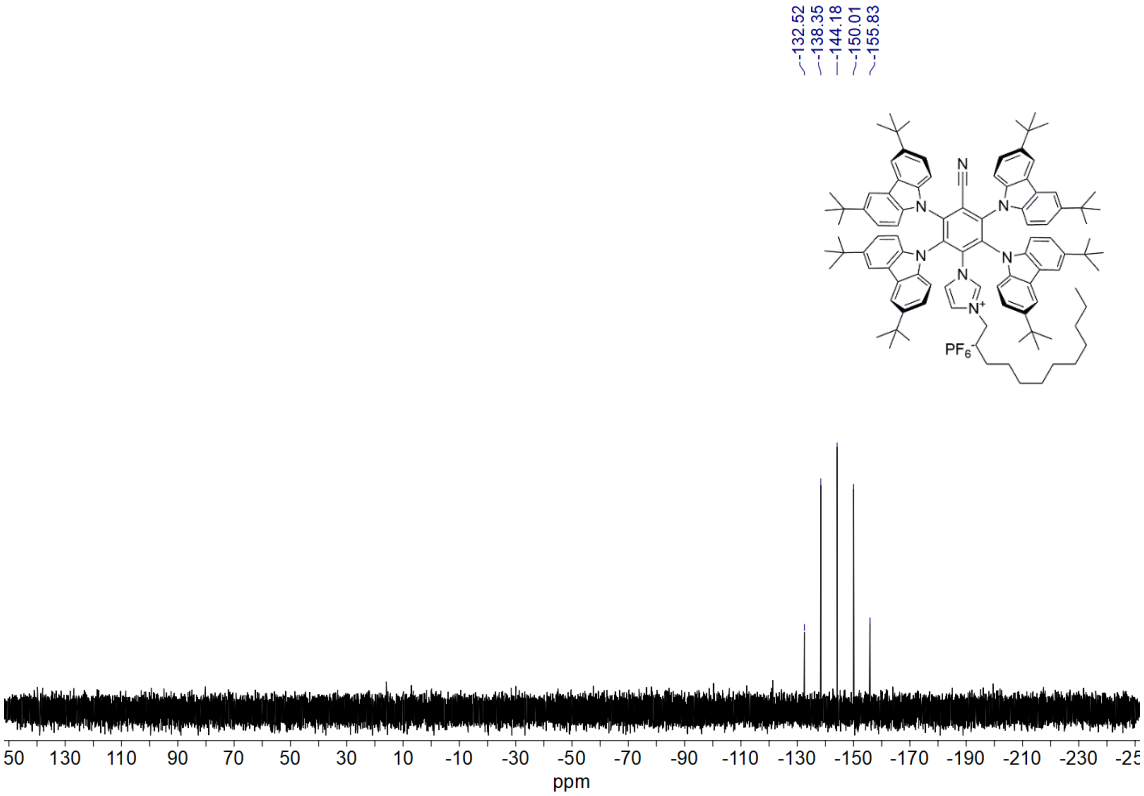


Figure A6.5: ^{31}P NMR spectrum of **[4^{tBu}CzBNImC12]PF$_6$** (CD_3CN).

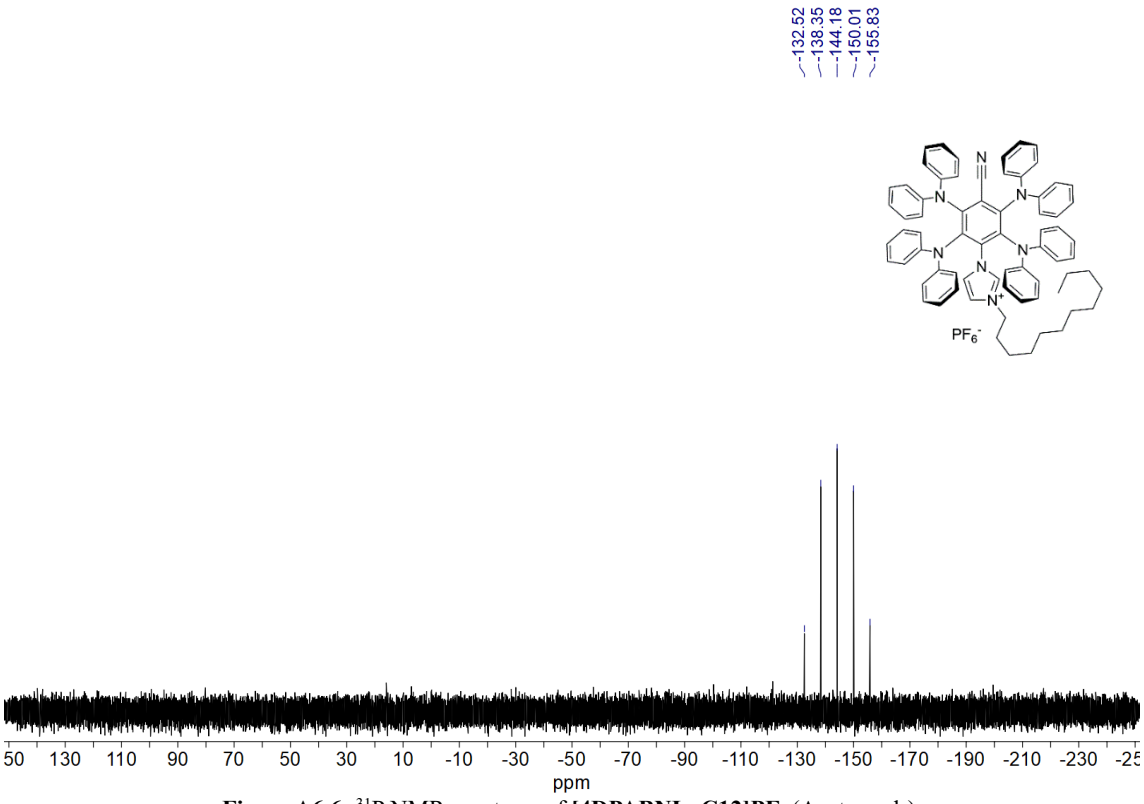


Figure A6.6: ^{31}P NMR spectrum of **[4DPABNImC12]PF$_6$** (Acetone-d_6).

6.4 ^{19}F NMR Spectra

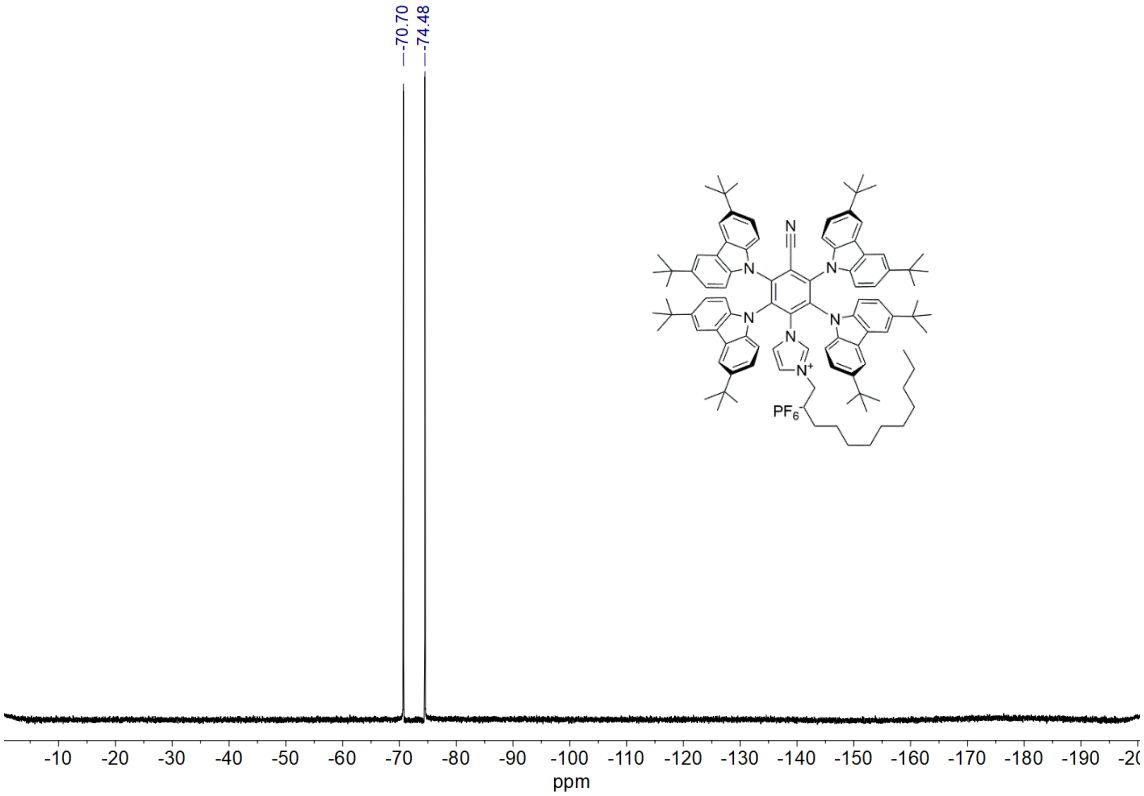


Figure A6.7: ^{19}F NMR spectrum of **[4^{tBu}CzBNImC12]PF$_6$** (CD_3CN).

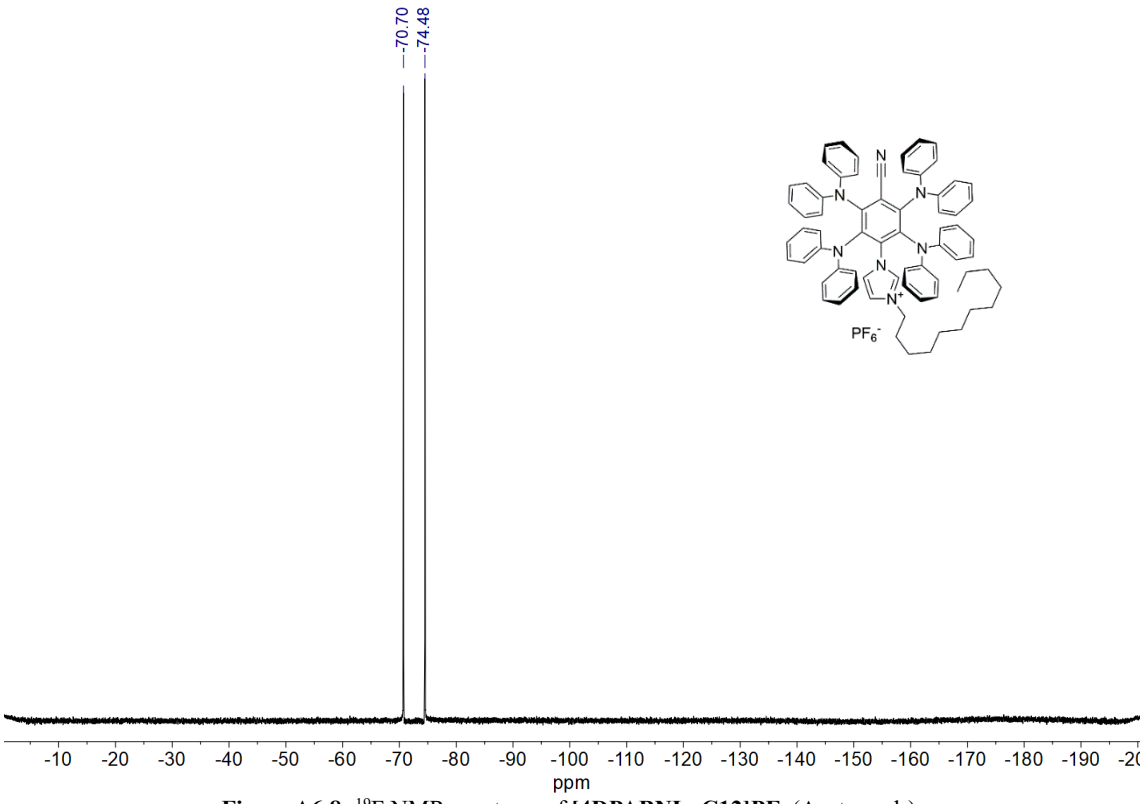


Figure A6.8: ^{19}F NMR spectrum of **[4DPABNImC12]PF$_6$** (Acetone-d_6).

6.5 Absorption-excitation spectra (solution) comparisons

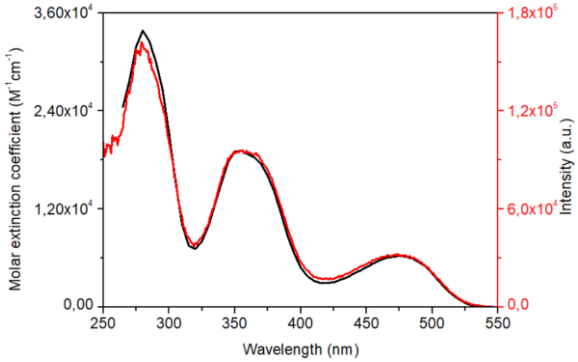


Figure A6.9: Absorption (black line) and excitation (red line) spectra of **[4^{tBu}CzBNImC12]PF$_6$** in dichloromethane.

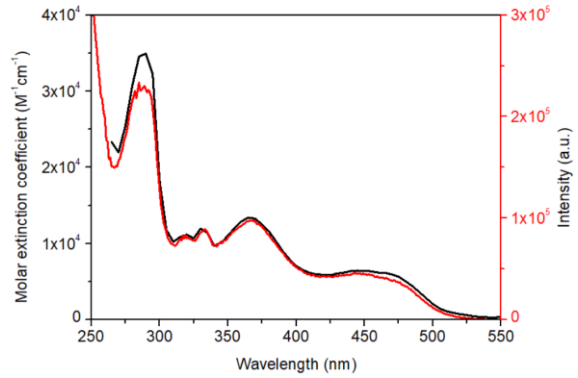


Figure A6.10: Absorption (black line) and excitation (red line) spectra of **[4DPABNImC12]PF$_6$** in dichloromethane.

6.6 Luminescence decay curves (solution)

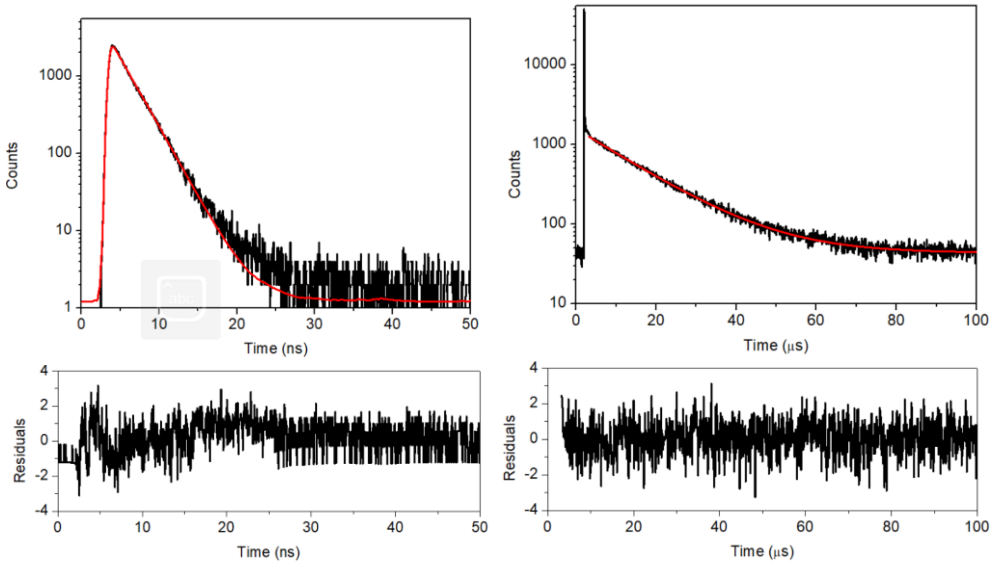


Figure A6.11: Luminescence decay curves of **[4^{tBu}CzBNImC12]PF$_6$** in Ar-purged dichloromethane solution with their fittings and residuals. Left: decays in the nanosecond scale; Right: decays in the microsecond scale.

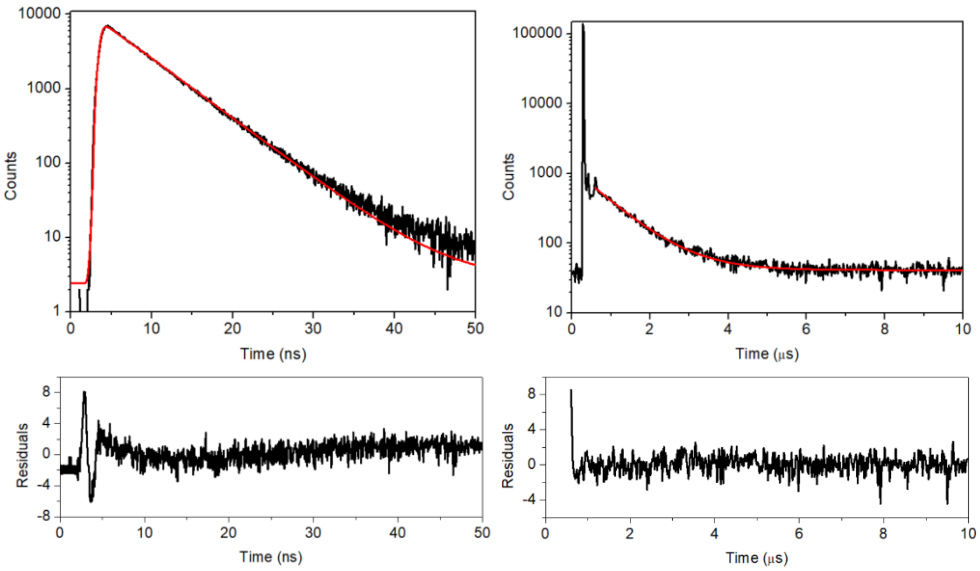


Figure A6.12: Luminescence decay curves of **[4DPABNImC12]PF$_6$** in Ar-purged dichloromethane solution with their fittings and residuals. Left: decays in the nanosecond scale; Right: decays in the microsecond scale.

6.7 Electrochemical and EIS characterization

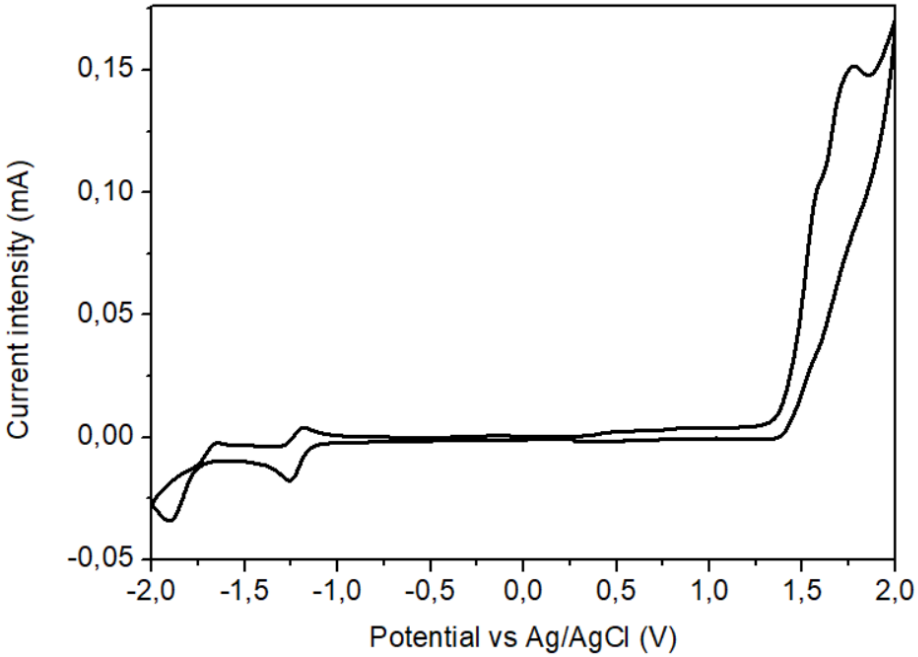


Figure A6.13: CV of **[4^{tBu}CzBNImC12]PF$_6$** in dichloromethane.

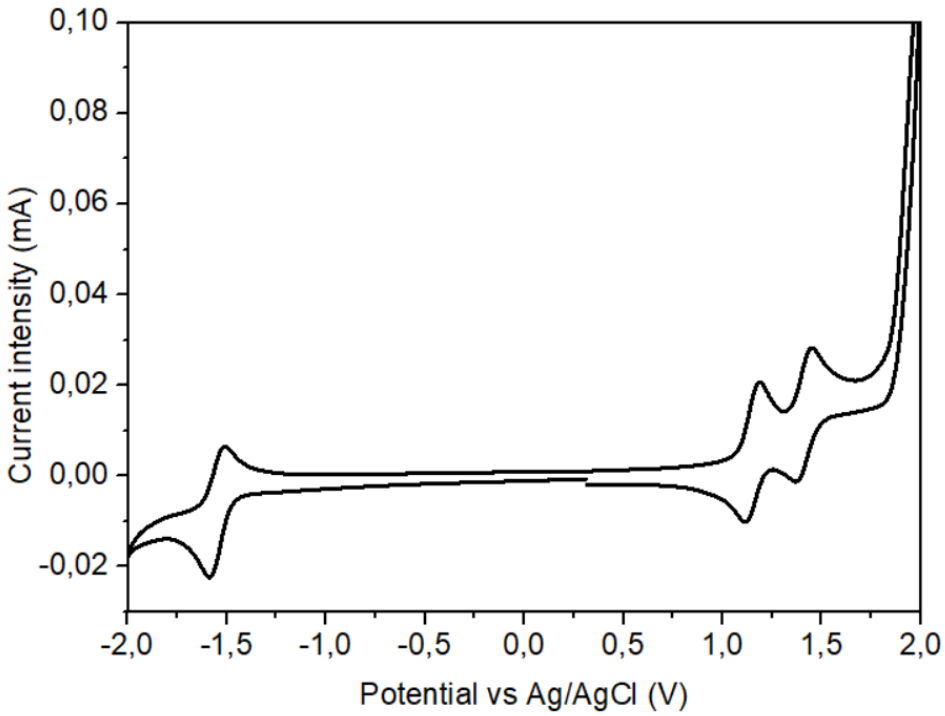


Figure A6.14: CV of **[4DPABNImC12]PF_6** in dichloromethane.

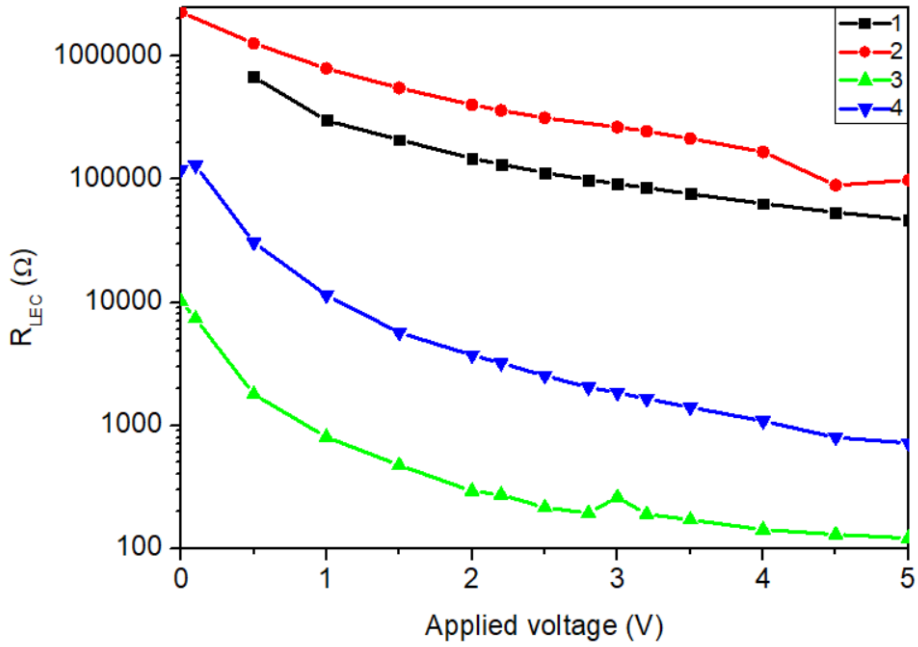


Figure A6.15: Resistance profile at different voltages in EIS assays conducted at 0-5 V for pristine **[4^{tBu}CzBNImC12]PF_6** (1), **[4^{tBu}CzBNImC12]PF_6** + 5% PMMA (2), pristine **[4DPABNImC12]PF_6** (3), **[4DPABNImC12]PF_6** + 5% PMMA (4) devices.

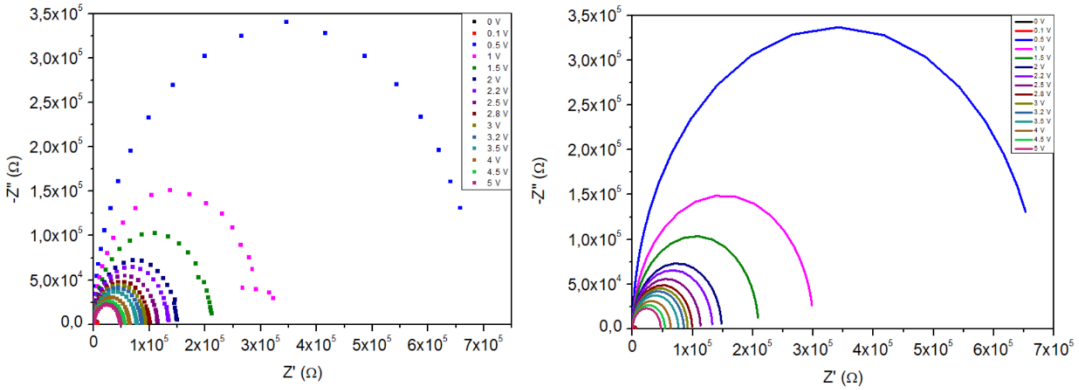


Figure A6.16: Nyquist plots at different voltages in static EIS assays conducted at 0 – 5 V of pristine **[4^{tBu}CzBNImC12]PF$_6$** device. Left: raw data, right: fitted data.

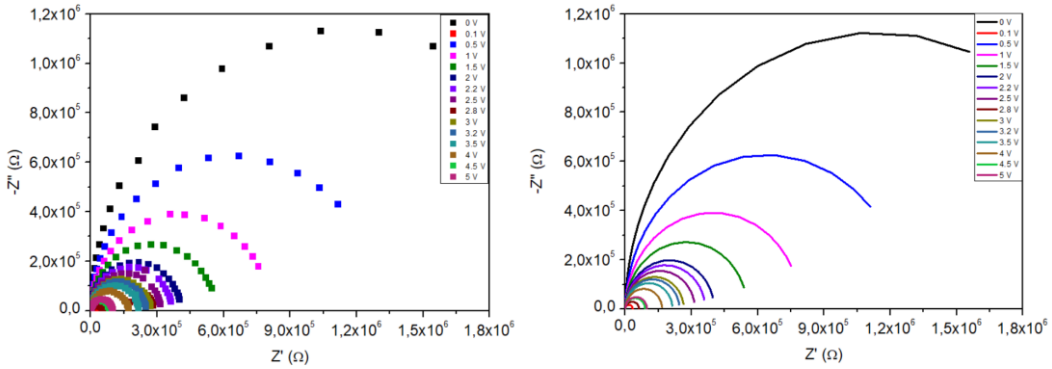


Figure A6.17: Nyquist plots at different voltages in static EIS assays conducted at 0 – 5 V of **[4^{tBu}CzBNImC12]PF$_6$** + 5% PMMA device. Left: raw data, right: fitted data.

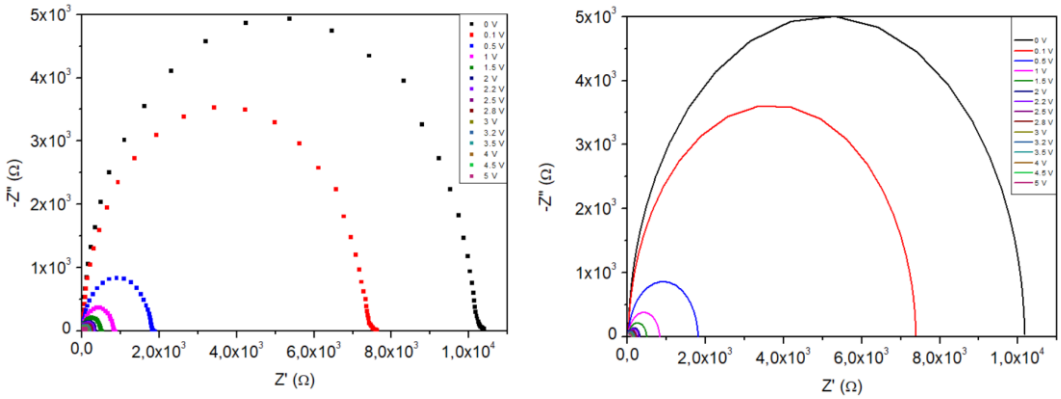


Figure A6.18: Nyquist plots at different voltages in static EIS assays conducted at 0 – 5 V of pristine **[4DPABNImC12]PF$_6$** device. Left: raw data, right: fitted data.

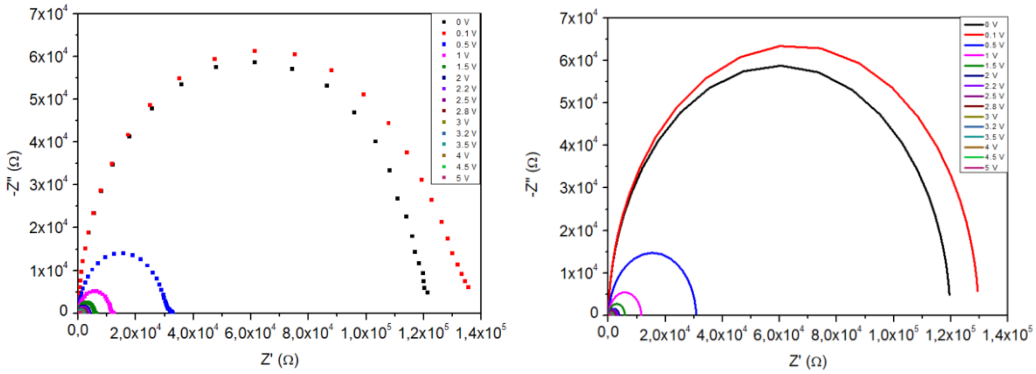


Figure A6.19: Nyquist plots at different voltages in static EIS assays conducted at 0 – 5 V of **[4DPABNImC12]PF_6** + 5% PMMA device. Left: raw data, right: fitted data.

6.8 Emission spectra (Single-Guest thin film)

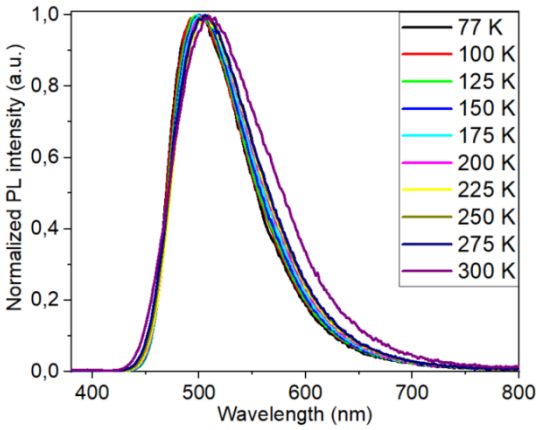


Figure A6.20: Emission PL spectra at different temperatures of **4^{tBu}CzBNIm** pristine thin film.

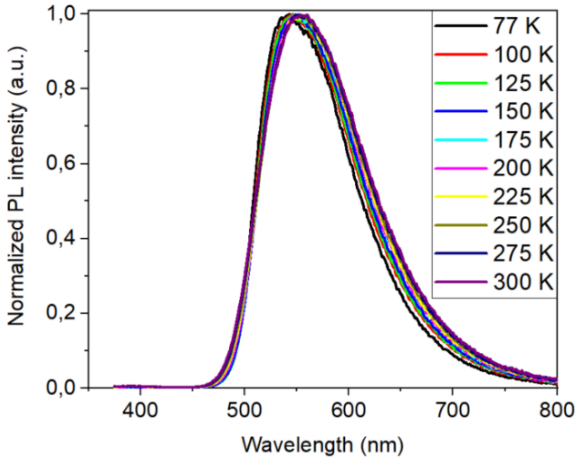


Figure A6.21: Emission PL spectra at different temperatures of **[4^{tBu}CzBNImC12]PF_6** pristine thin film.

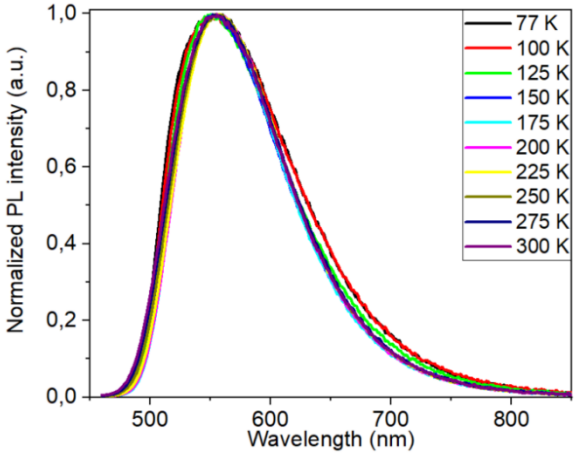


Figure A6.22: Emission PL spectra at different temperatures of **4DPABNIm** pristine thin film.

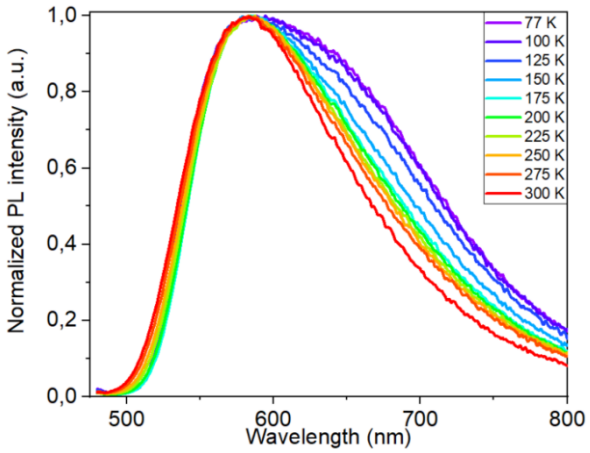


Figure A6.23: Emission PL spectra at different temperatures of **[4DPABNImC12]PF_6** pristine thin film.

6.9 Excitation spectra (Single-Guest thin film)

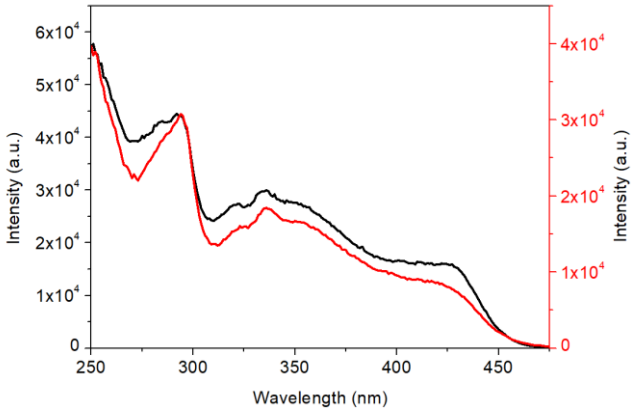


Figure A6.24: Excitation spectra at 77 K (black curve) and 300 K (red curve) of **4^{tBu}CzBNIm** pristine thin film.

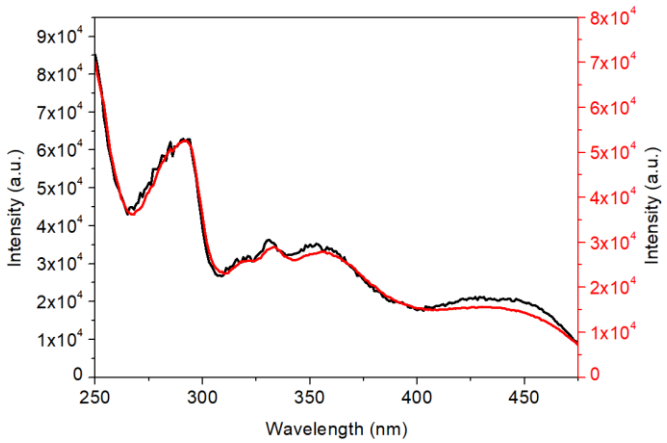


Figure A6.25: Excitation spectra at 77 K (black curve) and 300 K (red curve) of **[4^{tBu}CzBNImC12]PF$_6$** pristine thin film.

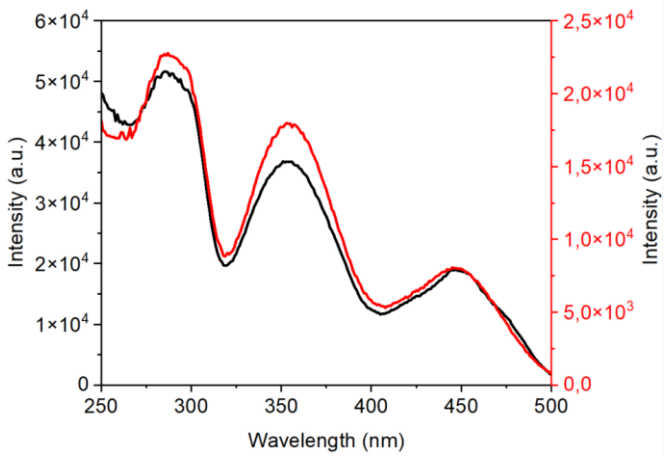


Figure A6.26: Excitation spectra at 77 K (black curve) and 300 K (red curve) of **4DPABNIm** pristine thin film.

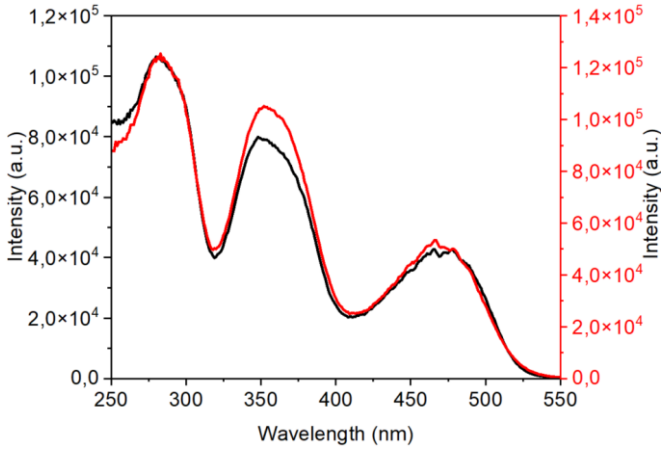


Figure A6.27: Excitation spectra at 77 K (black curve) and 300 K (red curve) of **[4DPABNImC12]PF$_6$** pristine thin film.

6.10 Luminescence decay curves (Single-Guest thin film)

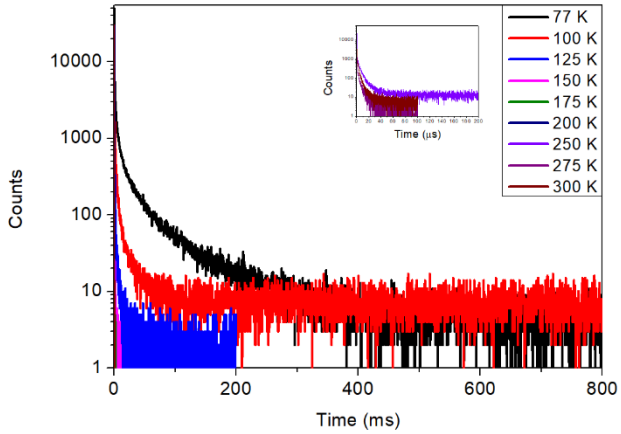


Figure A6.28: Luminescence decay curves at different temperatures of **4^{tBu}CzBNIm** pristine thin film under N_2 atmosphere.

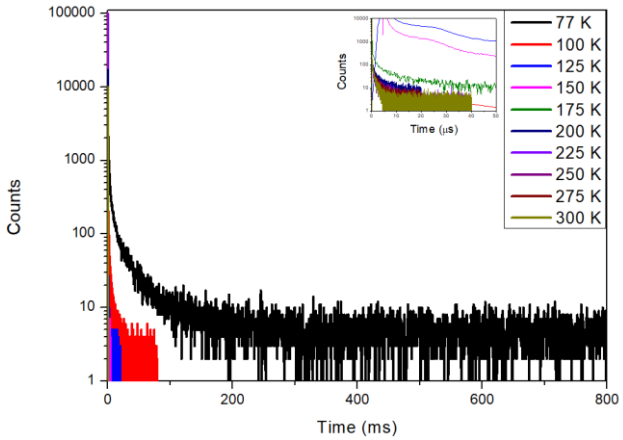


Figure A6.29: Luminescence decay curves at different temperatures of **[4^{tBu}CzBNImC12]PF$_6$** pristine thin film under N_2 atmosphere.

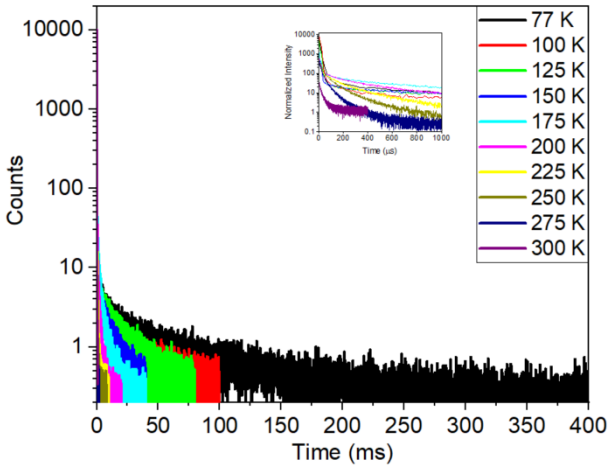


Figure A6.30: Luminescence decay curves at different temperatures of **4DPABNIm** pristine thin film under N_2 atmosphere.

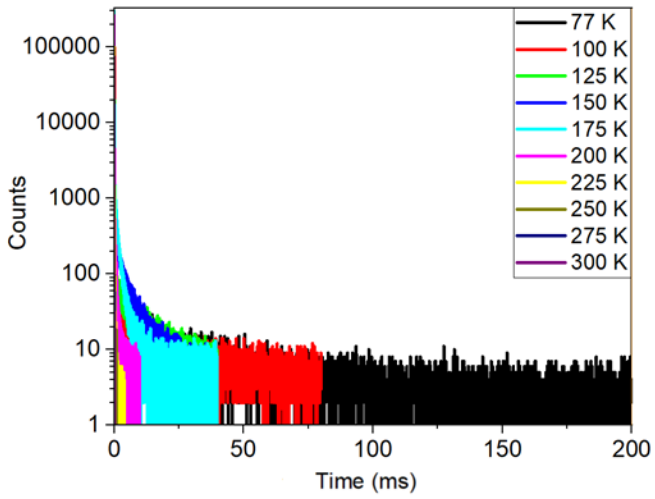


Figure A6.31: Luminescence decay curves at different temperatures of **[4DPABNImC12]PF_6** pristine thin film under N_2 atmosphere.

6.11 Time-dependent Luminance-Intensity-Voltage (Single-Guest thin film)

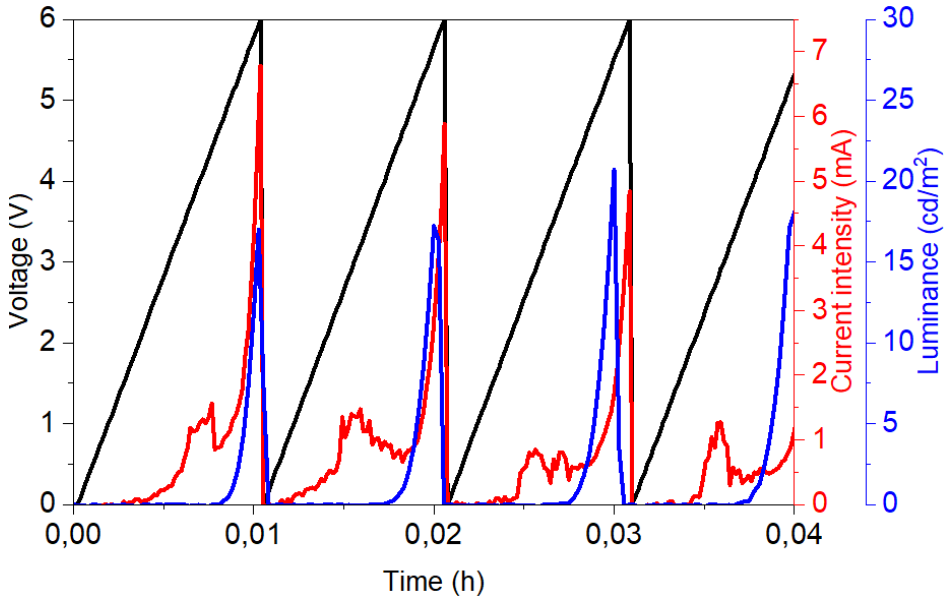


Figure A6.32: LIV profile of **4^{tBu}CzBNIm** + 5% PS + 20% $THABF_4$ device.

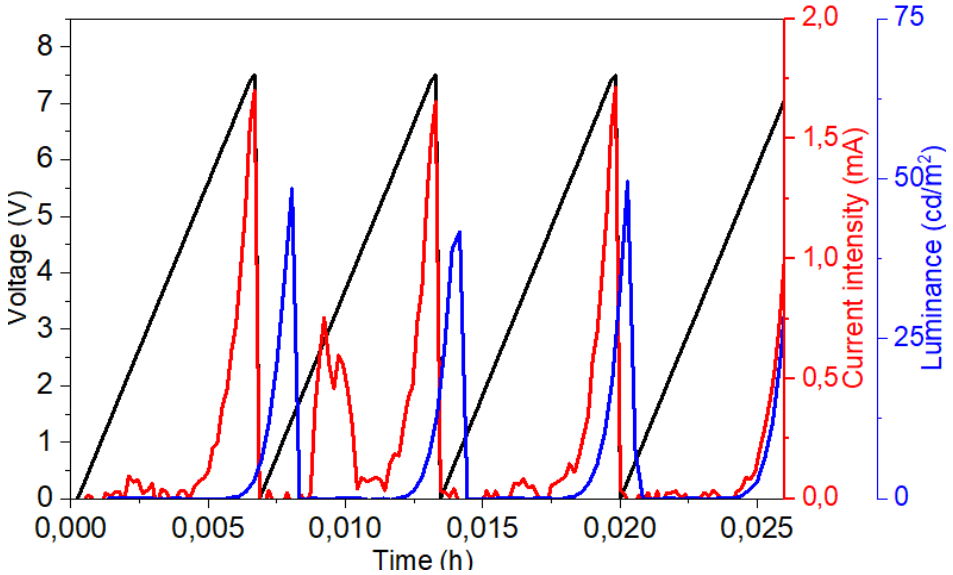


Figure A6.33: LIV profile of **4DPABNIm** + 5% PS + 20% $THABF_4$ device.

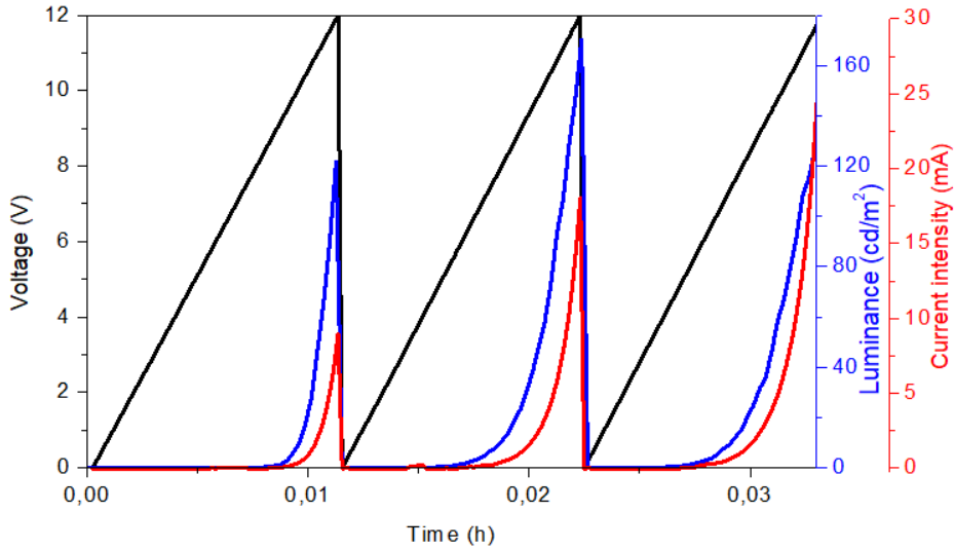


Figure A6.34: LIV profile of pristine **[4^{tBu}CzBNImC12]PF_6** device.

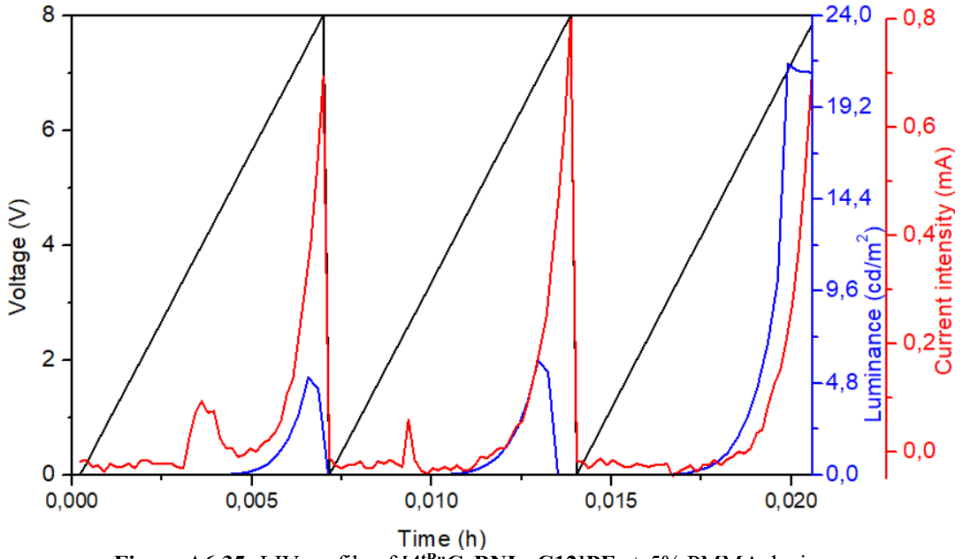


Figure A6.35: LIV profile of **[4^{tBu}CzBNImC12]PF$_6$** + 5% PMMA device.

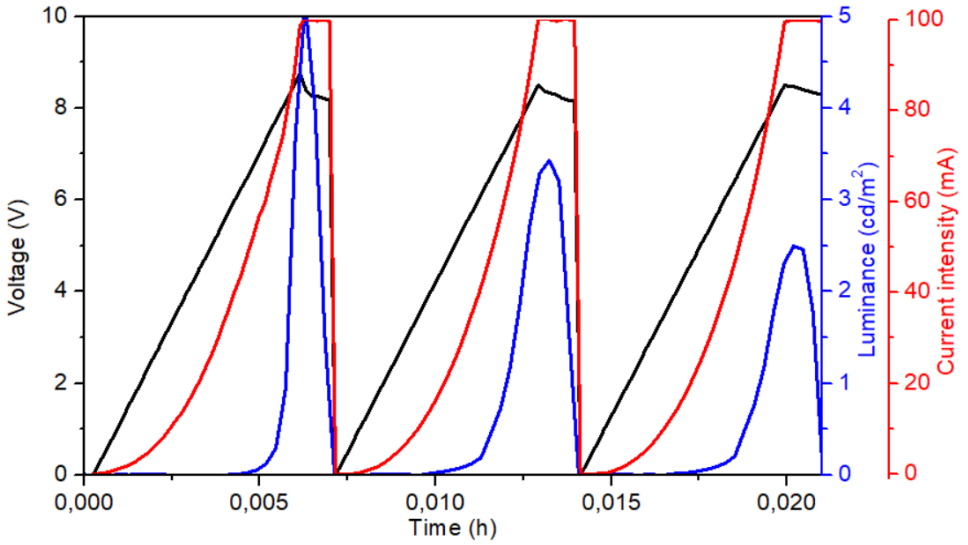


Figure A6.36: LIV profile of pristine **[4DPABNImC12]PF$_6$** device.

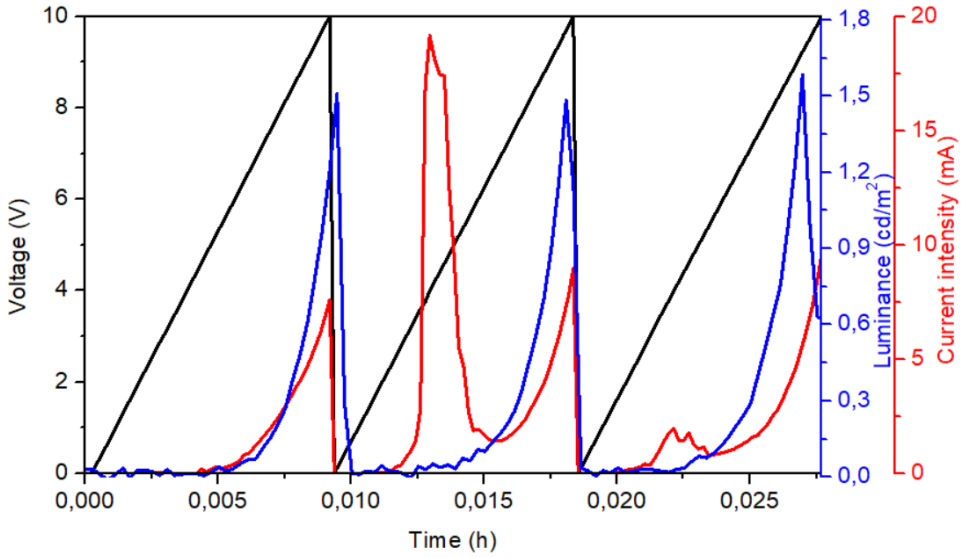


Figure A6.37: LIV profile of **[4DPABNImC12]PF_6** + 5% PMMA device.

6.12 Time-dependent average voltage and luminance profiles with pulsed current (Single-Guest LECs)

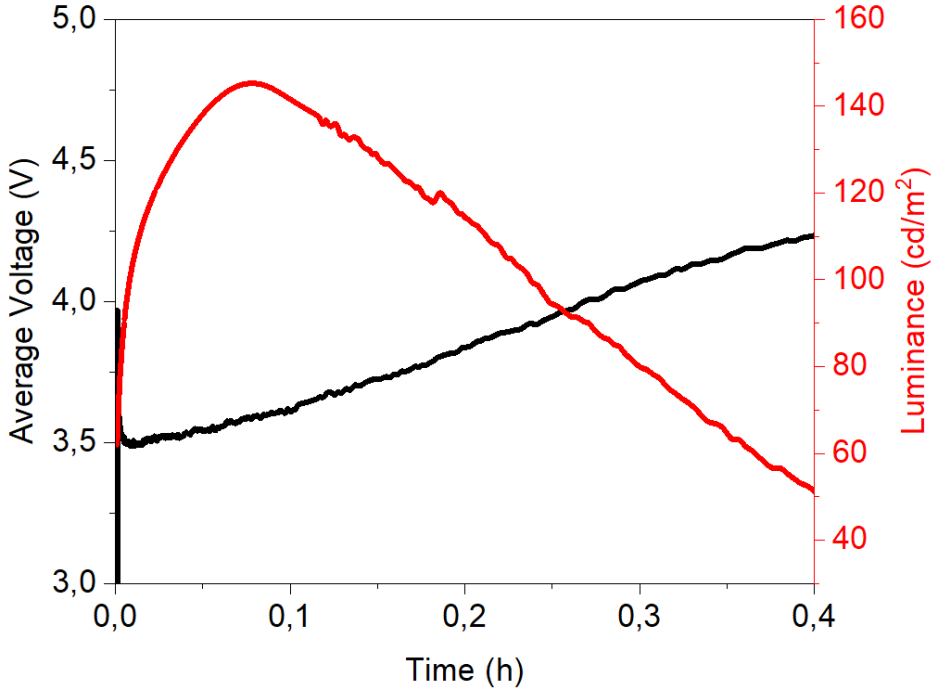


Figure A6.38: Average voltage (black curve) and luminance (red curve) versus time of pristine **4^{tBu}CzBNIm** device driven at pulsed 3 mA.

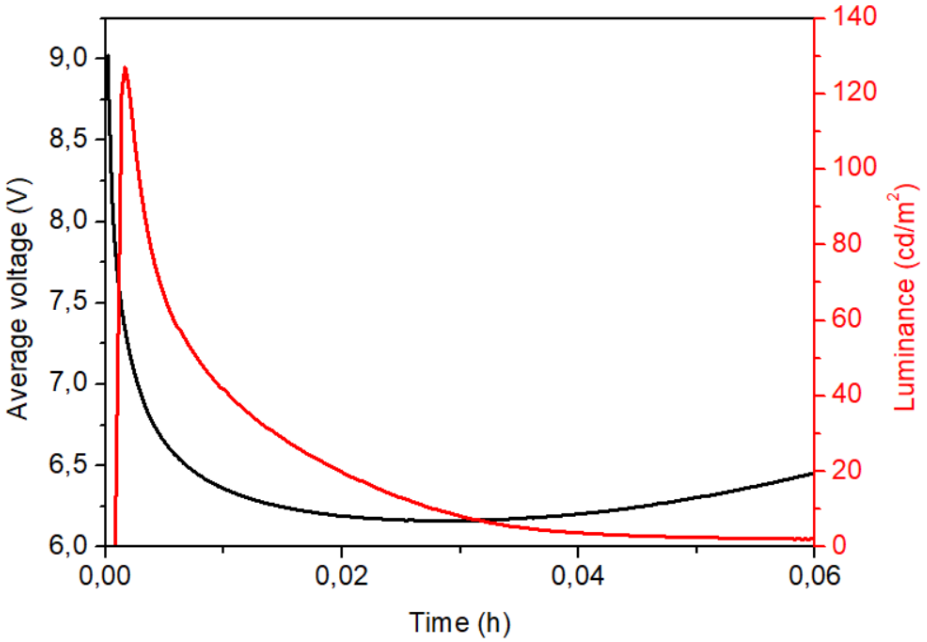


Figure A6.39: Average voltage (black curve) and luminance (red curve) versus time of pristine **[4^{tBu}CzBNImC12]PF$_6$** device driven at pulsed 3 mA.

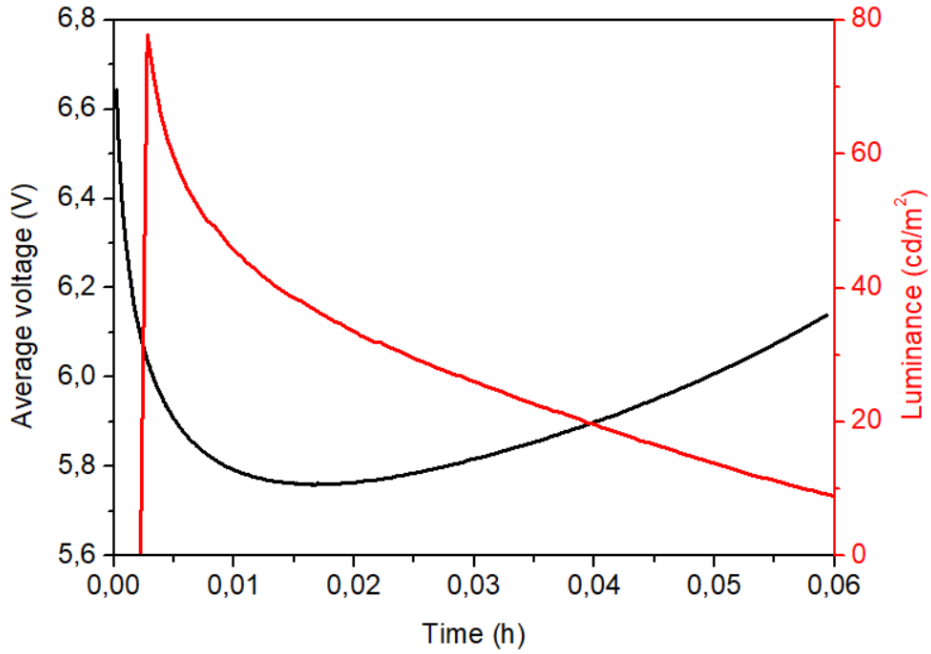


Figure A6.40: Average voltage (black curve) and luminance (red curve) versus time of pristine **[4^{tBu}CzBNImC12]PF$_6$** device driven at pulsed 5 mA.

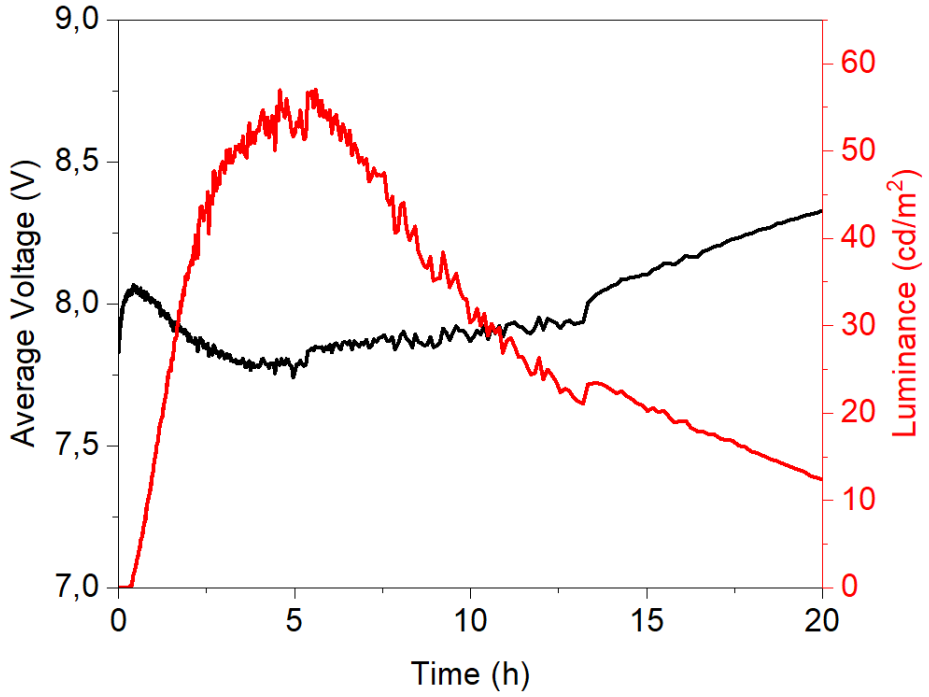


Figure A6.41: Average voltage (black curve) and luminance (red curve) versus time of **4DPABNIm** + 5% PMMA device driven at pulsed 5 mA.

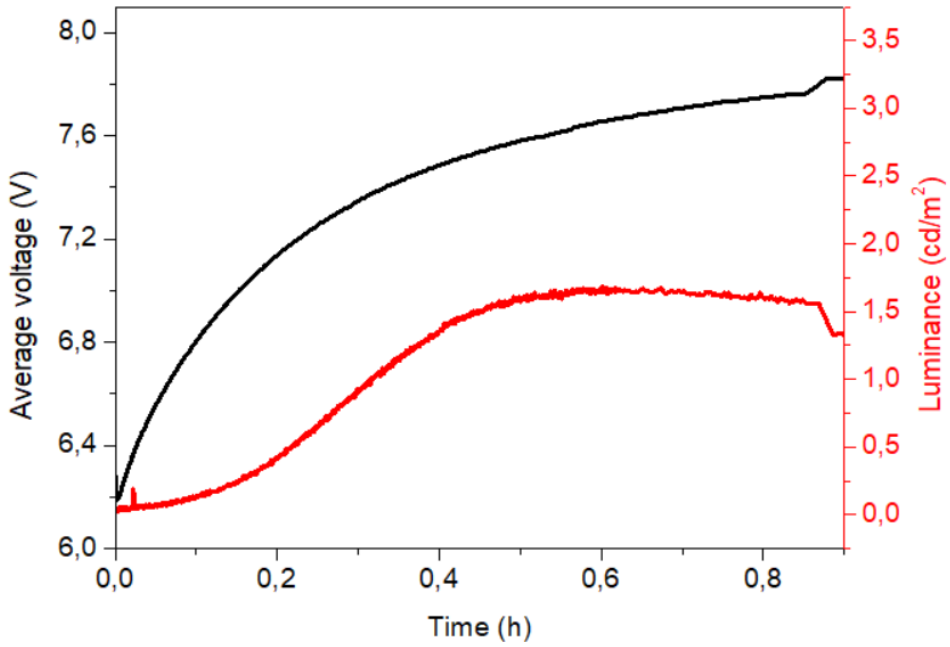


Figure A6.42: Average voltage (black curve) and luminance (red curve) versus time of pristine **[4DPABNImC12]PF_6** device driven at pulsed 40 mA.

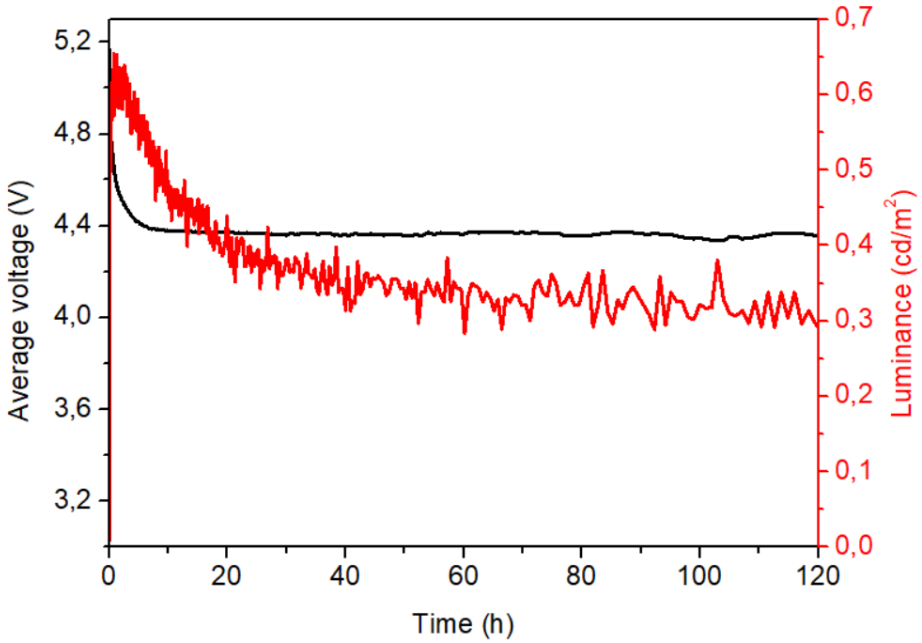


Figure A6.43: Average voltage (black curve) and luminance (red curve) versus time of **[4DPABNImC12]PF_6** + 5% PMMA device driven at pulsed 5 mA.

6.13 Emission spectra (Host-Guest thin film)

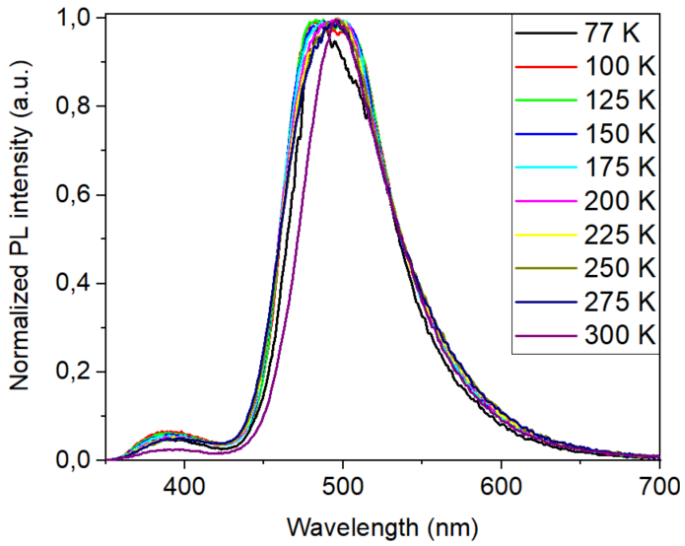


Figure A6.44: Emission PL spectra at different temperatures of **4^{tBu}CzBNIm** Host-Guest thin film (tCP:OXD-7:$THABF_4$:**4^{tBu}CzBNIm** 100:100:6.6:15) under N_2 atmosphere.

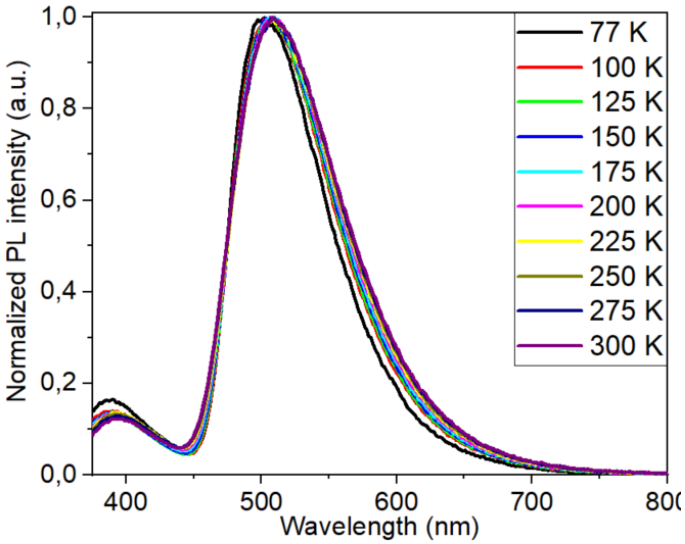


Figure A6.45: Emission PL spectra at different temperatures of [**4^{tBu}CzBNImC12]PF$_6$** Host-Guest thin film (tCP:OXD-7:THABF$_4$:[**4^{tBu}CzBNImC12]PF$_6$** 100:100:6.6:15) under N_2 atmosphere.

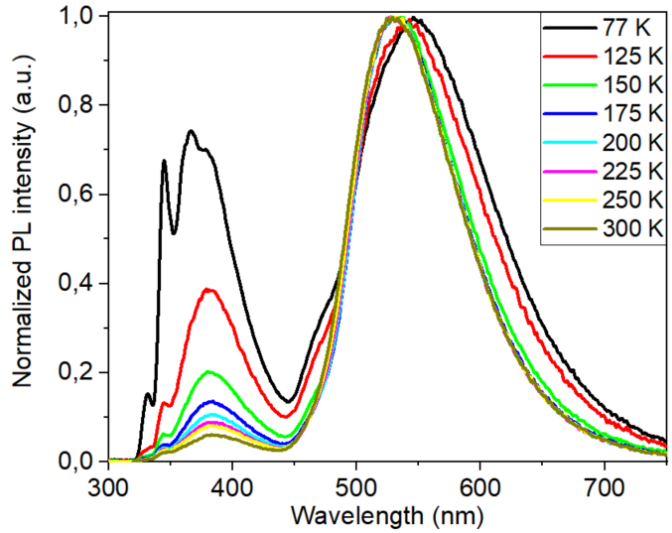


Figure A6.46: Emission PL spectra at different temperatures of **4DPABNIm** Host-Guest thin film (tCP:OXD-7:THABF$_4$: **4DPABNIm** 100:100:6.6:15) under N_2 atmosphere.

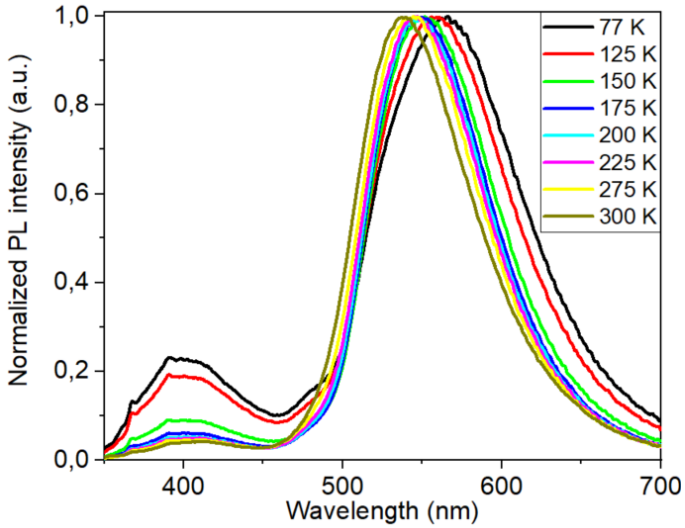


Figure A6.47: Emission PL spectra at different temperatures of **[4DPABNImC12]PF_6** Host-Guest thin film (tCP:OXD-7:$THABF_4$:**[4DPABNImC12]PF_6** 100:100:6.6:15) under N_2 atmosphere.

6.14 Excitation spectra (Host-Guest thin film)

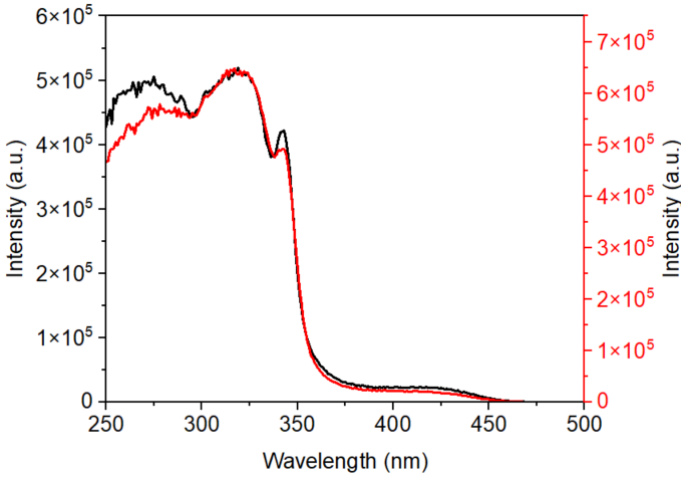


Figure A6.48: Excitation spectra at 77 K (black curve) and 300 K (red curve) of **4^{tBu}CzBNIm** Host-Guest thin film (tCP:OXD-7:**4^{tBu}CzBNIm**:$THABF_4$ 100:100:6.6:15).

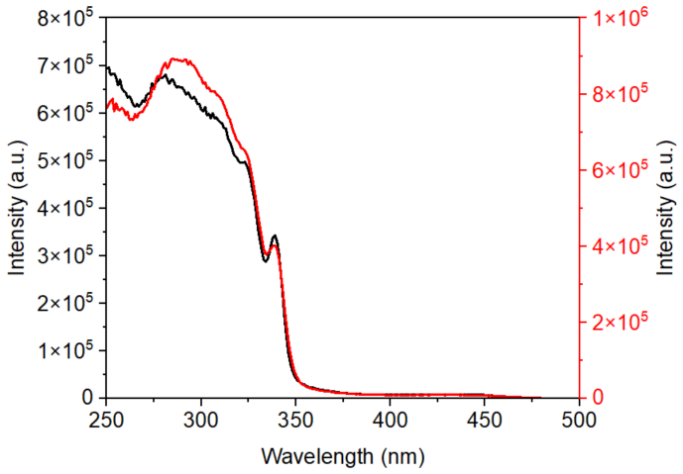


Figure A6.49: Excitation spectra at 77 K (black curve) and 300 K (red curve) of **[4^{tBu}CzBNImC12]PF$_6$** Host-Guest thin film (tCP:OXD-7:**[4^{tBu}CzBNImC12]PF$_6$**:THABF$_4$ 100:100:6.6:15).

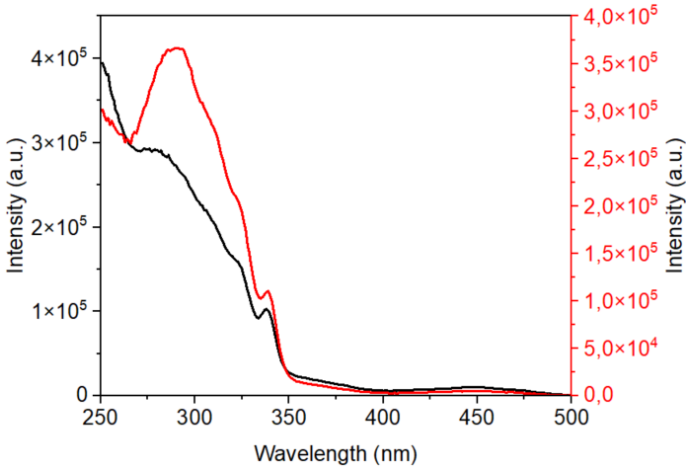


Figure A6.50: Excitation spectra at 77 K (black curve) and 300 K (red curve) of **4DPABNIm** Host-Guest thin film (tCP:OXD-7:**4DPABNIm**:THABF$_4$ 100:100:6.6:15).

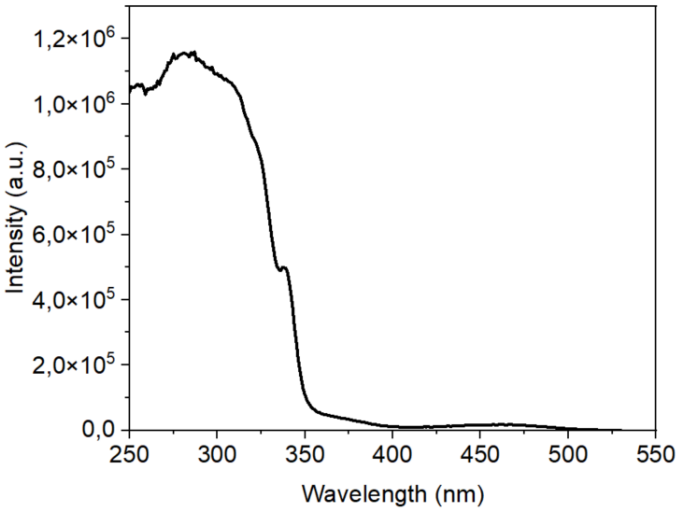


Figure A6.51: Excitation spectra at 300 K (black curve) of **[4DPABNImC12]PF$_6$** Host-Guest thin film (tCP:OXD-7:**[4DPABNImC12]PF$_6$**:THABF$_4$100:100:6.6:15).

6.15 Luminescence decay curves (Host-Guest thin film)

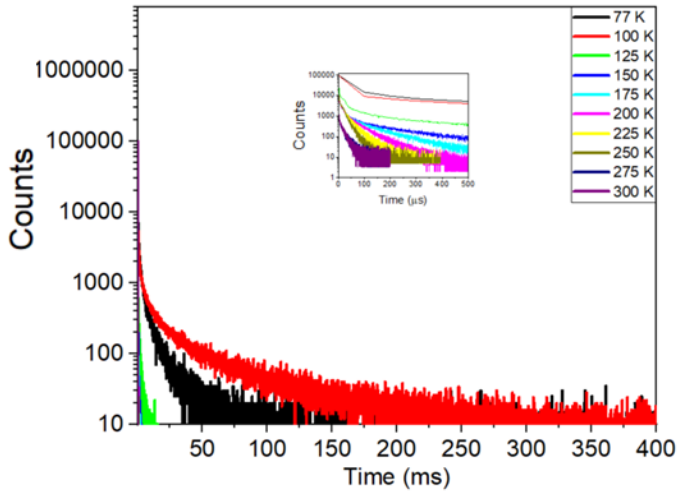


Figure A6.52: Luminescence decay curves at different temperatures of **4^{tBu}CzBNIm** Host-Guest thin film (tCP:OXD-7:**4^{tBu}CzBNIm**:$THABF_4$ 100:100:6.6:15) under N_2 atmosphere.

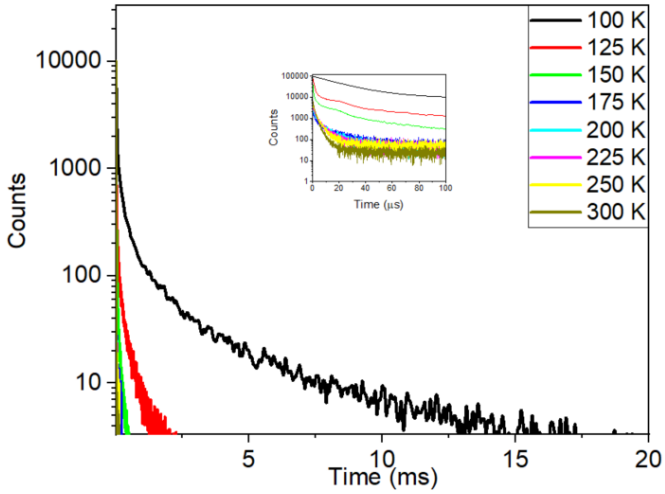


Figure A6.53: Luminescence decay curves at different temperatures of **[4^{tBu}CzBNImC12]PF_6** Host-Guest thin film (tCP:OXD-7:**[4^{tBu}CzBNImC12]PF_6**:$THABF_4$ 100:100:6.6:15) under N_2 atmosphere.

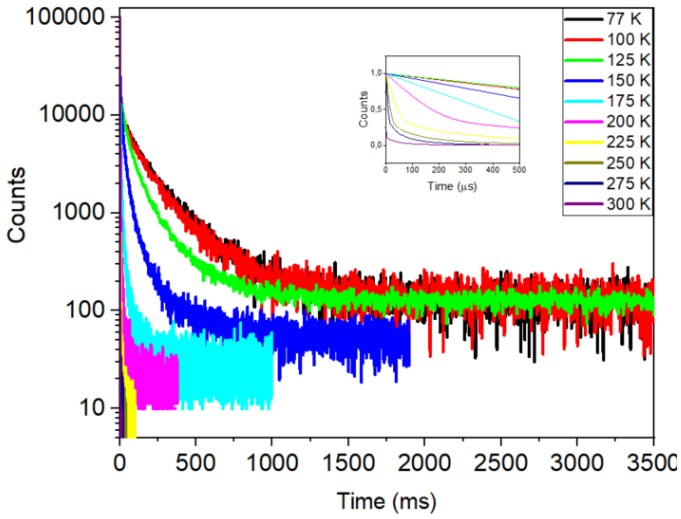


Figure A6.54: Luminescence decay curves at different temperatures of **4DPABNIm** Host-Guest thin film (tCP:OXD-7:**4DPABNIm**:THABF$_4$100:100:6.6:15) under N_2 atmosphere.

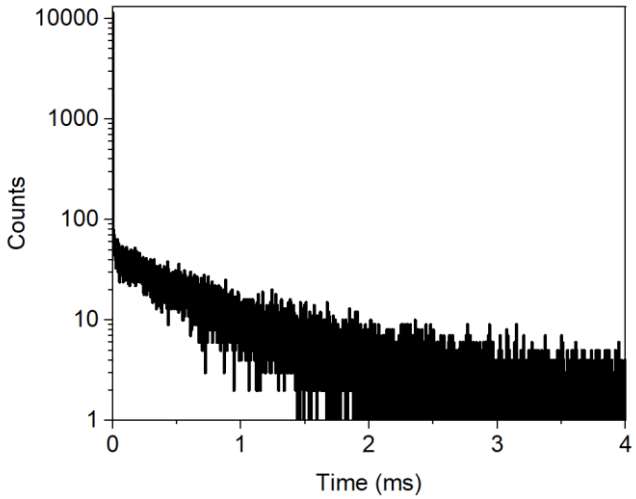


Figure A6.55: Luminescence decay curves at 300K **[4DPABNImC12]PF$_6$** Host-Guest thin film (tCP:OXD-7: **[4DPABNImC12]PF$_6$**:THABF$_4$100:100:6.6:15) under N_2 atmosphere.

6.16 Time-dependent average voltage and luminance profiles with pulsed current (Host-Guest LECs)

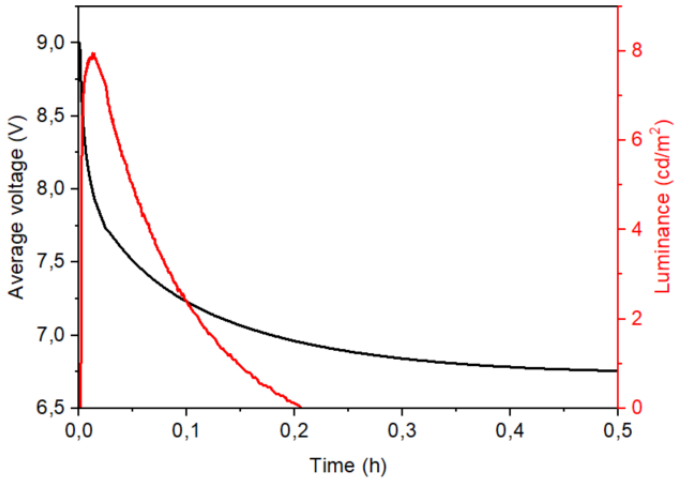


Figure A6.56: Average voltage (black curve) and luminance (red curve) versus time of **4^{tBu}CzBNIm** Host-Guest device driven at pulsed 5 mA (tCP:OXD-7:**4^{tBu}CzBNIm**:THABF$_4$ 100:100:6.6:15).

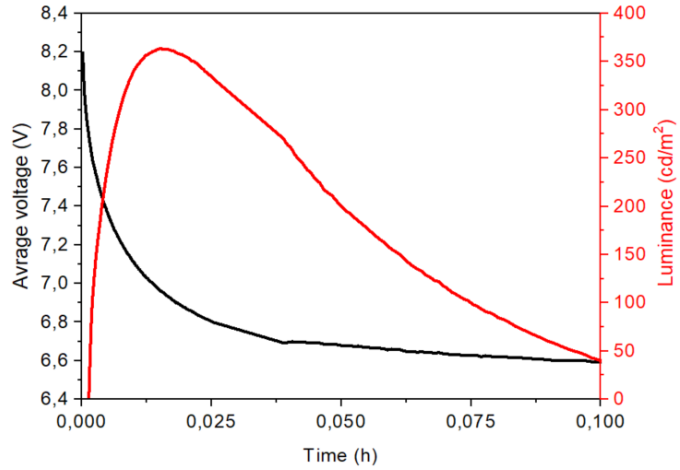


Figure A6.57: Average voltage (black curve) and luminance (red curve) versus time of **[4^{tBu}CzBNImC12]PF$_6$** Host-Guest device driven at pulsed 5 mA (tCP:OXD-7:**[4^{tBu}CzBNImC12]PF$_6$**:THABF$_4$ 100:100:6.6:15).

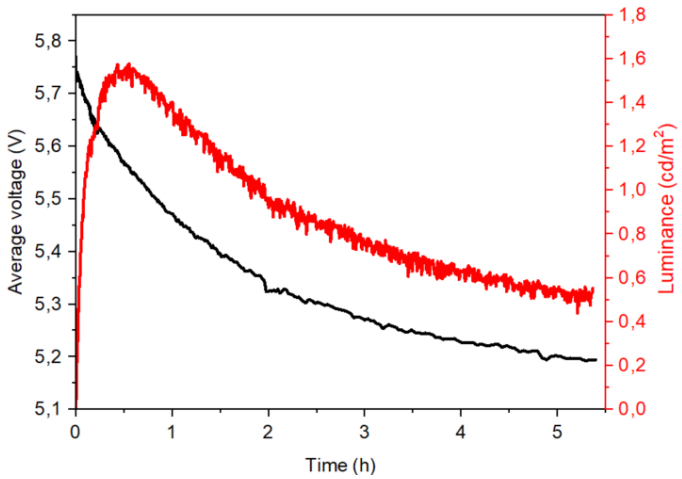


Figure A6.58: Average voltage (black curve) and luminance (red curve) versus time of **4DPABNIm** Host-Guest device driven at pulsed 5 mA (tCP:OXD-7:**4DPABNIm**:$THABF_4$ 100:100:6.6:15).

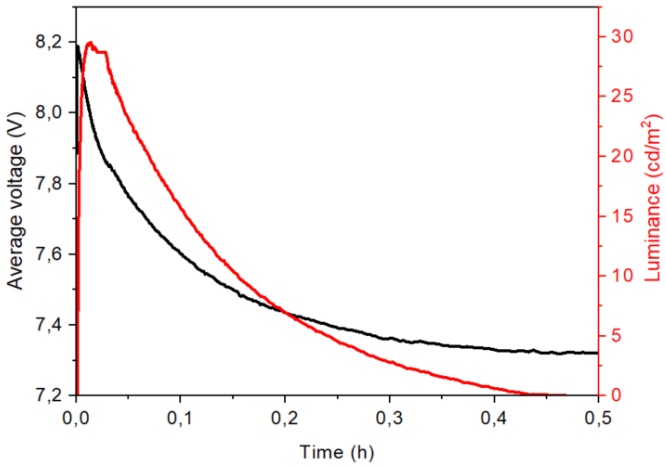


Figure A6.59: Average voltage (black curve) and luminance (red curve) versus time of **[4DPABNImC12]PF_6** Host-Guest device driven at pulsed 5 mA (tCP:OXD-7:**[4DPABNImC12]PF_6**:$THABF_4$ 100:100:6.6:15).

Acknowledgments

Prof. Sabrina Antonello (University of Padua) is acknowledged for her scientific assistance for the cyclic voltammetries at different scan rates reported in **Chapter 4**.

Dr Ilaria Fortunati (University of Padua) is acknowledged for her assistance in emission spectra, excitation spectra and lifetime decay measurements.

Dr. Nicola Demitri (Elettra Sincrotrone Trieste) is acknowledged for the XRD characterization of single crystals.

Dr. Marco Roverso and Prof. Sara Bogialli (University of Padua) are acknowledged for HR-MS experiments.

M.Sc. Alessandro Fracassa and Prof. Giovanni Valenti (University of Bologna) are acknowledged for the electrochemical and electrochemiluminescence characterization of the compounds reported in **Chapter 2**.

M.Sc. Luca M. Cavinato, Dr. Youssef Atoini and Prof Ruben D. Costa (Technical University of Munich) are acknowledged for the photophysical characterization of the thin films reported in **Chapter 6** and for the hosting during the abroad period.